École Doctorale : SIReNa - Sciences et Ingénierie des Ressources Naturelles

Thèse

Présentée et soutenue publiquement pour l'obtention du titre de

DOCTEUR DE L'UNIVERSITE DE LORRAINE

Mention : Géosciences

par **Aurélien RANDI**

Modélisation expérimentale de l'injection de solutions enrichies en CO_2 dans un doublet géothermique. Étude des impacts géochimiques en proche puits

Soutenue publiquement le12 Février 2021

Membres du jury :

Rapporteurs :	M. Vincent Lagneau	Professeur, MINES ParisTech, Fontainebleau
	Mme Catherine Noiriel	Maître de Conférences HDR, Université Paul Sabatier, Toulouse
Examinateurs :	Mme Linda Luquot	Chargée de Recherche au CNRS, Université de Montpellier
	M. André Lecomte,	Professeur, Université de Lorraine, Nancy
	M. Jérôme Sterpenich	Professeur, Directeur de thèse, Université de Lorraine, Nancy
	M. Jacques Pironon	Directeur de Recherche au CNRS, Co-directeur de thèse, Université de Lorraine, Nancy
Membre invité :	M. Christophe Kervévan	Chef de projet senior, BRGM, Orléans

---

UMR 7359 GeoRessources, Faculté des Sciences et Technologies, 54500, Vandoeuvre-lès-Nancy

Une seule certitude suffit à celui qui cherche…

Albert Camus

REMERCIEMENTS

Ce travail de recherche a été initié dans le cadre du projet CO2-DISSOLVED soutenu par l'ANR et le GIS Géodénergies. La thèse s'est déroulée au sein du laboratoire GeoRessources sur la thématique de l'altération des roches carbonatées et du ciment périphérique au cuvelage métallique d'un puits d'injection composant un doublet géothermique. Ce travail est le fruit d'une collaboration entre plusieurs domaines de compétences représentés par des acteurs d'horizons variés dont les approches et les compétences multiples m'ont enrichi personnellement et ont contribué à l'aboutissement de ma thèse. Ce manuscrit vient donc ponctuer cinq années d'échanges, d'apprentissage, de réflexions, de constructions, d'expérimentations, d'écriture … et de réécriture qui m'ont permis de vivre de grands moments qui sont passés de la joie à l'allégresse, mais également aux doutes permanents. Cette partie me permet donc de remercier les personnes concernées et relate des moments de partage intervenus au cours d'une aventure professionnelle mais avant tout humaine.

Evidemment, mes remerciements s'adressent avant tout à mes deux directeurs de thèse et néanmoins collègues (voire plus que cela) : **Jérôme Sterpenich** et **Jacques Pironon**. Merci de m'avoir catapulté dans cette entreprise et d'avoir cru en mes capacités à pouvoir réaliser une thèse en parallèle de mes activités professionnelles. Votre confiance et la liberté que vous m'avez accordées à avancer dans mes recherches au gré de mes idées ont été un moteur qui m'a permis de m'épanouir et d'aller jusqu'au bout de cette expérience. Les « ouais, c'est pas mal » de Jérôme et les « c'est un peu long, j'ai fatigué sur la fin » de Jacques ont participé sans aucun doute à parfaire le contenu de ce manuscrit. Merci d'avoir su être attentif à mon travail et présent au bon moment.

Tout d'abord, j'adresse ma gratitude aux membres du jury avec qui j'ai, en toute sincérité, passé un excellent moment, quoique lointain, lors de ma soutenance… après une nuit plus que courte. Merci pour l'intérêt porté à mon travail et pour les échanges très constructifs que nous avons eus. Merci donc à mes rapporteurs, Mme **Catherine Noiriel** et M. **Vincent Lagneau** ainsi qu'aux examinateurs, Mme **Linda Luquot**, M. **André Lecomte** et M. **Christophe Kervévan** pour m'avoir fait l'honneur de juger mes travaux. J'exprime en particulier ma gratitude à Messieurs Lagneau et Lecomte pour m'avoir suivi tout au long de ces années (et il y en a eu) lors des réunions d'avancement et pour leur précieux conseils ainsi que pour leur bienveillance à mon égard. Je tiens à manifester une reconnaissance particulière à M. Christophe Kervévan, porteur du projet CO2-DISSOLVED, sans qui ce travail n'aurait pas été possible. Merci de m'avoir permis de vivre des expériences inoubliables (une pensée spéciale aux WISKHEY SISTERS). Enfin, Mesdames Noiriel et Luquot, je vous ai tellement lues que ce fut un plaisir de mettre des visages sur des noms. La situation n'ayant malheureusement pas permis de discuter plus longuement de nos travaux transverses autour d'une boisson.

Ainsi, tout a commencé à l'éclosion du projet CO2-DISSOLVED (2013 !!) dont ma participation au long de ces années a été très enrichissante sur le plan professionnel, scientifique et technique en raison de la pluralité et de la diversité des partenaires composant le consortium du projet. Je tiens notamment à remercier M. **Nicolas Marty**

pour ses précieux conseils sur la réactivité des ciments, M. **Dominique Thierry** pour avoir modélisé numériquement mes expériences, Mme **Marie-Hélène Bedellem** et M. **Hevré Traineau** pour m'avoir éclairé sur les techniques de forages à l'échelle industrielle ainsi que Mme **Christelle Castillo**, M. **Yann Le Gallo** et l'équipe américaine composée de Mme **Kathleen O'Neil** et M. **Gerald Blount**.

La première tâche qui m'a été confiée a constitué à mettre en place un banc d'essai expérimental. Il m'a donc fallu, dans un premier temps, concevoir ce dernier et acheter le matériel nécessaire ; ce qui m'a occupé un bon moment. Pour cela, je voudrais adresser un mot chaleureux à l'égard de l'équipe administrative de GeoRessources pour le travail réalisé lors de ma thèse, toujours avec de la sympathie à mon égard (Mme **Rachida El Ouardani**, Mme **Laurence Moine**, Mme **Stéphanie Trombini**, Mme **Karine Lepelletier** et Mme **Marie Morel**). La mise en place de ce banc d'essai (avec qui j'ai passé beaucoup de temps en tête à tête et que je remercie de ne jamais m'avoir fait faux bond) sur le site d'ARTEM a également fait partie de mes occupations pendant une bonne période. L'implantation du système a nécessité d'adapter la salle d'expérimentation initialement non équipée pour ce type de manip. Cette mission n'aurait pu aboutir sans l'aide de l'équipe technique d'ARTEM qui a toujours su répondre à mes besoins. Un grand merci donc à Messieurs **Laurent Payre**, **Laurent Kaltenecker**, **Jean-Charles Lukas** ainsi qu'à **Thomas** et **Jérôme Dehaye**). Enfin, la réalisation de ce banc d'essai MIRAGES-2 n'aurait pas pu être complétement abouti sans les conseils de Messieurs **Philippe Chopineau** et **Sylvain Pelatan** mais surtout sans les usinages du magicien de la pièce qui sauve, notre mécanicien **Gilles Bessaque**.

Ensuite, il m'a été indispensable de me familiariser avec mon matériau de compagnie qui m'a suivi durant toute cette aventure ; à savoir la roche carbonatée. Vaste monde que celui des carbonates auquel j'ai été initié avec l'aide d'une dream-team composée de M. **Bernard Lathuilière** et M. **Cédric Carpentier** (« we got the funk »). Je vous exprime une grande marque d'affection pour le temps précieux que vous m'avez octroyé et pour l'effort que vous avez fourni à la relecture de mon « lonnnnnnng » chapitre initial sur les carbonates mais également pour votre regard critique sur la qualité du travail fourni. La maîtrise de la roche étudiée n'aurait également pas été possible sans sa caractérisation. A ce sujet, je souhaite adresser mes sincères remerciements à Messieurs **Yves Géraud** et **Laurent Schumacker** pour leur formation sur les us et coutume des mesures pétrophysiques. Merci Yves pour l'accès au matériel et le temps accordé et merci Laurent pour tes explications « fines ». J'en profite également pour adresser une pensée aux anciens thésards de l'école de géologie de Nancy qui n'ont jamais été avares de conseils concernant le fonctionnement des machines mais aussi de sourires et d'échanges divers et variés: Mme **Claire Bossenec,** M. **Sebastien Haffen** et M. **Vivien Navelot**. Concernant la inspection du « tout petit », je tiens à remercier grandement M. **Andréï Lecomte** pour les analyses MEB de qualité. Ces analyses ne sont rendues possibles qu'après préparation des échantillons. Je remercie donc également M. **Mohammed Moumni** (Allez le Sluc !) pour les carottages de « ma roche ». Merci pour l'apprentissage et pour les discussions et désolé pour les taches de graisse sur le t-shirt. Un grand merci également à la team de « lithopréparation » : M. **Alexandre Flammang** et M. **John Moine** pour leur aide dans la préparation des lames minces et le café toujours chaud.

Enfin, que dire de Messieurs **Vitaliy Privalov** et **Chrisophe Morlot** à qui je dois l'optimisation de l'analyse de mes résultats expérimentaux. Vitaliy : Щиро дякую вам за все, що ви зробили для мене. Я надовго запам'ятаю наші моменти, коли ми обговорювали мої « WORMHOLES » біля образів Крістофа. Без вас ця теза не була б настільки успішною. Я також надовго запам'ятаю наші побічні дискусії. Quant à toi, Christophe, Monsieur le Blancôtois (j'ai fait mes recherches), the « best of the merge and of the curvature », merci pour le transfert de savoir, les conseils et surtout le temps d'accès à ta plateforme de tomographie aux rayons-X. Grace à toi, j'ai pu « voyager » dans mes « wormholes » pour en comprendre leur comportement. Je tiens, dans le même élan, à témoigner mes plus sincères remerciements et mon entière gratitude à M. **Fabrice Golfier** pour le temps précieux accordé, ses enseignements, ses suggestions critiques, ses orientations constructives et ses conseils qui m'ont grandement permis d'aboutir à la matérialisation actuelle de mon travail. Quelle chance d'avoir le « Monsieur du diagramme Pe-Da » comme conseiller !

Je salue également tous les autres collègues de GeoRessources pour leurs présence, conseils et soutien : Mme **Régine Mosser-Ruck** (dont la bienveillance à mon égard est une force au quotidien), Mme **Odile Barres** (en attendant la Suisse), Mme **Judith Sausse** (mon modérateur de Jérôme), Mme **Anne-Sylvie André-Mayer** (rassurante et arrangeante jusqu'au bout du bout), Mme **Catherine Lorgeoux** de même que Mme **Marie-Camille Caumon** (dont les conseils et remarques au moment du sprint final m'ont beaucoup aidé), M. **Philippe De Donato**, Mme **Cécile Fabre**, M. **Raymond Michels**, Mme **Isabella Pignatelli**, Mme **Delphine Martin**, Mme **Camille Gagny**, M. **Julien Mercadier**, M. **Antonin Richard**, M. **Aurélien Eglinger**, Mme **Chantal Pfeiffer**, M. **Dimitri Laurent** et M. **Rémi Mazerolles** (dernier voisin de bureau qui a pu m'entendre pester de façon non négligeable lors de la rédaction finale du mémoire).

Il est également bon d'être épaulé en dehors du monde professionnel, je me permets d'inclure dans mes remerciements mes amis de toujours, mes « best » et d'attribuer une mention spéciale à : **Thibault**, **Fix**, **Julien**, **Priscille**, … la liste est bien trop longue mais je n'oublie pas les autres! Je remercie également l'équipe de basket du Haut du Lièvre de m'avoir permis d'extérioriser mon trop plein de stress au cours d'entrainements intenses.

Pour finir, Je tiens à remercier mes parents, pour leur soutien, leur amour inconditionnel et les valeurs qu'ils m'ont inculquées. Merci à mon frère, je ne peux m'empêcher de penser que là d'où tu es, tu m'envoies une force indéfectible qui m'aide à surmonter les épreuves de la vie.

Et je terminerai par remercier les trois femmes de ma vie : ma femme **PHUONG** et mes deux filles **SAHARA** et **SALOME** ; merci d'illuminer ma vie de votre amour.
JE VOUS AIME !

TABLE DES MATIERES

RESUME ETENDU EN FRANÇAIS_____ 14

INTRODUCTION GENERALE_____ 35

PARTIE 1 – LE PROJET CO2-DISSOLVED

PART 1 – THE CO2-DISSOLVED PROJECT

I. PRINCIPE_____ 42

II. RISQUES LIES A LA PARTIE STOCKAGE DU PROJET_____ 45

PARTIE 2 – ETAT DE L'ART

PART 2 – STATE OF THE ART

I. LES ROCHES CARBONATEES_____ 50

I.1. Caractéristiques pétrographiques des roches carbonatées_____ 50

I.2. Caractéristiques pétrophysiques des roches carbonatés_____ 52

I.2.1. La porosité (l'espace poreux)_____ 52

I.2.2. La perméabilité_____ 55

I.2.3. La surface spécifique (interface fluide /roche) et la surface réactive_____ 56

I.3. Nomenclature et classification des roches carbonatées_____ 57

II. APPROCHE THEORIQUE DE LA REACTIVITE DES RESERVOIRS CARBONATES PAR FORÇAGE HYDROGEOCHIMIQUE ANTHROPIQUE_60

II.1. Système calco-carbonique et réactions de dissolution/ précipitation (échelles microscopiques)_____ 61

II.1.1. Dissolution du CO_2_____ 61

II.1.2. Aspect thermodynamique des phénomènes de dissolution/précipitation_ 63

II.1.3. Aspect cinétique des phénomènes de dissolution/précipitation_____ 66

II.1.3.1. Mécanisme de contrôle de la vitesse globale de réaction_____66

II.1.3.2. Paramètres définissant la cinétique de dissolution/ précipitation_ 68

II.2. Transport réactif dans une roche calcaire poreuse (classification des modèles de dissolution (introduction Pe-Da)_____ 70

II.2.1. Description du transport réactif multi-échelle_____ 70

II.2.2. Adimensionnement du transport réactif et classification des déformations 72

PARTIE 3 – APPROCHE EXPERIMENTALE

PART 3 – EXPERIMENTAL APPROACH

I. INTRODUCTION_____ 80

II. MATERIALS_____ 81

II.1. Carbonate rock sample selected for experiments: the "Lavoux limestone"_____ 81

II.2. Description of the injection well materials_____ 83

II.2.1. Cement_____ 83

II.2.2. Injection tube steel_____ 85

III. PRE-DIMENSIONING MODELING OF THE MIRAGES-2 EXPERIMENTS 86

III.1. Procedure of the numerical experiment used to define the injection conditions of the flowthrough experiments_____ 86

III.2. Results_____ 88

III.2.1. Impact of the flowrate_____ 88

III.2.2. Impact of the amount of dissolved CO_2 in the injected solution_____ 89

III.3. Conclusion of the pre-dimensioning modeling_____ 91

IV. THE EXPERIMENTAL BENCH: MIRAGES-2_____ 91

IV.1. Sample design and preparation process_____ 91

IV.2. Description of the MIRAGES-2 experiment_____ 93

IV.2.1. Device for the CO_2/solution mixture _____ 95

IV.2.2. Device for the radial injection of the CO_2 rich solution (MIRAGES-2)____ 96

IV.2.3. In-situ thermodynamic and chemical monitoring of the experiment_____ 98

V. EXPERIMENTAL PROTOCOL_____ 99

V.1. Protocol of injection_____ 99

V.2. Determination of the initial fluid chemistry and preparation procedure 100

VI. DESCRIPTION OF THE EXPERIMENT_____ 101

VII. CHARACTERIZATION OF PRE- AND POST- EXPERIMENTAL SAMPLES 103

VII.1. Investigation of the petrophysical properties of the rock_____ 103

VII.1.1. Permeability_____ 103

VII.1.2. Porosimetry_____ 104

VII.1.2.1. Concept_____ 104

VII.1.2.2. Protocol of measurement and data acquisition_____ 105

VII.1.3. Sampling protocol of the pre- and post-petrophysical analyses_____ 106

VII.2. Investigation of the evolution of the structural properties of rock by imaging_____ 107

VII.2.1. Thin section observation_____ 107

VII.2.2. Scanning Electron Microscopy (SEM)_____ 108

VII.2.3. X-Ray micro-tomography_____ 109

VII.2.3.1. Concept and data acquirement procedure_____ 109

VII.2.3.2. Image processing protocol_____ 111

VII.2.3.3. Surface roughness analysis protocol_____ 113

*VII.2.3.3.1. Surface curvature concept*_____ 113

VII.2.3.3.2. Image processing protocol for surface curvature analysis _____ 116

VII.2.3.4. Description of the analyzed samples_____ 118

VII.2.4. *In* and *ex-situ* chemical analysis_____ 119

VII.2.4.1. *In-situ* high pressure pH measurement_____ 119

*VII.2.4.1.1. Image Materiel and method*_____ 119

*VII.2.4.1.2. pH probes calibration*_____ 120

VII.2.4.2. *In-situ* Raman spectroscopy under high pressure/high temperature hydrothermal conditions_____ 121

*VII.2.4.2.1. In-situ Raman: material and method*_____122

*VII.2.4.2.2. Results of the in-situ Raman calibration at 20°C*_____124

*VII.2.4.2.3. in-situ Raman calibration at 60°C*_____ 126

VII.2.4.3. Solution chemistry analysis by ICP-AES and ion chromatography (IC)_____ 126

PARTIE 4 – MODÉLISATION EXPÉRIMENTALE DE L'INJECTION DE CO_2 SOUS FORME DISSOUTE EN RÉSERVOIR GEOLOGIQUE : RESULTATS ET OBSERVATIONS

PART 4 – EXPERIMENTAL MODELLING OF THE INJECTION OF CO_2 IN DISSOLVED FORM IN GEOLOGICAL RESERVOIR: RESULTS AND OBSERVATIONS

I. INITIAL CHARACTERIZATION OF THE ROCK SAMPLES_____130

I.1. Petrographic analysis_____130

I.2. Petrophysical analysis_____133

I.3. Chemical analysis_____135

II. MINERAL REACTIVITY OF THE LIMESTONE ROCK SAMPLES FOLLOWING THE INJECTION OF CO_2-RICH SOLUTIONS: RESULTS AND OBSERVATIONS

II.1. Results of in-situ data acquisition_____ 136

II.1.1. Pressure/Temperature and mass flow recording_____ 136

II.1.2. pH measurement_____ 138

II.1.3. Carbonate speciation_____ 139

II.2. Chemical analysis of the aqueous solution_____ 142

II.3. Sample alteration: Structural characterization_____ 144

II.3.1. Macroscopic observation (post-experimental core-plug external observation and CT-scan images analysis)_____ 144

II.3.2. Petrophysical parameters_____ 150

II.3.2. Microscopic observation (SEM)_____ 151

PARTIE 5 – DISCUSSION : EVOLUTION SPATIO-TEMPORELLE DES PHENOMENES DE TRANSPORT REACTIF

PART 5 – DISCUSSION: SPATIO-TEMPORAL EVOLUTION OF REACTIVE TRANSPORT PHENOMENA

I. pH VARIATION AND MASS BALANCE 158

II. DOMINANT MECHANISMS IN THE INITIATION OF DISSOLUTION PATTERNS: A DIMENSIONLESS NUMBER DISCUSSION 164

III. SPATIO-TEMPORAL EVOLUTION OF THE DISSOLUTION PROCESS 168

IV. EVIDENCE OF PRECIPITATION PHENOMENA 171

PARTIE 6 – CONTRÔLE STRUCTUREL D'UN RÉSEAU DE DISSOLUTION DANS UN RÉSERVOIR CALCAIRE SOUMIS A L'INJECTION RADIALE D'UNE SOLUTION SATURÉE DE CO_2

PART 6 – STRUCTURAL CONTROL OF A DISSOLUTION NETWORK IN A LIMESTONE RESERVOIR FORCED BY RADIAL INJECTION OF CO_2 SATURATED SOLUTION

ABSTRACT 182

PAPER 183

CONCLUSION 209

NOMENCLATURE 217

REFERENCES BIBLIOGRAPHIQUES 222

LISTE DES FIGURES 240

LISTE DES TABLEAUX 249

ANNEXES 251

RESUME DE THESE 299

ABSTRACT OF THE THESIS 301

RESUME ETENDU (FRANÇAIS)

I. INTRODUCTION

Face à la problématique de l'accroissement du phénomène d'effet de serre [1] et afin de répondre au défi, défini en 2015 lors de la conférence de Paris (COP21), de limiter le réchauffement de la planète à 1,5°C [4], la France s'est fixé l'objectif d'une transition énergétique axée sur une économie décarbonée [5]. Cette stratégie de neutralité carbone s'emploie à mettre en œuvre la technologie de Captage et Stockage du CO_2 (CSC) afin de réduire les émissions liées au secteur industriel [5]. Le CSC consiste en une combinaison de technologies permettant de capter le CO_2 provenant de sources d'émissions importantes telles que les centrales thermiques à combustibles fossiles ou les aciéries, de le transporter de la source vers un lieu de stockage adapté permettant de confiner le CO_2 sur le long terme dans un réservoir géologique profond [6]. Il existe dans le monde de nombreux réservoirs propices au stockage géologique du CO_2. Les aquifères salins profonds (profondeur d'au moins 800 mètres assurant un état supercritique du CO_2) fournissent la part la plus importante de la capacité de stockage et sont assez bien distribués géographiquement [7]. Les projets en cours prévoient généralement l'injection du CO_2 à l'état supercritique, maximisant ainsi les quantités stockées. En France, le développement à grande échelle du CSC est cependant limité en raison d'incertitudes économiques (coût important de mise en œuvre), d'absence de régimes juridiques et financiers appropriés ou encore par manque d'infrastructures existantes (par exemple les réseaux de pipelines nécessaires au déploiement commercial généralisé du CCS) et se heurte régulièrement à une opposition sociétale locale. En outre, la filière CSC française semble n'être applicable qu'à un nombre limité de sites industriels, principalement les gros émetteurs (centrales de production d'énergie ou encore les aciéries, cimenteries, raffineries, usines chimiques et pétrochimiques…) [3].

Face à ces différents verrous, l'émergence de projets à plus petite échelle apparaît alors comme une solution alternative. Parmi les options suggérées, le projet CO2-DISSOLVED à l'origine de ces travaux de thèse, propose un nouveau concept hybride CCS qui vise à coupler la récupération d'énergie géothermique et la séquestration du CO_2 sous forme dissoute en aquifères salins à proximité d'une source d'émission industrielle. Le projet ouvre de nouvelles opportunités pour des solutions de stockage local dédiées aux faibles émetteurs (< 150 000 tCO_2/an) et constitue une voie intéressante de valorisation de la réinjection de la saumure géothermale, démontrant ainsi qu'une réelle synergie entre le stockage de CO_2 et les activités géothermiques peut exister. L'approche CO2-DISSOLVED repose sur la technologie d'un doublet géothermique basse enthalpie standard qui consiste à pomper une saumure chaude par un puits producteur afin d'en récupérer les calories en surface par le biais d'échangeurs pour les besoins de l'usine émettrice de CO_2 voire pour alimenter un réseau de chaleur environnant. La saumure géothermale refroidie est ensuite chargée en CO_2 dissous avant d'être réinjectée dans le même aquifère via un second puits dit "injecteur", à proximité immédiate de la source émettrice (Fig. 1).

Cette approche offre aux industriels un gain énergétique par le bénéfice direct et local des calories produites, un gain financier par le revenu généré par l'utilisation de cette énergie verte produite et un bénéfice environnemental avec une empreinte carbone réduite. En outre, l'option d'injecter le CO_2 sous forme dissoute par rapport à l'état supercritique offre des avantages notables en termes de réduction de risques [27]. L'absence de phase gazeuse et les effets de densité favorables (l'eau salée riche en CO_2 réinjectée est légèrement plus dense que l'eau de formation) permettent de s'affranchir des problèmes inhérents à l'approche « classique » comme la migration de la saumure et du CO_2 dissous vers les formations géologiques sus-jacentes.

De plus, l'utilisation de deux puits pour le pompage et la réinjection dans la même formation va permettre d'éviter la montée en pression de l'aquifère, inévitable dès lors que le CO_2 supercritique y est injecté massivement par un puits unique. Enfin, le système repose sur une technologie parfaitement maitrisée (le doublet géothermique).

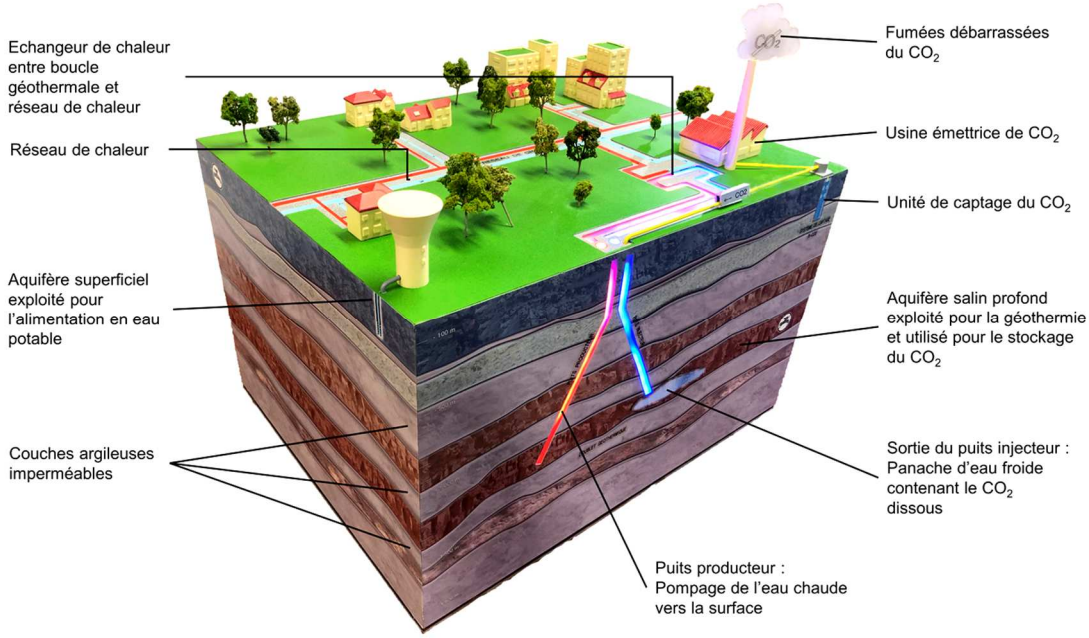

Figure 1 : Représentation schématique du concept CO2-DISSOLVED combinant le stockage du CO_2 sous forme dissoute et la récupération de chaleur géothermique via un système de doublet (http://co2-dissolved.brgm.fr/).(@BRGM)

L'ajout de CO_2 dissous dans la solution saline injectée génère cependant de nouvelles contraintes qui doivent être prises en compte dans la conception et le dimensionnement de l'ensemble du système. En effet, l'injection d'une eau acidifiée enrichie en CO_2 devrait induire une réactivité accrue avec la roche encaissante à proximité immédiate du puits d'injection, notamment en présence de minéraux carbonatés. Les réactions du fluide acide avec la roche vont provoquer des changements des propriétés pétrophysiques de la formation hôte caractérisées par une modification de la porosité et de la perméabilité [6,11,12,13,14]. Le comportement à long terme du réservoir pourra alors être modifié en termes d'injectivité, d'efficacité de stockage et d'intégrité. De même, l'eau saline contenant du CO_2 sera beaucoup plus agressive pour le tubage du puits que la solution saline classiquement réinjectée dans d'un doublet géothermique classique.

Le développement à l'échelle pilote et industrielle impose alors une identification complète des risques. Cette tâche nécessite de considérer et d'évaluer l'impact environnemental et surtout de prédire l'évolution du réservoir hôte et des matériaux de puits sur une longue période (environ 50 ans).

L'option d'injecter le CO_2 en réservoir géologique sous forme dissoute a été beaucoup moins étudiée que l'injection standard de CO_2 supercritique. En effet, la grande majorité des études sur le sujet simule la zone extérieure (ou périphérique) à la zone proche-puits, environnement où le CO_2 commence à se dissoudre dans l'eau salée et où le déséquilibre chimique est maximal [22]. La technologie de captage et d'injection propre au concept CO2-DISSOLVED va provoquer un déséquilibre chimique immédiat en sortie de casing entre les phases en présence. Une bonne compréhension des phénomènes complexes induits aux abords directs du puits d'injection apparaît alors essentielle pour fournir les modèles d'évaluation des risques fiables (prévention de fuites, intégrité du réservoir, interférence avec un aquifère voisin…) et l'aide au dimensionnement du doublet (positionnement optimal pour optimiser la productivité). Pour ce faire, l'altération expérimentale à l'échelle du pilote de laboratoire des roches et des matériaux de puits est une bonne alternative pour alimenter les bases de données des modèles prédictifs à l'échelle du doublet.

L'objectif principal de cette thèse consiste alors à mettre en place un banc d'essai de laboratoire reproduisant au plus près les conditions d'un puits d'injection avec ses différentes interfaces (ciment/casing, ciment/réservoir et ciment/réservoir/couverture). Ce banc assure une certaine souplesse expérimentale garantissant la possibilité de tester une large gamme de solides (ciment, roche encaissante, casing) et de compositions du fluide injecté (CO_2, gaz co-injecté, eau saline) dans des conditions géologiques variées (pression, température, gradients de température et de pression, temps de résidence). En effet, ce sont ces paramètres qui vont contrôler les mécanismes réactionnels (dissolution/précipitation). Le design développé offre également au fluide la capacité de circuler librement dans l'espace poral de l'échantillon. Le système expérimental est impacté par l'hétérogénéité structurale et texturale de la roche et permet donc d'investiguer la relation spatiale entre la distribution des discontinuités (microfailles, microfissures, changements de lithologie, de faciès…) dans l'échantillon et les phénomènes de dissolution ou de précipitation aux abords du puits. De plus, ce banc d'essai garantit l'acquisition d'une quantité importante de données géochimiques *in situ* permettant de modéliser numériquement le transport réactif induit.

De cette façon, les résultats aideront à :

- valider la sélection des matériaux de construction du puits afin de minimiser tout dommage potentiel relatif à la présence du CO_2 dissous,
- valider les conditions opératoires de la phase d'injection (débits, concentration de CO_2,…),
- quantifier les taux et les figures de dissolution/précipitation pour assurer une meilleure injectivité,

- optimiser l'emplacement des puits producteur et injecteur à partir de l'interprétation spatiale de la morphologie des réseaux de dissolution afin de maximiser la durée de vie des installations géothermiques ainsi que la séquestration du CO_2.

Ce mémoire se focalise principalement sur l'étude de la réactivité géochimique et des modifications hydrodynamiques associées d'un aquifère salin carbonaté en région proche puits suite à l'injection d'une solution riche en CO_2. Les résultats permettent également l'étude structurale des réseaux de dissolution générés dans un matériau hétérogène. L'évolution de l'interface ciment-roche est également suivie et le rôle tampon du ciment sur le pH est discuté. Cette étude expérimentale couplée à une modélisation numérique menée dans le cadre du projet CO2-DISSOLVED s'inscrit ainsi dans une approche « risques, performance et aide à la décision ».

II. MODELISATION EXPERIMENTALE

II.1. Approche expérimentale

Afin de répondre au mieux aux besoins du projet CO2-DISSOLVED, un protocole expérimental original a été développé. Dans un premier temps, un pré-dimensionnement a été opéré à l'aide d'un outil numérique de modélisation dans le but de déterminer les conditions expérimentales optimales, en termes de pression, température, quantité de CO_2 dissous, débit d'injection de la solution expérimentale acide et durée d'injection. Ainsi, les conditions limites qui engendreraient des transferts de masse trop importants ou trop faibles et ne permettraient pas une étude significatives des phénomènes couplés de dissolution/précipitation, ont pu être éliminées. De la même façon, la concentration maximale de CO_2 pouvant être dissoute sans engendrer de phénomène d'exsolution au sein du système a également pu être spécifiée. Le dispositif expérimental instrumenté appelé MIRAGES-2 (acronyme de " Modèle d'Injection RAdiale pour Gaz à Effet de Serre") a ensuite été conçu et mis en service au cours de cette thèse. Il permet de simuler efficacement, à l'échelle du laboratoire, la dynamique d'injection du CO_2 en région proche puits. La particularité du banc d'essai développé concerne, en premier lieu, la conception de l'éprouvette à contraindre. En effet, sa configuration reproduit un puits d'injection de taille décimétrique assurant une injection " radiale " de la solution expérimentale tout en simulant la présence des différentes interfaces (ciment/acier, ciment/roche réservoir et potentiellement ciment/roche réservoir/roche couverture). Il peut être souligné l'originalité et la singularité du banc d'essai MIRAGES-2. En effet, l'injection radiale au cœur d'un échantillon de roche décimétrique composé des différents matériaux d'un puits d'injection a rarement été réalisée dans le cadre d'études expérimentales de géo-séquestration des gaz acides. Les caractéristiques techniques du système permettent une injection isotrope du fluide et une circulation libre dans la matrice rocheuse de l'échantillon et non pas orientée comme c'est le cas dans les expériences unidirectionnelles de type " core holder ". De cette façon, le rôle détaillé des hétérogénéités structurales de la roche sur l'évolution de ses propriétés pétrophysiques au cours du temps peut être investigué.

De plus, une attention particulière a été portée sur l'acquisition des données physico-chimiques (pression, température, pH, concentrations de différentes espèces aqueuses, etc.) et de nouveaux outils ont été développés pour la mesure *in situ* (sonde Raman Haute Pression / Haute Température, sonde pH Haute Pression / Haute Température, débitmètre Haute Pression).

Une description complète des caractéristiques des différents matériaux avant et après les expériences a également été réalisée. Une observation pétrographique de la roche en lame mince et sur des cassures fraîches, couplée à l'imagerie 3D par micro-tomographie aux rayons X a été utilisée pour décrire la microstructure de la roche. Des données quantitatives ont également été obtenues par le biais de mesures pétrophysiques (porosité, perméabilité) et des analyses chimiques (ICP-MS). Les échantillons expérimentaux entiers ont été analysés par micro-tomographie aux rayons X avant et après les expériences afin de caractériser l'évolution de la géométrie du réseau poreux.

En complément, un protocole de traitement des données post expérimentales issues des analyses par tomographie à rayons X a été développé. Cette méthode a permis la caractérisation qualitative et quantitative de l'évolution de la topologie du réseau poreux suite aux processus de dissolution/précipitation.

II.2. Design expérimental et protocole

II.2.1. Description de l'échantillon

Le choix de la roche à contraindre repose sur le contexte géologique du bassin sédimentaire de Paris, principalement la formation de " l'Oolithe Blanche " (Bathonien) du Dogger, qui a été identifiée comme une cible pertinente pour la mise en œuvre d'un pilote industriel dans les conditions attendues [146 ; 147 ; 148 ; 149]. Un analogue naturel, le "Calcaire de Lavoux" a alors été sélectionné pour réaliser les carottes expérimentales car ses caractéristiques pétrophysiques lui confèrent de bonnes propriétés d'écoulement et donc d'injectivité. Les échantillons ont été prélevés en affleurement dans la carrière de Chauvigny, dans le Sud-Ouest du bassin de Paris.

D'un point de vue textural, le calcaire de Lavoux est un "packstone" à "grainstone" principalement composé d'oolithes micritiques, de peloïdes et de bioclastes (Fig. 2a, b). Le volume poreux a été partiellement rempli par une phase liante constituée d'une matrice micritique, de ciment sparitique syntaxial de grande taille (100 - 1000µm) et de calcite sparitique rhomboédrique (ou équant) de taille moyenne (10-50µm) (Fig. 2a, c).

Les analyses pétrophysiques ont mesuré une porosité totale connectée de 24,73%. Cette porosité a une distribution bi-modale avec des familles d'entrée de pores moyens à 0,42 µm et 3,08 µm correspondant respectivement à la porosité intra- (microporosité) et inter-(mesoporosité) oolitiques. Les macropores peuvent atteindre une taille maximale de 300 µm. La perméabilité de la roche est anisotrope avec une perméabilité verticale k_v de 46,5 mD et horizontale k_h de 73,8 mD. D'un point de vue chimique, le calcaire de Lavoux est composé à 98% de carbonate de calcium (calcite pure et calcite faiblement magnésienne).

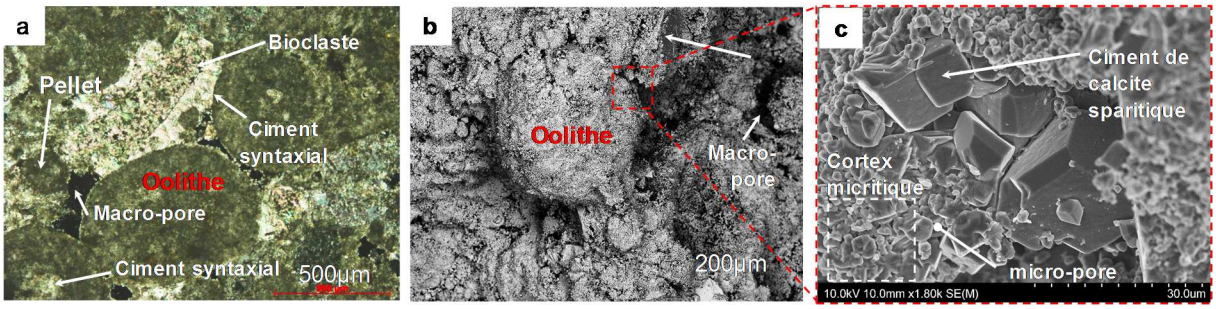

Figure 2 : Illustration de la texture du calcaire de Lavoux: (a) Observation microscopique sur lame mince (lumière polarisée). Il est possible de visualiser la fabrique de la roche avec les oolithes et les ciments syntaxiaux autour d'un fragment d'échinoderme. Les zones sombres correspondent à la porosité, (b) Observation par MEB (en mode électrons secondaires SE) du calcaire de Lavoux. Vue d'ensemble de la surface montrant l'oolite et les macro-pores. (c) Focus sur le cortex micritique et les ciments de calcite sparitiques.

L'éprouvette utilisée pour reproduire un puits d'injection à échelle réduite (Fig. 3 a) consiste en un tube métallique ou non (longueur = 119 mm, diamètre interne = 4,5 mm, diamètre externe = 6,35 mm) vissé à un anneau de téflon (diamètre = 25 mm, épaisseur = 2 mm) et scellé à la carotte de roche (diamètre externe = 100 mm, longueur = 100 mm) avec un ciment Portland de classe G. La roche a été carottée dans un bloc de calcaire de Lavoux de façon perpendiculaire au litage sédimentaire, à l'exception d'une expérience où l'échantillon a été carotté à 55° par rapport à la stratification (Fig 3c). Cet angle correspond à l'angle maximum prévu lors de la conception du puits d'injection à l'échelle du pilote industriel (Fig. 3b). Cette configuration permet de simuler étroitement les conditions d'exploitation, et plus particulièrement d'étudier l'influence de la fabrique rocheuse sur les figures de dissolution/précipitation.

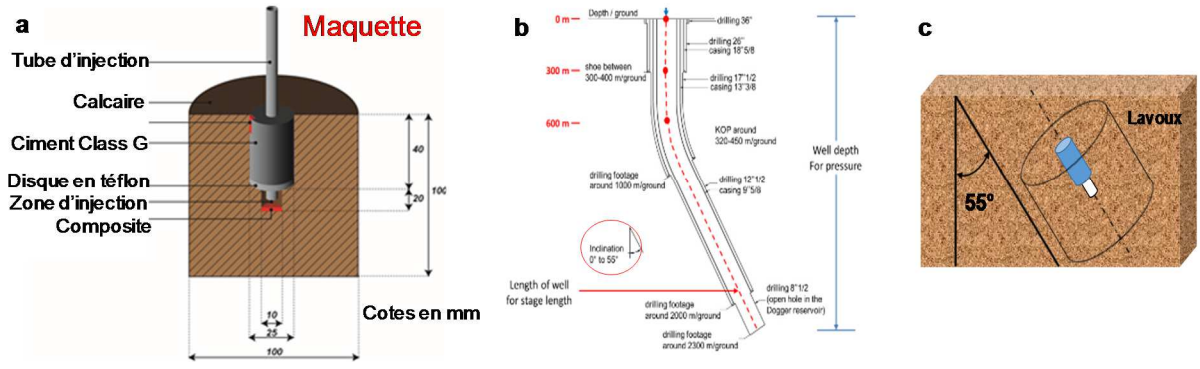

Figure 3 : (a) Vue schématique de l'échantillon simulant le puits d'injection sur le banc d'essai MIRAGES-2. (b) Conception typique d'un puits d'injection [170] avec l'angle maximum prévu (cercle rouge) à la profondeur du trou ouvert. (b) Carottage de l'échantillon simulant l'angle du forage du pilote industriel.

Le ciment est, quant à lui, préparé selon le protocole API-ISO 10426-A avec un rapport Eau/Ciment de 0,44. Après hydratation, le ciment est principalement composé de portlandite ($Ca(OH)_2$), de silicates de calcium hydratés (CSH), de silicates bi/tri calciques non hydratés (C2S et C3S) et d'autres phases mineures contenant de l'aluminium, des sulfates (ettringite) et du fer. L'acier utilisé dans notre expérience est un acier inoxydable austénitique 316 (nom d'acier standard EN X5CrNiMo17-12-2).

II.2.2. Banc d'essai MIRAGES-2 et protocole expérimental.

Le dispositif expérimental MIRAGES-2 est composé de deux éléments principaux (Fig. 4). Le premier est consacré à la solubilisation du CO_2 de façon maitrisée dans la solution d'injection expérimentale. Il est principalement constitué d'une cuve de mélange de 5 litres ("autoclave de mélange") équipé de capteurs de niveau assurant un remplissage continu de la solution. Le second permet de réaliser l'injection en continu et à débit constant de la solution monophasique riche en CO_2 dans le " puits miniature " de laboratoire par le tube d'injection, et ce, dans des conditions de pression et de température contrôlées. Il est composé d'un "autoclave d'injection" de 2 Litres à l'intérieur duquel sont installées les éprouvettes. L'injection du fluide enrichi en CO_2 est réalisée à débit constant à l'aide d'un pompe seringue double couplée à un débitmètre massique. Pendant les expériences, des mesures régulières du pH et de la chimie de la solution sont effectuées avec des sondes *in situ* à l'entrée et à la sortie de l'échantillon. La procédure expérimentale se déroule en deux étapes : i) une période de cure pendant laquelle l'échantillon est soumis aux conditions du réservoir dans un système fermé. Cette période dure environ 10 jours et permet l'hydratation des phases cimentaires dans les conditions du réservoir. ii) une période d'injection (ou de vieillissement) d'une durée définie pendant laquelle le fluide est injecté radialement dans la zone d'injection de l'éprouvette (Fig. 3a).

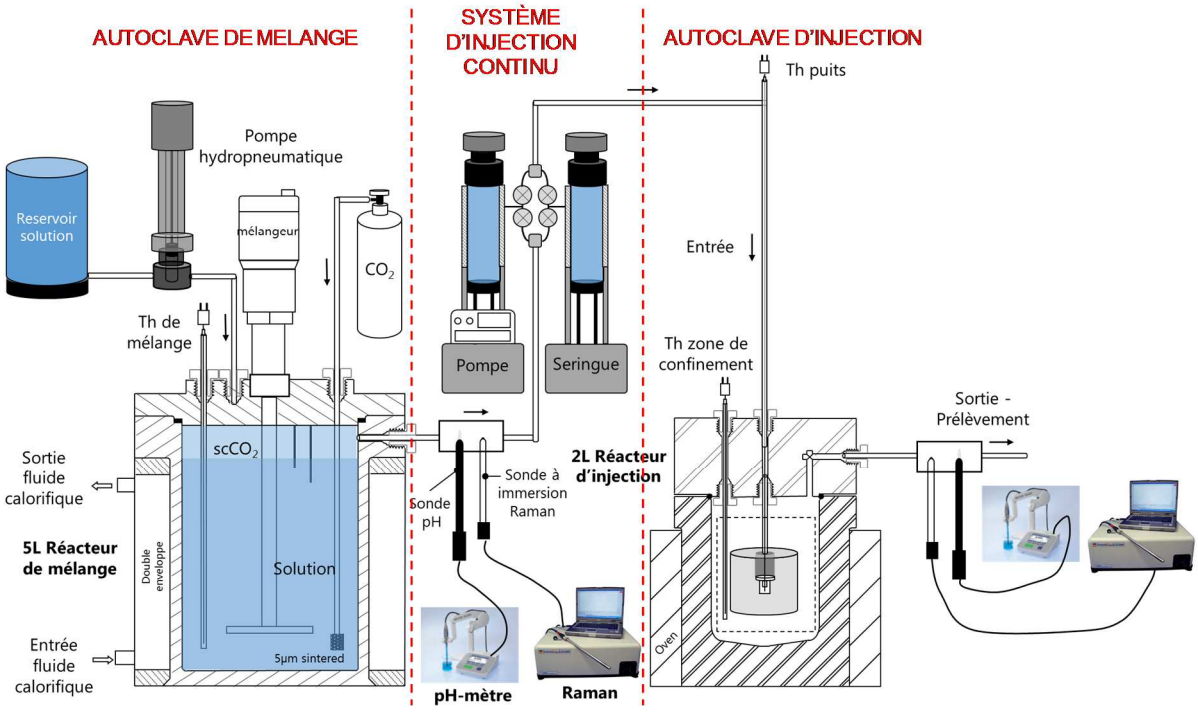

Figure 4 : Schéma de principe du banc d'essai d'injection continue d'une solution monophasique riche en CO_2 (MIRAGES-2) en condition de réservoir géologique.

III. EXPERIENCES REALISEES

Les conditions retenues pour les expériences sont les suivantes : Pression = 120 bars, Température = 60°C, débit d'injection = 150 g · h^{-1}, concentration de CO_2 dans une eau équilibrée avec de la calcite = 0,93 mol · $kg^{-1}$$_{d'eau}$ ($P_{(CO_2)}$ = 30 bar à 20°C) et = 0,88 mol · kg^{-1} d'eau dans une solution saline (15 g de NaCl · L^{-1}) équilibrée avec de la calcite. Sept expériences ont été réalisées afin d'étudier les effets de la durée d'injection (12h, 24h, 25j, 10j, 21j correspondant respectivement aux Exp #2, #3, #4, #5 et #6), de la salinité de la solution injectée (Exp #7) et de l'orientation du puits d'injection par rapport à la stratification de la roche (Exp #5). Avant de réaliser toute expérience d'injection de solution acide, une " expérience blanche " (Exp #1) est réalisée afin d'étudier le comportement du système suite à l'injection d'une solution d'eau pure non-saturée et à l'équilibre avec la pression atmosphérique de CO_2.

Les différentes conditions expérimentales sont listées dans le tableau 1.

Expériences	Pression (bar)	Température (°C)	Débit ($g.h^{-1}$)	Durée d'injection	Chimie de la solution injectée	Solubilité du CO_2 dans la solution réactive ($mol.kg^{-1}$$_{sol}$)	Inclinaison du carottage
Exp #1	120	60	150	20 jours (20d)	Eau milliQ	0	90°
Exp #2	120	60	150	12 heures (12h)	Eau équilibrée (15mg/kg_{sol} $CaCO_3$)	0.93	90°
Exp #3	120	60	150	24 heures (24h)	Eau équilibrée (15mg/kg_{sol} $CaCO_3$)	0.93	90°
Exp #4	120	60	150	2.5 jours (2.5d)	Eau équilibrée (15mg/kg_{sol} $CaCO_3$)	0.93	90°
Exp #5	120	60	150	10 jours (10d)	Eau équilibrée (15mg/kg_{sol} $CaCO_3$)	0.93	55°
Exp #6	120	60	150	21 jours (21d)	Eau équilibrée (15mg/kg_{sol} $CaCO_3$)	0.93	90°
Exp #7	120	60	150	20 jours (20d)	Eau équilibrée (30 mg/kg_{sol} $CaCO_3$ + 15g/L NaCl)	0.88	90°

Tableau 1 : Résumé des expériences. L'angle de l'orientation du carottage dans le bloc de calcaire est défini par rapport au litage.

IV. RESULTATS ET DISCUSSIONS

IV.1. Réactivité de la roche réservoir : Analyse structurale.

L'investigation de la pétrofabrique de l'éprouvette réalisée par micro-tomographie aux rayons X a permis une visualisation interne de l'évolution de l'architecture du réseau de dissolution suite à la percolation du fluide.

Pour toutes les expériences, l'investigation de l'espace vide des échantillons de roche calcaire démontre la présence d'un front de dissolution radial anisotrope de structure ramifiée et complexe qui se développe sur toute la hauteur des parois du puits vers l'ensemble du volume rocheux (Fig. 5). Ces chemins de dissolution préférentiels sont appelés " wormholes ", ils sont de tailles mésoscopiques et sont définis comme dominants [129].

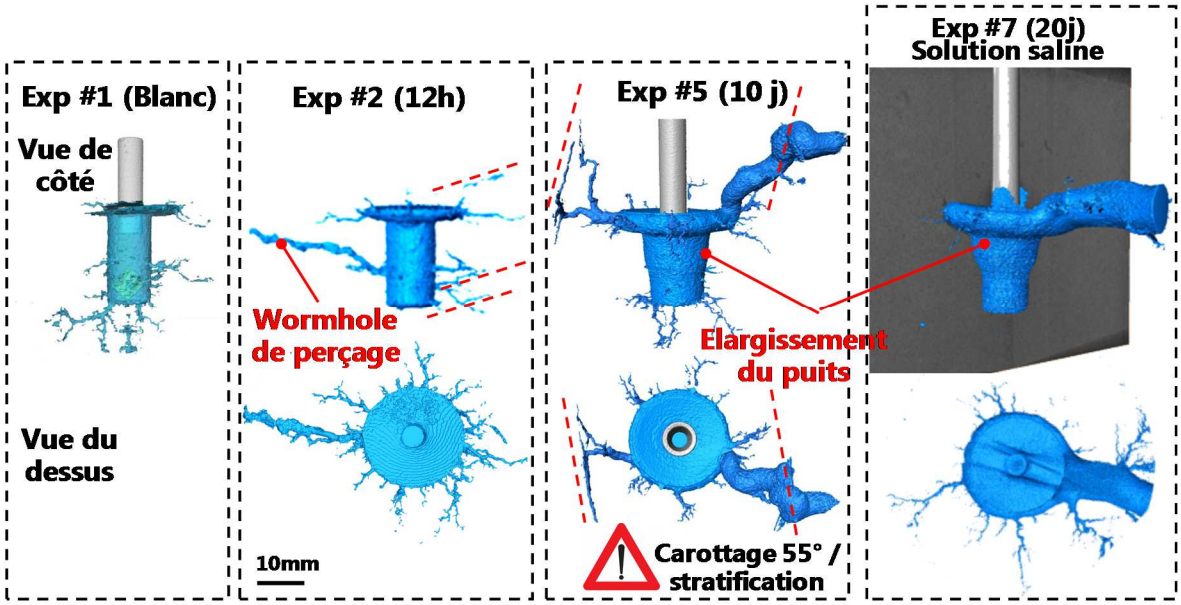

Figure 5 : Illustration 3D des figures de dissolution issue de l'imagerie 3D par tomographie à rayons X. (Vues latérale et supérieure). Exp #1: expérience blanche, Exp#2 : expérience de 12h sans sel, Exp#5 : expérience de 10 jours sans sel et Exp#7 : expérience de 20 jours avec sel. La couleur bleue correspond aux zones de vide au sein de la carotte avec une résolution de 60 µm. Les traits pointillés rouges soulignent les changements de direction des figures de dissolution

Dans le cas de l'injection de solutions acidifiées au CO_2, le réseau de dissolution est plus complexe que dans le cas d'une eau pure ; les wormholes entrent en compétition lors de leur développement et un " wormhole " dit principal perce la carotte. Une fois la carotte percée, ce " wormhole principal " vient drainer la majorité du fluide aux dépens des autres qui sont alors définis comme des " wormholes morts ".

Les morphologies spatiales de ces chenaux hautement conducteurs semblent comparables pour toutes les expériences, exceptées pour l'expérience de 10 jours (Exp #5) où l'échantillon de roche a été foré à 55° par rapport au litage.

Enfin, à partir de 10 jours d'injection, le puits expérimental de forme initialement cylindrique devient conique avec un élargissement continu de sa partie supérieure.

IV.2. Evolution de l'interface ciment-roche.

Après expérience, la carotte est coupée en deux et des lames minces sont réalisées au niveau de zones d'intérêt dont l'interface ciment-roche. La figure 6a représente l'observation microscopique d'une lame mince issue de l'expérience de 21 jours sans sel. Une investigation détaillée a été accomplie à partir d'observations par microscopie électronique à balayage (MEB) (Fig. 6b) en électrons rétrodiffusés.

Les résultats révèlent que l'injection de la solution riche en CO_2 n'a en aucun cas altéré la cohésion mécanique entre le ciment et la roche réservoir où aucune fracture ou fissure significative n'est observée.

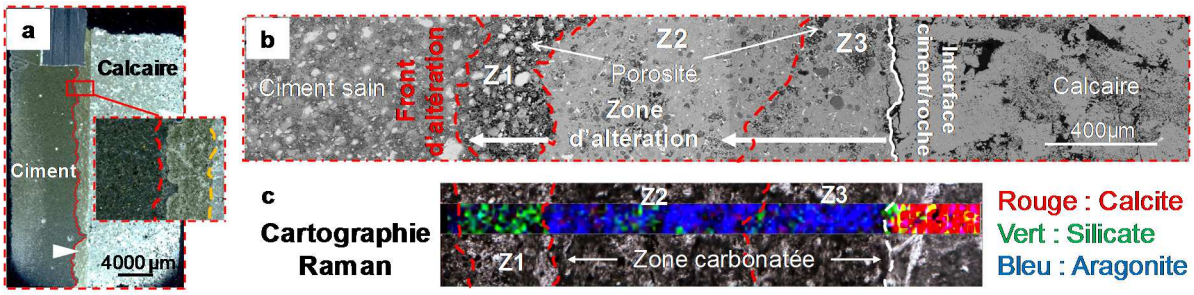

Figure 6 : a) Détail de la lame mince de l'interface ciment-roche avec la zone altérée du ciment (flèche blanche) délimitée par la ligne rouge. Le carré rouge correspond à un focus sur la transition entre le ciment altéré (couleur blanchâtre et brune) et le ciment non altéré (couleur sombre) délimitée par une ligne pointillée rouge. b) Image MEB (BSE) dévoilant l'altération du ciment divisée en trois zones pour l'expérience de 21j sans sel (Exp #6). c) Cartographie Raman à l'interface roche/ciment montrant une forte carbonatation du ciment avec précipitation d'aragonite.

Néanmoins, une zone réactive parallèle à l'interface se développe depuis l'interface vers le cœur du ciment. Les observations MEB (Fig. 6b) soulignent une subdivision de la zone de réaction en 3 sous-zones distinctes (Fig. 6b) largement décrites dans la littérature [54, 190]. Une première sous-zone (Z1) adjacente au ciment non altéré est identifiée. Cette sous-zone est une région appauvrie en portlandite et de porosité plus élevée. Dans les deux autres sous-zones (Z2 et Z3), une matrice dense est détectée avec des précipitations intimement liée à la matrice cimentaire. Le transfert de masse du calcium depuis la zone 1 dominé par le processus de diffusion [76 ; 192 ; 193, 194] couplé à la diffusion des ions carbonates de la solution injectée induit la précipitation de polymorphes secondaires de carbonate de calcium.

L'analyse Raman indique que ces précipitations secondaires correspondent à de l'aragonite (Fig. 6c). La zone proche de l'interface avec la roche (Z3) est plus poreuse que la zone intermédiaire (Z2). Ce phénomène s'explique par une dissolution partielle des carbonates secondaires induite sous l'action de la solution acide renouvelée. Dans les sous-zones Z2 et Z3, les C2S et C3S sont remplacés par une phase de silice amorphe.

IV.3. Chimie de la solution et mécanismes réactionnels.

L'analyse des données *in-situ* du pH issues des diverse expériences (Fig. 7) a été couplée à un travail de modélisation numérique effectué avec le logiciel PHREEQC afin d'interpréter les interactions (et les processus associés) de la solution acide injectée avec les matériaux en fonction du temps et de la salinité.

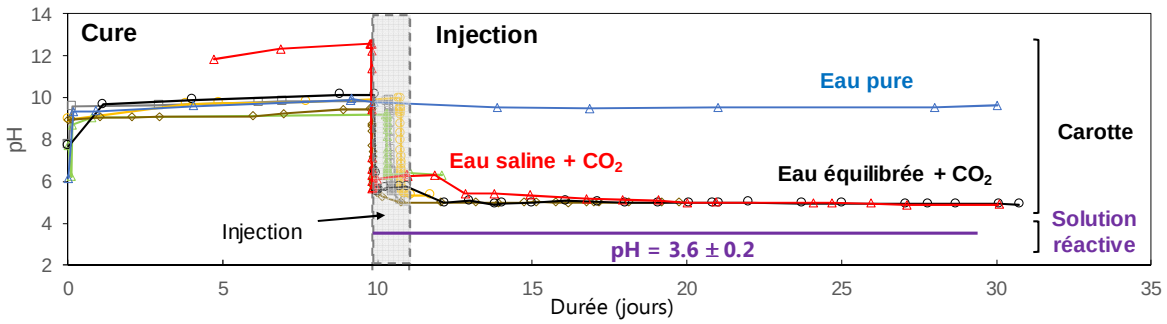

Figure 7 : Mesures des valeurs du pH de la solution en sortie de carotte en fonction du temps pour les différentes expériences. Légende : Courbe bleu : Exp #1 Blanche ; Courbes Jaune, Vert, Marron, et Noire respectivement Exp #3, #4, #5 et #6 d'injection d'eau sans sel et Rouge : Exp#7 d'injection d'eau saline ; courbe Violette : solution réactive injectée.

Le rôle du ciment sur la zone proche puits est dans un premier temps investigué. Pour ce faire, une modélisation géochimique de systèmes simples à 60°C a été réalisée. Ce travail a permis de déterminer des valeurs de pH d'une solution à l'équilibre thermodynamique avec les principales phases solides composant le ciment. Les résultats (Fig. 8) démontrent l'impact majeur de la phase cimentaire sur la valeur du pH de la solution environnante. La valeur du pH expérimental de 10 enregistrée pendant la période de cure (Fig. 7) est proche des résultats calculés pour un système à l'équilibre avec le CSH1.6 et la calcite ou avec la calcite et l'ettringite. Ce pH étant atteint très rapidement (Fig. 7), l'impact de la portlandite sur le pH de la solution est considéré comme mineur. Ces résultats confirment le contrôle des phases CSH et de l'ettringite sur le pH du milieu aqueux pendant la cure.

Minerals	pH
Calcite	9.13
Portlandite	11.36
Ettringite	10.39
CSH1.6	10.5
Calcite+Portlandite	11.36
Calcite+Ettringite	10.39
Calcite+CSH1.6	10.5

Figure 8 : pH à l'équilibre avec différentes phases minérales à 60°C. Calculs réalisés avec PHREEQC et la base de données Thermoddem.

Durant la période d'injection, la présence de la solution réactive riche en CO_2 (valeur expérimentale de pH mesurée à 3,6 à l'équilibre à 20°C (Fig 7, courbe violette) induit une diminution quasi instantanée du pH de la solution interstitielle initiale de la roche et conduit à une réactivité accrue des minéraux du ciment et de la roche dont le mécanisme dominant est la dissolution. Pendant les 2 premiers jours d'injection, une compétition entre les carbonates et la phase cimentaire contrôle la valeur du pH aux alentours de 6. Les observations au microscope électronique à balayage ont révélé, principalement pour l'expérience sans sel, un front réactif dans le ciment à l'interface avec la roche (Fig. 6b et c).

La présence de CO_2 en solution engendre, entre autres, un lessivage du calcium (et du magnésium) du ciment provenant principalement de la dissolution de la portlandite et des CSH, de la lixiviation des C2S et C3S restants et, dans une moindre mesure, de la dissolution de l'ettringite (AFt) et du monosulfate (AFm). Le ciment participe donc activement à l'augmentation de la concentration en calcium (et en magnésium) en solution. Une fois les différentes phases du ciment dissoutes ou carbonatées, le pH est alors contrôlé par un équilibre dynamique entre le renouvellement continu de la solution riche en CO_2 et la dissolution des minéraux carbonatés associée à celle des phases CSH du ciment. L'évolution à long terme du pH atteint alors la valeur stable de 4,9 suite aux 20 jours d'injection de la solution riche en CO_2 (Fig.7).

Pour les expériences avec une solution saline, la cohésion mécanique de l'interface entre le ciment et la roche et également conservée. Cependant, la zone d'altération est beaucoup moins importante avec seulement 2 zones réactives délimitées correspondantes aux zones Z1 et Z2. Ces résultats tendent à démontrer que la présence de sel en solution et son effet inhiberait la dégradation du ciment.

Les analyses chimiques de la solution expérimentales dont les principaux résultats remarquables concernent l'évolution de la concentration en calcium (Fig. 9a) et en magnésium (Fig. 9b) au cours des expériences montrent une augmentation significative de leurs concentrations après injection pour les expériences avec une solution riche en CO_2.

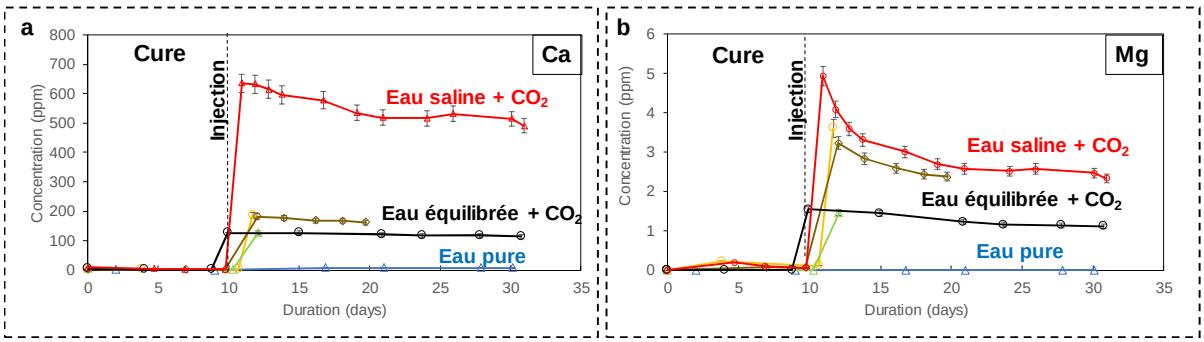

Figure 9 : Analyse chimique (ICP-AES) des échantillons collectés lors des différentes expériences. Les concentrations en (b) ions calcium et (c) magnésium ont été mesurées à la sortie de la carotte et sont tracées en fonction de la durée de l'expérience. Légende : Courbe bleue : Exp #1 Blanche ; Courbes Jaune, Vert, Marron, et Noire respectivement Exp #3, #4, #5 et #6 d'injection d'eau sans sel et Rouge : Exp#7 d'injection d'eau saline.

L'augmentation de la concentration du calcium en solution provient donc du couplage entre la dissolution de la roche calcaire et la réactivité du ciment avec des valeurs maximales atteintes très rapidement après 1 jour d'injection (Fig. 9a : $[Ca^{2+}]$ = 126-212 mg · kg^{-1} et $[Mg^{2+}]$ = 1,5 à 3,3 mg · kg^{-1} en fonction de l'expérience).

La quantité totale de calcium dissous a été déterminée pour chaque expérience à partir des données expérimentales. La figure 10 illustre son évolution en fonction du temps et de la nature de la solution injectée.

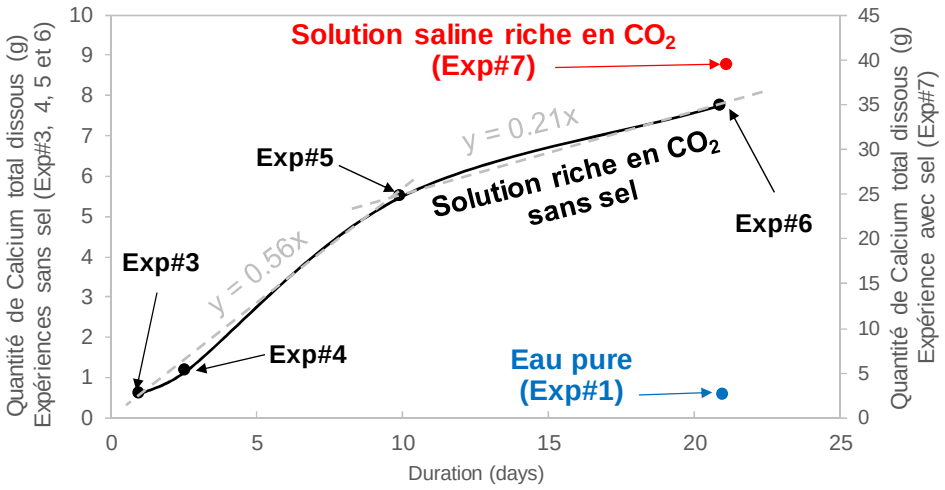

Figure 10: Evolution de la quantité de calcium total dissous en g (courbe noire) pour les expériences sans sel (Exp# 3, 4, 5 et 6). Les pentes des 2 courbes en pointillés correspondent aux taux de dissolution de la calcite (en g/jours) calculés à partir des points de mesure de la courbe noire. Le point bleu correspond à la quantité de calcium total dissous pour l'expérience blanche d'injection d'eau pure (Exp#1) et le point rouge pour l'expérience avec sel (Exp#7).

Pour les expériences sans sel, une diminution du taux de calcite dissoute est observée à partir de 10 jours. Cette tendance est également soulignée par la diminution continue de la concentration en calcium dans la solution expérimentale une fois le pic maximal atteint (Fig. 9a). Ce phénomène s'explique d'une part par l'apparition des chemins de dissolution préférentielle qui entraine une diminution de plusieurs ordres de grandeur de la surface réactive [44] et du taux de réaction de la calcite [177], et d'autre part par la baisse du taux d'altération du ciment avec le temps due à la présence de la zone de forte carbonatation qui joue le rôle de barrière à la diffusion des ions dissous.

Les différents résultats mettent également en évidence une dissolution du calcium beaucoup plus marquée pour les expériences en présence de sel avec une concentration maximale en solution 5 fois plus importante (Fig. 9a : $[Ca^{2+}]$ = 636 mg · kg^{-1}). Ils s'expliquent par une augmentation de la solubilité de la calcite en présence de NaCl en solution même si la $P_{(CO_2)}$ est plus faible et la concentration en carbonate en solution moins importante en raison de l'effet de "salting out".

Les modélisations géochimiques relatives à la réactivité seule de la roche dans les conditions de nos expériences ($P_{(CO_2)}$ déduite pour le système expérimental $CaCO_3/CO_2/H_2O$ à l'équilibre de 56,2 bar correspondant à une fugacité du CO_2 de 44,7 bar et une température de 60°C) avec et sans sel réalisée avec le logiciel PHREEQC et la base de données phreeqc.dat montrent des résultats cohérents avec les observations expérimentales. La concentration calculée de calcite dissoute égale à $2.38x10^{-2}$ mol · kg^{-1} pour l'eau pure et légèrement supérieure en solution saline (mais moins que pour les observations expérimentales) avec une valeur calculée de $3,07x10^{-2}$ mol · kg^{-1}. Il faut également remarquer que les concentrations en calcium dissous mesurées dans la solution expérimentale sont plus faibles pendant toute la période d'injection de la solution acidifié ($0,39x10^{-2}$ mol.kg^{-1} pour l'expérience sans sel

et 1,3x10^{-2} mol.kg^{-1} pour l'expérience avec la solution saline) que celles calculées à l'équilibre thermodynamique avec le code PHREEQC. Cette remarque reflète un déséquilibre constant de la solution par rapport à la calcite confirmant un mécanisme global prédominant de dissolution dans le système pendant toute la durée de l'injection.

IV.4. Evolution des propriétés pétrophysiques de la roche et mécanismes associés

Les images 3D issues de l'analyse par tomographie aux rayons-X des carottes post-expérimentales (Fig. 5) ont montré que l'injection du CO_2 sous forme dissoute a généré un front de dissolution immédiatement au point d'injection. Ces instabilités ont été engendrées par une rétroaction entre les réactions chimiques du fluide avec la roche et le transport des espèces en solution qui se traduit par une localisation du flux dans plusieurs voies préférentielles (" wormholes ") [200; 201]. L'utilisation des nombres adimensionnels de Péclet (*Pe*) de Damköhler (*Da*) a permis de définir le processus dominant (c.-à-d., diffusion, advection ou cinétique de réaction) qui contrôle les phénomènes de dissolution induits par la présence d'acide carbonique. Le nombre de Péclet (*Pe)* exprime l'importance relative du transport par dispersion et/ou diffusion par rapport au transport par advection. Le nombre de de Damkhöler (*Da)* traduit, quant à lui, l'agressivité de la solution vis-à-vis de la roche pour une échelle de longueur donnée (*Da* = fraction d'acide consommée par rapport à la quantité d'acide amenée par convection ou par diffusion). Les résultats des calculs obtenus dans le cadre de cette études ont permis de démontrer que le transport diffusif est dominant (Pe et Da<1) dans les pores de la roche dont les diamètres d'entrée sont les plus petits (0,05 à 7 µm). Dans les macro-pores (300 µm), c'est l'advection (Pe>>1) qui est le mécanisme de transport dominant. Au vu du fort déséquilibre chimique et de la forte réactivité de la roche face à l'injection de la solution enrichie en CO_2, le processus de dissolution global est principalement contrôlé par la cinétique de la réaction chimique (Da>>1) et il est de nature non-uniforme préférentiellement le long des principales voies d'écoulement (macro-pores connectés ou fragilités préexistantes). Ces résultats démontrent que, pour une roche naturelle, les hétérogénéités physiques et structurales (distribution de la taille d'entrée de pores, présence de failles ou de fissures) et minéralogiques, spécifiques à chaque matrice rocheuse, exercent une influence majeure dans le mécanisme de transport réactif, en accord avec les travaux de Noiriel et al., 2015 [204], Smith et al., 2013 [43] et Menke et al., 2017 [199].

Ainsi, le développement spatial et la vitesse de propagation des wormholes qui drainent la majorité du fluide constamment renouvelé sont principalement gouvernés par la pétrofabrique jusqu'à ce qu'un " wormhole " principal atteigne l'extrémité de la carotte. La percée de la carotte est alors responsable d'une évolution des mécanismes de transport réactif dans le temps en fonction de la localisation dans la carotte. En effet, elle modifie la distribution spatiale de la vitesse d'écoulement de la solution au sein de la roche, avec l'existence simultanée de régions d'écoulement préférentiel et de régions de faible écoulement voire de zones stagnantes. La première conséquence concerne l'élargissement progressif du diamètre de chenal dominant au travers duquel circule la majorité du fluide sous l'effet d'une lente érosion chimique.

Une autre répercussion relative au perçage de la carotte est la déformation du puits après 2,5 jours d'injection, conséquence d'une dissolution "uniforme" accrue de sa partie supérieure (Fig. 5). La transformation de la géométrie du puits est attribuée aux modifications de la conductivité hydraulique au sein de ce dernier couplées à des forces de flottabilité (rôle de la gravité). Ces instabilités sont, en effet, liées à un contraste de densité au point d'injection entre la solution fraichement injectée et la solution du puits enrichies en minéraux dissous [219, 220]. Ce phénomène souligne la dépendance spatio-temporelle des modèles de dissolution, essentiellement liée à l'évolution de la structure rocheuse et aux modifications localisées des mécanismes de transport réactif dominants.

Enfin, malgré un environnement acide sous saturé vis-à-vis de la calcite, plusieurs observations microscopiques ont révélé la présence d'une recristallisation localisée sous différentes formes : i) des calcites rhomboédriques au niveau d'une matrice micritique (Fig. 11a) et ii) des agrégats de calcite polyédrique à la surface des oolithes observés sur les parois des " wormholes mésoscopiques morts " (Fig. 11b) (zones correspondant aux régions de faible écoulement définies précédemment). En outre, l'analyse de la projection 2D de la totalité des " wormholes " issus des images acquises par la technique de tomographie aux rayons-X (Fig. 11 c et d) dévoile une diminution significative de la densité de ces " méso-wormholes " avec le temps.

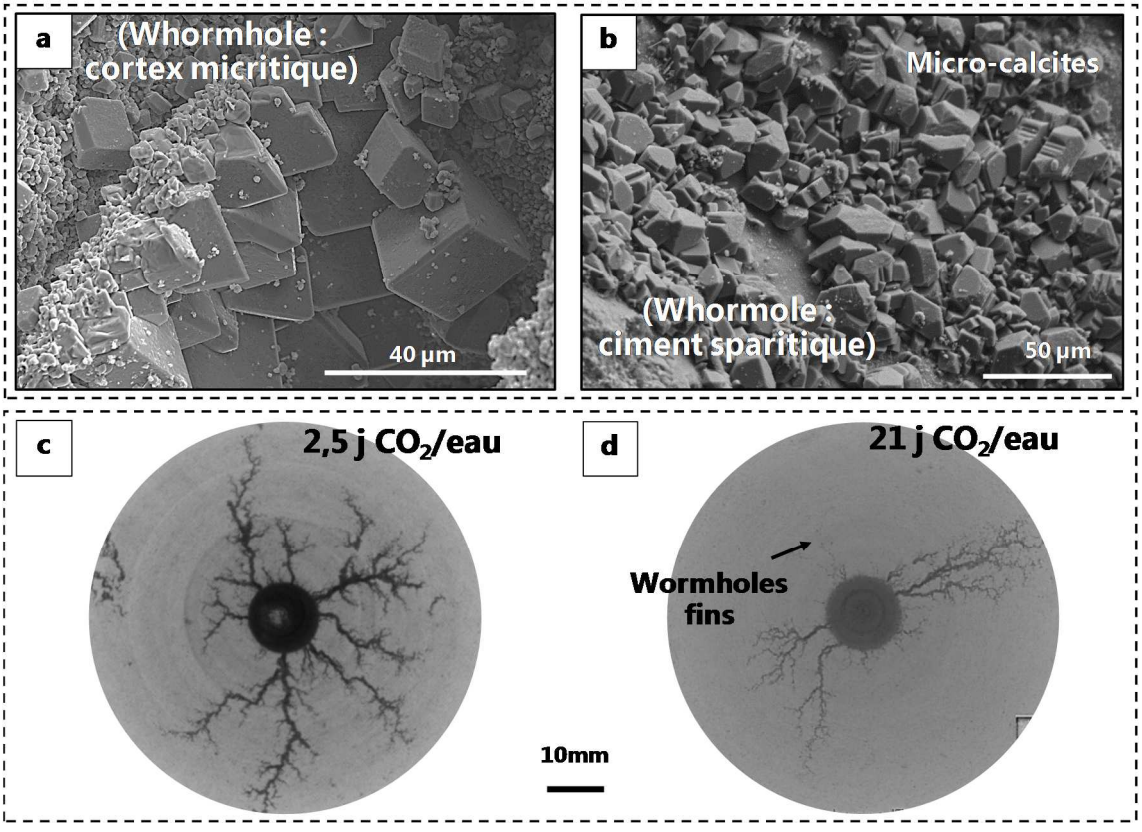

Figure 11 : Observation MEB (BSE) de la carotte issue de l'expérience de 21 jours sans sel : (a) amas de calcite rhomboédrique lisse se développant sur le cortex micritique de la paroi d'un " wormhole secondaire ". (b) agrégats de micro-calcites polyédriques néo-formées à la surface de ciments sparitiques situés sur la paroi d'un " wormhole secondaire ". Observations tomographiques des projections des " wormholes " par superpositions des stacks d'images pour les expérience sans sel (c) de courte durée (2,5 jours) et (d) de longue durée (21 jours).

Les " wormholes morts " apparaissent également beaucoup plus fins pour les expériences de longue durée (Fig. 11d). Ces observations sont d'autant plus importantes qu'elles sont corrélées à la diminution de la concentration en carbone total en solution en sortie de carotte pendant les 10 premiers jours d'injection (Fig. 12). A partir d'un protocole d'analyse des images 3D segmentées, une quantification de l'évolution de la rugosité de ces "wormholes morts" a pu être effectuée. Une cartographie de la topographie des parois des wormholes a donc été réalisée pour chaque expérience sans sel en utilisant le concept de courbure de surface comme descripteur local des irrégularités de surface en 3D. Les résultats ont démontré une augmentation graduelle de ces irrégularités pour les wormholes situés au niveau bas du puits ; augmentation imputée à des précipitations secondaires.

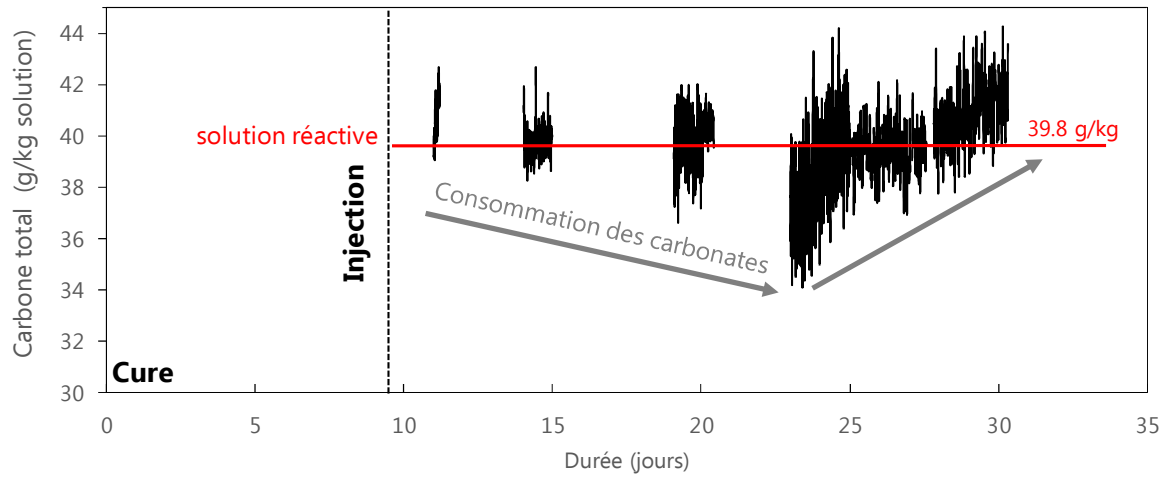

Figure 12 : Expérience de 21j d'injection de solution équilibrée chargée en CO_2 sans sel (Exp#6): Evolution des valeurs de concentrations en carbone inorganique total à l'entrée (rouge) et à la sortie (noir) de l'échantillon en fonction du temps (en kg par kg de solution).

Ces différentes observations et analyses cumulées nous amènent donc à corréler la modification des caractéristiques géométriques des "wormholes morts" en partie basse du puits à un processus de précipitation consécutif à la percée de la carotte. Ces phénomènes de précipitation entraînent alors la réduction du diamètre de ces wormholes voire leur colmatage.

Afin d'expliquer la présence de ces précipitations, l'hypothèse d'une modification locale des interactions fluide-roche suite à l'évolution des mécanismes de transport dominants des espèces en solution, est avancée. Ces bouleversements locaux font suite à l'évolution de la chimie des fluides et de la conductivité hydraulique du milieu poreux après perçage de la carotte.

Dans les aspérités composant les parois des " wormholes morts " qui fournissent une surface spécifique importante (largement corrélée au taux de nucléation hétérogène [225 ; 232]), la réaction chimique initialement contrôlée par la cinétique de réaction devient contrôlée par le transport diffusif des ions en solution. La modification du transport dominant dans ces zones devenues stagnantes engendre un gradient de concentrations des espèces dans la couche limite diffusive à l'interface fluide-roche.

Une sursaturation locale par rapport à la calcite peut alors se produire à l'échelle du pore en raison d'une légère diminution de la $P_{(CO_2)}$ locale liée à la consommation du CO_2 (Fig. 12) et à une augmentation conjointe locale du pH. A ceci s'ajoute un lessivage des ions Mg (Fig. 9b) et Sr (connus pour leur caractère inhibiteur de la précipitation des carbonates) initialement libérés par le ciment qui a pour conséquence une diminution locale de la solubilité de la calcite. La faible sursaturation locale corrélée à un taux rapide de précipitation de calcite peut être suffisante pour permettre la nucléation hétérogène de cristaux de calcite sur les défauts de surface existants où les énergies de surface sont plus faibles [233, 234].

V. MORPHOLOGIE DES RESEAUX DE DISSOLUTION ET RELATIONS AVEC LE CONTEXTE STRUCTURAL

Dans cette partie, une attention particulière est accordée à l'interprétation de la morphologie et de l'orientation des figures de dissolution observées suite à l'injection de la solution acidifiée au CO_2. L'analyse des réseaux artificiels de " wormholes " à travers les différentes expériences menées a permis d'identifier un contrôle directionnel des chenaux de dissolution qui se répètent dans chaque expérience.

Une investigation structurale multi-échelle a ainsi été menée afin de définir le rôle des défauts de la formation hôte, hérités des contraintes tectoniques régionales, sur la direction de propagation des voies de dissolution.

L'orientation initiale des " wormholes principaux " de perçage observés au cours des expériences MIRAGES-2 sont parallèles à la contrainte de compression maximale σ_1, suivant la fente de tension T, direction de plus faible résistance. Ces " wormholes principaux " subissent ensuite un changement de direction contrôlé par le réseau de fractures existant au sein de la roche. L'ensemble des wormholes générés se propagent ainsi dans les volumes affectés par la fracture de cisaillement dextre principal Y (champs de contraintes affectant la zone de Chauvigny où les échantillons de Lavoux ont été prélevés) et par la combinaison des fractures de cisaillement synthétiques R1 et antithétiques R2. De plus, les fractures de cisaillement antithétiques R2, composées de minéraux insolubles résiduels, s'organisent en surfaces slickolitiques qui peuvent constituer des barrières à l'écoulement des fluides. La distribution de la perméabilité et la géométrie de propagation des wormholes s'en trouve alors impactées.

Les résultats ont ainsi mis en évidence le phénomène du contrôle structural de la géométrie spatiale du réseau de dissolution comme le démontre la corrélation entre la direction des différents wormholes et le champ des contraintes régionales principales. L'interaction de l'intra-stratification, du système de fractures et de leurs environnements cinématiques contrôle largement l'orientation des wormholes induits par l'injection d'une solution riche en CO_2.

Les résultats peuvent être mis en œuvre dans l'évaluation des risques liés à l'implantation d'un projet industriel CCS, comme une information supplémentaire sur l'incertitude spatiale et morphologique de figures de dissolution émergentes.

VI. CONCLUSION

Cette thèse soutenue dans le cadre du projet CO2-DISSOLVED intervient dans l'étude de faisabilité technique d'un nouveau concept couplant la récupération d'énergie géothermique au captage et au stockage local du CO_2 sous forme dissoute dans un aquifère salin profond. L'objectif principal est de développer un pilote de recherche à l'échelle du laboratoire en amont de la mise en place d'un pilote industriel.

Le travail réalisé a consisté à étudier l'impact géochimique de l'acidification d'une solution aqueuse par la dissolution du CO_2 sur i) l'altération des minéraux carbonatés dans le réservoir géothermique et sur ii) la phase cimentaire et le tubing composant le puits d'injection. Le développement d'un banc expérimental approprié simulant les conditions réelles est essentiel pour décrire les modifications physico-chimiques et pétrophysiques induites. Les résultats expérimentaux doivent aussi contribuer à valider les modélisations numériques à l'échelle d'une roche réservoir.

Un dispositif expérimental unique (MIRAGES-2) a été mis en place avec succès. Il simule un puits d'injection à l'échelle réduite, qui permet au fluide de circuler librement dans la matrice rocheuse de l'échantillon. De cette manière, le système expérimental rend possible la prise en compte de l'hétérogénéité structurale et texturale de la roche et permet ainsi de comprendre la relation spatiale entre la distribution des discontinuités dans l'échantillon (micro-failles, micro-fissures, changements de porosité, distribution granulométrique...) et l'évolution des phénomènes de dissolution générés par l'injection de la solution acidifiée. De plus, le banc d'essai MIRAGES-2 considère l'impact de la phase cimentaire dans la réactivité globale du système. Il permet également l'acquisition d'une quantité importante de données géochimiques *in-situ* qui contribuent à améliorer les paramètres d'entrée des simulateurs de transport réactif et ainsi à réduire les incertitudes relatives aux scénarios de stockage géologique du CO_2.

Sept expériences d'écoulement radial dans des conditions géologiques (P= 120 bar et T = 60°C) ont été réalisées sur plusieurs durées (de 12 heures à 21 jours) avec de l'eau douce et une solution saline équilibrées, toutes deux enrichies en CO_2 ($P_{(CO_2)}$ = 30 bar). Elles ont été couplées à des outils originaux d'analyse chimique *in-situ* de la solution aqueuse développés au laboratoire GeoRessources (sondes Raman HP/HT *in-situ*) et désormais utilisés en routine. Le pH a également été contrôlé à l'aide d'instruments de mesure *in-situ*. Une étude microscopique de la matrice rocheuse à différents endroits a été réalisée et la technique d'imagerie par tomographie aux rayons X a été utilisée pour la visualisation 3D et la quantification de l'évolution de l'architecture et de la topographie du milieu poreux.

Les résultats ont montré que l'injection de la solution chargée en CO_2 déclenche des déséquilibres géochimiques importants à proximité immédiate du puits dus à la diminution du pH, entraînant un réarrangement de l'espace poral suite à des processus de dissolution/précipitation. La dissolution est dominée par la cinétique de réaction (limitée par le transfert de masse) qui, couplée à une importante force motrice convective, se traduit par l'apparition d'un réseau dendritique radial sous forme de chenaux définis comme "wormholes dominants". La percée de la carotte par un

" wormhole principal " induit une discontinuité du champ de vitesse qui perturbe la propagation des autres " wormholes ". Le " wormhole dominant " draine alors la quasi-totalité du fluide injecté et contrôle les transferts de masse empêchant l'alimentation en réactifs des autres " wormholes " qui deviennent des zones stagnantes. De plus, suite au perçage de la carotte, un couplage complexe entre des effets de contrastes densitaires au sein du puits, de modification de la conductivité hydraulique en région proche puits et de réactivité chimique conduit à une modification de la forme du puits d'injection qui devient conique avec le temps en raison d'une dissolution préférentielle de la partie supérieure.

Des cristaux de calcite néoformés ont été détectés à différents endroits de la carotte suite aux expériences longue durée. Ces précipitations sont attribuées à des gradients de pH locaux dans le voisinage immédiat de l'interface ciment-roche et à des changements locaux de l'indice de saturation (évolution des concentrations d'ions en solution tels que Ca^{2+}, Mg^{2+} ou Sr^{2+}, modification du transport réactif dominant) dans les zones stagnantes suite à la percée de la carotte.

La comparaison avec l'échelle régionale des résultats expérimentaux a permis de démontrer le contrôle structural de la propagation des réseaux de dissolution comme le démontre la corrélation entre la direction des différents "wormholes" et le champ de contrainte régional. Les résultats ont révélé que les nombreuses hétérogénéités de l'échantillon (fissures, fractures, déformation des pores...) acquises lors d'épisodes cinématiques intenses contrôlent les figures de dissolution induites par l'injection de fluides riches en CO_2.

Les résultats expérimentaux de MIRAGES-2 fournissent donc une base solide pour déterminer un scénario d'injection et un cadre assurant la sécurité opérationnelle du procédé CO2-DISSOLVED. En effet, les résultats obtenus réduisent sérieusement les incertitudes spatiales et morphologiques liées au développement des figures de dissolution localisées en confirmant le rôle clé des hétérogénéités structurales de la roche réservoir. Ils démontrent l'importance d'intégrer, à l'échelle de la maille dans les modèles numériques prédictifs de terrain, la variabilité spatiale des propriétés hydrodynamiques induites par la réactivité géochimique. Un des intérêts principaux en amont de la mise en œuvre du doublet géothermique serait, par exemple, de pouvoir optimiser le positionnement du puits de production par rapport au puits d'injection (loin des fractures potentiellement existantes) afin de minimiser la percée du système et d'augmenter la durée de vie du doublet et l'efficacité du stockage à long terme. La modification du puits est également un paramètre majeur à prendre en compte. En effet, une dissolution compacte trop importante du puits pourrait impacter la résistance mécanique du réservoir créant ainsi des instabilités et un endommagement du puits injecteur.

Enfin, par analogie, les précipitations observées dans les zones stagnantes et un colmatage potentiel de la porosité aux abords du puits pourraient se produire lors d'une opération d'arrêt d'injection. Ce phénomène altérerait l'hydrodynamique du système lors du redémarrage de la phase d'injection.

En perspectives et puisque le système simulé dans cette étude était relativement simple, il serait utile d'étudier d'autres type de roches réservoirs (silico-clastiques par exemple) ayant une histoire tectonique différente et percolées par des fluides plus complexes. Ceci permettrait de suivre la réponse de différents types de réservoirs (réactivité différente des silicates en milieu CO_2) et des matériaux de puits (pas d'effet tampon carbonate dans une roche siliceuse) à l'injection de CO_2 dissous. L'application de cette étude au stockage géologique du CO_2 nécessite également de connaître et quantifier les régimes de contraintes mécaniques qui ont une influence sur la solubilité des minéraux et qui ne sont pas considérés dans cette étude.

– INTRODUCTION GÉNÉRALE –

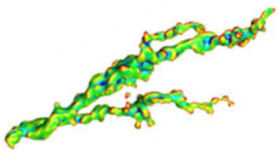

Présentation du contexte général

La prise de conscience de l'urgence climatique date des années 70-80 avec en 1979 la première Conférence mondiale sur le climat à Genève. Le 5ème rapport du GIEC (Groupe Intergouvernemental d'Expert sur l'Evolution du Climat) de 2014 [1] a clarifié le rôle des activités anthropiques et de la hausse continue de la demande énergétique mondiale dans l'accroissement du phénomène d'effet de serre. Le dioxyde de carbone, en tant que produit primaire de l'oxydation ou de la combustion des énergies fossiles contribue ainsi pour environ 66 %[1] au forçage radiatif des GES à longue durée de vie (3,1 $W.m^{-2}$ au total) et est responsable à 82% de son augmentation au cours des dernières décennies [2]. Les émissions globales de la France ont été estimées, en 2017, à 441 $MtCO_2$ équivalent/an [3]. Face au défi défini en 2015 lors de conférence de Paris (COP 21) de limiter avant 2050 le réchauffement climatique à 1,5°C [4], la France s'est fixé l'objectif d'une transition énergétique axée sur une économie décarbonée [5]. Cette stratégie de neutralité carbone s'emploie à mettre en œuvre la technologie de Captage et Stockage du CO_2 (CSC) afin d'atteindre une réduction de 5 Mt CO_2/an des émissions liés au secteur industriel [5]. Plusieurs autres voies de recherche sont actuellement explorées (l'amélioration de l'efficacité énergétique, l'usage de combustibles à faible empreinte carbone tels que le gaz naturel, l'hydrogène ou l'énergie nucléaire, l'augmentation des puits biologiques de carbone, les technologies telles que la capture directe d'air (DAC), le déploiement des énergies renouvelables telles que l'éolien, le solaire, l'hydraulique et la production de carburants de synthèse issus de sources d'énergie verte (bioénergie),…) et joueront un rôle grandissant dans l'évolution d'une économie à faibles émissions de carbone. Cependant, elles ne peuvent constituer une réponse complète et suffisante. Les technologies de capture à partir de gros émetteurs de CO_2 et de stockage en réservoir géologique ou d'utilisation industrielle apparaissent comme des solutions efficaces pour atteindre les scénarios les plus ambitieux.

Le concept de CSC correspond à une chaîne intégrée de technologies consistant (1) à capter et isoler le CO_2 émis par une unité industrielle, (2) à le transporter de la source vers un lieu de stockage adapté et enfin (3) à l'injecter et le stocker sur le long terme dans un réservoir géologique profond [6].

Les trois formations géologiques généralement concernées pour le stockage du CO_2 sont: les gisements de gaz ou de pétrole déplétés (ou en cours d'exploitation) dont la capacité de stockage globale mondiale est estimée entre 675 et 900 $GtCO_2$ [7], les gisements de charbons non exploitables (entre 40 et 200 $GtCO_2$ [7]) et les aquifères salins profonds qui est l'option offrant la plus grande capacité de stockage (1 000 à 10 000 Gt CO2) [7]. En France, le potentiel de captage et stockage de CO_2 est évalué à 24 $MtCO_2$/an, notamment au sein des grands bassins sédimentaires tels que le bassin parisien. L'injection dans les formations salines profondes peut être réalisée en mer (off-shore) ou sur terre (on-shore). En Europe, le stockage est pour le moment principalement réalisé en mer (bassin de la mer du Nord/Sleipner) où la perception du

[1] Ce pourcentage est calculé comme la contribution relative du gaz mentionné à l'augmentation du forçage radiatif global causé par tous les gaz à effet de serre à longue durée de vie depuis 1750.

public à l'égard des activités off-shore est différente de celle des préoccupations locales on-shore.

Actuellement, 23 projets à grande échelle, dont la majorité est directement liée à la récupération assistée du pétrole (RAP ou CO_2-EOR), sont opérationnels ou en construction dans le monde (Fig. 1) pour une capacité de stockage de 40 Mtpa (Méga tonnes par an) de CO_2 soit moins d'1% des émissions de l'Union européenne. 18 projets commerciaux sont actuellement en cours, dont 10 recensés aux Etats Unis et 9 sous la forme de RAP.

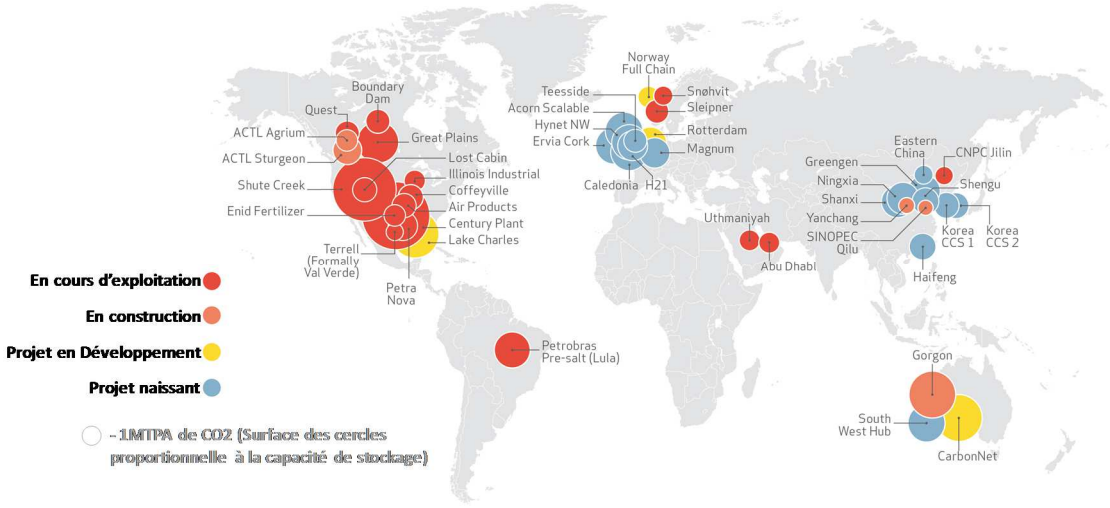

Figure 1 : Liste des installations de CSC à grande échelle en opération, en construction ou en phase de projet (Source : Global CCS Institut (2018). Global status of CCS 2018).

En France, le développement à grande échelle du CSC est cependant limité en raison d'incertitudes économiques (coût important de mise en œuvre), d'absence de régimes juridiques et financiers appropriés ou encore par manque d'infrastructures existantes (par exemple les réseaux de pipelines nécessaires au déploiement commercial généralisé du CCS) et se heurte régulièrement à une opposition sociétale locale. Ce dernier point est d'ailleurs en grande partie responsable du manque de soutien de la part des instances gouvernementales à traduire un contexte législatif qui inciterait à la mise en œuvre d'exploitations de CSC. L'instauration d'une taxe carbone comme mécanisme de pénalisation des principales sources émettrices est un élément fondamental dans le processus de décision des exploitants. Cependant, le cours de la tonne de CO_2 qui varie d'un pays à l'autre, est actuellement insuffisant. Plafonné en Europe en dessous de 10 euros la tonne jusqu'en 2018, des aménagements dans la règle du "quota CO_2" par l'Union Européenne conduit à une augmentation du cours qui atteint 26 euros aujourd'hui [8]). Elle offre ainsi aux entreprises privées un bénéfice marginal par rapport à l'investissement important requis.

La filière CSC française semble de plus n'être applicable qu'à un nombre limité de sites industriels, principalement les gros émetteurs (centrales de production d'énergie ou encore les cimenteries, raffineries, usines chimiques et pétrochimiques…). Face aux différents verrous, l'émergence de projets isolés à plus petite échelle apparaît alors comme une solution alternative.

Parmi l'éventail d'offres technologiques de séquestration du CO_2 anthropique, le couplage entre CSC et géothermie s'affiche comme option d'énergie verte d'intérêt et d'avenir comme cela a été souligné dans un rapport de l'IEAGHG (International Energy Agency of the GreenHouse Gases) [9]. L'association du captage à la production d'énergie verte apporte en effet une plus-value qui améliorerait la viabilité économique du CSC [10, 11] tout en assurant une empreinte carbone négative à l'industriel. Initialement, ces applications utilisent le CO_2 sous forme supercritique à des fins de récupération d'énergie géothermique généralement optimisée par la production d'électricité [12 ; 13 ; 14 ; 15]. Plusieurs stratégies de système géothermique stimulé (SGS) [16 ; 17] ou autres projets pilotes [18] (GEOSYNERGY [19] au Danemark, CarbFix [20] en Islande, Wallula Basalt Pilot Project [21] aux Etats-Unis ou encore GeoThermae en Croatie) ont émergé depuis une vingtaine d'années. Cependant, les opportunités réelles de mise en œuvre restent limitées de par les incertitudes concernant la gestion du risque mais surtout par une disponibilité concomitante limitée de ressources géothermiques et de grands émetteurs de CO_2.

L'alternative recommandant une dissolution de surface du CO_2 dans une saumure préalablement extraite et le choix de cibler des petits émetteurs industriels (10 à 100 $ktCO_2$/an/doublet) pourraient faire office de pont entre les projets pilotes de grande ampleur et la mise en place d'opérations matures de CSC ciblant de grosses sources industrielles de CO_2. Ce concept de stockage de CO_2 combinant une injection sous forme dissoute à la récupération de chaleur géothermique, n'avait encore, à l'ébauche du projet CO2-DISSOLVED à l'origine de cette étude, jamais été décrit dans la littérature.

Objectif de l'étude

L'implantation de toute installation industrielle impose une identification complète des risques sur l'ensemble du système afin d'en évaluer les impacts possibles sur l'environnement et la santé humaine. Dans le cadre du projet CO2-DISSOLVED proposant l'injection du CO_2 sous forme dissous dans l'eau de réservoir, une réactivité accrue à proximité immédiate du puits d'injection va être induite du fait de la formation d'acide carbonique, en particulier en présence de minéraux carbonatés. De même, la solution acidifiée sera beaucoup plus agressive pour les différents éléments du puits (ciment, casing) qu'un fluide géothermal issu d'un doublet géothermique conventionnel.

La grande majorité des études sur l'impact des interactions chimiques entre un fluide riche en CO_2 et la roche, le casing ou le ciment interviennent dans le contexte d'une injection de CO_2 en réservoir géologique sous forme « supercritique ». La zone simulée correspond à la région extérieure (ou périphérique) à la zone d'injection du puits, environnement où le CO_2 commence à se dissoudre dans l'eau salée et où le déséquilibre chimique est maximal [22]. Il en est de même pour les études d'impact de la réactivité du CO_2 dans le cadre d'un système CO_2-SGS (Système Géothermique Stimulé) [23 ; 24]. La technologie de captage et d'injection propre au concept CO2-DISSOLVED va provoquer une réactivité immédiate en sortie de casing entre les phases en présence. Une bonne compréhension des phénomènes complexes induits

aux abords du puits d'injection apparaît alors essentielle pour fournir des modèles d'évaluation des risques fiables (prévention de fuites, intégrité du réservoir, interférence avec un aquifère voisin…) et d'aide au dimensionnement du doublet (positionnement optimal pour optimiser la productivité du process). Pour ce faire, l'altération expérimentale des différents matériaux étudiés est une bonne alternative afin d'agrémenter les bases de données des modèles prédictifs à l'échelle du doublet.

L'objectif principal de mon implication dans ce projet consiste alors à mettre en place un banc d'essai de laboratoire reproduisant au plus près les conditions d'un puits d'injection avec ces différentes interfaces (ciment/casing, ciment/réservoir et ciment/réservoir/couverture). Il doit assurer une certaine souplesse expérimentale garantissant la possibilité de tester une large gamme de matériaux (ciment, roche, casing) et de compositions du fluide injecté (CO_2, gaz co-injecté, eau saline) dans des conditions géologiques variées (pression, température, gradient de température et de pression, temps de résidence). Le design développé doit également offrir au fluide la capacité de circuler librement dans l'espace poral de l'échantillon. De cette façon, le système expérimental considère l'hétérogénéité structurale de la roche et permet d'investiguer la relation spatiale entre la distribution des discontinuités (microfailles, microfissures, changements de lithologie, de faciès…) dans l'échantillon et l'évolution des phénomènes de dissolution ou de précipitation aux abords du puits.

De plus, ce banc d'essai doit garantir l'acquisition d'une quantité importante de données géochimiques *in situ* permettant de modéliser numériquement le transport réactif induit.

De cette façon, les résultats aideront à :

- valider la sélection des matériaux de construction du puits afin de minimiser tout dommage potentiel relatif à la présence du CO_2 dissous,
- valider les conditions opératoires de la phase d'injection (débits, concentration de CO_2,…),
- vérifier les conditions thermiques locales en sortie de puits d'injection,
- quantifier les taux et les figures de dissolution/précipitation pour assurer une meilleure injectivité,
- optimiser l'emplacement des puits producteur et injecteur à partir de l'interprétation spatiale de la morphologie des réseaux de dissolution. Une prévision de la migration du panache de CO_2 permettra de maximiser la durée de vie des installations géothermiques ainsi que la séquestration du CO_2.

Ce mémoire se focalisera principalement sur la réactivité géochimique d'une roche calcaire et l'étude structurale des réseaux de dissolution générés. La réalisation de cette étude expérimentale couplée à une modélisation numérique servira d'outil d'aide à la décision dans une démarche sécuritaire du projet CO2-DISSOLVED.

– PARTIE 1 –
LE PROJET CO2-DISSOLVED

– PART 1 –
THE CO2-DISSOLVED PROJECT

I. Principe

Le projet CO2-DISSOLVED est soutenu par l'ANR et le GIS Géodénergies. Il est piloté par le BRGM et il a la vertu de regrouper dans son consortium des partenaires multidisciplinaires (CFG Service, ENERTME, GEOGREEN, IRENE, le laboratoire d'économie d'Orléans, Pi-Innovation, l'UMR 5319 passage et l'UMR 7359 GeoRessources). Son objectif est d'évaluer la viabilité d'un concept novateur combinant l'injection et le stockage de CO_2 anthropique sous forme dissoute en aquifères salins et la récupération de chaleur géothermique [25 ; 26]. Ce concept cible les petits émetteurs industriels (< 150 kt/an) qui ne sont généralement jamais intégrés dans des projets de CSC. L'approche repose sur la technologie d'un doublet géothermique basse enthalpie standard qui consiste à pomper une saumure chaude par un puits producteur afin d'en récupérer les calories en surface par le biais d'échangeurs puis de réinjecter, dans le même aquifère, la saumure refroidie chargée en CO_2 dissous par un second puits, à proximité immédiate de la source émettrice (Fig. 2).

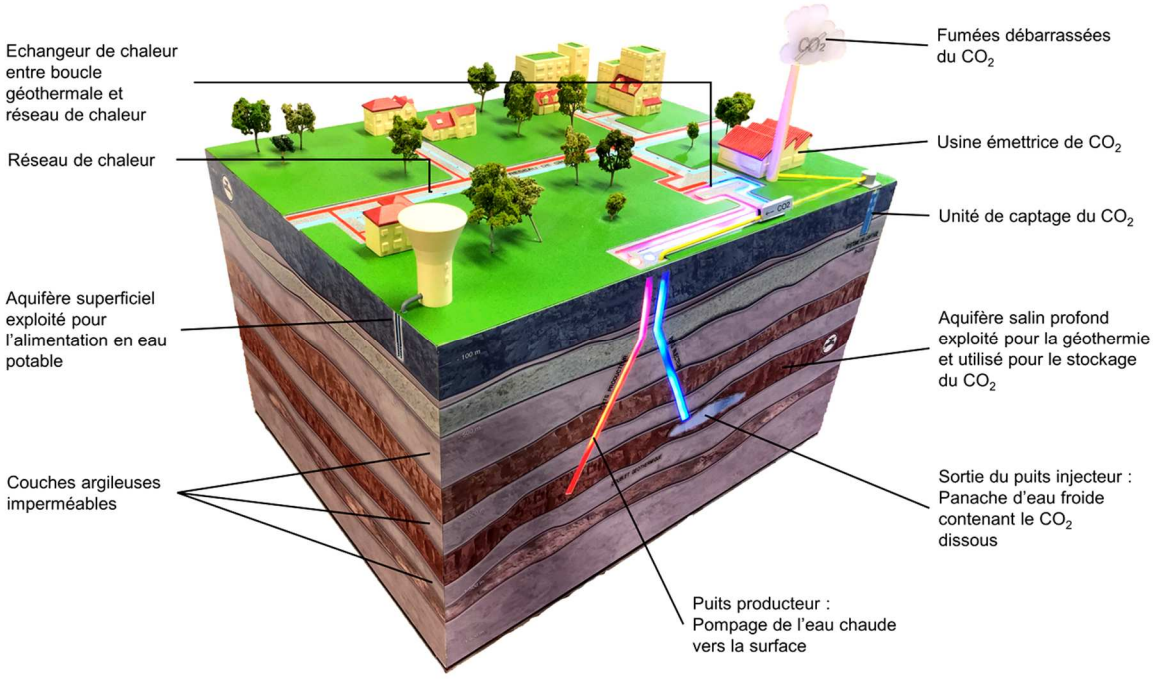

Figure 2 : Représentation schématique du concept CO2-DISSOLVED combinant le stockage du CO_2 sous forme dissoute et la récupération de chaleur géothermique via un système de doublet (http://co2-dissolved.brgm.fr/).(@BRGM)

Cette approche offre aux industriels plusieurs avantages :

- un gain énergétique par le bénéfice direct et local des calories produites pour les besoins en chauffage du process industriel impliqué et/ou pour alimenter un réseau de chaleur urbain environnant,

- un gain financier par le revenu généré par l'utilisation de cette énergie verte produite qui permettra, entre autres, de valoriser l'investissement relatif aux coûts des infrastructures propres aux étapes de captage et d'injection. À ces revenus peuvent s'ajouter les crédits « carbone » dont la valeur pourrait être revue à la hausse dans les années à venir. De plus, le projet ayant vocation à être une solution locale, les coûts liés au transport de CO_2 sont minimisés.

- un bénéfice environnemental avec une empreinte carbone négative directement liée à la séquestration des gaz à effet de serre en bassin sédimentaire.

En outre, l'option d'injecter le CO_2 sous forme dissoute par rapport à l'état supercritique offre des avantages notables en termes de réduction de risques et de potentiel de minéralisation accélérée [27]. L'absence de phase gazeuse et les effets de densité favorables (l'eau salée riche en CO_2 réinjectée est légèrement plus dense que l'eau de formation) permettent de s'affranchir des problèmes inhérents à l'approche « classique » comme la montée en pression du réservoir, la migration de la saumure et du CO_2 vers les formations géologiques sus-jacentes.

Une étude préliminaire réalisée dans le cadre du projet a inventorié pour trois pays (France, Allemagne et Etats-Unis) [25] les candidats potentiels à l'application industrielle du concept CO2-DISSOLVED. En France (Fig. 3) les émetteurs répertoriés au nombre de 650 représentent 25% de la totalité des émetteurs de CO_2 référencés.

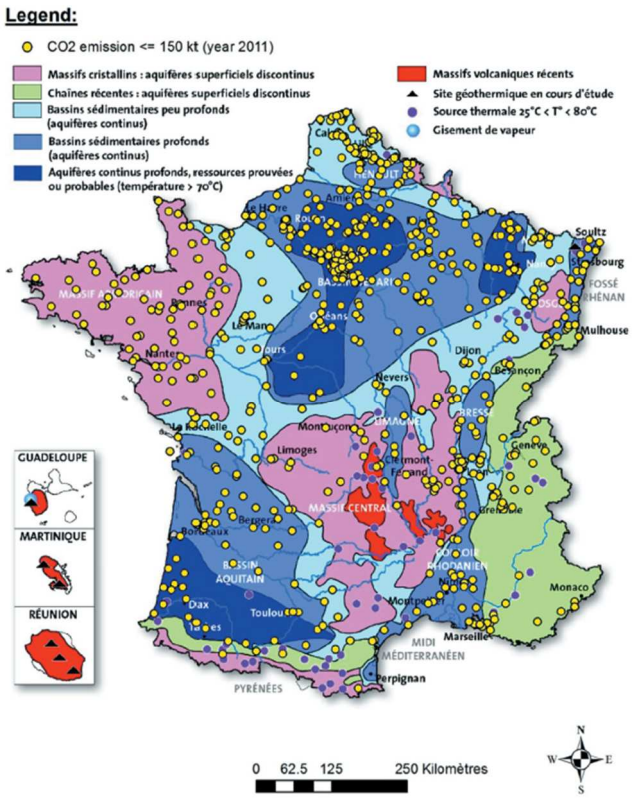

Figure 3: Petits à moyens émetteurs industriels de CO_2 (ca. 10-150 kt/yr) et sites géothermiques sur la carte géologique de la France simplifiée (Castillo et al., 214 [28] ; (Points jaunes, données IREP 2011)).

Le caractère innovant du projet réside aussi dans le choix d'une technologie double de captage et de dissolution en puits profonds (propriété du partenaire américain du projet Partnering in Innovation (Pi-innovation)) initialement conçue pour des applications de RAP et de SGE [29]. En résumé, le premier aspect de cette solution technologique (dénommée Pi-CO_2) propose un procédé de séparation post-combustion qui utilise l'eau comme solvant physique pour capter le CO_2. Elle consiste en une boucle fermée remplie d'eau, composée d'un absorbeur naturel et d'un désorbeur par inversion de pression, le tout installé dans un puits étanche profond (ca. 300-600 m) de large diamètre (ca. > 1 m). Ce puits artificiel fonctionne alors comme une enceinte close profonde qui permet d'imposer au gaz une gamme de pressions hydrostatiques : de la pression atmosphérique jusqu'à 60 bar environ. Ainsi, les gaz émis par l'industriel sont injectés dans l'eau de ce réacteur naturel et les deux phases circulent dans un système d'absorption par transfert de masse en cascade (Mass Transfer System MTS en anglais). La pression naturellement imposée permet ainsi de maximiser la solubilisation du CO_2 dans l'eau qui est ainsi séparé des gaz annexes non dissous dans les mêmes conditions thermodynamiques. L'eau chargée retourne ensuite à la surface depuis le MTS et est soumise à une pression de moins en moins importante ce qui permet le dégazage de CO_2 quasi pur. Les autres gaz sont par la suite séparés de façon séquentielle en surface. Les dimensions du système de séparation MST ne permettent pas de l'intégrer directement en tête du puits d'injection et nécessite donc la mise en place d'un puits annexe pour l'abriter (Fig. 4). Il est évidement possible d'utiliser une des technologies de captage existantes (amines, membranes,…) mais en gardant à l'esprit leurs incidences économiques et environnementales moins favorables.

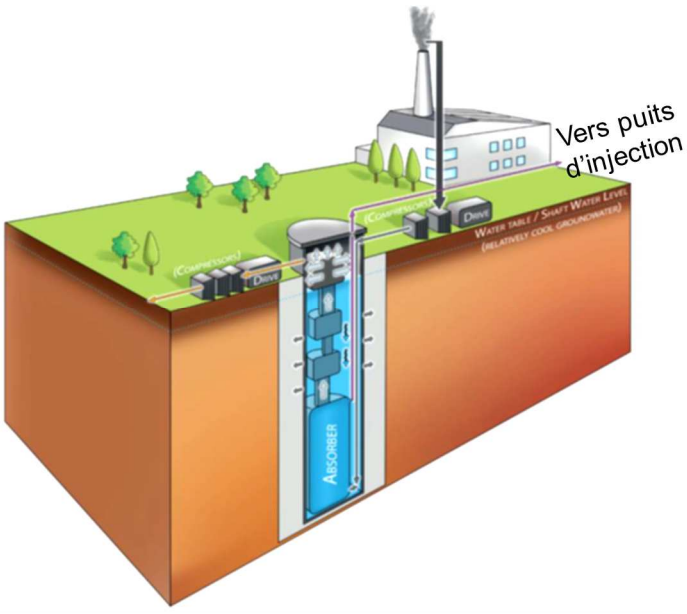

Figure 4 : Pi-CO2 : Prototype de technologie de captage du CO_2 par absorption avec un système de transfert de masse en cascade (adsorber) (@BRGM).

Une fois séparé, le flux de CO_2 capté est acheminé vers le puits d'injection sous forme gazeuse. La solution technique proposée pour l'injection du CO_2 sous forme dissoute est alors d'utiliser un barboteur positionné à une profondeur appropriée dans le puits

d'injection en fonction du débit massique de CO_2 à injecter et de la limite de solubilité de ce dernier dans la saumure. Sous l'effet du débit et des conditions de pression et de température en profondeur (20 bar en tête de puits), ce système garantit la dissolution totale du CO_2 avant son arrivée dans l'aquifère hôte.

Deux types de designs sont alors proposés en fonction des quantités de CO_2 concentrées dans le flux de gaz :

- quand les gaz de combustion contiennent une concentration très élevée en CO_2 comme dans le cas d'une oxy-combustion, l'unité de séparation n'est pas nécessaire. Le CO_2 pourrait alors être directement co-injecté avec de l'eau dans le puits d'injection.

- Lorsque la teneur en CO_2 dans les fumées émises est plus faible, dépassant une valeur seuil de 10%, ce qui est le cas le plus général, la mise en place du procédé de séparation des gaz annexes est nécessaire en amont du système de co-injection placé dans le puits injecteur.

Une modélisation chimique et thermodynamique a été réalisée et montre d'excellentes prédictions de la solubilité du CO_2 dans les conditions proposées et de sa séparation des fumées par solubilisation différentielle [29]. Une modélisation de l'écoulement des fluides multiphasiques a également démontré que la configuration du système proposée permettrait d'atteindre l'équilibre et que le transfert de masse associé assurerait la récupération par solubilisation de 90% du gaz d'intérêt dans le solvant physique (solution aqueuse) après 12 étapes de fonctionnement en cascade. En parallèle, les premiers tests techniques ont donné des résultats très satisfaisants au stade du banc d'essai de laboratoire ainsi qu'à l'échelle du pilote industriel [30].

II. Risques liés à la partie stockage du projet

Dans le cas d'un projet novateur lié à une technologie originale, comme c'est le cas pour CO2-DISSOLVED, une méthodologie d'évaluation des risques spécifiques et de calcul de leur criticité doit être développée, d'autant plus que la filière émergente du CSC dans son ensemble ne bénéfice, à l'heure actuelle, que d'un retour d'expérience limité. Pour les besoins du projet, seuls les risques liés au stockage et au bon comportement du site et des forages pendant la phase opérationnelle ont été examinés. Les risques liés aux installations industrielles de surface seront pris en compte lorsque la technologie et les procédés seront arrivés à maturité. Enfin, le projet ayant vocation à proposer un intérêt économique à l'industriel impliqué, les risques associés à la performance de l'installation doivent également être pris en compte.
Les risques relatifs au stockage sont différents de l'approche classique d'une injection sous forme supercritique en raison du choix d'une stratégie de « dissolution de surface ». Dans un premier temps, l'injection de la saumure refroidie riche en CO_2 renforce le contraste de densité de telle sorte que l'eau injectée migre naturellement vers les couches les plus profondes de l'aquifère. De cette façon, les risques de migration du CO_2 par effet de densité vers les couches supérieures sont très faibles.

De plus, l'utilisation concomitante des 2 puits du doublet (pompage et réinjection) dans la même formation dispensera l'aquifère de stockage de la surpression induite lorsque le CO_2 y est injecté massivement sous forme supercritique. Les perturbations hydrodynamiques et géochimiques attendues resteront théoriquement principalement localisées autour des deux puits, réduisant significativement le déplacement non maîtrisé de la saumure sous l'effet de la mise en place de la bulle de gaz qui est observée dans l'approche CSC standard.

Bien que minimisés, les risques inhérents à l'injection du CO_2 sous forme dissoute doivent encore être étudiés principalement à cause des interactions chimiques entre la solution réinjectée, les minéraux formant la roche et les matériaux du puits d'injection.

Ainsi, quatre familles de risques principaux spécifiques ont été retenues pour l'application propre à CO2-DISSOLVED [31 ; 32]:

1. *Le recyclage thermique* : Cet aspect ne concerne pas directement les phénomènes impactant l'homme ou l'environnement mais plutôt les évènements préjudiciables à la productivité du process. Le recyclage thermique se définit par l'arrivée du fluide réinjecté, après exploitation de ces propriétés thermiques, au niveau du puits de production. Une diminution progressive de l'écart thermique exploitable peut avoir lieu limitant ainsi la rentabilité de l'installation. L'exploitation du doublet serait alors remise en cause. La présence du CO_2 sous forme dissoute dans la solution réinjectée modifiera les propriétés thermiques et physiques du fluide ainsi que les propriétés pétrophysiques de la roche (augmentation de la perméabilité entre les deux puits du doublet). Ces modifications pourraient alors diminuer le temps de percée du doublet et donc la durée de vie des opérations. De la même façon l'arrivée du panache de CO_2 dissous au niveau du puits de production engendrerait la saturation du système en CO_2 et donc l'impossibilité de piéger le CO_2 nouvellement capté.

2. *L'exsolution massive du CO_2 dans le réservoir* : Une éventuelle chute de la pression au sein du réservoir lors d'un arrêt d'injection ou des conditions biologiques locales pourrait déplacer la limite de saturation du CO_2 dans la saumure. En conséquence, ces variations entraineraient un dégazage du CO_2 préalablement dissous avec un risque de surpression et une perturbation mécanique de la roche réservoir avec une migration des fluides incontrôlée.

3. *L'impact géochimique du CO_2 sur le réservoir* : Le CO_2 dissous après son captage va acidifier la solution au niveau du puits froid. Son injection induira alors des phénomènes complexes dans la zone d'intérêt « proche puits ». Les résultats principaux des études réalisées sur les interactions fluides-roches induites par la percolation d'une solution enrichie en CO_2 [*e.g.* 33 ; 34 ; 35 ; 36 ; 37 ; 38 ; 39 ; 40 ; 41 ; 42 ; 43 ; 44 ; 45 ; 46 ; 47 ; 48 ; 49] démontrent que différentes figures de dissolution peuvent naître suite à l'injection d'une solution acidifiée en fonction des conditions opératoires imposées (pression, température, débit d'injection, concentration en CO_2,…). Des phénomènes de

précipitations peuvent également être observés en raison de différents gradients chimiques et thermodynamiques induits par le déséquilibre du système [33, 46, 47, 50]. Suivant la nature des phénomènes générés, l'espace poral est réorganisé et les caractéristiques pétrophysiques de la roche sont modifiées. Le comportement à long terme du réservoir pourra alors être modifié en termes d'injectivité, d'efficacité de stockage et d'intégrité (modification des propriétés mécaniques de la roche réservoir ou couverture) avec les risques conjoints de perte d'étanchéité.

4. *L'impact géochimique du CO_2 sur les éléments du puits d'injection (dégradation mécanique)*: Une saumure acidifiée soumet les matériaux de puits (ciment/casing) à un environnement beaucoup plus agressif qu'une saumure froide injectée dans le cadre d'un doublet géothermique classique. Les mécanismes d'altération chimique résultant peuvent engendrer des faiblesses sur les éléments mais également sur la cohésion mécanique entre les différentes interfaces (ciment/roches, ciment/tubing) et ainsi générer des chemins de fuites compromettant l'intégrité du puits. Les diverses investigations expérimentales [e.g. 51 ; 52 ; 53 ; 54 ; 55 ; 56 ; 57 ; 58 ; 59 ; 60 ; 61 ; 62 ; 63 ; 64 ;65 ; 66 ; 67 ; 68 ; 69 ; 70 ;71 ; 72] et numériques [e.g. 58 ; 71 ; 72] réalisées dans un contexte de stockage géologique du CO_2 montrent que la dégradation du ciment (souvent du ciment Portland) par le CO_2 est limitée par des phénomènes de diffusion qui tendent à créer une couche superficielle où les carbonates précipitent, entrainant une diminution de la porosité et de la perméabilité avec augmentation de la résistance mécanique et de la dureté du matériau. Cette couche protège la partie plus profonde du ciment des dégradations chimiques. Cependant la variation de certains facteurs tels que le débit d'injection du mélange acidifié ou encore la présence initiale de fragilités dans le ciment sain peuvent, dans certains cas, aboutir à une augmentation de la perméabilité via la création de microfissures. Une concentration de microfissures au niveau des différentes interfaces pourrait alors causer un endommagement de la matrice solide sous l'effet de contraintes mécaniques nouvelles [73]. Ces observations de laboratoires ont été confirmées au travers de simulations géochimiques [74, 75, 76] sur des durées représentatives d'un site opérationnel. Ces études attestent bien de la possible existence de ciment carbonaté, mais sans jamais conclure à une perte d'intégrité de la gaine cimentaire si cette intégrité existait avant injection du CO_2.

– PARTIE 2 –
ÉTAT DE L’ART

– PART 2 –
STATE OF THE ART

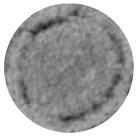

I. LES ROCHES CARBONATÉES

L'intérêt des secteurs industriel et scientifique pour les réservoirs carbonatés est principalement stimulé par leur rôle économique majeur dans l'industrie du pétrole et du gaz. En effet, plus de 60 % des réserves mondiales d'hydrocarbures sont contenues dans des roches calcaires ou dolomitiques [77]. Les formations carbonatées jouent également un rôle majeur dans les systèmes naturels, essentiellement dans le domaine de l'hydrogéologie. Elles représentent d'importantes réserves d'eau douce, ressources de plus en plus exploitées principalement dans le domaine agricole. Ces aquifères carbonatés sont grandement surveillés et protégés des contaminations extérieures [78]. En outre, en raison du regain d'intérêt actuel pour le développement durable et les énergies renouvelables, les eaux salines des formations carbonatées impropres à la consommation par l'homme, constituent des réservoirs d'intérêt pour l'exploitation géothermique. Ces réservoirs de fluide ont souvent des propriétés pétrophysiques avantageuses en termes de porosité (capacité de la roche à contenir un fluide), de perméabilité (capacité d'une roche à laisser circuler un fluide) et d'injectivité. Ces caractéristiques offrent un volume disponible important qui légitime également leur sélection comme hôtes géologiques potentiels pour le stockage souterrain du CO_2.

Dans le cadre de notre étude, la compréhension et la modélisation associée de l'évolution des propriétés hydrauliques d'un réservoir carbonaté suite à l'injection d'une solution riche en CO_2 et des processus impliqués nécessitent donc une caractérisation fine de la roche étudiée. La connaissance du contexte géologique et des processus de formation de la roche carbonatée avec ses paramètres intrinsèques texturaux reste essentielle pour comprendre les mécanismes physico-chimiques induits par nos contraintes expérimentales. En effet, l'évolution des propriétés pétrophysiques de la roche hôte sera contrôlée par son hétérogénéité à toutes les échelles (de l'échelle micro à l'échelle du réservoir) et également par les incertitudes sur la cinétique de réaction des minéraux carbonatés au contact d'une solution saline saturée en CO_2. Ce chapitre résume ainsi les principales caractéristiques des systèmes carbonatés.

I.1. Caractéristiques pétrographiques des roches carbonatées

Les propriétés physiques d'une roche carbonatée différent selon la taille, la forme, la disposition et les proportions des éléments pétrographiques qui la composent. Ces éléments peuvent être classés en trois groupes principaux [79]: 1) les grains (origine, nature, densité, taille et forme des éléments de la roche), 2) la phase de liaison entre ces grains (nature minéralogique de la matrice ou du ciment, son abondance et la répartition de la taille des grains) et 3) l'espace poreux (type de porosité).

- **Les grains carbonatés** (appelé également allochèmes-allochems).

Ces éléments sont de différents types en fonction de leur origine (ici, seuls les quatre types de grains les plus courants sont discutés) :

- *Intraclaste* (Intraclast): Ce grain de carbonate est d'origine détritique et provient de la désagrégation et du transport d'un sédiment carbonaté préalablement lithifié et érodé peu après sa formation (érosion par les vagues, émersion...). Le matériel est transporté sur de courtes distances et re-sédimenté proche du lieu d'érosion.

- *Bioclaste*: Fragments d'organismes marins également appelés grains squelettiques (tests d'échinodermes, coquilles de bivalves,...)

- *Péloïde*: Ce sont des grains micritiques (calcite très finement cristallisée) de forme subsphériques à ovoïdes et de taille uniforme. Ils sont dépourvus de structure interne. Leur taille est limitée à 0,5 mm et ils peuvent être d'origine fécale (pellets) ou être issus d'un remplacement complet de grain par les phénomènes de micritisation destructive, ou de la dégradation/remaniement de divers autres grains.

- *Ooide*: Grain sphérique de forme régulière, constitué d'un nucleus et d'un cortex périphérique, issu de la précipitation chimique (ou biochimique) de la calcite ou de l'aragonite autour du nucleus. Les nucleii sont généralement formés par un bioclaste, un intraclaste ou un grain de quartz. La taille des grains varie entre 0,5 et 2 mm. Le cortex est composé d'un arrangement de cristaux fibreux initialement de calcite magnésienne ou d'aragonite et de nanocristaux de micrite. Les cristaux sont organisés en lamines concentriques. Les cristaux fibreux présentent une disposition tangentielle, radiaire (Fig. 5).

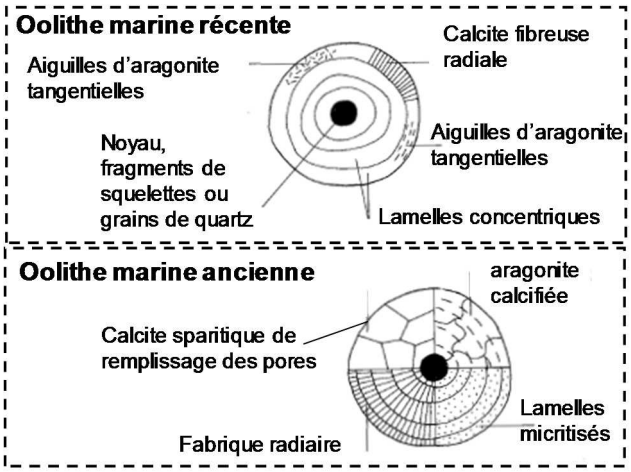

Figure 5 : Composition des oolithes marines récentes et plus anciennes [79].

- **La phase de liaison**

Les différents allochèmes qui composent le squelette de la roche sont généralement entourés d'un matériau intergranulaire composé d'une fine matrice carbonatée ou d'un ciment plus grossier :

- *Matrice (matrix)*: Boue carbonatée microcristalline (<4 µm), appelée micrite, sédimentée en même temps que les grains. Les micrites proviennent d'une précipitation chimique ou biochimique, de la désagrégation d'organismes marins comme les algues vertes ou de la bioérosion de tests calcaires et soutiennent les allochèmes existants. Les micrites constituent la matrice de la plupart des roches calcaires. La présence d'une boue micritique indique un environnement calme (environnement protégé peu profond comme les lagunes ou les récifs, ainsi que les environnements marin plus profonds situés en dessous de la limite d'action des vagues...).

Après leur dépôt et durant la diagenèse, les micrites peuvent subir des surcroissances ("néomorphisme") augmentant la taille des cristaux : Selon la taille du grain, on obtient des microsparites de 4 à 10 µm ou des pseudosparites (>10 µm) (Folk., 1959) [80].

- *Ciments de calcite sparitique (spar cement)*: Il s'agit de calcite transparente ou translucide avec une taille des cristaux >4µm qui constitue le ciment de remplissage des pores entre les grains. Ces cristaux résultent de processus de précipitation minérale post-dépositionnel. En fonction de leurs formes et arrangements, il est possible d'identifier plusieurs types de ciments sparitiques [79] : (1) Ciments palissadiques ou aciculaires (en frange fibreuse), (2) Ciments de blocage et ciments syntaxiaux.

I.2. Caractéristiques pétrophysiques des roches carbonatés.

Les caractéristiques pétrophysiques des roches carbonatés conditionnent le volume de stockage potentiel d'un sédiment et influencent les figures de dissolution que peut générer l'injection d'une solution acidifiée. Une roche réservoir contient une certaine quantité d'espaces vides (les pores), qui peuvent contenir un ou plusieurs fluides miscibles ou non (gaz ou eau) et à travers laquelle, dans le cas de notre étude, le CO_2 dissous va se déplacer. Ces pores, et particulièrement leur interconnexion, sont des éléments clés car ils contrôlent la circulation de la solution acide et donc l'accessibilité du CO_2 aux phases minérales. Dans le contexte d'un processus d'injection, d'autres caractéristiques du système, telles que les surfaces réactives, sont aussi importantes que la porosité et la perméabilité car elles contrôlent les cinétiques de réaction. Cette section passe en revue ces propriétés essentielles décrivant un milieu poreux.

I.2.1. La porosité (l'espace poreux).

La porosité se définit comme le pourcentage de volume de vide qui peut être occupé par des fluides dans le sédiment *cad* le rapport entre le volume de vide et le volume total de la roche. Le volume poreux peut apparaître sous forme des pores isolés et non communicants ou sous forme de pores directement interconnectés permettant, dans cette configuration, la percolation du fluide [81]. Le milieu poreux est donc un concept légèrement différent de celui de porosité car il s'intéresse principalement à la topologie de ces interconnexions entre les pores. Le remplissage des volumes poreux dépend

des diamètres d'accès (*access diameters*), ou seuil (*threshold*) d'entrée de pores également appelé gorges (*pore throat*). Certains « bras mort » peuvent également être connectés au réseau mais ils ne contribuent pas à l'écoulement du fluide (Fig. 6).

L'ensemble de l'espace poreux d'une roche ne peut donc pas être considéré comme entièrement disponible à l'écoulement d'un fluide. Par conséquent, la porosité totale comprend :

- **La porosité effective** (*effective porosity*): également appelée porosité libre qui est produite par l'interconnexion des vides. Cette porosité contribue au mouvement des fluides dans la roche.

- **La porosité fermée** (*closed porosity*): qui correspond aux vides entièrement fermés et non connectés. Cette porosité non connectée peut parfois avoir un rôle important dans les interactions fluide-roche lorsque le transport est dominé par la diffusion.

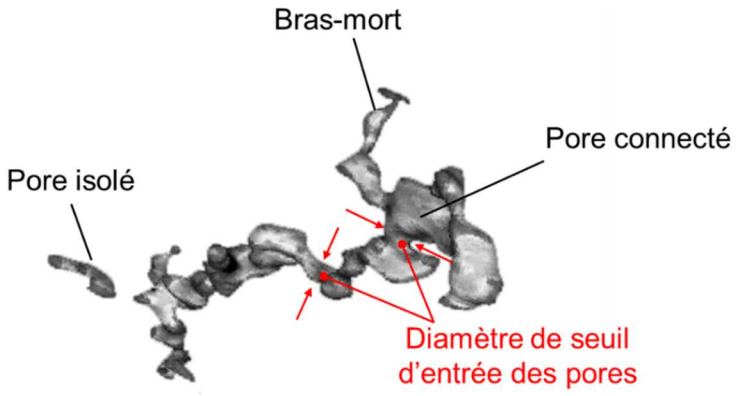

Figure 6 : Les différents types de pores.

Les différentes tailles des pores du milieu poreux d'une matrice rocheuse sont regroupées en trois catégories distinctes de porosité en fonction du diamètre moyen d'entrée de pores [82] : la micro, la méso et la macro-porosité (Fig. 7).

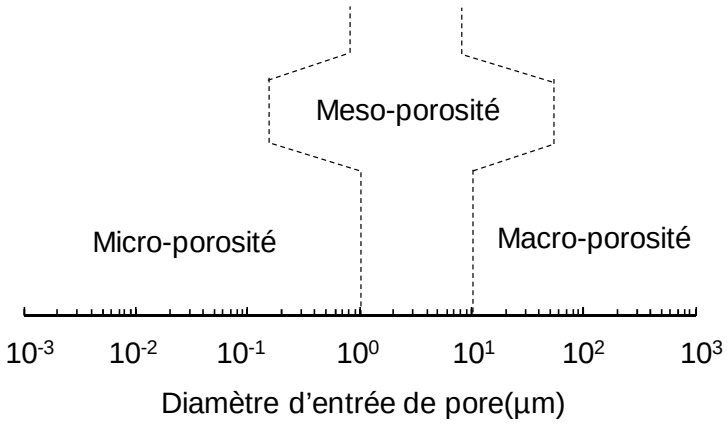

Figure 7 : Classification des familles de taille de pores dans la matrice rocheuse en fonction du diamètre d'entrée de pore [82].

Plusieurs auteurs ont établi des classifications plus spécifiques du système poreux des roches carbonatées en fonction de la taille et forme moyennes des pores, de leur interconnexion et de l'impact de la sédimentation initiale. La classification de Choquette et Pray [83] (Fig. 8) est la plus fréquemment utilisée.

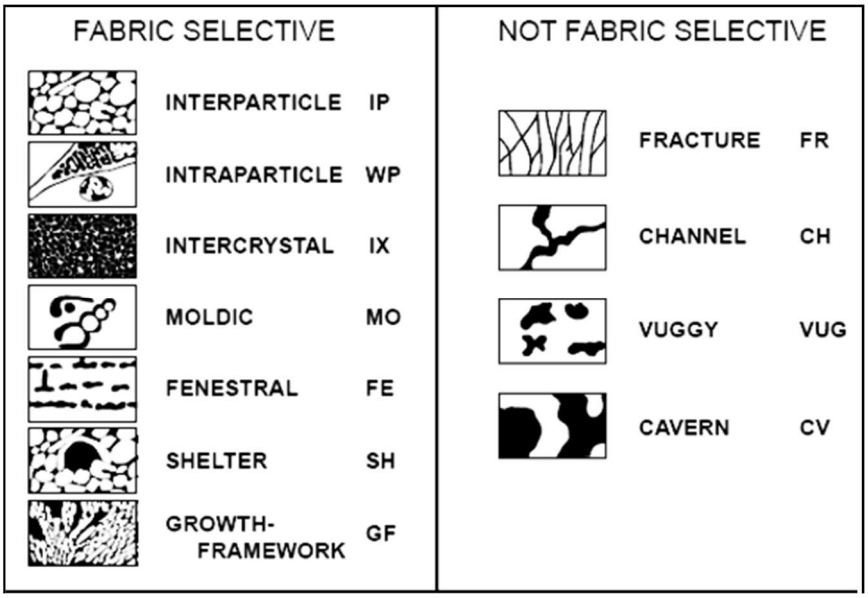

Figure 8 : Classification des différents types de porosité d'une roche carbonatée selon Choquette et Pray [83].

Au premier ordre, la porosité peut être divisée en deux grand types : (1) la porosité "**liée à la fabrique**" ("fabric sélective porosity") contrôlée par la texture initiale du sédiment, (2) la **porosité "indépendante de la fabrique"** ("not-fabric sélective porosity") qui n'a pas de causalité particulière avec l'élément constitutif du sédiment initial. Dans la **porosité "liée à la fabrique"**, la taille des grains ainsi que leur disposition spatiale sont les premiers paramètres qui influencent l'échelle de taille des vides, du plus fin au plus grossier. Il est possible de distinguer la porosité primaire présente dès le dépôt et la porosité secondaire issue de processus diagénétiques post-dépôt qui modifient le volume des pores mais également leur morphologie. La **porosité " indépendante de la fabrique"** est, quant à elle, forcément secondaire et liée principalement à des phénomènes de dissolution.

La porosité primaire regroupe, i) la porosité inter-granulaire (*intergranular*) située entre les grains. La plupart du temps, elle correspond aux macropores non obstrués et elle est généralement réduite progressivement au cours de la diagenèse, ii) la porosité intra-granulaire (*intergranular*) située à l'intérieur des grains. Elle est définie comme la microporosité et est souvent rapidement réduite par la croissance syntaxiale des ciments calcitiques [84], iii) la porosité fenestrée (*fenestral*) liée à la présence de vacuoles alignées initialement remplies de gaz dans les tapis stromatolitiques, iv) la porosité d'ombrelle (*shelter*) située sous certains bioclastes, v) la porosité de récifs (*growth-framework*) formant des vacuoles entre la trame construite de certaines bioconstructions.

La porosité secondaire se développe lors des phénomènes de remplacement comme par exemple lors de la dolomitisation avec l'apparition d'une porosité inter-cristalline (*intercystal*) ou lors de phénomènes de dissolution d'éléments figurés donnant une porosité moldique (*moldic*) où la forme du pore secondaire reflète la forme du grain dissous.

La porosité secondaire indépendante de la texture initiale ("non sélective") est liée à des phénomènes de fracturation ou de dissolution aboutissant à la formation de vacuoles ou de conduits karstiques de taille pluri-centimétriques à pluri-kilométriques (*fracture, channel, vuggy, cavern*).

La structure des réseaux poreux est donc très complexe. L'éventail des tailles de seuil d'accès aux pores, la complexité géométrique (également appelé sinuosité), l'interconnexion et la topologie de l'espace poral affectent de manière significative le transport des fluides au sein d'une roche carbonatée. Le facteur utilisé pour décrire cette complexité structurelle est dénommé *tortuosité*. Il n'existe pas de définition universelle de la tortuosité. Selon le domaine d'étude, différents types de mesure sont utilisés : la *tortuosité géométrique*, la *tortuosité hydraulique*, *la tortuosité de diffusion* et autres [85]. La *tortuosité géométrique* est la plus fondamentale et est définie, pour un réseau de pores tortueux, comme le rapport entre la longueur du "chemin tortueux" et une ligne droite. Tous ces aspects ont un impact sur les processus de conduction, d'advection et de diffusion et contrôlent les propriétés de transfert comme la perméabilité. Cependant, pour les besoins de notre étude, seules les valeurs de porosités totale et libre seront mesurées à partir de la technique de porosimétrie au mercure décrite dans la partie expérimentale.

I.2.2. La perméabilité

La perméabilité correspond à l'autre caractéristique essentielle d'un milieu poreux. Elle correspond à la capacité d'une roche à laisser un fluide s'écouler à travers son espace poreux. L'injectivité et le déplacement d'une solution injectée dans une roche carbonatée sont fortement contrôlés par ce paramètre. Cette notion est définie comme intrinsèque, car elle est étroitement liée à la distribution et à la forme du milieu poreux (structure et connectivité des pores), au type de fluide injecté et aux conditions externes en termes de gradient de pression [86]. Deux types de perméabilité sont identifiés : 1) La perméabilité relative à la matrice et 2) la perméabilité relative aux fractures. La première est une propriété spécifique de la roche à l'échelle des pores et a un impact significatif dans les interactions fluide-roche. La seconde dépend de l'orientation, des dimensions et des connexions entre les fractures à l'échelle du réservoir. Cette dernière a un impact préférentiel sur l'aspect directionnel du transport d'un fluide à travers une roche. La perméabilité n'est cependant que partiellement liée à la porosité. Une roche peut être définie par une porosité élevée mais une faible perméabilité dans le cas où la majorité des espaces poreux ne sont pas connectés. L'unité principale est le m^2. Elle peut également être exprimée en Darcy (D) (1D = $0.97 \cdot 10^{-12}$ m^2). Dans notre étude, seules les mesures de la perméabilité intrinsèque seront effectuées sur des échantillons mésoscopiques (cm) en utilisant de l'azote. L'équipement est décrit dans la partie expérimentale.

I.2.3. La surface spécifique (interface fluide /roche) et la surface réactive

La surface spécifique est un autre facteur géométrique important du milieu poreux. Elle se définit comme le rapport entre la surface totale des vides interstitiels (S_V) et le volume total du milieu (V_T). La surface spécifique est en corrélation directe avec les cinétiques de réaction d'un solide (sorption, dissolution, précipitation,...) car elle est la seule zone accessible pour un fluide réactif. Compte tenu de la complexité de structure d'une roche carbonatée propre à son histoire sédimentaire et diagénétique, il n'est pas aisé de déterminer cette surface susceptible de réagir dans un environnement loin de l'équilibre thermodynamique.

Afin d'étayer ce phénomène, une première constatation peut être établie quant à la variabilité de la relation entre la masse d'un minéral et sa surface qui est fonction du type de matériau cristallin. En effet, à titre d'exemple, un ciment sparitique syntaxial (Fig. 9a) dont la surface est quasi plane aura une surface de contact avec le fluide beaucoup moins importante qu'un amas de micro-sparite ou qu'un cortex oolitique composant une oolite (Fig. 9b). La cinétique de réaction locale sera alors différente [87].

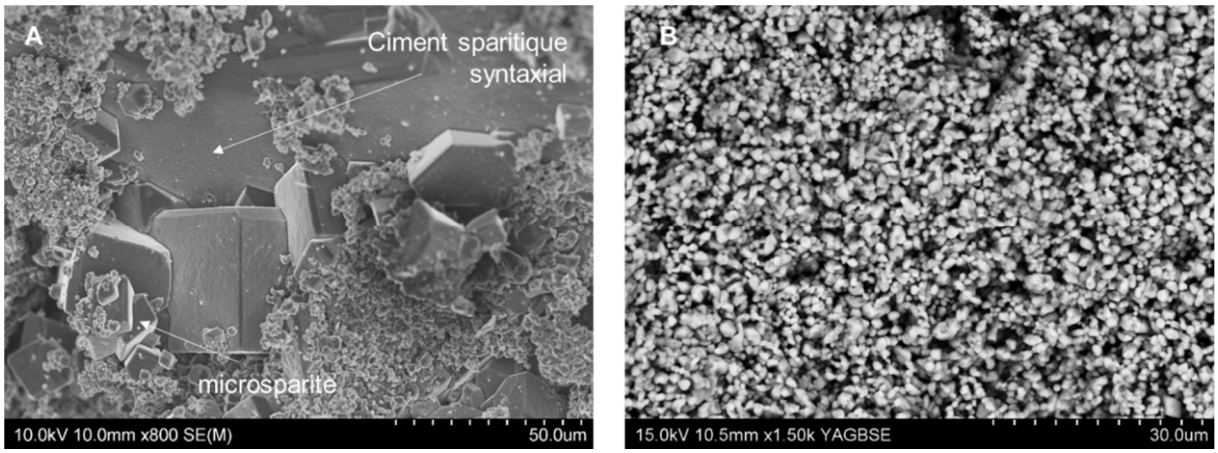

Figure 9 : Observations MEB sur calcaire de Lavoux sain de la surface 1) d'un monocristal de calcite (sparite) et d'une calcite finement cristallisée (microsparite) (cette étude) et 2) d'un cortex micritique microcristallin (cette étude).

Un modèle développé par Brunauer et al. [88] permet l'appréciation de la surface spécifique dite BET S_{BET} (pour Brunauer, Emmett et Teller) à partir de mesures d'adsorption de gaz à la surface du minéral. Les techniques de microscopie à force atomique (AFM) ou d'interférométrie par balayage permettent également une bonne caractérisation physique des surfaces aux échelles micro et nanométrique.

Plusieurs expériences réalisés sur des roches calcaires et utilisant ces différentes techniques ont permis de démontrer qu'une surface endommagée tend à réagir plus rapidement qu'une surface lisse en raison de l'existence d'un excès d'énergie superficielle [89 ; 90 ; 91]. Ce phénomène s'explique par une distribution anisotropique des sites réactifs à leur surface régissant les cinétiques réactionnelles de nombreux matériaux cristallins.

Une seule fraction de la surface spécifique sera donc concernée par les mécanismes réactionnels [87 ; 92]. Deux catégories de sites réactifs de surface sont répertoriées [93] (Fig. 10): la première correspond aux terrasses (flat terraces) situées au niveau des régions plates d'un monocristal et la deuxième aux dislocations comme les escaliers (steps, correspondant à des couches partiellement surélevées), les coins, trous ou encore les replis "kink" au niveau desquels le taux de réactions y est plus important.

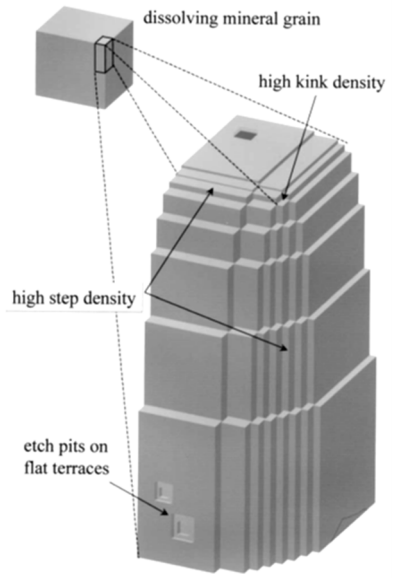

Figure 10 : Représentation schématique de l'hétérogénéité réactive du mécanisme de dissolution à la surface d'un cristal de calcite par la répartition des différents sites de dissolution préférentielle [94].

La prise en compte de ces caractéristiques inhérentes à la morphologie de surface de la matrice carbonatée nécessite donc de faire intervenir un nouveau paramètre, la surface réactive S_r. Dans le cadre de notre projet, les valeurs utilisées proviennent de la littérature et sont issues d'analyses de calcaires prélevés dans la même zone d'échantillonnage de notre calcaire de Lavoux et dont les caractéristiques sont extrêmement proches.

I.3. Nomenclature et classification des roches carbonatées

Les roches carbonatées ont des origines très variées, principalement biologiques. La coexistence des grains initiaux, des vides, des fluides et de la matrice ainsi que leur évolution dans le temps dépendent directement de la relation entre l'environnement de dépôt et l'histoire de leur enfouissement. La grande instabilité chimique des sédiments carbonatés et leur réactivité mécanique peuvent induire des changements minéralogiques et texturaux très importants peu après le dépôt. Ces divers phénomènes conduisent à la genèse d'une structure rocheuse très complexe et hétérogène qui est, comme nous l'avons vu précédemment, fonction de la distribution spatiale des différents composants, de l'abondance du ratio ciment/matrice et de la variabilité des propriétés texturales intrinsèques (type de ciment).

Ainsi afin de pouvoir définir les différents types de roches carbonatées, de nombreuses classifications ont été proposées par plusieurs auteurs. Les plus couramment utilisées sont les classifications de Folk [95 ; 96] et Dunham [97] modifiée par Embry & Klovan [98]. Les deux paramètres fondamentaux utilisés dans la classification des carbonates sont les types ou l'abondance des grains et la nature des phases de liaison.
Dans le cadre de cette étude, nous ne nous attarderons que sur la classification de Dunham.

La classification de Dunham (Fig. 11) a été établie pour permettre une reconnaissance des différentes familles de roches carbonatées, principalement en fonction de leurs propriétés texturales. Cette classification traite plus spécifiquement de l'hydrodynamisme au moment du dépôt via la quantité de grains présents et le type de phase de liaison. Elle permet d'identifier la multiplicité des origines des calcaires à travers leur origine sédimentaire. Dunham se concentre donc sur le transport des grains initiaux. Il clarifie le rôle de l'énergie dans l'accumulation des sédiments et l'impact sur chaque fabrique rocheuse. Ainsi, les critères de différenciation des classes au sein de la classification de Dunham sont : la présence ou l'absence de boue (définie comme la fraction de taille inférieure à 20 µm), la disposition des grains (grains liés ou non) et la proportion de grains par rapport aux phases de liaison au moment du dépôt. La cohésion organique des composants initiaux de la roche est un autre paramètre dans la distinction des carbonates. Lorsque les dépôts de carbonates sont composés de coquilles transportées, de restes de squelettes ou de fragments bioclastiques érodés, l'entassement est défini comme *allochtone*. En revanche, lorsque les fragments squelettiques des carbonates biogéniques n'ont pas migrés hors de leur environnement de formation, la fabrique résultante est dite *autochtone*.

Les trois principales subdivisions sont :

- Roche contenant une matrice micritique (**roche allochtone** contenant de la boue) :

- *Mudstone* : Roche carbonatée micritique contenant moins de 10 % de grains. La boue provient de dépôts subvenus dans une eau très calme.

- *Wackestone* : Roche carbonatée à phase de liaison micritique contenant plus de 10 % de grains non jointifs. Cette roche se forme avec un taux de précipitation rapide dans un environnement avec des courants faibles et de courte durée.

- *Packstone* : Calcaire à grains en grande partie jointif, mais contenant une matrice micritique (boueuse). Ce calcaire est défini comme un sédiment carbonaté à énergie relativement faible, ce qui indique qu'il a été déposé dans un environnement à activités limités mais dont l'énergie a permis la présence de grains avec un taux rapide de formation de micrite.

- Roche contenant un ciment sparitique (**roche allochtone** dépourvue de boue micritique) :

- *Grainstone* : grains jointifs déposés les uns sur les autres en l'absence de boue micritique et liés par un ciment. Cette classe de carbonate est représentative d'un dépôt dans un environnement turbulent, ce qui signifie qu'elle a été exposée à une forte action des vagues. Le volume des pores est rempli par des précipitations tardives.

  - Roche biologiquement liée.

- *Boundstone :* Lorsqu'il existe des preuves que des sédiments carbonatés étaient liés par des phénomènes biologiques au moment du dépôt. Cette classe est également définie comme autochtone.

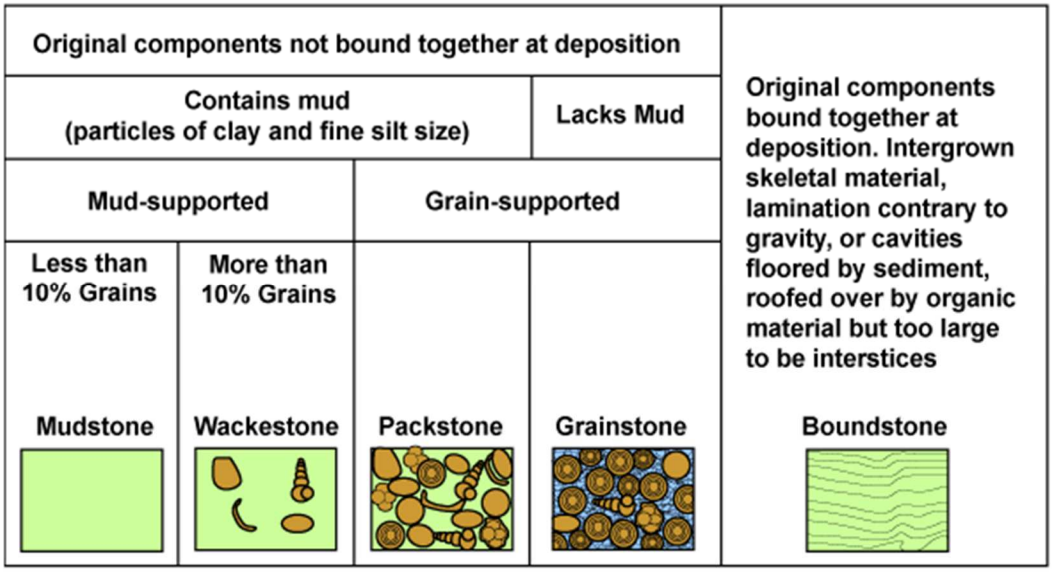

Figure 11 : Classification des roches carbonatées selon la texture de dépôt par Duhnam [96].

Lorsque la texture de dépôt n'est pas reconnaissable, le sédiment carbonaté est appelé calcaire cristallin ou dolomie cristalline (Fig. 12).

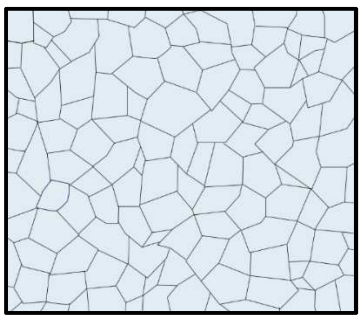

Figure 12 : Texture d'un calcaire cristallin ou dolomie cristalline.

II. APPROCHE THÉORIQUE DE LA RÉACTIVITE DES RÉSERVOIRS CARBONATÉS PAR FORÇAGE HYDROGÉOCHIMIQUE ANTHROPIQUE

L'introduction forcée de la solution acidifiée au CO_2 dans un aquifère profond carbonaté va induire toute une série de processus en réponse aux perturbations des équilibres chimiques existants. La dissolution et la précipitation des carbonates sont les deux principaux phénomènes induits dans le système CO_2/Eau saline. Leur cinétique de réaction est déterminée par trois mécanismes indépendants qui peuvent tous être déterminant à des degrés différents en fonction des conditions environnantes:

- La cinétique de conversion du CO_2 aqueux en acide carbonique H_2CO_3, qui constitue l'agent agressif dans le processus de dissolution du $CaCO_3$.

- La cinétique de dissolution/précipitation de la phase limite à l'interface entre le solvant constitué de CO_2 dissous (+sels) et de $CaCO_3$ dissous et la roche calcaire.

- Transport de masse des espèces présentes en solution Ca^{2+}, HCO_3^-, CO_3^{2-}, CO_2 et H_2CO_3, par convection, dispersion ou par diffusion moléculaire à partir de et vers l'interface entre les phases liquides et solides.

L'importance d'appréhender ces processus majeurs générés par l'acidification de la roche repose principalement sur les effets occasionnés sur la micro et macrostructure de la roche. En effet les interactions (ou la compétition) entre les réactions géochimiques produites et l'écoulement du fluide peuvent engendrer des changements significatifs de la matrice rocheuse à l'échelle microscopique et une évolution importante des propriétés macroscopiques telles que la porosité, la perméabilité [48] ou encore la surface spécifique de la roche [99]. Ces modifications se répercutent alors localement sur les lignes de courant et les propriétés hydrauliques relatives à la mobilité de la saumure riche en CO_2 [33]. Elles peuvent également être à l'origine de dommages à la formation, non loin du puits ou encore fragiliser la tenue du ciment [100 ; 101 ; 102] et entrainer la fin prématurée des opérations de stockage.

Nous considérons donc dans ce chapitre les notions de géochimie de base des carbonates de calcium en rappelant le système calco-carbonique ainsi que quelques notions thermodynamiques et cinétiques sur ces espèces. Dans un second temps sera exposé le couplage des réactions chimiques aux phénomènes de transport encore appelé "transport réactif" ainsi que ses effets sur la géométrie de l'écoulement en conditions géologiques.

II.1. Système calco-carbonique et réactions de dissolution/ précipitation (échelles microscopiques)

II.1.1. Dissolution du CO_2

Le concept de base du projet CO2-DISSOLVED étant axé sur la solubilisation naturelle du CO_2 en solution saline, la compréhension de ce processus physico chimique est essentielle.

La quantité de CO_2 dissous dans le système sera principalement fonction des paramètres pression, température et salinité (force ionique). Il existe de nombreuses études expérimentales et de modèles analytiques développés pour les mesures de solubilité du CO_2 en solution dans les conditions de séquestration géologique [e.g. 103 ; 104 ; 105 ; 106 ; 107]. Dans le cadre de notre étude, la solubilité sera calculée en fonction des différentes variables par le modèle thermodynamique de Duan et al [108].

Dans la gamme T-P-force ionique couverte par le modèle de Duan (273-533 K / 0-2000 bar et 0-5 mol of NaCl per kg), les tendances montrent que la solubilité du CO_2 augmente avec la pression (Fig. 13a) et diminue avec une augmentation de la force ionique des sels (Fig. 13b). La diminution de la solubilité avec la salinité se traduit par l'effet du "salting-out" [109]. Elle varie également avec la température dans les deux systèmes binaire CO_2-H_2O et ternaire H_2O-CO_2-NaCl. Comme il est possible de le visualiser figure 13a, à basse pression (< 100 bar), la solubilité du CO_2 diminue progressivement avec la température. Pour des pressions plus élevées (>100 bar), la solubilité du CO_2 tend à diminuer avec la température jusqu'à atteindre un minimum avant de ré-augmenter modérément pour les pressions proches des conditions du réservoir géologique ciblé (120-200 bar).

En aquifère, sur la gamme des conditions pertinentes d'un projet de CCS, la solubilité du CO_2 est donc quasiment indépendante de la température, mais a une forte dépendance à la pression et à la teneur en sel dissous.

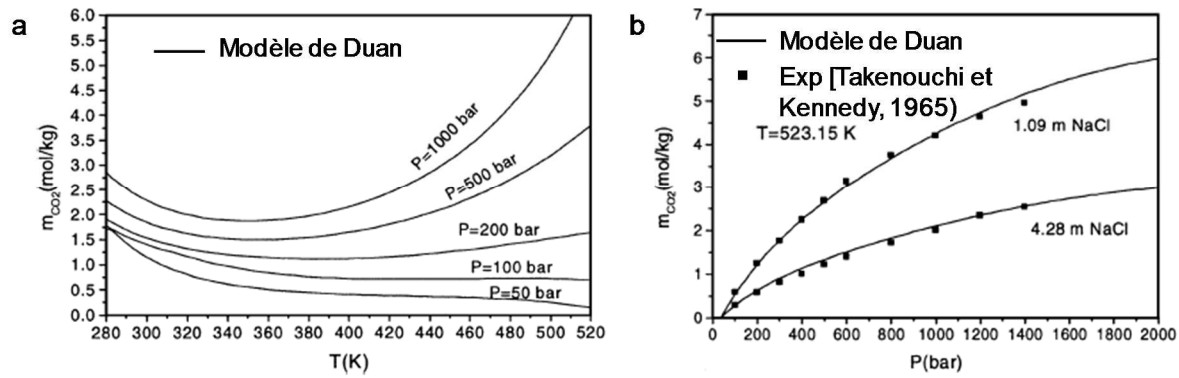

Figure 13 : a) Solubilité du CO_2 dans l'eau pure en fonction des paramètres pression et température [108] et b) pour différentes concentrations de NaCl en fonction de la pression [108 ; 109].

Une fois dissous, le CO_2 aqueux s'hydrate avec les molécules d'eau pour former un acide faible, l'acide carbonique. L'acide carbonique ainsi formé se dissocie en ion hydrogénocarbonate et en ion carbonate. La dissociation des expèces carbonatés est fortement dépendente du pH de la solution.

Les réactions entre phase aqueuse et gaz sont rapides. La réaction d'équilibre s'écrit :

$$CO_{2(g)} \Leftrightarrow CO_{2(aq)} \quad (1)$$

A faible pression, la solubilité est fixée par la loi de Henry. Ainsi la quantité de gaz dissous exprimée en mole/kg est déterminée par l'équation :

$$[CO_2]_{(aq)} = K_H . P_{(CO_2)} \quad (2)$$

avec, K_H la constante de Henry exprimée en mole.kg^{-1}.kPa^{-1} et $P_{(CO_2)}$ la pression partielle du CO_2 dans la phase gazeuse en kPa.

La pression partielle est déterminée de la manière suivante :

$$P_{(CO_2)} = \alpha_{CO_2} . P \quad (3)$$

où α_{CO_2} est la fraction molaire de CO_2 dans le gaz et P la pression totale.

Le CO_2 aqueux va s'hydrater et former de l'acide carbonique suivant l'équilibre :

$$CO_{2(aq)} + H_2O \Leftrightarrow H_2CO_3 \qquad K_0 = \frac{(a_{H_2CO_3})_{eq}}{(a_{CO_{2(aq)}})_{eq}} = 10^{-1.79} \quad (4)$$

Cet acide se dissocie ensuite pour créer les différentes espèces ioniques HCO_3^- et CO_3^{2-} en équilibre avec l'eau selon les réactions acido-basiques suivantes :

$$H_2CO_3 \Leftrightarrow H^+ + HCO_3^- \qquad K_{a_1} = \frac{(a_{H^+})_{eq}(a_{CO_3^{2-}})_{eq}}{(a_{H_2CO_3})_{eq}} = 10^{-6.26} \quad (5)$$

$$HCO_3^- \Leftrightarrow H^+ + CO_3^{2-} \qquad K_{a_2} = \frac{(a_{H^+})_{eq}(a_{CO_3^{2-}})_{eq}}{(a_{HCO_3^-})_{eq}} = 10^{-10.13} \quad (6)$$

Les valeurs des différentes constantes thermodynamiques K_H, K_o, K_{a1}, K_{a2} à 60°C (conditions expérimentales de notre étude) sont issues de Shock et al., 1988 [110].

Le pH joue un rôle fondamental car il contrôle l'espèce carbonatée dominante. Dans nos conditions d'expériences qui seront décrites plus tard (120 bars – 60°C – eau pure), pour des pH inférieurs à 6,29, l'H_2CO_3 sera l'espèce dominante. Si le pH est compris entre 6,29 et 10,14, l'ion hydrogénocarbonate prédominera. Enfin pour des pH supérieurs à 10,14, c'est l'ion CO_3^{2-} qui sera majeur.

II.1.2. Aspect thermodynamiques des phénomènes de dissolution/précipitation.

L'environnement proche puits, suite à l'injection d'une solution riche en CO_2 dissous, correspondra à un système CO_2(g)-$CaCO_3$(s)-$H_2O_{(aq)}$ (+ sels) dont le pH, en raison de la présence d'acide carbonique, va diminuer très rapidement et dans lequel les réactions décrites ci-dessus seront couplées à la dissolution des minéraux carbonatés primaires (calcite, aragonite, dolomite, magnésite, calcite magnésienne...). La précipitation de minéraux carbonatés secondaires pourra également advenir dans des zones plus ou moins éloignées [33] du point d'injection dans des conditions de sursaturation favorables (présence de cations, augmentation du pH v).

A pH faible (et donc $P_{(CO_2)}$ élevée) et dans une solution sous saturée, la calcite est attaquée par l'acidité de la solution.

$$CaCO_{3(s)} + H^+ \Leftrightarrow Ca^{2+} + HCO_3^- \quad (7)$$

Plusieurs phénomènes entrent en compétition dans le système calcite-CO_2-eau. D'une part l'augmentation de la $P_{(CO_2)}$ entraine une diminution du pH par production d'acide carbonique, favorisant la dissolution de la calcite. D'autre part la $P_{(CO_2)}$ entraine une augmentation de la concentration en espèces carbonatées qui, en accord avec le principe de Le Chatelier, tendra à stabiliser la calcite. On est donc dans un système tampon.

L'état de saturation d'une solution vis-à-vis des minéraux carbonatés est déterminé en comparant le produit d'activité ionique (noté IAP ou Q) au produit de solubilité du minéral donné par :

$$CaCO_{3.(s)} \Leftrightarrow Ca^{2+} + CO_{3(aq)}^{2-} \qquad K_{ps_1} = (a_{Ca^{2+}})_{eq}(a_{CO_3^{2-}})_{eq} = 10^{-8.74} \quad (8)$$

La valeur du produit de solubilité K_{ps_1} donnée pour l'équation (11) correspond à celle de la calcite déterminée à 60°C [110].

Le produit d'activité ionique est défini sous la même forme que la constante d'équilibre thermodynamique mais il intègre les activités réelles (et non à l'équilibre) des ions en solution:

$$Q = \left(a_{Ca^{2+}}\right)_{rel}\left(a_{CO^{2-}_3}\right)_{rel} \quad (9)$$

Le déséquilibre thermodynamique au sein du fluide poral suite à l'injection de la solution riche en CO_2 est alors mesuré par l'indice de saturation Ω de la solution. Il correspond au quotient du produit d'activité ionique sur le produit de solubilité :

$$\Omega_{Calcite} = \left(\frac{Q}{K_{ps}}\right) \quad (10)$$

Ainsi, lorsque Ω=1, la solution est en équilibre thermodynamique avec le minéral considéré. Si Ω<1, la solution est sous saturée vis-à-vis du minéral et celui-ci se dissout. Enfin, dans le dernier cas où Ω>1, la solution est dite sursaturée et le minéral sera susceptible de précipiter.

Le degré de saturation est également fonction des deux autres paramètres principaux que sont la température et la pression. L'influence de la pression (augmentation de la solubilité de la calcite corrélée avec celle de la pression) est cependant de deuxième ordre par rapport à celle de la température. Cette dernière, de par son augmentation, entrainera une solubilisation moins importante de la calcite.

Enfin, la présence d'impuretés (Mg^{2+}, Mn^{2+}, Fe^{2+}, …) modifie les équilibres réactionnels décrits précédemment [111, 112]. Les valeurs des produits de solubilité K_{ps} et des vitesses associées seront différentes. La figure 14 illustre bien les variations de solubilité en fonction de ces différents critères pour des conditions définies à 25°C et 1 bar.

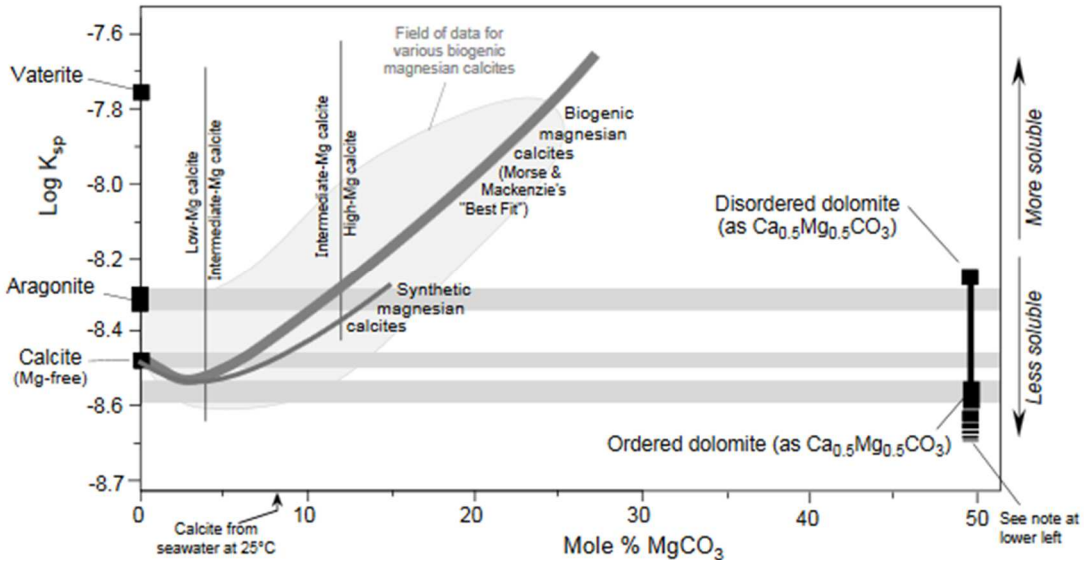

Figure 14: Solubilité de la calcite magnésienne en fonction de la teneur en $MgCO_3$ dans la roche (Morse et Mackenzie., 1990 [113]: données pour la calcite, Mg-calcite et aragonite, Langmuir., 1997 [114] : données pour la calcite et l'aragonite).

A titre d'exemple, le produit de solubilité de l'aragonite est légèrement plus faible que celui de la calcite, ce qui signifie que parmi ces deux polymorphes, l'aragonite est moins stable que la calcite dans ces conditions de pression et de température. De même la solubilité d'une calcite magnésienne avec environ 2% de Mg est inférieure à celle de la calcite pure, tandis que les calcites avec une substitution de 12-15% de Mg sont cinq fois plus solubles que l'aragonite [113].

La présence de ces ions étrangers peut également influer sur la structure cristalline et donc la morphologie des cristaux précipités. Dans le cas majoritaire du magnésium, ses propriétés inhibitrices vont affecter la direction (et la vitesse) de croissance par la substitution des ions Ca par Mg (effet d'empoisonnement au Mg).

Ainsi, dans un environnement ou circule un fluide caractérisé par un fort rapport Mg/Ca, la croissance des cristaux se fait préférentiellement selon l'axe c (cristaux fibreux de calcite magnésienne ou d'aragonite, cf. Fig. 15). A contrario, dans un fluide peu concentré en magnésium, la croissance des cristaux tend vers une forme cristalline équigranulaire.

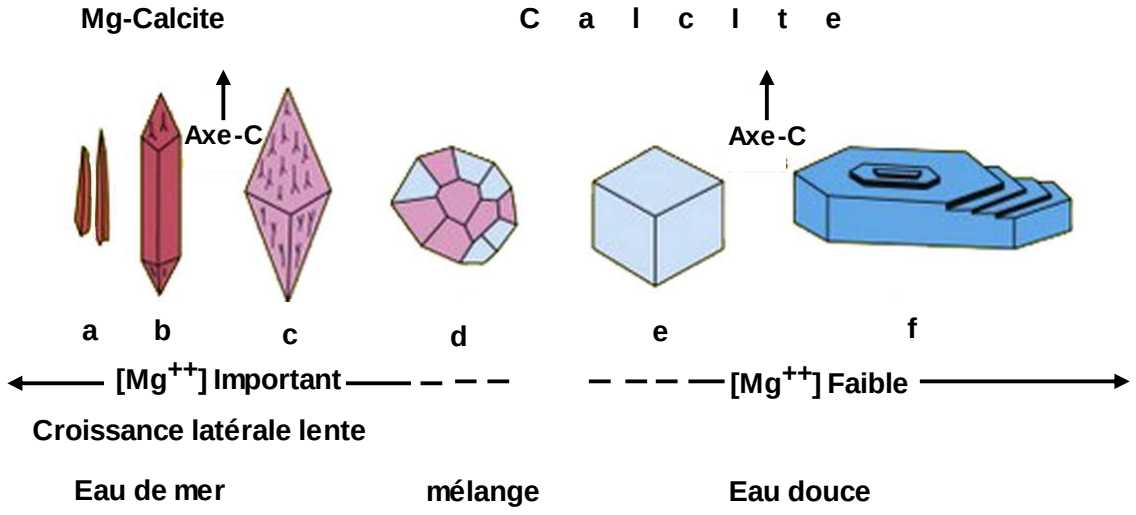

Figure 15 : Habitus des croissances des cristaux de calcite en fonction du ratio Mg/Ca en condition naturelle [115, 116].

Enfin, il est à noter l'influence de la force ionique sur la solubilité des minéraux eux-mêmes. On a vu que le sel provoquait un effet de "salting out" impliquant une baisse de la solubilité du CO_2 dans la phase aqueuse. Mais il est également à noter que l'augmentation de la salinité de la solution entraine une augmentation de sa force ionique qui a une action sur les coefficients d'activité des ions en solution. La figure 16 présente l'évolution du coefficient d'activité des ions CO_3^{2-} et Ca^{2+} en fonction de la force ionique de la solution à 60°C dont les calculs sont présentés en annexe A. On voit que le coefficient est très sensible à la force ionique et que pour une force ionique de 0.25 correspondant à 15 g.L^{-1} de NaCl, les coefficients d'activité sont de 0.28 et 0.24 pour le calcium et le carbonate respectivement. Si le produit d'activité ionique pour une solution diluée vaut $Q_{(0)} = a_{Ca^{2+}} \times a_{CO^{2-}_3} = m_{Ca^{2+}} \times m_{CO^{2-}_3}$, il vaut $Q_{(0.25)} = 0.28 m_{Ca^{2+}} \times 0.24 m_{CO^{2-}_3}$ pour une solution à 15 g.L-1 de NaCl. Donc $Q_{(0)} = 15 Q_{(0.25)}$

En réalité, la force ionique d'une solution d'eau pure à l'équilibre avec la calcite sera non-nulle donc l'écart sera moindre. Toutefois, l'augmentation de la salinité de la solution entraîne une augmentation sensible de la solubilité apparente de la calcite.

De plus, l'ajout de cholures en solution favorise la complexation des ions calcium et par conséquent, augmente la solubilité apparente de la calcite. Cependant les calculs thermodynamiques montrent un effet limité de ce phénomène dans les gammes de salinité étudiée.

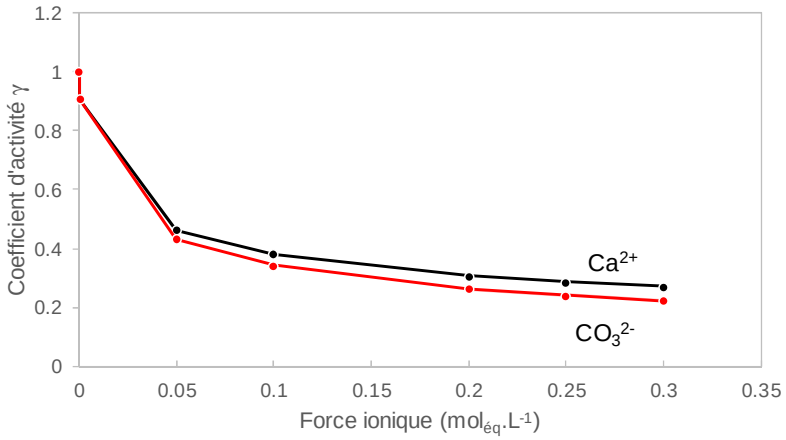

Figure 16 : Evolution des coefficients d'activité de Ca^{2+} et CO_3^{2-} calculés à l'aide de la loi de Debye-Hückel en fonction de la force ionique de la solution à 60°C.

II.1.3. Aspect cinétique des phénomènes de dissolution/précipitation

Les réactions décrites jusqu'à présent ont été exprimées d'un point de vue thermodynamique vis-à-vis d'un environnement que nous pourrions assimiler à un réacteu. Leurs états d'équilibre sont caractérisés par les états énergétiques initiaux et finaux du système de façon indépendante du facteur temps et sans tenir compte des mécanismes réactionnels et de leurs cinétiques. Dans le cadre de notre étude, la connaissance des cinétiques, des taux de dissolution/précipitation des minéraux ainsi que des mécanismes mis en jeu en conditions d'aquifères profonds est essentielle. De plus, les phénomènes de transport qui impacteront la dynamique générale de l'environnement proche puits suite à l'injection de la solution riche en CO_2 jouent également un rôle prépondérant dans l'évolution du système.

II.1.3.1. Mécanisme de contrôle de la vitesse globale de réaction

Les processus physico-chimiques qui interviennent durant les réactions de dissolution/précipitation d'un minéral dans un fluide se décomposent en cinq étapes [117] (Fig. 17):

1. Transport par diffusion ou advection des réactifs vers la surface du solide.

2. Adsorption des réactifs à la surface du solide et migration à la surface des sites actifs.

3. Réaction chimique entre les réactifs adsorbés et le minéral (cette étape peut comporter différentes sous-étapes telles que la rupture et la formation de liaisons chimiques [118] et migration hors des sites réactifs).

4. Désorption des produits de surface.

5. Migration des produits loin de la surface.

La vitesse de réaction globale résulte donc de deux mécanismes distincts : 1) le détachement ou l'incorporation des ions à la surface du minéral suite aux réactions chimiques proprement dites, c'est le "surface reaction effect" (étapes 2-3 et 4) le transport diffusionnel des espèces aqueuses dissoutes issues des réactions de surface au travers d'une couche interfaciale (ou diffussive boundary layer en anglais) appelé le "transport effect" (étape 1 et 5). [119]

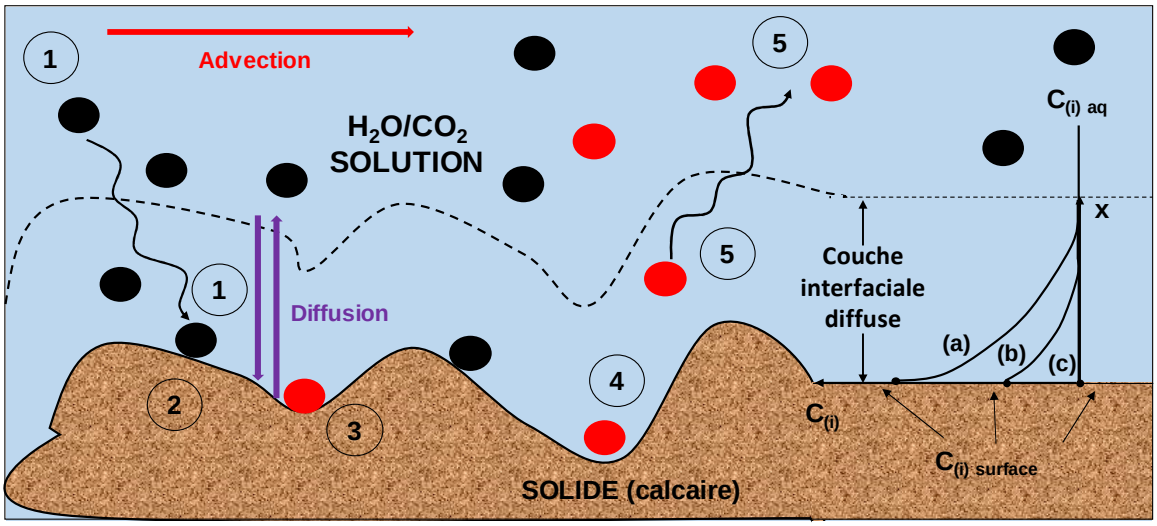

Figure 17 : Schéma représentant les cinq étapes élémentaires observées lors des processus de dissolution/précipitation d'un minéral à son interface avec la solution aqueuse. A droite du schéma, il est possible de visualiser l'évolution des concentrations au sein de la couche interfaciale lors du contrôle de la dissolution d'un solide (a) par le transport diffusif, (b) contrôle mixte, ou (c) par la réaction de surface (modifié d'après Madé., 1991 [120]).

La cinétique globale de réaction est alors gouvernée par l'étape la plus lente appelée également étape limitante. Ainsi, si la réaction chimique de surface est beaucoup plus lente que le transport des espèces en solution alors la cinétique globale est dite contrôlée par la réaction de surface. La concentration d'une espèce i à la surface du minéral ($C_{i(surf)}$) sera la même que la concentration dans la phase aqueuse ($C_{i(aq)}$) (Fig. 17). Si c'est la cinétique de transport la plus lente alors la cinétique globale est dite limitée par le transport de matière (ou transfert de masse) au sein de la phase aqueuse. Dans ce cas, la concentration de l'espèce i à la surface du minéral sera différente de celle présente dans la phase aqueuse. Il se forme alors un gradient de concentration dans la couche interfaciale entre cette surface et la solution au travers de laquelle le transport est principalement diffusif (Fig.17 droite). Dans un scénario où circule un fluide acide au travers des pores d'une matrice rocheuse ou de fractures pré-existantes, le renouvellement de la solution au voisinage de la surface sera accentué par les phénomènes liés à l'agitation (advection et dispersion). Une augmentation de cette agitation diminuera l'épaisseur de la couche interfaciale et augmentera donc la concentration de l'espèce i en solution [121].

II.1.3.2. Paramètres définissant la cinétique de dissolution/ précipitation

Les variations de la vitesse de réaction entre une fluide et une roches sont liés d'une part à l'environnement dans lequel a lieu l'interaction (Température, pH, P_{CO_2} , présence d'inhibiteurs, agitation du milieu…) mais également aux propriétés de surface des minéraux (défauts cristallins…) et à l'hétérogénéité minéralogique de la roche.

La mesure de la vitesse de réaction de la calcite a fait l'objet de nombreuses études aux échelles nano et microscopiques (dont Morse et Advison 2002 [93] et Morse et al., 2007 [122] en ont fait une analyse globale). Deux études particulières de Pokrovsky et al., 2009 [123] (25 <T< 150 °C et 1 < P_{CO_2} < 55 atm) et Peng et al., 2015 [124] (25 <T< 100°C et 60< P_{CO_2} <138 atm) ont été réalisées en conditions thermodynamiques représentatives d'un aquifère salin profond soumis à une injection de CO_2. Pour les conditions attendues dans nos expériences, les auteurs ont démontré experimentalement l'impact de la température, de la P_{CO_2} et du pH associé sur les taux de dissolution (Fig. 18a et b). L'impact de la force ionique jusqu'à 1 molaire NaCl est quant à lui relativement modéré [123].Les résultats démontrent également l'influence de l'hydrodynamisme sur l'épaisseur de la couche limite (couche interfaciale diffuse Fig. 17) et donc sur la concentration des espèces dissoutes en solution [124] (solubilité augmente avec l'effet dynamique).

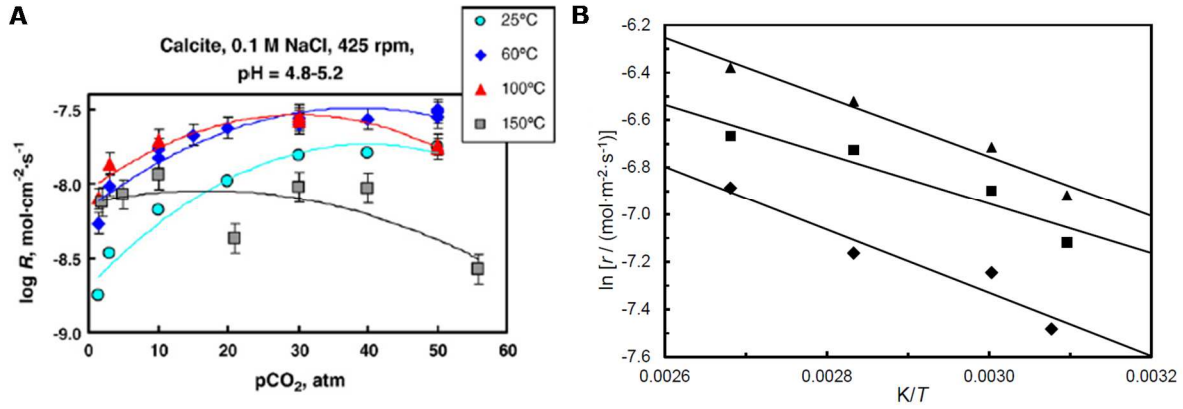

Figure 18: Vitesses de dissolution de la calcite en fonction de a) la P_{CO2} à différentes températures [123] et b) de l'inverse de la température pour différentes pression de CO_2 [124]. ◆, P_{CO_2} = 6 MPa; ■, P_{CO_2} = 10 MPa et ▲, P_{CO_2} = 13.8 MPa [124].

La nature de la surface de contact entre la roche et le fluide réactif ainsi que la fraction réactive impliquée dans les réactions de dissolution/précipitation ont également un impact direct sur le taux de réaction mais également sur l'évolution de l'état de surface de la roche. La rugosité de surface locale à l'échelle microscopique est fonction de la nature des éléments composant la matrice rocheuse (grains carbonatés, phase de liaison,…). A titre d'exemple, dans le cas de la dissolution d'une roche calcaire, un monocristal composant les ciments sparitiques n'a pas la même distribution d'énergies de surface qu'une micrite. Fischer et al (2012) [87] ont comparé la distribution des taux de dissolution sur les surfaces d'un monocristal et d'une micrite en mesurant les

hauteurs de recul des surfaces par dissolution à l'aide de la technique d'interférométrie à balayage vertical. Les spectres montrent une distribution distincte des taux réactifs sur leur surface globale et une déformation différente de leurs surfaces (Fig. 19a). Plusieurs études expérimentales ont confirmé ces observations [44 ; 125]. Ainsi, un monocristal sera dominé par une dissolution hétérogène au niveau des sites réactifs définis paragraphe I.2.3 sous forme de puits de dissolution (etch pit) et de plateaux ; avec un retrait progressif de la matière (Fig. 19b). Une matrice composée de grains micritiques se dissoudra quant à elle de façon plus aléatoire sur une surface plus réactive car composée d'une quantité de sites réactifs plus importants (spectre plus élargi Fig. 19a).

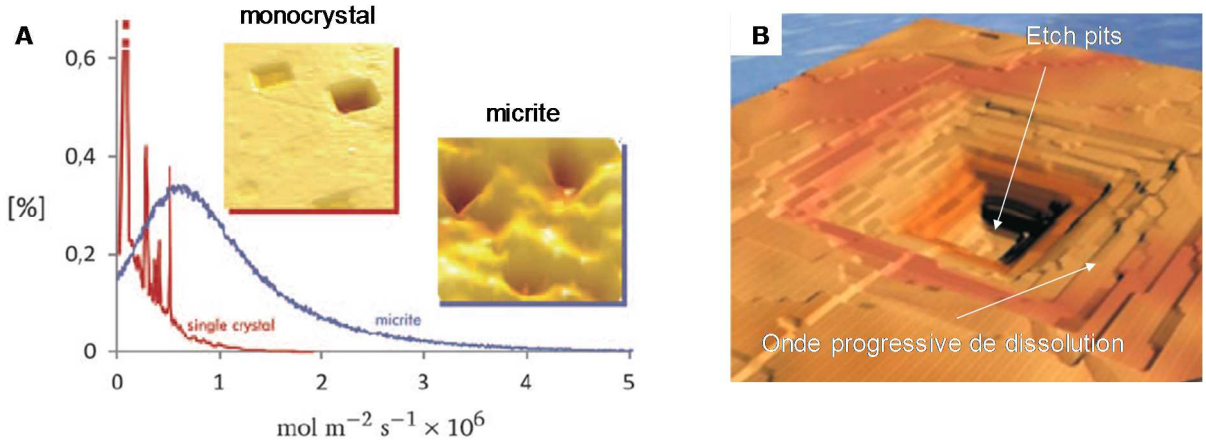

Figure 19 : Comparaison des spectres représentant la distribution des vitesses de dissolution à la surface d'un monocristal et d'une micrite. Les images AFM correspondent aux états de surface propres à chaque échantillon [125]. b) Simulation de la formation d'un puits de dissolution sur le site d'un défaut de dislocation avec la génération d'ondes progressives de dissolution [126].

La cinétique de dissolution est donc propre à chaque type de cristal du fait de leur surface réactive différente. Cependant, il est intéressant de noter que malgré des mécanismes de dissolution et des cinétiques différents, le taux de dissolution global n'est que faiblement impacté [126].

Bien évidemment, l'évolution morphologique de la surface de la matrice rocheuse suite à l'injection continue d'une solution acide fera évoluer le nombre de sites réactifs [125] et la valeur de la surface réactive S_r. De la même façon, elle modifiera la rugosité des parois en la lissant [89] ou en augmentant la rugosité, par la formation de cavités plus ou moins profondes.

Ainsi, pour les analyses globales de dissolution dans le domaine des géosciences, l'équation la plus commune pour décrire le taux de dissolution global d'un minéral carbonaté prenant en compte les différents paramètres influants s'écrit [117]:

$$r = -\frac{dn_{\min}}{dt} = k_r S_r = k_m S_r \prod_i [a_i]^j (1-\Omega^n)^{n'} \quad (11)$$

où r est la vitesse de dissolution locale à la surface du minéral (mol.s^{-1}), $n_{\min}$ le nombre de moles du minéral, k_r est la constante cinétique globale de la réaction chimique (mol.m^{-2}.s^{-1}), k_m est la constante cinétique intrinsèque au minéral m (mol.m^{-2}.s^{-1}), S_r est la surface réactive du minéral (m^2), a_i correspond à l'activité de l'espèce i influençant la réaction, soit comme catalyseur (si l'exposant j > 0), soit comme inhibiteur (si j < 0), Ω est l'indice de saturation.

Dans cette équation, il apparaît également que l'état de saturation du système influence la cinétique de dissolution par le terme $(1-\Omega)$. Ce dernier annule la vitesse lorsque l'équilibre thermodynamique est atteint.

Dans le cadre de notre étude, le taux de dissolution global sera déterminé à partir des données expérimentales de Pokrovsky et al., 2009 [123] acquises dans les conditions de nos expériences (P_{CO_2} = 30 bars et *T* = 60°C). La valeur de *r* est calculée à partir de l'équation polynomiale de second ordre suivante :

$$\log r = A + B * P_{CO_2} + C * \left(P_{CO_2}\right)^2 \quad (12)$$

Où A, B et C sont des paramètres empiriques qui dépendent de la température et du pH (Tableau 1) pour un environnement soumis à un pH dont la valeur est comprise entre 4,8 et 5,2.

Température	C	B	A	R²
25	-0,000601	0,0480	-8,69	0,96
60	**-0,000456**	0,0351	**-8,16**	**0,9**
100	-0,000557	0,0335	-8,04	0,89
150	-0,000302	0,0101	-8,13	0,5

R² correspond au coefficient de corrélation

Tableau 1 : Paramètres de l'équation (12) décrivant la dépendance du taux de dissolution de la calcite à la P_{CO_2} (pour 4,8<pH<5,2).

II.2. Transport réactif dans une roche calcaire poreuse (classification des modèles de dissolution (Introduction des nombres *Pe-Da*)

II.2.1. Description du transport réactif multi-échelle

Les solutions interstitielles saturant un environnement géologique naturel peuvent être soit quasi stationnaires (« stagnantes ») soit en mouvement (écoulement laminaire ou turbulent) par rapport à la surface de la matrice solide. L'injection, par le biais d'un ouvrage approprié, d'une solution enrichie en CO_2 dans un réservoir carbonaté est un processus dynamique. Afin de spécifier les phénomènes engendrés par l'injection de ce soluté réactif, il est nécessaire de coupler les modèles "statiques" qui définissent à

l'échelle microscopique (par le *transfert* des ions en solution) la réactivité entre le fluide et la roche aux différents mécanismes de *transport* en milieu poreux qui contraignent ce déséquilibre chimique moyen à l'échelle macroscopique. Le transport est donc un paramètre fondamental dans notre système car il fournit la force motrice aux réactions qui ont lieu en introduisant continuellement le fluide hors d'équilibre par rapport à la phase solide réactive. L'étude des impacts géochimiques en région proche puits équivaut donc à une problématique de transport réactif en milieux poreux saturé, avec ou sans hétérogénéités locales (fissure, fractures) dans lequel trois mécanismes principaux de transport agissent conjointement (Fig. 20) : l'advection, la dispersion et la diffusion.

- L'advection (ou convection) : implique le transport de la matière dissoute ou en suspension dans le champ de vitesse du fluide en mouvement dont la valeur moyenne U est définie par la loi de Darcy.

- La dispersion cinématique : le milieu poreux étant très hétérogène, les éléments au sein du fluide vont parcourir différents chemins tortueux à des vitesses moyennes de propagation différentes qui sont fonction de la variabilité des dimensions et longueurs de pores (Fig. 20a). De plus, au sein même d'un pore ou de ses gorges d'accès (pore-throat), le phénomène de friction imputable à la viscosité du fluide entraine une distribution des profils de vitesses microscopiques sous une forme parabolique avec une valeur maximale au centre du pore et minimale le long des parois (due aux forces de frottements à ce niveau) (Fig. 20b) [127]. Ces fluctuations multiples de vitesse entraînent une dilution du soluté, appelée dispersion cinématique. A toutes les échelles, il est nécessaire de surimposer à l'advection cette composante de dispersion aléatoire dont le coefficient s'exprime sous une forme tensorielle, suivant une direction longitudinale dans le sens de l'écoulement et transversale dans les deux directions perpendiculaires à l'écoulement.

- La diffusion est un phénomène physique qui peut être défini comme un mouvement aléatoire lié à l'agitation des particules qui a pour conséquence un flux net de migration des régions à forte concentration vers les régions à faible concentration entraînant ainsi un mélange progressif du soluté à l'échelle macroscopique (Fig. 20c). La diffusion est un phénomène fortement lié à la température du milieu (selon la loi d'Arrhenius) ainsi qu'à la nature de l'ion concerné, la pression et la composition du fluide. En milieu poreux, la diffusion moléculaire est également contrainte par la configuration de l'espace poral, le mouvement des particules étant limité par les interfaces solides. Il en résulte un coefficient de diffusion moléculaire dit effectif D_{eff} plus faible que le coefficient de diffusion moléculaire standard D_m.

A l'échelle macroscopique, pour un fluide en mouvement, il est nécessaire d'introduire la notion de dispersion hydrodynamique qui associe la diffusion moléculaire et la dispersion cinématique.

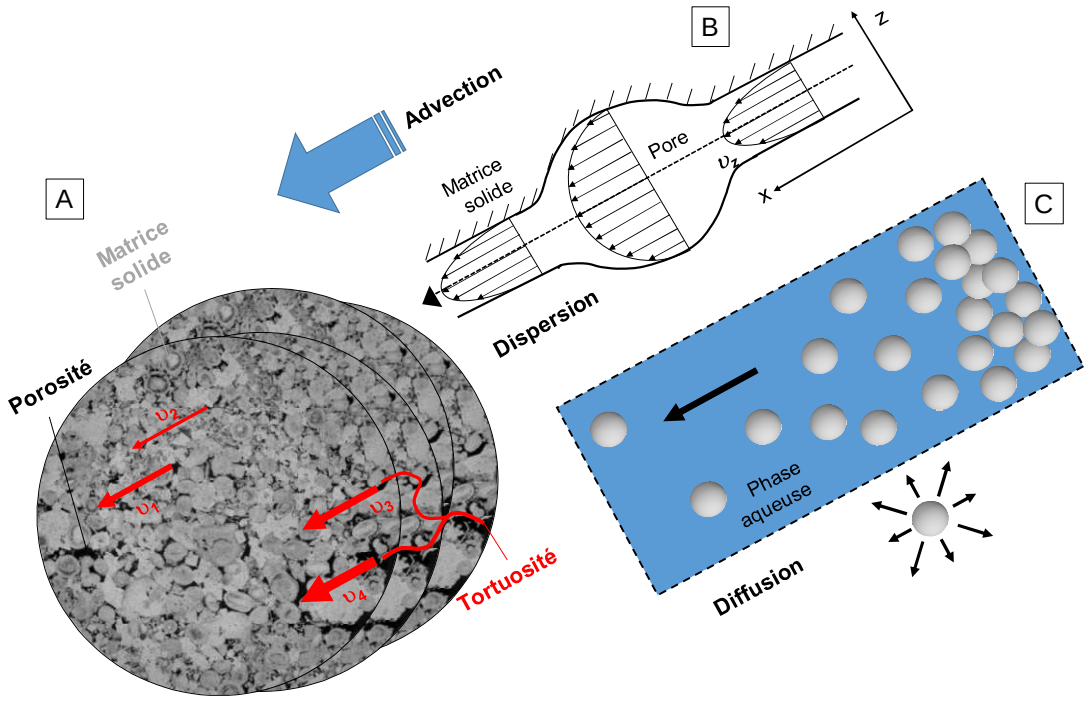

Figure 20: Représentation schématique des différents mécanismes intervenant lors du transport hydraulique d'éléments conservatifs dans un milieu poreux saturé a) Mise en évidence de l'influence de la tortuosité et de la géométrie des pores sur le mécanisme de dispersion ; les images représentent l'accumulation de stacks acquis par tomographie aux rayons X sur les échantillons de calcaire (cette étude) b) Influence des phénomènes de frictions sur le mécanisme de dispersion au sein d'un pore et c) mécanisme de diffusion.

II.2.2. Adimensionnement du transport réactif et classification des déformations

Afin de caractériser l'évolution du milieu poreux provoquée par la réactivité du fluide acide introduit, nous utiliserons deux nombres adimensionnels qui gouvernent le processus limitant et les motifs d'altération engendrés [128 ; 129 ; 130 ; 131]: les nombres de Péclet et de Damkhöler dont la détermination diffère selon l'échelle d'observation choisie.

Le nombre de Péclet décrit le mécanisme de transport dominant. Ce nombre est défini comme l'importance relative entre le flux de transport par advection par rapport au flux de transport par diffusion (ou dispersion) moléculaire [132].

A l'échelle microscopique : $$Pe = t_D \times \frac{1}{t_A} = \frac{l^2}{D_m} \times \frac{\upsilon}{l} = \frac{\upsilon l}{D_m} \quad (13)$$

Où t_D correspond au temps caractéristique de diffusion et t_A d'advection (en s), υ correspond à la vitesse interstitielle advective moyenne (m.s^{-1}), l la longueur caractéristique du système étudié (m) qui dépendra de l'échelle considérée (par exemple diamètre moyen d'entrée de pore ou longueur de l'échantillon pour un milieu poreux ou ouverture dans le cas d'étude de réactivité dans les fractures) et D_m le coefficient de diffusion moléculaire de Ca^{2+} en solution (m^2.s^{-1}).

Un faible nombre de Péclet (*Pe* << 1) est représentatif d'un milieu dans lequel le processus de transport dominant est la diffusion. A contrario, pour un nombre de Péclet important (*Pe* >> 1), la convection est le processus de transport dominant avec une dispersion du soluté d'ordre majoritairement longitudinal et très peu diffusif. Dans le cas de valeur transitoire (*Pe* ≈ 1), les deux processus influencent le transport de façon quasiment similaire.

Le nombre de Damköhler traduit l'agressivité de la solution vis-à-vis de la roche et est défini, pour une échelle de longueur donnée, comme la fraction d'acide consommé (vitesse de réaction chimique) par rapport à la quantité d'acide amenée par convection (vitesse du fluide) ou par diffusion. Le nombre de Damköhler se détermine de deux façons selon que le système étudié est principalement convectif *Da* (Eq. 14) ou diffusif *Da** (Eq. 15). Ce deuxième nombre *Da**, également appelé le nombre cinétique est fréquemment utilisé dans les études sur la dissolution d'un minéral ; il est défini comme le rapport entre le flux d'acide consommé par la réaction chimique et le flux diffusif et il permet de s'affranchir de la vitesse du fluide [133].

$$Da = t_A \times \frac{1}{t_R} = \frac{l}{\upsilon} \times \frac{S_r k_r(T)}{\phi C_{eq}} = \frac{S_r k_r(T)\, l}{\phi C_{eq}\, \upsilon} \qquad (14)$$

$$Da^* = t_D \times \frac{1}{t_R} = \frac{l^2}{D_m} \times \frac{S_r k_r(T)}{\phi C_{eq}} = \frac{S_r k_r(T) l^2}{\phi C_{eq} D_m} \qquad (15)$$

Où t_R correspond au temps caractéristique de la réaction (en s), $k_r(T)$ correspond à la constante cinétique à la température *T* en s^{-1}, S_r est la surface spécifique en contact avec le fluide réactif en $m^2_{minéral}.m^{-3}_{solution}$, l la longueur caractéristique considéré (m), ϕ la porosité connectée et C_{eq} la concentration en ions Ca^{2+} en équilibre avec la calcite en $mol.L^{-1}$. De la même façon que pour le nombre de Péclet, le nombre Da dépend fortement de l'échelle de longueur considérée.

Le nombre de Damköhler nous renseigne donc sur le mécanisme réactionnel limitant (cf. II.1.2.1). A faible valeur de *Da ou Da** (<< 1) la réaction est contrôlée par la réaction de surface alors qu'à des valeurs importantes de *Da ou Da** (>> 1), c'est le transfert de masse qui est limitant.

Le degré d'équilibre entre les propriétés de transport et la cinétique de réaction va alors engendrer différentes figures de dissolution qui sont fonction du débit massique de l'injection et du processus réactionnel limitant (Fig. 21) [46 ; 134 ; 135; 136 ; 137 ; 138 ; 139].

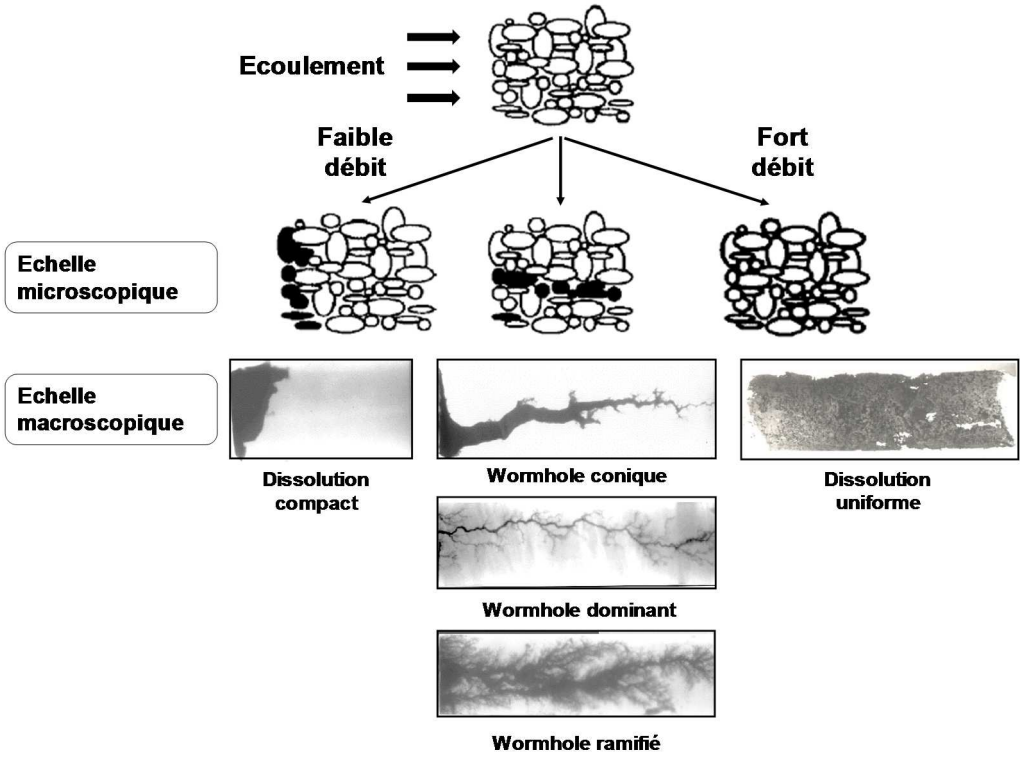

Figure 21 : Représentation schématique des différents régimes d'altération obtenus expérimentalement aux échelles microscopiques [130] et macroscopiques [131].

1. *Régime de dissolution compact* : À des taux d'injection suffisamment faibles (*Pe*<<1), la diffusion est le mécanisme dominant du transport de l'espèce acide. Pour un *Da**<<1, l'acide est complètement consommé lorsqu'il pénètre dans la matrice poreuse. Malgré les hétérogénéités présentes dans la roche, le front réactif est stable et de nature compacte.

2. Régime de *"wormhole conique"* : Pour des débits légèrement plus importants (*Pe* et *Da** intermédiaires), des instabilités à l'échelle du pore commencent à se développer, instabilités pouvant évoluer sous forme de chenaux préférentiels au sein du milieu poreux appelés trous de vers (« wormholes »). L'augmentation du débit entraine un renforcement de l'advection axiale mais le transport de l'espèce acide par diffusion reste dominant. Les effets diffusifs tendent alors à éroder les parois à l'entrée du wormhole avec comme conséquence l'apparition d'une forme conique.

3. Régime de *"wormhole dominant"* : Pour des débits intermédiaires (*Pe* proche ou > 1), le transport convectif devient dominant et lorsque le taux de réaction est relativement important par rapport à la diffusion (*Da* > 1), l'espèce acide est transportée et consommée préférentiellement dans les diamètres d'entrée de pores (pore-throats) les plus grande, le long des chemins d'écoulement, dont la déformation conduira à l'apparition de wormholes cylindriques et allongés de haut conductibilité hydraulique. Cette forme est imputable au temps de séjour minimal de l'acide dans le wormhole qui se concentre à l'extrémité de ce dernier.

4. Régime de *"wormhole ramifié"* : A plus haut débit, l'intensité du transport par advection axiale devient plus important que le taux de réaction (*Da* faible). L'acide injecté n'est alors pas complétement consommé au niveau du front de dissolution. L'acide résiduel est alors transporté dans plusieurs directions en fonction des hétérogénéités rencontrées par le mécanisme de dispersion. Apparaissent alors plusieurs ramifications dérivées du wormhole. Ce régime est marqué par un front de dissolution plus épais et propagé.

5. Régime de *dissolution uniforme* : En imposant un très haut débit et pour des faibles taux de réaction (réaction limitante à *Da* << 1), apparaît un équilibre à l'échelle du pore. La majorité de l'espace poreux connait des vitesses relativement élevés. Le soluté est alors consommé progressivement les long des diamètres d'entrée de pores (indépendamment de la forme et taille de pore) et les produits de la réaction sont ainsi éloignés efficacement de la surface de la matrice rocheuse. Ainsi, le fluide réactif renouvelé est continuellement exposé à la surface entière de la roche conduisant à une augmentation uniforme de la porosité.

Plus récemment Menke et al., 2016 [140] ont défini un nouveau régime de dissolution pour des nombres de *PeDa* jusqu'alors représentatifs du régime de dissolution uniforme : un fort *Pe* (fort débit d'acide continu alimentant en permanence l'ensemble de l'espace poreux en réactif) et un faible *Da* (vitesse de réaction lente par rapport aux transports diffusif et adjectif). Les auteurs ont dénommé ce phénomène chenalisation ("channeling"). Ce régime engendre des instabilités sous forme de chemins réactifs préférentiels mais diffère légèrement du phénomène de wormholing (Fig. 22). Il souligne l'importance de prendre en compte la structure initiale de la matrice (à l'échelle du pore dans l'étude) en l'associant aux conditions d'écoulement pour définir le type d'altération.

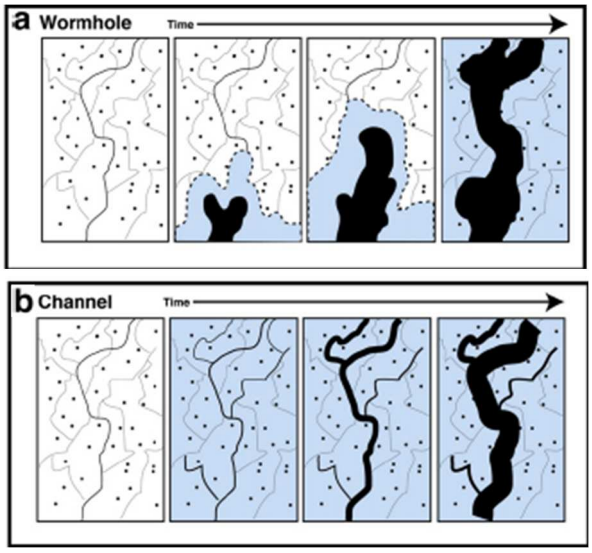

Figure 22 : Représentation schématique des régimes de dissolution [140] (a) de type wormholing et (b) de type " channeling ". L'espace poreux est représenté en noir ; les points noirs correspondent à la porosité intra-granulaire ; la solution réactive est en bleu et la roche en blanc.

En régime de wormholing, les chenaux formés dominent l'écoulement et limitent la consommation des réactifs aux alentours de leurs bordures limitant ainsi le transport du réactif dans le reste de l'espace poreux (Fig. 22a). Dans le cas du régime de type "channeling", le débit est plus important ; il va alimenter le réseau poreux très rapidement (comme dans le cas d'un régime uniforme) mais les hétérogénéités de la roche vont donner lieu à la formation de chemins préférentiels (Fig. 22b), qui par la suite vont bien entendu drainer principalement le fluide assurant l'alimentation de la majorité du réactif à une portion plus limitée de la surface de la roche.

Un diagramme de comportement permettant de cartographier les différents régimes de propagation et ainsi définir les conditions de transition entre les régimes en fonction des deux seuls nombres de *Pe* et *Da* a été proposé par Golfier et al., 2002 [139] à partir de travaux experimentaux et de modélisation de transport réactif (Fig. 23). Ce diagramme a été validé par d'autres auteurs (par exemple [35 ; 46 ; 141]) dans des conditions similaires de dissolution mais également dans le cas de la réaction inverse (précipitation) [142 ; 143]. N'étant pas encore défini à l'époque, le régime dit de "channeling" n'apparait pas.

Il ressort de ce diagramme que le nombre de Péclet n'influence pas les transitions entre les régimes de wormholes dominants, wormholes ramifiés et dissolution uniforme, mais qu'elles dépendent directement du nombre de Damköhler. Dans notre cas d'étude ou le débit d'injection sera relativement important en région proche puits, le mécanisme de transport par convection apparait comme étant le mécanisme qui dominera le transport (cinétique limité par la diffusion) ce qui est plutôt propice à la formation de wormhole dont la forme dépendra du débit imposé [144]. De plus, dans un premier temps, le nombre de Damköhler sera le plus affecté (de par l'influence du facteur cinétique k) par l'ajout de CO_2 dans la solution injectée. L'injection d'une solution riche en CO_2 engendrera donc, dans le cas de notre étude, des phénomènes plutôt instables dont la géométrie sera principalement fonction de Da.

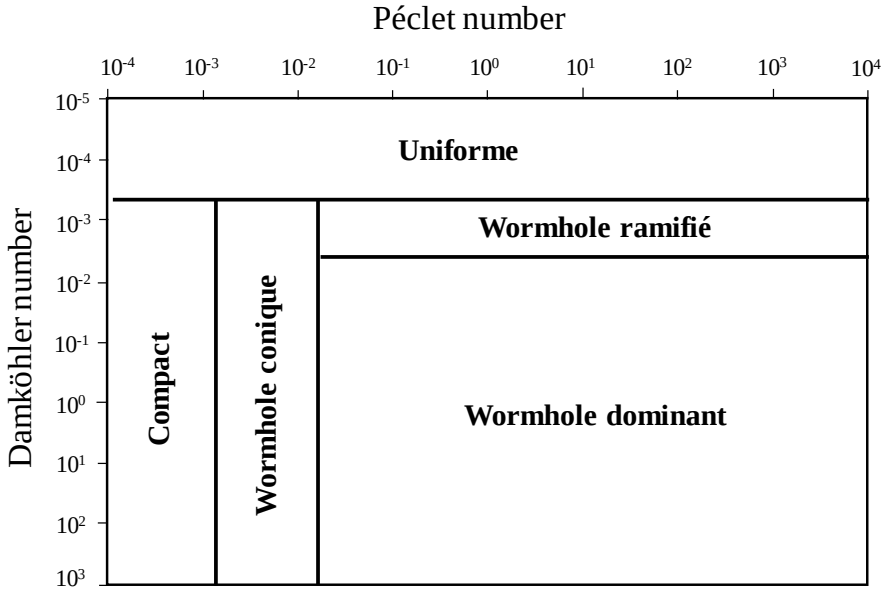

Figure 23 : Diagramme de prédiction des transitions entre les différentes figures de dissolution en fonction des nombres adimensionnels Pe-Da [139].

Ce diagramme a donc un intérêt pratique pour un expérimentateur car il permet soit en amont des expériences, d'anticiper le régime de dissolution en fonction du débit imposé et ainsi de minimiser les nombres d'expériences ; soit en aval des expériences, d'identifier les mécanismes dominants à l'origine des figures de dissolution observées.

Enfin, il est nécessaire de souligner que les lignes de transition entre les différentes figures de dissolution sont mobiles et dépendent i) de la concentration d'acide fixée et exprimée par le nombres adimensionnel dit de pouvoir acide N_{ac} (Equation 16) [135] (masse de solide dissous par unité de masse de roche concernée), ii) du nombre adimensionnel de Darcy N_D (Equation 17) qui détermine l'importance relative du terme de Darcy sur le terme visqueux de Stokes ainsi que iii) du facteur de forme F (Equation 18) propre au système expérimental.

$$N_{ac} = \frac{\phi C_{ac_0} \beta}{(1-\phi)\rho_{calcite}} \quad (16)$$

$$N_D = \frac{k}{x_1^2} \quad (17)$$

$$F = \frac{x_1}{x_2} \quad (18)$$

Avec C_{ac_0} moyenne volumique intrinsèque de concentration acide imposée en entrée (% acide dans la solution) en kg.m^{-3}, ϕ la porosité du milieu poreux, β le coefficient stoechiométrique de la réaction égale à 1 dans notre cas. $\rho_{calcite}$ la masse volumique du minéral (kg.m^{-3}), k la perméabilité du milieu poreux (m²) et x_1 la longueur maximale de propagation du front réactif (la longueur entre la surface du puits et l'extrémité extérieure de la carotte), x_2 la hauteur initiale de contact entre la solution et la roche (hauteur du puits).

Ces nombres adimensionnels permettent donc de définir les phénomènes à l'origine des figures émergentes suite à la réactivité entre la solution interstitielle acide et la roche. Comme nous l'avons déjà discuté précédemment, au-delà des processus physico-chimique mis en jeu, les zones réactives vont être fortement dépendantes de l'hétérogénéité minéralogique de l'échantillon étudié qui engendrera des gradients de réactivité (les phénomènes de dissolution/précipitation n'impacteront pas obligatoirement l'ensemble du réseau poreux). De plus, la répartition de ces zones réactives sera également fortement dominée par la distribution des défauts qui pilotera le taux de réaction et les processus limitants.

NOTE

Ce travail de thèse intervenant dans le cadre de participations à 2 projets regroupant plusieurs partenaires internationaux, il a fait l'objet de 2 livrables rédigés en anglais décrivant la méthodologie développée ainsi que les résultats principaux obtenus. Ceci explique la langue de rédaction des parties 3, 4, 5 et 6.

– PARTIE 3 –
APPROCHE EXPÉRIMENTALE

– PART 3 –
EXPERIMENTAL APPROACH

I. INTRODUCTION

In order to best meet the needs of the CO2-DISSOLVED project, an original experimental protocol has been developed. The context of the project requires the injection, at a constant flowrate, of a CO_2-rich aqueous phase in a reservoir rock to investigate the geochemical processes induced by the disruption of existing chemical equilibria and their effect on the hydraulic properties. The experimental setup thus reproduces at the laboratory scale the injection conditions in near well region in term of pressure, temperature, flowrate, rock type, well material (cement, casing) and fluid chemical composition. The special feature of the considered test bench relates, in the first instance, to the design of the sample to be constrained. Indeed, the sample configuration replicate a laboratory-scale injection well by imposing the "radial" injection of a CO_2-saturated solution and by reproducing the different interfaces (cement/steel, cement/reservoir and potentially cement/reservoir/cover). A radial injection in the heart of a centimeter rock sample has rarely been performed in the framework of CCS research. This configuration allow the fluid to freely flow through the rock matrix of the sample. By this mean, the experimental system will consider the structural heterogeneity of the rock. In addition, the acquisitions of physico-chemical data (pressure, temperature, pH, concentrations of different aqueous species, etc.) are optimized during the experiments. For this purpose, a variety of original in situ measurement techniques (High Pressure / High Temperature Raman probe, High Pressure / High Temperature pH probe, High Pressure flowmeter) were implemented.

In addition, a protocol for processing data from the non-invasive method of X-ray tomography has been developed. This method allow the qualitative and quantitative characterization of the evolution of the rock sample morphology due to the dissolution/precipitation processes.

The selected rock for the experiments, the pre-dimensioning modeling, the experimental set-up and the various tools used in the characterization of pre- and post-experiment samples are presented in the following paragraphs. A special attention will be paid to the specific in-situ Raman measurement and the CT-scan data treatment methods.

II. MATERIALS

II.1. Carbonate rock sample selected for experiments: the “Lavoux limestone”.

Beyond the assessment of the technical applicability of the new CCS concept CO2-DISSOLVED, the best injection strategy requires to select a geological environment appropriate to the project constraints. The geological context of the Paris sedimentary basin appears to be conducive to the implementation of an industrial pilot in the expected conditions [146; 147]. The “Oolithe Blanche Formation” (Bathonian) of the Dogger has been predominantly identified as the most promising host formation for a CCS industrial application [148; 149]. Several studies underline the quality of this reservoir in term of porosity (18.3% according to Lopes et al., 2010 [150]; between 1 and 26.8%, with an average value of 15.5 % according to Delmas et al., 2010 [151], between 11.6% and 23.4%, with an average value of 17% according to Casteleyn et al., 2010 [152]) and permeability data (from 10 mD in the outcrops area to 2 D in the geothermal production layers [152]). These petrophysical characteristics provides good flow properties and good injectivity. The reservoir is 70-80 meters thick and it rests at depths of more than 1500 m in the central part of the Paris Basin. The “Oolite Blanche Formation” thus offers a large spatial extent and available pore volume for CO_2 storage. The aquifer is characterized by pressure and temperature conditions varying respectively between 120 and 200 bar and between 50 and 80°C and by a salinity of 2 to 20 $g.L^{-1}$ [149]. Furthermore, the existence of a cap-rock of impermeable argillaceous rocks (Callovo-Oxfordian) would ensure the integrity of the storage. Finally, these formations are close to major CO_2 emitters.

In order to perform experimental procedures of acidic injection, a natural analog of the “Oolithe Blanche Formation”, the “Lavoux limestone” was used. The main selection criteria considered were i) a structural and textural homogeneity for a good reproducibility of results and ii) good flow properties that would enable a good injectivity. This limestone has been studied as part of different projects on themes such as the development of methodologies for measuring petrophysical data of a rock [153], the numerical modeling of the microstructure of a porous rock in order to comprehend the effect of this microstructure on the rock macroscopic behavior [154], or, as in our field of research, the experimental study of the geochemical [38], petrophysical [39 ; 155] or chemomechanical [156; 157; 158] behavior of a porous limestone in contact with CO_2. The “Lavoux limestone” is considered as almost a mono-mineral material and its high porosity and good permeability allow the fluid percolation, without excessive stress and pressure gradient to be imposed.

The “Lavoux limestone” is located in the geological area called “Poitou Threshold”, in the Poitou-Charentes Region between the Paris basin to the northeast and the Aquitaine basin to the southwest (Fig. 24). This carbonate rock belongs to the Dogger (50–200 m thick) as the “Oolithe Blanche Formation” and it is dated more precisely from the Upper Callovian age. The deposits are outcropping in two sequences in many quarries near the city of Poitiers as shown in Figure 24, which represents the geological section of the Poitou threshold.

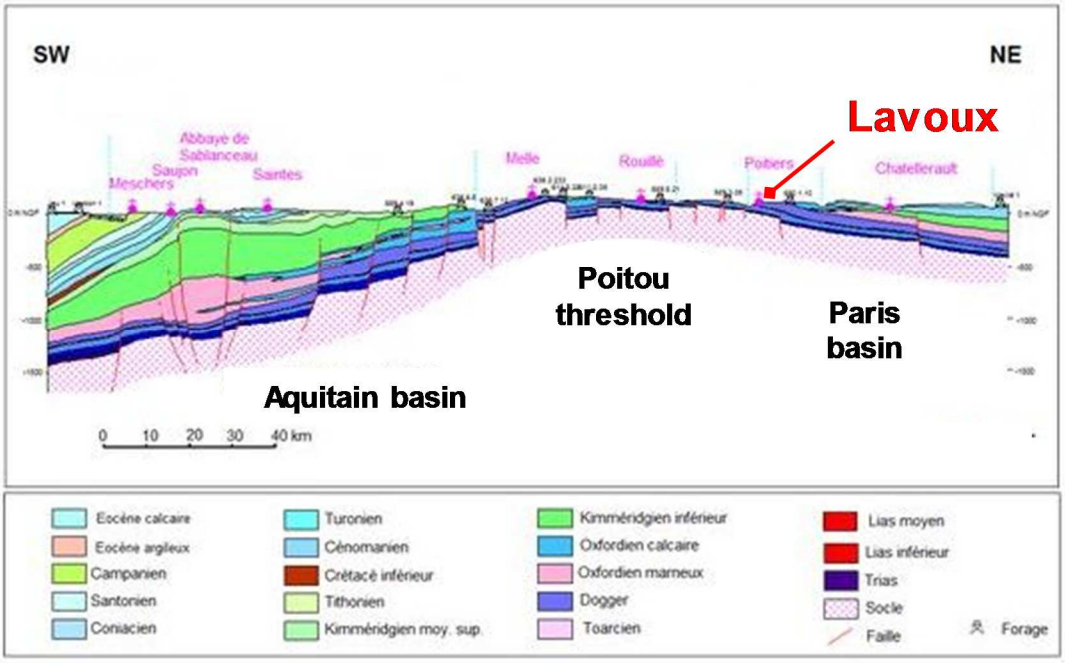

Figure 24: Geological SW-NE cross-section. Source BRGM, modified.
http://sigespoc.brgm.fr/spip.php?article33

The limestone of this formation corresponds to an oolitic limestone. In the restricted area of the sampling location (around Chauvigny), beds alternate between wackestone/packstone and coarse grained ooid grainstone with bivalve and equinoderm debris cemented by a sparry calcite [159]. This limestone is informally called “Oolite miliaire” due to the millimetrics size of the grains or “yellow Lavoux” with coarse grains. It is characterized by a porosity of 12 to 24%.

The sedimentary series of the western Paris Basin is affected by several normal faults. The major Hercynian accidents are oriented NW-SE and structure the region governing Cenozoic fracturing. The main accidents NW-SE correspond to the Montreuil-Bellay, Lusignan and Partenay faults (Fig. 25).

The results of observation campaigns [160] on the outcrops of the Jurassic limestone in the Poitiers area has established four main preferential fracturing directions: N20-30, N95, N110-135 and N170-00 (Fig. 26). The dips are mainly sub-vertical (Fig. 27). Another study concerning a multi-scale characterization of a heterogeneous aquifer also carried out in the Poitiers area by IFPEN in 2005 have found three main orientation families in formations of Bajocian and Bathonian stages: N50, N120 and N170 [161], which are close to the previous ones. All these regional fractures affect the Jurassic series of the Lavoux.

The “Lavoux limestone” selected for our experiment was sampled by the owner in a quarry (“Carrière de La Vienne”) located near the villages of Lavoux and Chauvigny, just a couple of km from the East of Poitiers (Fig. 25).

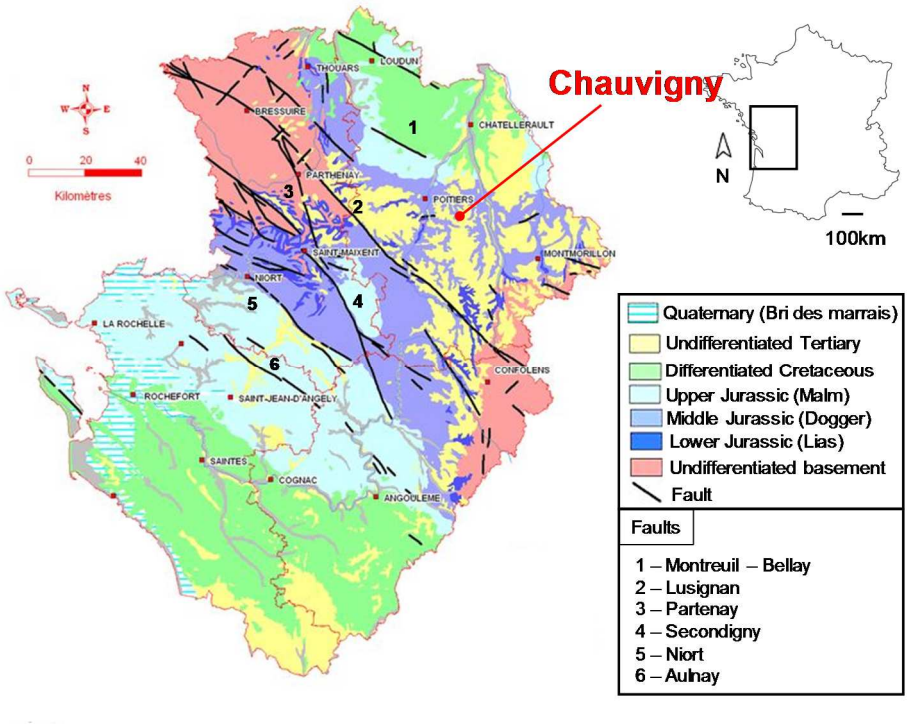

Figure 25: Location of the major faults in the studied area on a simplified geological map of the Poitou-Charentes region. Source BRGM, modified.
http://sigespoc.brgm.fr/spip.php?article33

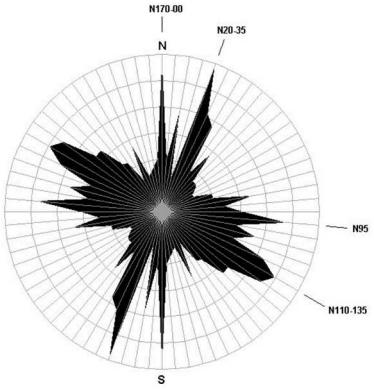

Figure 26: Main directions of the regional fractures [160].

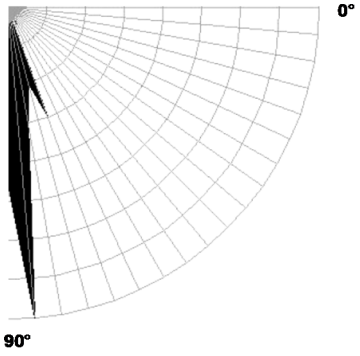

Figure 27: Dominant dip [160].

II.2. Description of the injection well materials

II.2.1. Cement

Cement is a hydraulic binder, which means that it is a finely grinded materiel which hardens by hydration reaction when combined with water. The Portland cement is manufactured by heating limestone with clay and quartz bearing clastic material to about 1450°C in a kiln. The resulting mixture called the clinker is ground with gypsum to make a fine Portland cement powder.

For the description of the cement phase, the chemists use a specific nomenclature. The first letter of the each oxide composing the cementitious materials is used to lighten the usual handwriting where each chemical element is mentioned. The main oxide are listed below:

- C = CaO (calcium oxide)
- S = SiO_2 (silicon oxide)
- H = H_2O or OH- (water or hydroxides)
- A =Al_2O_3 (Alumina)
- F = Fe_2O_3 (iron oxide)

The Portland class G is an anhydrous grain powder essentially composed of clinker and calcium sulphate. The four major phases forming during cooking are as follows [162]:

- 50 to 70 % alite (tricalcium silicate, C3S or Ca_3SiO_5),
- 15 to 30 % belite (dicalcium silicate, C2S or β-Ca_2SiO_4)
- 5 to 10 % aluminates (ferrite and tricalcium aluminate C3A or $Ca_3Al_2O_6$),
- 5 to 15 % ferrite (calcium aluminoferrite, C4AF with high substitution of Fe or Al),
- and small amounts (~2 %) of the added gypsum

The chemical composition of the Portland class G powder used in the study is presented in table 2. The analyses of the majors and traces elements were carried out by ICP-OES at the analytical research facility SARM (Service d'Analyse des Roches et des Minéraux) which is part of the Centre de Recherches Pétrographiques et Géochimiques (CRPG).

Chemical composition (Major components)	SiO_2	Al_2O_3	Fe_2O_3	MnO	MgO	CaO	Na_2O	K_2O	TiO_2	P_2O_5
weight (%)	18.31	2.96	3.27	0.04	1.56	52.37	0.12	0.37	0.32	0.28

Chemical composition (Trace elements)	Ba	Cr	Ni	Sr	Zn
weight (%)	0.016	0.011	0.005	0.080	0.011

Table 2: Chemical composition (weight %) of the Portland class G anhydrous powder (ICP-OES analysis): Major components and trace elements.

The addition of water to the Portland cement powder causes the dissolution of the anhydrous phases of the cement. The result is the formation of hydrated compounds:

- Portlandite CH ($Ca(OH)_2$),

- Hydrated calcium silicate CSH,
- And other minor phases containing aluminium, iron, and sulphate (Ettringite, Monosulfoaluminate, Katoïte silicate and gypsum).
- It is also possible to find remaining non-hydrated di/tri-calcium silicates (C2S and C3S)

The CSH is the mineral that provides the mechanical cohesion of the cement [163; 164] with an initial Ca to Si molar ratio at around 1.7/1.8. The final mineral composition of the cement after hydration and setting according to thermodynamic equilibrium [195] is presented in table 3. The given phases are those used in the thermodynamic database “Thermoddem”.

Portland Cement Class G	Formula	Composition (% Vol)
CSH_1.6	$Ca_{1.6}SiO_{3.6}$:2.58H_2O	38.10%
Portlandite	$Ca(OH)_2$	26.10%
Ettringite	$Ca_6Al_2(SO_4)3(OH)_{12}$:26H_2O	13.80%
Katoite_Si1	$Ca_3Al_2SiO_4(OH)_8$	10.50%
C3FH6	$Ca_3Fe_2(OH)_{12}$	5.50%
Hydrotalcite	$Mg_4Al_2O_7$:10H_2O	5.40%
Calcite	$CaCO_3$	0.60%

Table 3: Mineralogical composition of the class G hydrated cement. [165]

The hardened cement paste consists of a solid, porous phase and an aqueous phase resulting from the mixing water. Located in the space between the minerals, the interstitial is the product of the dissolution of the anhydrous compounds in water and the equilibrium with the hydrates. The electroneutrality of the solution is ensured by the release of hydroxide ions. The pH is thus very high, above 13 at room temperature.

II.2.2. Injection tube steel

The used steel in our experiment is an austenitic stainless steel 316 (EN standard steel name X5CrNiMo17-12-2). 316SS has a good pitting corrosion resistance and an excellent resistance to sulfates, phosphates and other salts. Its chemical composition is presented in table 4.

Chemical composition	C	Si	Mn	P	S	Cr	Ni	Mo	N
weight (%) min	-	-	-	-	-	16	10	2	-
weight (%) max	0.08	1	2	0.045	0.03	18	14	3	0.1

Table 4: Chemical composition (Weight %) of injection tube steel (316SS) (@Autoclave Maxitech)

III. PRE-DIMENSIONING MODELING OF THE MIRAGES-2 EXPERIMENTS.

After the material selection, the key parameters to be considered in the dimensioning of the test-bench are the pressure and temperature, the duration, the flowrate, and the concentration of dissolved CO_2 in the injected solution.

The choice of the deep formation (1200 m) of the Dogger aquifer of the Paris Basin as a potential host formation, led us to define the experimental conditions of the sample confinement as follows : Pressure = 120 bar and Temperature = 60°C.

The duration, the injection rate and the $P_{(CO_2)}$ are defined by using numerical codes.

III.1. Procedure of the numerical experiment used to define the injection conditions of the flowthrough experiments.

This work was carried out in collaboration with BRGM as a part of the project.

The numerical experiment used to measure the impact of the CO_2 dissolved injection on the carbonate rock is based on a coupling algorithm between chemistry and transport.

The chosen model does not reproduce the processes in details but it is used to define the orders of magnitude for the "worst case" in terms of reactivity (pure calcite, equilibrium) (Fig. 28): it simulates the injection of a CO_2 laden water in a calcite core sample in order to maximize the reactivity.

The model is based on 2 systems in series. The first is the volume of water contained in the core-plug (with estimated dimensions of a cylindrical calcite sample of 10 cm x 10 cm with 20% of porosity i.e. a volume of 0.2 x 785 cm^3 = 185 cm^3); the second corresponds to the autoclave filled with the solution corresponding to a volume of 2000 cm^3 minus the volume of the core-plug (785 cm^3) to give a final volume of 1215 cm^3.

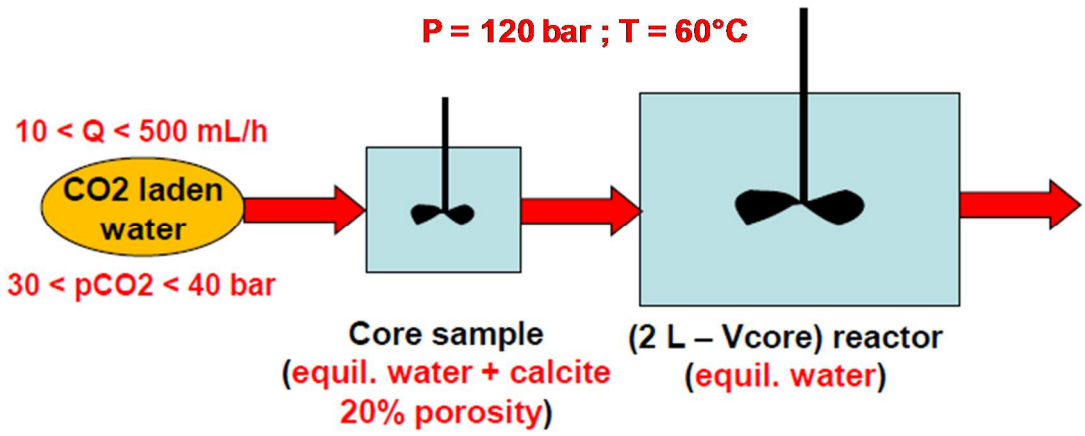

Figure 28: Simplified model for the pre-dimensioning of the MIRAGES-2 experiment.

This model takes into account:

- The non-ideality of the initial gas phase. The water is balanced with the fugacity of CO_2, significantly different from the total pressure of the system (reservoir conditions). The fugacity coefficient is estimated from the model of Duan et al., 2003 [108].
- The variation of the residence time within the core as the calcite is dissolved
- The complete speciation of aqueous species.

The model does not consider:

- The spatialization of the phenomenon, especially within the core plug. Indeed, the reactor is considered as perfectly stirred and the results are averaged from significant volumes.
- The kinetics of chemical recations.
- The real amount of dissolved CO_2. An overestimation is indeed considered as a security factor.

The protocol used a dedicated numerical tool based on two pre-existing modules:

- For the chemistry: the geochemical program PHREEQC [166] is used with the THERMODDEM database (downloadable from the BRGM website).
- For reactive transport, a ‘classical’ perfect stirred tank equations without source term (Neptunix simulator) is used.

The coupling schema implemented in the numerical tool is based on a purely non-iterative sequential (SNI) method [167]. This simple method is based on breaking down the calculation into two steps:

- Step 1: *TRANSPORT (Δt)* = the N chemical elements are transported during the Δt time step, assuming that no chemical reaction occurs.
- Step 2: *CHEMISTRY (Δt)* = the reactor is considered as a closed system (batch); the N chemical elements contained in the reactor are divided into different species that react with each other and with the stationary phases (minerals) during the time step.

The corresponding algorithm can then be written:

<u>Loop</u> on time

<u>Loop</u> on the N chemical elements

TRANSPORT (Δt)

<u>End loop</u> on the chemical elements

<u>Loop</u> on the n reactors

CHEMISTRY (Δt)

<u>End loop</u> on the n reactors

<u>End loop</u> on time

Several test cases were then carried out under geological conditions (120 bar, 60°C) by varying different parameters in order to evaluate their influence on the defined model.

III.2. Results

III.2.1. Impact of the flowrate

A constant pressure $P_{(CO_2)}$ = 30 bar is considered for the different injection flowrates. The results are presented in figure 29 in terms of pH values in the solution of the core sample and in the reactor.
An almost instantaneous drop of the pH value at high injection rates is observed in the two systems with an equilibrated value of 4.9. For the low rate (≤ to 10 mL.h^{-1}), this value is reached over a slightly longer period of time (10 days) in the reactor.

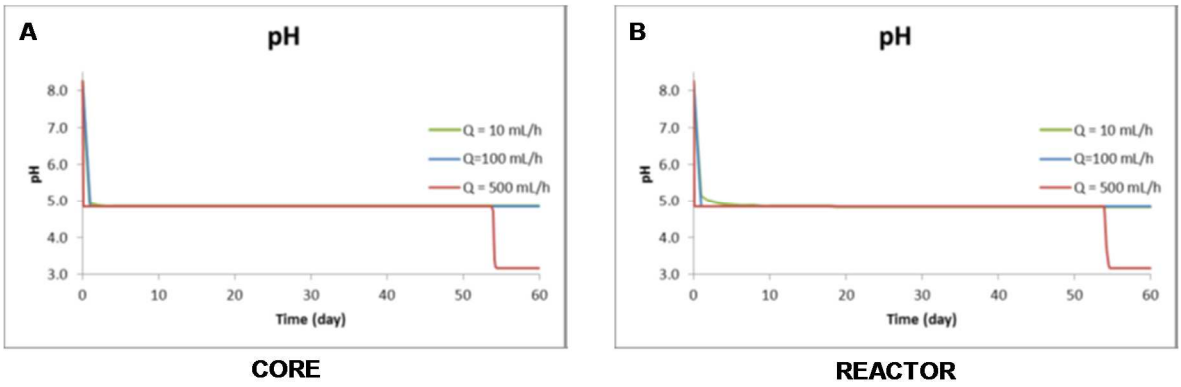

CORE **REACTOR**

Figure 29: Evolution of the pH values of (a) the aqueous solution in the core sample and (b) the aqueous solution in the reactor with time depending on the injection flowrate.

Other results depicting the impact of the flowrate on the dissolution rate of the rock are visible in figure 30 in terms of porosity changes of the core sample and saturation index with respect to calcite in the reactor.

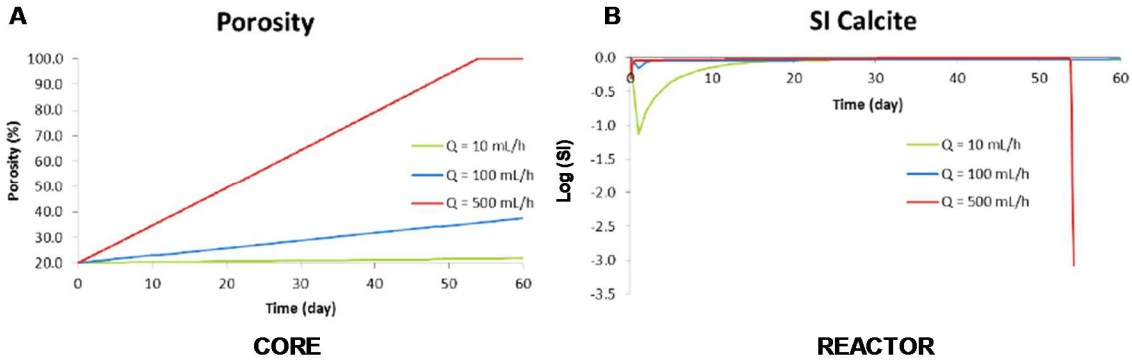

Figure 30: Evolution of (a) the porosity of the core sample with time depending on the injection flowrate and (b) evolution of the saturation index for calcite in the reactor with time and for different injection flowrates.

This modelling demonstrates that the flowrate strongly influences the calcite dissolution rate. The core-plug is completely dissolved after 54 days of injection for a flowrate of 500 $mL.h^{-1}$. Moreover, for a flowrate ≤ to 100 $mL.h^{-1}$, the solution in the reactor remains at equilibrium with calcite over a long period of time, implying that the calcite core sample is not entirely dissolved (Fig. 30b). The equilibrium for a very low flowrate (≤ to 10 $mL.h^{-1}$) is reached after 20 days. For this flowrate, the impact on the rock structure is weak with a minimal increase in porosity after 60 days.

III.2.2. Impact of the amount of dissolved CO_2 in the injected solution

Three simulations were carried out for two $P_{(CO_2)}$ in the injected solution at a constant injection flowrate of 100 $mL.h^{-1}$. The results are presented i) in figure 31 in terms of pH evolution of the solution in the core sample and in the reactor and ii) in figure 32 in terms of porosity change in the core sample and evolution of the saturation index for calcite in the reactor.

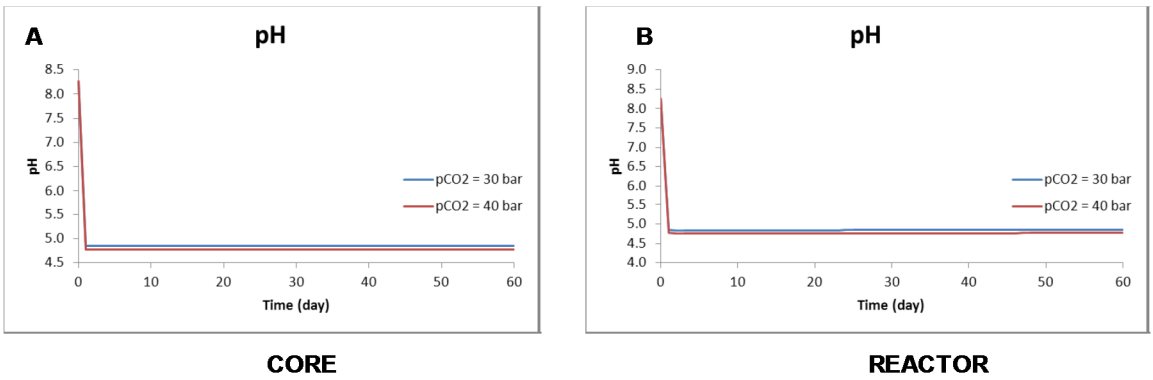

Figure 31: Evolution of the pH values of (a) the aqueous solution in the core sample and (b) the aqueous solution in the reactor with time depending on the $P_{(CO_2)}$ of the injected solution.

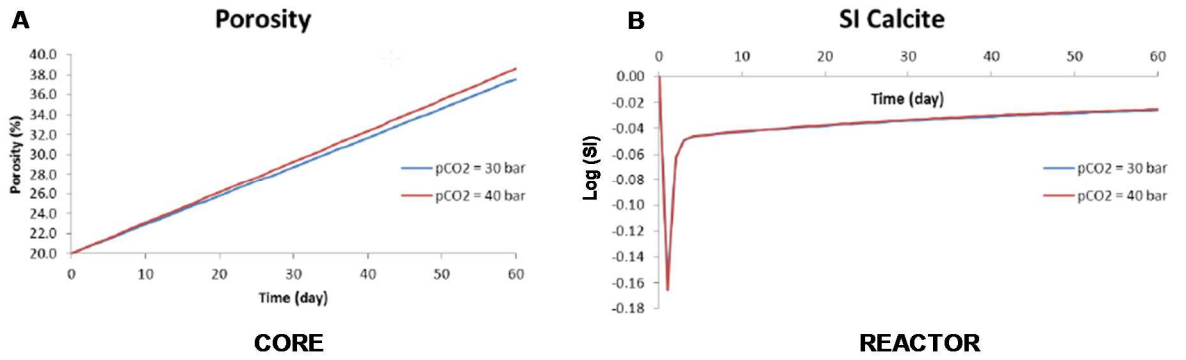

Figure 32: Evolution of (a) the porosity of the core sample with time as a function of the $P_{(CO_2)}$ and (b) evolution of the saturation index for calcite in the reactor with time as a function of the $P_{(CO_2)}$ in the injected solution.

These results show that the initial $P_{(CO_2)}$ in the injected solution has a limited effect on the calcite dissolution rate in the core and on the calcite saturation index in the reactor.

The third test-case concerns the evolution of the $P_{(CO_2)}$ in the 2 considered systems with time (Fig. 33) for the two different $P_{(CO_2)}$ in the reactive solution.

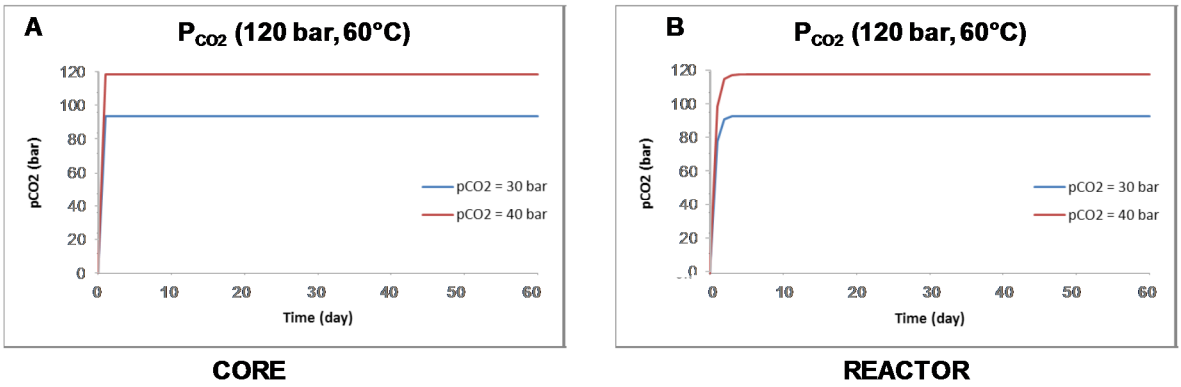

Figure 33: Evolution of the total $P_{(CO_2)}$ in (a) the core sample and (b) in the reactor with time depending on the $P_{(CO_2)}$ in the injected solution.

The increase of the $P_{(CO_2)}$ in the core-plug and the reactor aqueous environment corresponds to the time required for the CO_2 solubilization. When $P_{(CO_2)}$ in the injected solution is near 40 bar, the bulk CO_2 pressure in the reactor is closed to the confinement pressure. In this case, the thermodynamic conditions become conducive to a CO_2 degassing phenomenon.

III.3. Conclusion of the pre-dimensioning modeling

The pre-dimensioning modeling of the MIRAGES2 experiments under realistic storage conditions (120 bar – 60°C) demonstrates that, on the one hand, with a too high injection flowrate of CO_2 laden solution, the total dissolution of the calcite sample can occur. On the other hand, a low flow rate over a short period of time would lead to minimal dissolution of calcite with limited variation of porosity. These extreme conditions would therefore provide a high or limited modification of the rock matrix, limiting the study of the coupled phenomena of dissolution/precipitation. The initial pressure of CO_2 considered in the tests (30 and 40 bar) has no significant effect on the calcite dissolution. However, a risk of CO_2 degassing in the core-plug environment has to be considered when a too high amount of CO_2 ($P_{(CO_2)}$ > 40bar) is dissolved in the reactive solution. It is therefore recommended to use a flowrate between 10 and 150 $mL.h^{-1}$ for a long-term experiment. It is also recommended to use a solution for injection with a CO_2 pressure lower than 35 bar to avoid bubbling effect.

As a result of this pre-dimensioning work and in order to avoid the different risks pointed up, the maximum values of the different parameters are defined as follow:

- Pressure = 120 bar / Temperature = 60°C
- $P_{(CO_2)}$ in the injected solution ≤ 40 bar (at 20°C)
- Flowrate ≤ 150 $mL.h^{-1}$
- Maximum duration of the ageing (injection) ≤ 54 days.

IV. THE EXPERIMENTAL BENCH : MIRAGES-2

The so-called MIRAGES (Modèle d'Injection RAdiale de Gaz à Effet de Serre) experimental device was initially designed by GeoRessources for application to supercritical CO_2 injection [168; 169]. It mimics an injection well at the $1/20^{th}$ scale. In this study, we present the design of the experimental sample and a new experimental device (MIRAGES-2) that was specifically designed for the injection of aqueous solution with dissolved CO_2 under P-T conditions.

IV.1. Sample design and preparation process

The core assemblage used to reproduce a scaled-down injection well (Fig. 34) consists of either a metallic or a non-metallic tube (length = 119 mm, internal diameter = 4.5 mm, external diameter = 6.35 mm) screwed to a Teflon ring (diameter = 25 mm, thickness = 2 mm) and cemented to the core plug (external diameter = 100 mm, length =100 mm) with a class G Portland cement.

The ratio L/H between the different walls of the well and the edges of the limestone sample is 1.1. For the purposes of the study, a piece of composite material that could be used instead of steal for the well casing due to a better resistance to corrosion issues, can be placed at the injection zone or at the interface between the reservoir and the cement at the upper part of the core-plug.

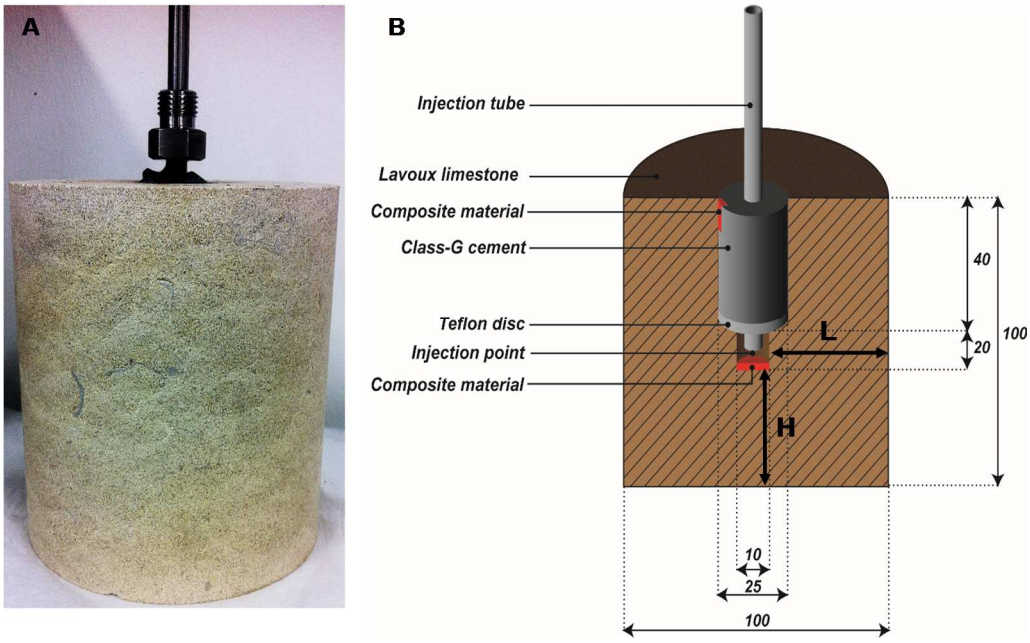

Figure 34: (a) View of the injection well scale-model. (b) Schematic view of the injection well of the MIRAGES-2 experiment. Dimensions are given in millimeters.

All the core-plug tested in the experiments are drilled in a Lavoux limestone block, perpendicular to the sedimentary bedding except for one experiment where the core-plug is drilled at 55° with respect to the bedding (Fig 35b) corresponding to the maximum provided angle of the injection well design (Fig 35a). This design makes it possible to closely simulate the operating conditions but more specifically to investigate the influence of the rock fabrics on the dissolution patterns and locations.

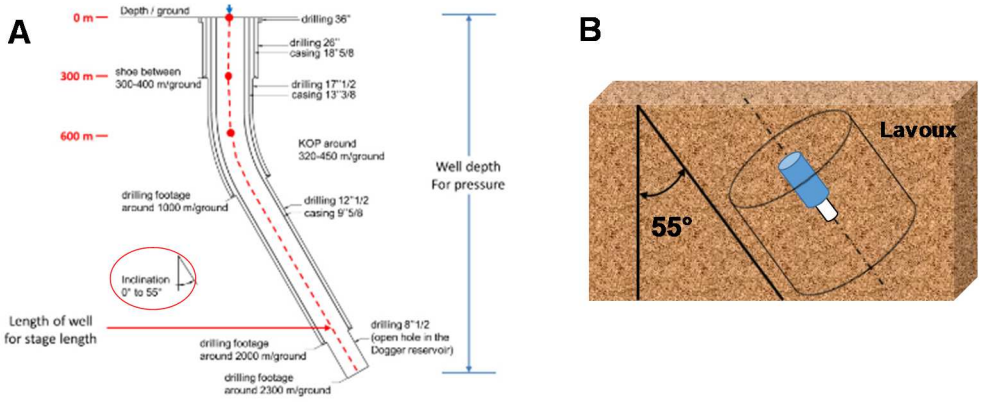

Figure 35: (a) Typical injection well design [170] with the maximum provided angle (red circle) at the open hole depth. (b) Core sampling of the sample simulating the borehole angle on the field.

The mixing of the cement with water is done according to the API-ISO 10426A norm:

- Mixing water:
  The used water is demineralized

- Blending amount (class G cement):
  Water 349 ± 0.5 g
  Cement 792 ± 0.5 g

- Mixing protocol:

  - Place the water in the blender
  - Use the blender at 4000 ± 200 rpm during 15 s while the cement is added in a continuous way
  - Then use the blender at 12000 ± 500 rpm during 35 ± 1s.

- The cement is then cast in the specified area where the injection tube is located. The Teflon disc screwed into the lower part of the tube prevents the cement from clogging the injection zone.

IV.2. Description of the MIRAGES-2 experiment

The experimental device (Fig. 36) I have built is divided in two parts: the first one is devoted to the CO_2-solution mixing process, and the second one enables to perform the injection of the CO_2-rich solution in the laboratory "miniature well" through the injection well, under controlled pressure and temperature conditions. The overall schematics of the MIRAGES-2 core flow experiment is presented in figure 37.

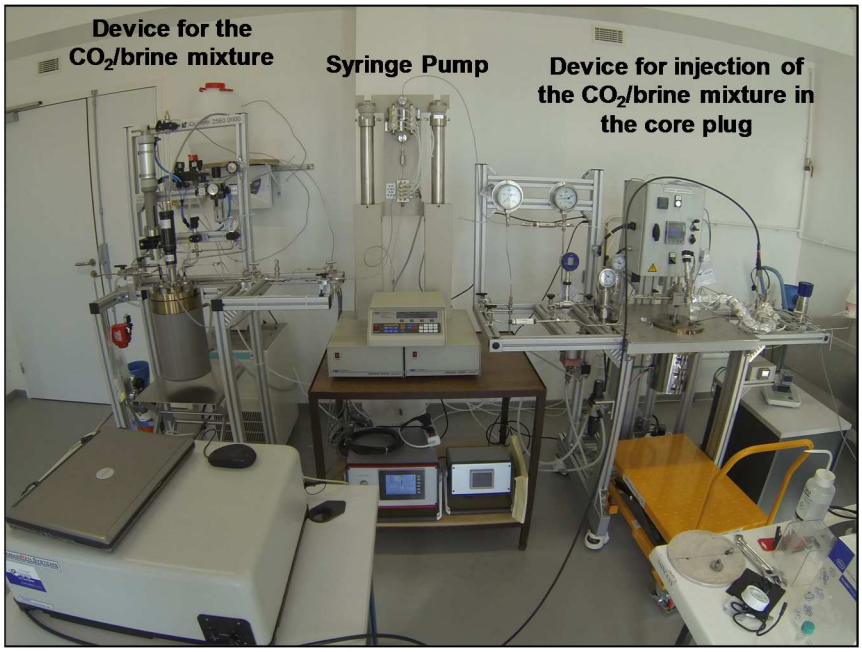

Figure 36: Global view of the MIRAGES-2 radial flowthrough test bench.

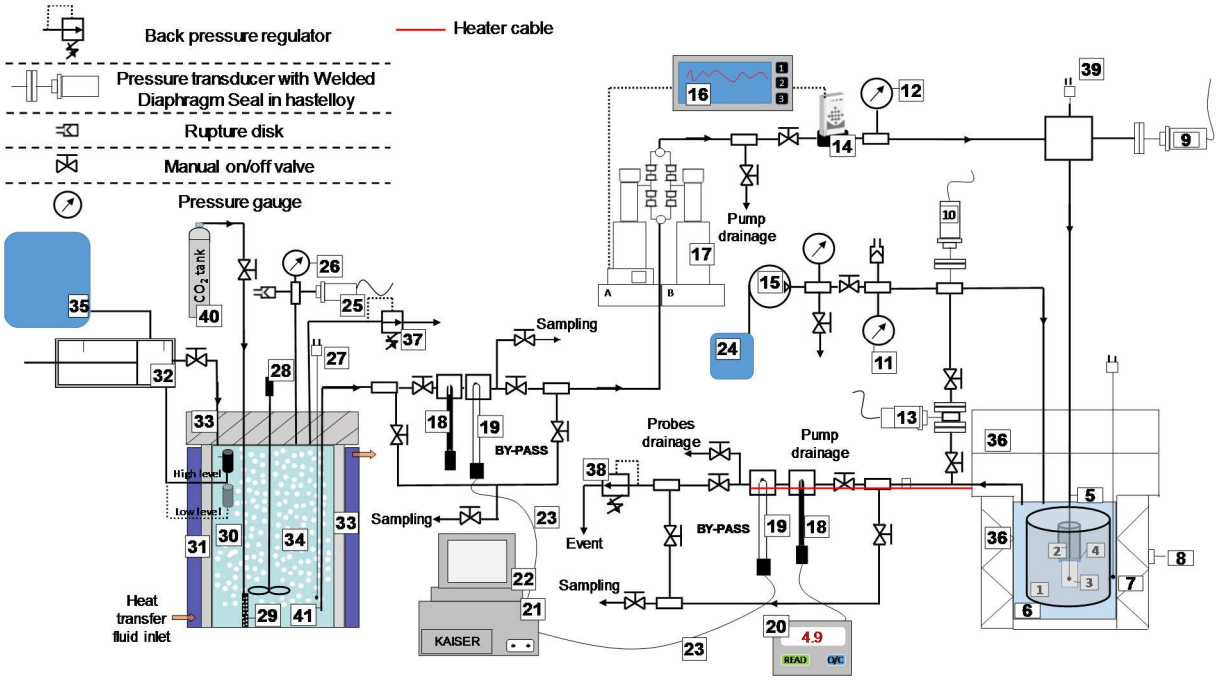

1 Core Sample
2 Cement
3 Injection zone
4 Teflon washer
5 Injection tube
6 Aqeuous solution
7 Confinement zone thermocouple (injection autoclave)
8 Oven Thermocouple
9 Injection pressure transducer (injection autoclave)
10 Confinement pressure transducer (injection autoclave)
11 Confinement pressure gauge (injection autoclave)
12 Injection pressure gauge (injection autoclave)
13 Differential pressure measuring transducer (injection autoclave)
14 Mass flowmeter
15 Hydropneumatic pump for water
16 Control unit of the pump controlled by the flow-meter
17 Syringue pump
18 In situ pH probe
19 In situ Raman probe
20 pH meter
21 Raman spectrometer
22 Raman data acquisition station
23 Optic fiber
24 Water tank
25 Mixing autoclave pressure transducer
26 Mixing autoclave pressure gauge
27 Confinement thermocouple of the mixing autoclave
28 Static stirrer
29 5 µm sintered
30 Level sensor
31 Heating jacket
32 Syringe for brine pressurisation
33 Mixing autoclave
34 CO_2/aqeuous solution mixture
35 Salted water inlet pré-balanced and filtered tank
36 Injection Autoclave
37 Back pressure regulator for CO_2 (mixing autoclave)
38 Back pressure for CO_2/brine mixture (injection autoclave)
39 Injection zone thermocouple (injection autoclave)
40 CO_2 tank
41 Dipe tube for mixture collection

Figure 37: Schematics of the MIRAGES-2 MIRAGES-2 radial flowthrough test bench.

IV.2.1. Device for the CO_2/solution mixture

This device aims at preparing the appropriate CO_2/H_2O (or saline water) mixing in order to obtain a monophasic aqueous solution containing the desired quantity of dissolved CO_2 (Fig. 38).

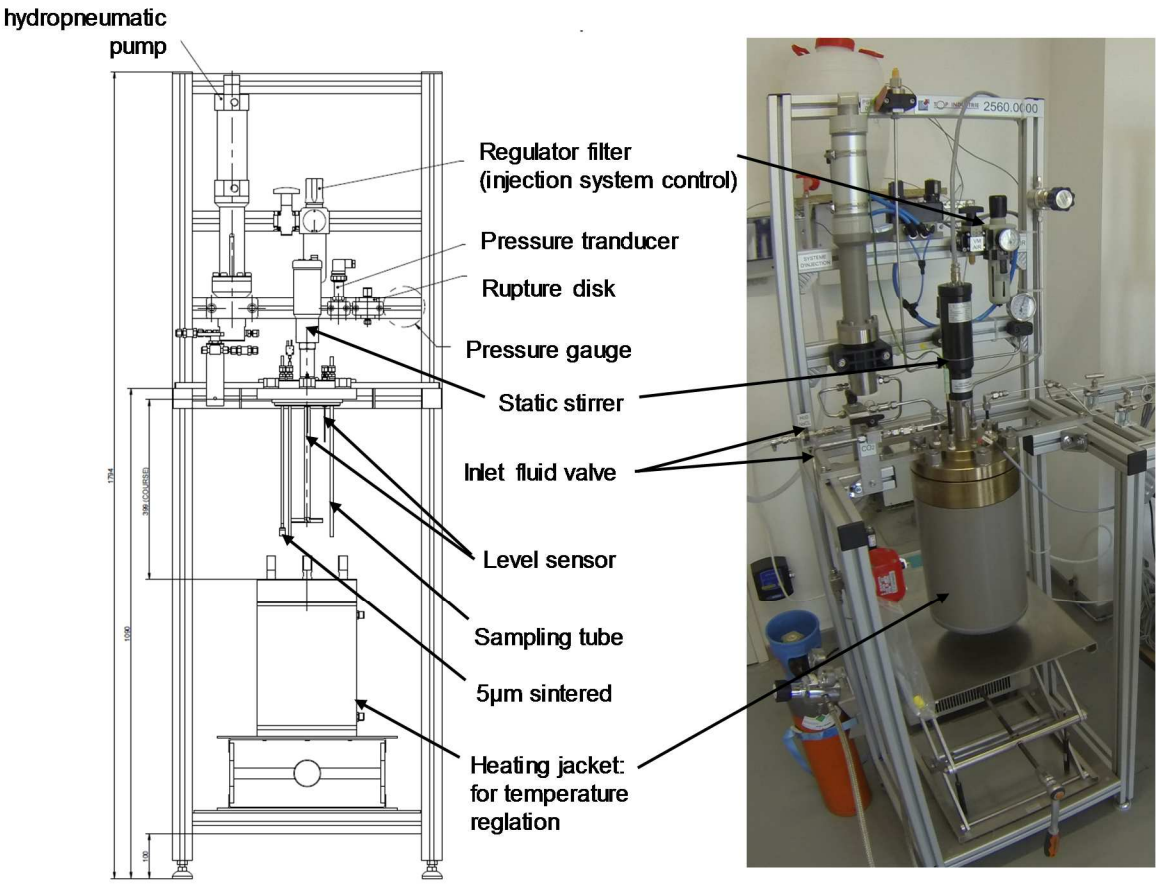

Figure 38: 5 liters mixing device plan (solubilization system).

The mixing vessel is a 5 liters autoclave made of stainless steel (316L-X2CrNiMo 17-12-2). The reactor walls and the cover are coated with a triple layer of Teflon (Fig.37, item 33) to avoid corrosion problems due to the CO_2/brine solution. The body of the autoclave is surrounded by water-cooled temperature jackets to maintain the mixture at the desired temperature (a chiller is used to regulate the heat transfer fluid). The system is filled with water or saline water with a hydropneumatic pump (10 cc) (Fig. 37, item 32 and Fig. 38) controlled by a water level sensor (Fig. 37, item 30) linked to a control unit station. This pump is machined in A-236 alloy (X6NiCrTiMoVB25-15-2). The nickel and chromium contents of this metal provide resistance to corrosion and oxidation. The vessel is supplied with CO_2 through a pressurized bottle (Fig. 37, item 40). The CO_2 goes through a 5 µm sintered made in 316 SS (Fig. 37, item 29 and Fig. 38) and the solubilization is optimized with a static stirrer (Fig. 37, item 28 and Fig. 38). A back pressure regulator prevents overpressure during the reinjection of the solution by the hydropneumatic pump (Fig. 37, item 37 and Fig. 38). The entire system can withstand up to 60 bar at 150°C.

Once the CO_2-brine equilibrium is reached, the solution exits from the bottom part of the autoclave using a dip tube (Fig. 37, item 41). A by-pass system is placed at the outlet of the tube to enable chemical in-situ analysis of the mixture. It consists of (1) a Raman probe (Fig. 37, item 19) connected to the system via a metal tee connector measuring the in-situ CO_2 concentration in the solution without any sampling constraints, (2) an in-situ pH probe (Fig 37, item 18) and (3) valves dedicated to the sampling of the solution for its analysis. The in-situ analytical equipment as well as the calibration and measurement protocols are detailed in paragraph V.3.1 and V.3.2. At the output of the by-pass, the water with dissolved CO_2 fills a high pressure double syringe pump (Fig. 37, item 17 and Fig. 39) for the mixture injection in the second autoclave containing the core sample. This second autoclave named MIRAGES-2 is described in the next paragraph.

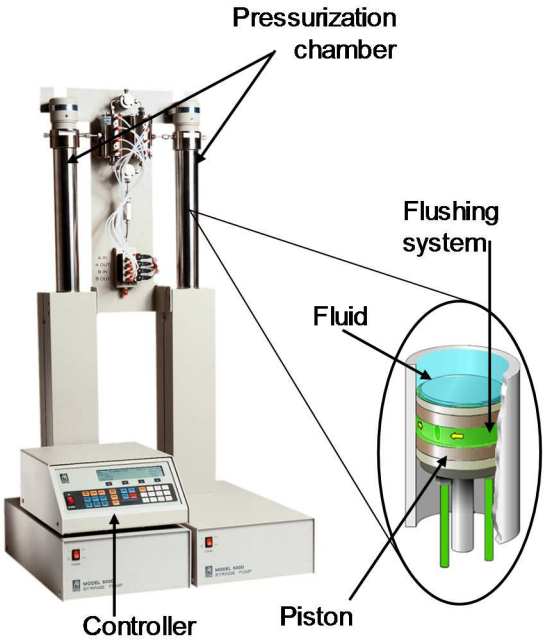

Figure 39: Double syringe pump (@Teledyne ISCO, model 500D).

IV.2.2. Device for the radial injection of the CO_2 rich solution (MIRAGES-2)

The experimental device MIRAGES2 is based on a 2 liters autoclave (Fig. 37, item 36 and Fig. 40) made of stainless steel (316L-X2CrNiMo 17-12-2) with a triple Teflon coating on the wall of the vessel and on the cover lid. This setup enables to inject the aqueous solution containing dissolved CO_2 through a core plug immersed in an aqueous solution (Fig. 40).

Injection will be performed at constant flow rate using the double syringe pump (Teledyne Isco, Model 500D) coupled to a liquid mass Coriolis flow meter (Fig. 37, item 14) via a control unit (Fig. 37, item 16). This coupling allows working with injection pressures from 0 to 200 bar, with a flow rate ranging between 0.01 and 500 $g.h^{-1}$ (accuracy of 0.01 $g.h^{-1}$). The control unit continuously records the flow rate in $g.h^{-1}$as well as the density of the percolating fluid.

Due to the expected high chemical reactivity of the CO_2-brine mixture, the pumps are made of durable and corrosion resistant material (NITRONIC 50). Moreover, the pistons are made up of a flushing system to avoid some possible snatch on the wall of the pressurization chamber caused by the salt (Fig. 40). To perform the injection in the core plug, a metallic tube (Fig. 37, item 5), is screwed onto the lower part of the lid of the 2 Liters autoclave (Fig. 40a). The confinement pressure is controlled by a hastelloy back pressure regulator (Fig. 37, item 38) and the temperature in the autoclave is reached using a MICA heater band and regulated by a devoted station.

At the outlet, the fluid flows through a by-pass system equipped with high pressure and temperature probes to acquire pH values and Raman spectra (Fig.37, items 18 and 40c). The probes are heated with a heater cable in order to keep the same temperature as in the MIRAGES-2 autoclave. The liquid sampling for chemical analyses is also possible thanks to a sampling valve. The use of a bypass system makes possible the regeneration of the pH probe and a regular calibration.

The autoclave can also be filled and pressurized by water for the pre-injection period by using a hydro-pneumatic pump (Fig. 37, item 15).

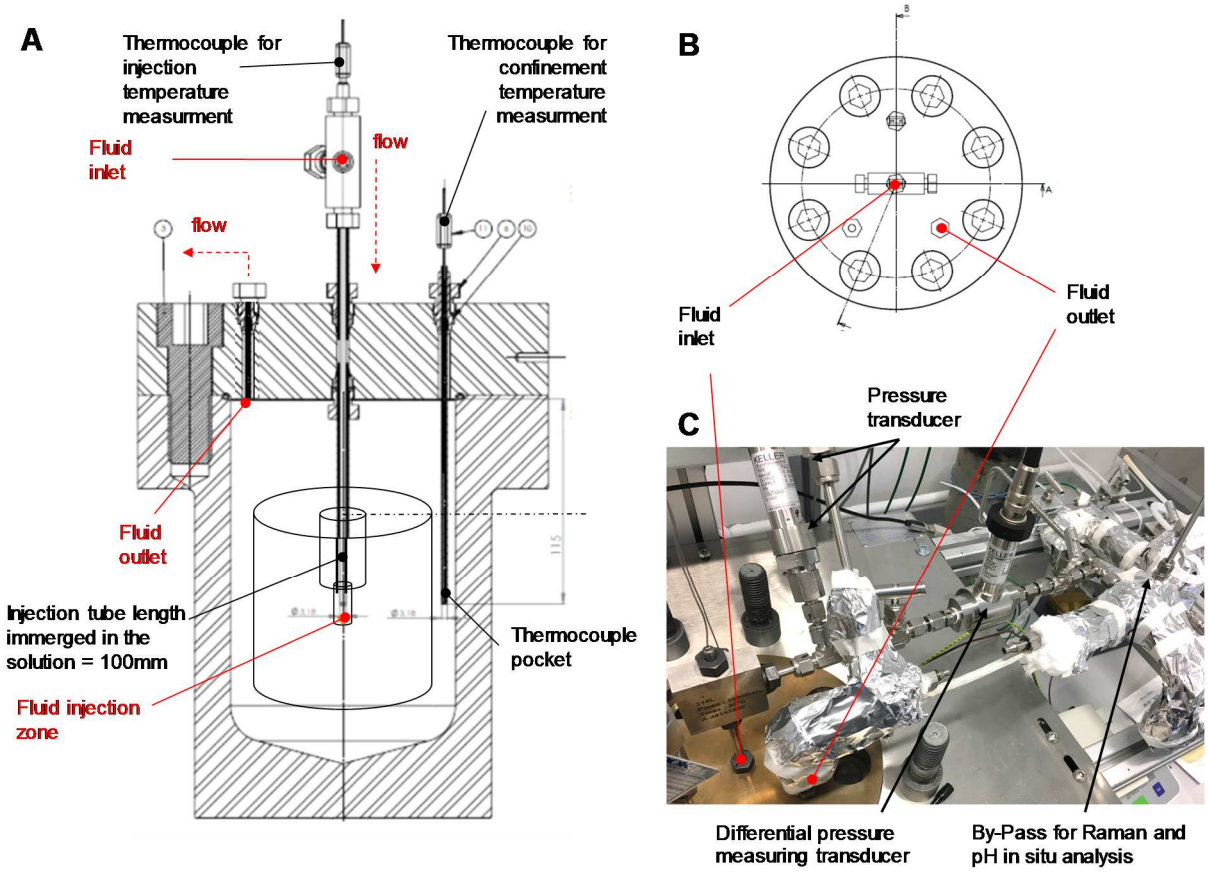

Figure 40: (a) Schematic drawing of the radial injection device MIRAGES-2 (b) Top view of the MIRAGES-2 lid (c) Front view of the various pressure measuring transducer and in-situ probe locations in the system.

High pressure rated check valves are introduced at strategic points in the system to avoid reverse flow in case of momentary pressure differences or pressure drops, preventing harmful damage to the system equipment. Moreover, rupture disk are also introduced in the two parts of the system to avoid any overpressure.

IV.2.3. In-situ thermodynamic and chemical monitoring of the experiment

The two autoclaves of the experimental device are equipped with electronic sensors for pressure-temperature measurements and recordings. In the MIRAGES2 injection autoclave, the pressure is measured at the injection point (Fig. 37, item 9) and in the confining zone (Fig. 37, item 10) with two high accuracy hastelloy flush diagram pressure transducers. The same configuration is applied for the temperature measurement at the injection point (Fig. 37, item 39 and Fig. 40a) and the confining zone (Fig. 37 item 7 and Fig. 40). To ensure accurate differential pressure measurements between the inlet and the outlet of the core plug, a hastelloy flush diagram differential pressure transducer (Fig. 37, item 13) is placed between the two zones. The measurement of the pressure drop ΔP between the inlet and the outlet of the sample is motivated by its ability to notice changes in permeability within the core-plug during the flowthrough experiments. In unidirectional flowthrough experiments studies using 1-D dimension column, according to Darcy's law, the ratio of the volumetric flow rate Q ($m^3.s^{-1}$) over the pressure difference ΔP is directly related to the permeability of the sample *k* (m^2), by:

$$k = -\frac{\mu L}{S}\frac{Q}{\Delta P} \quad (19)$$

Where L is the length of the core-plug sample in the flow ridrection (m), S is the cross-sectional area of the sample (m^2) and μ is the dynamic viscosity of the fluid (Pa.s). Permeability values are reported in mD.

But, the 3D configuration of our experiments will not allow the experimental determination of the evolution of the permeability of the sample in real time.

During the experiment, regular measurements of the pH and of the dissolved CO_2 species are carried out with in situ probes (see paragraph VII.2.4.1). A regular calibration of the probes is performed before, during, and after the experiment to improve the accuracy of the measurements.

A modelling of the heat transfer by forced convection in the channel flow of injection was carried out [171] in order to determine the expected temperature at the injection point and also to validate the experimental data. The protocol modeling as well as the calculations and results are reported in appendix B.

The theoretical temperature in the injection well is expected at 59.7°C. No thermal gradient are expected at the vicinity of the injection zone.

V. EXPERIMENT PROTOCOLS

V.1. Protocol of injection

Before each experiments, X-ray computed tomography (CT) analysis is performed on the near well region of the cores in order to ensure that no anomaly which could prevent the injection or be the source of leakage (especially at the cement-rock interface) exist. The core-plug is then placed in the MIRAGES-2 injection autoclave. The autoclave is filled with the experimental solution defined in V.2.

The system is then pressurized with a hydrodynamic pump (Fig. 37, item 15) and heated in order to perform the hydration of the cement in the sample under the reservoir conditions. This operation is called "***cure***" and lasted approximately 10 days for each experiment.

CO_2 was dissolved at an average temperature of 20°C and a pressure close to 30 bar in the 5 liters mixing autoclave 24 hours before the beginning of its injection in the core-plug in order to reach the equilibrium.

Once the cure is achieved, the syringe pump (Fig. 39) is used to inject continuously the solution (pure water, CO_2-rich acidified water or brine) from the mixing autoclave (Fig. 38) to the center of the core plug placed into the MIRAGES-2 injection autoclave (Fig. 40). Following the pre-dimensioning modeling, the injection flow rate is set to 150 gram per hour ($g.h^{-1}$). The temperature of the system is set to 60 °C and the confining pressure is set to 120 bar thanks to the back pressure regulator. This step is called "***ageing***".

The 5 liters mixing autoclave is continuously feed with the CO_2-free initial solution by the coupling between the water level sensors located in the autoclave and the hydro-pneumatic pump connected upstream to the device. A pressure reducer provides a stable required CO_2 pressure from a B5 tank.

During experiment, the solution is sampled at the outlet of the two autoclaves in order to perform chemical analyses of major and traces elements. At each sampling time, 20 mL of solution are used to analyze the concentrations of ionic species and especially the sulfates. The solution is filtered at 0.22 µm before analysis. Similarly, 20 mL of solution is sampled to analyze the concentrations of cations (calcium, magnesium, strontium, aluminum and iron) in aqueous solution. The sample is then filtered at 0.25 µm. 400 µl of concentrated HNO_3 (65%) is added in order to stabilize the solution. The samples are then stored at 4°C until analyze.

The quantity of dissolved CO_2 is continually determined by Raman analysis. These measurements are carried out alternatively in the injected solution and in the experimental one (at the level of the two by-pass system) because the Raman spectrometer used does not allows two simultaneous spectra recording.

V.2. Determination of the initial fluid chemistry and preparation procedure

The experimental protocol also requires the definition of a fluid chemistry that ensures the non-reactivity of the rock during the cure period in the P-T conditions of the experiments. A pre-dimensioning calculation of solubility equilibrium of calcite in pure water is done to avoid the dissolution of the core-plug during the cement hydration phase **("cure"** period).

The geochemical program PHREEQC [166] is used to simulate the equilibrium state of the calcite between the rock sample and the water in the imposed physical conditions (P=120 bar / T= 60°C). We consider that the influence of the pressure is negligible on aqueous species. At 60°C and without CO_2, the calculated solubility of calcite in pure water is 15.6 $mg.kg^{-1}_{water}$.

The experimental protocol implies to fill preliminarily the 5 liters mixing autoclave with the equilibrated solution to adjust the temperature at 20°C before starting to solubilize the CO_2. During this period, the fugacity of CO_2 in contact with the solution is 0.0004 bar. Under these conditions, the results of modelling shows that the dissolved mass of calcite at equilibrium with pure water is 57.5 $mg.kg^{-1}_{water}$. The concentration of 15.6 mg of calcite dissolved in 1 kg of pure water will thus not induce precipitation of carbonate phase during the duration of the temperature equilibration.

As a consequence, a solution composed by 15 $mg.kg^{-1}_{water}$ of $CaCO_3$ is used to limit the dissolution of the core-plug during the cure period for experiment with dissolved CO_2 in water without salt.

Concerning the salinity parameter, the brine of the Dogger reservoir has a salinity between 2 and 20 $g.L^{-1}$ [149]. The chloride and sodium ions represent 90 % in weight of the total salinity [172]. For the experiment with saline solution; the chosen salinity is of 15 $g.L^{-1}$ of NaCl. A modelling allowing the calculation of the amount of calcite at equilibrium with a solution of 15 $g.L^{-1}$ of NaCl in the cure period conditions was carried out. The results led us to prepare an equilibrated solution composed of 30 mg of $CaCO_3$ in 1 kg of water.

Another key point is the fluid state in each part of the experimental device. Indeed, the percolation fluid has to remain monophasic. The pre-dimensioning modeling demonstrated that the $P_{(CO_2)}$ in the injected solution has to be ≤ 40 bar (at 20°C). The CO_2 solubility both in the mixing and the MIRAGES2 autoclaves are calculated using the thermodynamic model of Duan for the given pressure, temperature, and salinity [108]. In the experimental conditions of injection (60°C, 120 bar), the solubility of CO_2 in pure water is 1.12 $mol.kg^{-1}$. A $P_{(CO_2)}$ of 30 bar injected at 20°C in the 5 liters mixing device correspond to a theoretical solubility of 0,93 $mol.kg^{-1}$, well below that calculated in the MIRAGES2 conditions. This concentration theoretically prevents from any CO_2 bubbling in the MIRAGES2 autoclave. A $P_{(CO_2)}$ of 30 bar is thus set in the reactive solution. For the experiments with the saline solution the same $P_{(CO_2)}$ of 30 bar is imposed, corresponding to a theoretical CO_2 solubility of 0.88 $mole.kg^{-1}$. This value is well below the theoretical solubility of CO_2 in a 15 $g.L^{-1}$ of NaCl solution under reservoir

conditions calculated at 1.08 mole.kg^{-1}. The aqueous species of CO_2 are analyzed by Raman spectrometry before injection in order to ensure that the system has reached the expected equilibrium.

VI. DESCRIPTION OF THE EXPERIMENTS.

The final experimental conditions are defined as follows:

- Confinement pressure P_{conf} = 120 bar
- Confinement temperature T_{conf} = 60°C
- Theoretical concentration of dissolved CO_2 in the injected equilibrated water = 0.93 mol · kg^{-1} of water: Preparation of the acidic solution at a partial pressure of dissolved CO_2 $P_{(CO_2)}$ = 30 bar at 20°C
- Theoretical concentration of dissolved CO_2 in the injected equilibrated saline solution = 0.88 mol · kg^{-1} of brine: Preparation of the acidic solution at a partial pressure of dissolved CO_2 $P_{(CO_2)}$ = 30 bar at 20°C
- NaCl concentration in the injected brine = 15 g.L^{-1} of water
- $CaCO_3$ concentration in the injected water = 15 mg.kg^{-1} of solution
- $CaCO_3$ concentration in the injected saline water = 30 mg.kg^{-1} of solution
- Flowrate = 150 g.h^{-1}
- Duration of "**cure**" = 10 d

The different variable parameters for our experiments were as follows:

- Duration of the "**ageing**" (Time of injection): 12 h ; 24 ; 2.5 d ; 10 d ; 21 d. corresponding respectively to the Exp #2, #3, #4, #5 and #6
- The chemistry of the injected solution (water or saline solution) (Exp #7).
- The inclination of the core drilling (55° vs. perpendicular to the bedding) (Exp #5)

Finally, before performing any acidic injection experiment, a "blank experiment" (Exp #1) is carried out in order to study the behavior of the system following the injection of an unsaturated solution at equilibrium with the atmospheric pressure of CO_2.

The various experimental conditions are listed in table 5.

Experiments	Pressure (bar)	Temperature (°C)	Flowrate ($mg.h^{-1}$)	Duration of injection	Solution chemistry	CO_2 solubility in the reactive solution ($mol.kg^{-1}_{sol}$)	Core-drilling orientation
Exp #1	120	60	150	20 days (20d)	milliQ water	0	90°
Exp #2	120	60	150	12 hours (12h)	equilibrated water ($15mg/kg_{sol}$ $CaCO_3$)	0.93	90°
Exp #3	120	60	150	24 hours (24h)	equilibrated water ($15mg/kg_{sol}$ $CaCO_3$)	0.93	90°
Exp #4	120	60	150	2.5 days (2.5d)	equilibrated water ($15mg/kg_{sol}$ $CaCO_3$)	0.93	90°
Exp #5	120	60	150	10 days (10d)	equilibrated water ($15mg/kg_{sol}$ $CaCO_3$)	0.93	55°
Exp #6	120	60	150	21 days (21d)	equilibrated water ($15mg/kg_{sol}$ $CaCO_3$)	0.93	90°
Exp #7	120	60	150	20 days (20d)	Equilibrated water ($30 mg/kg_{sol}$ $CaCO_3$ + 15g/L NaCl)	0.88	90°

Table 5: Sum up of experiments. The angle of the core-drilling orientation in the limestone boulder is done with respect to the bedding.

VII. CHARACTERIZATION OF PRE- AND POST- EXPERIMENTAL SAMPLES

A complete description of the mineral composition of the sample as well as the architecture of its porous network before and after experiments were performed.

The workflow for the description of the rock and the extracted information are detailed in figure 41. A petrographic observation of the rock in thin section and fresh fractured rock ("Fresh" means that rock samples have not undergone any experimental treatment), coupled with X-ray tomographic imaging performed on cylindrical samples of 10 mm x 10 mm was used to describe the microstructure of the rock. Quantitative data were also obtained through petrophysical measurements (porosity, permeability) and mineralogical analysis. The whole core-plug was analyzed by X-Ray micro-tomography before and after experiments.

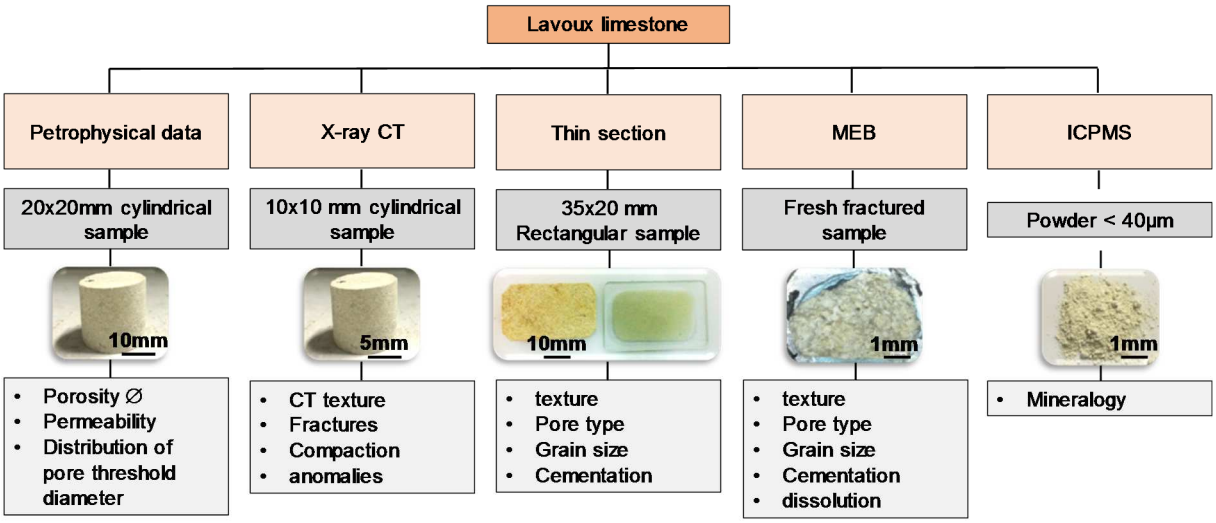

Figure 41: Workflow on the rock analysis.

VII.1. Investigation of the petrophysical properties of the rock.

VII.1.1. Permeability

The method used here is the nitrogen gas permeability.

The measurement device (Fig. 42) consists of: (1) the Hassler cell; the sample is surrounded with a tight plastic membrane and the assembly is placed in the cell. The membrane is used to apply a confining pressure on the one hand, and on the other hand an injection pressure through the rock, (2) the confining system made up of a pressure transducer and a drain, (3) the "head" system made up of a pressure transducer and a drain, (4) the foot system made up of a pressure transducer, a mass flow meter and a micrometric valve to control the output flowrate. The pressure and flow data are recorded thanks to a Keithley 2700 D.A.S multimeter [173].

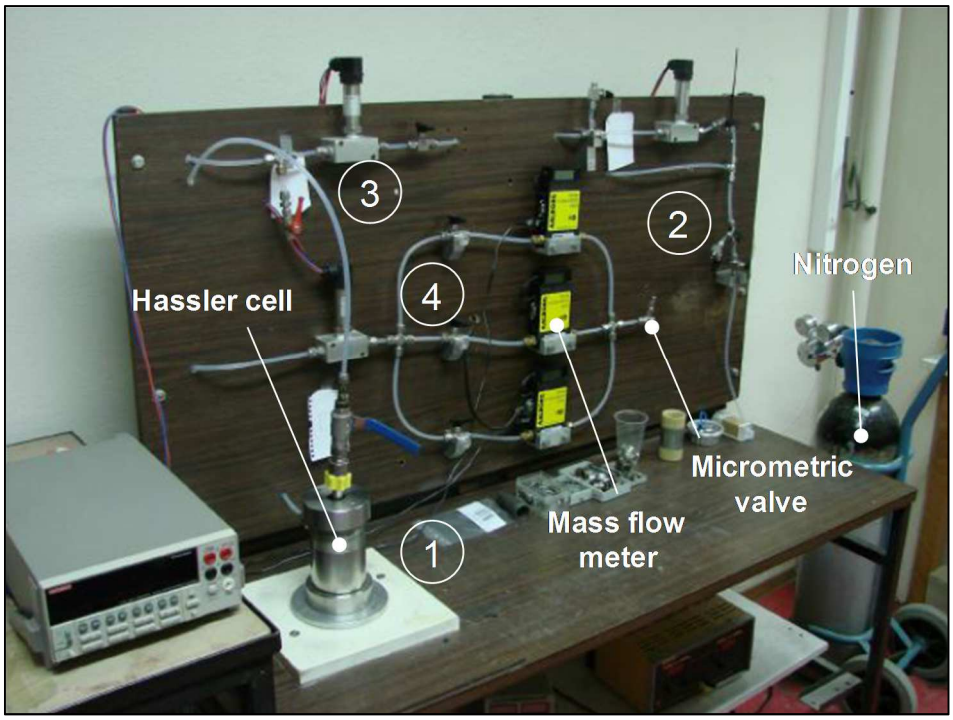

Figure 42: Data acquisition device of nitrogen permeability: 1) Hassler cell, 2) Confining system, 3) "head" system and 4) "foot" system.

The core sample dimensions are: diameter X height = 20 X 20 mm.
The assembly composed by the rock sample in the membrane is placed in the Hassler cell. In the first step, the confining pressure is applied. Then the gas flow is imposed through the sample from the "head" system to the "foot" system. The measurement of the different pressure and of the gas flow rate lasts between 0.5 and 3 hours. The data are then processed using a spreadsheet methods and the absolute permeability is calculated.

Permeability values are reported in millidarcies, (1 mD ≈ 0.987. 10^{-15} m^2). This instrument allow to measure permeability ranging from approximately 0.0001 up to 100 mD. The permeability analysis was performed under the supervision of Yves Géraud at GeoRessources lab.

VII.1.2. Porosimetry.

VII.1.2.1. Concept

The pore network analysis tool is the mercury porosimetry. It determines the total pore volume, the pore radius and the relative abundance of the void in the sample. It also evaluates the open and connected porosities.

Mercury is used as a non-wetting liquid, with a contact angle between the mercury and the rock upper to 90°. As a consequence, Hg will not spontaneously penetrate pores by capillary action, it must be forced into the pores by the application of an external pressure. This one depends on the pore radius invaded by the mercury.

The required equilibrated pressure is inversely proportional to the size of the pores, only slight pressure being required to intrude mercury into large macropores, whereas much greater pressures are required to force mercury into small pores. Mercury porosimetry analysis is thus the progressive intrusion of mercury into a porous structure under stringently controlled pressures. From the pressure versus intrusion data, the instrument generates volume and size distributions.

The measurements were obtained using the Micrometrics Autopore IV 9200 series. This instrument can reach pressures ranging from approximately 0.004 up to 220 MPa which correlate to pores from about 307 µm to 0.005 µm.

VII.1.1.2. Protocol of measurement and data acquisition.

The rock sample are the same than for the permeability analysis. This analysis is performed in a second stage because the filling of the sample with mercury clogs the porosity of the rock which can't be re-used after measurement.
The measurements proceed in two phases: (1) a low pressure phase with pressure from 0.01 to 0.150 MPa and (2) a high pressure phase with pressure from 0.150 to 220 MPa. To perform analysis measurement, the sample is loaded into a penetrometer (Fig. 43). The penetrometer is sealed and placed in a low pressure chamber. A pressure of 50 µm of mercury is applied in order to remove air before the penetrometer's cup and capillary stem are automatically backfilled with mercury. As pressure on the filled penetrometer increases, mercury intrudes into the sample's pores, beginning with those pores of largest diameter. This requires that mercury moves from the capillary stem into the cup. As the cannula is surrounded by a metal plating, it is possible to measure the decreasing of capacitance of the condenser formed by the metal plating and the mercury of the cannula. These data determine the volume of mercury injected in the porous network of the sample every time the pressure increases. From these data, it is possible to plot cumulative pore volume versus entry pore radius (Fig. 44a), thereby producing a pore-size distribution histogram (Fig. 44b).

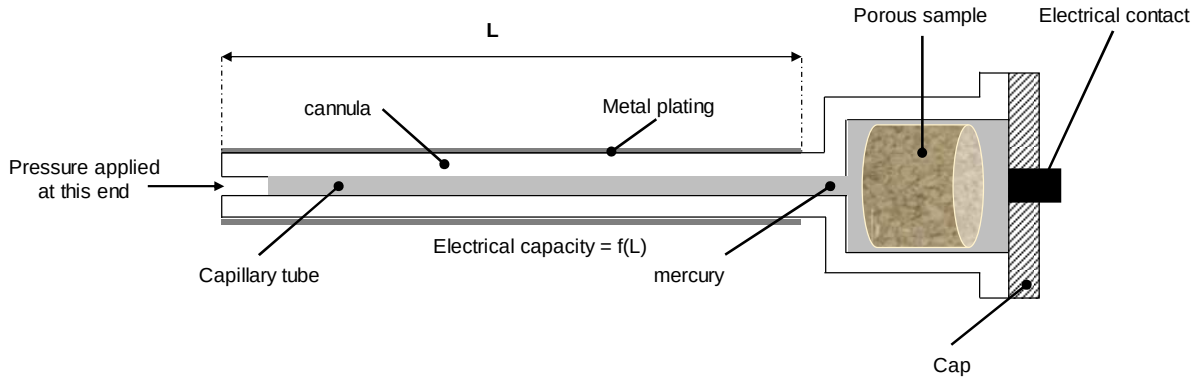

Figure 43: Plan of a penetrometer used for the measurements of porosity by injection of mercury. The cannula is covered with a metallic film.

Once the pressure of 0.150 MPa is reached, the penetrometer filled by mercury is weighed and placed in the high pressure chamber filled by oil. The oil allows to apply an isotropic pressure to the mercury. The pore space is thus overgrown.

At the end of this second phase, the total connected porous volume is determined. This phase is followed by a pressure decreasing phase to 0.15 MPa. Then a new pressure increasing phase is done up to 220 MPa. This last step allows the characterization of the free porosity of the rock. The difference between the total connected porosity and the free porosity corresponds to the trapped porosity (Fig. 44a) [173].

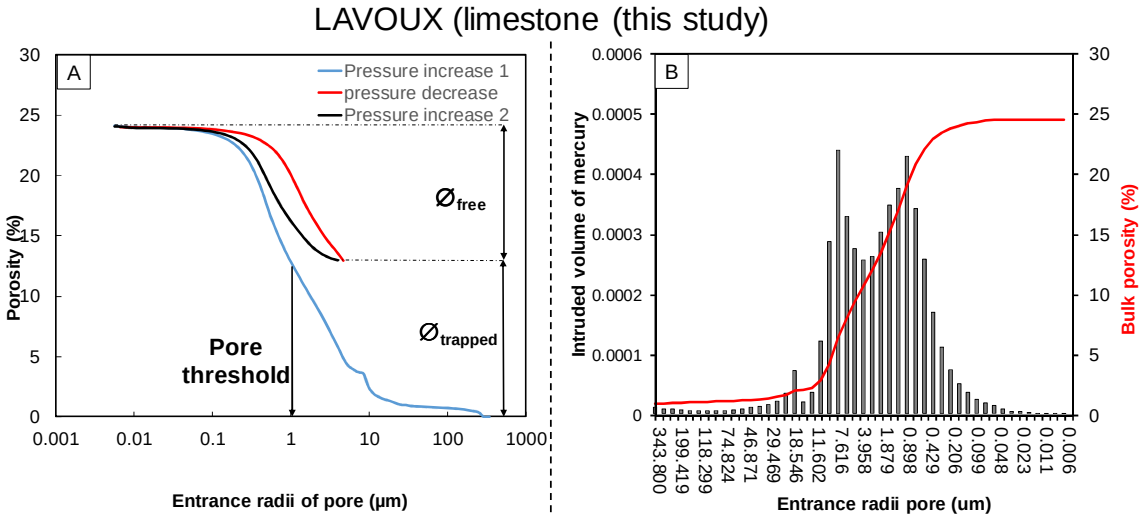

Figure 44: a) Curves obtained by injection of mercury on a 20 x 20 mm sample of Lavoux limestone used in this study (∅free = free porosity, ∅trapped = trapped porosity). b) Histogram of distribution of entrance radii of pores for bulk porosity of limestone (1st injection of Hg porosity).

The average diameter of access to the porosity is determined and corresponds to the abscissa of the inflexion point of the curve of first injection (Fig. 44a). This point corresponds to the threshold of percolation.

The mercury porosimetry analyses were performed under the supervision of Yves Géraud at GeoRessources lab.

VII.1.3. Sampling protocol of the pre- and post-petrophysical analyses.

Six cylindrical samples cored in the direction perpendicular to the horizontal sedimentary bedding of the rock (Kv permeability) and one cored vertically (Kh permeability) at different part of the Lavoux block were used for the native petro-physical properties analyses. After each experiments, 5 samples with the same dimensions were drilled at different regions of the core-plug especially at the vicinity of the edge (Fig. 45). 30 samples have thus be analyzed after experiments performing Purcell tests (porosity) and the standard method of nitrogen (permeability). It should be noticed that no evidence of the existence of high permeability zones in the small rock sample has to be emphasized to validate the data and to realize a comparative analysis between the experiments.

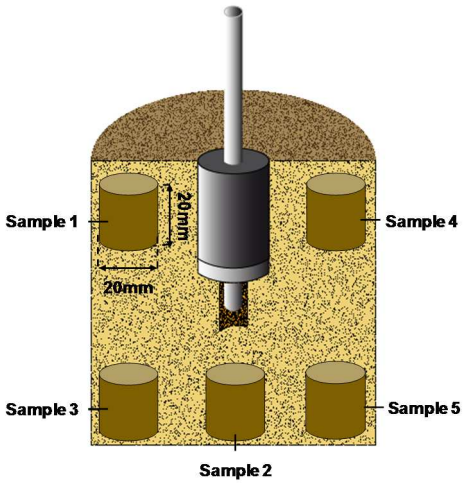

Figure 45: Location of the 20 mm diameter X 20 mm height cylinders sampled for the post-experimental petrophysical analysis.

VII.2. Investigation of the evolution of the structural properties of rock by imaging

VII.2.1. Thin section observation.

Thin sections are prepared after core-plug cutting (Fig. 46). The thickness of the thin sections is around 30 µm and the dimensions are 35 X 20 mm (L X l). They are used before experiments to identify the microstructure of the rock *i.e* the carbonate grains and the binding phase. After experiment, thin sections are made to mainly investigate the alteration of the cement phase and also possible dissolution or precipitation patterns. They are examined using standard optical microscope, SEM or Raman equipment.

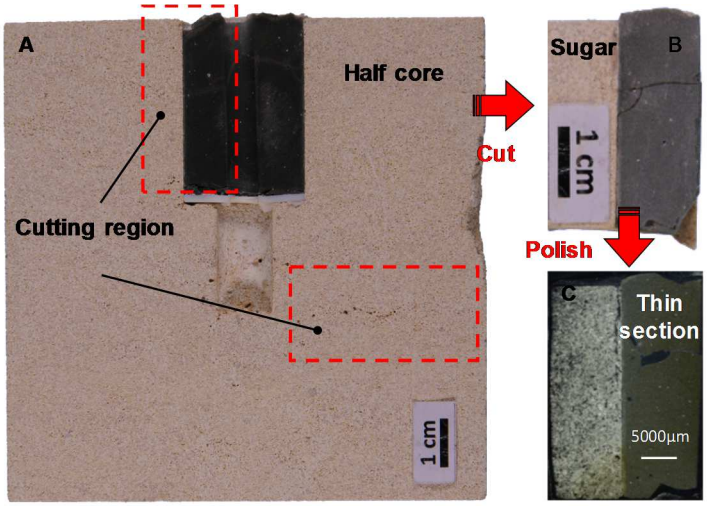

Figure 46: Model of preparation protocol of thin sections used in the study (example of the sample extracted from the blank experiment): (a) The core-plug is first split in two identical parts by following the diameter of the core, (b) Sugars are cut in specific areas of the core-plug (c) and sugar are finally polished at 30 µm before carbon covering.

VII.2.2. Scanning Electron Microscopy (SEM)

The SEM is a microscope that uses electrons instead of light to form an image. It uses a focused beam of high-energy electrons to generate a variety of signals at the surface of solid specimens. The signals deriving from electron-sample interactions are mainly due to secondary electrons (SE), backscattered electron (BSE) and X photons:

- ***Secondary electrons*** are very sensitive to the topography of the sample. Imaging with secondary electrons consequently provides information about morphology and surface topography. The study of the initial and aged samples gives information about the morphology of dissolution features and the location of precipitated phases.

- ***Back Scattered Electron*** result from elastic scattering of the primary beam with the nucleus of the atom at the sample surface. The likelihood of backscattering increases with the atomic number (Z) of the material. High-Z materials give a stronger signal (brightness) than low-Z materials, thereby giving image contrast from element mass differences. This technic gives an image of the chemical composition of the sample.

- ***X photons***: The ionic bombardment of the sample surface by the primary electrons of high energy also leads to X photon emissions. The wavelength of the X photons emissions depends on the targeted atoms. The X photon analysis gives the chemical composition of the sample.

Two types of samples are studied with SEM:

- ***Fresh fractured rock*** pieces are sampled at different locations of the core-sample (wall of the injection zone, wall of the dissolution pattern). This observation is used to visualize the crystals morphology and its evolution after experiment. Samples are examined using a Hitachi FEG S4800 high-resolution scanning electron microscope coupled to a wavelength-dispersion spectrometer (WDS) with an accelerating voltage set to 15 or 20 kV in SE or BSE mode.
- ***Thin sections*** are examined using a JEOL J7600F field-effect with an accelerating voltage set at 15 or 20 kV.

Free water is removed from the samples to avoid vaporization under vacuum. The fresh fractured rock are placed in an oven at 120°C during 24h. The fresh fractured rock and the thin section need to be electrically conductive by covering the sample with a thin layer of carbon.

SEM analyses are performed at the Electronic Microscopy and Microanalysis platform of GeoRessources laboratory.

VII.2.3. X-Ray micro-tomography

VII.2.3.1. Concept and data acquirement procedure.

X-Ray micro-tomography is a non-destructive and non-invasive technique used to explore the architecture of solid samples in 3-D with a spatial resolution that can reach less than one micrometer. In this work, tomography is used to access to the pore network and its evolution during the different experiments.

The principle of this technique is based on the measurement of the attenuation coefficients of a solid through which an X-ray photon beam passes. When a X-ray photon passes through a material, it interacts with the different components of the medium. The incident X-ray photons progressively disappear as they pass through the solid matrix. This phenomenon is called “attenuation”.

The level of attenuation depends on the characteristics of the radiation (frequency, wavelength and energy), but also on the thickness of the material as well as its density (and thus its porosity) and chemical composition. The absorbed beam are recorded with a photon detector X. This detector measures the X-Ray attenuation and quantify the linear attenuation coefficient μ, defined from Lambert-Beer’s law:

$$I/I_0 = \exp(-\mu h) \quad (20)$$

where I_0 is the incident X-ray intensity and I is the intensity remaining after the X-ray passed through a sample with thickness h.

The density variation is at the origin of the contrast detected in radioscopy of absorption of the X-rays. The obtained projections on the detector, supply 2-D radiographies in 16 bits. Image acquisition is repeated under different angles of rotation. The obtained sections are then reconstructed using the appropriate algorithms forming a three-dimensional image of the sample. This technique reveals the characteristics of the internal structure of the sample: size, shape, spatial distribution of the elements relative to each other, heterogeneities and defects (pores, inclusions, mineral phases ...).

The acquisition device (Fig. 47a) is made of: (1) a X-Ray generator (defined by its range of energy), (2) a rotation platform where the sample is located and (3) a data acquisition system composed of a X-ray detector with a CCD (Charge Coupled Device) camera (2-D-pixel arrays).

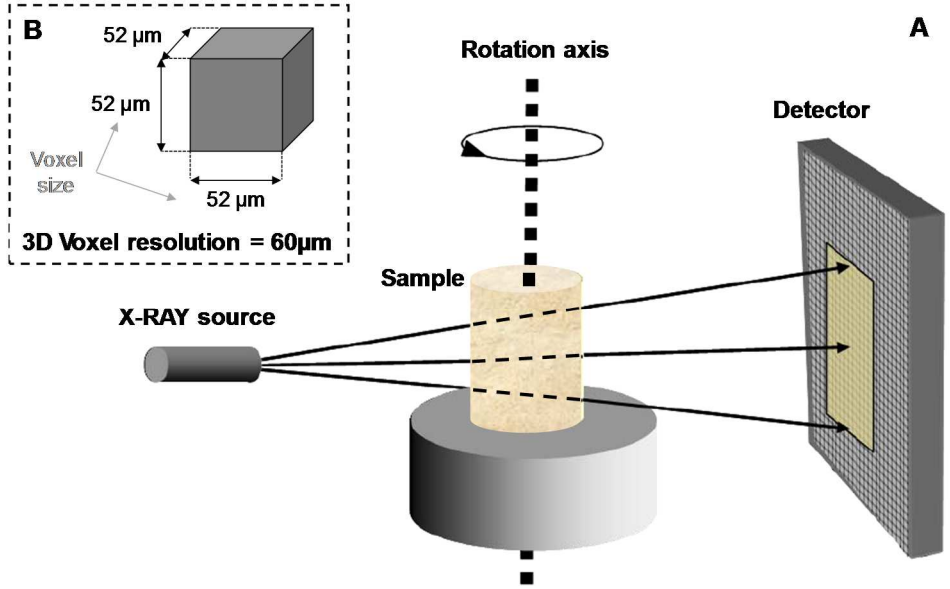

Figure 47: (a) Schematic layout of X-Ray microtomograph. (b) Voxel size and 3-D voxel resolution depending of the sample size of this study (example of the 10 x 10 cm cylindrical sample).

The voxel (3-D pixel or elementary cube generated by a pixel) which is the basic elementary unit of the reconstructed 3-D volume (Fig. 47b) has a resolution that ranges from 0.8 µm to 80 µm per voxel as a function of the sample size and the span length between source/detector and source/sample.

In this study the whole core-plugs (10 X 10 cm) before and after injection are analyzed. For the fine characterization of the initial rock at the microscopic scale, the selected cylindrical samples are of 20 X 20 mm. The studied samples were illuminated in series of experiments by X-ray beam generated in a 100 to 145 kV micro-focus X-ray tube-generator depending of the sample size. Registration of absorbed beam was recorded as a set of radiographic images collected around the object at different viewing angles by the help of X photon CMOS 5 Mp digital image sensor. The several different parameters of acquisition are defined in Table 6.

SAMPLE TYPE	***GEOMETRY***	***ACQUISITION***		***DETECTOR***		***X-RAY***	
	Resolution (µm/voxel)	Angular interval (°)	Number of radiographies	Number of average acquisition of the grey level	Exposure time (ms)	X-ray tube of nanofocus tension (kV)	Beam intensity (µA)
Cylindrical 10 x 10 cm	60	0.24	1500	5	1250	145	300
Cylindrical 20 x 20 mm	11.7	0.21	1700	4	1000	100	50

Table 6: Acquisition parameters for X-ray tomography of the whole core-plug used in the different experiments and for the cylindrical sample used for the characterization of the rock. The radiographies numbers is the number of images acquired by the detector, it depends on the angular interval between two successive radiographies.

The X-ray tomograph used in this study is a Nanotom Phoenix (GE). The analyses are performed at the Tomography Platform of the GeoRessources laboratory. For digital geometry processing and following 3-D visualization, exploration and quantification analysis of dissolution patterns VGStudio 2.2 and Avizo THERMOFISCHER software packages were used.

VII.2.3.2. Image processing protocol.

Following the analysis, the multitudes of acquired radiographic projections are stored in a digital format. The 2-D X-ray data are set into a 3-D raw image in 16-bit by Radon transform.

Each voxel of the image corresponds to a gray level correlated to the linear attenuation coefficient of the object at this location. The global 16-bit encoded volume has a grey scale ranging from 0 to 65 535 (Fig. 48a). An anisotropic diffusion filter is then applied to the image in order to easily delimit the solid matrix to the porous volume (Fig. 48b). A segmentation work of the images (also called thresholding and depending of the operator) is then used in order to delimit the outlines of the areas of interest mentioned above. The file then becomes binary with two phases, one corresponding to the solid and the other to the void. The mineral phase corresponds to the lightest phase (at the right of the thresholding value) and the porous volume the darkest.

On macroscopic samples; the 3-dimensional visualization of the geometry of the dissolution patterns is then possible (Fig. 48c and d).

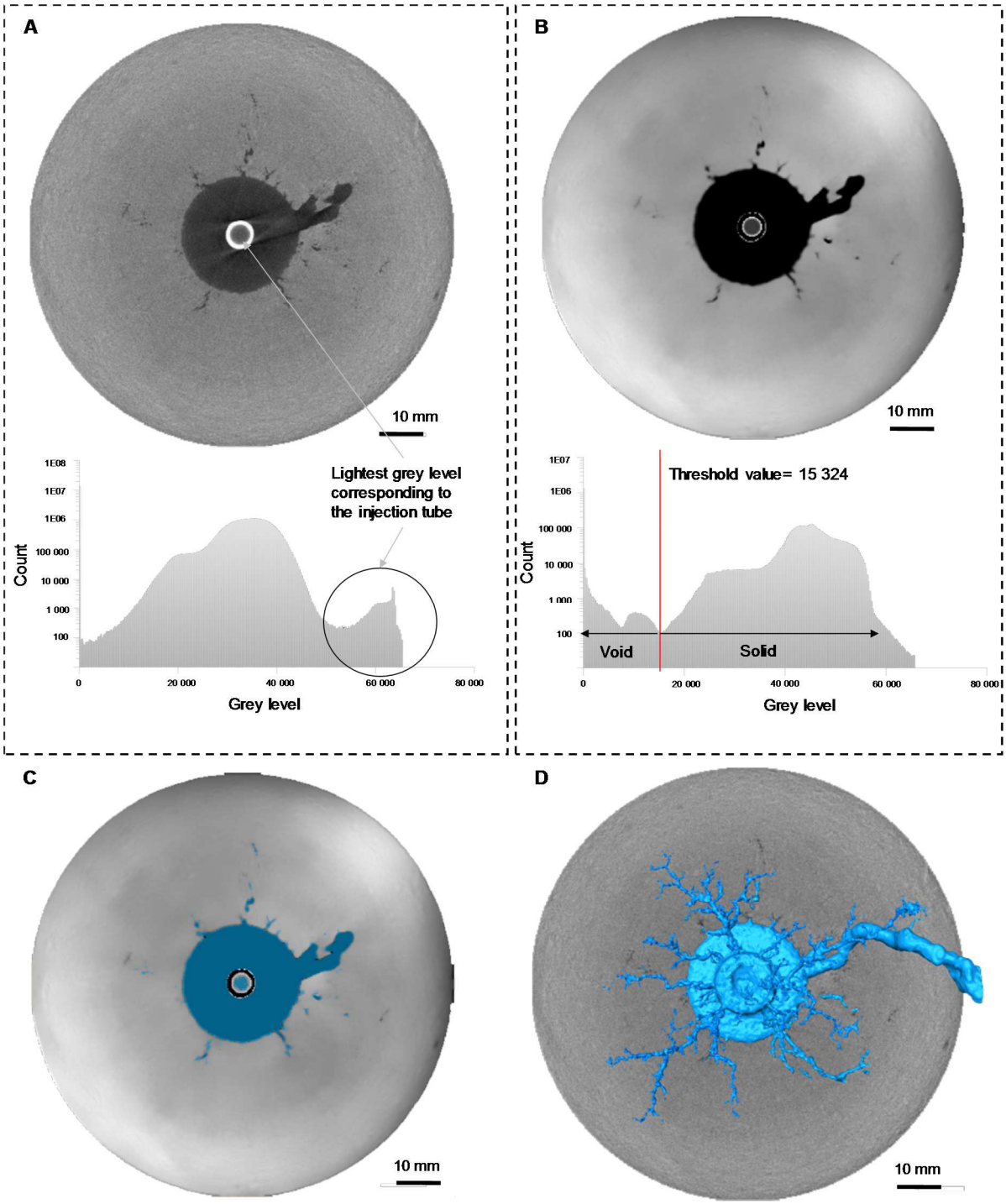

Figure 48: a) 2-D-slice of the reconstructed raw image encoded in 16-bit with the corresponding histogram of the grey level. It should be noticed that the circled part at the right end of the histogram corresponds to the stainless steel injection tube. b) 2-D Image filtered using an anisotropic diffusion filter with the corresponding filtered histogram of the grey level. The red line corresponds to the solid/void interface. This step made the artifacts related to the injection tube disappear. c) 2-D image of the delimitation of the porous network (in blue) within the segmented image (using the thresholding value). d) Projection of 3-D reconstruction in the XY plane using a generalized marching cubes algorithm.

VII.2.3.2. Surface roughness analysis protocol.

VII.2.3.2.1. Surface curvature concept

For the needs of the study, the three-dimensional structure of the material after experiments, mainly the geometry of the dissolution networks, must be characterized. From the topography of the induced dissolution pathways, a cartography of their surface roughness, according to their location in the core-plug is carried out. An analysis protocol of the segmented images obtained after processing is established to provide an estimation of the evolution of the curvature of the inner surface of the dissolved volumes. The option to apply the concept of surface curvature as a local descriptor of surface irregularities in 3-dimensions is motivated by its ability to approximate a delimited surface as a quadratic shape.

The notion of surface curvature has been initially developed in the field of 3-D object reproduction to optimize the approximation of the surface aspect by structuring a 3-D mesh as fine as possible. In the geosciences, the oil industry has integrated the concept of curvature, at the kilometric scale (regional), for their applicability to seismic interpretation [174]. On a mapped surface, curvature analysis is very effective at delimiting faults and fault geometries or visualize surface lineaments. It highlights drainage patterns for understanding well drainage efficiency and in the mapping of hydrocarbon migration pathways [175].

At the pore scale, the measurement of interfacial curvatures between two fluids or between a solid and a liquid has allowed the measurement of contact angles that quantify the wettability and control of capillary pressure [176; 177; 178]. This methods constructed on curvature computation was developed to determine the associated mobilization of the non-wetting phase within the porous network.

The use of the surface curvature data is planned at a micro- and centimetric scale as part of our study.

In a 2-dimensional Euclidean plan, the term curvature is defined by the property that describes the rate of direction change of a curve $\mathscr{C}$ at two adjacent points, in a given direction with respect to the arc length. By locally approximating the curve by its tangent circle named the “osculating circle”, its radii R can be measured (Fig. 49). The curvature κ for a particular P point on the curve is thus equal to the reciprocal of the radius of the “osculating circle” at that point:

$$\kappa = \frac{1}{R} \quad (21)$$

From a quantitative point of view; for a straight line, the center of the oscillating circle is at infinity and therefore its curvature is equal to zero. Conversely, the smaller the circle, the greater the value of the curvature. In terms of geometrical interpretation; the normal vectors at each points and more precisely the displacement of these vectors along the curve, are used as an indicator of the effects of curvature. The curvature is negative if the arrangement of 2-D nearby surface normal vectors N aims towards the center of the osculating circle. In this case the n vectors converge and the curvature is

defined as concave. In the opposite case, the curvature is positive if the arrangement of 2-D nearby surface normal vectors N aims in the opposite direction of the osculating circle. The n vectors diverge and the curvature is defined as convex (Fig. 49). This property is independent of the orientation of the surface.

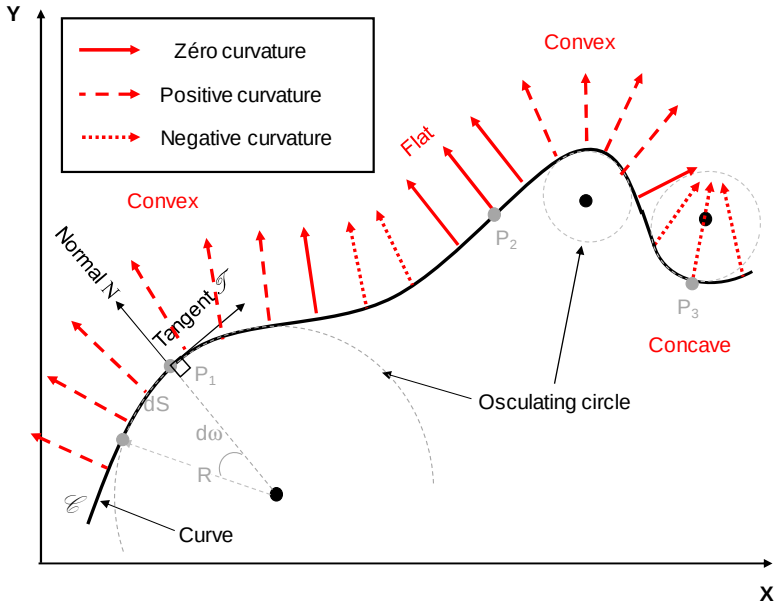

Figure 49: Definition of curvature κ : the curvature at a considered point P on a curve is defined as the rate of change of an angle $d\omega$ with respect to the arc length dS. The "ideal" tangent circle (which best fits the arc) is called the "osculating circle" and the curvature correspond to: $\kappa = \frac{d\omega}{dS} = \frac{2\pi}{\pi R} = \frac{1}{R}$. N are the vectors normal to the curve at each point P. The convergence (convexity), divergence (concavity) or parallelism (flatness) of nearby surface normal vectors allow to define the sign of the curvature which are respectively positive, negative or zero.

The curvature of a surface can also be described in a three-dimensional space based on the same concept (Fig.50). This is known as surface normal curvature. While the curvature of a plane curve is defined by a scalar and a unique number, the extension of the concept of curvature in three dimensions requires to consider another dimension. It is thus defined by a tensor (a 2 X 2 matrix) and 2 numbers established below. At a P point on the surface, we consider a rotating radial plane, perpendicular in P to the tangent plane T to the surface. This plane intersects the considered surface in a radial curves (Fig. 50a). Each of these curves is related to its curvature in P. There are an infinite number of tangential directions at that point and thus an infinity of orthogonal radial plane (white dotted line Fig. 50b for example) defined by it coefficients of surface normal curvature. Two major curvatures κ_{min} and κ_{max}, with extreme values, respectively the minimum and maximum normal curves, are used to characterize the normal curvatures at a P point (Fig. 50b). The planes corresponding to these two main curvatures have the property of being unique and orthogonal. From these maximum and minimum curvatures, two key curvature indicators can be defined: The "average curvature" κ_{mean} which is defined as the average of the main curvatures (Equation 22) and the "Gaussian curvature" which is the product of the curvatures (Equation 23).

$$\kappa_{mean} = \frac{\kappa_{\min} + \kappa_{\max}}{2} \quad (22)$$

$$\kappa_{gauss} = \kappa_{\min} * \kappa_{\max} \quad (23)$$

In this study, the “mean curvature” is used as a local descriptor of the degree of concavity or convexity of the rock matrix surface. These local specificities are associated to surface changes and enable to approximate the roughness of rock surface. As in 2-D dimensions, the sign of the curvature value will define the shape of the curvature, i.e. a positive curvature means that the surface is convex and a negative curvature is indicative of a concave surface. As the image proceeding is performed by considering the void as the zone of interest, a local negative value will indicate that the surface portion is curved in the direction of the void and a positive value in the direction of the solid phase. A zero value will mean that the surface is flat in at least one direction (Fig. 50c).

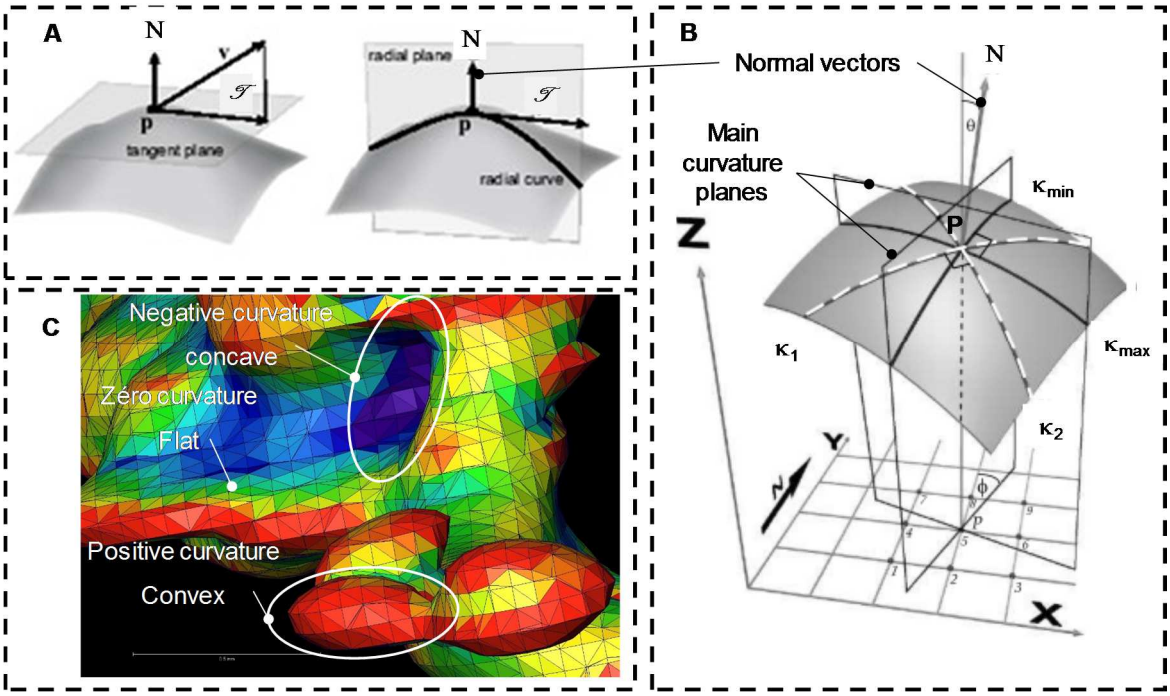

Figure 50: a) Reproduction in 3-dimensions of the tangential and normal radial plans at a P point of a curved surface, b) Curvature in three-dimensions ([174] modified): a 3-D surface is intercepted by an infinity of orthogonal plans with their associated curvature (κ_1 and κ_2 for example). For the definition of the key curvature indicator, only the minimum (κ_{min}) and maximum (κ_{max}) values of the curvature, which are called major curvatures, are used. c) Illustration of the local appearance of the surface according to the sign of the main curvatures (the colored part on the figure refers to a 3-D simulation of a dissolved volume observed in this study).

VII.2.3.2.2. Image processing protocol for surface curvature analysis

To approximate the distribution of surface curvature that define the geometry of the rock/void interface, the elaborated method of analysis firstly requires an average smoothing of the voxels composing the processed images by triangulation. An automatic meshing is generated using the “generate surface” module in the Avizo THERMOFISCHER software package. The creation of this triangular approximation of the non-planar surface patches is performed using a generalized marching cubes algorithm developed by Hege et al 1997 [179]. This algorithm is mainly built on the subdivision of a grid cell into a number of smaller sub-cells as depicted in simplified form in the following diagram:

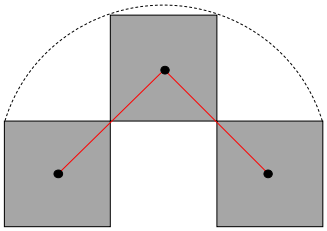

Figure51: Simplified diagram of the surface meshing algorithm by cell triangulation. [179]

This step has the additional advantage of increasing the resolution of the image (from 60 to 37 µm). The rock/void interface is thus represented as a triangular surface composed of a large number of triangles (Fig. 52a and b).

The next step consists in calculating the curvatures of the newly generated triangular discrete surface. For this purpose, the “curvature” module is used. The algorithm produce a surface field with curvature values or curvature vectors being defined on the surface's triangles. The eigenvalues and eigenvectors of the approximate quadric form corresponds to the principal curvature values and to the direction of principal curvature (which are called curvature vectors: black and withe arrows (Fig. 52b and c). Both eigenvector are tangent to the surface, and orthogonal to each other. The normal planes are defined by the normal vectors (red arrow Fig. 52b and c). The module calculates all the normal surface curvature related to the inverse radius of the circle fitting the curve defined as the interception between the surface (or tangential) and the radial (or normal) plane (Fig.52 c). An important input parameter to be specified is the number of neighbors of a given triangle that it is necessary to consider in order to define the surface for which curvature information should be computed. If the value of the input (nLayers) is one, then only triangles sharing a common edge with a given triangle are considered to be neighbors of this triangle. For larger value of nLayers, successively larger neighborhoods are taken into account (Fig. 52c red numbers). In the study, two successive layers are taken into account.

As we mentioned above, the output data of the “curvature” module we considered is the “mean curvature”, *ie* the surface scalar field containing the mean of the principal curvature values. This value is negative in strictly concave region and positive in strictly convex region (Fig. 52d and e). The extreme absolute values of the surface curvature are equal to $|5 \cdot 10^{-3}|$ and $|7.85 \cdot 10^{-4}|$ corresponding respectively to an average oscillating circle radius of 200 µm and 21 500 µm (Fig.52d).

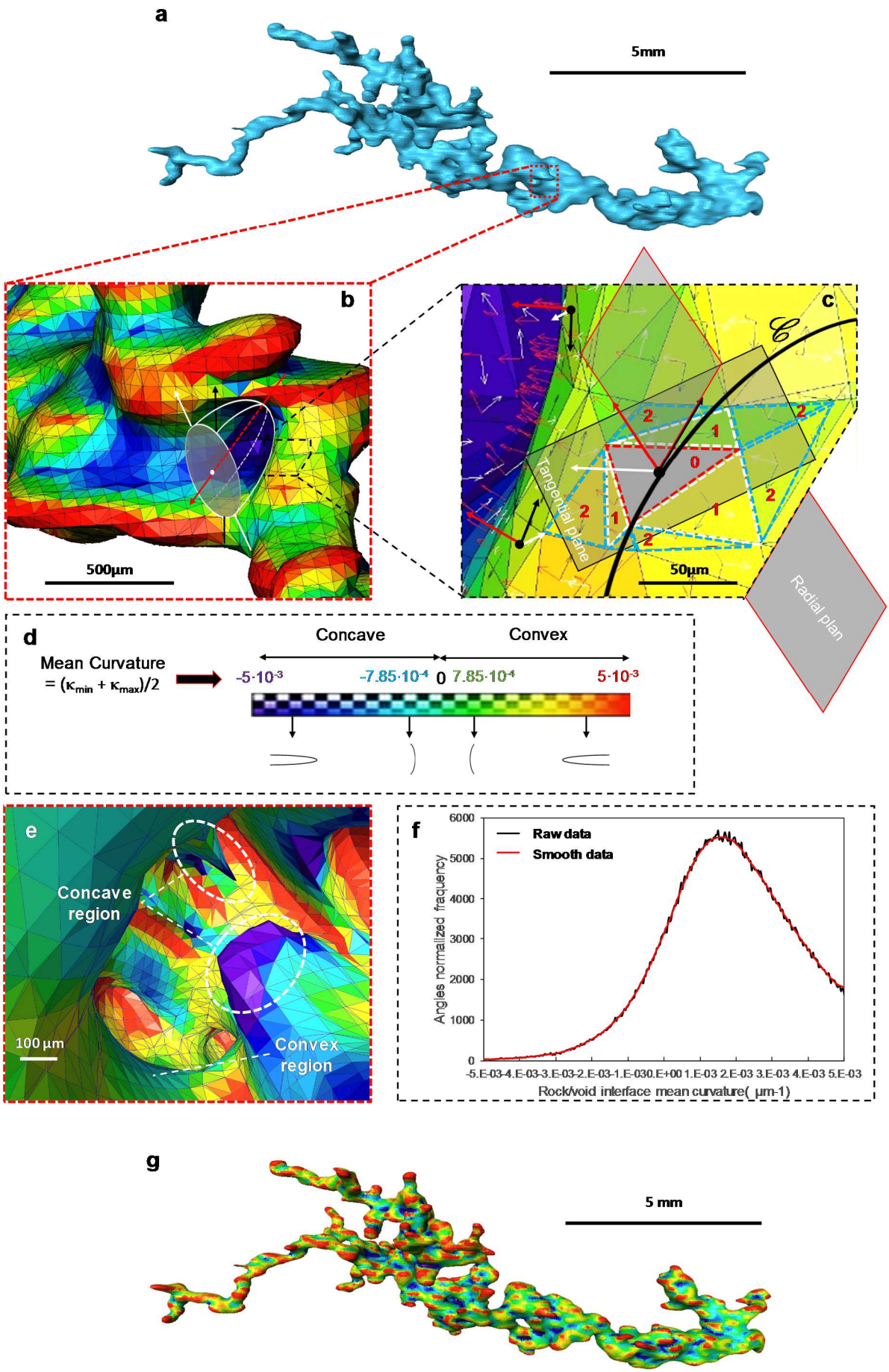
a
5mm
b
500µm
c
50µm
Tangential plane
Radial plan
d
Concave
Convex
Mean Curvature
= (κmin + κmax)/2
-5·10-3
-7.85·10-4
0
7.85·10-4
5·10-3
e
Concave region
Convex region
100 µm
f
Raw data
Smooth data
Angles normalized fraquency
Rock/void interface mean curvature(µm-1)
g
5 mm

Figure 52: Image processing for surface curvature analysis workflow a) Typical 3-D reconstruction of a post-experimental dissolution arrays after tomographic image processing (threshold volume in voxel). (b) Reconstruction of the 3-D image (rock/void interface) by smoothing the surface in triangular coordinates. The colorations correspond to the different values of surface mean curvatures (c) Illustration of the curvature calculation at a given point. The black and withe arrows represents the orthogonal eigenvectors of the surface curvature in the plane T tangential to the surface. The red arrow corresponds to the normal eigenvector. The module calculates the major normal surface curvatures of the curve located at the interception between the surface defined by a given number of neighboring triangles (numbers in red) and the radial plane. d) Mean curvature color map with considered extreme value. e) Inside view of the porosity network depicting the idea of convexity and concavity of curvatures. f) Evolution of the curvature of the rock-void interface for the selected interface. The black line corresponds to the distribution of the raw data surface curvature and the red line to the smoothing of these data (moving average) g) Mean curvature color map across the initial rock/void interface analyzed.

The display of the curvature distribution according to the data object of the triangular surface is carried out from the module “Surface view”. The scalar field is evaluated at the vertex positions of the surface (Fig 52c) and colors will be assigned (depending of the surface curvature value) onto the surface using a color map (Fig. 52g). The nature as well as the extremes of the color chart can be defined by the operator (Fig. 51d). An option (“histogram” module) finally computes the histogram of the data values of the surface curvature. The histogram illustrates the normalized frequency of value intervals corresponding to the rock/void interface curvatures in μm^{-1} (Fig. 52f). It depicts the distribution of the calculated surface curvature. The data range over which the histogram is to be computed is set from -5.10^{-3} to 5.10^{-3}. Data higher and lower than these extremes are also calculated by the algorithm but will not appear on the various graphs. The number of intervals of the data range is arbitrarily divided into 330.

VII.2.3.3. Description of the analyzed samples.

At the microscopic scale, several pieces of rock were arbitrarily selected from the Lavoux boulder in order to define the grains and to classify the type of porosity constituting the rock. In addition, it can provide information on the micro-structural aspect of the rock.

At the macroscopic scale, before experiment, a 3-D reconstruction of the near well region is performed to confirm (1) the good mechanical cohesion between the rock and the cement and (2) that the injection tube is not plugged by the cement. Moreover, the pre-experimental analysis can also be used to highlight, at the centimetric scale, the presence of structural weaknesses specific to the rock sample such as meso-fractures or meso-faults. The use of a high-resolution X-ray micro-tomograph can also highlights the layers structure of the rock or even variations in the density of specific significant areas with different porosity. The post-experimental analysis allows to provide information on spatial models of the generated dissolution network in internal structure of the post-mortem samples generated by the injection of CO_2-rich solution.

Finally, **the method for estimating the curvatures of the internal surface** of the dissolved area will allow to study the evolution of their roughness with time.

VII.2.4. *In* and *ex-situ* chemical analysis

The pH and chemical composition of the fluid (ions and dissolved CO_2 concentrations) at the outlet and the inlet of the core-plug were monitored throughout the different experiments. These measurements will provide information on the chemical interactions between the fluid and the rock. In-situ pH measurement coupled with in-situ analysis of carbon species concentration in solution by Raman spectroscopy will allow continuous monitoring of carbon speciation and concentration in solution.

VII.2.4.1. *In-situ* high pressure pH measurement

VII.2.4.1.1. Image Materiel and method.

The continuous *in-situ* pH monitoring was performed with commercial high pressure *in-situ* silver-silver chloride electrode probes (ENDRESS + HAUSER CONDUCTA INC#, USA) at temperatures of 20°C and 60°C. The probes are inserted in the system using a 316SS tee (Fig. 53a). They are located in the by-pass at the outlets of the two autoclaves. The components (tubes and tees) of the by-pass positioned after the MIRAGES-2 injection autoclave are heated at 60°C thanks to a heater cable. As a consequence, the measurements are performed on the percolating fluid in the same pressure/temperature conditions than in the experimental autoclaves. The liquid junction metal is porous Teflon and the probe material is 316SS and glass (Fig. 53b). The probes have a pH range from 0 to 14. The working conditions of the electrodes are normally limited to 70 bar and 105°C. However the pressure header located at the top of the probes allows to work up to 150 bar, but this conditions of use reduced the lifetime of the probes.

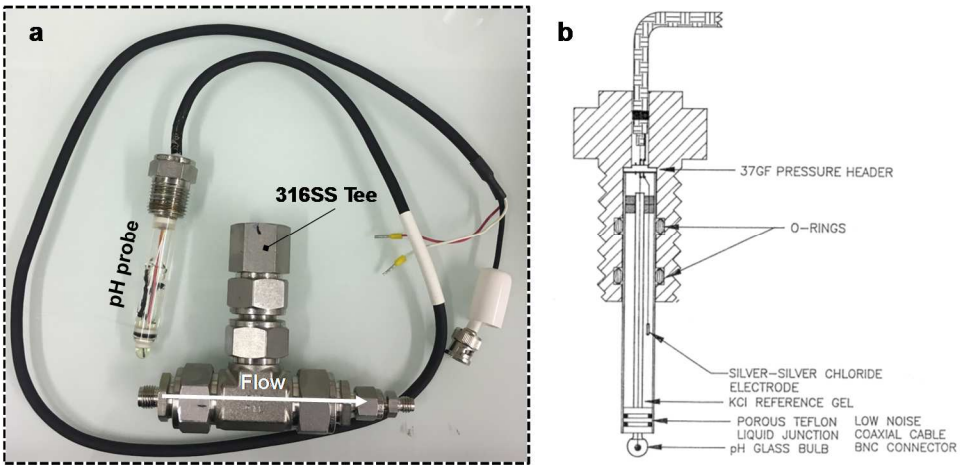

Figure 53: a) HP/HT in situ pH probe with its cable and 316SS tee allowing it implementation in the MIRAGES-2 test bench. b) Scheme of the probe with the different components (@Hendress and Hauser Conducta INC).

The pH determination is based on the electric potential measurement between a pH and a reference electrodes. The potential measured by the electrode bathing in a hydrogen flow is inversely proportional to the pH of the solution. A calibration in experimental conditions with buffer solutions of known pH is required. This calibration gives a relationship between the *in-situ* pH and the measured potential of the pH probe *E*, relative to the reference probe. For a given temperature of measurement, the electrode behavior is described by the Nernst equation: (Equation 24):

$$E = A - \frac{\beta \times R \times T \times \ln(10)}{F} \times pH \qquad (24)$$

Where A is a constant (the intercept of the function) for a series of measurements and a given temperature. This constant depends on the state of the data channel at one time and temperature. β is a coefficient characteristic of the data channel during a given period (this coefficient evolves with the electrode wear and is close to 1 (generally >0.98)), R is the universal gas constant in $J \cdot mol^{-1} \cdot K^{-1}$, T the absolute temperature in K and F the Faraday constant in coulombs C. $(\beta \times R \times T \times ln(10))/F$ is the slop of the function. It also depends on the temperature. The more β is close to 1, the more the behavior of the probe is closed to the “ideal” behavior of Nernst. At 20°C and 60°C, the slop is respectively equal to ~ 59.16 mV/pH and ~ 65 mV/pH) [180].

The calibration curve has to be consistent with the Nernst behavior. Calibrations are performed before and after each run to apply the proper correction due to a possible probe drift over time (the pressure conditions modifying the state of the data channel with time). The position of the probe in a by-pass system allows to remove it during experiment for maintenance or calibration purposes.

In our experimental conditions, the calibration with standard pH buffer is effective for the pH measurement of the brine solutions (15 $g \cdot L^{-1}$ of NaCl). In these conditions of salinity, the potential of the reference probe is poorly affected by the ionic strength of the measured solution.

During experiments, several probes were destroyed due to a too high depressurization after measurement.

VII.2.4.1.2. pH probes calibration

Standard calibration: The pH probes are calibrated at 20°C and 30 bar (conditions in the mixing autoclave) and at 60°C and 120 bar (condition in the MIRAGES-2 autoclave) with three buffer solutions of known pH.

Figure 54 shows the relationship between the *in-situ* pH and the measured potential of the pH probes before and after the 21d experiment without salt. These calibration results demonstrate that the potential of the probes gives linear responses as a function of pH.

It also reveal that the difference of calibration slopes before and after experiment are not significant. The slope is about 57-58 mV per pH unit for the calibration at 20°C and 64 mV per pH at 60°C. This values are in good agreement with the literature data [180].

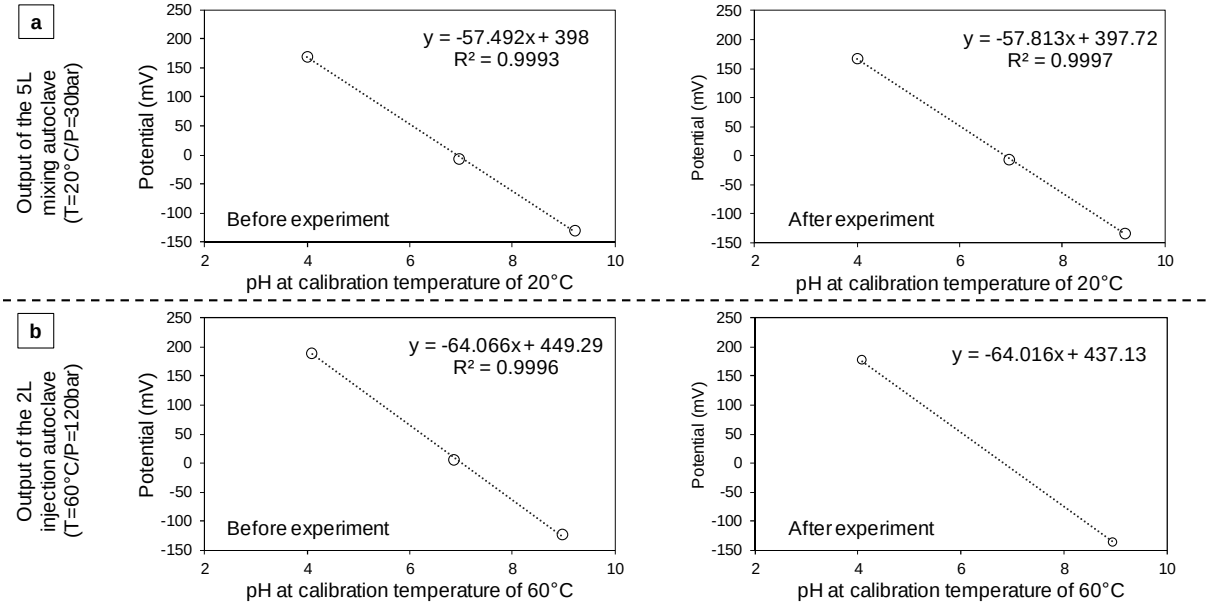

Figure 54: Calibration curves of high pressure pH probes showing the electrode potential as a function of pH for two different calibration steps, before and after the end of the 21d injection experiment without salt (a) Output of the 5L mixing autoclave and (b) output of the MIRAGES-2 autoclave.

VII.2.4.2. *In-situ* Raman spectroscopy under high pressure/high temperature hydrothermal conditions.

The Raman spectroscopy is a technique of molecular analysis dedicated to the study of solids, liquids and gases. It is based on inelastic scattering of monochromatic light, usually from a laser source. Inelastic scattering means that the frequency of photons in monochromatic light changes upon interaction with a sample. Photons of the laser light are absorbed by the sample and then reemitted. Frequency of the reemitted photons is shifted up or down in comparison with original monochromatic frequency, which is called the “Raman Effect”. This shift provides information about vibrational, rotational and other low frequency transitions specific to each molecule. Scattered light is collected with a lens and is sent through interference filter or spectrophotometer to obtain Raman spectrum of a sample. A Raman spectrum is thus a plot of the intensity of Raman scattered radiation as a function of its frequency difference from the incident radiation (usually in units of wavenumbers, cm^{-1}). This difference is called the “Raman shift”.

Within the framework of our experiments, this technique is used for in-situ data acquisitions of CO_2 solubility in the injected solution and the speciation of carbonate in the effluent solution after interaction with the sample.

VII.2.4.2.1. In-situ Raman: material and method.

Original Equipment: The usual experimental and analytical techniques for the determination of CO_2 solubility in solution (water or brine) under geological P/T conditions are based on the sampling of the phases before analysis by chromatography, mass spectrometry or weighing [108, 181]. However, the sampling operation may induce a perturbation of the system (pressure and temperature decrease, fluid displacement), which can be of a great influence under conditions where the system is close to instability. The recent development of immersion optic probes makes possible the in-situ solubility measurements by Raman spectroscopy under controlled pressure.

A new method developed by the GeoRessources laboratory [182] allows the continuous in-situ monitoring of the CO_2 concentration in aqueous solution under high pressure/temperature conditions.

The technical apparatus for the in-situ Raman analysis is a Kaiser RXN1 Raman spectrometer. This is a portable compact system (Fig. 55a) connected to a Raman optic head with an optical fiber (Fig. 55a). This Raman head is connected to the in-situ Raman probe (Fig. 55a) which consists in an Alloy C-276 tube composed of an optic lens and a sapphire window. The emission wavelength of the laser is 532 nm with a power of ~ 25 mW at the sample. The laser beam passes through the optical fiber, the probe and the sapphire window before interacting with the sample. The Raman signal generated by the light-matter interaction is sent to the spectrometer by the optical fiber. The signal is thus collected and filtered toward a CCD detector cooled down to −40°C by Peltier effect. This system allows Raman spectra to be collected in-situ and simultaneously from 175 to 4325 cm^{-1} with a resolution of ~ 3 cm^{-1} at 1400 cm^{-1}. The length of the immersion probes is of 6 inches and the diameter is of ¼". They can operate up to 450°C and 200 bar.

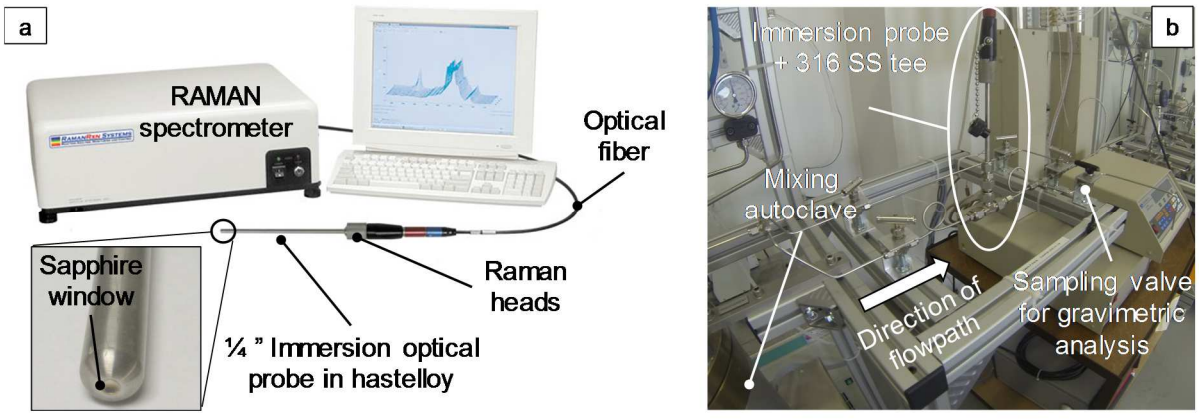

Figure 55: Description of Kaiser RXN1 Raman spectrometer (a). Implementation of the probe on the test bench (b): the probe is crimped to a 316 SS tee with ¼" connection, the laser is focused at the center of the tee where the solution flows continually.

The Raman probes are coupled to the MIRAGES2 test bench by crimping on a 316SS tee (Fig. 55b). Two probes are set up, i) one located in a by-pass system after the 5 liters mixing autoclave to measure and check the amount of dissolved CO_2 in solution before injection in the core-plug ii) and the other one located in a by-pass system after the MIRAGES-2 autoclave to determine the carbonate speciation in effluent solution coming from the core-plug. Each by-pass is equipped with a connection that enabled regular on-line sampling of the fluids (Fig. 55b).

Spectrometer response, Raman shift wavenumbers and laser wavelength are calibrated using cyclohexane, a Neon lamp and a white lamp respectively with a known continuous emission spectrum (HCA calibration accessory, Kaiser Optical Systems). The acquisition time and the number of accumulations are defined in a way to optimize the signal-to-noise ratio, usually 30 s and 8 accumulations. The dark is subtracted and spectra are corrected from the instrument function (intensity calibration on).

Raman data processing: The concentration of dissolved CO_2 in solution is determined by correlating the peak Intensity ratio of the Fermi doublet characteristic of the dissolved CO_2 with the wavenumbers ν_1 at 1276 cm^{-1} and ν_2 at 1384 cm^{-1} normalized to the H_2O bending vibration band (δ_1 ~ 1640 cm^{-1}) with the amount of CO_2 in solution (mole.kg^{-1} of solution). The range of wavenumbers covered by the integration for dissolved CO_2 is 1150 to 1450 cm^{-1} and 1450 to 1850 cm^{-1} for water (Fig. 56. The ratio I_{CO_2}/I_{H_2O} is calculated using the HGSLabSpec software (@Horiba Jobin-Yvon).

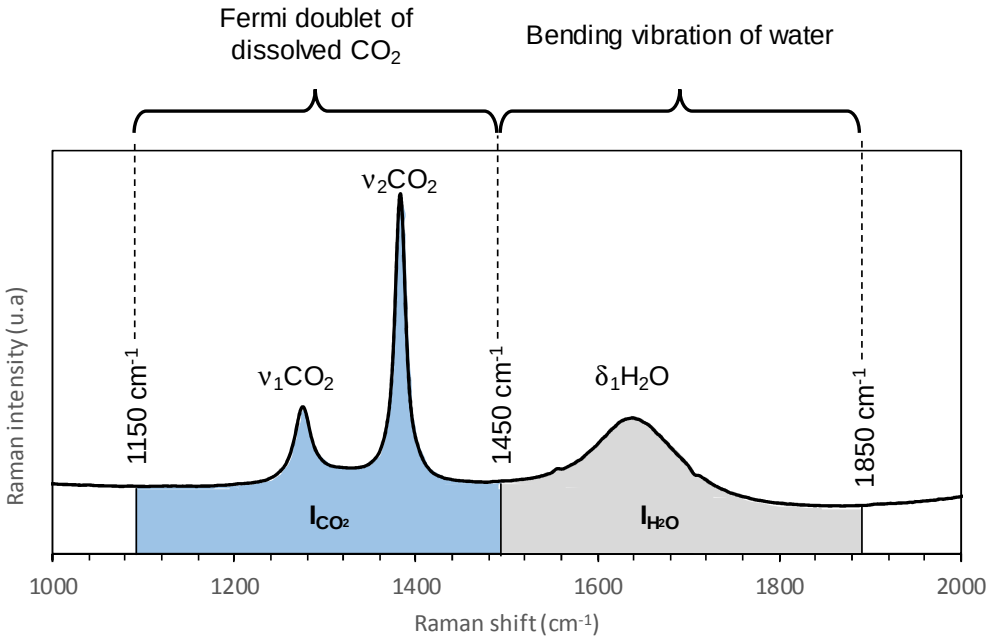

Figure 56: Typical Raman spectra of dissolved CO_2 in pure water acquired with the in-situ Raman probes at 20°C/30bar.

Calibration: As for any analytical device, a calibration is required before experiments. The calibration of the Raman probe is carried out by measuring the area pic ratio of CO_2/H_2O (I_{CO_2}/I_{H_2O}) at 20°C (temperature of the 5 liters device) for different pressures. The ratio is calculated and plotted as a function of dissolved CO_2 concentration. The solubility of CO_2 in water is calculated using the thermodynamic model of Duan et al. (2003) [108] for each pressure/temperature conditions.

The concentration of dissolved CO_2 is also determined by gravimetric method; on the one hand, to validate the choice of the Duan model as a reference for the data of CO_2 solubility and on the other hand to confirm the validity of the computed CO_2 solubility value during experiments. A validation stage of the gravimetric method is also carried out in a first instance.

The experimental procedure for the Raman calibration of dissolved CO_2 concentration measurements at 20°C and the gravimetric method of total carbonate concentration measurement are described in the appendix C.

VII.2.4.2.2. Results of the *in-situ* Raman calibration at 20°C

The calibration is done with five CO_2 pressure conditions (20 – 25 – 30 – 35 and 40 bar) in pure water at 20°C. Between 4 and 149 spectra are recorded continuously at each P/T conditions every 5 minutes. For each acquisition, the I_{CO_2}/I_{H_2O} ratio is calculated and reported in a graph as a function of time (Fig 57. b). The equilibrium of solubility is considered when the curve reaches a plateau.

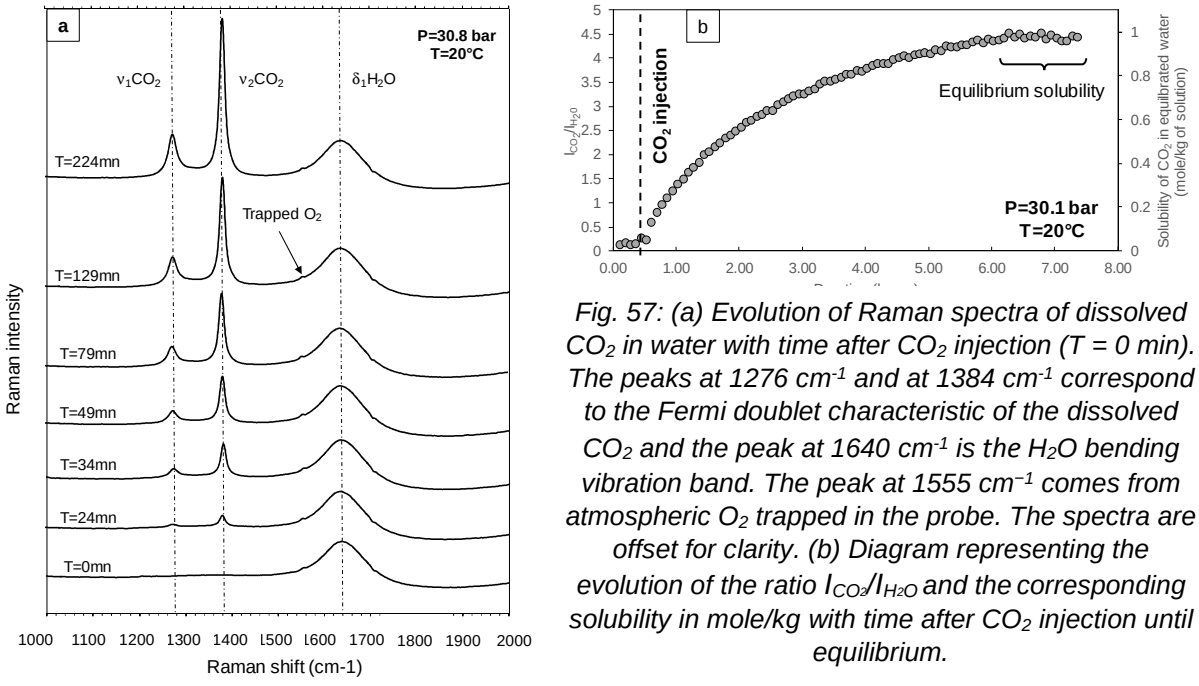

Fig. 57: (a) Evolution of Raman spectra of dissolved CO_2 in water with time after CO_2 injection (T = 0 min). The peaks at 1276 cm^{-1} and at 1384 cm^{-1} correspond to the Fermi doublet characteristic of the dissolved CO_2 and the peak at 1640 cm^{-1} is the H_2O bending vibration band. The peak at 1555 cm^{-1} comes from atmospheric O_2 trapped in the probe. The spectra are offset for clarity. (b) Diagram representing the evolution of the ratio I_{CO_2}/I_{H_2O} and the corresponding solubility in mole/kg with time after CO_2 injection until equilibrium.

Raman spectra collected in the aqueous phase as a function of time at 20°C and 30.8 bar are presented figure 57a. At t = 0 min, the only signal comes from the OH vibration bending band of water at 1640 cm^{-1}. The intensity of this vibration does not vary with time after CO_2 injection and can be considered as an internal standard.

Once the CO_2 is injected, the CO_2 Fermi doublet band of dissolved CO_2 at 1276 cm^{-1} and 1384 cm^{-1} becomes visible very quickly. The intensity of the Fermi doublet increases with time until the equilibrium of solubility is reached. At equilibrium, the Raman signal becomes stable and the variations of I_{CO_2}/I_{H_2O} are very weak (Fig. 57b). The average of these I_{CO_2}/I_{H_2O} values at equilibrium is used to determine the CO_2 solubility thanks to the thermodynamic model of Duan and Sun (2003) [108] and the appropriate calibration curve.

The results are summarized in appendix D. The experimental standard uncertainty 2σ is calculated on the ratio I_{CO_2}/I_{H_2O}. The relative standard uncertainty defined by $\sigma_r = {\sqrt{\sigma}}/{n}$ (with n the number of measurement) is also determined.

A calibration curve (Fig. 58) is calculated by fitting the data with a straight line and an intercept fixed to zero. The slop of the calibration curve is equal to 4.20 with an uncertainty on the I_{CO_2}/I_{H_2O} ratio of 0.03 at 95%. The adjusted R^2 is equal to 0.9352.

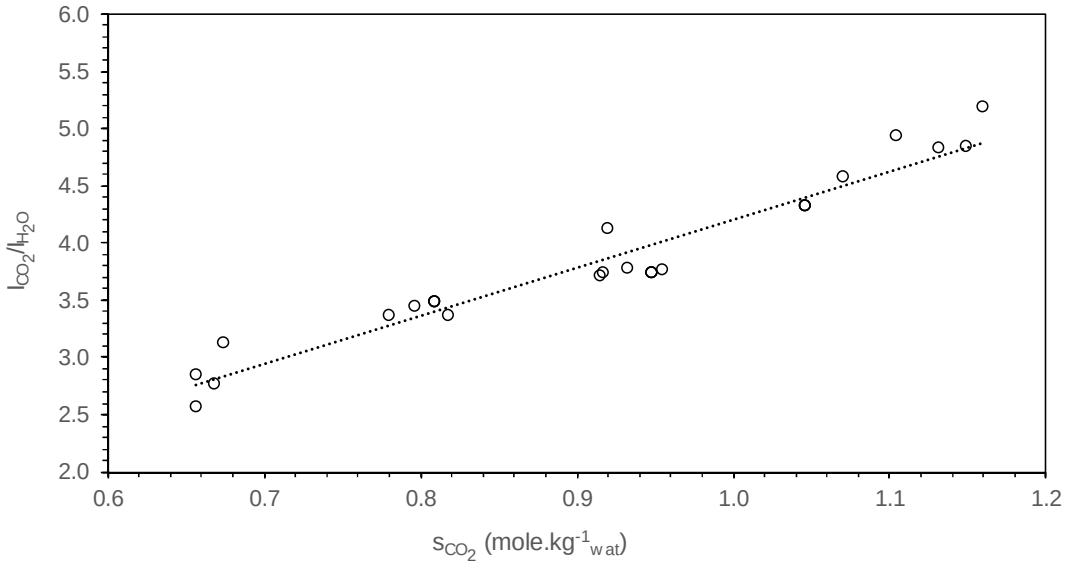

Figure 58: I_{CO2}/I_{H2O} peak intensity ratio as a function of CO_2 solubility (mol.kg$^{-1}_{water}$) calculated from the thermodynamic model of Duan and Sun (2003) [108] at 20°C.

Thus, for our experiment, the CO_2 solubility (mol.kg$^{-1}_{water}$) is calculated thanks to the in situ Raman probes using the equation 25:

$$disolved\ CO_2 = \frac{{I_{CO_2}}/{I_{H_2O}}}{4.20} \quad (25)$$

VII.2.4.2.3. *in-situ* Raman calibration at 60°C

For the measurement of the amount of dissolved CO_2 in water at the output of the core-plug at 60°C and 120 bar, the data of experimental measurements of co-solubility of the CO_2/H_2O system at 65°C done by Caumon et al (2016) [182] are used. The calibration curve of I_{CO_2}/I_{H_2O} peak intensity ratio as a function of CO_2 solubility ($mol.kg^{-1}_{wat}$) at 65°C has been calculated by fitting the data with a straight line with a slope equal to 4.91 ± 0.03 (95%) and an intercept fixed to zero. For our experiment, the CO_2 solubility is calculated using the equation 26:

$$disolved\ CO_2 = \frac{{}^{I_{CO_2}}\!/_{I_{H_2O}}}{4.91} \quad (26)$$

Since the correlation between the peak intensity ratios I_{CO_2}/I_{H_2O} and the CO_2 dissolved in solution ($mol \cdot kg^{-1}_{wat}$) is established, the amount of CO_2 dissolved in water before and after the injection in the core-plug is continually measured during our experiments. A sampling of the solution is done from time to time in order to check, with the gravimetric method, if there is no drift of the Raman measurement during the different experiments especially the long-term experiments.

VII.2.4.3. Solution chemistry analysis by ICP-AES and ion chromatography (IC)

The device allows regular fluid sampling at the outlet of the core-plug for chemical analysis by ICP-AES and/or ion chromatography. Changes in the concentration of specific elements (mainly Ca^{2+} in our case) can provide information on the chemical behavior of the rock and the dissolution rate.

The coupling of these additional method is interesting because it enables to establish precise mass balances of the elements composing the studied system.

ICP-AES: The inductive coupled plasma spectrometry is an analytical technique used to precisely measure the concentrations of almost all the chemical elements of a solid or in aqueous solution. A high temperature plasma source is used to dissociate the sample into its constituent atoms or ions, exciting them to a higher energy level. They return to their ground state by emitting photons of a characteristic wavelength depending on the element present. This light is recorded by an optical spectrometer. When calibrated against standards, the technique provides a quantitative analysis of the original sample. This technics is used here to determine the concentrations of cations (calcium, magnesium, strontium, aluminum and iron) in aqueous solution. The measurement uncertainties are of 5% for a concentration > 100 $\mu g.L^{-1}$ and of 5 $\mu g.L^{-1}$ for a concentration between 5 and 100 $\mu g.L^{-1}$. The limit of quantification is of 5 $\mu g.L^{-1}$.

Ion chromatography: This technics measures concentrations of ionic species by separating them with a resin. The retention time of different species determines the ionic concentrations in the sample. In our experiments, only the concentration of sulfate in aqueous solution is determined thanks to the IC technic. The measurement uncertainties are of 6% for a concentration > 330 $\mu g.L^{-1}$ and of 20 $\mu g.L^{-1}$ for a concentration <330 $\mu g.L^{-1}$. The limit of quantification is of 50 $\mu g.L^{-1}$ according to the ISO standard 11-352.

The solution chemistry analyses were carried out at chemical analysis platform of the Interdisciplinary Laboratory for Continental Environments (LIEC).

– PARTIE 4 –

MODÉLISATION EXPÉRIMENTALE DE L'INJECTION DE CO_2 SOUS FORME DISSOUTE EN RÉSERVOIR GEOLOGIQUE : RESULTATS ET OBSERVATIONS

– PART 4 –

EXPERIMENTAL MODELLING OF THE INJECTION OF CO_2 IN DISSOLVED FORM IN GEOLOGICAL RESERVOIR: RESULTS AND OBSERVATIONS

I. INITIAL CHARACTERIZATION OF THE ROCK SAMPLES

I.1. Petrographic analysis.

The microscopic observation on the fresh fractured rock samples and thin sections of the studied Lavoux limestone reveals predominantly the presence of microporous micritic ooids and accessory pellets and bioclasts (echinoderm fragments,…) (Fig. 59a, b and c). The porous volume has been partially filled by a binding phase consisting in a micritic matrix, large size syntaxial sparitic cement (100 – 1000µm) and moderate size rhombohedral (or equant) sparitic calcite (10-50µm) (Fig. 59d, e and f) resulting from an early diagenesis.

The ooids are made up of concentric micritized lamella composed by calcite micro-crystals (Fig. 59b and c). Their shape is almost spherical and their size ranges from 200 to 600 µm. The fine-grained carbonate constituting the micritic cortex of the ooids has different size and shape. To describe these microcrystalline calcite types, the classification of Deville de Periere et al. (2011) [183] is used (Fig. 60). It is mainly based on the crystal morphology and the type of inter-crystal contact. In our samples, the crystal shape is defined as subrounded to micro-rhombic with inter-crystalline contact punctic to locally coalescent (Fig. 59d and f).

The large syntaxial cement corresponds to calcite overgrowths around echinoderm clasts (Fig. 59a, b and e) and can reach a size of several hundreds of micrometers. They are characterized by a slightly irregular surface. Traces of alteration are readily apparent on their surface in the form of crevasses (Fig. 59e).

The use of SEM also enabled a fine observation of the small rhombohedral sparitic crystals classified as blocking cement (Fig. 59d). They are localized in the micritic cortex and apparently have the micrite crystals as nuclei. They appear as a fringe around the ooids and do not totally occlude the macroporosity (Fig. 59b).

According to the classification of Dunham., 1962 [97], the Lavoux limestone can be defined as a packstone to grainstone.

The micro-CT analysis provides a broader overview of our experimental samples. Core samples of 10 X 10mm parallel to the bedding of the Lavoux limestone are analyzed to obtain a 2D/3D reconstruction with a resolution of 5 µm. A sub-horizontal cross-section (top view) of a sample is shown in figure 60. The lightest grey levels correspond to the rock matrix. The CT-scan displays a partial dissolution of the nucleus of some ooids (Fig. 61a). In micro-CT, echinoderm fragments are difficult to identify due to their chemical composition and crystallographic structure similar to that of cement.

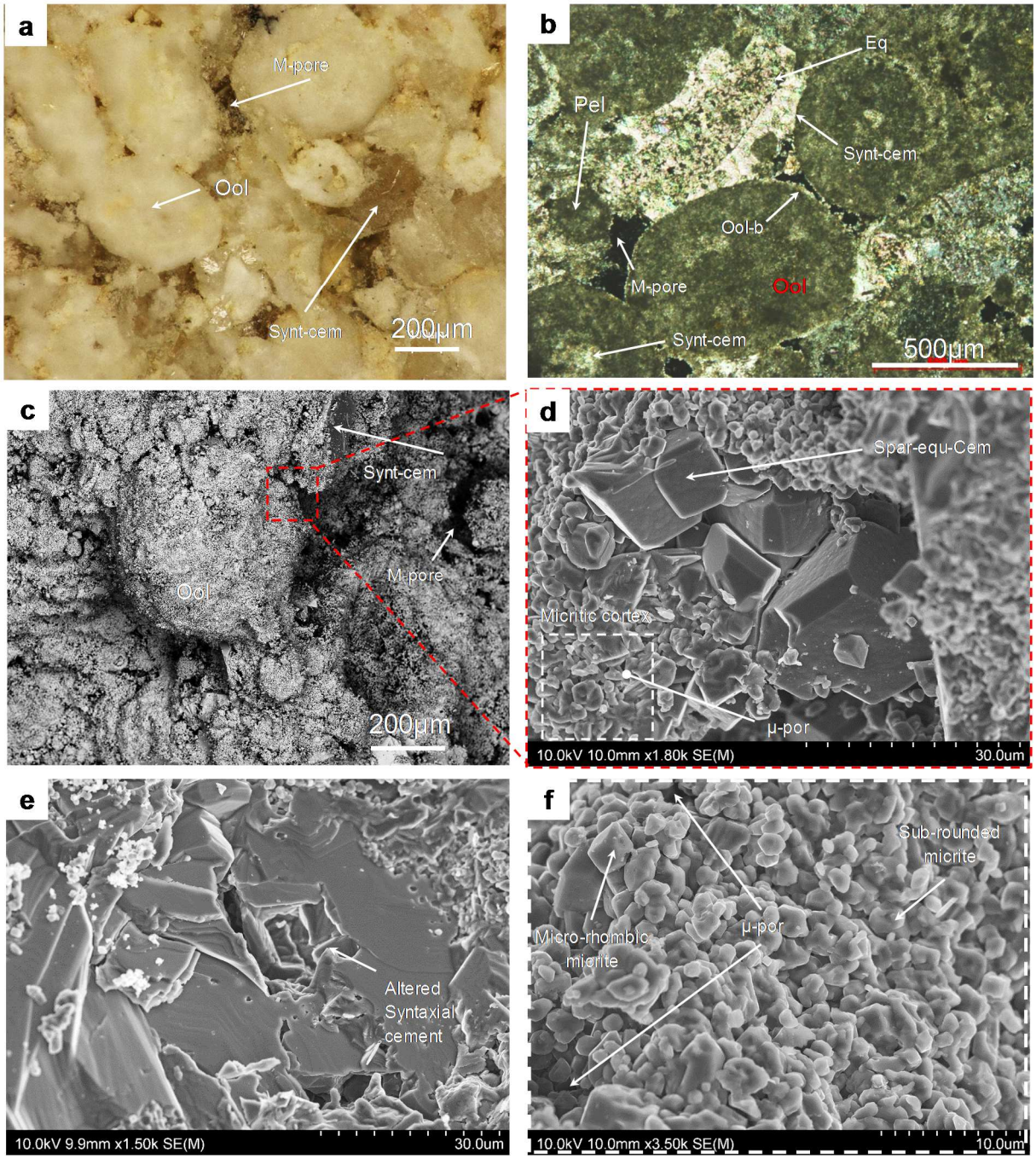

Figure 59: Illustration of the Lavoux limestone texture: (a) microscopic observation on a fresh sample, (b) microscopic observation on thin section (polarized light). We can see the fabric of the rock with the ooids (Ool) and the syntaxial cementation (Synt-cem) around an echinoderm fragment (Eq) and also the oolitic fringe (ool-b). The dark areas correspond to the porosity, (c) SEM observation (in SE Secondary Electrons mode) of Lavoux limestone. Overview of the surface showing the ooid (oolite), syntaxial cement (synt-cem) and macropores (M-pore) (d) with micritic cortex and sparitic equant cement (Spar-equ-cem).(e) Syntaxial cement with dissolution pits (f) Focus on the micritic cortex and the microporosity (µ-por).

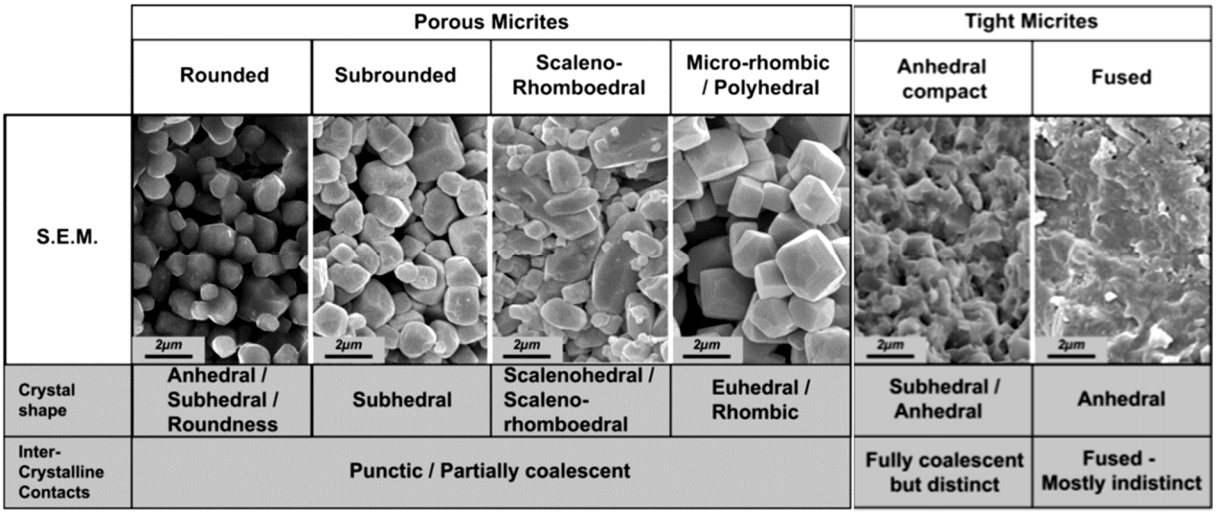

Figure 60: Classification of micritic micro-textures from Deville de Periere et al. (2011) [183], mainly based on crystal morphology and type of inter-crystal contact.

In a structural aspect, the 2D CT-scans reveals characteristic microstructures such as micro-stylolites (Fig. 61b). Finally, we also observe regularly arranged microscale planar fractures along which we record small amounts of dextral and sinistral shear displacements (Fig. 61a and b).

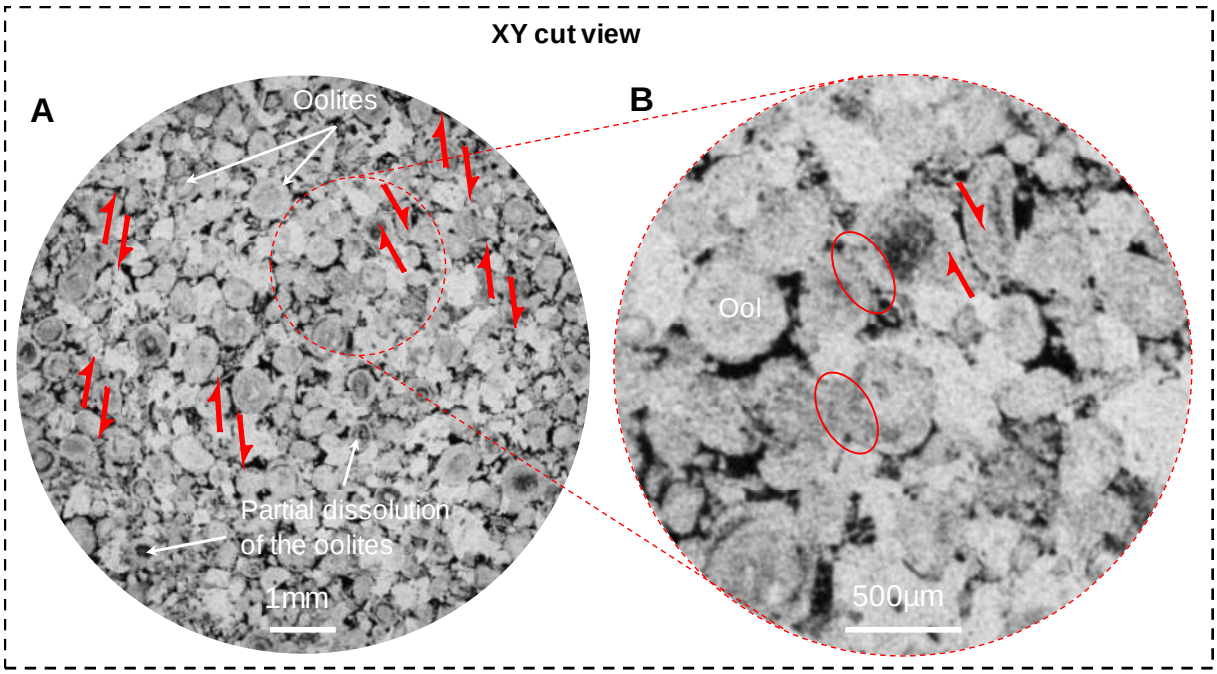

Figure 61: CT scans of a sample of the Lavoux limestone (resolution 5 µm) with the rock fabric in grey and the porosity in black. (a) Sub-horizontal cross-section showing the arrangement. Of Oolites and cements. The nucleus of some oolites are partially dissolved. Some potential micro-fracture are also visible (double red arrows) (c) Focus on the oolites and sparitic cement: The CT-scan displays stylolitic contacts of ooids (red circles arrows) and some grains interpenetration due to a chemical compaction during burial (large red arrows).

I.2. Petrophysical analysis.

Petrophysical analyses were performed with focus on porosity and permeability parameters.

A visual investigation is firstly performed on a sub-vertical cross-section (side view) of the 2D CT-scans from the tomographic analysis of the 10 X 10mm cylindrical sample (Fig. 62). The darkest grey levels represent the porosity of the rock. In accordance with the image resolution, this porous space corresponds to the macro-porosity. The intermediate grey levels correspond to microporous grains (a voxel thus integrates void and solid). Indeed, this gray level is darker than for pure material because the X-rays cross more easily through the material and are representative of a less dense microporous area.

At this scale, it emerges from the CT-scan of figure 60 and 61 that the macro-porosity is neither vertically nor horizontally well connected. The connection between macropores is supported by the micro-porosity. It appears that a partial dissolution of the nucleus of the ooids enlarged the intra-ooid pores and also created mesopores (Fig. 62). This phenomenon leads to a heterogeneous aspect of the internal structure of the ooids. Three types of ooids can thus be distinguished. The first one corresponds to ooids with a nucleus completely dissolved. Their center appears very dark. The second type of ooids has a high microporous nucleus. The grey level of some areas of the center of the ooids thus appears darker. The third type is made of a highly crystallized nucleus and are whiter on CT images.

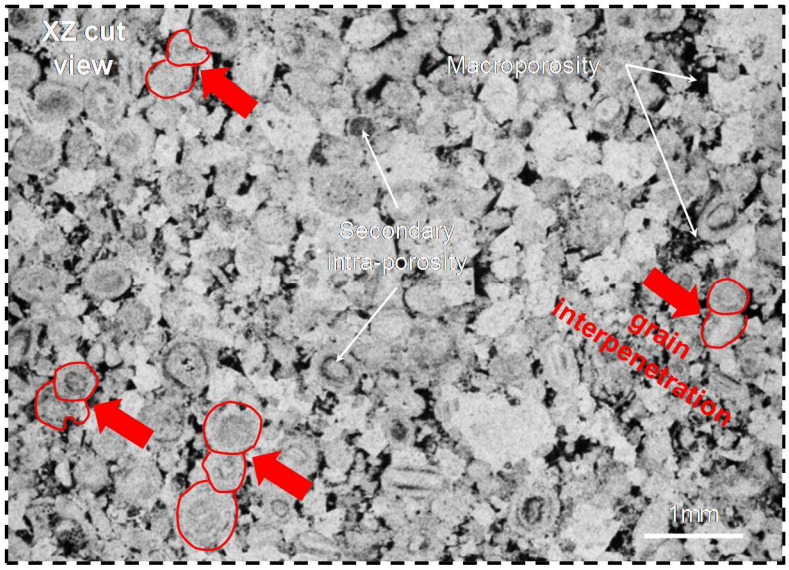

Figure 62: CT scans of a sample of the Lavoux limestone (resolution 5 µm) with the rock fabric in grey and the porosity in black. (a) Sub-vertical cross-section: the dark area in the ooids corresponds to a partial secondary dissolution of the intra-porosity and the large red arrows show some grains interpenetration due to a chemical compaction during burial.

The sub-vertical visualization of the studied rock also reveals some grain–to–grain interpenetration (Fig. 62) generated by chemical compaction during the burial of the rock. This phenomenon completely clogs the space between two ooids.

From a quantitative point of view, Table 7 presents the values of petro-physical results for the different fresh samples cored at different parts of the boulder. Values show a good homogeneity of the rock with an average total bulk connected porosity equal to 24.73% which is in accordance with the data found in the literature on the Lavoux limestone (between 12 and 26.33%) [38; 154; 155; 187; 188; 189].

Samples	Hg prosity (%)			Density of the solid skeleton ρ_s (g/cm^3)	Access diameter (µm)	N_2 permeability k (mD)
	Total	Free	Trapped			
Samples cored in the direction perpendicular to the horizontal sedimentary bedding of the rock						
Initial sample1	24.04	9.16	14.88	2.69	1.69	51.2
Initial sample2	24.56	9.21	15.34	2.69	1.66	58.2
Initial sample3	23.05	10.02	13.03	2.63	1.17	48.7
Initial sample4	25.78	12.17	13.60	2.67	1.30	31.8
Initial sample5	25.17	13.34	11.83	2.62	1.25	42.3
Initial sample6	25.79	12.50	13.30	2.68	1.24	50.5
Average	**24.73**	**11.07**	**13.66**	**2.66**	**1.38**	**K_v = 46.5**
Samples cored in the direction parallel to the horizontal sedimentary bedding of the rock						
Initial sample 7	**23.36**	**9.34**	**14.02**	**2.66**	**1.54**	**K_h = 73.8**

Table 7: Petro-physical properties (Total, free and trapped porosity, permeability k_v and k_h) of Lavoux limestone: initial cylindrical samples cored in the direction perpendicular and parallel to the horizontal sedimentary bedding.

The free porosity (or effective porosity) (11.07%) represents an important fraction of the bulk connected porosity. The average pore entry diameter is of 1.38 µm. The method of nitrogen permeability results in a high intrinsic permeability with an average value of k_v = 46.5 mD. The permeability in the rock is anisotropic. Indeed, the permeability k_h parallel to the bedding equal to 73.8 mD is greater than for the vertical direction. The relevant permeability tensor will influence the velocity field in the core sample. We can expect a dependent flow rate of the injected solution in a direction oriented by the bedding. Concerning the absolute specific mass value of the solid skeleton (2660 kg.m^{-3}), this value is consistent with that of calcite (2700 kg.m^{-3}).

Figure 63 shows the porous spectrum of the Lavoux limestone obtained from the first mercury injection with a mercury pressure up to 400 MPa. Samples have a bi-modal porosity distribution with peaks at 0.42 µm and 3.08 µm. The range between 0.03 and 1.46 µm is the smaller one and corresponds to intra-ooid porosity (microporosity). The other family of pores, between 1.46 and 5.1 µm corresponds to the inter-ooids pores (mesoporosity).

The petro-physical analysis describes the Lavoux limestone as a porous rock due to the large size of both intra and inter-ooids pores. The macropores can reach a maximum size of 300 µm.

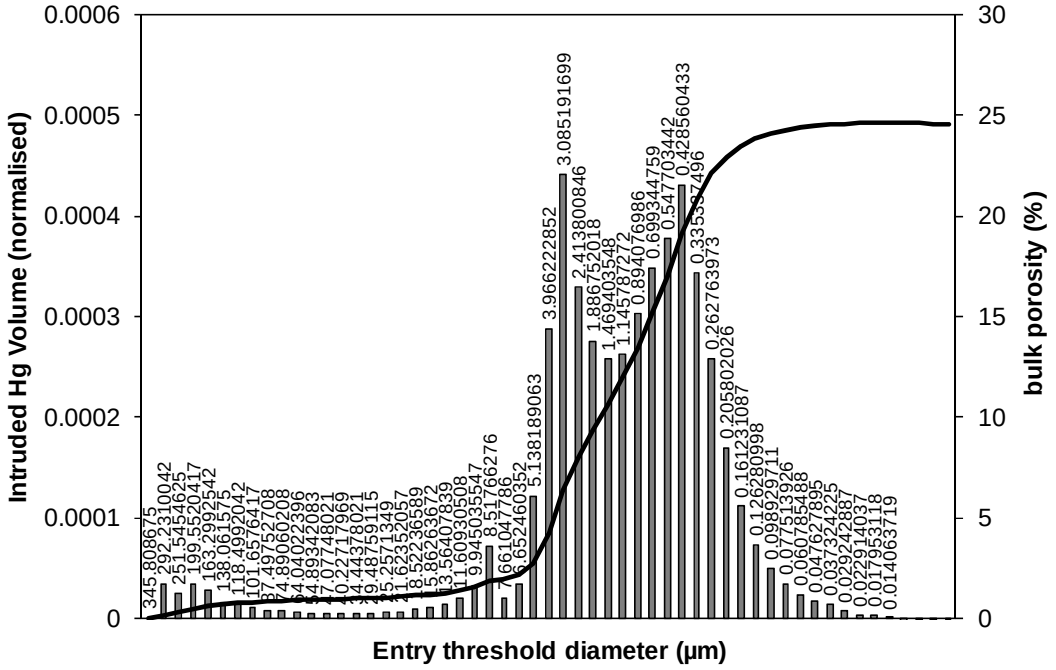

Figure 63: Purcell test (Hg porosimetry) on the Lavoux limestone (first injection). Pore size distribution (porous spectrum) is for bulk porosity.

These investigations justify the choice of the Lavoux limestone as an adapted rock for flowthrough experiments. Its petrophysical characteristics are suitable for a hydraulic forcing without imposing a too severe pressure gradient within the rock. The injection will thus not generate an excessive stress that could fracture the rock and invalidate the experience.

I.3. Chemical analysis

The chemical characterization performed on Lavoux limestone by ICP-ES (Inductively Coupled Plasma Emission Spectroscopy) shows that the material is composed of 98% of calcium carbonate and contains traces of aluminium, iron and silica due to a small amount of accessory minerals (Table 8). Magnesium is also present, with 0.28 wt% of MgO. The Mg/Ca and Sr/Ca ratio is equal to 5×10^{-3} and the ratio Sr/Ca is equal to 3.3×10^{-4}. The Lavoux limestone can thus be considered as a quasi mono-mineral limestone mainly composed of calcite.

Major elements	SiO_2	Al_2O_3	Fe_2O_3	MnO	MgO	CaO	Na_2O	K_2O	TiO_2	P_2O_5
weight (%)	0.06	0.03	0.11	0.01	0.28	56.25	<LD	<LD	<LD	<LD

Trace elements	Sr	Zn
ppm	133.9	14.9

Table 8: Chemical composition of the Lavoux limestone (ICP-ES).

II. MINERAL REACTIVITY OF THE LIMESTONE ROCK SAMPLES FOLLOWING THE INJECTION OF CO_2-RICH SOLUTIONS: RESULTS AND OBSERVATIONS

II.1. Results of in-situ data acquisition.

This paragraph presents the evolution of the various parameters recorded during the experiments conducted. It provides, on the one hand, a control of the conditions imposed on the system and, on the other hand, a detailed overview of the behavior of the system during the different injection durations.

II.1.1. Pressure/Temperature and mass flow recording

Recording of CO_2 pressure-temperature parameters used for the preparation of the reactive solution in the 5 liters mixing autoclave are presented in figure 64. The evolution of the pressures-temperatures-ΔP (between injection and confining) and flowrate data recorded in the MIRAGES-2 autoclave during the experiment are detailed in figures 65 for the for the 21d CO_2/water injection experiment. The different curves representing the evolution of the parameters with time for the others experiments are displayed in the appendix E. The pressure-temperature data monitoring in the mixing autoclave are exposed exclusively for the 2.5d, 10d and 21d long term experiments with and without saline solution.

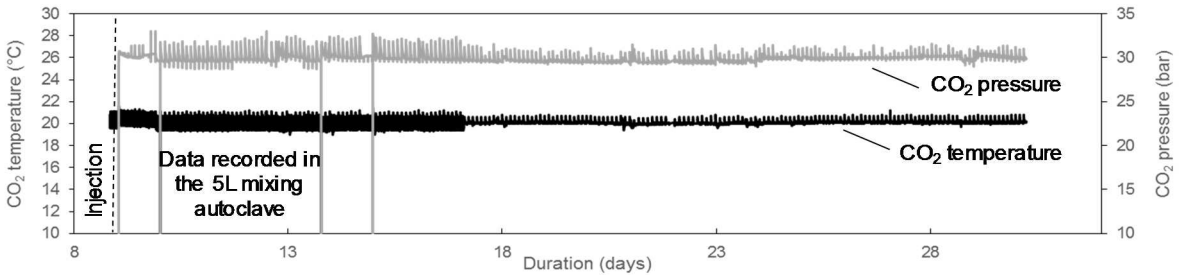

Figure 64: Evolution of temperature and CO_2 pressure in the mixing autoclave (5 Liters) for the 21d experiment without salt.

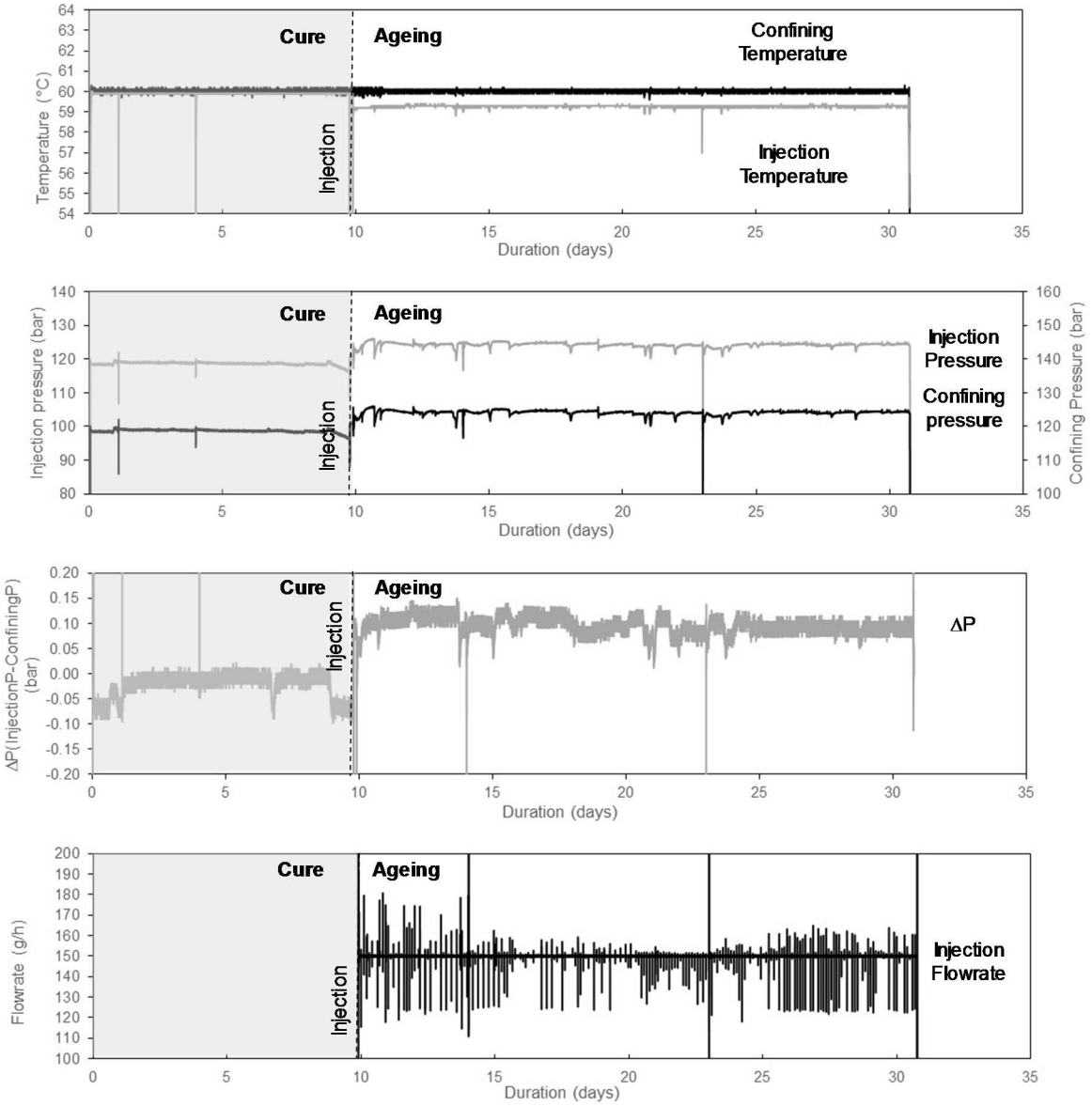

Figure 65: Evolution of pressures (confining and injection), temperatures (confining and injection), ΔP (between injection and confining) and injection flowrate in the MIRAGES-2 autoclave during the 21d experiment without salt.

The cure lasted between 9.1 and 10.7 days and 2 to 74 liters of solution were injected in the core-plugs during the ageing period depending on the experimental duration. A summary of the average experimental data recorded during the different experiments are displayed in appendix F.

The average recorded data of CO_2 pressure and temperature in the 5 liters mixing autoclave are consistent with the expected operating conditions (T = 20°C and $P_{(CO_2)}$ ~ 30 bar) during all the injection period. Slight and regular increases in pressure and temperature are generated during the filling stage of the autoclave by the hydrodynamic pump (Fig. 64). The equilibrium is quickly re-established by the temperature control system of the autoclave and the discharge of the over-pressure by the back-pressure regulator.

During the **"cure"** period, the pressure and temperature applied on the sample in the MIRAGES-2 autoclaves remained stable with a temperature of 60°C and a pressure close to 119 bar (Fig. 65). Significant variations of pressure and temperature (injection) are observed sporadically due to the sampling of solution for chemistry analysis. Brief decrease in pressure was observed (~10 bar) during the **"cure"** period of some experiments but this pressure drops have no consequence on the core-plug.

During the **"ageing"**, the confining temperature remained stable at 60°C while the temperature at the injection point was 59.8°C. This value exactly corresponds to the temperature calculated with the thermal modelling in appendix B. It confirms that the injection of the solution at 20°C doesn't generate any temperature gradient in the near-well region. Similarly, the pressure of confinement remained very stable with values ranging between 118.5 and 122.2 bar as a function of the experiment. The pressure gradient between the inlet and the outlet of the core-plug slowly increased during the first few days of injection before reaching a steady state with a value close to 0.8 bar for the short term experiments (12h and 24h) and an average value close to 0.05 bar during the other experiments (2.5, 10 and 21 d). It has to be noticed that these last values are equals or closed to the accuracy of the differential pressure measuring transducer. The difference of the two orders of magnitude measured is mainly due to the location of the two connections of the measuring device in the system which have been modified for optimization. These findings reveal the difficulty to establish, at the core scale in the configuration of the experiment, a relationship between the evolution of the ΔP value and that of the petrophysical properties of the rock, mainly the permeability. This aspect will be not investigate.

The flowrate injection was stable at 150 $g.h^{-1}$ for all the experiments. The very punctual variation observed are due to the steps of pump filling or to the action of the back pressure regulator implying variations of the pressure in the system. For the 20d blank experiment with pure water, the injection was stopped during 10 hours after 19.6 days. This artefact led to pressure drop and to a rise of temperature. The confinement temperature finally reached the confinement temperature very quickly. It was due to a technical problem with the injection pump.

II.1.2. pH measurement

Measurements were performed at the outlet of the 2 parts of the system to give information about the pH values of the injected reactive fluid and the core-plug aqueous environment. The evolution of the pH of the solutions with time is presented in figure66.

Injected solution: The pH measured in the injected solution remains constant during all the experiments. The average value is of 3.6±0.2 with 30 bar of CO_2 dissolved in pure water equilibrated with 15 $mg.kg^{-1}$ of $CaCO_3$. For experiment with saline solution, the average value is 0.2 pH unit lower than for experiment without salt.

Cure period: The measurements indicate that the pH increased abruptly to values between 9.2 and 10.1 for the experiment without salt. The pH reaches a higher value of 2.5 pH unit when saline solution enriched with CO_2 is injected.

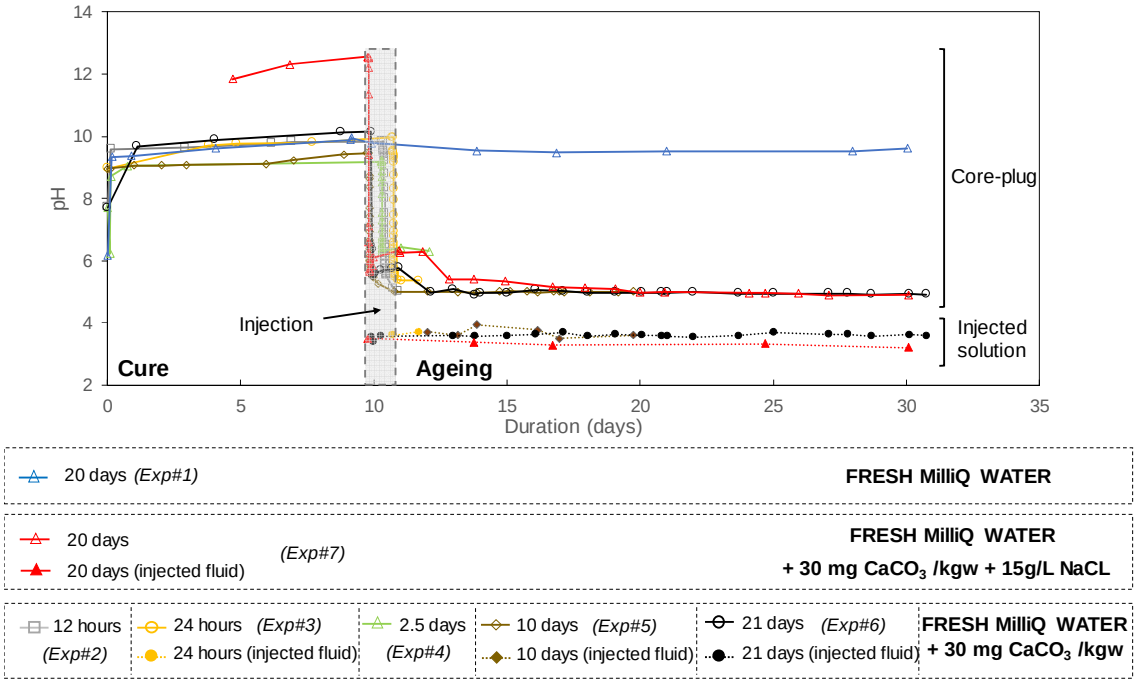

Figure 66: pH measurements of the injected solution and of the solution at the outlet of the core-plug during the different experiments.

Ageing period: For the blank experiment, a slight decrease of the pH occurs during the first 8 days of the injection of fresh pure water in the core-plug with a value dropped from 9.8 to 9.4. The pH then remained relatively constant until the end of the experiment.

For the experiments with CO_2, as soon as the CO_2 rich acidified solutions is injected, the pH dropped to a first step of 6.0 - 6.2 for all experiment during the first 1 to 3 hours of injection. Then a sill lasting 1 or 2 days is followed by a new acidification with values reaching 5.0 to 5.4 depending of the experiments. Over longer period of time (10 and 21 d), the pH was close to 5 until the 12 days of injection. A slight decrease in the pH value and a dynamic equilibrium until 4.9 - 5 is the observed for the 17 last days of injection.

II.1.3. Carbonate speciation

The acquisition of 700 and 2034 Raman spectrum was performed and processed for the in-situ chemical analysis of the injected solution and the experimental solution respectively for the long-term experiments with and without salt (20d of injection).

For the experiment without salt, the values of total carbon concentrations in solution measured at the inlet and outlet of the core-plug as well as the distribution of carbonate species are visible in table 9. Figure 67 displays the evolution of the total carbon concentration with time.

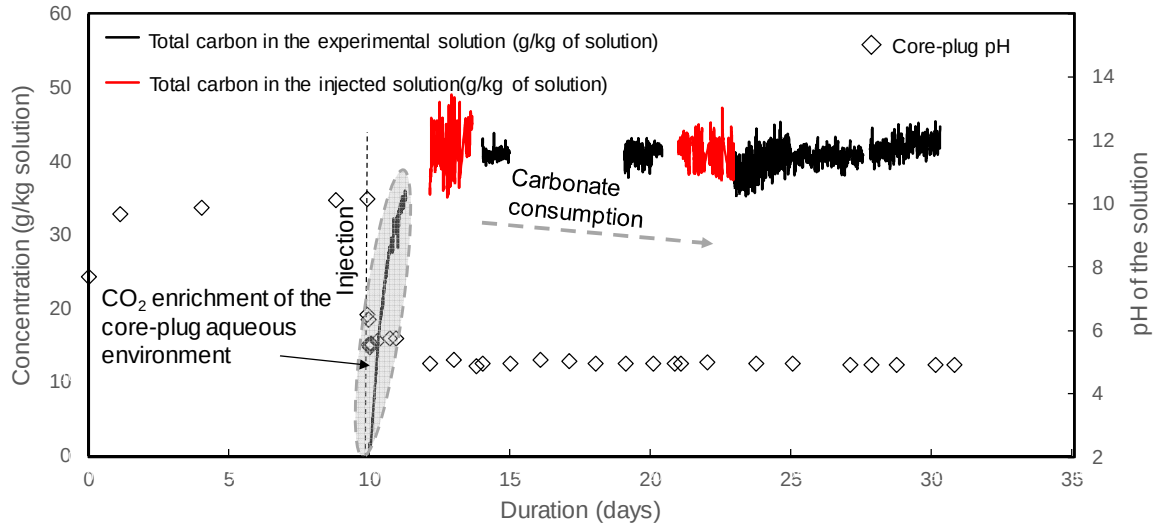

Figure 67: 21d experiment of injection of CO_2 laden equilibrated solution without salt: Evolution of the pH values and total inorganic carbon concentrations at the inlet and outlet of the core-plug with time (in kg per kg of solution).

The average amount of aqueous CO_2 in the experimental solution sampled at the outlet of the core-plug reaches a sill after 2 days of injection (38.07 $g.kg^{-1}$ of solution *i.e.* 0.93 $mol.kg^{-1}$) (Table 9). The total carbon concentration in solution is roughly the same in the inlet and outlet of the core-plug during the 3 following days of injection (Table 9). The total carbon concentration in the experimental solution tends to decrease during the following 10 days and remains slightly below the concentration in the injected solution. The values of the last 6 days show carbon concentrations closed to that of the injected solution.

No CO_2 degassing was reported during our experiments.

	2-5 days of injection	9-11days of injection	12-14 days of injection	15-20 days of injection
aqueous CO_2 (g/kg solution) *injected solution*	39.78	39.78	39.90	39.90
aqueous CO_2 (g/kg solution) *experimental solution*	38.07	37.94	35.96	38.23
HCO_3^- (g/kg of solution) *experimental solution*	1.724	1.72	1.591	1.69
Total carbon (g/kg of solution) *injected solution*	**39.81**	**39.81**	**39.93**	**39.93**
Total carbon (g/kg of solution) experimental *solution*	**39.79**	39.66	**37.55**	**39.92**

Table 9: Concentration of the total inorganic carbon in the injected and experimental solutions at different period of the "ageing" of the 21d injection experiment without salt. Distribution of carbonated species $CO_{2(aq)}$ and HCO_3^- in the experimental solution.

For experiment with salt, 300 and 2600 Raman spectrum was processed. The results are presented figure 68 and table 10.

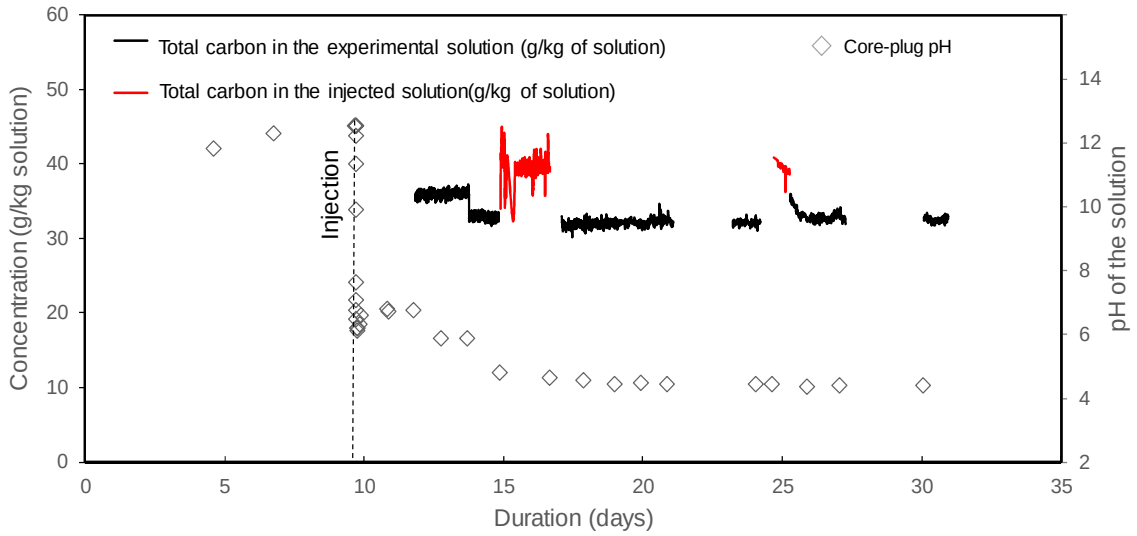

Figure 68: 20d experiment injection of CO_2 laden equilibrated solution with salt: Evolution of the pH values and total inorganic carbon concentrations at the inlet and outlet of the core-plug with time.

	1-5 days of injection	7-15days of injection	15-20 days of injection
aqueous CO_2 (g/kg solution) *injected solution*	39.26	39.26	39.38
aqueous CO_2 (g/kg solution) *experimental solution*	31.82	31.55	32.27
HCO_3^- (g/kg of solution) *experimental solution*	2.809	0.45	0.417
Total carbon (g/kg of solution) *injected solution*	**39.29**	**39.29**	**39.41**
Total carbon (g/kg of solution) experimental *solution*	**35.02**	**32.01**	**32.69**

Table 10: Concentration of the total inorganic carbon in the injected and experimental solutions at different period of the "ageing" of the 21d injection experiment without salt. Distribution of carbonated species $CO_{2(aq)}$ and HCO_3^- *in the experimental solution.*

The total carbon concentration in the experimental solution with salt reaches a first still of concentration of 35.02 $g.kg^{-1}$ of solution (0.8 $mol.kg^{-1}$) due to the first step of pH value of 6. Once the pH decrease, the total carbon concentration also decrease until a value close to 32 $g.kg^{-1}$ of solution (0.74 $mol.kg^{-1}$) which is constant until the end of injection. The recorded concentrations of carbonate species in the experimental solution are lower than the quantity in the injected solution throughout the experience.

II.2. Chemical analysis of the aqueous solution.

Regular sampling of the aqueous solution was performed at the outlet of the core-plug (experimental solution) during the cure and ageing periods of the experiments with an occurrence of 1 to 7 days. As a consequence, 1 to 4 sampling were done during the cure and 1 to 11 during the ageing depending on the experiments. A first sampling of the injected solution was also done at the beginning of each experiments.

The analytical results of the experimental solutions are summarized in appendix G, H and I. The values are plotted as a function of time for each element (sulfates ions, calcium, magnesium, strontium, aluminum, and iron) (Fig. 69). It should be noticed that for the blank experiment, strontium and aluminium was not measured.

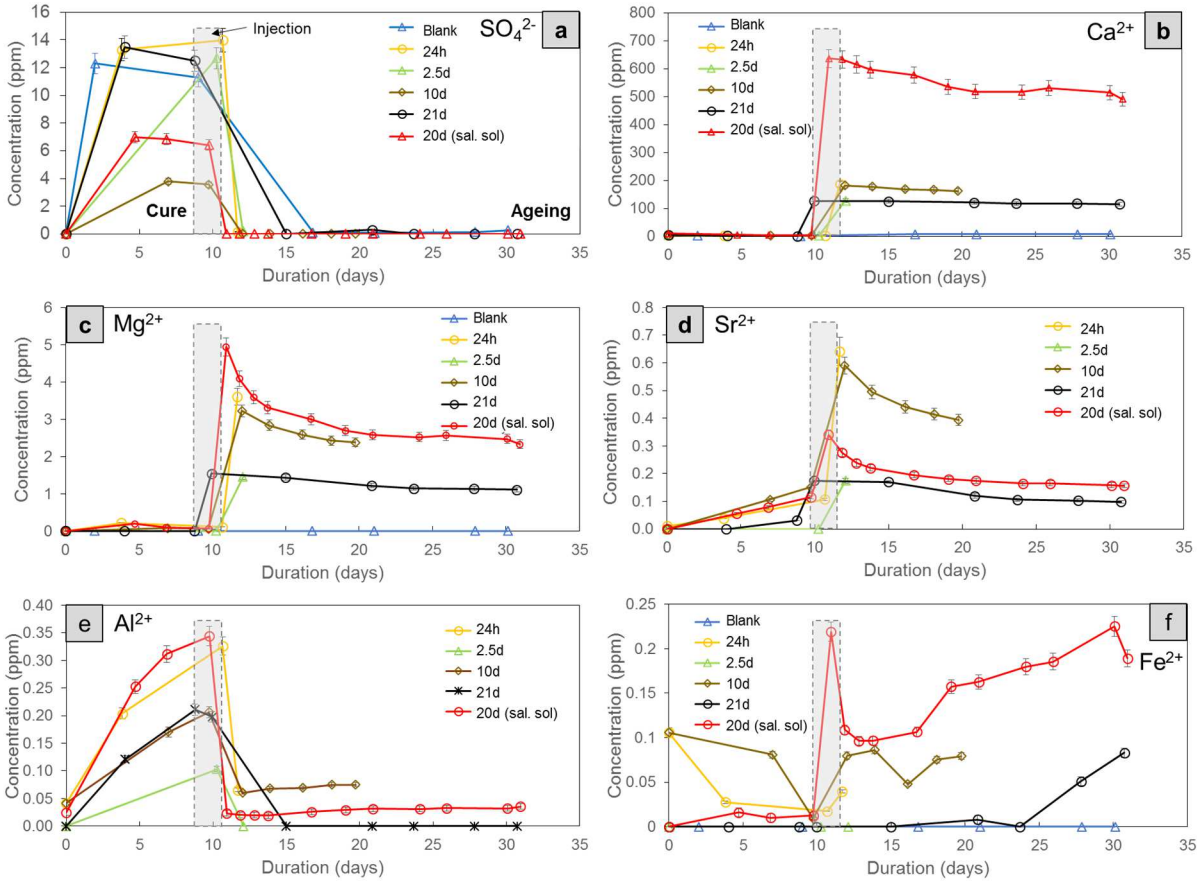

Figure 69: Chemical analysis (ICP-AES) of the samples collected during the different experiments. The concentrations of (a) sulfates ions, (b) calcium, (c) magnesium, (d) strontium, (e) aluminum and (f) iron were measured at the outlet of the core-plug are plotted as a function of the duration of experiment. (Sal.sol corresponds to saline solution).

- **Anions:** There was no sulfate in the initial solution. Once the solutions were in contact with the core-sample, the SO_4^{2-} concentrations increased during the "cure" period. The evolution of the sulfates concentrations in solution follows the same trend for experiments with and without salt. The sulfates reached a concentration between 3.6 and 14 mg/kg of solution depending on the experiment.

After injection, the SO_4^{2-} concentration decreases abruptly reaching a near-zero values induced by dilution in the renewed solution.

- **Cations:** Significant changes in the chemistry of experimental solutions are observed during experiments.

A first remark can be mentioned regarding the concentration of **calcium** in the initial solution. The measured concentration (≈ 5 $mg.kg^{-1}$ for the experiment without salt and ≈ 10 $mg.kg^{-1}$ for the experiment with NaCl) corresponds to the expected value. These analyses demonstrate that the calcium carbonate used to create the injected solution was entirely dissolved during the protocol of preparation. The **calcium** concentration slightly decreased during the cure for all the experiments. It can be related to the basification of the solution.

For the blank experiment, only **Ca** concentration increases in the experimental solution reaching a relatively constant value closed to 7.9 $mg.kg^{-1}$ after 8 days of injection and until the end of experiment.

For the experiment with CO_2-rich solution, once the injection started, the results show a significant increase of the **Ca** concentrations together with **Mg** and **Sr**. These alkaline-earth elements have similar behaviors for all the experiments. The maximum concentration is reached very quickly after 1 day of injection. The amount of calcium is 5 times higher when a saline solution flows through the rock. These peaks in calcium concentrations are immediately followed by a gradual and smooth decrease until a 9 to 10% reduction for the long –term experiment without salt. This coefficient of variation of Ca is two times higher (21%) for the experiments with saline solution. The ensuing decrease is also more significant for Mg and Sr cations with a variation close to 50% for all the experiment.

The Mg/Ca and Sr/Ca ratios are plotted as a function of time for the long-term experiment without (10d and 21d) and with (20d) salt in the reactive solution (Fig. 70). The two ratios increase during the cure and tend to decrease after injection. The fractionation of the element is always higher in the experimental solution than in the initial fresh rock.

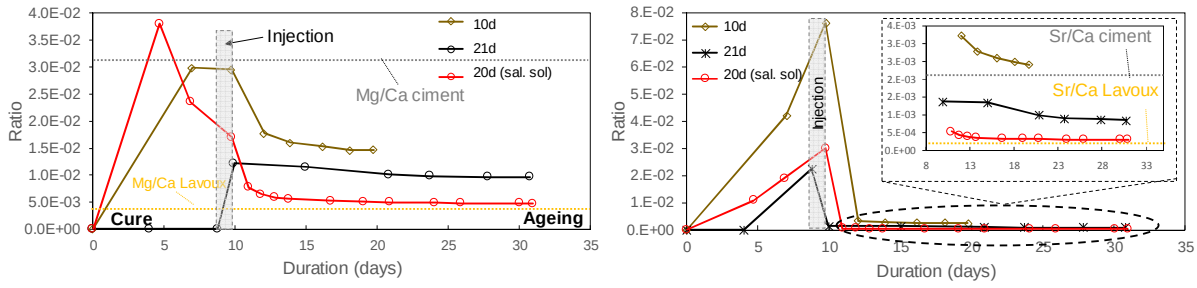

Figure 70: Evolution of the Mg/Ca and Sr/Ca ratios as a function of time for the long-term experiment without (10d and 21d) and with (20d) salt in the reactive solution. The data are compared with the initial element ratio in the cement and the fresh rock.

The **Al** content increases during the cure period in each experiment reaching a value between 0.1 and 0.35 $mg.kg^{-1}$. It becomes very low or undetectable after the injection of the different solutions.

Iron shows different behaviors between the experiments. The **Fe** content is close to zero at the end of the cure. After injection of pure water, no iron is found in the solution until the end of the experiment. When a solution enriched in CO_2 is injected, traces of **Fe** are detected after only 1 days (between 0.1 and 0.22 $mg.kg^{-1}$). A continuous increase of Fe concentrations is observed after the injection of saline solution.

II.3. Sample alteration: Structural characterization

II.3.1. Macroscopic observation (post-experimental core-plug external observation and CT-scan images analysis)

Figure 71 shows the several core-plugs observed after experiment at the macroscopic scale.

For the blank experiment, nor visible changes neither apparent trace of dissolution are visible on the surface of the sample.

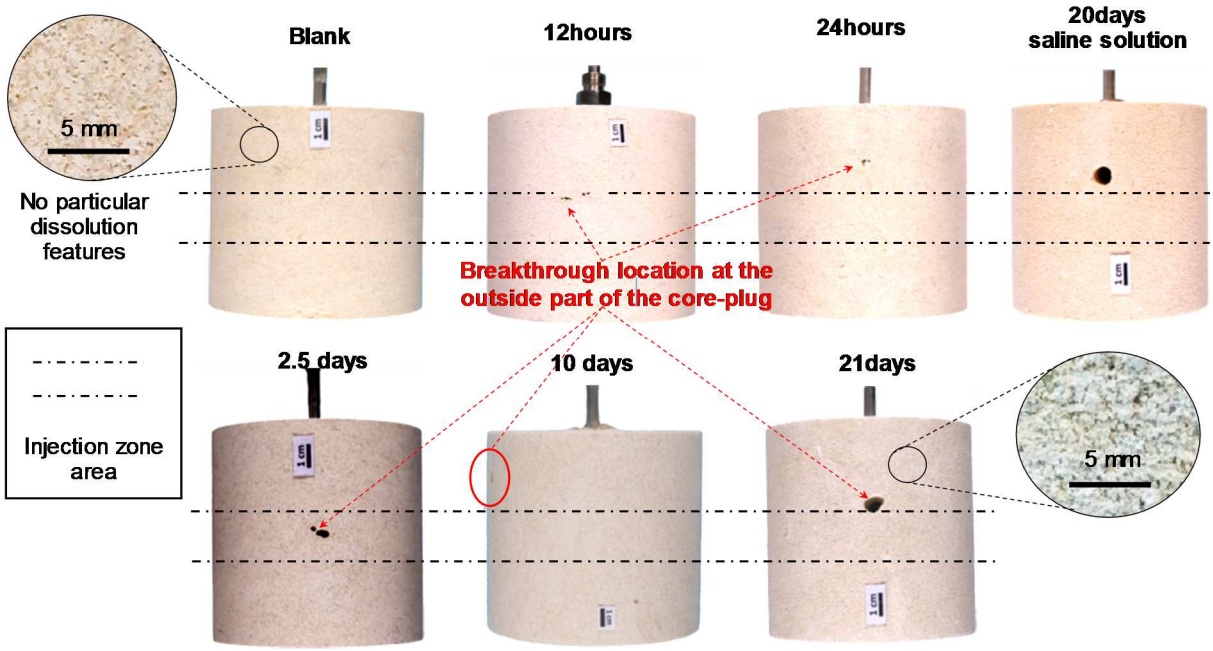

Figure 71: View of the samples after experiment and after drying for 24h at room temperature. For the blank and 21d experiment without salt, focus are carried out in order to check the external surface state of the core-plug.

The examination on the other block samples revealed that, in all experiments with CO_2-rich solution, the core-plugs show millimetric to centimetric holes visible on the surface of the plug. These holes appeared after only 12 hours of injection at the level of the injection surface or slightly above (Fig. 71). Their diameters increase with the duration

of injection. The surface state of the core-plugs is also marked by a visible increase of its roughness which seems to correspond to an inter-oolitic dissolution features from 10 days onwards.

The core-plugs are cut in two identical parts by following the core diameter in order to carry out petrographic and chemical analyses from thin sections or small rock samples. Figure 72 shows the cross sections of the core-sample with the different materials (rock, cement, injection tube) for the blank, the 2.5d and 20d experiment without salt and 21d experiment with salt.

The core plugs show holes visible on the wall of the well (Fig. 72b) corresponding to the origin of the dissolution pattern. A preferential cylindrical channel of dissolution with a large diameter extends from the wall of the well to the outer surface of the core-plug of the 20d experiment with salt (Fig. 72a). The dissolution of the well (Fig 72b) with an enlargement of its upper part is clearly evident for experiments lasting several days with and without salt.

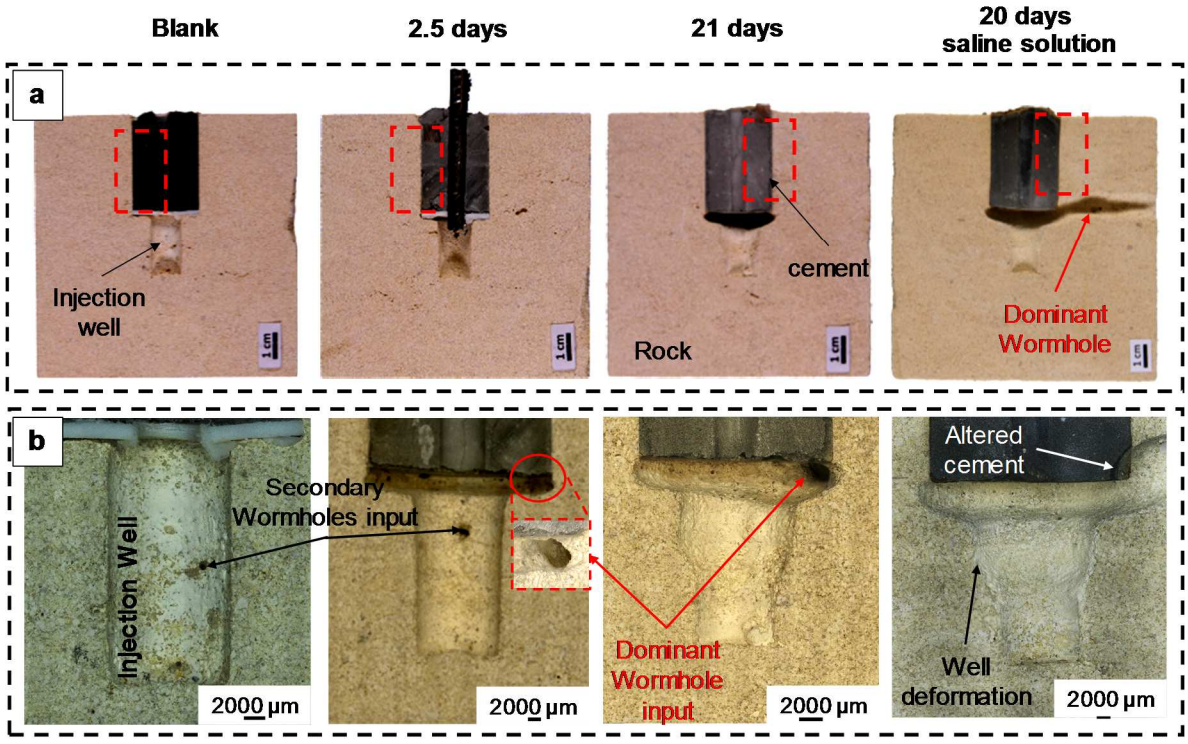

Figure 72: a) Cross section of the core-sample showing the different materials (rock, cement) for the blank, 2.5d and 20d experiment without salt and 21d experiment with salt. The red dotted lines correspond to the area selected for microscopic observations of the cement/rock interface. b) Overview of the injection well of the core plug after experiments with the zone of appearance of the wormholes.

The structural investigation performed with X-Ray micro- tomography was performed by using the Image processing protocol explained in paragraph VII.2.3.2. This technic allows an internal visualization of the macro-porosity network due to the fluid flow impact on the rock fabric.

The 3D tomography images of the dissolution arrays architecture and their connection integrity after experiments are presented in figure 73.

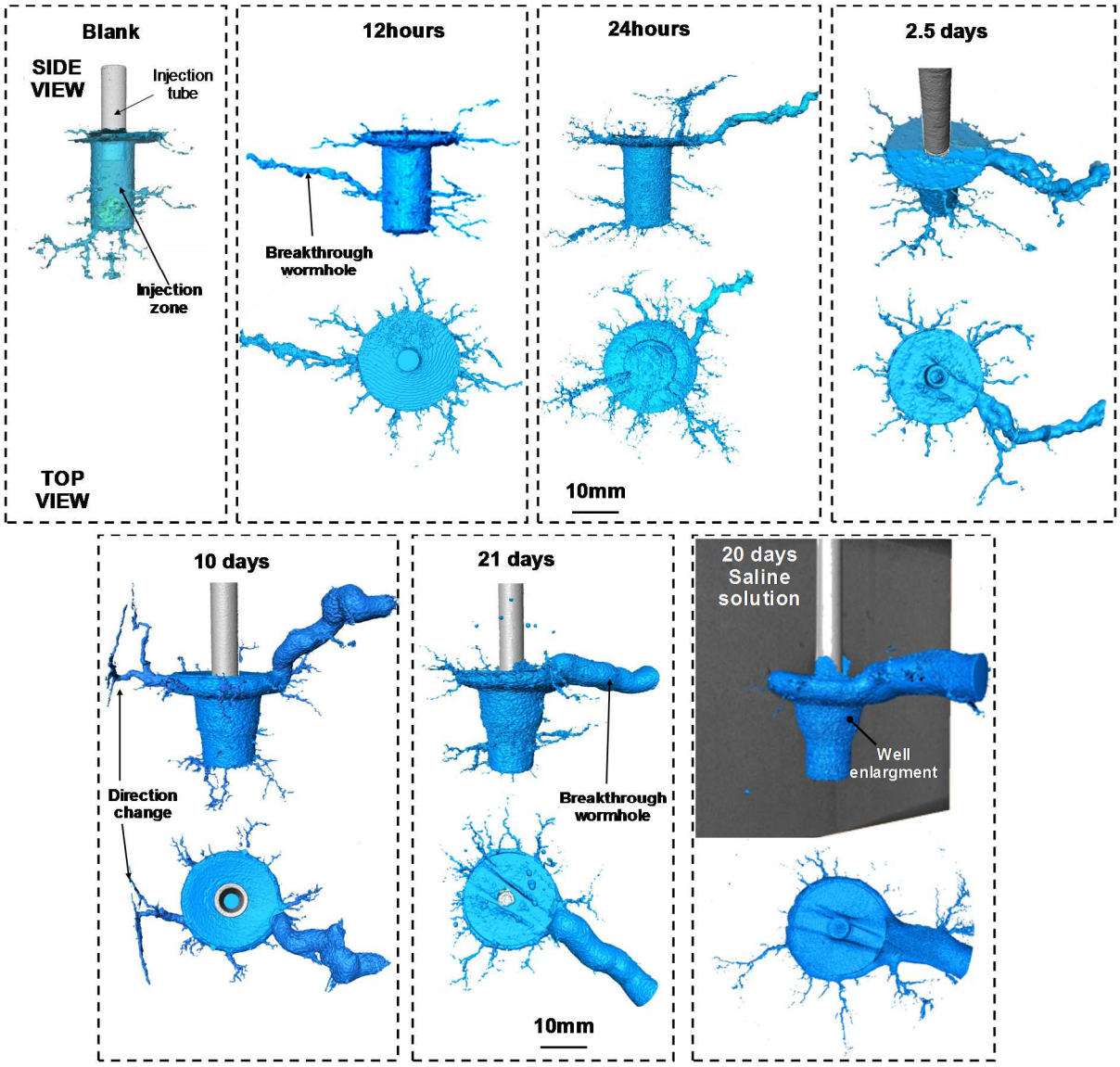

Figure 73: 3D display of dissolution patterns from X-ray tomography. (Side and top views). Experiments: blank, from 12h to 21 d without salt and 20 d with salt. The blue color corresponds to the void areas in the core with a resolution of 60 µm.

For all the experiments, the investigation of the hollow space shows the alteration of the carbonated rock matrix. A radial dissolution front develops from the injection wellbore to the whole rock volume.

For the blank experiment, a ramified and complex predominant channels of dissolution – called wormhole – forms mainly at the base of the injection surface.

For the flow-through radial experiments of CO_2 laden solutions, the injection also generated these wormholes from the injection zone (Fig. 73). These preferential pathways are created at different vertical locations over the entire height of the open hole. After only 12 hours, a single dominant wormhole breaks through the rock sample.

These main wormholes are emerging from different part of the well depending on the experiments but they appeared mainly at the upper part where a mechanical fragility should have been generated during the building of the core-plug (Fig.72b). The spatial morphologies of these highly conductive channel looks comparable except for the 10d experiment where the rock sample was drilled at 55° with respect to the bedding. From 10 days of injection, the experimental wellbore with initial cylindrical shape becomes conical with a continuous enlargement of its upper part.

In order to examine the several wormholes in a more detailed way, a projection of the least dense elements (the void) was then performed on the acquired images by combining all the reconstructed CT-slice on a given thickness. This step was executed with the VG STUDIO software by using the Ticklab option. XY Top view an XZ side view of all the generated wormhole can thus be visualized respectively on the same image. Figure 74 shows the two different views for all the experiment with dissolved CO_2. The location of the XZ Top view images have been processed are visible on XZ side view (Fig. 74 “purple lines”). It should be noticed that the samples are oriented according to their location in the autoclave at the end of the experiment (referred to the fluid inlet and outlet on the images).

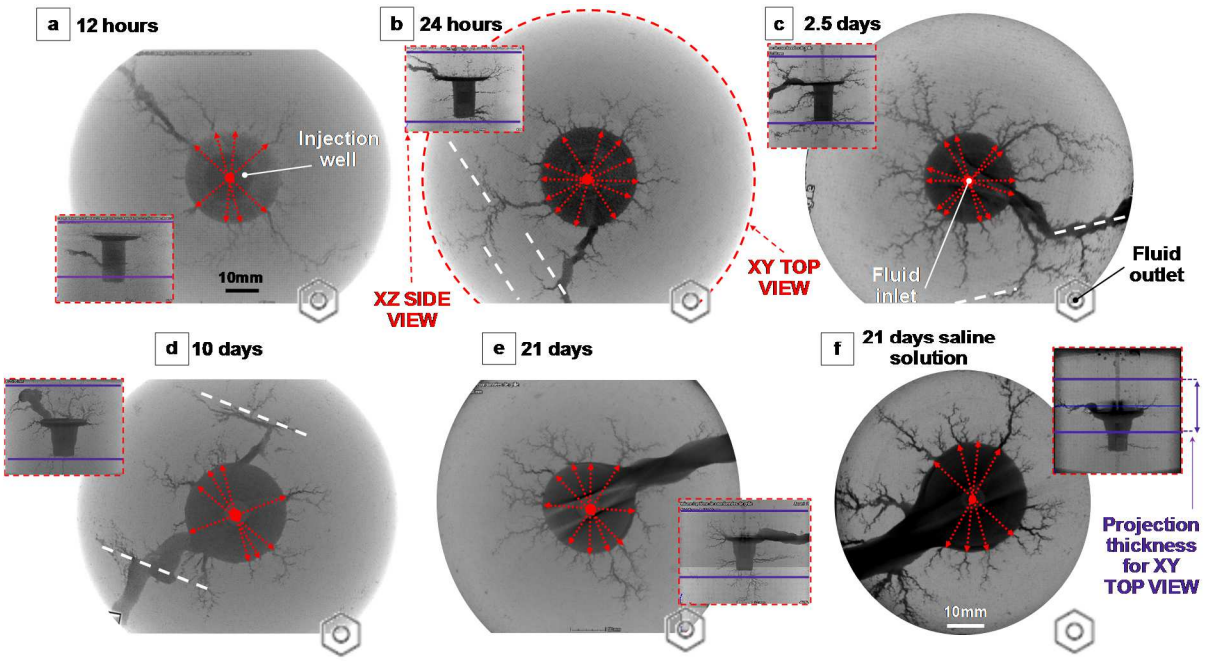

Figure 74: XZ side view (Square images surrounded by red dotted lines) and XY TOP View (Circular images surrounded by red dotted lines) projection of all wormholes by superimposition of CT-scans on a thickness defined on the XZ view (purples lines). a) 12 h, b) 24 h, c) 2.5 d, d) 10 d, e) 21 d experiment without salt and f) 20 d experiment with salt. The red dotted arrows located in the injection well highlight the axisymmetry of the wormholes' origin sites. The white dotted lines in b), c) and d) underline a drastic change of the initial direction of predominant wormholes. The presence of the nut corresponding to the fluid outlet gives information on the orientation of the core at the end of the experiment.

Images processing reveals that the generated wormholes are thin with few tortuous secondary ramifications.

For all the experiment, the main wormhole are generated randomly from various directions and not systematically in the direction of the fluid discharge (fluid outlet).

Despite a basic isotropic injection process from the bottom hole, a prominent anisotropy of the multilevel dissolution pathways is observed. For the 10d experiment, a similar drastic change in the initial direction of the two mains wormholes is observed (Fig.74 d white dotted line and Fig. 73).

A brief investigation was also carried out at the interface between cements and rock. The half core-plugs were cut in 30 X 20 mm samples (see Fig. 72, for their location) in these specific areas to make polished cross sections for microscopic observations (Fig. 75a). A detailed observation was obtained thanks to SEM analysis (Fig. 75b) in back scattering electron mode. The results reveal a good mechanical cohesion and the absence of fractures or cracks between the cement and the limestone for all the experiments. Nevertheless, a reactive zone parallel to the interface develops from the interface into the cement zone.

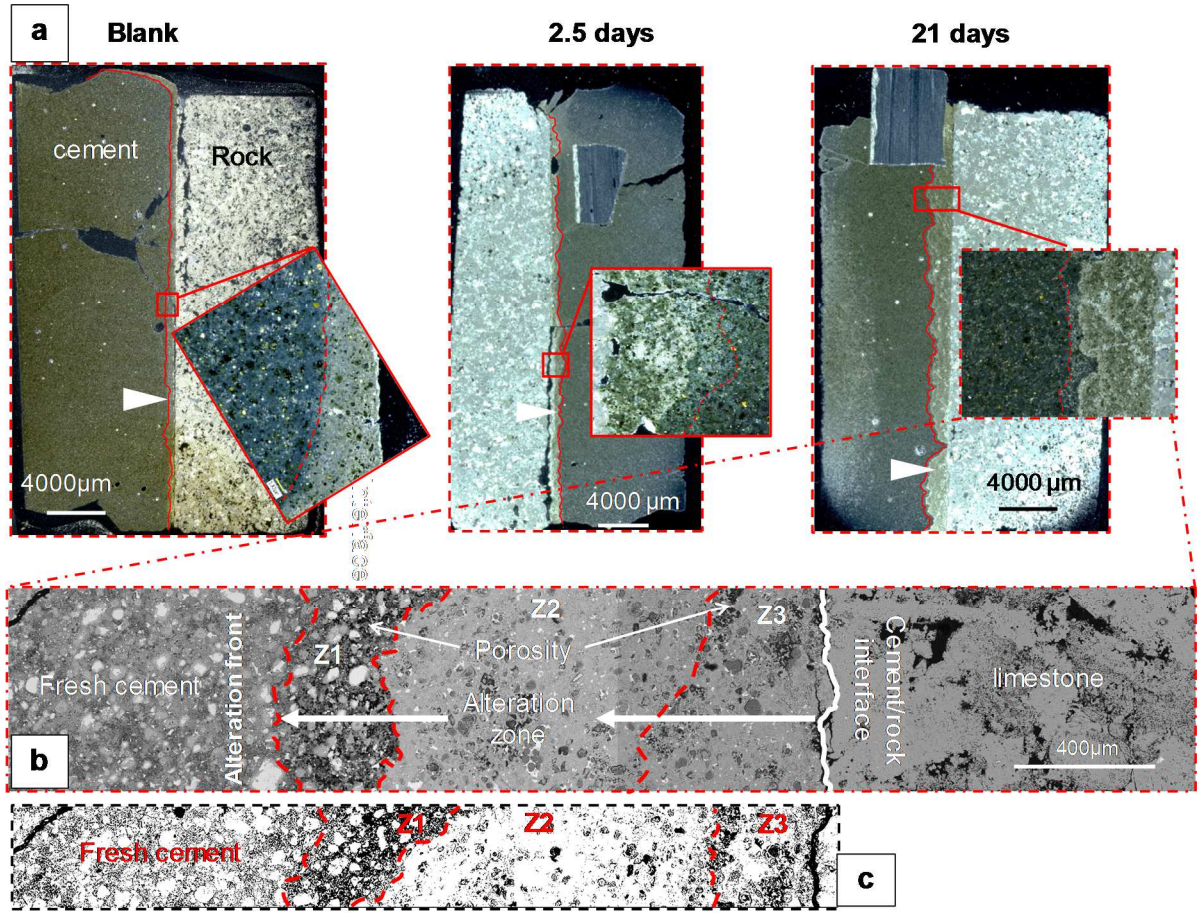

Figure 75: a) Detail of the thin section of the rock-cement interface with altered zone of the cement (with arrows) delimited by the red line. The red square corresponds to a focus on the transition between reacted (whitish and brown color) and unreacted cement (dark color) delimited by a red dotted line. b) SEM (BSE) picture showing the cement alteration divided in three zones for the 21d experiment without salt. c) Binarization of the SEM image (ImagJ software).

For the blank experiment, the cement at the interface turns light grey after injection of pure water at equilibrium with atmospheric CO_2 (Fig. 75a). For 10d and 21d experiment without salt, we can identify different distinct layers in the altered zone.

The cement adjacent to the limestone has turned orange-brown and the cement closed to the unaltered cement has changed to light grey (Fig. 75a).

The SEM observations underline the subdivision of the reaction zone in 3 zones (Fig. 75b). A first zone (Z1), with a higher porosity, where the CSH matrix is dissolved, can be identified. In the two other zones (Z2 and Z3), a dense matrix is detected. The area close to the interface with the rock (Z3) appears more porous than the intermediate zone (Z2). The binarization of the SEM images performed with the ImageJ software highlights this density variation between the different zones (Fig. 75c).

The same images analyzes was performed at the cement-rock interface on the post-experimental sample of the 20d experiment with saline solution (Fig. 76). The mechanical cohesion of the interface is also preserved. Moreover, the alteration zone appears less prominent with only 2 reactive zones underlined (Z1 and Z2).

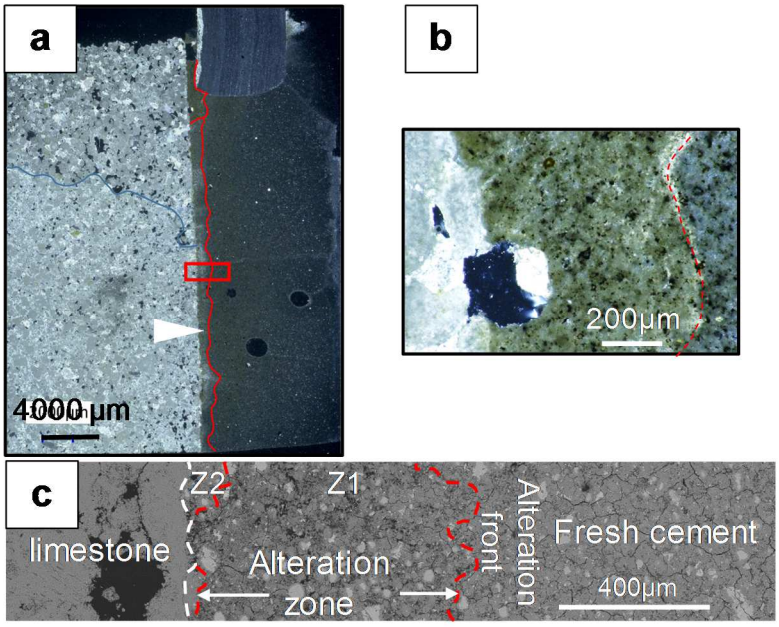

Figure 76: 20d experiment with salt a) Detail of the thin section of the rock-cement interface with altered zone of the cement (with arrows) delimited by the red line. The red square corresponds to a focus on b) the transition between reacted (orange-brown color) and unreacted cement (dark color) delimited by a red dotted line. b) SEM (BSE) picture showing the cement alteration divided in 2 zones.

A discussion on the cement degradation with additional analysis (Raman mapping for chemical analysis) is available in the paper by Randi et al. (2017) “Experimental and numerical simulation of the injection of a CO_2 saturated solution in a carbonate reservoir: application to the CO2-DISSOLVED concept combining CO_2 geological storage and geothermal heat recovery” published for the 13th International Conference on Greenhouse Gas Control Technologies (GHGT-13) in Lausanne, Switzerland (Appendix J).

II.3.1. Petrophysical parameters

For each experiment, Purcell tests (porosity) and the standard method of nitrogen (permeability) was performed on 5 cylinders of rock of 20mm diameter X 20 mm height size sampled at different locations of the core-plug especially at the vicinity of the edge, far from the wormholes network (Fig. 45). No evidence of the existence of high permeability zones representative of high conductive dissolution pathways was emphasized in the small rock sample. This remarks indicates a structural homogeneity of the investigated samples and the reliability of the estimated mean values.

The analysis of the average porous spectrum displays a modification of the pore entry diameters distribution from 24 hours of injection (Fig. 77).

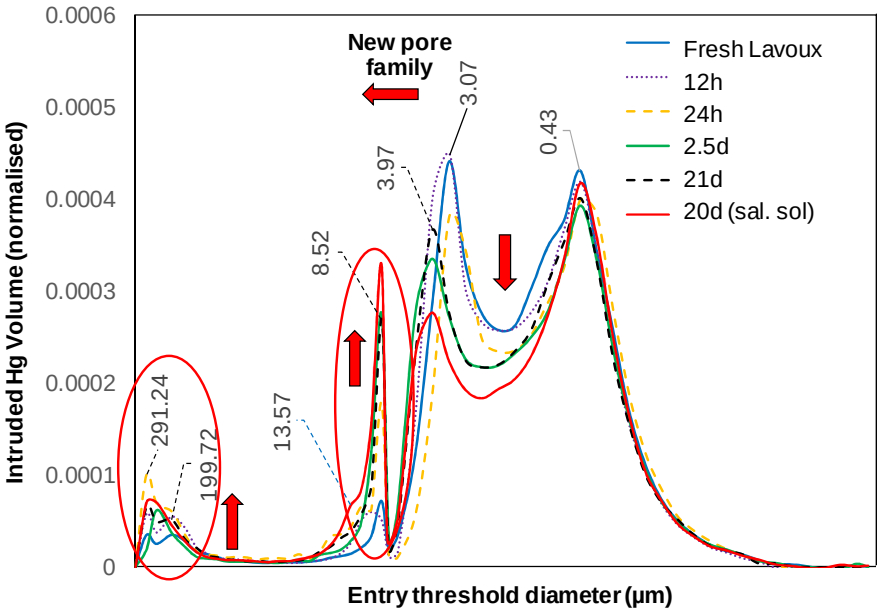

Figure 77: Evolution of the average pore size distribution with time from the sample drilled at different location in the post-experimental core-plug.

The initial bi-modal distribution of the porous network becomes tri-modal with the appearance of a new pore throat family. The pore size family between 7 and 20 µm initially limited increase significantly at the expanse of the native mesoporous family (1.46 - 5.1µm). An increase of the numbers of macropores (100 to 300µm) is also detected. These observations is an indicator of a dissolution exclusively occurring in the biggest pore throat. Indeed, the intra-ooids pore (0.43µm) are poorly affected. These changes appear over the first 2-3 days of injection and tend to stabilize in the following days. However, despite the appearance of a new pore-throat family, the petrophysical properties of the studied areas are not impacted. The average values of porosity and permeability determined for the aged sample range respectively between 23 and 26.5% and between 45 and 120 mD while the fresh rock was initially defined by a porosity of 24.49% and a permeability of 46.47 mD.

II.3.2. Microscopic observation (SEM)

SEM observations are performed on different fresh fractured rock cautiously sampled at different parts of the core plug (without mechanically altering the zone of interest) in order to describe the petrographical evolution of the limestone before and after experiment.

The first series of observation focuses on the injection wall of the well. SEM image (Secondary electron mode) of a natural sample (Fig. 78a) shows the initial texture of the Lavoux limestone (also Fig. 59) which allows a comparison with the post-experimental samples.

After injection of pure water, the SEM images reveal the starting point of small wormholes on the wall of the injection well (Fig. 78b). These “small size” holes have a diameter of about 10 to 20 µm.

The flow of CO_2-charged water in the limestone also induced disseminated holes in the micritic matrix from 5 to 15 µm diameter (Fig 78b, c, d, white arrows). Similarly, the inter-crystalline porosity tends to increase with a dissolution of the micrites composing the oolites.

Specific scaled-down SEM observations exhibit the evolution of the dissolution textures of calcite minerals. The injection of under-saturated distillated water induces changes in the shape and contact of the micrite crystals on the walls of the injection wellbore.

The micrites are partially dissolved and, following the classification of micrite microtexture proposed by Deville de Periere et al. (2011) (Fig. 60) [183], become mainly rounded with punctic to partially coalescent contacts (Fig. 79b) compared to an initial subrounded to microrhombic crystal morphology (Fig. 79a).

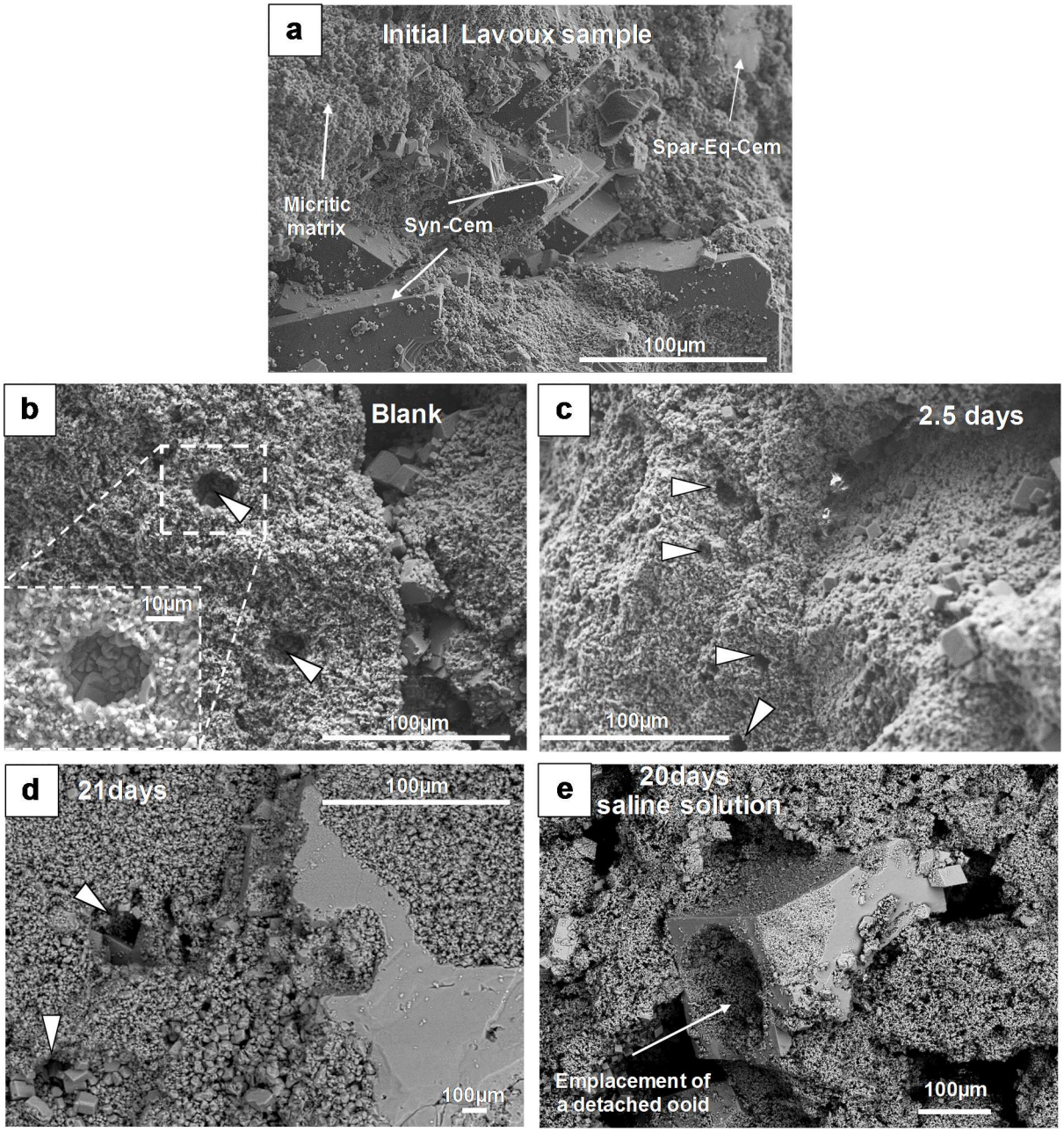

Figure 78: SEM images (in SE Secondary Electrons mode) of the surface state of fresh fractured rock of (a) the initial microstructure of the Lavoux limestone composed of oolitic grains, microporous micritic matrix, sparitic rhombohedral calcite (Spar-Eq-Cem) and syntaxial cement (Syn-Cem). SEM images of the wall of the well from (b) the blank (c) 2.5, (d) 21d experiment without salt and (e) 20d experiment with salt. Holes of dissolution appear in the micritic matrix (white arrows) for all experiments. This new intra-oolitic porosity is from 5 to 20 µm in diameter.

After 21 days of percolation of the CO_2 acidified solution with and without salt, the dissolution process affects the microporous micritic matrix of the carbonate sample in a more significant way. Micrites are subrounded with highly altered surfaces which are linked together with bridges (Fig 79.c and d). The density appears to be less important than for the fresh sample with an increased intercrystalline porosity. This porosity appears more important when a saline solution is injected.

These microscopic modifications significantly alter the arrangement of pores and their interconnectivity at the injection point.

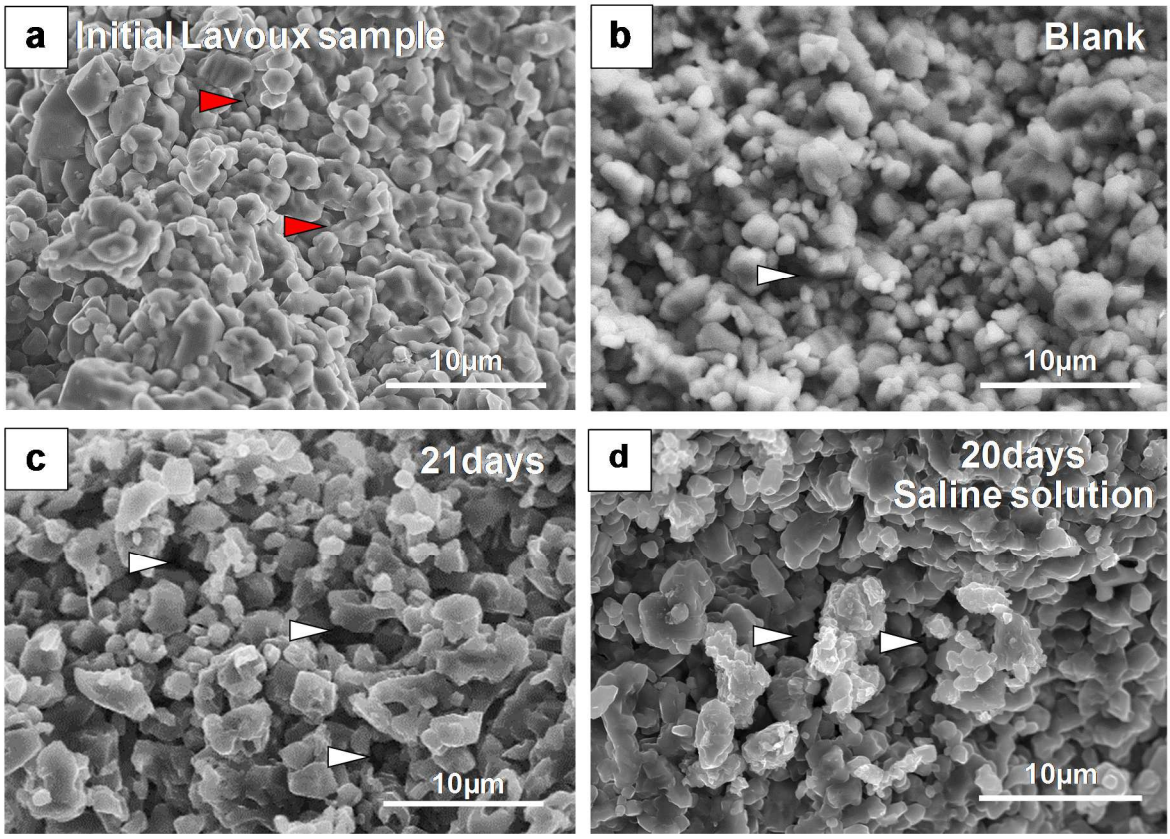

Figure 79: SEM images (in SE mode) of the micritic microtextures observed (a) in the natural limestone rock before experiment on the wall of the injection well (b) after 20 days injection of unsaturated distillated water and (c) after 21 days injection of aggressive CO_2-charged water and (d) salt. Red arrows correspond to the initial intra-oolitic microporosity and white arrows to an increase of this micoporosity.

The presence of fibrous and sometimes hollow crystals of calcite at the surface of syntaxial cements (Fig. 80) has also been noticed. The same phenomenon is observed on the surface of the internal walls of the predominant wormholes (the observations are done at the outer part of the core-plug for Fig. 80c).

These assemblies of calcite peaks are the results of the continuous heterogeneous dissolution initially in the form of etch pits at the surface of sparitic cement.

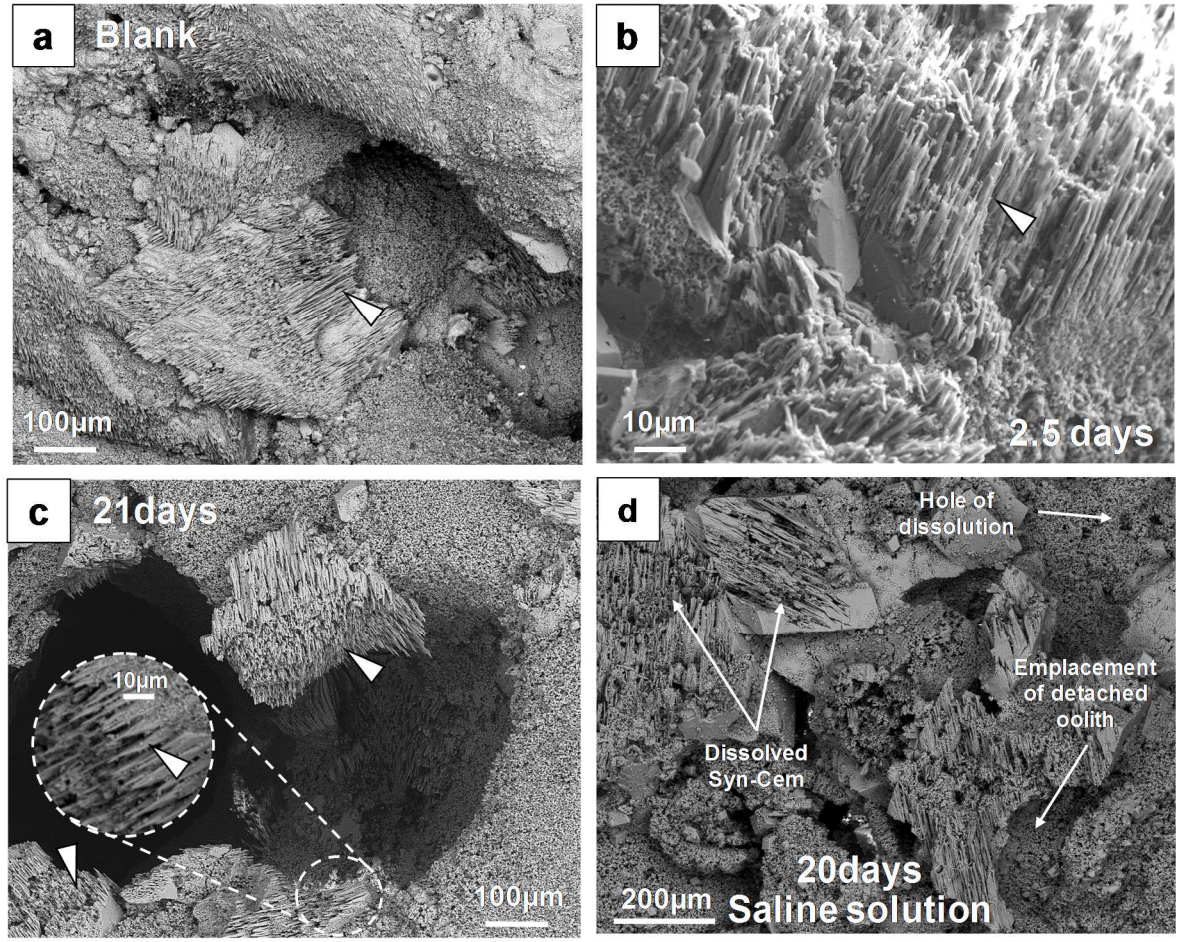

Figure 80: SEM images (Secondary electrons) focusing the observation of fibrous crystal (white arrows) covering (a) the surface of the entry of a wormhole in the blank experiment with unsaturated distillated water and the internal walls of wormholes for experiment of (d) 2.5 days and (c) 21 days of injection of dissolved CO_2. (d) (BSE mode) Surface state of the wellbore after injection for the 20d experiment with salt.

For the long-term experiment (21 d) without salt, an important amount of euhedral micro-caclites of different sizes (15 µm in maximum size) is observed at the surface of the ooliths at the immediate vicinity of the cement phase (Fig. 81a).

Unaltered rhombohedral calcites appear on the surface of the micritic matrix lining the walls of secondary mesoscopic wormholes developed (Fig. 81b). Neo-formed polyhedral micro-calcites (µ-calc) of approximately 10 to 30 µm in size also cover homogeneously the surface of oolites (Fig. 81c).

Concerning the long-term experiment with salt, the study of the internal walls of secondary wormholes underlines the concomitant existence of dissolved micrites and altered sparitic cement and at their immediate vicinity, the occurrence of neo-formed smooth rhombohedral calcite (Fig. 81d).

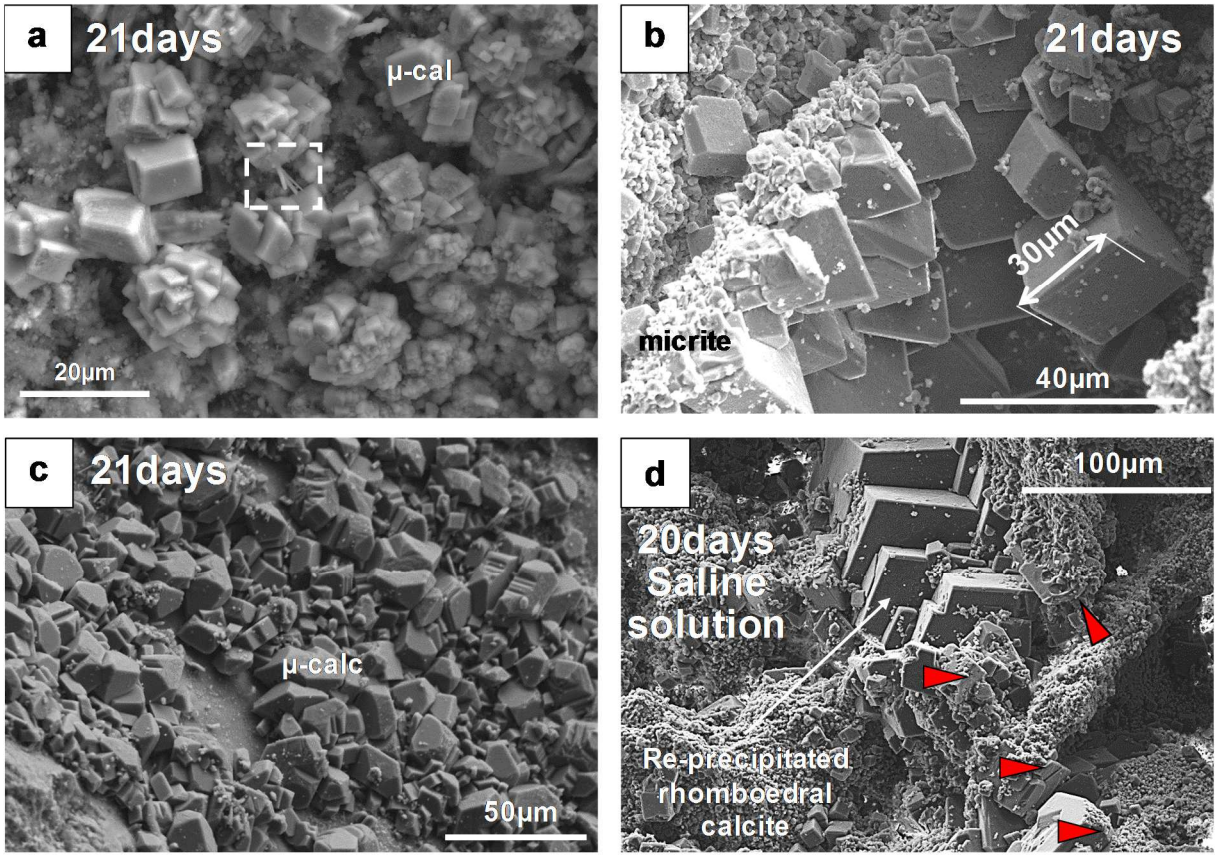

Figure 81: SEM observation (BSE mode): 21d experiment without salt: (a) Aggregates of euhedral micro-calcite (µCal) crystals covering the surface of the oolith at the cement-rock interface. The dotted white square corresponds to aragonite needles (b) Clusters of smooth rhombohedral calcite growing on the wall of a secondary wormhole and (c) Aggregates of neo-formed polyhedral micro-calcite on the surface of ooliths located on the wall of secondary wormholes. 20d experiment with salt: (d) Clusters of smooth rhombohedral calcite growing on the wall of a secondary wormhole.

– PARTIE 5 –
DISCUSSION : ÉVOLUTION SPATIO-TEMPORELLE DES PHÉNOMENES DE TRANSPORT RÉACTIF

– PART 5 –
DISCUSSION: SPATIO-TEMPORAL EVOLUTION OF REACTIVE TRANSPORT PHENOMENA

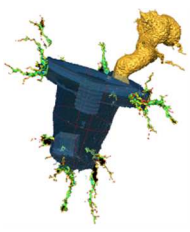

I. pH VARIATION AND MASS BALANCE

During the MIRAGES-2 experiments, CO_2 dissolved in aqueous phase (with or without salt) was radially injected at 150 $g.h^{-1}$ in limestone core-plugs under reservoir conditions of 120 bar and 60°C during different durations.

A reactive fluid in equilibrium with a $P_{(CO_2)}$ = 30 bar was continuously prepared at 20°C in a dedicated reactor during all the experiments. The measured concentration of dissolved CO_2 in the injected solution was of 0.89 $mol.kg^{-1}$ and 0.91 $mol.kg^{-1}$ for the long-term experiment with and without salt respectively (Tables 9 and 10). These measured values are very close to the expected concentrations calculated with the Duan model [108] which demonstrates that i) the solution is at equilibrium with the gas phase and ii) the efficiency of the in-situ Raman measurement technic.

In order to perform geochemical modeling, we consider the system with calcite and a solution in equilibrium with a fixed partial pressure of CO_2. For the experiment without salt, the equivalent CO_2 pressure was calculated by iteration performing simulation with PHREEQC software and phreeqc.dat database from the average CO_2 solubility measured in the experimental solution (39.2 $g.kg_{wat}^{-1}$ of pure water *i.e.* 0.89 $mol.kg^{-1}$) at 60°C and 120 bar of total pressure and the *in-situ* pH of 4.9. The deduced $P_{(CO_2)}$ for the experimental $CaCO_3/CO_2/H_2O$ system at equilibrium is of 56.2 bar (corresponding to a fugacity of CO_2 of 44.7 bar). This value will be used in the subsequent modelling especially for solubility calculation of the different species at equilibrium.

During the cure period, the initial aqueous solution is saturated with respect to calcite at 120 bar. The high pH values of 9.8 and 12 measured in the close system for the experiment with and without salt respectively are not only controlled by calcite but also by the cement phases. The role of each phase in the pH control can be envisaged taking into account the equilibrium pH of a solution with each phase. It is known that the high alkalinity (pH>12) in the first stages of the cements hydration is controlled by hydroxydes of alkaline metals (NaOH and KOH), followed by portlandite with pH values more than eleven. The long term pH will be mainly controlled by CSH phases and in a less extent by ettringite with pH closer to 10 [187]. Figure 82 clearly illustrates the change in the control of the solid phases composing the pore fluid on the pH value with time in a calcite/cement system. In addition, a geochemical modeling of simple systems at 60°C was also performed to establish pH values according to a thermodynamic equilibrium with the main solid phases composing the cement with or without calcite in solution. The results are shown in table 11. These results demonstrate the major impact of the cement phase on the pH value of the surrounding solution. The experimental pH of 10 is close to the results calculated for a system at equilibrium with the CSH1.6 and calcite or with calcite and ettringite. As this pH is reached very quickly (Fig. 66), the impact of the portlandite on the solution pH is minor. These results confirm the control of the CSH phases and of the ettringite on the pH of the core-plug aqueous environment during the cure. The salinity does not affect the pH value by more than 0.1 unit of pH and doesn't 'explain the difference between the experiment with and without salt.

The sulfate and aluminum concentrations recorded during this cure period (Fig. 69) are likely due to the dissolution of ettringite and the monosulfate composing the hydrated cement.

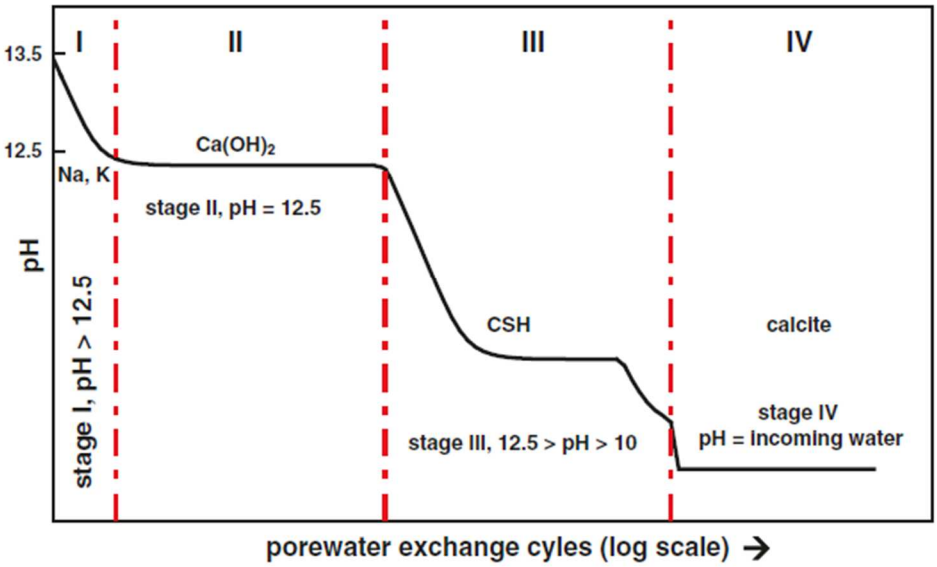

Figure 82: Schematic diagram of the evolution of the pore water pH as a function of the number of water exchange cycles. It illustrates the different stages of cement degradation due to the infiltration of a calcite equilibrated water at 25°C and depicts the major solid phase controlling the fluid composition and the corresponding pore water pH. Ochs (2016) [186] modified from Berner (1992) [188] and Andra (2005) [189].

Minerals	pH
Calcite	9.13
Portlandite	11.36
Ettringite	10.39
CSH1.6	10.5
Calcite+Portlandite	11.36
Calcite+Ettringite	10.39
Calcite+CSH1.6	10.5

Table 11: pH at equilibrium with different mineral phases at 60°C. Calculation with PHREEQC and Themoddem database.

Once the injection starts, the mixture between the interstitial CO_2-free fluid (initially at equilibrium with the host rock and the cement) and the CO_2-rich solution modifies the nature of the ionic species in solution. Aqueous CO_2 becomes the dominant species with a small amount of bicarbonate ions.

The presence of this reactive solution (pH = 3.6 at equilibrium at 20°C) induces a sudden drop in pH of the initial experimental solution and leads to the enhanced dissolution of minerals of both cement and rock.

Concerning the CO_2/rock interaction, the formed weak acid reacts with the porous matrix and leads to a mass transfer according to the following equation of calcite dissolution:

$$CaCO_{3(s)} + 2H^+ = Ca^{2+} + 2CO_{2(aq)} + H_2O \quad (27)$$

During the 2 first days of injection, a competition between the carbonate and the cement phases controls the pH value.

The SEM microscopic observations has revealed, especially for the experiment without salt, a reactive front in the cement arising from the interface with the rock and which is divided in three different alteration zones (Z1, Z2 and Z3) (Fig. 75b) widely described in the literature [54, 190]. The zone 1 adjacent to the unaltered cement is a region depleted in portlandite. Indeed, the high porosity is attributed to the leaching of this mineral characterized by a dissolution rate significantly faster (r = 2.24 X 10^{-8} mole.m².s^{-1} at 25°C) than for the CSH phases (r = 2.75 X 10^{-12} mole.m².s^{-1} at 25°C) according to Marty et al (2009) [191]. The zone 2 is defined as the carbonated zone. Within the cement phase, the mass transfer of the calcium from the zone 1 dominated by the diffusion process [76; 192; 193, 194] coupled to the diffusion of the carbonate ions of the injected solution induce the precipitation of secondary calcium carbonate polymorph, mainly aragonite in our experiment (appendix J [195]). This phenomenon is responsible for the low permeability of the zones Z2 and Z3 with a more important calcium concentration than in the fresh cement. In these 2 reactive zones, the remaining C2S and C3S are leached and replaced by amorphous silica. The zone Z3 located at the rock/limestone interface undergoes, in a second step, the action of the renewed acidic solution which induces the partial dissolution of the secondary carbonates (Fig. 75c). Water-soluble calcium bicarbonate then forms, which can easily diffuses out of the cement matrix. This outer leached region is defined in the litterature as a decarbonated zone mainly composed of amorphous silica gel [54]. The calcium contribution from the cement thus mainly comes from the dissolution of portlandite and CSH, the leaching of the remaining C2S and C3S and to a lesser extent from the dissolution of ettringite (AFt) and monosulfate (AFm).

The rate of degradation of the cement was controlled by the rate of dissolution of the calcium carbonate-rich layer, after its formation, and the diffusion through the fully degraded layers [194]. The thickness of the observed alteration front was measured at 40 points on the polished section of cement-rock interface selected samples for several experiments in order to calculate the mean rate of alteration.

For the blank experiment, the thickness is of about 404 ± 94 µm corresponding to an average alteration rate of **0.84 ± 0.19 µm.h^{-1}**. In the case of the injection of the acidic solution without salt (2.5 days and 21 days), the thickness of the alteration front is around 461 ± 151 µm after 2.5 days of injection and 1 607 ± 542 µm after 21 days corresponding respectively to an average rate of alteration of **7.44 ± 2.44** and

3.21 ± 1.08 µm.h^{-1}. The mean rate of cement alteration decreases with the duration of the experiment likely because the carbonated zones Z2 and Z3 play the role of a diffusion barrier. For the experiment with saline solution, the penetration depth is of 600 ± 171 µm (mean alteration rate = **1.18 ± 0.14 µm.h^{-1}**). These results from MIRAGES-2 experiments tend to demonstrate that the effect of salt in solution would inhibit cement degradation.

Other authors have studied the effects of carbonated brine on well cements [*e.g.* 54; 65; 194, and 196]. Duguid et al (2011) [194] performed a set of *dynamic* experiment using a $CaCO_3$-saturated brine enriched in CO_2 at pH 5 that simulated a limestone sequestration formation (T = 50°C, P = 100 bar, flowrate = 8.7 mL.min^{-1}). As a comparison, the alteration rate measured after 26 days of injection was of **0.92 ± 0.35 µm.h^{-1}** which is consistent with our observations of the sample submitted to the flowing of CO_2 rich saline solution. Other experiments of cement ageing with CO_2 saturated saline solutions without calcite performed in *static* mode have obtained a broad range of alteration rate. Thus, Barlet-Gouédard et al (2007) [53], Jobard et al (2013) [155], and Andac and Glasse (1999) [197] reported alteration rates of **0.63**, **0.26** and **0.32 µm.h^{-1}** respectively while Kutcho et al (2007) [54] obtained an alteration rate of **1.66 µm.h^{-1}** after 9 days of experiment. These variability are mainly attributed to the experimental set up, the test procedure (T, P, duration…) and the cement test specimen (class H cement, add of fly ash,…) used in each study. However, the values are mostly less than those obtained in the flowthrough experiment.

Once the different cement phases are dissolved or carbonated, the pH is then controlled by a dynamic equilibrium between the continuous renewal of the CO_2 rich solution and the dissolution of both the carbonate minerals and mainly the CSH phases of the cement as previously demonstrated. The long term evolution of the pH reaches a stable value of 4.9 for all the experiment with CO_2.

In order to propose a mass balance of the system, the total amount of dissolved calcite was determined. Considering an identical volume of rock at the beginning of each experiment, the total weight of dissolved calcite was estimated, for each experiment, from the total volume of the solution and the average calcium concentration $[Ca_{2+}]_{av}$ analyzed in the experimental solution.

$$\left(V_{init} + V_{inj}\right) \times \left[Ca_{2+}\right]_{av} \quad (28)$$

With V_{inj} is the total volume of injected solution and V_{init} the initial volume of the solution in the system equal to:

$$V_{init} = V_{auto} - \left[V_{core}\left(1-\phi\right)\right] \quad (29)$$

Where V_{auto} is the total volume of the system (autocalve), V_{core} corresponds to the initial core-plug volume and ϕ is the initial porosity of the core-plug.

The mass balance is summarized in Table 12. Figure 83 displays the total dissolved calcium as a function of time and of the nature of the injected solution.

Exp#	Duration (days)	Total injected volume of reactive solution (L)	Average dissolved Ca^{2+} concentration in the experimental solution (mg/kg)	**Dissolved Calcite (g)**
blank	21	71.2	7.9	**0.56**
Without salt	24	3.5	186.9	**0.65**
	2.58	10.3	112.5	**1.16**
	10	35.2	156.1	**5.49**
	20.9	73.7	105.2	**7.75**
Saline solution	21.16	74.3	529.57	**39.36**

Table 12: Total Amount of dissolved calcite after each experiment.

For the experiment without salt, the rate of dissolved calcite is of 0.56 g/days during the 10 first days of injection and is of 0.21 g/days for the 10 following days. This trends is also underlined for all the long-term experiments by the decrease of the calcium content in the experimental solution with time (Fig. 69).

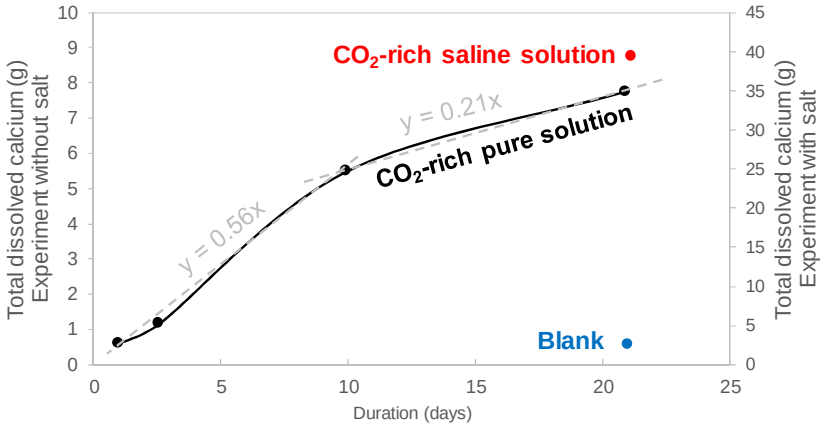

Figure 83: Evolution of the total dissolved calcium weight for each experiment.

The decrease of the calcium content was observed in laboratory studies of carbonate rock dissolution (linear flowthrough experiment) and was explained as the result of the wormholes emergence [44; 156; 198]. The appearance of preferential dissolution pathways which carry the majority of the injected fluid induces a decrease of several orders of magnitude of the specific surface area [44] and of the reaction rate [177].

In the MIRAGES-2 experiment, the lowering of the cement alteration rate with time can also be considered to explain the decrease of the calcium content of the expelled solution.

The experiment with salt results in a much higher dissolution of calcium (average calcium concentration in solution 3.3 times higher in the case of experiment with salt). As we explained in the paragraph II.1.2, even if the $P_{(CO_2)}$ is lower and the carbonate concentration in solution less important due to the “salting out” effect, the presence of NaCl in solution induces an increase of the calcite solubility. To illustrate this phenomenon, the calculation of the calcium solubility at equilibrium in a pure solution or enriched in NaCl (0.25 mole.kg^{-1} of NaCl) was performed at 60°C considering an acidification of the solution at a pH = 4.9 ($P_{(CO_2)}$ of 56.2 bar). This simulation was performed using the geochemical PHREEQC software and phreeqc.dat database. The results are consistent with the experimental observations with a calculated concentration of dissolved calcite equal to 2.38x10^{-2} mol.kg^{-1} for pure water and sligthly higher in saline solution with a calculated value of 3.07x 10^{-2} mol.kg^{-1}. However, the difference is less pronounced than in the experimental observations where the salt impact is more noticeable. It should also be noticed that the concentrations of the dissolved calcium measured in the experimental solution are lower throughout the injection period of the acidified fluid (0.39x10^{-2} mol.kg^{-1} for the experiment without salt and 1.3x10^{-2} mol.kg^{-1} for experiment with saline solution) than those calculated at thermodynamic equilibrium with PHREEQC code. This remark reflects a constant disequilibrium of the solution with respect to the calcite inducing an overall predominant mechanism of dissolution in the system during all the injection time.

These measured calcium concentrations in the effluent are in accordance with data found in the literature from experiments perfomed in Hassler cell (linear injection) under conditions similar to those imposed in this study. Luquot et Gouze., 2009 [37] and Menke et al., 2017 [199] have injected a CO_2-rich saline solution (pH values of 3.2 and 3.1 respectivly) under reservoir conditions (120 bar / 100°C for Luquot et al., 2009 [37] and 100 bar / 50°C for Menke et al., 2017 [199]) in a relatively chemicaly pure limestone cylindrical sample (oolitic limestone from the Mondeville formation of Middle Jurassic age of the Paris basin for Luquot et al., 2009 [37] and a Portland basebed limestone for Menke et al., 2017 [199]) whose pore structures are closed to that of the Lavoux limestone. During the percolation of the acidic fluid in the core-plug, the maximum concentrations of calcium in solution of 1.26x10^{-3} mol.L^{-1} (Luquot et al., 2009 [37]) and 10^{-3} mol.L^{-1} (Menke et al., 2017 [199]) were obtained while we have measured a maximum concentration of 1.56 mol.L^{-1} in the MIRAGES-2 experiment with NaCl. These differences coul be explained on the one hand by the configuration of the experimental set-up. Indeed the radial configuration of the injection in the MIRAGES-2 test bench induces a larger rock pore volume exposed to the acidic fluid in comparison to the linear configuration. On the other hand, the calcium release from the cement phase also contributes to the higher calcium concentration in our experiments.

II. DOMINANT MECHANISMS IN THE INITIATION OF DISSOLUTION PATTERNS (DIMENSIONLESS NUMBER ANALYSIS)

Numerous experimental and numerical studies on the reactivity of carbonate rocks in acidic environment have demonstrated that injection of supercritical CO_2 in an aqueous media leads to a structural reorganization and modification of their petro-physical properties with respect to the geochemical processes involved (dissolution/precipitation). The permeability as well as the porosity of the rocks are modified, mainly near the injection well.

In experimental laboratory conditions specific to CO2-DISSOLVED project, the CO_2 is injected in aqueous form. A dissolution front is thus generated immediately at the injection point of the injection well.

The dissolved ions are then transported by hydrodynamic dispersion or by molecular diffusion spreading out in the system. Feedbacks between chemistry and transport of species induce instabilities that result in flow localization in several preferential pathways [200; 201]. The mass transfers are then directly related to the evolution of the pore structure with regard to the involved reactive transport phenomena.

The published literature underlines the diversity of dissolution patterns (Fig.21) initiated by the injection of acidic solution in carbonated reservoirs, which depend on different factors such as the intrinsic characteristics of the rock (nature, permeability, heterogeneity, reactivity,…), the spatial distribution of minerals in heterogeneous rocks, the original brine composition, the process parameters (injection flowrate, CO_2 concentration,…) and the thermodynamic conditions (Pressure, Temperature) [35; 36; 131]. These parameters impose a degree of equilibrium between the reactions, advection, and diffusion processes impacting the rock matrix structure [130].

Unidirectional linear percolation experiments of CO_2-enriched fluids through a core-flood carbonated rock sample have been performed by different authors in experimental conditions close to those targeted in our experiments [33; 37; 42; 196; 199]. The results have demonstrated that the reaction rate of calcite at the limestone surface is so fast that most of the pore space in the near-well region is submitted to a transport-limited dissolution regime [46; 199; 202]. Localized dissolution emerges with the appearance of “dominant type wormholes” [*e.g. 37; 43; 135; 156; 203*]. The observations of the radial dissolution network architecture in the core-plug after our experiments displays the same structure of “dominant wormhole” (Fig. 73 and 74).

As the studied rock is “considered” as a relative homogeneous porous medium, a dimensionless number analysis using the Péclet-Damköhler numbers (*Pe-Da*) (Equation 13, 14 and 15) is performed for the experiment without salt. This discussion is initiated to highlight the cautious use of the *Pe-Da* numbers with natural rock where structural and mineralogical heterogeneities, specific to each rock matrix exert a major influence in the reactive transport mechanism as already pointed out by Noiriel et al., 2015 [204], Smith et al., 2013 [43] or by Menke et al., 2017 [199].

As a reminder, the Pe locally corresponds to the the ratio of advection rate to diffusion rate and the Da number to the ratio of the reaction rate to the dominant mass transport rate. The use of these dimensionless numbers mainly depends on the considered scale (micro or macroscopic) and the definition of the meaningful lengthscale, critical parameters for both *Pe* and *Da* calculation. Indeed, apart from a simple tube-like geometry, it is difficult to define an adequate characteristic length. This task is especially tricky in the study of a porous network where the fluid pathways are tortuous and highly connected. In this discussion, two different approaches are considered.

The first approach considers the average dimension of the conduits carrying the fluid into the rock matrix *i.e* the pore. Ths scale of study allows the comparison of our experimental results with those obtained by Golfier et al., 2002 [139] based on 2-D flat Hele-Shaw cells experiments. Indeed, the incorporation of the calculated values in the *PeDa* behavior diagram (Fig. 23) which delimits the boundaries between the different dissolution patterns is enabled as soon as the study is performed at the microscopic scale.

Assuming that geochemical instabilities are triggered at the surface of the injection well located in the middle of the rock sample, the average pore access diameter, measured by mercury porosimetry, is used as the characteristic length scale for both *Pe* and *Da* number. Table 13 provides parameter values used in the different dimensionless number calculations.

The dominant transport mechanism is determined using the *Pe* parameter (Eq. 13). The interstitial velocity included in the *Pe* determination is defined as the specific flux per cross-sectional area in $m.s^{-1}$:

$$v_{inj} = \frac{Q_{inj}}{(S_{lat} + S_{bot})\phi} \quad (30)$$

Where Q_{inj} is the fluid flow rate ($m^3.s^{-1}$), $S_{lat} = 2\pi r_{well} h_{well}$ is the lateral surface of the experimental wellbore, $S_{bot} = \pi r_{well}^2$ is the bottom surface and ϕ the total bulk connected porosity.

The calculated value of the *Pe* number is equal to **0.15** which means that diffusion mass transfer is slightly faster than convective transport. But, as the value is very close to one, the two processes have an influence on the transport of the ions in solution.

As the system is partially dominated by the diffusive transport, the Damköhler number, is calculated using the equation 15. The calcium concentration in the solution at equilibrium and the reactive specific surface area involved in the Da calculation have to be determined. The modeling performed in paragraph **I**. gives a calcium concentration of 2.38×10^{-2} $mol.kg^{-1}$ at equilibrium in a solution at 60°C for a $P_{(CO_2)}$ of 56.2 bars.

The specific surface area of the initial Lavoux limestone is calculated using:

$$S_r = \rho_{calc}(1-\phi) \times A_{BET} \quad (31)$$

Where ρ_{calc} is the density of calcite (kg.m^{-3}) measured by mercure porosimetry and A_{BET} is the BET specific surface area (m^2.kg^{-1}) determined by Vincent et al (2011) [153] for a similar fine ooid grainstone with internal cement sampled in the same Lavoux region.

The calcite dissolution rate is determined as a function of the $P_{(CO_2)}$ using the empirical equation 12 given by Pokrovsky et al (at 60°C and pH = 4.9) [123]. The corresponding dissolution *r* is equal to 4.21x10^{-4} mol.m².s^{-1}.

The calculated value of *Da** is of **0.08**. It thus means that transport rates are higher than reaction kinetics and that the dissolution is here reaction limited.

Parameters	Values	
Injected fluid flow rate	4.11×10^{-8} m.s^{-1}	
Well radius	5×10^{-3} m	
Well length	2×10^{-2} m	
Average pore access diameter	1.31×10^{-6} m	
D_m, *(60°C)*	2×10^{-9} m².s^{-1}	[36]
r_+ (T) (acid + neutral mechanism, 60°C)	4.21×10^{--4} mol.m².s^{-1}	[123]
ρ_{calc}	2.66 ×10^3 kg.m^{-3}	[this study]
Porosity ∅	0.2479	
A_{BET}	6.9 ×10^2 m².kg^{-1}	[153]
C_{eq}	2.4 ×10^{-2} mol.m^{-3}	
C_{ac0}	16.64 kg.m^{-3}	
k	4.59×10^{-14} m²	
x_1	0.0425 m	
x_2	0.02 m	

Table 13: Parameters used for the dimensionless number calculations.

Finally, in order to adjust the quantitative boundaries between the different regimes in accordance with our experimental conditions, the dimensionless number N_{ac} (acid power number), the Darcy number N_D and the shape factor F specific to our experimental sample, which impact these different limitations, are also estimated using equations 16, 17 and 18. The calculated values are equal to N_{ac} = 2.03 · 10^{-3}, N_D = 2.54 · 10^{-11} and F = 2.1.

According to the Péclet/Damköhler diagram (Fig. 84), the results confirm that the dissolution pattern initiated at the microscopic scale near the injection point is defined as “dominant wormhole”.

However, the obtained values are not really in accordance with the dominant mechanism expected. Indeed, the highly conductive wormholes with few rammifications generated in our experiments correspond to a dispersion of the solute mainly longitudinal and diffusion-limited while the estimated dimensionless numbers at the pore scale rather denote a predominance of the diffusive process.

This comment is mainly due to the choice of the meaningful lengthscale. The previous selected value corresponds to the mesoscopic average pore access diameter calculated over a large range of values. A macro-porosity also composed the porous network of the rock. If we consider for example the macropores family of 300 µm, the corresponding *Pe* is equal to **35**. In this case, the convection is the dominant transport mechanism. The calculated *Da* number using equation 14 is thus equal to **124** corresponding to a transport-limited dissolution behaviour. It is important to take this particularity into account in the definition of the dominant mechanism involved knowing that the transport will be dominated by advection in the biggest pore and by diffusion in the smallest ones.

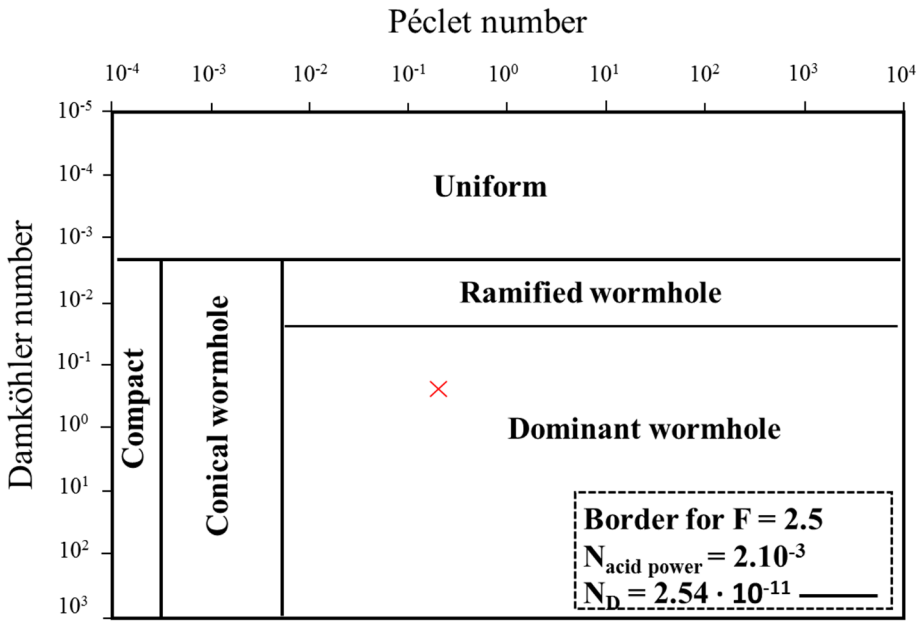

Fig. 84: Quantitative schematic diagram representing the dissolution pattern depending on Péclet and Damköhler numbers [139]. The Red Cross corresponds to the theoretical estimated *Pe-Da** values.

Another approach consequently consists in specifying the representative dimension of the area where the reactions can occur as the characteristic length of our system. In the literature, the commonly chosen experimental parameter in predominantly unidirectional end-to-end injection experiments on cylindrical samples is the core length.

In the configuration of the MIRAGES-2 experiments, the appropriate characteristic length is defined as the average distance between the contact surface of the well with the inlet fluid and the vertical and horizontal outer part of the core-plug (L = 0.0425m).

The obtained values for *Pe* with the macroscopic approach is $\approx 5x10^3 > 10^3$. This high *Pe* value confirms that, at the beginning of the injection, the diffusive transport is clearly negligible. The properties of the reactive front is therefore mainly governed by the *Da* number. With this approach, as the transport mechanism is dominated by advection, the *Da* is calculated using equation 14. *Da* is thus equal to $1.76x10^4$. The high value of *Da* reveals that the dissolution process is controlled by the mass transfer due to a high chemical disequilibrium and the high reactivity induced. The dissolution is non-uniform and occurs preferentially along the main flow paths.

This aspect therefore reflects the singularities of the use of these dimensionless numbers at each scale and also the importance of integrating the structural and mineralogical heterogeneities. Indeed, the carbonate rocks represent complex micro-environments characterized by a complex structural organization with variable distributions, forms and interconnexions of its porous network. Thus, even if the samples appear relatively homogeneous, structural weakness inherited from its diagenetic history can induce a variability in fluid flow and in the anistropic propagation of dissolution channels. The demonstration of the structural control of the rock on the dissolution network is developed in part 6.

III. Spatio/temporal evolution of the dissolution processes

The dimensionless number analysis has allowed to identify the dominant mechanism which initially drives the generation of the dissolution channels. It has also underlined the importance of considering the specific features of the carbonates rocks in terms of pore structure (pore size distribution, presence of microcracks) in the understanding of the spatialization of the dissolution regime with time. As the acidic solution is continuously injected, the pore space heterogenity is evolving as well as the velocity field. These modifications impact the dynamic of fluid-solid interactions and can induce local modifications of characteristic transport and reaction times. The *Pe-Da* numbers spatially and temporally change as the geometrical properties of the rock are modified. The MIRAGES-2 experiments has allowed the observation and the understanding of the spatial behavior of the dissolution patterns over time which is a significant parameter in establishing a post-injection predictive scenario.

Several studies, some of which are very recent, mainly focus on the appearance and growth of these dissolution channels as well as on the flow dynamics related to their evolution [e.g; 130; 137; 138; 141; 144 ; 205; 206; 207; 208; 209; 210; 211] taking into account the structural heterogeneities of the rock.

In the configuration of the MIRAGES-2 experiments; as the CO_2 enriched solution is injected, a pressure gradient is generated at the level of the surface of the wellbore. Coupled with the high chemical reactivity between the solution and the rock, this

pressure gradient induces instabilities mainly in the largest pores [208; 212, 213] or surface defects [208; 209; 214; 215].

The reactive fluid penetrates these preferential percolation zones and initiates the development of the “dominant wormholes”. Once a wormhole is generated, a pressure gradient constraints the surrounding rock matrix and inhibits the initiation of other wormholes. The field pressure remains unaffected from a certain distance of the firstly generated wormholes and other wormholes may appear (Fig. 85).

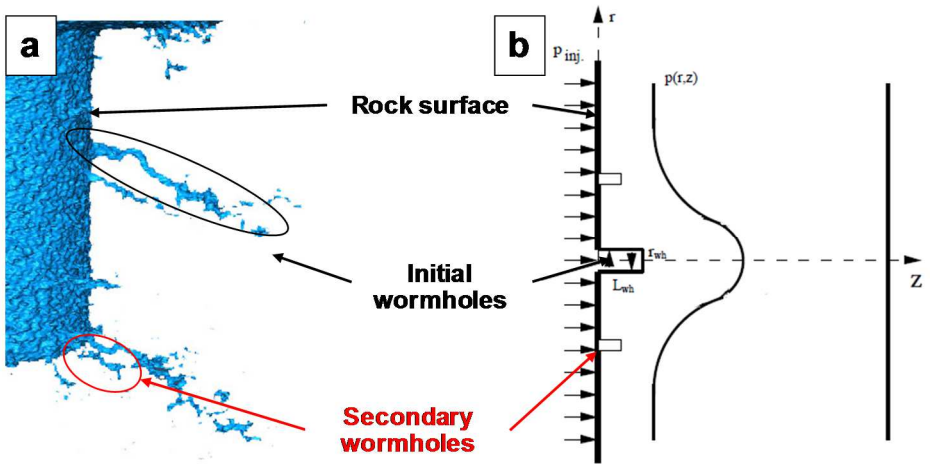

Figure 85: (a) 3D display from X-ray tomography analysis results of wormholes initiated from the surface of the well (10 days injection experiment without salt). (b) Schematic view of the wormholes’ formation on rock surface [212].

The fluid thus preferentially flows in these incipient channels of higher permeability. This trend is resulting in the non-uniformity increase of the solid matrix. The significant continuous flowrate of the acidic solution imposes a concentration of the reactant at the tip of the wormhole close to that of the injected solution despite acid consumption by the walls of the wormhole. These generated wormholes extend along the core-plug at the expense of the rest of the rock matrix. A competition between this preferential channels then drives the spatial dynamics of dissolution over time [137; 216]. This mechanism is intrinsically related to the structural and mineralogical characteristics of the rock. Longer wormholes carries the majority of the fluid preventing the growth of the smaller adjacent ones. This “secondary” shorter wormholes attract less and less inflow until they stop growing [144]. They can be defined as “dead wormholes”. Thus, the density of wormholes decreases as the length of penetration increases (Fig. 74). This process occurs until a single dominant wormhole (named the “breakthrough wormhole”) breaks through the core-plug. It should be noticed that, under laboratory conditions at the decimetric scale, the pressure differential at the both ends declines sharply when the tip of a main wormhole is close to the external part of the core. An "end effect" then appears, which increases the speed of penetration of this wormhole until the breakthrough of the sample [217]. This phenomenon has been confirmed by numerical experiment [138; 141]. In the MIRAGES-2 experiments, the “breakthrough wormhole” reaches the core-plug periphery very early, after less than 12 hours of injection (Fig. 74).

The core-plug breakthrough is responsible for an evolution of the reactive transport mechanisms over time depending on the location in the core-plug.

On the one hand, the process of localized dissolution actively contributes to the hydraulic conduction of the injected fluid. The consequence is an intrinsic increase of the injectivity at the immediate vicinity of the well. The flow of acidic solution is mainly concentrated in the “breakthrough wormhole” in which the characteristic reaction time becomes much greater than the transport time. The solute transport is “advective dominant” in the flow direction. The dominant channel gradually widens under the effect of a slow chemical erosion of the walls matrix (Fig. 74).

On the other hand, despite this dominant non-unifom and important localized dissolution, modifications of the petrophysical characteristics of the rock in area away from the wormholes have been detected (Fig. 77). An overall alteration of the porous media composing the volume of the rock sample was highlighted with the appearance of a new pore-throat families of larger diameters, mainly during the first days of injection. This changes in pore structure in regions away from the highly conductive channels have also been observed by Gharbi et al., 2013 [42] during reactive transport experiments.

Moreover, the post-experimental observations at the level of the wellbore clearly confirm thereon, that the dissolution phenomena over time are not limited to the “dominant wormholes” pattern. Indeed, the conical aspect of the upperpart of the injection zone (Fig. 73) after 2.5 days is indicative of a time dependent enhanced uniform dissolution. Figure 86a depicts the evolution of the wellbore geometry with time.

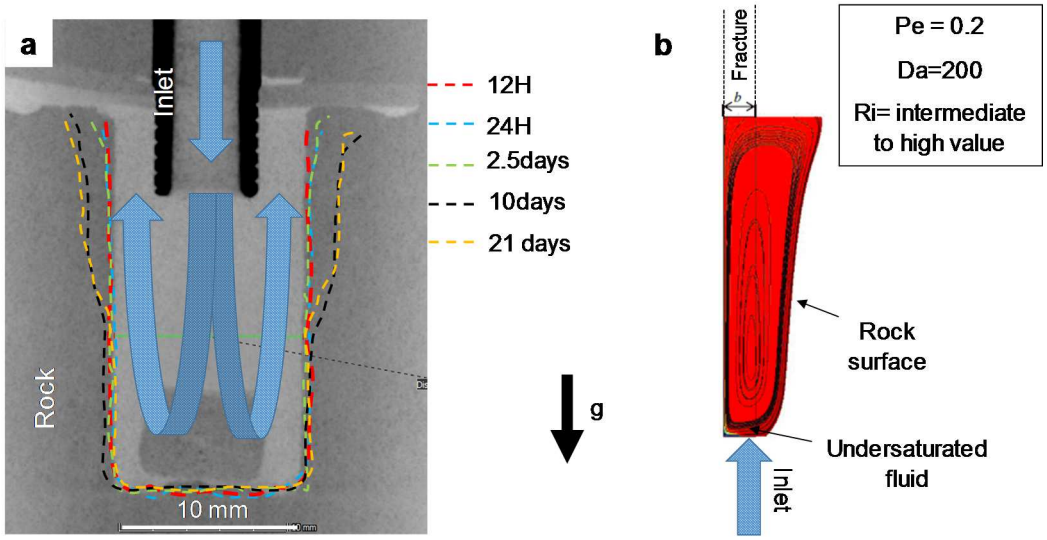

Figure 86: (a) Time dependent evolution of the well geometry. The large blue arrows indicate the fluid inlet within the injection well. The background photo illustrates the well shape of an initial sample. The different color dotted lines show the final geometry of the well for several time of acidic injection. (b) Example of Numerical buoyancy-dominated dissolution patterns obtained for Pe-Da numbers expected at the injection well after the core-plug breakthrough for intermediate to high value of the Richardson dimensionless number which reflects the significance of the buoyancy force [218]. g is defined as the gravity vector ($L.T^{-2}$).

As mentioned above, the breaktrough of the core plug modifies the spatial distribution of the flow speed of the solution within the core-plug, with the concomitant existence of preferential flow regions and low flow regions.

At the level of the well, the convection driving force is reduced modifying the local *Pe*-*Da* numbers with a potential decrease of *Pe* and increase of *Da*. Moreover, the enrichment of the interstitial solution of the near-well region with dissolved minerals may generate some instabilities with density contrast between the fresh injected solution and the well solution [219; 220]. The impact of the buoyancy force must be considered to discuss the geometrical changes of the well with time. In a vertical system of preferential fluid percolation, where the coupled mechanisms of chemical reaction, transport (mainly convective) and buoyancy drive the dissolution pattern, the predominance of buoyancy forces results in an upward dissolution [218; 219; 221]. Figure 86b illustrates the aperture variations of a vertical fracture filled with a fully saturated brine solution where pure water was injected under conditions equivalent to those of the MIRAGES-2 experiments after the core-plug breakthrough (low *Pe*, high *Da* and intermediate to high *Ri*) [218]. The numerical simulation of this investigation was performed considering a laminar regime (as in our experiments; see appendix B) and integrating the dimensionless number of Richardson *Ri*. This parameter includes the buoyancy force *i.e.* the difference of the mass fraction of species in solution between the saturated brine solution and the injected undersaturated solution. The results show this upwards dissolution as observed at the level of the injection zone. The modification of the well geometry in the MIRAGES-2 experiment is thus the result of coupled buoyant (role of the gravity) and convection forces. This phenomenon underlines the time dependence of the dissolution processes basically linked to the evolution of the rock structure and the resulted changes in hydrodynamics features.

IV. EVIDENCE OF PRECIPITATION PHENOMENA

Several microscopic observations have revealed the presence of localized recrystallization under different forms: i) rhombohedral calcites at the level of a micritic matrix and ii) aggregates of polyhedral calcite on ooliths surface observed on the walls of “dead mesoscopic wormholes” and iii) aggregates of euhedral µ-calcite have growth on ooliths surface at the immediate vicinity of the cement-rock interfaces (Fig. 81).

In addition to these observations, the density of these "meso-womrholes" emerging from the experimental wellbore tends to decrease with time. The 2D projection of wormholes imaged by CT-scans allows the counting of the numbers of existing wormholes (Fig. 87). The comparison between the different experiments (*i.e.* times of injection and solution salinity) is legitimated by the identical images resolution during the X-ray Computed Tomography analysis.

The number of wormholes ranges from 35 to 46 for the short-term experiments while it drops to 27-28 for the long-term experiments. This trend is clearly noticeable at the base of the injection well (Fig. 87).

Moreover, for the long-term experiments with and without salt, the wormholes are very thin compared to those of the 2.5d experiment without salt.

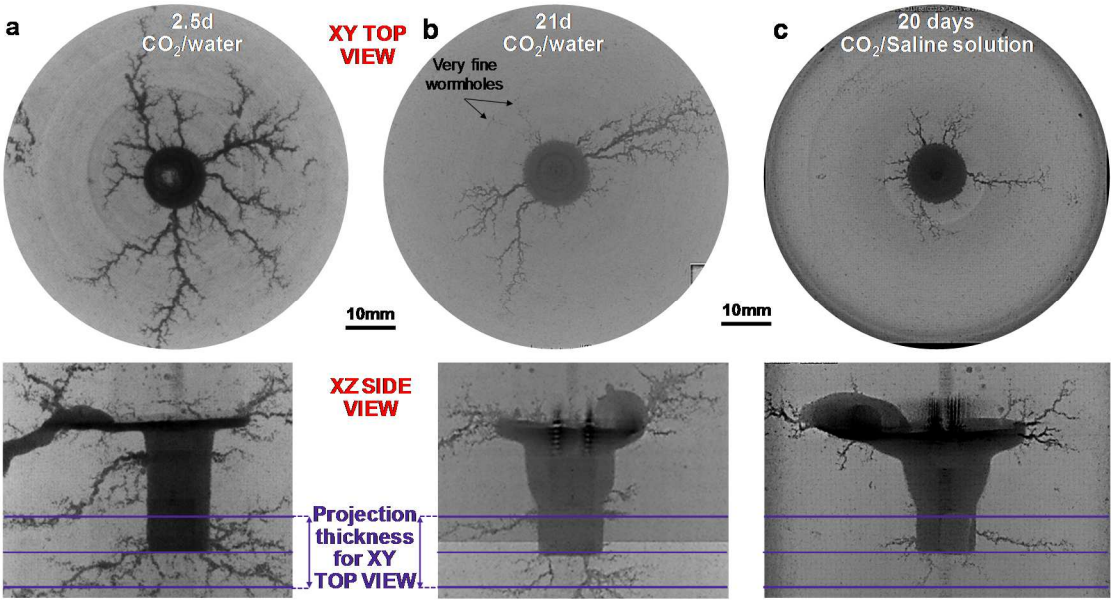

Figure 87: XY TOP view and XZ side view of projections of wormholes initiated at the bottom part of the well by superimposition of the CT-scans. The thickness of the projection for the XY Top views is defined on the XZ view (purples lines) for the short-term (a) 2.5d, and long-term experiments (b) without and c) with salt.

During core-plug preparation, the samples were drilled in the same block of rock and no major cracks were detected in the pre-experimental computed tomography (CT) inspection. Initial preferential pathways driving the majority of the injected solution since the beginning of the ageing period are thus not at the origin of these density contrasts. Precipitation phenomenon resulting in the reduction of dead wormholes diameters or even their clogging can thus be suggested. Such precipitation has already been observed in the context of the experimental injection of CO_2 saturated solution in carbonated reservoir conditions [36; 37; 44; 222; 223]. Neo-formed calcites were mainly detected in low flow or stagnant area mimicking the zone far from the injection point (low $P_{(CO_2)}$).

An investigation of the evolution of the surface roughness of the dead wormholes with time was carried out. The protocol of the local analysis of surface curvatures (Part 3, paragraph VII.2.3.2.2) as a descriptor of the average surface irregularities was used. The distribution of the frequency of mean curvature κ_{mean} value is calculated for defined surfaces.

Figure 88 illustrates the two extreme examples encountered in the MIRAGES-2 experiment. The images 88a and 88c depict a typical wormhole from the blank experiment with a relatively smooth surface characterized by a majority of convex curve.

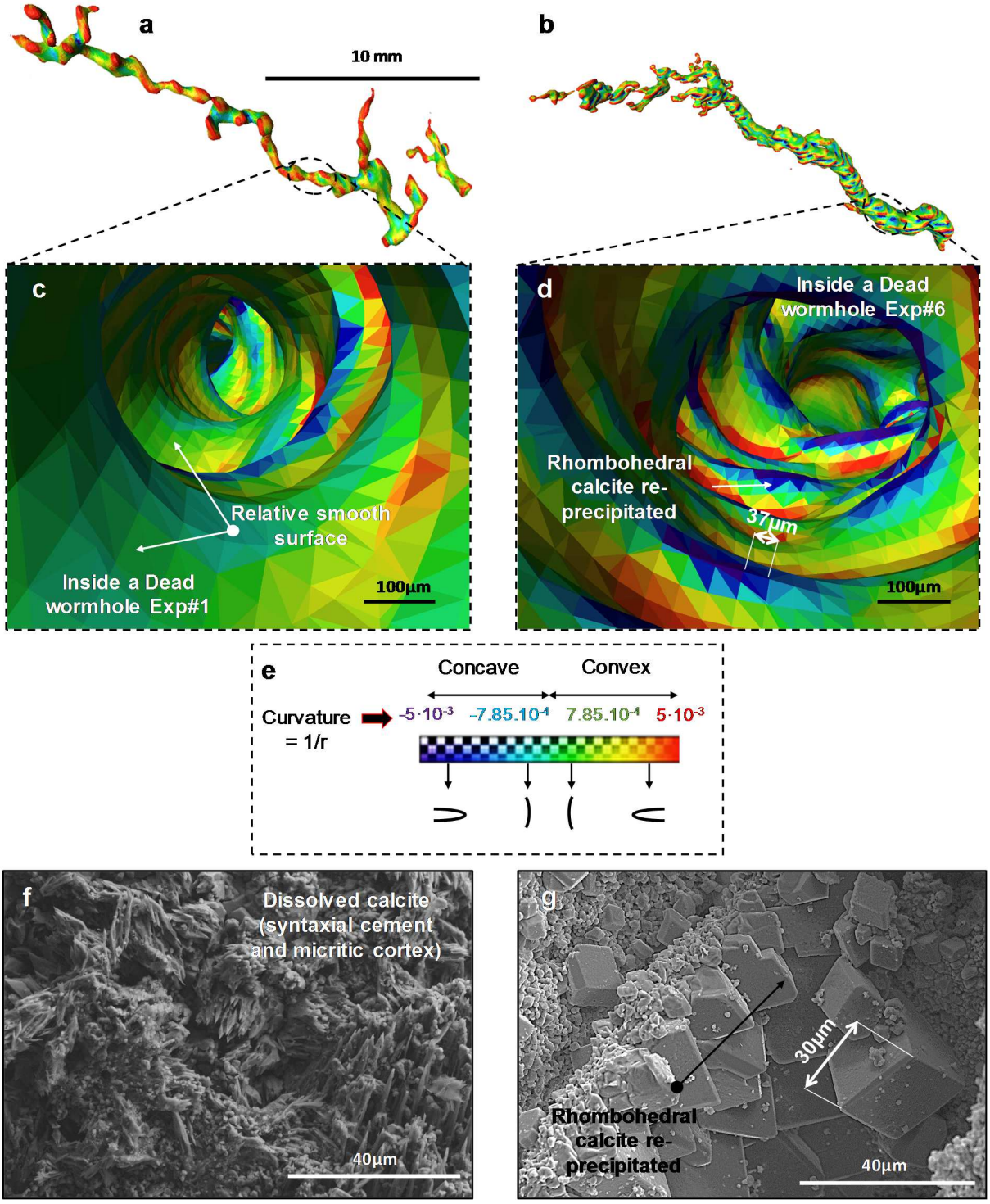

Figure 88: Extraction of a 3D model of an isolated wormhole after the analysis of the curvature distribution of its surface for (a) the blank experiment and (b) 21d experiment without salt. (c) Inside view of the isolated wormholes from the blank experiment displaying the surface triangles used to determine the distribution of curvatures. The color of the triangles depends on the sign and the value of the calculated curvatures. (d) 21 d experiment without salt. (e) Color map corresponding to the rate of concave (toward the interior of the wormhole) or convex (toward the rock matrix) curvatures. SEM observations (secondary electrons) of the walls of the dead wormholes for (f) the blank with a micritic cortex and syntaxial cement partially dissolved and for (g) 21 d experiment without salt with a dissolved micritic cortex and a possible re-precipitated rhombohedral calcites.

Images 88b and d displays a wormhole selected from the 21 days experiments without salt. The roughness of the surface is characterized by alternating zones with concave (blue) and convex (yellow to red) curves indicative of the presence of surface heterogeneities.

The SEM images of the microscopic aspect of the surface of the wormholes from the blank experiment depicts weak surface anomalies characterized by a microscopic heterogeneous dissolution feature of the micritic matrix and the syntaxial cements (Fig. 88f) [44; 224]. The corresponding roughness is not sufficiently marked to be perceptible on the micro-CT images on cm-sized samples resulting in a smooth aspect. The SEM observation of the 21d experiment without salt (Fig. 88g) displays a surface alteration marked by a micritic cortex partially dissolved and noticeable smooth and unaltered rhombohedral calcites on the surface. The edge size of these crystals is big enough to be characterized with this method (Fig. 88d).

The wormholes are not inspected individually but by location: i) the wormholes initiated at the top of the well and ii) those initiated at the bottom of the well (Fig. 89)

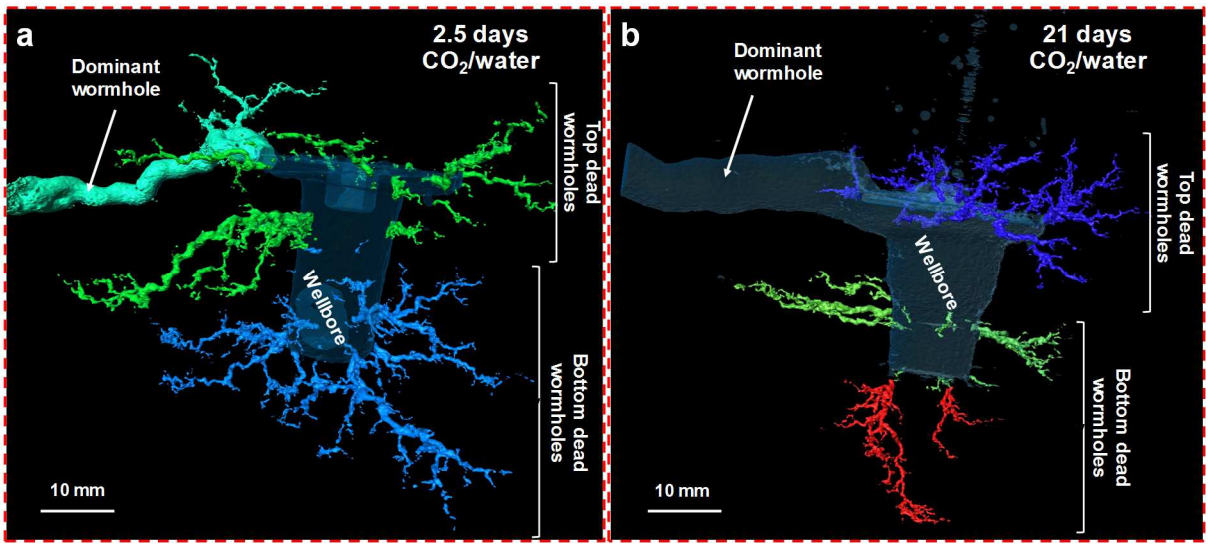

Figure 89: 3D model of the analyzed wormholes for experiments without salt (a) 2.5d injection: in green the wormholes initiated at the top of the well and in light blue at the bottom of the well. b) 21d injection: in dark blue the wormholes initiated at the top of the well and in green and red at the bottom of the well.

The results are presented in a diagram reporting the frequency of normalized angles over a range from $-5{\cdot}10^{-3}$ to 5.10^{-3} μm^{-1} (corresponding to a minimum value of 200 µm R_{curv} *i.e.* radius of curvature). The κ_{mean} values corresponding to a concave R_{curv} < 200 µm are anecdotal and are included in the lowest family of κ_{mean}. The smallest convex κ_{mean} are not considered because they mainly correspond to the tip of the several wormholes. Figure 90 shows the distribution of curvatures for both selected volumes of wormholes. As expected, the majority of calculated curvature are mainly convex due to the cylindrical form of the wormholes with an average radius of curvature of 740 µm at the top of the well (Fig. 90a) and of 700 µm at the bottom of the well (Fig. 90b).

The average radius of curvature calculated on the walls of the wormholes initiated during the blank experiment is equal to 1000 µm (Fig. 90a and b).

A very low surface in the concave zone exists. This trend depicts a smooth aspect of the wall indicative of a relative uniform dissolution as observed in figure 88c.

The curvatures data, which illustrate the presence of localized surface defaults associated to possible precipitation, correspond to the lowest negative concave values. The cumulative frequency of the measured curvatures shows an increase, with time, of areas with strong concavity around the bottom part of the well with a significant presence after 21 days of injection (7% of the total surface) (Fig. 90d). This effect is not reproducible for the upper part with a random behavior (Fig. 90c). This trend should be representative of precipitation cluster over the dead wormholes surface.

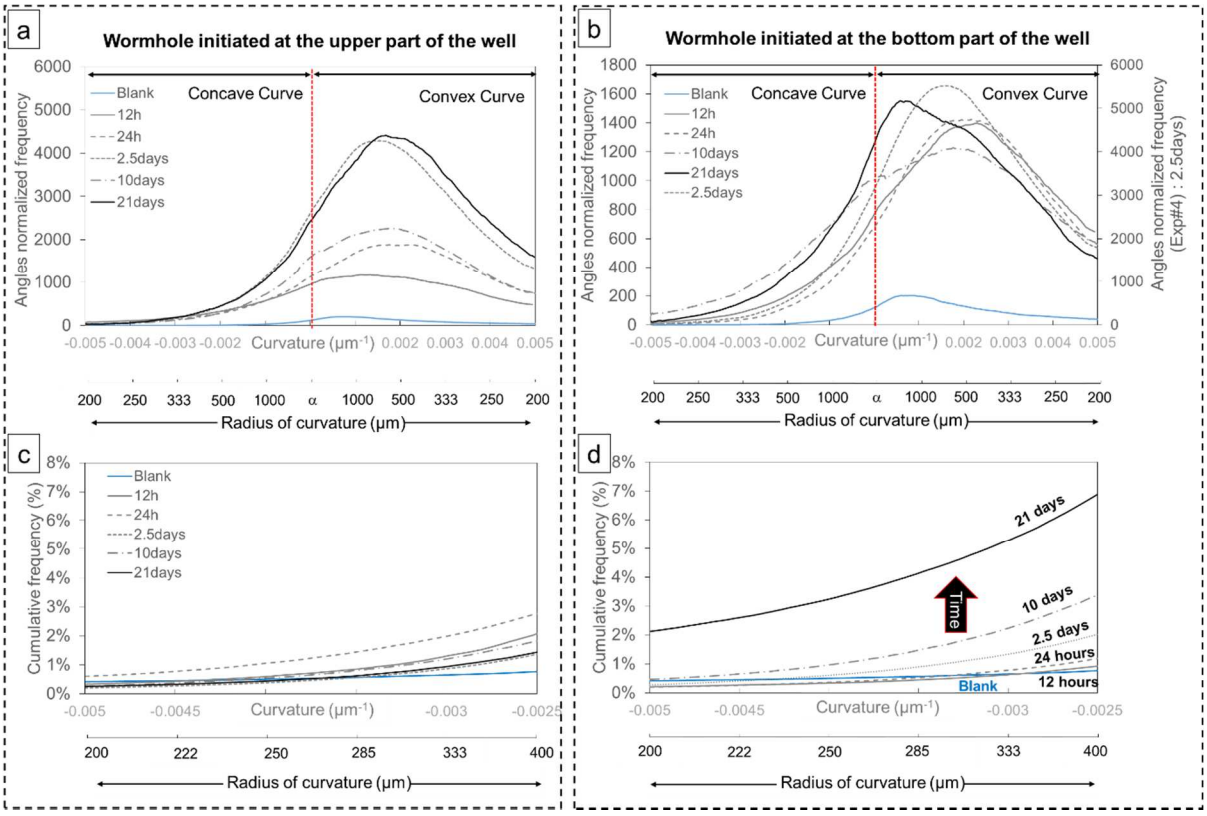

Figure 90: Time dependent histogram of the total surface mean curvature of the walls for "dead wormhole" selected (a) at the upper part of the well and (b) at the bottom part of the well. (c) Comparison of the cumulative frequency of curvatures with strong concavity (Radius of curvature from 200 to 400 µm) for the wormholes generated from the upper part of the well according to the different experiments and (d) from the bottom part of the well.

The cumulative observations of i) neo-formed calcite among the wall of "dead mesoscopic wormholes", ii) an obvious decrease of the wormholes density at the bottom part of the well and the presence of very thin ones, and iii) an increase of the surface irregularities at the overall scale of the "dead wormholes", lead us to correlate the geometrical characteristics change with a precipitation process as a consequence to the core-plug breakthrough.

The presence of precipitation in an acidic environment, under-saturated with respect to calcite, is not quite intuitive. It is also difficult to consider the phenomenon of precipitation close to equilibrium. The majority of neo-formed calcite crystals rising in such kind of experiment was observed under specific conditions such as an alkaline environment [225], a low flowrate and a low $P_{(CO_2)}$ [37], or in the case of the injection of oversaturated solution [33; 222]

Jobard et al., 2013 [155] have simulated, during 30 days in a static reactor reproducing the CO_2 sequestration geological conditions (pressure, saline aqueous environment) with a pH of 4.6-4.9, a thermal gradient (100 – 35 °C) on a crushed oolitic Lavoux limestone, similar to the one used in this study. The imposed thermal gradient induces a 10 % mass transfer of the initial rock matrix from the cold area where a dissolution process mainly affects the oolitic cortex toward the warmed area where re-crystallization occurs in the form of micro-calcite aggregates covering the surface of the ooliths composing this zone. The hypothesis of a thermal gradient between the injection zone and the near well region of our experimental system as the origin of the observed precipitations could be advanced in a first time. However, the temperature computed from the thermal modeling performed in appendix B and the experimental temperature data recorded are of 59.7°C in the injection zone. This implies that a 0.3°C temperature gradient is imposed which is too low to induce an important mass transfer. The thermal gradient theory can thus not be retained.

The hypothesis of changes in local thermodynamic conditions and local saturation index can then be suggested. During the expansion of the wormholes in the first days of injection, a micro-surface roughness may have developed on their walls due to the combined effects of i) particles detachment (Fig 78f) [34; 45; 226], ii) heterogeneities of reactive surface areas and reaction rates in the polycrystalline calcite (presence of sparitic cement and micritic grains) [44; 224; 227] and iii) the potential presence of insoluble components [228]. The walls of the “dead wormholes”, initially submitted to a strong reactivity in contact with the injected fluid, become stagnant zones due to fluid flow velocity and pressure gradients within the sample following the breakthrough [44; 177]. The chemical forcing are thus modified with a decrease over time of the reactivity of the carbonate phase caused by the modification of the dominant transport process from an advective to a diffusive one at the fluid-reactive rock interface (low *Pe* and High *Da*). The complex internal geometry of these newly stagnant zone with defects and defects driven reactions [229] can expect significant local, real-time deviations of pH-P conditions. A decrease of the $P_{(CO_2)}$ can occur leading to a slight decrease of the calcite solubility. The consumption of protons during the earlier dissolution process may also have resulted in a rise of pH.

Moreover, variations of local concentrations of specific elements in solution over time, such as calcium or other alkaline earth elements such as Mg and Sr, may cause a local decrease of the calcite solubility (Fig. 14) [114]. Concerning the Mg and Sr ions, they can form complexes with the other ions in solution and can decrease the ionic strength. They can also adsorb on the surface of a growing crystal modifying its surface tension and interfacial energy [230]. They act as inhibitors of the precipitation process of calcium carbonate and their presence results in an increase of the nucleation time and

a decrease of the rate of crystal growth [230]. Mg^{2+} has a higher impact than Sr^{2+} on these phenomena [115, 231]. The presence of these ions can also influence the crystal structure and thus the morphology of the precipitated crystals. The inhibitory properties of Mg will affect the direction (and the speed) of growth because of its substitution with Ca (the Mg poisoning effect). A fluid with a low **Mg** concentration will generate a spiral growth regime [115; 116] (Fig. 14 right) at the surface of a calcite crystal. A local decrease of these ions concentrations in solution close to the fluid-reactive rock interface can be a factor which promotes the initiation of crystal growth.

The chemical analysis of the experimental solution demonstrates that the behaviour of the Ca, Mg and Sr ions in solution is characterized by a significant increase resulting from the injection of the CO_2-rich solution followed by a continuous decrease over time. The Mg and Sr partitioning between the solid (cement and rock) and the solution composing the system is also to be studied.

Indeed, Mg/Ca and Sr/Ca ratios in the different phases (Fig. 70) evolve during the static (cure) and dynamic (ageing) stages of the experiments. These two ratios are always higher in the aqueous experimental solution than in the fresh Lavoux limestone during all the experiments. This phenomenon demonstrates the contribution of the cement phases in the enrichment of Mg and Sr in the solution. To confirm this hypothesis, chemical analysis of Mg and Ca contents in the altered and unaltered zone of the cement was performed by SEM using the JEOL J7600F scanning electron microscope.

The Figure 91 shows the evolution of the **Mg** concentrations in weight percent and the **Mg/Ca** ratio in the different zones of the altered cement (21d experiment without salt sample).

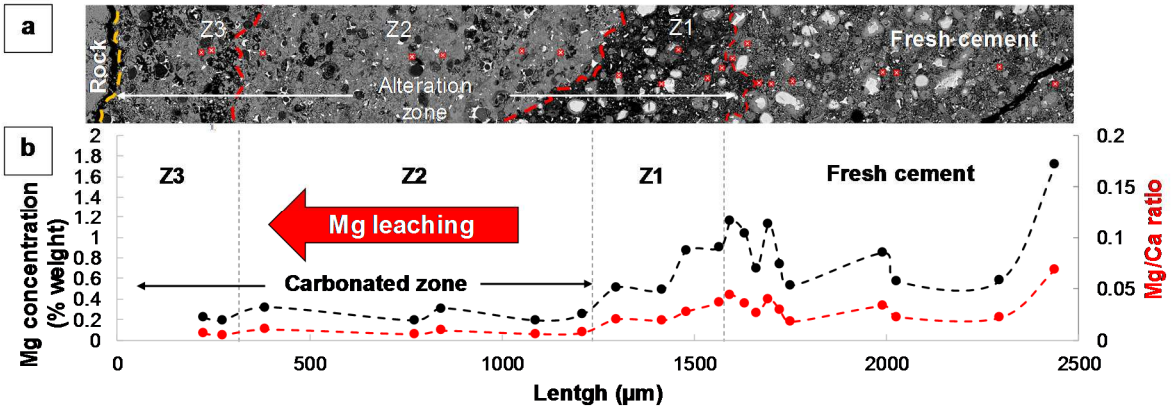

*Figure 91: a) SEM (BSE) picture showing the cement alteration divided in three zones and the unaltered cement for the 21d experiment without salt. Red crosses correspond to the analysis points. b) Evolution of **Mg** concentrations (black line) and **Mg**/**Ca** ratio (red line) along the cement.*

The average **Mg**/**Ca** ratio of 0.033 measured in the fresh cement corresponds to the value determined in the initial cement powder (Table 2) which demonstrate the reliability of the results. The **Mg** concentrations measured in the carbonated zones Z3 and Z2 are lower than in the fresh cement.

These observations indicate a **Mg** leaching during the cement alteration process. In a CO_2-saturated water, the formation of a leached zone within the matrix of a highly carbonated layer of an altered cement has already been observed during laboratory leach tests [197].

The behavior of the **Sr** element in the experimental solution could also originate from this phenomenon.

The decrease of Mg/Ca and Sr/Ca ratios over time with the continuous renewal of the CO_2 laden solution can be attributed to a less important contribution of the cement phase following its carbonation. The faster decrease of Mg and Sr concentrations in solution with regard to the calcium one have an impact, to a minor degree, on the calcite solubility in the experimental solution. A modeling was performed in a system at 60°C imposing a $P_{(CO_2)}$ of 56.2 bars and different Mg concentrations close to our experimental value. 5 simulations were performed with Mg concentrations varying from 0 to 10^{-3} mol.kg^{-1}.

The results confirm a slight increase of calcite solubility with a Mg enrichment of the solution (Fig. 92).

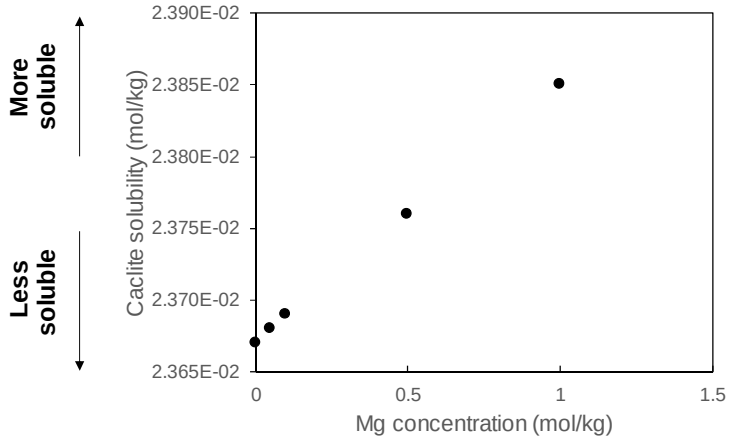

*Figure 92: Evolution of Calcite solubility as a function of the **Mg** concentration in solution.*

Thus, the dynamic of fluid-solid interactions may have locally changed as a result of the modification of transport properties and the induced changes of thermodynamics conditions. In the asperities and the multiplicity of crystalline surface imperfection providing an important specific surface area (largely correlated the rate of heterogeneous nucleation [225; 232]), the chemical reaction has became transport controlled by diffusion. A local oversaturation with respect to the calcite may occur at the pore scale due to poorly mixed conditions, a slight decrease of the $P_{(CO_2)}$, a pH rise, the release of Mg and Sr ions and a chemical gradient in the diffusive boundary layer at the fluid-rock interface. This weak local oversaturation correlated to a fast rate of calcite precipitation may be sufficient to allow the heterogeneous nucleation of calcite crystals on existing surface defects where the free surface energies are lower [233, 234].

Along the cement/rock interface, the nucleation of newly crystalized euhedral micro-calcites covering the grains can be attribuated to a pH gradient influenced by the cement phases that favor crystalline growth.

– PARTIE 6 –
CONTRÔLE STRUCTUREL D'UN RÉSEAU DE DISSOLUTION DANS UN RÉSERVOIR CALCAIRE SOUMIS A L'INJECTION RADIALE D'UNE SOLUTION SATURÉE DE CO_2

– PART 6 –
STRUCTURAL CONTROL OF A DISSOLUTION NETWORK IN A LIMESTONE RESERVOIR FORCED BY RADIAL INJECTION OF CO_2 SATURATED SOLUTION

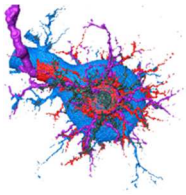

ABSTRACT

The 3D exploration of the architecture of dissolution arrays following the injection of CO_2-laden solution has demonstrated the existence within samples of preferential directions of “attracted” dissolution resulted in systems of highly conductive channels, referred as wormholes from the injection point to the exterior of the samples. In this part, a special attention is paid to the prominent anisotropic aspect of the multilevel dissolution pattern despite the injection process basically isotropic from the bottom hole.

This observations strongly suggest the presence of an initial anisotropy in samples of the Lavoux formation even before experimental treatment. Despite of the dramatic differences in initial conditions of experiments, *i.e.* duration of treatment under reservoir conditions, and, more specifically, different composition of injected fluids, results obtained are thus able to identify prominent directional control of patterns reoccurring in each dataset.

A structural investigation was conducted to define the role of the defaults of the host formation inherited from the regional stress on the direction of propagation and the morphology of the dissolution network (wormholes). A scale invariance, regional tectonic, and geomorphic patterns analyses was used as tools for azimuthal referencing of experimentally obtained dissolution arrays and connection with fault and fracture networks at different scales. The analogy noticed between the spatial propagation of artificially induced wormholes and conduit initiation and growth of cavities in a karst system has motivated this approach. The principal mechanism of a preferable dissolution pattern nucleation developed along zones of structural weakness represented by faults and different scale fractures has been explored.

The results have highlighted the phenomenon of the structural control of the spatial geometry of the dissolution network, as shown by the correlation between the direction of the different wormholes and the main regional stress field. The interplay of intra-stratification, fracture systems, and their kinematical environment largely controls the dissolution pattern induced by CO_2-rich fluids.

These results can be implemented in the risk assessment as an additional information on the spatial spatial and morphologic uncertainties in characteristic shapes for growing dissolution structures.

This part corresponds to the article published in the international peer-reviewed open access journal of geoscience in 2019. Privalov et al. (2019): Structural Control on Dissolution Network in Limestone Reservoir Forced by Radial Injection of CO2 Saturated Solution: Experimental Results Coupled with X-ray Computer

geosciences

MDPI

Article

Structural Control of a Dissolution Network in a Limestone Reservoir Forced by Radial Injection of CO_2 Saturated Solution: Experimental Results Coupled with X-ray Computed Tomography

Vitaliy Privalov *, Aurélien Randi *, Jérôme Sterpenich, Jacques Pironon and Christophe Morlot

- GeoRessources UMR7359 CNRS, Université de Lorraine-CREGU, BP70239 Vandoeuvre-les-Nancy, France; jerome.sterpenich@univ-lorraine.fr (J.S.); jacques.pironon@univ-lorraine.fr (J.P.); christophe.morlot@univ-lorraine.fr (C.M.)
- Correspondence: vitaliy.privalov@gmail.com (V.P.); aurelien.randi@univ-lorraine.fr (A.R.)

Received: 9 October 2018; Accepted: 28 December 2018; Published: 9 January 2019

- **Abstract:** This study was conducted in the framework of the PILOT CO_2-DISSOLVED project, which provides an additional approach for CO_2 sequestration, with the aims of capturing, injecting, and locally storing the CO_2 after being dissolved in brine. The brine acidity is expected to induce chemical reactions with the mineral phase of the host reservoir. A set of continuous radial CO_2 flow experiments was performed on cylindrical carbonate rock samples under geological storage conditions. The objective was to interpret the dissolution network morphology and orientation involved. To explore the three-dimensional architecture of dissolution arrays and their connection integrity within core samples, we used computed tomography. A structural investigation at different scales revealed the impact of the rock heterogeneity on the dissolution pathways. The initial strike of the observed mesoscopic wormholes appears to be parallel to dilatational fractures, with a subsequent change in major trends of dissolution along master shears or, more specifically, a combination of synthetic shears and secondary synthetic shears. Antithetic shears organize themselves as slickolitic surfaces, which may be fluid-flow barriers due to different mineralogy, thus affecting the permeability distribution-wormhole growth geometry induced by CO_2-rich solutions.

Keywords: CO_2-rich aqueous solution; radial injection; dissolution array; X-ray computed tomography; morphology of wormhole; regional strike-slip zone; Riedel shears; artificial karstification pattern

1. Introduction

Capture, transport, and subsequent injection of anthropogenic CO_2 into deep geological horizons of highly-permeable sedimentary rocks effectively reduces atmospheric emissions of CO_2 derived from the combustion of fossil fuels. The injection of CO_2 into deep geological formations uses technologies that have been traditionally applied and verified by the oil and gas industry. However, validating potential storage reservoirs from the standpoint of environmental risks, which may arise from uncertainties in geometrical characteristics of leakage pathways from injection wells into adjoining stratigraphic intervals, is crucial. Leakage of CO_2 could have various impacts, including contamination of groundwater, which affects local health and safety.

Considerable attention has been paid to the suitability of horizons at depths of approximately 1500 m in the central part of the Paris Basin (France) for supercritical CO_2 storage installation. These include 70–80-m-thick oolitic carbonate horizon from the Dogger and uppermost carbonate formation of Oolite

Blanche Series [1,2], which lie directly beneath impermeable argillaceous rocks of Callovian–Oxfordian age. The Oolite Blanche Series can be observed in outcrops at the basin edges, wherein these limestones have been extensively excavated (e.g., in the vicinity of Poitiers and Chauvigny, where Lavoux limestone is still being quarried). This formation serves as an aquifer with moderate salinity that has been used for geothermal projects for more than 40 years.

In accordance with previous experiments [3–5], the reactivity of Lavoux limestone (mainly composed of calcite) is sensitive to pH and, therefore, to the partial pressure (P) of CO_2 in the interstitial solution. Thermodynamic calculations [4] have demonstrated that the volume of dissolved calcite is obviously limited by storage conditions due to the H_2O-CO_2-calcite equilibrium in closed systems. However, these limitations occur at some edges of the dissolution front away from the injection well, where CO_2 is transported along attractive planes of diffusion. Rahbari and Saberi [6] introduced a mathematical model of the growth of this three-dimensional (3D) pattern, where diffusion process, as a 3D Brownian motion, was controlled by the attractive planes. Owing to the complex internal geometry of solute flow paths, including sink conduits and blind pockets, we can expect significant local, real-time deviations of pH-P conditions, which are responsible for dissolution and contemporaneous re-precipitation in some domains of the host rock. According to Fischer and Lüttge [7], the heterogeneity of polycrystalline calcite causes a pattern of fluid flow velocity gradients that retroact on surface dissolution rates. Direct observations using atomic force microscopy, optical interferometry, surface spectroscopy, and related instrumental approaches have provided significant advancements in our understanding of mineral dissolution, in which kinetics are typically dominated by the distribution of defects and defect-driven reactions [8], which may constitute a critical contribution to whole rock reactivity.

Since 2012, the French National Research Agency (ANR) launched the CO_2 DISSOLVED research project [9,10], employing the Carbon Capture and Storage (CCS) concept based on environmentally-friendly technology integrating a geothermal doublet system consisting of two wells targeted for a deep saline aquifer in a carbonate reservoir. The first injection well is used for injecting and storing CO_2 in dissolved form produced by low tonnage emitters, whereas the second production well is employed for simultaneous geothermal energy recovery. This study was conducted in the framework of the PILOT CO_2-DISSOLVED project (funded by the Scientific Interest Group Geodenergies) with the ultimate aim of careful site selection for understanding the geometrical characteristics of possible CO_2 leakage pathways from the injection well during implementation of the forthcoming industrial pilot demonstration project. For this purpose, a test bench (MIRAGES-2), mimicking an injection well at a 1/20 scale (rock/cement/tubing), was developed by the GeoResources Laboratory to allow the continuous radial injection of a CO_2-rich aqueous solution under geological storage conditions.

The characteristics of the dissolution network within reservoir rocks were produced by CO_2-like and more complex fluid-carbonate rock alterations. These are critical for defining possible injection scenarios for feasibility studies related to installation and safe, long-term exploitation of a CCS industrial pilot demonstration project.

2. Investigation and Methodology of MIRAGES-2 Experiments

2.1. Experimental Protocol

The MIRAGES devices were initially designed by GeoResources Laboratory (Nancy, France) to validate the numerical simulations of modes of behavior and the interaction of casing materials (steel, composite materials) with reservoir rocks, including estimation of induced corrosion effects during and after injection of supercritical CO_2 under geological conditions of pressure and temperature. A detailed depiction of MIRAGES experimental devices was provided by Sterpenich et al. [11].

The main objective of a series of new experiments using the MIRAGES-2 [12] device was to obtain a physical and chemical model of the formation of the dissolution arrays linked to the injection of aggressive fluids of different compositions under realistic temperature-pressure storage conditions occurring in the Dogger formation of the Paris basin at a 1500 m depth.

A set of 8 experiments was performed on cylindrical samples of the Lavoux limestone extracted from monolithic bulk samples quarried at the subsurface level from Chauvigny within the *Vienne* River valley (France).

The samples of limestones (Figure 1b) were inserted into a batch reactor made of stainless steel 316SS with a triple Teflon (MAXIMATOR® France, Rantigny, France) coating on the wall of the vessel and the cover lid to avoid corrosion problems (CO_2 + NaCl), which was connected to a coupled system composed by a dual syringe pump (A500 Teledyn ISCO, Lincoln, NE, USA) and liquid mass Coriolis flow meter (Bronkhorst®, Montigny-Les-Cormeilles, France) allowing a continuous and constant injection of aqueous solutions in the core-plug containing dissolved CO_2 and with or without salt (Figure 1a).

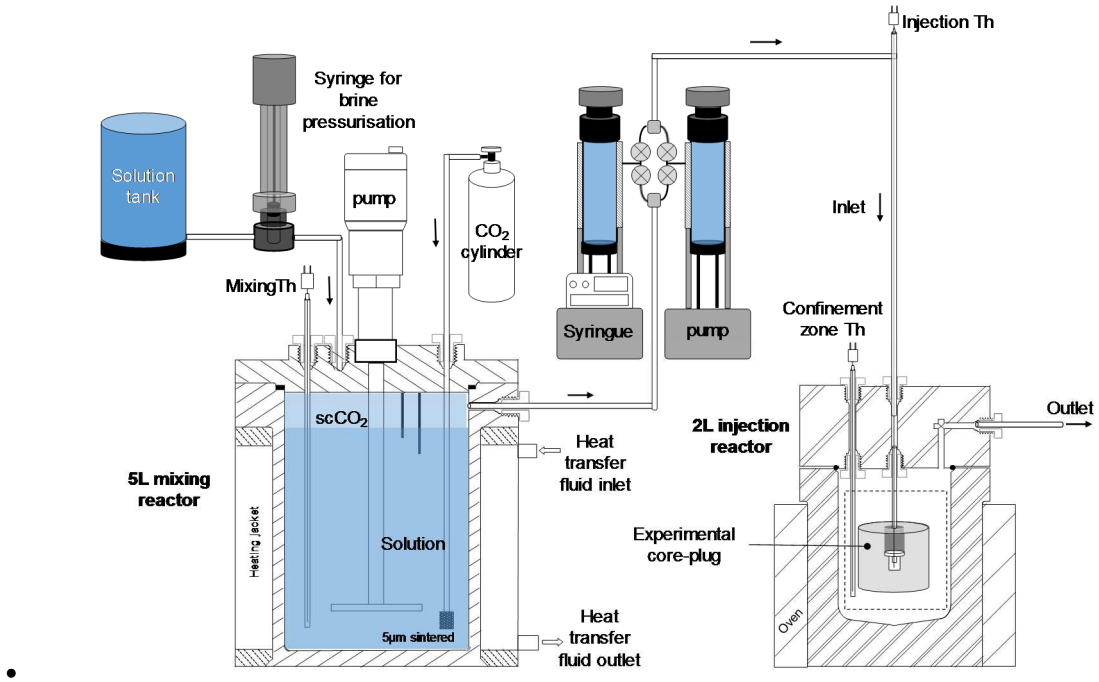

(**a**)

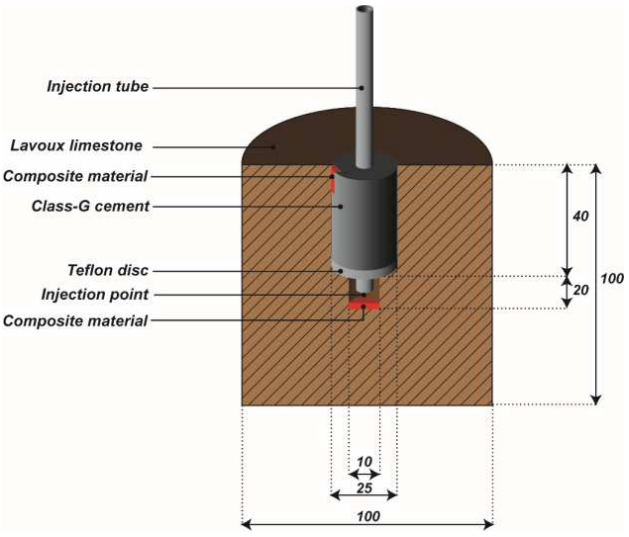

(**b**)

Figure 1. (**a**) Experimental device (MIRAGES-2) used to inject the CO_2-rich solution in the core-plug under controlled conditions of pressure, temperature, and flow rate; (**b**) schematic view of the core-plug and the injection well. Dimensions are provided in millimetres.

Core-plugs were forced into the MIRAGES-2 device for different regimes of treatments with injections of specific fluids: Pure water with atmospheric CO_2 presence (experiment #1), short-term (experiments #2, #6, and #9), and long-term (experiments #3 and #7) with CO_2-dissolved fluids and CO_2-rich saline fluid (experiments #4 and #8; 15 g/L NaCl). All experiments were conducted under thermodynamic conditions similar to real reservoir simulation parameters (e.g., pressure P = 120 bar, temperature T = 60 °C) with a constant rate of fluid injection (150 g/h). All experiments except experiment #1 were performed with dissolved $CaCO_3$ (15 mg/kg) to limit the initial dissolution of the core-plug during the cure period. Refer to previous studies [12,13] for a complete description of the experiment.

Experiment #7 (9.8 days of forced injection into sample equilibrated water with 15 mg of $CaCO_3$/kg of solution and 0.929 mole/kg of CO_2) was carried out for imitation of the real inclination of an injection well (55°) proposed for the pilot project. The conditions of the 8 performed experiments are summarised in Table 1.

Table 1. Summary of the conditions for the performed experiments.

Experiment No./X-ray CT Resolution	Drilling Inclination	Composition of Fluid Injected with Permanent Flow Rate 150 g/h	Time of Curing [1] (Days)	Time of Ageing [2] (Days)	Volume of Injected Fluid (L)
#1/100 μm	⊥	pure water at equilibrium with atmospheric CO_2 = 0.0372 mole/kg	9.10	21.00	71.18
#2/60 μm	⊥	water + 15 mg/L $CaCO_3$ + dissolved CO_2 (CO_2 solubility of the injected solution = 0.94 mole/kg)	10.27	2.58	10.32
#3/60 μm	⊥	water + 15 mg/L $CaCO_3$ + dissolved CO_2 (CO_2 solubility of the injected solution = 0.94 mole/kg)	9.90	20.90	73.70
#4/60 μm	⊥	water + 30 mg/L $CaCO_3$ + 15g/L NaCl + dissolved CO_2 (CO_2 solubility of the injected solution = 0.89 mole/kg)	9.78	21.16	74.32
#6/60 μm	⊥	water + 15 mg/L $CaCO_3$ + dissolved CO_2 (CO_2 solubility of the injected solution = 1.01 mole/kg)	10.77	0.99	3.49
#7/60 μm	#55°	water + 15 mg/L $CaCO_3$ + dissolved CO_2 (CO_2 solubility of the injected solution = 0.93 mole/kg)	9.80	9.95	35.15
#8/60 μm	⊥	water + 30 mg/L $CaCO_3$ + 15 g/L NaCl + dissolved CO_2 (CO_2 solubility of the injected solution = 0.88 mole/kg)	10.02	7.93	27.89
#9/60 μm	⊥	water + 15 mg/L $CaCO_3$ + dissolved CO_2 (CO_2 solubility of the injected solution = 0.96 mole/kg)	10.37	0.52	2.00

⊥ Cores were drilled perpendicularly to the bedding. [1] Time of subjecting sample to the reservoir thermodynamic conditions in a close system. [2] Time of fluid injection under reservoir conditions.

2.2. X-ray Computed Tomography and Scanning Electron Microscopy

To explore the 3D architecture of dissolution arrays and their connection integrity within core samples, we performed computed tomography (CT) using the X-ray Nanotom Phoenix GE system (GE Inspection Technologies®, Limonest, France) at the GeoResources Laboratory, with resolutions varying from 52 μm to 100 μm/voxel. X-ray CT is a non-destructive technique of assessing the density-dependant internal structure of a solid specimen by recording the attenuations of the levels of X-rays after passing through the sample.

The studied samples were illuminated by an X-ray beam with a constant adjustment 145 Kv 300 μm X-ray generator. The dissolution patterns in the internal structure of studied samples were recorded on a 5 Mpx flat panel sensor as a set of radiographic images. The tomography collected 1500 viewing angles (1 radiography by 0.24 degree) for reconstructing the 3D models.

For digital geometry processing and the following 3D visualization, exploration, and quantification analysis of dissolution patterns, VGStudio 2.2 (Volume Graphics, Heidelberg, Germany) and Avizo 9.2 (ThermoFischer Scientific, Hillsbro, OR, USA) software packages were used.

The scanning electron microscope, TESCAN VEGA3 (TESCAN, Brno-Kohoutovice, Czeck Republic), equipped with an energy dispersive X-ray (EDS) detector, was used for microstructural and chemical characterisation of selected fracture surfaces.

3. Experimental Results

Matrix acidizing of the carbonate rocks was triggered by the injection of aggressive fluids in a set of eight different experiments. These experiments generated sets of dissolution arrays, which appeared to be due not only to continuous uniform alteration or the stochastic branch working in porous limestone medium, but also to the physical and chemical competition between enlarging unitary flow paths and tectonically-induced conduits and barriers, involving both fluid-reservoir rock dissolution and precipitation interactions.

3.1. Reactivity of Lavoux Limestone after Comptuted Tomography Inspection

The injection of aggressive fluids promoted dissolution of the limestone in the studied samples from the injection point to the exterior of the samples. After CT inspection, the core plugs demonstrated dissolution networks visible on the CT scans and 3D models (Figure 2).

Notably, prominent anisotropy of the multilevel dissolution pathways was observed, whereas the injection process was basically isotropic from the bottom hole. This strongly suggests the presence of an initial anisotropy in the samples of the Lavoux formation even before experimental treatment. Despite the dramatic differences in the initial experimental conditions, including the duration of the treatment under reservoir conditions and different compositions of injected fluids, the results identify *recurrent directional control of patterns* in each dataset. It appears that the similarity of the dissolution pathways repeated in all experiments must be more than a coincidence. Specifically, the experiments demonstrated that preferential directions "attracted" dissolution and resulted in systems of highly conductive channels, referred to as wormholes. Especially *prominent, similar patterns* in the dissolution arrays can be seen by comparison of the CT scans with related 3D models in pairs of experiments (#1, #2, #3, and #4) presented in Figure 2.

Prior to the experiments, we considered the existence of pre-existing fabrics and related preferential directions that were pronounced in the samples. These directions could facilitate wormhole propagation and the overall growth of the entire dissolution pattern.

(a)

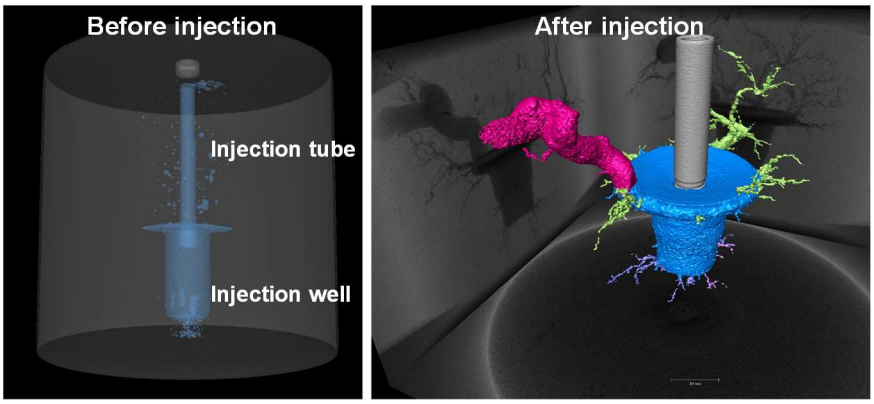

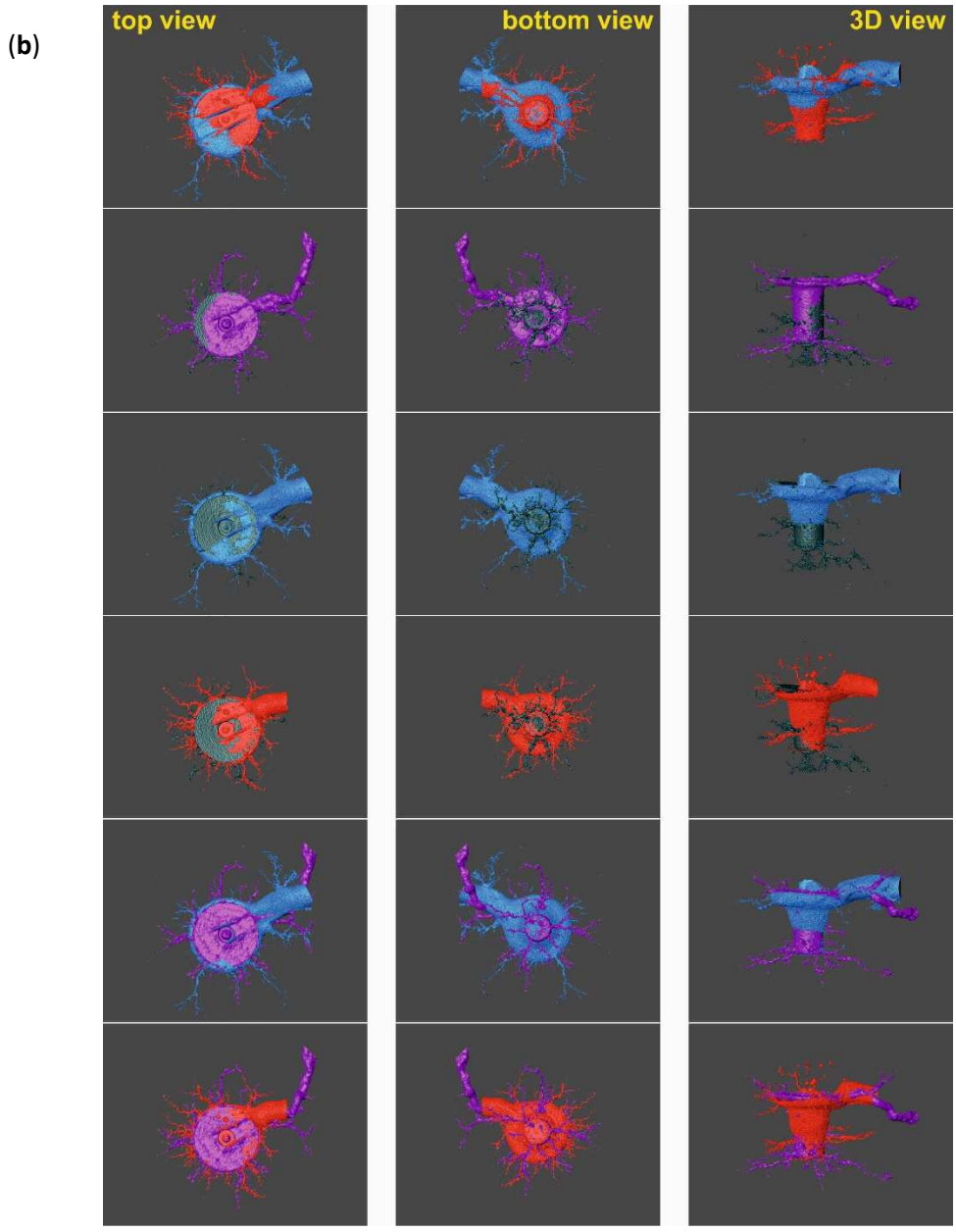

Figure 2. (**a**) Computed Tomography (CT) scan of injection well vicinity before and after injection of CO_2-rich solution. Notice the development of a dissolution network with one dominant wormhole (pink) after 10 days of injection; (**b**) comparison of obtained dissolution arrays (top views, bottom views, and 3D models) based on CT scan results in pairs of experiments. Different colors correspond to the experiment number: Grey is #1, purple is #2, red is #3, and blue is #4. Vertical columns of images correspond to: **Left**–top view in horizontal plane; **middle**–bottom view in horizontal plane; **right**–side 3D view in vertical plane.

3.2. Similarities of Subsequent Dissolution Development in Natural Environments and Artificial Wormhole Propagation from the Standpoint of the Influence of Pre-Existing Structural Discontinuities

Researchers have been looking for the mechanism for wormhole formation and various models to describe this process have been proposed [14–19]. However, there is still no consensus on global wormhole theory. Most of the traditional models [14] advocate the hypothetic random distribution of pores in the shape of cylindrical tubes, with their enlargement being a response to aggressive fluid injection.

Experimental studies of wormhole formation have used a variety of porous systems, including plaster dissolved by water [15], limestone cores treated with acid [16], and salt packs dissolved with under-saturated salt solution [17]. Multiple types of dissolution networks along discreet rock fractures and their zones have been reported [17–19]. This approach to wormhole distribution analysis resembles the conduit initiation and growth of cavities in a karst system, and can be referred to as the principal mechanism of a preferable dissolution pattern nucleation developed along zones of structural weakness represented by faults and fractures of different scales.

The high-permeability subsurface horizons are typically derived from biological and igneous processes and chemical reactions between rocks and fluids, including greenhouse gases, such as carbon dioxide. In sedimentary basins, natural accumulations of relatively pure CO_2 and CO_2 dissolved in formation waters have been found in a number of different types of sedimentary rocks, especially in limestones, dolomites, and sandstones, with a variety of seals and a range of trap types, reservoir depths, and CO_2-bearing phases. Geological storage of CO_2 dissolved in formation waters occurred as a natural process in carbonate rocks (e.g., limestones) for millions of years and this natural laboratory provides a basis for understanding possible scenarios of the behavior of industrial CO_2 storage in carbonate lithology formations.

More specifically, long-term natural storage of CO_2 in carbonate rock aquifers are most likely accompanied by artificial karstification due to acidic water-rock interactions. Conduit initiation and progressive growth of cavities in a karst system are usually assumed to be controlled by non-linear kinetics [20] that allow CO_2-enriched aggressive water to penetrate geological formations. In most cases, this process mainly occurs along zones of structural weakness represented by faults and fractures on different scales [21,22].

Moreover, competition exists between conduit evolution along different fractures, and many karst corridors are closely related, not only with open tension fractures, but also with relatively tight strike-slip faults [20]. The structural network of faults and fractures, recognizable both at the surface and inside the karst systems in the transpressional structure of the Italian Dolomites, has been interpreted to be consistent with a Riedel shear system [23]. The existence of preferential orientations of conduits within karst networks has been demonstrated [24]. The structural relationship between fault families and the preferential orientation of cave survey data was identified within the Picos del Europa Mountains (Spain) [22] and a dextrally reactivated shear zone was recognized [25].

Reactions of dissolution—precipitation during experimental injection of CO_2 into a limestone reservoir—predominantly occur within the fractures, which serve as preferential paths for fluid flow [26]. However, the specifics of the laboratory equipment being used in this study [26] forced unidirectional transport of aggressive liquid into the specimen, with subsequent propagation of the dissolution pattern within fractures exclusively oriented along the maximal gradient of the fluid flow. This means that the effect of natural sample heterogeneity and permeability anisotropy caused by fracturing and layering on dissolution pattern structure is beyond the scope of such experiments. The ability to induce radial fluid flow in relation to an injection point is one of the major advantages offered by the MIRAGES-2 device, which ultimately helps to identify and quantify experimental results from the standpoint of understanding the spatial relation between the fracture distribution in a specimen and the subsequent dissolution development in natural environments of limestones reservoirs.

3.3. Structural Arrangement of Planar Microfractures in Samples of the Lavoux Limestone from X-ray Computed Tomography

We performed a detailed examination of CT scans of fresh samples of Lavoux limestones with a 5 μm resolution in sub-horizontal sections and observed regularly arranged microscale planar fractures along which we recorded small amounts of dextral and sinistral shear displacements (Figure 3a).

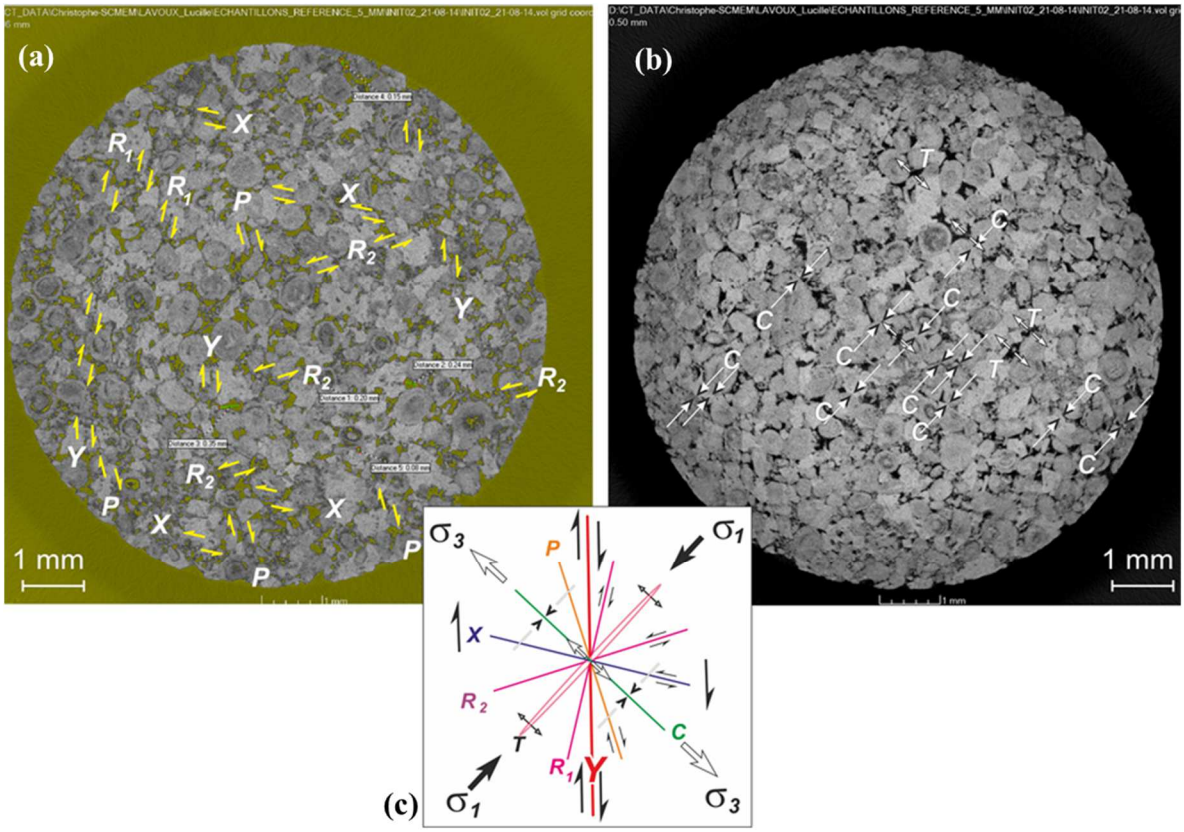

Figure 3. (**a**) CT scans of a sample of the Lavoux limestone (resolution 5 μm) in sub-horizontal sections with delineation within them at microscale-level planar fractures of Y, R_1, R_2, P, and X types with identification of the direction of shear displacement (double yellow arrows); (**b**) stylolitic contacts of ooids C (white arrows), and dilatational joints; (**c**) Note, CT scans and the constructed (on the basis of interpretation of obtained kinematic types of fractures) model of formation of subsidiary fractures (modified from Hancock [27]) within dextral strike-slip zone are not azimuthally referenced.

These shear-stress-affected surfaces contain minute brecciated fragments abraded from larger ooids grooved and cracked particles. Fractures propagated mainly along ooidal grain boundaries, but also several intra-ooidal cracks with lateral shifting of grain fragments are recognised (Figure 3a). Also, tension fractures (T) or dilatational joints with no displacement parallel to the sidewalls of the fracture and tectonically-induced stylolitic contacts of ooids, as a product of intergranular pressure-solution, are visible (Figure 3b).

The presence of stylolitic planes (C) in horizontal sections is often an indication of a volume loss within the deforming material under main compressive tectonic stress (σ_1) perpendicular to the stylolites. The tectonic stylolites in the WNW–ESE direction in the mid-Jurassic oolitic reservoirs in the Paris Basin were described previously by Granier and Staffelbach [28], who indicated that compressional stress (σ_1) was applied from NNW–SSE directions (azimuth N150° E). Also, specific lineations, orthogonal to stylolites, have been delineated and interpreted as dilatational joints (T). Here, fracture surfaces exist normal to the main tensile stress during joint formation.

A total set of fractures identified within horizontal CT scans could be generated within the dextral strike-slip zone with the principal direction, Y, in the classical framework scheme of development of the set of subsidiary structures within the strike-slip zone [27]. These subsidiary structures consist of:

- Conjugated dextral synthetic (R_1) and sinistral antithetic (R_2) Riedel shears;
- conjugated dextral synthetic P and sinistral antithetic X shears; and
- *stylolitic planes* (C) perpendicular to the main compressive stress, σ_1.

- Tension fractures (dilatational joints) were T perpendicular to the main tensile stress, σ_3, which formed parallel to the strain ellipse short axis, C.

All these fissures or microfaults are connected to one another, forming the specific pattern of an anastomosing network of fissures (Figure 3c). Additional support for the presence within the studied samples of microcracks induced by strike slip faulting may be obtained from the analysis of the vertical sections of Lavoux limestones with the help of binary filtration of CT scans. The vertical section (Figure 4a) demonstrates the presence of both features, i.e., elements of intra-stratification and characteristic shapes of minute-scale flower structures [29], which can be interpreted as upward splaying shear microfaults. These findings are in good agreement with previously published results of geostructural surveys within the Saint-Maixent-l'École mapping sheet located in the vicinity of Chauvigny [30]. The faults inferred from the Mesozoic formations tend to join downward into single strands in the same way (Figure 4b), as we documented for high-resolution CT scans of millimeter-scale fragment of Lavoux limestone specimen.

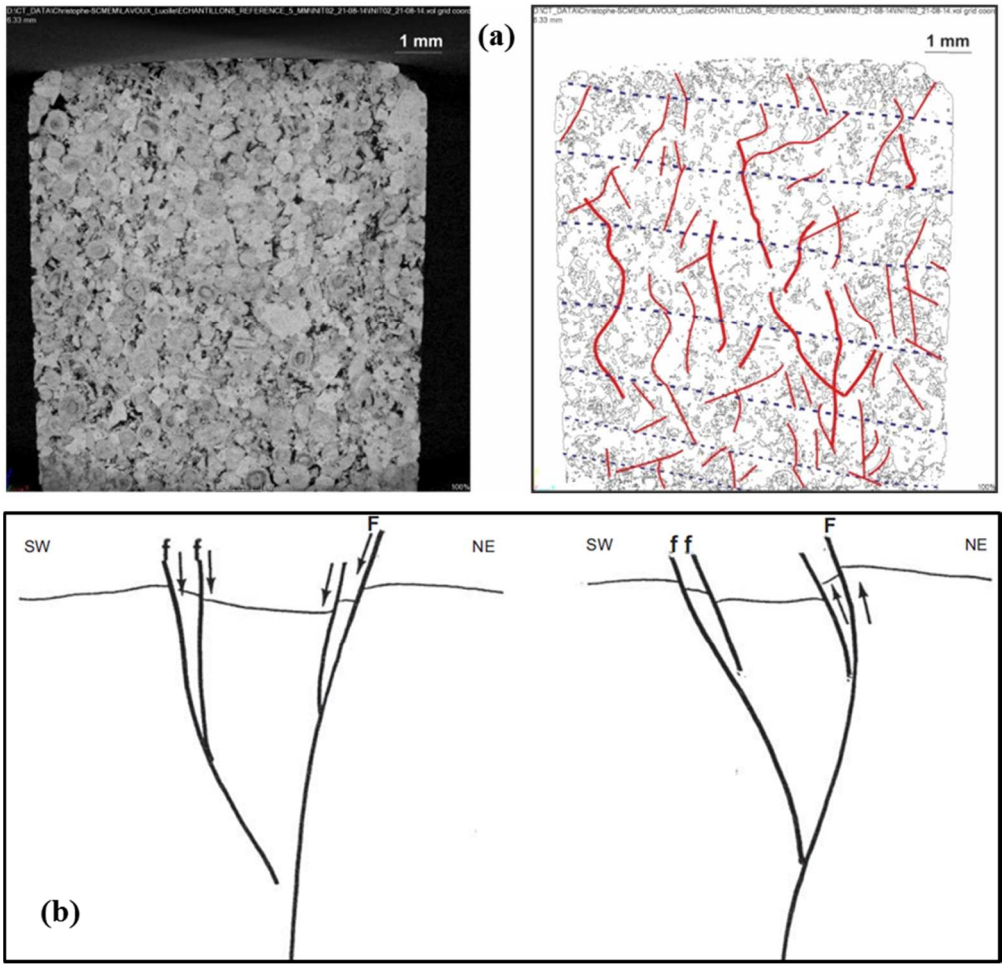

Figure 4. (**a**) CT scans of samples of Lavoux limestone in the vertical section with delineation within at the microscale-level microlayer boundaries (dashed blue lines) and upward splaying shear microfaults (red lines); (**b**) structural data of the Saint-Maixent-l'École graben [30]; this segment of the Southern Armorican Shear Zone is located ~80 km southwest of Chauvigny. The major faults "F" inherited the Variscan basement faults and complimentary sedimentary carapace's antithetic faults "f" tend to join downward into single strands, forming a specific pattern of flower structures as a typical marker of lateral movements associated with strike-slip zones. Note, this structural interpretation of the regional tectonic structure of the study area (**b**) is compatible with our results of microfaults' matrix interpretation (**a**). Note also for (**b**) the regional scale (several tens of km) to be compared with the centimetric scale in (**a**).

Here, localization of discrete microfractures corresponds to inherited mechanical anisotropy caused by millimeter-scale sedimentary layering. From our premise of preferential direction of dissolution arrays obtained within the results of MIRAGES-2, experiments should be related to precursors of brittle microcracks nucleation, resulting from the influence of the natural strike-slip stress field that affected the Lavoux limestones in-situ within the Chauvigny quarry location.

The azimuthal referencing systems of revealed microcracks in the Lavoux samples were derived using scale invariance and regional tectonic and geomorphic patterns analyses.

3.4. Scale Invariance, Regional Tectonic, and Geomorphic Patterns Analyses as Tools for Azimuthal Referencing of Experimentally Obtained Dissolution Arrays and Connection with Fault and Fracture Networks at Different Scales

The scale invariance of geological phenomena is one of the first concepts taught to students of geology [31]. Without the scale bar, it is mostly impossible to determine whether the delineated fracture pattern is a result of the interpretation of satellite imagery, aerial photographs, outcrop-scale documentation, or fault damage zone inspection after visual core observation, even if these are nano-fissure systems obtained from X-ray CT scans. There is ground truth of experimentally-derived similarities between shear zones of different magnitudes [25]. Zooming into details of arrangements of discrete brittle and semi-brittle fractures within shear zones of different scales [27,29,32] proves that there is no principal difference between processes of crustal mega-scale, local meso-scale, and even micro-scale shear zone formation in terms of the arrangement of subsidiary faults and their kinematic types.

Can we use this scale invariance phenomenon to derive a suitable solution for azimuthal referencing systems of microcracks deduced from CT scans in the samples of the Lavoux limestone? We think this is possible if we consider the information about trends of tectonic structures, topography, and drainage patterns of the area of the adjoining place of sampling. The Chauvigny site and the related quarry are located within the Vienne River valley. The outcrop and quarry, formed during the Jurassic period, rests in a depression between two Variscan structural highs: The Armorican Massif and the French Massif Central (Figure 5).

The tectonic patterns and kinematic characteristics of the Dogger formation are poorly understood. However, the typical underlying structural grain recognized in both the Southern Armorican Massif and the north-western edge of the French Massif Central is the presence of dextral transcurrent strike-slip faults within the frame of the Southern Armorican Shear Zone (SASZ; Figure 5).

During Variscan times, the Armorican Massif underwent deformations related to a major continental collision between Gondwana and Laurussia [34]. These resulted in the development of large dextral shear zones, including the SASZ, whose occurrence has been traced to the north-western edge of the French Massif Central. The dextral strike-slip component of the displacement is widely recognized across the Middle-Late Paleozoic Europe along NW–SE- and W–E-striking subconcentric wrench faults, e.g., Biscay-Pyrenees, Northern and Southern Armorican, Bristol Channel-Bray-Vittel, and North Artois faults [35,36].

Numerous neotectonic paleostress reconstructions, analyses of focal mechanism of earthquakes, and borehole breakouts across the entire Paris basin suggest that this right-lateral deformation of NW–SE- and W–E-striking subconcentric wrench faults is still ongoing. Shear patterns within the SASZ of Variscan age were independently mapped by different authors [37,38]. However, microseismical data showed that the SASZ is still a geodynamically active zone clearly pronounced in geomorphic patterns extracted from satellite imagery [39].

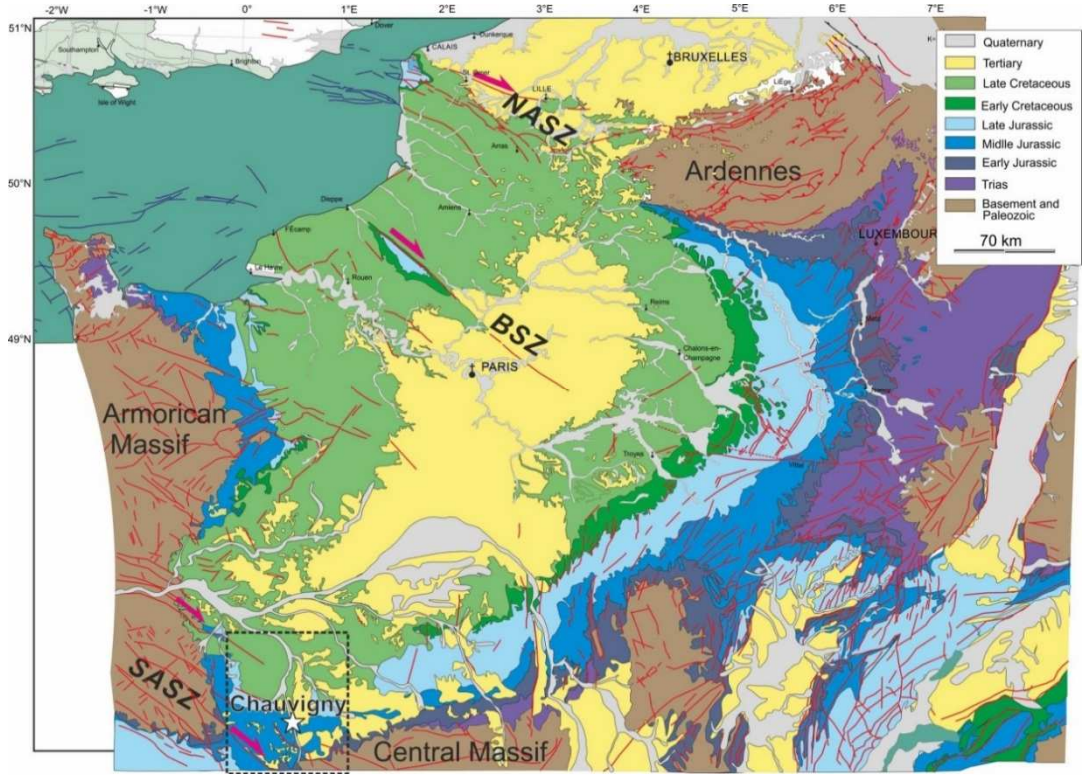

Figure 5. Geological map of the Paris Basin modified from the geological map of FRANCE (BRGM: Bureau de Recherches Géologiques et Minières - French geological survey) [33]. The rectangle with a dashed border shows the location of the frame of digital elevation model (DEM) for the Vienne Department region being used for the analysis of morpholineaments represented on Figures 6 and 7. SASZ—South Armorican dextral shear zone; BSZ—Bray dextral shear zone; NASZ—North Artois dextral shear zone. The white star marks the position of the Chauvigny quarry.

Gunzburger and Magnenet [40] used the up-to-date extensive synthesis of a huge database of outstandingly dense stress measurements in the Paris Basin obtained by ANDRA (the French radioactive waste management agency) in the framework of the feasibility study of underground nuclear waste storage. They confirmed that, on average, the major horizontal stress, σ_1, in the sedimentary cover of the basin has a constant NW–SE orientation, which is similar to the orientation of σ_1, generally accepted in the underlying basement. This means that Jurassic sediments overlying the Southern Armorican Shear Zone (SASZ) must be affected by this right lateral strike-slip faulting here. One of the possible methods to determine the proper spatial position studied in MIRAGES-2 device samples and fracture networks is to study these issues over the terrain overseen by the entire Vienna Department.

There is considerable evidence [41] that river valleys or, broadly speaking, ravine-gully networks follow tectonic structures, which are, to a large extent, determined by neotectonic processes and the related stress-field. This geomorphic phenomenon of neotectonically-controlled drainage networks is closely related to selective erosion process within zones of structural weakness.

A number of researchers [41,42] have used similarities between morpholineaments extracted from drainage patterns and mapped joint-fault distribution for identifying structural trends and delineating structure that have are buried, deep-seated, or masked by younger sediments. Analysis of digital models of land surface and river valleys, and ravine-gully networks by means of numerical geomorphology, provides a basis for recognizing faults and understanding their mutual arrangement and kinematic types. According to Scheidegger [41], joints controlling drainage networks and river valleys fragments are of tensile and shear origin and can be used as an effective instrument to reconstruct the neotectonic stress field.

So, to find a solution with azimuthal referencing of revealed fractures in the Lavoux samples, we decided (1) to delineate morpholineaments based on analysis of digital elevation models (DEM) of the land surface and (2) to perform spatial analysis of drainage patterns.

Figure 6 exhibits the shaded-relief elevation and drainage patterns in the Vienna Department area. Yellow dashed lines within Figure 6b correspond to morpholineaments extracted from a shaded-relief elevation visualization model. The lineaments visible here show the primary WNW–ESE orientation trending the SASZ as well as the lineations of subsidiary submeridional and sublatitudinal faults that appeared because of the dextral reactivation of the shear zone. However, the most spectacular evidence of right lateral reactivation of the SASZ and identification of trends of the principal and subsidiary fault systems is the fact that its formation can be derived from an analysis of drainage network patterns.

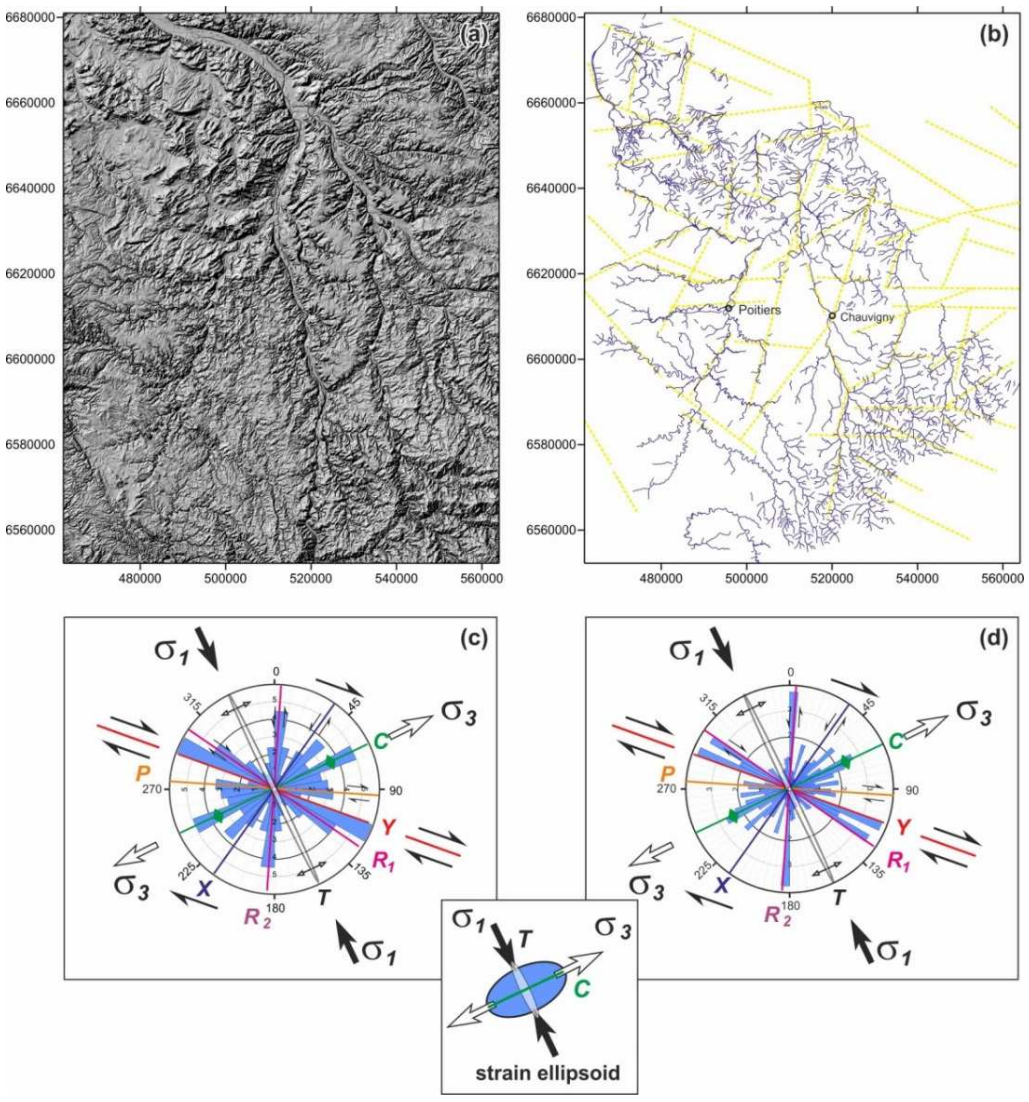

Figure 6. (**a**) Shaded-relief elevation and (**b**) drainage patterns in the area of the Vienna Department. (**c**,**d**) show drainage segment orientations in the rose diagrams with differentially assigned petal widths (10° and 5°, respectively). (**b**) Yellow dashed lines correspond to morpholineaments extracted from a shaded-relief elevation visualization model. The lowermost detail demonstrates a neotectonic strain ellipsoid orientation responsible for the formation of the recent drainage network.

Results of this analysis are presented in Figure 6c,d as drainage segment orientations in rose diagrams with differentially assigned petal widths (10° and 5°, respectively). The major petal anomalies within the constructed rose diagrams are critically dependent on the main neotectonic stresses directions and the strain ellipsoid.

Both the most frequent drainage WNW–ESE-orientated lineations in Figure 6d coincide with the striking domain of the main dextral Y-shears and dextral R_1-shears. The angle between the bulk shear-zone boundary (or Y-shears) and R_1-shears is ~15°, which corresponds to a $\phi/2$ ratio [27], where ϕ = 30 ± 2° is the internal friction angle of the host rock (Lavoux limestone) involved in strike-slip deformations.

Other drainage segment orientation extremes within the study area reflect submeridional NNE–SSW striking R_2 sinistral shears, ENE–WSW striking compressional structures C (stylolitic planes within reversed faults and related compressional fold structures), dextral sublatidional P-shears, and sinistral X-shears.

The strike of principal shear zone Y (azimuth 105–110°) and internal arrangement of subsidiary structures: R_1 (azimuth 120–125°), R_2 (azimuth 0–5°), C (azimuth 60–65°), P (azimuth 90–95°), and X (azimuth 30–35°), are consistent with the strain ellipsoid where the principal compression stress (σ_1) is 150–155°, with trending and extension stress (σ_3) of 60–65°. Both principal stresses (σ_1 and σ_3) are lying sub-horizontally in the strike-slip stress regime.

Actually, the Vienna River's deflecting and meandering pattern (Figure 7a) can be represented by a combination of segments of a set of faults developed due to the right lateral reactivation of the SASZ.

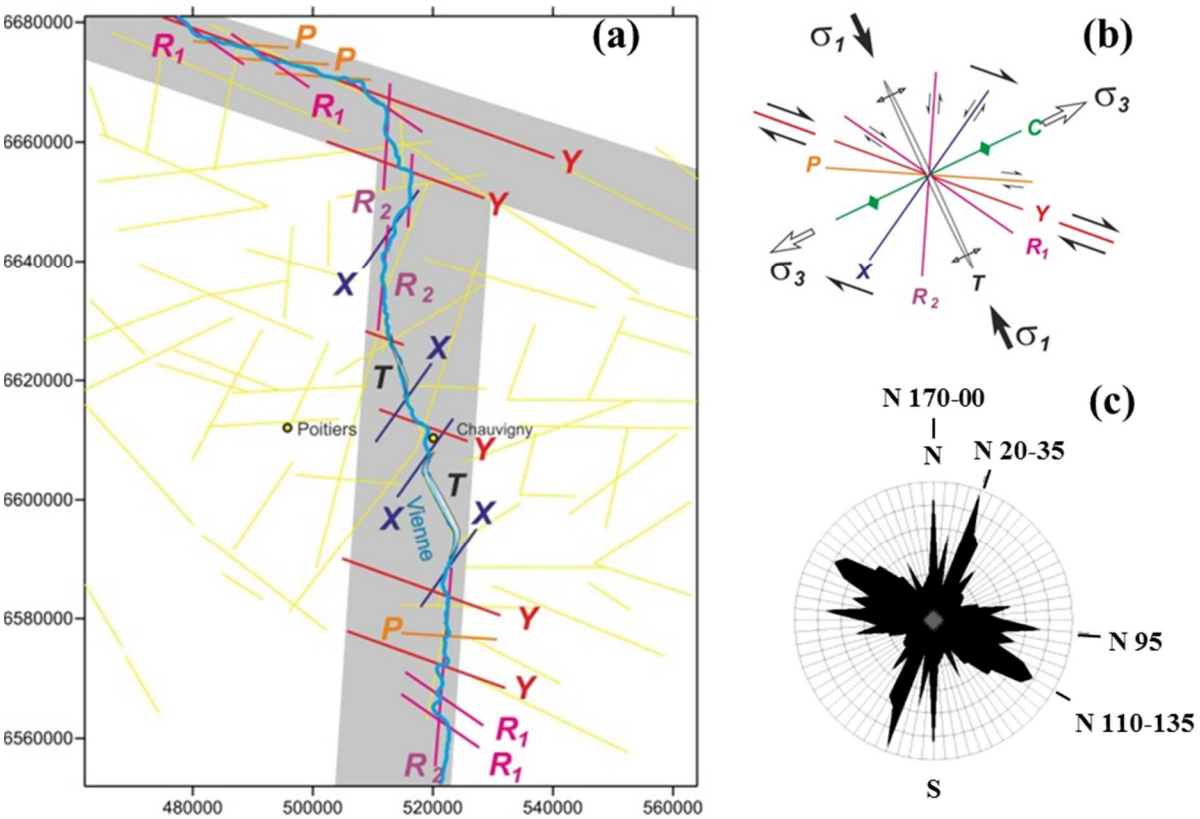

Figure 7. (**a**) Representation of major and minor trends of the Vienne River valley (shown by the blue line) derived from topography DEM as a combination of 105–110°, trending master shears Y, complimentary shears of R_1 (azimuth 120–125°), P (azimuth 90–95°), R_2 (azimuth 0–5°), X (azimuth 30–35°) types, and 150–155°, trending extensional joints T in a lazy S-shape. We inferred from the analysis of drainage patterns in the Vienna Department the azimuth of σ_1, the maximum principal stress in the strike-slip regime, is about N150–155° E. Yellow dashed lines represent morpholineaments extracted from the shaded-relief elevation visualization model (Figure 6b). Grey zones correspond to two major directional clusters of the Vienne River valley represented by the master Y shears and secondary antithetic R_2 shears. (**b**) Fractures orientation from this study. (**c**) Fractures identification from the Poitou threshold" [43].

All major trends of the Vienne river valley seen in the topography DEM are represented by two major clusters corresponding to master Y shear and secondary R_2 shear directions. However, the entrenched river's meanders appear to be composed of a number of differently-oriented straight segments controlled by fractures (lineaments). Streams follow these lineaments represented by master shears Y and complimentary shears of R_1, P, R_2, and X types, as well as dilatational fractures, T.

In accordance with Cornet and Röckel [44], the statistical distribution of the tension fracture orientations, identified within both the Dogger and the Oxfordian limestones of the Paris basin, exhibits a strong preferential orientation in the N150–155° E direction, i.e., parallel to the maximum horizontal stress direction developed during the Alpine tectonic orogeny.

The trend of extensional fissures, T (azimuth 150–155°), is relatively weakly expressed in the rose diagram for the entire drainage pattern of the study region. However, it becomes important for the Vienne River in the area just south and north of Chauvigny and seems to be morphologically and rheologically related to the outcropping, which is a relatively narrow strip of brittle Lavoux limestone. The characteristic lazy S-shape of the dilatational fracture, T, was created by the right lateral faulting along the set of master Y-shears, whose strikes correspond to the direction of the SASZ. We inferred from the analysis of drainage patterns in the Vienna department (Figures 6 and 7) the azimuth of σ_1, the maximum principal stress, is about N150–155° E.

These results are in good agreement with the general features of neotectonic stress reconstructions for the Poitou threshold and adjoining massifs summarized in previous publications (Figure 7c) [43–45]. Thermal remote sensing data allowed us to define the relation between fracturing and basement cover. Several observation studies of the outcrops of the Jurassic limestone defined the main directions of the preferential fractures (linked to the tectonic of the region). The cumulative rose diagram presented in this study (Figure 7b) confirms that the topolineaments controlling the Vienne River valley geometrical pattern developed in concert with two families of regional fractures: (1) Y, R_1, and P shears and (2) R_2 and X shears. The slight maximum corresponding with tension fractures T is visible on this rose diagram.

3.5. Deciphering Spatial Orientations of Preferential Propagation of Dissolution Arrays after Experiments

Since Lavoux limestone sampled in-situ were affected by regional strain within a crustal-scale shear zone, we assumed that our samples, even without being subjected to the action of a regional stress field after extraction from the quarry, bear strain scars, i.e., fractures that can control or at least affect the morphology of the wormhole network.

The mechanical anisotropy caused by regional tectonic stresses in samples before experimental treatment seems to be a plausible factor for deciphering the spatial orientations of preferential propagation of experimentally-obtained dissolution conduits. The identical initial microstructure of samples extracted from one bulk sample of Lavoux limestone provides a strong basis for meaningful comparison of results. The azimuthal referencing of dissolution arrays was performed via rotation of obtained horizontal CT scans to provide the best fit in terms of an alignment for discrete fragments of dissolution arrays (which revealed microcracks enlarged by a dissolution process) with the scheme of orientations of kinematically-defined and mutually-crosscutting fracture sets inferred from regional tectonic and geomorphic patterns analyses (Figures 6 and 7).

Azimuthally-referenced CT scans of dissolution arrays and principal wormhole morphology, derived from the results of a spatial comparison of the results of experiments #1, #2, #3, and #4 (Figure 8) strongly support the influence of a principal displacement zone corresponding with bulk shear displacement Y (azimuth 105–110°) on the studied samples' right lateral reactivation within the limits of the SASZ, which affected the Dogger Formation in the region of sampling Lavoux limestone (Chauvigny quarry).

A total set of subsidiary Riedel system structures identified within horizontal CT scans of fresh samples (Figure 3) and samples after experiments (discrete fragments of dominant wormhole and entire dissolution patterns) demonstrate a strain ellipsoid, where the principal compression stress (σ_1) is

150- 155° and extension stress (σ_3) is 60–65°. Both principal stresses (σ_1 and σ_3) are lying sub-horizontally in the strike-slip stress regime.

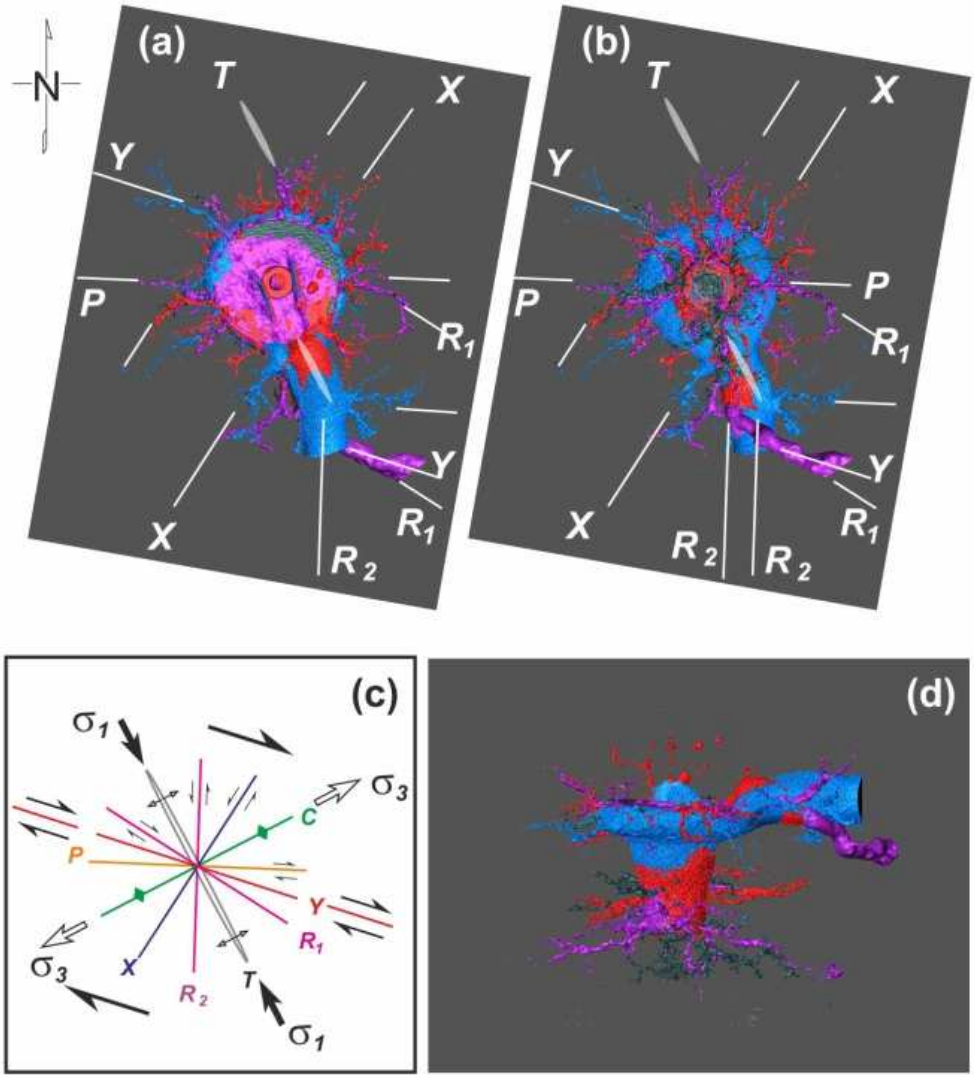

Figure 8. Azimuthally referenced structural control of dissolution arrays and principal wormhole morphology derived from the results of a spatial comparison of the experimental results: #1 (shown in grey), #2 (shown in purple), #3 (shown in red), #4 (shown in blue) in the framework of depicted orientations of fractures (**c**) appeared to be pronounced in the original sample of Lavoux limestones: (**a**) top view; (**b**) bottom vertically mirrored view; and (**d**) side 3D view.

4. Discussion

The spatial geometry of progressively dissolving limestone media affected by CO_2-rich solution injection into a well remains poorly understood. The most critical issue is the question about the morphology of the growing dissolution cavity, which could be theoretically represented by three possible scenarios.

The first scenario assumes mean dissolution rates in limestone with an appearance of a dissolution array of quasi-isometric shape that grew due to the stable dissolution front propagating in relatively homogeneous porous media. Here, mineral dissolution always occurs at the same distance from the injection point. The second scenario assumes an appearance of a dendritic dissolution pattern resulting from stochastic dissolution branchworking in porous limestone medium, where permeable regions have already inherited a pre-existing ramified pattern of chaotically connected macro-pores.

The third scenario supposes the highly channelized shape of dissolution arrays targeting fractures and zones of structural weakness. In radial flow, the last scenario provides a basis for considerable 3D variation in distances between the dissolution front and the injection point of the well. This variation might be subsequently eventualized in the trend in the dominating single principal wormhole as a potential leakage pathway from the injection well into adjoining stratigraphic intervals.

The results of our experimental studies, with the help of the MIRAGES-2 device, indicate the ground proof of the third scenario, where localized fast preferential fluid pathways are dependent on the pre-existing fracture network. We documented quick directional dissolution front propagation in the final scene of the dominant wormhole development in most cases of CO_2-rich solution injection into core specimens, prominently pronounced even for relatively short time-driven experiments, #9 (12 h ageing, Figure 9) and #6 (24 h ageing, Figure 10).

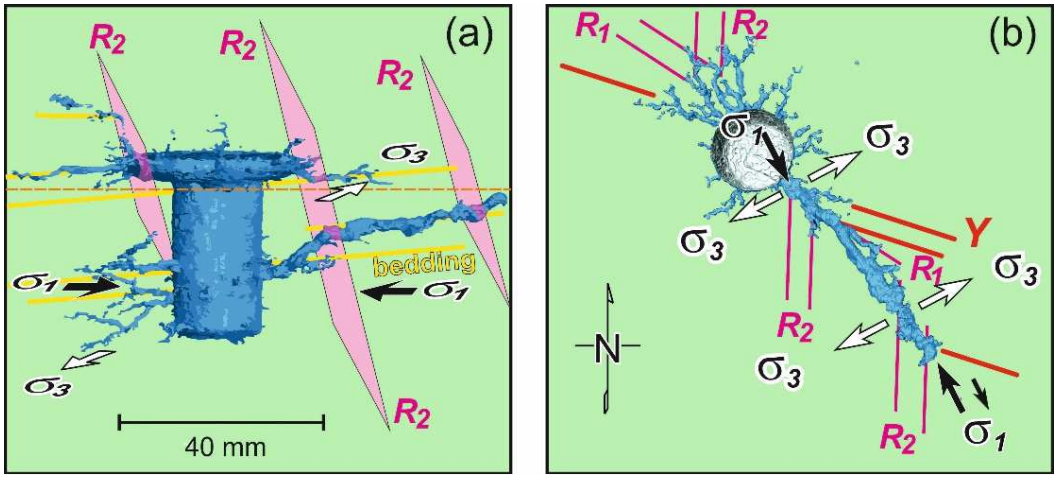

Figure 9. Results of structural interpretation of dissolution network/wormhole morphology for experiment #9 (12 h of CO_2-rich solution injection into sample): (**a**) 3D model and (**b**) top view of the 3D model after CT inspection, horizontally cut at the level of the orange dashed line within inset (**a**).

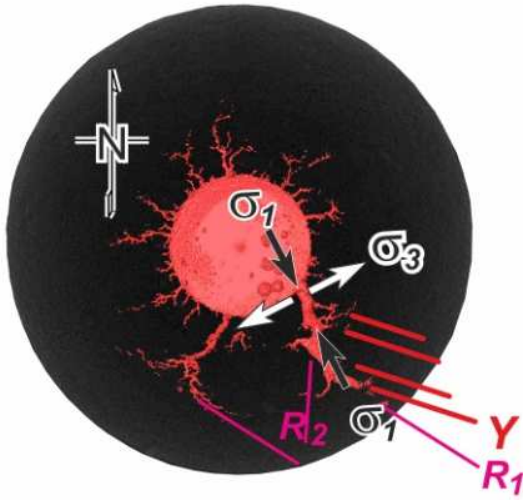

Figure 10. Results of structural interpretation of the dissolution network/wormhole morphology for experiment #6 (24 h CO_2-rich solution injection into the sample).

Additional information about the distribution of dissolution networks and azimuthally referenced wormholing morphology trends were experimentally revealed after structurally interpreting the results of experiment #7 (Figure 11). From a technical point of view, experiment #7, with a core plug drilled at 55°, seems to important because it was performed to mimic the real inclination of a pilot project injection well.

The results of 2D and 3D delineating of the dominant wormhole (Figure 11) indicate the non-horizontal saltatory mechanism of its propagation inside the core specimen. The spatial trend of the wormhole was governed by the interplay of both distributions, including the fracture systems with dramatically variable conductivity, which might serve as regions of attractors or obstacles for dissolution pathways, and intra-stratification (bedding) elements within the entire sample structure.

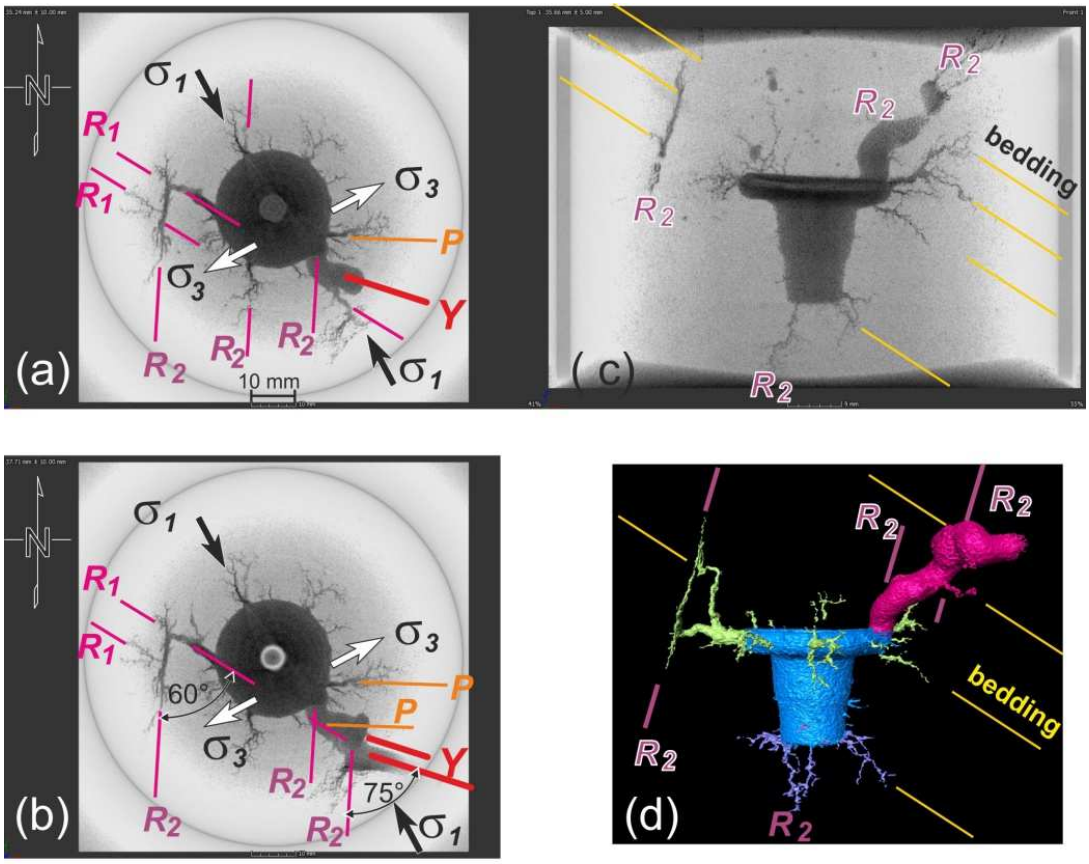

Figure 11. Results of structural interpretation of dissolution network /wormhole morphology for experiment #7 (10 days of CO2-rich solution injection into sample drilled with inclination imitating injection well): horizontal CT scans showing progressive development of the principal wormhole from the level closed to the injection point (a) to the level closed to the top of cylindrical sample (b); vertical CT scan in E-W direction (c); 3-D model (d), wherein principal wormhole is shown in pink.

So, on horizontal CT scans obtained of the dissolution mosaic (Figure 11a,b), it is shown that conjugated Riedel shears, R_1 and R_2, intersected with one another and produced typical zones of strike-slip deformations with a rhombic block pattern. A model of experimental observations was reported with the angle of radial separation of discrete wormhole precursors 60° from each other under radial flow wormholing [46], which accommodates the effects of permeability anisotropy caused by natural fracturing.

From our point of view, this angle reflects the angle between the conjugated Riedel shears, $60° = 90° - \varphi$ [27], where $\varphi = 30 \pm 2°$ is the internal friction angle of the host rock (Lavoux limestone) involved in strike-slip deformations. Notably, in some cases, the rhombic pattern of dissolution consists of fragments of master dextral Y-shears and antithetic sinistral R_2 shears, intersecting each other at an angle of about $75° = 90° - \varphi/2$ [27] (Figure 11a,b).

The initial strike of the observed mesoscopic wormholes appears to be NNW–SSE, trending parallel to dilatational fractures T (azimuth 150–155°), with a subsequent change in the major trends of dissolution along the master Y shears (azimuth 105–110°) or, more specifically, including the combination of synthetic R_1 shears and secondary synthetic P shears.

Practically, the same trend governing the wormhole strike is depicted in the rose diagram of the skeleton model constructed for the principal wormhole developed during experiment #7 (Figure 12).

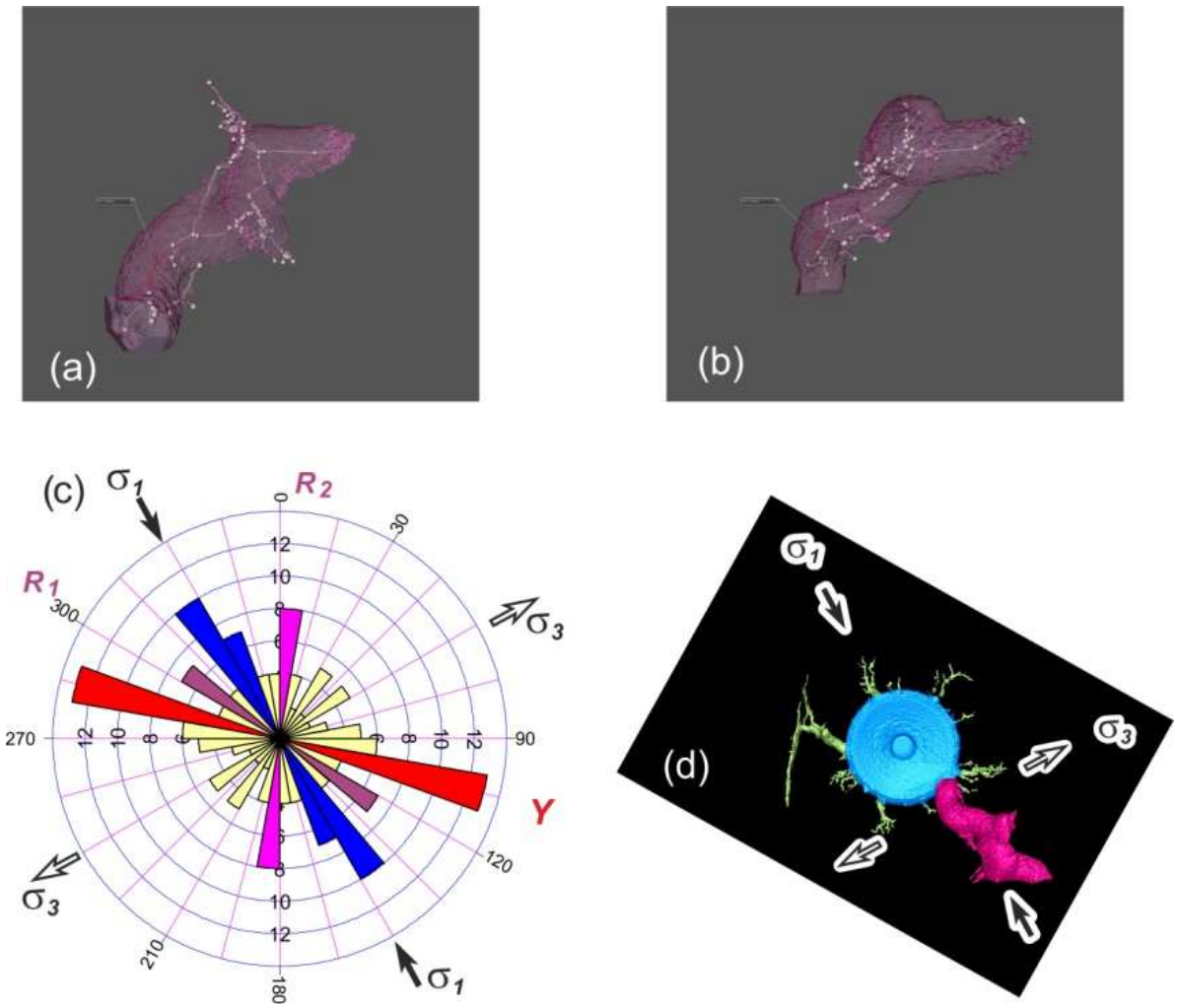

Figure 12. Skeleton model from CT 3D visualization of the principal wormhole represented as the (**a**) bottom and (**b**) vertical view of experiment #7. (**c**) Rose-diagram depicting the preferential directions of the growing principal wormhole, (**d**) which is shown in pink in the top view of the 3D model.

The revealed antithetic R_2 shears served as obstacles for dissolution pathways, creating conditions for "jumping" a wormhole from one level to another elevated level (Figures 9–12).

Microstructural analysis of the studied sample (experiment #7) via binary filtration of high-resolution photographs of the R_2 fracture wall demonstrated that this antithetic Riedel shear organizes itself as a rough indented surface due to the presence of slickolitic teeth oblique to the surface of shear displacement (Figure 13).

At this millimeter scale, small conic dissolution pits are visible parallel to the maximum compressive stress, σ_1.

Additional proof of the presence of conically shaped localized slickolitic teeth was derived for the same wall at the micron scale with the help of Scanned Electronic Microscope (SEM) image analysis. The teeth inclined to the wall of the fracture fossilized signatures of the stress field clearly indicate the strike-slip kinematic type of this fracture (Figure 14).

Figure 13. Correlation of results obtained with help of the CT 3D model in (**a**) the W–E direction and (**b**) microstructural analysis of a high-resolution photo of the vertical section of the studied sample for experiment #7 with outcrop scale structural patterns in the quarry excavating the Lavoux limestones. Note, the elements of the roughness for the slickolitic surface of R_2 shears affected the dissolution pathways and geometric shape of the principal wormhole, shown in pink in the inset in (**a**).

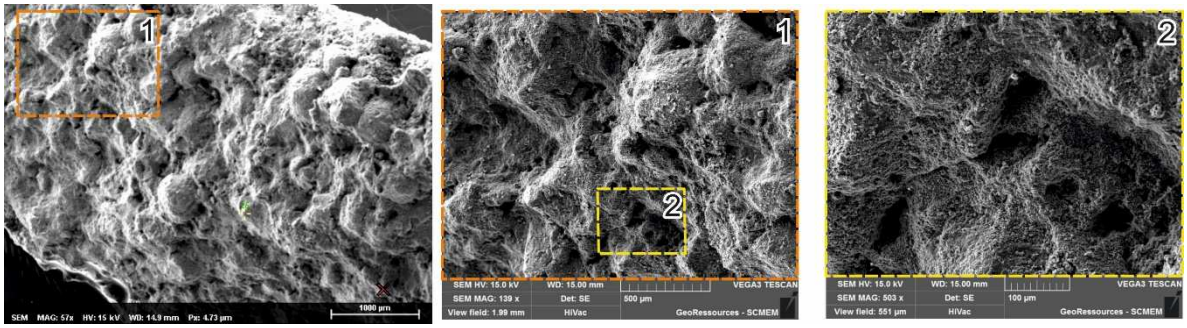

Figure 14. Multiscale Scanned Electronic Microscope (SEM) details of conical slickolites within the wall of the R_2 shear within the studied sample (experiment #7).

The microslickolitic topography (combination of dissolution picks and pits) demonstrates the similar behavior over a range of scales studied. From our point of view, this serves as the main reason for generating both in-situ significant roughness and a related drop in conductivity within domains of the antithetic R_2 shears. This feature can be illustrated by calculating the 3D distribution of the mean curvature, H, for the surfaces of the dominant wormhole and subsidiary dissolution arrays extracted from CT images for experiment #7 with following 3D visualization using Avizo software. In mathematics, the mean curvature, H, of a surface, S, is a measure of the surface deviation from a flat plane. First, a surface (S), as a triangular approximation of the extrinsically segmented volumes of the entire dissolution pattern, was created. Second, the mean curvature (H) was calculated using the formula:

$$H = (k_1 + k_2)/2, \quad (1)$$

where k_1 and k_2 are the principal curvatures of the curves resulting from the intersection between the surface, S, and orthogonal planes containing the normal vectors. An invariant under rotation, the principal curvatures were calculated considering direct neighbours to a certain triangle of the surface.

The constructed 3D model of the mean curvature distribution (Figure 15a) indicates that highly curved (shown in red), and highly indented rough regions of the surface, *S*, strongly gravitated to domains of R_2 shears, with partial propagation along bedding surfaces. Note the prominent positive anomaly of the mean curvature recorded within the node of intersection of the principal wormhole with the R_2 fracture plane (Figure 15b), which acted as an impermeable barrier. Here, a fluid flow touched the steep dipping fracture seal, providing the hopping extension of the dominant wormhole into the upper levels, where tectonically-induced preferential direction facilitated its further growth. Irrespective of the precise mechanism controlling surface reactivity, our results indicate that, beyond the R_2 fracture domain, the surface of the wormhole is almost polished, which is why it is characterized by minimal values of the mean curvature (shown in blue).

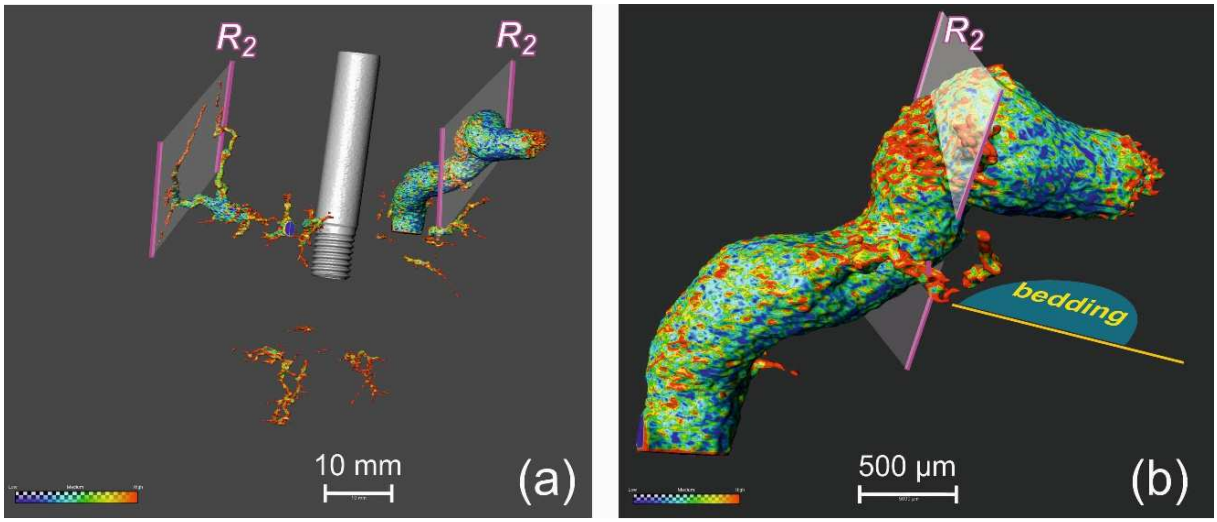

Figure 15. 3D model of the mean curvature distribution, H, for (**a**) the entire dissolution pattern and (**b**) the principal wormhole. Maximally and minimally curved areas are shown in red and in blue, respectively.

A question can be raised concerning the difference in conductivity for conjugated R_1 and R_2 shears. Instead of the classical theory of failure mechanics predicting equitable growth of two sets of Riedel shears, physical experiments and field observations in granular rocks [47] suggest that R_1 shears developed much better than R_2 shears. In most of the studied cases, shear failure within the strike-slip zone starts with the primary development of a set of R_1 fractures. Continuous, but narrow, zones of R_1 structures are composed of individual shear fractures, R_1, linked by transfer zones containing en-echelon arranged dilatational jogs—tensile joints and normal faults, T [48,49]. Closely spaced, but relatively short, R_2 fractures develop later due to secondary restraining in the spatially overlapping bridges between the already developed R_1 fractures [47]. Therefore, R_2 fractures are usually more subjected to local stress concentration and can be interpreted as a combination of tight shears and compressive jogs (micro-thrusts) serving as damper valves for sub-horizontal fluid conduction.

This point of view explains the multiscale asperity of surfaces for the antithetic R_2 shears caused by the presence of tectonically-induced slickolitic peaks and pits, which may constitute fluid-flow barriers due to their different mineralogy, thus affecting the permeability distribution—wormhole growth geometry induced by CO_2-rich fluids.

Preliminary chemical analyses of Lavoux limestone within fragments of slickolitic surface of R_2 shear and beyond by means of SEM TESCAN VEGA3, equipped with an N EDS detector, revealed a discrepancy in the chemical concentration of Si (1.34–2.76%), Al (1.17–2.55%), and Mg (0.24–0.59%), which were pronounced only within the R_2 shear wall. The concentration of those elements beyond the fracture of the R_2 shear type were almost zero.

This result supports the concept of dropping reactivity rates in experimental limestone core-plugs along the slickolitic surfaces of R_2 shears. These fracture surfaces are affected by residual insoluble minerals that have already precipitated during the tectonically-driven dissolution of calcite.

Little is known about the growth process of cavities induced by aggressive fluid treatments in Lavoux limestones, especially in terms of their spatial position and morphology throughout subsequent dissolution phases. However, formation of an initial dissolution pathway parallel to the maximal compressive stress, σ_1, or in the direction of least resistance, is not surprising when considering the analogical influence of local stresses on the spatial control of opening magma-chamber ruptures and dyke injecting [50]. Hydraulic fractures in fracking technology are of tensile origin and in-situ stress predetermines their orientation. Their propagation trends parallel to the maximum horizontal stress, σ_1 [51]. During underground mining activity in a burst-prone coal seam, the primary elongated rock-and-gas outburst cavity is also oriented in the direction of the σ_1 axis [52].

5. Conclusions

Numerous experimental core injecting flow tests have documented the formation of highly conductive cylindrically channelized carbonate matrix acidizing, which may result in wormholing as rapid and mostly complete tunnelling within host rocks.

This study highlights the phenomenon of the structural control of the propagation of the dissolution network, as shown by the correlation between the direction of the different wormholes and the main regional stress field. The interplay of intra-stratification, fracture systems, and their kinematical environment largely controls the dissolution pattern induced by CO_2-rich fluids.

The formation of a primary dissolution pathway tends to start along a tensile fracture, T, with subsequent growth of the artificial cavity (wormhole), controlled by the existing network of fractures. The most prominent artificial "karstification" arrays propagate in volumes affected by master Y shears, synthetic R_1 shears, and antithetic R_2 shears.

Antithetic shears, R_2, organize themselves as slickolitic surfaces, which may act as fluid-flow barriers due to their different mineralogy, thus affecting the permeability distribution—wormhole growth geometry induced by CO_2-saturated solutions.

As an important and reasonable tool to document the spatial control of limestone surface reactivity and wormholing propagation, we propose using 3D mapping of the mean curvature of the dissolution array.

We conclude that inferred tectonically-triggered control of the initiation and subsequent evolution of the dissolution pattern create possibilities for the implementation of industrial CCS projects because our results seriously reduce the spatial and morphologic uncertainties in characteristic shapes for growing dissolution structures.

Author Contributions: Conceptualization, V.P., A.R., J.S., and J.P.; Data curation, C.M.; Formal analysis, V.P. and C.M.; Funding acquisition, J.S.; Investigation, A.R.; Project administration, A.R., J.R. and J.P.; Software, C.M.; Supervision, J.P.; Writing—original draft, V.P., A.R. and J.R.

Funding: This work was supported and financed by the Scientific Interest Group Geodenergies through the PILOTE CO_2-DISSOLVED project (ANR-10-IEED-0804 PILOTE CO_2 DISSOLVED).

Acknowledgments: The authors would like to acknowledge Maxime Dargent for technical assistance in SEM analyses. Our acknowledgements go to Robert Rainbird (Natural Resources Canada and Geological Survey of Canada) for fruitful comments and significant improvement of English text.

Conflicts of Interest: The authors declare no conflict of interest. The founding sponsors had no role in the design of the study; in the collection, analyses, or interpretation of data; in the writing of the manuscript; or in the decision to publish the results.

References:

1. Grataloup, S.; Bonijoly, D.; Brosse, E.; Dreux, R.; Garcia, D.; Hasanov, V.; Lescanne, M.; Renoux, P.; Thoraval, A. A site selection methodology for CO_2 underground storage in deep saline aquifers: Case of the Paris Basin. *Energy Procedia* 2009, *1*, 2929–2936, doi:10.1016/j.egypro.2009.02.068.
2. Brosse, E.; Badinier, G.; Blanchard, F.; Caspard, E.; Collin, P.Y.; Delmas, J.; Dezayes, C.; Dreux, R.; Dufournet, A.; Durst, P.; et al. Selection and Characterization of Geological Sites able to Host a Pilot-Scale CO_2 Storage in the Paris Basin (GéoCarbone-PICOREF). *Oil Gas Sci. Technol. Rev. IFP* 2010, *65*, 375–403, doi:10.2516/ogst/2009085.
3. Le Guen, Y.; Renard, F.; Hellmann, R.; Brosse, E.; Collombet, M.; Tisserand, D.; Gratier, J.P. Enhanced deformation of limestone and sandstone in the presence of high fluids. *J. Geophys. Res. Solid Earth* 2007, *112*, doi:10.1029/2006JB004637.
4. Sterpenich, J.; Sausse, J.; Pironon, J.; Géhin, A.; Hubert, G.; Perfetti, E.; Grgic, D. Experimental ageing of oolitic limestones under CO_2 storage conditions: Petrographical and chemical evidence. *Chem. Geol.* 2009, *265*, 99–112, doi:10.1016/j.chemgeo.2009.04.011.
5. Jobard, E.; Sterpenich, J.; Pironon, J.; Corvisier, J.; Jouanny, M.; Randi, A. Experimental simulation of the impact of a thermal gradient during geological sequestration of CO_2: The COTAGES experiment. *Int. J. Greenh. Gas Control* 2013, *12*, 56–71, doi:10.1016/j.ijggc.2012.11.001.
6. Rahbari, S.H.E.; Saberi, A.A. Attracted diffusion-limited aggregation. *Phys. Rev. E* 2012, *86*, 011407, doi:10.1103/PhysRevE.86.011407.
7. Fischer, C.; Lüttge, A. Beyond the conventional understanding of water–rock reactivity. *Earth Planet. Sci. Lett.* 2017, *457*, 100–105, doi:10.1016/j.epsl.2016.10.019.
8. Lüttge, A.; Arvidson, R.S.; Fischer, C. Fundamental Controls of Dissolution Rate Spectra: Comparisons of Model and Experimental Results. *Procedia Earth Planet. Sci.* 2013, *7*, 537–540, doi:10.1016/j.proeps.2013.03.115.
9. Kervévan, C.; Beddelem, M.-H.; O'Neil, K. CO2-DISSOLVED: A Novel Concept Coupling Geological Storage of Dissolved CO_2 and Geothermal Heat Recovery—Part 1: Assessment of the Integration of an Innovative Low-cost, Water- based CO_2 Capture Technology. *Energy Procedia* 2014, *63*, 4508–4518, doi:10.1016/j.egypro.2014.11.485.
10. Kervévan, C.; Beddelem, M.-H.; Galiègue, X.; Le Gallo, Y.; May, F.; O'Neil, K.; Sterpenich, J. Main Results of the CO2-DISSOLVED Project: First Step toward a Future Industrial Pilot Combining Geological Storage of Dissolved CO_2 and Geothermal Heat Recovery. *Energy Procedia* 2017, *114*, 4086–4098, doi:10.1016/j.egypro.2017.03.1549.
11. Sterpenich, J.; Jobard, E.; El Hajj, H.; Pironon, J.; Randi, A.; Caumon, M.-C. Experimental study of CO_2 injection in a simulated injection well: The MIRAGES experiment. *Greenh. Gases Sci. Technol.* 2013, *4*, 210–224, doi:10.1002/ghg.1389.
12. Randi, A.; Sterpenich, J.; Morlot, C.; Pironon, J.; Kervévan, C.; Beddelem, M.H.; Fléhoc, C. CO2-DISSOLVED: A Novel Concept Coupling Geological Storage of Dissolved CO_2 and Geothermal Heat Recovery—Part 3: Design of the MIRAGES-2 Experimental Device Dedicated to the Study of the Geochemical Water-Rock Interactions Triggered by CO_2 Laden Brine Injection. *Energy Procedia* 2014, *63*, 4536–4547, doi:10.1016/j.egypro.2014.11.487.
13. Randi, A.; Sterpenich, J.; Thiéry, D.; Kervévan, C.; Pironon, J.; Morlot, C. Experimental and Numerical Simulation of the Injection of a CO_2 Saturated Solution in a Carbonate Reservoir: Application to the CO2-DISSOLVED Concept Combining CO_2 Geological Storage and Geothermal Heat Recovery. *Energy Procedia* 2017, *114*, 2942–2956, doi:10.1016/j.egypro.2017.03.1423.
14. Schechter, R.S.; Gidley, J.L. The change in pore size distribution from surface reactions in porous media. *AIChE J.* 2004, *15*, 339–350, doi:10.1002/aic.690150309.
15. Daccord, G.; Lenormand, R. Fractal patterns from chemical dissolution. *Nature* 1987, *325*, 41–43, doi:10.1038/325041a0.
16. Hoefner, M.L.; Fogler, H.S. Pore evolution and channel formation during flow and reaction in porous media. *AIChE J.* 2004, *34*, 45–54, doi:10.1002/aic.690340107.
17. Gouze, P.; Noiriel, C.; Bruderer, C.; Loggia, D.; Leprovost, R. X-ray tomography characterization of fracture surfaces during dissolution. *Geophys. Res. Lett.* 2003, *30*, doi:10.1029/2002GL016755.

18. Detwiler Russell, L. Permeability alteration due to mineral dissolution in partially saturated fractures. *J. Geophys. Res. Solid Earth* 2010, *115*, doi:10.1029/2009JB007206.
19. Szymczak, P.; Ladd, A.J.C. Wormhole formation in dissolving fractures. *J. Geophys. Res. Solid Earth* 2009, *114*, doi:10.1029/2008JB006122.
20. Gabrovšek, F.; Dreybrodt, W. A model of the early evolution of karst aquifers in limestone in the dimensions of length and depth. *J. Hydrol.* 2001, *240*, 206–224, doi:10.1016/S0022-1694(00)00323-1.
21. Ford, D.; Williams, P. Introduction to Karst. In *Karst Hydrogeology and Geomorphology*; Wiley-Blackwell: Hoboken, NJ, USA, 2013; pp. 1–8, ISBN 978-1-118-68498-6.
22. Ballesteros, D.; Jiménez-Sánchez, M.; García-Sansegundo, J.; Borreguero, M. SpeleoDisc: A 3D quantitative approach to define the structural control of endokarst: An application to deep cave systems from the Picos de Europa, Spain. *Geomorphology* 2014, *216*, 141–156, doi:10.1016/j.geomorph.2014.03.039.
23. Sauro, F.; Zampieri, D.; Filipponi, M. Development of a deep karst system within a transpressional structure of the Dolomites in north-east Italy. *Geomorphology* 2013, *184*, 51–63, doi:10.1016/j.geomorph.2012.11.014.
24. Collon, P.; Bernasconi, D.; Vuilleumier, C.; Renard, P. Statistical metrics for the characterization of karst network geometry and topology. *Geomorphology* 2017, *283*, 122–142, doi:10.1016/j.geomorph.2017.01.034.
25. Nijman, W.; Savage, J.F. Persistent basement wrenching as controlling mechanism of Variscan thin-skinned thrusting and sedimentation, Cantabrian Mountains Spain. *Tectonophysics* 1989, *169*, 281–302, doi:10.1016/0040-1951(89)90092-9.
26. Garcia-Rios, M.; Luquot, L.; Soler, J.M.; Cama, J. Influence of the flow rate on dissolution and precipitation features during percolation of CO_2-rich sulfate solutions through fractured limestone samples. *Chem. Geol.* 2015, *414*, 95–108, doi:10.1016/j.chemgeo.2015.09.005.
27. Hancock, P.L. Brittle microtectonics: Principles and practice. *J. Struct. Geol.* 1985, *7*, 437–457, doi:10.1016/0191-8141(85)90048-3.
28. Granier, B.; Staffelbach, C. Quick look cathodoluminescence analyses and their impact on the interpretation of carbonate reservoirs. Case study of mid-Jurassic oolitic reservoirs in the Paris Basin. *Carnets de Geologie* 2009, G2009_A07, doi:10.4267/2042/28795.
29. Sylvester, A.G. Strike-Slip Faults. *GSA Bull.* 1988, *100*, 1666–1703, doi:10.1130/0016-7606(1988)100<1666:SSF>2.3.CO;2.
30. Cariou, É.; Poncet, D.; Colchen, M.; Karnay, G.; Becqgiraudon, J.-F.; avec la collaboration de Branger, P.; Coirier, B.; Dubois, D.; Porel, G.; Thomassin, H. *Notice Explicative, Carte géol. France (1/50 000), feuille Saint-Maixent-l'École (611)*; BRGM: Orléans, France, 2006; 132p, ISBN 13: 978-2-7159-1611-1.
31. Scale invariance. In *Fractals and Chaos in Geology and Geophysics*; Turcotte, D.L., Ed.; Cambridge University Press: Cambridge, UK, 1997; pp. 1–5, ISBN 978-0-521-56733-6.
32. Tchalenko, J.S. Similarities between Shear Zones of Different Magnitudes. *GSA Bull.* 1970, *81*, 1625–1640, doi:10.1130/0016-7606(1970)81[1625:SBSZOD]2.0.CO;2.
33. *Carte Géologique de la FRANCE: 1/1 000000*; BRGM : Orléans, France: 2003; ISBN 978-7-159-21586-8.
34. Ballèvre, M.; Bosse, V.; Ducassou, C.; Pitra, P. Palaeozoic history of the Armorican Massif: Models for the tectonic evolution of the suture zones. *Comptes Rendus Geosci.* 2009, *341*, 174–201, doi:10.1016/j.crte.2008.11.009.
35. Badham, J.P.N.; Halls, C. Microplate tectonics, oblique collisions, and evolution of the Hercynian orogenic systems. *Geology* 1975, *3*, 373–376, doi:10.1130/0091-7613(1975)3<373:MTOCAE>2.0.CO;2.
36. Arthaud, F.; Matte, P. Late Paleozoic strike-slip faulting in southern Europe and northern Africa: Result of a right-lateral shear zone between the Appalachians and the Urals. *GSA Bull.* 1977, *88*, 1305–1320, doi:10.1130/0016-7606(1977)88<1305:LPSFIS>2.0.CO;2.
37. Jégouzo, P. The South Armorican Shear Zone. *J. Struct. Geol.* 1980, *2*, 39–47, doi:10.1016/0191-8141(80)90032-2.
38. Rolin, P.; Marquer, D.; Colchen, M.; Thieblemont, D.; Rossi, P. Progressive shortening axis rotation recorded by Variscan synkinematic granites: Example of the South Armorican shear zone in the Vendée (France). *Geodinamica Acta* 2008, *21*, 203–218, doi:10.3166/ga.21.203-218.
39. Yésou, H.; Rolet, J. Regional mapping of the South Armorican shear zone (Brittany, France) using remotely sensed SPOT imagery. *ISPRS J. Photogramm. Remote Sens.* 1990, *45*, 419–427, doi:10.1016/0924-2716(90)90032-7.
40. Gunzburger, Y.; Magnenet, V. Stress inversion and basement-cover stress transmission across weak layers in the Paris basin, France. *Tectonophysics* 2014, *617*, 44–57, doi:10.1016/j.tecto.2014.01.016.
41. Scheidegger, A.E. *Morphotectonics*; Springer: Berlin/Heidelberg, Germany, 2011; ISBN 978-3-642-18746-9.

42. Štěpančíková, P.; Stemberk, J.; Vilímek, V.; Košťák, B. Neotectonic development of drainage networks in the East Sudeten Mountains and monitoring of recent fault displacements (Czech Republic). *Geomorphology* 2008, *102*, 68–80, doi:10.1016/j.geomorph.2007.06.016.
43. Burbaud-Vergneaud, M. Fracturation et interactions socle couverture: Le seuil du Poitou [Fracturing and Interactions Crystalline Basement Overlays: The "Poitou threshold"]. Ph.D. Thesis, University of Poitiers, Poitiers, France, 1987.
44. Cornet, F.H.; Röckel, T. Vertical stress profiles and the significance of "stress decoupling." *Tectonophysics* 2012, *581*, 193–205, doi:10.1016/j.tecto.2012.01.020.
45. Bourbiaux, B.; Callot, J.P.; Doligez, B.; Fleury, M.; Gaumet, F.; Guiton, M.; Lenormand, R.; Mari, J.-F.; Pourpak, F. Multi-Scale Characterization of an Heterogeneous Aquifer Through the Integration of Geological, Geophysical and Flow Data: A Case Study. *Oil Gas Sci. Technol. Rev. IFP* 2007, *63*, doi:10.2516/ogst:2007029.
46. Gdanski, R. A Fundamentally New Model of Acid Wormholing in Carbonates. In Proceedings of the SPE European Formation Damage Conference, The Hague, The Netherlands, 31 May–1 June 1999; SPE-54719-MS, doi:10.2118/54719-MS.
47. Misra, S.; Mandal, N.; Chakraborty, C. Formation of Riedel shear fractures in granular materials: Findings from analogue shear experiments and theoretical analyses. *Tectonophysics* 2009, *471*, 253–259, doi:10.1016/j.tecto.2009.02.017.
48. Goncharov, M.A.; Rogozhin, E.; Frolova, N.S.; Rozhin, P.N.; Zakharov, V. Riedel megashears R' and the trend to gravitational equilibrium as main factors of tsunamigenic earthquakes. *Geodinamika i Tektonofizika* 2014, *5*, 939–991, doi:10.5800/GT-2014-5-4-0164.
49. Rao, G.; Lin, A.; Yan, B.; Jia, D.; Wu, X.; Ren, Z. Co-seismic Riedel shear structures produced by the 2010 Mw 6.9 Yushu earthquake, central Tibetan Plateau, China. *Tectonophysics* 2011, *507*, 86–94, doi:10.1016/j.tecto.2011.05.011.
50. Gudmundsson, A. How local stresses control magma-chamber ruptures, dyke injections, and eruptions in composite volcanoes. *Earth-Sci. Rev.* 2006, *79*, 1–31, doi:10.1016/j.earscirev.2006.06.006.
51. Huang, J.; Griffiths, D.V.; Wong, S.-W. In situ stress determination from inversion of hydraulic fracturing data. *Int. J. Rock Mech. Min. Sci.* 2011, *48*, 476–481, doi:10.1016/j.ijrmms.2010.08.018.
52. Sachsenhofer, R.F.; Privalov, V.A.; Panova, E.A. Basin evolution and coal geology of the Donets Basin (Ukraine, Russia): An overview. *Int. J. Coal Geol.* 2012, *89*, 26–40, doi:10.1016/j.coal.2011.05.002.

.

– CONCLUSION –

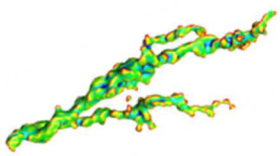

Why this study?

This thesis supported by the CO2-DISSOLVED project results from the technical feasibility study of a novel Carbon Capture and Storage concept coupling the recovery of geothermal energy with the capture and local storage of CO_2 dissolved in a deep saline aquifer. The main purpose is to develop a research pilot at the lab scale prior developing an industrial pilot demonstrator. As any innovative concept, the environmental impact, and especially the prediction of the evolution of the host reservoir and the well materials over a long period of time (around 50 years) shall be considered for the design of the whole system. The objectives of this work considers the geochemical impact of the acidification of the aqueous solution by CO_2 dissolution on i) the alteration of the carbonate minerals in the geothermal reservoir and ii) the cement phase and casing composing the injection well. The development of an appropriate simulation bench is thus essential for the description of the induced physico-chemical modifications. In addition, the experimental results must contribute to increase the predictive reliability of numerical modeling.

This present work allows the examination of the geochemical and hydrodynamic changes of the host carbonate aquifer during the continuous injection of a CO_2 rich solution at the laboratory scale. It especially highlights the propagation patterns of the dissolution channels in a heterogeneous carbonate material. The evolution of the rock-cement interface is also investigated and the role of pH buffer of the cement is discussed.

Experimental innovation and analytical coupling: a teamwork

A unique experimental device (MIRAGES-2) was successfully implemented. Most of the flowthrough equipments described in literature for the evaluation of the CO_2-brine-rock interaction impose a unidirectional linear transport of the aggressive fluid within the sample which directs the flow in an artificial way. The consequence of this boundary condition is that the heterogeneity of the sample and its permeability anisotropy are not taken into account at the centimeteric scale. The specific design of MIRAGES-2 allows the fluid to freely and radially flow through the rock matrix of the sample in any direction. In this way, the experimental system includes the structural and textural heterogeneity of the rock and thus makes it possible to understand the spatial relationship between the distribution of discontinuities (microfaults, microcracks, porosity changes, grain size distribution...) in the sample and the evolution of the dissolution phenomena generated by the injection of the acidified solution. Moreover, the MIRAGES-2 test bench considers the impact of the cement phase in the overall reactivity of the system. It provides the measurement of a significant amount of in situ geochemical data that contribute to improve the input parameters of the reactive transport simulators and thus reduce uncertainties in CO_2 geological storage scenarios.

Experimental achievement.

A set of 7 Radial flowthrough experiments under geological conditions (P= 120 bar and T = 60°C) has been performed over several durations (from 12 hours to 21 days) with equilibrated fresh water and equilibrated saline solution enriched in CO_2 ($P_{(CO_2)}$ = 30 bar). They were associated to original *in-situ* chemical analysis tools of the aqueous solution developed in the GeoRessources lab in collaboration with the industrial supplier (*in-situ* HP/HT Raman probes) and currently used routinely in the experimental field. The pH was also monitored using in-situ measuring instruments. Microscopic investigation of the rock matrix at different location were accomplished and X-ray computed tomography was used as a tool for the 3D visualization of the evolution of the architecture and the topography of the porous media at the core scale.

System reactivity: evolution in time and space

The injection of the CO_2 laden solution triggers significant geochemical disequilibria at the immediate vicinity of the well leading to a rearrangement of the pore space through dissolution and precipitation processes. Once the injection is activated, a radial dissolution front governed by the kinetics of reaction (mass-transfer limited) is the result of the pH decrease. This dissolution, coupled with an important convective driving force, generates a dendritic network as regular and thin channels defined as dominant wormholes. The native high initial permeability of the rock allows the development of several wormholes at different vertical location over the entire height of the experimental wellbore. Away from the wormholes, a homogeneous change in the distribution of pore entry diameters of the porous network is observed (size increase of the biggest pores). This observation underlines the impact of the dissolution process over the overall surrounding region of the well despite the presence of wormhole. The breakthrough of the core-plug induces a discontinuity of the velocity field disturbing the natural wormholes propagation. The dominant wormhole draw almost all the injected fluid and dominate the mass transfer preventing the feeding in reagents of the smallest ones, which become “dead wormholes”.

The hydrodynamics features within the well and in the contiguous area is also modified with a diversity of local streamlines. The fluid density contrast between the injected under-saturated fluid and the fluid charged with dissolved species involves the buoyancy effect impacts the dissolution patterns. The complex coupling between buoyancy, flow dynamics and chemical reaction lead to the modification of the shape of the wellbore which become conical with time as a result of an upward face dissolution.

The rare precipitates detected at different locations of the long-term post experiments core-plug are attributed to local pH gradients in the immediate vicinity of the cement-rock interface and to local saturation index disturbances (evolution of the $P_{(CO_2)}$, ions concentrations in solution such as Ca^{2+}, Mg^{2+} or Sr^{2+}, dominant reactive transport) in the dead wormholes considered as stagnant zone after the core-plug breakthrough.

The MIRAGES-2 experiments thus underlined the spatial and temporal heterogeneities of the geochemical processes engaged over a long period (in days) injection of CO_2 rich solution. Replacing the experimental results at the regional scale, it is concluded on the structural control of the propagation of the dissolution network, as demonstrated by the correlation between the direction of the different wormholes and the main regional stress field. The results revealed that a lot of heterogeneities in the sample (cracks, fracture, pore deformation…) were acquired during intense kinematic episodes and controls the dissolution patterns induced by the injection of CO_2-rich fluids.

Back to the scientific and technical benefits at the geothermal doublet scale

The CO2-DISSOLVED concept is an innovative approach which can actively contribute to the CCS deployment. The benefits offered by this project are both environmental and economic. The CO_2 storage in dissolved form reduce in a significant way the risk of buoyancy and potential CO_2 escaping to the surface. In addition, the use of two wells for the pumping and the re-injection into the same formation will prevent a pressure build-up in the aquifer. The expected hydrodynamic and geochemical disturbances should mainly be located around the two wells. We can still mention the benefit in terms of environmental impact provided by the capture technology which prevents the use of hazardous solvents. From an economic point of view, CO2-DISSOLVED offers a direct or indirect revenue source through the use or resale of the calories recovered by the geothermal doublet

Predicting operational risk at the well scale, at the geothermal doublet scale and at the reservoir scale is of crucial importance for the control of long-term storage performance. This task is necessary to enable the project's shift at the industrial pilot stage and to facilitate communication around the potential risks.

The most significant risk scenarios of the CO2-DISSOLVED technology concern the risks for people and environment and also the risks related to the efficiency of the facility (recovery of calories from the basement and CO_2 storage capacity). Several families of risk specific to the project have been identified (figure 93):

(1) Mechanical/chemical damage of the injection wellbore or the neighboring wells. The CO_2-rich solution migration toward a closed nearby borehole could also generate some potential leak by alteration of the sealing system. We demonstrated the ageing of cement under CO_2 rich saline solutions is responsible for the appearance of a carbonated zone at the interface with the rock. Cement porosity decreased, no steel alteration has been observed during the experiments. If cement and steel composition is the same in the neighboring wells and if the acidified solution reaches the wells, the experimental results demonstrate no evidence of damages. However the carbonation of cement probably modify its mechanical properties. Such evolution has not been tested in the present work.

(2) Clogging of the host reservoir in the near well region. The experiments demonstrate the injection of CO_2-rich aqueous fluid acts as an acidic solution creating dissolution voids in the form of wormholes and increasing the pore diameters. Precipitation products are limited in volume and always less than dissolution volumes even in the near well region where cement releases elements (Mg…) favorable to precipitation. However, the precipitation in stagnant zones as a result of local pressure fields' drop and the potential clogging in the near well region could occur during an injection stop operation. This phenomenon could alter the hydrodynamics of the system when restarting the injection phase.

(3) Loss of geothermal efficiency of the doublet. The potential risk of accelerating thermal recycling could also be triggered if the preferential dissolution patterns migrate towards the production well. The experiment results demonstrate channeling is improved by the presence of faults or other rock heterogeneities. If such heterogeneities intercept the injection and the production wells, they can become efficient drains for the CO_2-rich solution to reach early the production well.

(4) Generation of conflicts with neighborhood underground activities. A conflict of use with other sub-soil users (presence of other geothermal doublet, gas storages…) may also be considered especially in densely exploited aquifers. The principle of the CO2-DISSOLVED concept is to reduce the pressure increase of an aquifer where CO_2 gas is stored. Consequently there is no pressure increase that could modify the yield and security of neighborhood underground activities. However, our experiments demonstrate the presence of heterogeneities in the reservoir rock could create connections between activities. Such scenarios were not considered in the present work and request numerical approaches in further studies.

(5) Chemical/mechanical degradation of the caprock. A migration towards the cap rock interface would also generate potential risk of loss of sealing. However caprock-solution interaction has not been explored in the present study. Numerous previous works [235] were focused on CO_2 gas and CO_2 solution interaction with clay formations and concluded to very limited degradation of the caprock confinement properties.

(6) Contamination of fresh water in superficial aquifers. The likelihood of interfering with a neighboring aquifer can contaminate the fresh water. Such risk is mainly due to degradation of ancient wells crosscutting the superficial aquifer and the caprock of the targeted reservoir. However the concept of CO_2 dissolved project is based on the injection of a dense CO_2 rich saline solution with higher density than the fluid in the aquifer and it limited overpressure with pumping in the second well of the doublet. The injected solution should not reach the top of the reservoir rock formation and then the wells.

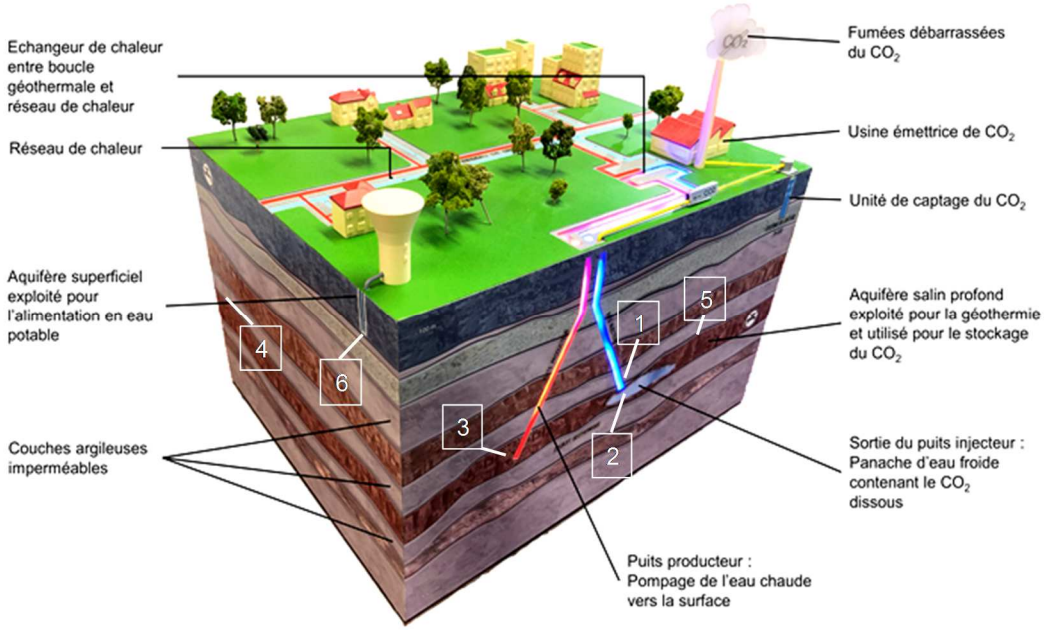

Figure 93: Location of the main risk events related to the CO2-DISSOLVED project

Contribution of the MIRAGES-2 experiment

The experimental contributions of MIRAGES-2 provide a powerful basis to predict the injection scenario and to define a framework to ensure the operational security. Indeed, the obtained results seriously reduce the spatial and morphologic uncertainties in characteristic shapes for growing dissolution patterns. The experiments performed during this work have confirmed that heterogeneities play a key role in the evolution of the processes induced by the disturbance of the near injection well area. Despite the prominent localized dissolution, the modification of the well is also a major parameter and could be the cause of geo-mechanical disruption which is important to prevent.

The extrapolation of phenomena and measurements from our laboratory experiments at the reservoir scale is however a difficult task. The constraint of geochemical upscaling and its coupling with mass transport is a major issue that has been raised many times. From an operational point of view, the reproduction by numerical simulation of the observed dissolution patterns at the laboratory scale and their spatial trends in a heterogeneous carbonate environment is challenging. This aspect is mainly attributed to the mesh scale used in a dynamic reservoir modeling (from a few hundred meters to a few kilometers) which is typically larger than the heterogeneity scale. The boundary conditions specific to our experimental set-up (breakthrough of the core-plug disturbing the system, sample specific heterogeneity…) can also limit the transfer of our observations at the field scale.

However, the results have demonstrated the importance of integrating the spatial variability of hydrodynamic properties induced by the geochemical reactivity at the mesh scale. The knowledge of the structural/textural and kinematics properties of the host reservoir, especially in the case of a heterogeneous carbonate reservoir is of prime importance for the design of the whole system.

Upstream of the geothermal doublet implementation, the positioning of the producing well in relation to the injection well could be optimized far from potential fractures in order to minimize the breakthrough of the system and increase the lifetime of the doublet and the efficiency of the long-term storage

Progress track and outlook

The system studied in this study was actually simple. It would be important to constrain different rocks (silicate, mixed silicate-carbonate, intense layering) with more complex fluids in order to determine the impact on the CO_2 storage capacity (less reactive sandstone) and on the well materials (no carbonate buffer effect). The application of this study to the geological storage of CO_2 also requires to simulate the mechanical strains specific to the reservoir. Indeed the mechanical factor is of a major importance because it modifies the solubility of solids in solution by several orders of magnitude. This aspect has also to be integrated in the numerical simulation.

NOMENCLATURE

α_{CO_2}	fraction molaire de CO_2 dans le gaz (-)
o	
a	paramètre de taille d'un ion en solution aqueuse (-)
A	constante correspondant au potentiel électrochimique de l'électrode de référence des sondes pH in-situ utilisées et qui intervient dans l'équation de Nernst pour une température donnée (mV)
A, *B* et *C*	constates empiriques (-)
a_i	activité chimique d'une espèce *i* en solution (mol.L^{-1})
A_{BET}	Surface spécifique BET (Brunauer, Emmett et Teller) (m²)
β	coefficient stœchiométrique de la réaction de dissolution de la calcite (-)
C	plan stylolitique
C_{ac0}	moyenne volumique intrinsèque de concentration acide imposée (kg.m^{-3})
C_{eq}	concentration en ions Ca^{2+} en équilibre avec la calcite (mol.kg^{-1})
$C_{i(aq)}$	concentration d'une espèce i dans la phase aqueuse (mol.kg^{-1})
$C_{i(surf)}$	concentration d'une espèce i à la surface du minéral (mol.kg^{-1})
Cp	capacité thermique massique (J.kg^{-1}.°C^{-1})
δ_1	bande de vibration de déformation de l'eau sur le spectre issu des analyses Raman (cm^{-1})
δ_{DBL}	épaisseur de la couche limite (m)
ΔP	différence de pression entre l'entrée et la sortie de l'éprouvette expérimentale (bar)
d	days (jours)
Da	nombre adimensionnel de Damköhler (-)
Da*	nombre adimensionnel de Damköhler cinétique (-)
D_e	diamètre d'échange thermique (m)
D_e	diamètre interne du tube d'injection expérimental (m)
D_i	diamètre hydraulique (m)
D_i	diamètre externe du doigt de gant du thermocouple au niveau de la zone d'injection de la carotte expérimentale (m)
D_m	coefficient de diffusion moléculaire (m².s^{-1})
dq_S	flux de chaleur (Joules)
dT_m	différence de température entre le milieu réactionnel et le fluide injecté (°C)
E_a	énergie d'activation (kg.m².s^{-2})
"f"	faille antithétique complémentaire
F	facteur de forme
"F"	Faille majeure
F	constante de Faraday (C)

$h(x)$	coefficient de transfert thermique moyen entre le fluide et le tube d'injection ($W.m^{-2}.°C^{-1}$)
h_{well}	hauteur du puits d'injection experimental (m)
I	Intensité (A)
I	force ionique (M)
I_{CO_2}	Aire du pic du CO_2 sur le spectre issu des analyses Raman (m^2)
I_{H_2O}	Aire du pic de l'eau sur le spectre issu des analyses Raman (m^2)
γ	coefficient d'activité ionique (-)
κ	courbure (μm^{-1})
ξ	paramètre utilisé dans les corrélations expérimentales de Lévêque (-)
k	perméabilité intrinsèque du milieu poreux (mD)
k_v	perméabilité verticale (mD)
k_h	perméabilité horizontale (mD)
k	conductivité thermique d'un fluide ($W.m^{-1}.°C^{-1}$)
K_H	constante de Henry ($mole.kg^{-1}.kPa^{-1}$)
k_m	constante cinétique intrinsèque au minéral m ($mol.m^{-2}.s^{-1}$)
$K_{(P,T)}$	constante d'équilibre thermodynamique
K_{ps_i}	produit de solubilité
$k_r(T)$	constante cinétique globale d'une réaction chimique à la température *T* ($mol.m^{-2}.s^{-1}$)
λ	Conductivité thermique d'un fluide ($W.m^{-1}.°C^{-1}$)
l	longueur caractéristique du système étudié (m)
L	longueur de la carotte dans la direction du débit de fluide (m),
μ	*v*iscosité dynamique du fluide ($kg.m^{-1}.s^{-1}$)
m	débit d'injection massique ($kg.s^{-1}$)
m_i	concentration d'une espèce *i* en solution ($mol.kg_{eau}^{-1}$)
ν_i	bande de vibration des pics correspondants au doublet de Fermi sur le spectre issu des analyses Raman (cm^{-1})
n	coefficient, indice, exposant
N	vecteur normal (-)
$n_{\min}$	nombre de moles d'un minéral (mol)
Nu	nombre adimensionnel de Nusselt (-)
pH	potentiel d'hydrogène
N_{ac}	nombres adimensionnel de pouvoir acide (-)
N_D	nombre adimensionnel de Darcy (-)
Φ	angle de friction interne d'une roche (°)
Ω	indice de saturation du milieu
ϕ_{tot}	porosité totale du milieu poreux (%)

ϕ_c	porosité connectée (%)
ϕ_{free}	porosité libre (%)
$\phi_{trapped}$	porosité piégée (%)
Ω	indice de saturation d'une solution
P	fracture synthétique de Skempton subordonnée à R_1 et R_2 ou absente
P	pression totale (bar)
P_{conf}	pression de confinement (bar)
P_{inj}	pression d'injection (bar)
$P_{(CO_2)}$	pression partielle de CO_2 en phase gazeuse (bar)
P_w	périmètre mouillé (m)
Pe	nombre adimensionnel de Péclet (-)
Pr	nombre adimensionnel de Prandlt (-)
Q	débit d'injection volumétrique ($mL.h^{-1}$)
$Q_{(P,T)}$	produit d'activité ionique (-)
$Q_{(0)}$	produit d'activité ionique pour une solution pure (-)
ρ_{solide}	masse volumique d'un solide ($kg.m^{-3}$)
r	vitesse de dissolution locale à la surface d'un minéral ($mol.s^{-1}$)
r_{well}	rayon du puits dinjection experimental (m)
R	rayon (m)
R^2	coefficient de détermination (-)
R	constante des gaz parfaits ($J{\cdot}mol^{-1}{\cdot}K^{-1}$)
R_1	fracture synthétique dextre de Riedel
R_2	fracture antithétique sinistre de Riedel
Re	Nombre adimensionnel de Reynolds (-)
Ri	Nombre adimensionnel de Richardson (-)
σ	écart type (-)
σ_1	contrainte principale majeure de compression
σ_3	contrainte principale majeure tensile
σ_r	incertitude standard relative (m)
S	surface (m^2)
s_{CO_2}	solubilité du CO_2 en solution aqueuse ($mol.kg^{-1}$)
S_r	surface réactive d'un minéral (m^2)
S_V	surface totale des vides interstitiels (m^2)
θ	angle (°)
t	temps(s)
T	fente de tension
T	température (°C)
T_{conf}	température de confinement (°C)
T_{inj}	température d'injection du fluide (°C)

t_A	temps caractéristique d'advection (s)
t_D	temps caractéristique de diffusion (s)
t_R	temps caractéristique d'une réaction chimique (en s)
υ	vitesse interstitielle advective moyenne ($m.s^{-1}$)
$\bar{v}$	vitesse moyenne entre les 2 tubes concentriques d'injection ($m.s^{-1}$)
V	volume (m^3)
x_1	longueur maximale de propagation du front réactif (longueur entre la surface du puits et l'extrémité extérieure de la carotte) (m)
x_2	hauteur initiale de contact entre la solution et la roche (hauteur du puits) (m)
Y	zone de cisaillement principale
z_i	charge d'un ion (-)

RÉFÉRENCES BIBLIOGRAPHIQUES

BIBLIOGRAPHICAL REFERENCES

[1] IPCC, 2014: Climate Change 2014: Mitigation of Climate Change. Contribution of Working Group III to the Fifth Assessment Report of the Intergovernmental Panel on Climate Change [Edenhofer, O., R. Pichs-Madruga, Y. Sokona, E. Farahani, S. Kadner, K. Seyboth, A. Adler, I. Baum, S. Brunner, P. Eickemeier, B. Kriemann, J. Savolainen, S. Schlömer, C. von Stechow, T. Zwickel and J.C. Minx (eds.)]. Cambridge University Press, Cambridge, United Kingdom and New York, NY, USA.

[2] Butler, J.H. and S.A. Montzka, 2019: The NOAA Annual Greenhouse Gas Index (AGGI), http://www.esrl.noaa.gov/gmd/aggi/aggi.html.

[3] Le Captage et Stockage géologique du CO2 (CSC) en France. Le CSC, un potentiel limité pour la réduction des émissions industrielles. Avis technique. ADEME (Agence de la transition énergétique). Juillet 2020. 44p. https://www.ademe.fr/sites/default/files/assets/documents/captage-stockage-geologique-co2_csc_avis-technique_2020.pdf

[4] Rogelj, J., D. Shindell, K. Jiang, S. Fifita, P. Forster, V. Ginzburg, C. Handa, H. Kheshgi, S. Kobayashi, E. Kriegler, L. Mundaca, R. Séférian, and M.V. Vilariño, 2018: Mitigation Pathways Compatible with 1.5°C in the Context of Sustainable Development. In: Global Warming of 1.5°C. An IPCC Special Report on the impacts of global warming of 1.5°C above pre-industrial levels and related global greenhouse gas emission pathways, in the context of strengthening the global response to the threat of climate change, sustainable development, and efforts to eradicate poverty [Masson-Delmotte, V., P. Zhai, H.-O. Pörtner, D. Roberts, J. Skea, P.R. Shukla, A. Pirani, W. Moufouma-Okia, C. Péan, R. Pidcock, S. Connors, J.B.R. Matthews, Y. Chen, X. Zhou, M.I. Gomis, E. Lonnoy, T. Maycock, M. Tignor, and T. Waterfield (eds.)], p. 135.

[5] Extrait de la SNBC révisée : https://www.ecologique-solidaire.gouv.fr/strategie-nationale-bas-carbone-snbc

[6] IPCC, 2005: IPCC Special Report on Carbon Dioxide Capture and Storage. Prepared by Working Group III of the Intergovernmental Panel on Climate Change [Metz, B., O. Davidson, H. C. de Coninck, M. Loos, and L. A. Meyer (eds.)]. Cambridge University Press, Cambridge, United Kingdom and New York, NY, USA, 442 pp.IPCC, Synthesis Report, Fifth Assessment Report (AR5), 2014

[7] GIEC 2007. Bilan 2007 des changements climatiques. Contribution des Groupes de travail I, II et III au quatrième Rapport d'évaluation du Groupe d'experts intergouvernemental sur l'évolution du climat [Équipe de rédaction principale, Pachauri,R.K. et Reisinger, A.].

[8] Marcu, A., Alberola,E., Caneill,J.Y., Mazzoni, M., Schleicher, S., Vailles, C., Stoefs, W., Vangenechten, D., et Cecchettil. F. (2019). I4CE. State of the EU ETS Report. https://www.i4ce.org/wp-core/wp-content/uploads/2019/05/2019-State-of-the-EU-ETS-Report-1.pdf

[9] Basava-Reddi L. (2010) - IEAGHG, "Geothermal Energy and CO2 Storage", 2010/TR3, August, 2010

[10] Pruess, K. On production behavior of enhanced geothermal systems with CO_2 as working fluid. Energy Conversion & Management 2008; 49: p. 1446-1454

[11] Randolph, J.B., Saar, M.O., 2011. Combining geothermal energy capture with geologic carbon dioxide sequestration: GEOTHERMAL ENERGY WITH CO_2 SEQUESTRATION. Geophysical Research Letters 38, n/a–n/a. https://doi.org/10.1029/2011GL047265

[12] Fouillac, C., B. Sanjuan, S. Gentier and I. Czernichowski-Lauriol (2004). Could Sequestration of CO_2 be Combined with the Development of Enhanced Geothermal Systems?, paper presented at Third Annual Conference on Carbon Capture and Sequestration, Alexandria, VA, May 3-6.

[13] Pruess, K., 2006. Enhanced geothermal systems (EGS) using CO_2 as working fluid—A novel approach for generating renewable energy with simultaneous sequestration of carbon. Geothermics 35, 351–367. https://doi.org/10.1016/j.geothermics.2006.08.002

[14] Azaroual, M., K. Pruess and C. Fouillac. (2007) - Feasibility of Using Supercritical CO_2 as Heat Transmission Fluid in the EGS Integrating the Carbon Storage Constraints, paper presented at ENGINE Workshop (Enhanced Geothermal Innovative Network for Europe), Volterra, Italy.

[15] Atrens, A.D., Gurgenci, H., Rudolph, V., 2009. CO_2 Thermosiphon for Competitive Geothermal Power Generation. Energy & Fuels 23, 553–557. https://doi.org/10.1021/ef800601z

[16] Brown, D.W., 2000. A hot dry rock geothermal energy concept utilizing supercritical CO2 instead of water, in: Proceedings of the Twenty-fifth Workshop on Geothermal Reservoir Engineering, Stanford University. pp. 233–238.

[17] Buscheck, T.A., Bielicki, J.M., Edmunds, T.A., Hao, Y., Sun, Y., Randolph, J.B., Saar, M.O., 2016. Multifluid geo-energy systems: Using geologic CO2 storage for geothermal energy production and grid-scale energy storage in sedimentary basins. Geosphere 12, 678–696. https://doi.org/10.1130/GES01207.1

[18] Torp, T. [2010] My House has Several Levels – Co-habitation of CO_2 Storage with Geothermal? International Conference: Geothermal Energy and CO_2 Storage, 10-11 February, Potsdam, Germany, 23-24

[19] Christensen, N.P. [2010] GeoSynergy: Combining CO_2 Storage and Geothermal Energy Production – A Case Study. International Conference on Geothermal Energy and CO_2 Storage, 10-11 February, Potsdam, Germany, 25

[20] Matter J.M. et al., "The CarbFix Pilot Project – Storing Carbon Dioxide in Basalt". Energy Procedia 4 (2011) pp. 5579-5585

[21] Zakharova, N.V., Goldberg, D.S., Sullivan, E.C., Herron, M.M., Grau, J.A., 2012. Petrophysical and geochemical properties of Columbia River flood basalt: Implications for carbon sequestration. Geochemistry, Geophysics, Geosystems 13. https://doi.org/10.1029/2012GC004305

[22] Lombard, J.M., Azaroual, M., Pironon, J., Broseta, D., Egermann, P., Munier, G., Mouronval, G., 2010. CO_2 Injectivity in Geological Storages: an Overview of Program and Results of the GeoCarbone-Injectivity Project. Oil & Gas Science and Technology – Revue de l'Institut Français du Pétrole 65, 533–539. https://doi.org/10.2516/ogst/2010013

[23] Fouillac, C., B. Sanjuan, S. Gentier and I. Czernichowski-Lauriol (2004). Could Sequestration of CO_2 be Combined with the Development of Enhanced Geothermal Systems?, paper presented at Third Annual Conference on Carbon Capture and Sequestration, Alexandria, VA, May 3-6.

[24] Ueda, A., Kato, K., Ohsumi, T., Yajima, T., Ito, H., Kaieda, H., Metcalfe, R., Takase, H., 2005. Experimental studies of CO2-rock interaction at elevated temperatures under hydrothermal conditions. GEOCHEMICAL JOURNAL 39, 417–425. https://doi.org/10.2343/geochemj.39.417

[25] Kervévan, C., Bugarel, F., Galiegue, X., Le Gallo, Y., May, F., O'Neil, K., Sterpenich, J., 2013. CO_2-Dissolved-A Novel Approach to Combining CCS and Geothermal Heat Recovery, in: Second EAGE Sustainable Earth Sciences (SES) Conference and Exhibition

[26] Kervévan, C., Beddelem, M.-H., Galiègue, X., Le Gallo, Y., Maye, F., O'Neil, K., Sterpenich, J., 2017. Main Results of the CO2-DISSOLVED Project: First Step toward a Future Industrial Pilot Combining Geological Storage of Dissolved CO_2 and Geothermal Heat Recovery. Energy Procedia 114, 4086–4098.

[27] Ahmad, N., Wörman, A., Sanchez-Vila, X., Jarsjö, J., Bottacin-Busolin, A., Hellevang, H., 2016. Injection of CO2-saturated brine in geological reservoir: A way to enhanced storage safety. International Journal of Greenhouse Gas Control 54, 129–144. https://doi.org/10.1016/j.ijggc.2016.08.028

[28] Castillo C., Knopf S., Kervévan C., May F. CO2-DISSOLVED: a novel concept coupling geological storage of dissolved CO_2 and geothermal heat recovery – Part 2: Assessment of the Potential Industrial Applicability in France, Germany, and the U.S.A. Submitted to the GHGT 12 Conference, Austin, TX, USA; Oct. 5-9, 2014.

[29] Blount, G., Gorensek, M., Hamm, L., O'Neil, K., Kervévan, C., Beddelem, M.-H., 2014. Pi-CO2 Aqueous Post-combustion CO_2 Capture: Proof of Concept Through Thermodynamic, Hydrodynamic, and Gas-Lift Pump Modeling. Energy Procedia 63, 286–292. https://doi.org/10.1016/j.egypro.2014.11.031

[30] Dupraz, S., Engevin, J., O'Neil, K. 2019. *Capturing CO_2 with water: tests of the Pi-CO2 lab-scale prototype. Final Report. BRGM/RP-69430-FR*

[31] De Lary, L., Manceau, J.C. 2015. CO2-DISSOLVED : coupling of the underground storage of dissolved CO2 and geothermal energy recovery – Preliminary risk study. Final Report. BRGM/RC-65363-FR

[32] Gravaud, I., Le Guénan, T. 2019 Projet PILOTE CO2-DISSOLVED : Rapport d'analyse préliminaire des risques liés à la partie sous-sol de l'exploitation. Final Report. BRGM/RP-68681-FR

[33] Wellman, T.P., Grigg, R.B., McPherson, B.J., Svec, R.K., Lichtner, P.C., 2003. Evaluation of CO2-brine-reservoir rock interaction with laboratory flow tests and reactive transport modeling, in: International Symposium on Oilfield Chemistry. Society of Petroleum Engineers.

[34] Noiriel, C., Bernard, D., Gouze, P., Thibault, X., 2005. Hydraulic properties and microgeometry evolution accompanying limestone dissolution by acidic water. Oil & gas science and technology 60, 177–192.

[35] Egermann, P., Bemer, E., Zinszner, B., 2006. An experimental investigation of the rock properties evolution associated to different levels of CO2 injection like alteration processes. paper SCA 34, 12–16.

[36] Izgec, O., Demiral, B., Bertin, H., Akin, S., 2008. CO2 injection into saline carbonate aquifer formations I: laboratory investigation. Transport in Porous Media 72, 1–24. doi:10.1007/s11242-007-9132-5

[37] Luquot, L., Gouze, P., 2009. Experimental determination of porosity and permeability changes induced by injection of CO2 into carbonate rocks. Chemical Geology 265, 148–159. doi:10.1016/j.chemgeo.2009.03.028

[38] Sterpenich, J., Sausse, J., Pironon, J., Géhin, A., Hubert, G., Perfetti, E., Grgic, D., 2009. Experimental ageing of oolitic limestones under CO2 storage conditions. Chemical Geology 265, 99–112. https://doi.org/10.1016/j.chemgeo.2009.04.011

[39] Radilla, G., Kacem, M., Lombard, J.M., Fourar, M., 2010. Transport Properties of Lavoux Limestone at Various Stages of CO2 -Like Acid-Rock Alteration. Oil & Gas Science and Technology – Revue de l'Institut Français du Pétrole 65, 557–563. doi:10.2516/ogst/2009081

[40] Gouze, P., Luquot, L., 2011. X-ray microtomography characterization of porosity, permeability and reactive surface changes during dissolution. Journal of Contaminant Hydrology 120-121, 45–55. https://doi.org/10.1016/j.jconhyd.2010.07.004

[41] I.M. Mohamed, J. He, H.A. Nasr-El-Din. Permeability change during CO2 injection in carbonate aquifers: experimental study SPE140979-SPE Americas E&P Health, Safety, Security, and Environmental Conference (2011) Houston, Texas, USA

[42] Gharbi, O., Bijeljic, B., Boek, E., Blunt, M.J., 2013. Changes in Pore Structure and Connectivity Induced by CO2 Injection in Carbonates: A Combined Pore-Scale Approach. Energy Procedia 37, 5367–5378. https://doi.org/10.1016/j.egypro.2013.06.455

[43] Smith, M.M., Sholokhova, Y., Hao, Y., Carroll, S.A., 2013. CO2-induced dissolution of low permeability carbonates. Part I: Characterization and experiments. Advances in Water Resources 62, 370–387. doi:10.1016/j.advwatres.2013.09.008

[44] Vialle, S., Dvorkin, J., Mavko, G., 2013. Implications of pore microgeometry heterogeneity for the movement and chemical reactivity of CO2 in carbonates. GEOPHYSICS 78, L69–L86. https://doi.org/10.1190/geo2012-0458.1

[45] Luquot, L., Roetting, T.S., Carrera, J., 2014. Characterization of flow parameters and evidence of pore clogging during limestone dissolution experiments. Water Resources Research 50, 6305–6321. https://doi.org/10.1002/2013WR015193

[46] Vialle, S., Contraires, S., Zinzsner, B., Clavaud, J.-B., Mahiouz, K., Zuddas, P., Zamora, M., 2014. Percolation of CO_2-rich fluids in a limestone sample: Evolution of hydraulic, electrical, chemical, and structural properties: CO2-rich fluids in a limestone. Journal of Geophysical Research: Solid Earth 119, 2828–2847. https://doi.org/10.1002/2013JB010656

[47] Menke, H.P., Andrew, M.G., Blunt, M.J., Bijeljic, B., 2016. Reservoir condition imaging of reactive transport in heterogeneous carbonates using fast synchrotron tomography — Effect of initial pore structure and flow conditions. Chemical Geology 428, 15–26. https://doi.org/10.1016/j.chemgeo.2016.02.030

[48] RATHNAWEERA, T. D., RANJITH, P. G. & PERERA, M. S. A. 2016 Experimental investigation of geochemical and mineralogical effects of CO2 sequestration on flow characteristics of reservoir rock in deep saline aquifers. Sci. Rep. 6, 19362.

[49] Singh, K., Anabaraonye, B.U., Blunt, M.J., Crawshaw, J., 2018. Partial dissolution of carbonate rock grains during reactive CO2-saturated brine injection under reservoir conditions. Advances in Water Resources 122, 27–36. https://doi.org/10.1016/j.advwatres.2018.09.005

[50] Luquot, L., Roetting, T.S., Carrera, J., 2014. Characterization of flow parameters and evidence of pore clogging during limestone dissolution experiments. Water Resources Research 50, 6305–6321. https://doi.org/10.1002/2013WR015193

[51] Jacquemet, N., Pironon, J., Caroli, E., 2005. A new experimental procedure for simulation of H2S + CO2 geological storage. Application to well cement aging. Oil & gas science and technology 60, 193–203.

[52] Barlet-Gouédard, V., Ramakrishnan, T.S., Bennaceur, K., Supp, M., Goffé, B., Rimmelé, G., Nelson, E., 2005. Mitigation Strategies for CO2 Migration through Wellbores. Schlumberger) Virginia, May.

[53] Barlet-Gouédard, V., Rimmelé, G., Goffé, B., Porcherie, O., 2007. Well Technologies for CO2 Geological Storage: CO2-Resistant Cement. Oil & Gas Science and Technology - Revue de l'IFP 62, 325–334. doi:10.2516/ogst:2007027

[54] Kutchko, B.G., Strazisar, B.R., Dzombak, D.A., Lowry, G.V., Thaulow, N., 2007. Degradation of well cement by CO2 under geologic sequestration conditions. Environmental science & technology 41, 4787–4792.

[55] Rimmelé, G., Barlet-Gouédard, V., Porcherie, O., Goffé, B., Brunet, F., 2008. Heterogeneous porosity distribution in Portland cement exposed to CO2-rich fluids. Cement and Concrete Research 38, 1038–1048. doi:10.1016/j.cemconres.2008.03.022

[56] Brandvoll, ø., Regnault, O., Munz, I.A., Iden, I.K., Johansen, H., 2009. Fluid–solid interactions related to subsurface storage of CO2 Experimental tests of well cement. Energy Procedia 1, 3367–3374. doi:10.1016/j.egypro.2009.02.125

[57] Carey, J.W., Svec, R., Grigg, R., Zhang, J., Crow, W., 2010. Experimental investigation of wellbore integrity and CO2–brine flow along the casing–cement microannulus. International Journal of Greenhouse Gas Control 4, 272–282. doi:10.1016/j.ijggc.2009.09.018

[58] Corvisier, J., Brunet, F., Fabbri, A., Bernard, S., Findling, N., Rimmelé, G., Barlet-Gouédard, V., Beyssac, O., Goffé, B., 2010. Raman mapping and numerical simulation of calcium carbonates distribution in experimentally carbonated Portland-cement cores. European Journal of Mineralogy 22, 63–74. doi:10.1127/0935-1221/2010/0022-1977

[59] Duguid, A., Scherer, G.W., 2010. Degradation of oilwell cement due to exposure to carbonated brine. International Journal of Greenhouse Gas Control 4, 546–560. doi:10.1016/j.ijggc.2009.11.001

[60] Liteanu, E., Spiers, C.J., 2011. Fracture healing and transport properties of wellbore cement in the presence of supercritical CO2. Chemical Geology 281, 195–210. doi:10.1016/j.chemgeo.2010.12.008

[61] Yalcinkaya, T., Radonjic, M., Willson, C.S., Bachu, S., 2011. Experimental study on a single cement-fracture using CO2 rich brine. Energy Procedia 4, 5335–5342. doi:10.1016/j.egypro.2011.02.515

[62] Abdoulghafour, H., Luquot, L., Gouze, P., 2013. Characterization of the Mechanisms Controlling the Permeability Changes of Fractured Cements Flowed Through by CO2 -Rich Brine. Environmental Science & Technology 130906110157009. doi:10.1021/es401317c

[63] Asahara, Y., Mito, S., Xue, Z., Yamashita, Y., Miyashiro, K., 2013. Chemical Impacts of CO2 Flooding on Well Composite Samples: Experimental Assessment of Well Integrity for CO2 Sequestration. Energy Procedia 37, 5738–5745. doi:10.1016/j.egypro.2013.06.496

[64] Luquot, L., Abdoulghafour, H., Gouze, P., 2013. Hydro-dynamically controlled alteration of fractured Portland cements flowed by CO2-rich brine. international journal of Greenhouse Gas Control 16, 167–179.

[65] Mason, H.E., Du Frane, W.L., Walsh, S.D., Dai, Z., Charnvanichborikarn, S., Carroll, S.A., 2013. Chemical and mechanical properties of wellbore cement altered by CO2-rich brine using a multi-analytical approach. Environmental science & technology 47, 1745–1752.

[66] Newell, D.L., Carey, J.W., 2013. Experimental Evaluation of Wellbore Integrity Along the Cement-rock Boundary. Environmental Science & Technology 47, 276–282. doi:10.1021/es3011404

[67] Wolterbeek, T.K.T., Peach, C.J., Spiers, C.J., 2013. Reaction and transport in wellbore interfaces under CO2 storage conditions: Experiments simulating debonded cement–casing interfaces. International Journal of Greenhouse Gas Control 19, 519–529. doi:10.1016/j.ijggc.2013.10.017

[68] Wolterbeek, T.K.T., Peach, C.J., Raoof, A., Spiers, C.J., 2016. Reactive transport of CO2-rich fluids in simulated wellbore interfaces: Flow-through experiments on the 1–6m length scale. International Journal of Greenhouse Gas Control 54, 96–116. doi:10.1016/j.ijggc.2016.08.034

[69] Jung, H.B., Kabilan, S., Carson, J.P., Kuprat, A.P., Um, W., Martin, P., Dahl, M., Kafentzis, T., Varga, T., Stephens, S., Arey, B., Carroll, K.C., Bonneville, A., Fernandez, C.A., 2014. Wellbore cement fracture evolution at the cement–basalt caprock interface during geologic carbon sequestration. Applied Geochemistry 47, 1–16. doi:10.1016/j.apgeochem.2014.04.010

[70] Walsh, H.E., Mason, W.L., Du Frane, S.A. Carroll., 2014a. Experimental calibration of a numerical model describing the alteration of cement/caprock interfaces by carbonated brine. Int. J. Greenh. Gas Control 22, 176–188. doi: 10.1016/j.ijggc.2014.01.004

[71] Lorek, A., Labus, M., Bujok, P., 2016. Wellbore cement degradation in contact zone with formation rock. Environmental Earth Sciences 75. doi:10.1007/s12665-015-5114-z

[72] Choi, B.-Y., Lee, H., Chae, G.-T., Kim, T., Kim, J.-C., 2016. Alteration processes of cement induced by CO2-saturated water and its effect on physical properties: Experimental and geochemical modeling study. Chemie der Erde - Geochemistry 76, 597–604. doi:10.1016/j.chemer.2016.10.001

[73] Fabbri, A., Corvisier, J., Schubnel, A., Brunet, F., Goffé, B., Rimmele, G., Barlet-Gouédard, V., 2009. Effect of carbonation on the hydro-mechanical properties of Portland cements. Cement and Concrete Research 39, 1156–1163. https://doi.org/10.1016/j.cemconres.2009.07.028

[74] Carey, J.W. Lichtner, P.C.: "Computational studies of two-phase cement-CO2-brine interaction in wellbore environments". 2011. SPE Journal, 940-948.

[75] Huet, B., Tasoti, V., Khalfallah, I., 2011. A review of Portland cement carbonation mechanisms in CO2 rich environment. Energy Procedia 4, 5275–5282. https://doi.org/10.1016/j.egypro.2011.02.507

[76] Matteo, E.N. Scherer, G.W.:, 2012. Experimental study of the diffusion-controlled acid degradation of Class H Portland cement. International Journal of Greenhouse Gas Control, 7, pp 181–191.

[77] Sheng, J., 2013. Enhanced Oil Recovery Field Case Studies. Gulf Professional Publishing, 772 pp.

[78] Garing, C., Luquot, L., Pezard, P,A., Gouze, P. Geochemical investigations of saltwater intrusion into the coastal carbonate aquifer of Mallorca, Spain. December 2013. Applied Geochemistry 39:1-10 DOI: 10.1016/j.apgeochem.2013.09.011

[79] Tucker, M.E., Wright, V.P., 1990. Carbonate sedimentology. Blackwell Science, UK

[80] Folk, R.L., 1959, Practical petrographic classification of limestones: American Association of Petroleum Geologists Bulletin, v. 43, p. 1-38.

[81] Norton, D., Knapp, R. 1977. Transport phenomena in hydrothermal systems: The nature of porosity. American Journal of science 277, 913-936

[82] Katsube, T.J.. 1981. Pore structure and pore parameters that control the radionuclide transport in crystalline rocks. Proc. Tech. Prog., International Powder and Bulk Solids Handling and Processing, Rosemont, Ill., May 12–14, 1981? pp. 394-409

[83] Choquette, P.W. and Pray, L.C. 1970. Geologic Nomenclature and Classification of Porosity in Sedimentary Carbonates. American Association of Petroleum Geologists Bulletin, 54, 207-250

[84] Selley, Richard C. (2000). Applied Sedimentology. London: Academic Press

[85] Ghanbarian, B., A. G. Hunt, R. P. Ewing, and M. Sahimi. 2013. Tortuosity in Porous Media: A Critical Review. Soil Sci. Soc. Am. J. 77:1461-1477. doi:10.2136/sssaj2012.0435

[86] Homand, F., Duffaut, P. (2000) Manuel de mécanique des roches (Tome 1 Fondements). Les Presses de l'Ecole des Mines de Paris. Paris : Comité Français de Mécanique des Roches, 265 p

[87] Fischer, C, Arvidson, RS and Lüttge, A (2012) How predictable are dissolution rates of crystalline material? Geochimica et Cosmochimica Acta, 98. 177-185. doi:10.1016/j.gca.2012.09.011.

[88] Brunauer S., Emmet P. H. et Teller E. A. [1938] Adsorption of gases in multimolecular layers. Journal of the American Chemical Society 60, 309-319.

[89] Fischer, C. & Luttge, A. 2007. Converged surface roughness parameters. A new tool to quantify rock surface morphology and reactivity alteration. AmericanJournal of Science, 307, 955–973.

[90] Levenson, Y. & Emmanuel, S. 2013. Pore-scale heterogeneous reaction rates on a dissolving limestone surface. Geochimica et Cosmochimica Acta, 119, 188–197

[91] Kirstein, J., Hellevang, H., Haile, B.G., Gleixner, G., Gaupp, R., 2016. Experimental determination of natural carbonate rock dissolution rates with a focus on temperature dependency. Geomorphology 261, 30–40. https://doi.org/10.1016/j.geomorph.2016.02.019

[92] Rickard D. et Sjöberg E. L. [1983] Mixed kinetic control of calcite dissolution rates. American Journal of Science 283, 815-830.

[93] Morse J. W. et Arvidson R. S. [2002] The dissolution kinetics of major sedimentary carbonate minerals. Earth-Science Reviews 58, 51-84.

[94] Arvidson, R.S., Ertan, I.E., Amonette, J.E., Luttge, A., 2003. Variation in calcite dissolution rates: Geochimica et Cosmochimica Acta 67, 1623–1634. https://doi.org/10.1016/S0016-7037(02)01177-8

[95] Folk, R.L., 1959, Practical petrographic classification of limestones: American Association of Petroleum Geologists Bulletin, v. 43, p. 1-38.

[96] Folk, R.L., 1962, Spectral subdivision of limestone types, in Ham, W.E., ed., Classification of carbonate Rocks-A Symposium: American Association of Petroleum Geologists Memoir 1, p. 62-84.

[97] Dunham, R. J., 1962, Classification of carbonate rocks according to depositional texture. In: Ham, W. E. (ed.), Classification of carbonate rocks: American Association of Petroleum Geologists Memoir, p. 108-121.

[98] Embry, AF, and Klovan, JE, 1971, A Late Devonian reef tract on Northeastern Banks Island, NWT: Canadian Petroleum Geology Bulletin, v. 19, p. 730-781.

[99] Noiriel, C., Luquot, L., Madé, B., Raimbault, L., Gouze, P., van der Lee, J., 2009. Changes in reactive surface area during limestone dissolution: An experimental and modelling study. Chemical Geology 265, 160–170. https://doi.org/10.1016/j.chemgeo.2009.01.032

[100] Vernoux J.F., M. Degouy, H. Machard de Gramont, R. Galin (2002) –Etude bibliographique sur le suivi des risques engendrés par les forages profonds sur les nappes d'eau souterraine du bassin Seine-Normandie, rapport BRGM/RP-51312-FR, 70 pages, 14 figures, 1 tableau, 2 annexes

[101] Gombert, P., Thoraval, A., 2010. Etat des connaissances sur les risques liés au stockage géologique du CO2. Rapport n°1 : les risques en phase d'injection. INERIS/DRS-08-95145-11842B. 117p., 3 annexes.

[102] Bouc, O., 2008. Construction de scénarios d'évolution pour le stockage géologique du CO2, méthode et application. BRGM/RP-56592-FR, 108p, 23 ill, 3 annexes.

[103] Z. Li, M. Dong, S. Li, L. Dai, Densities and solubilities for binary systems of carbon dioxide + water and carbon dioxide + brine at 59 ◦C and pressures to 29 MPa, J.Chemical and Engineering Data 49 (2004) 1026–1031.

[104] Y. Liua, M. Houa, G. Yanga, B. Han, Solubility of CO2 in aqueous solutions of NaCl, KCl, CaCl2 and their mixed salts at different temperatures and pressures, J. Supercritical Fluids 56 (2011) 125–129.

[105] Ruth Jacob, Beverly Z. Saylor, CO2 solubility in multi-component brines containing NaCl, KCl, CaCl2 and MgCl2 at 297K and 1–14MPa,Chemical Geology,Volume 424, 2016, Pages 86-95,ISSN 0009-2541, https://doi.org/10.1016/j.chemgeo.2016.01.013.

[106] R.M. El-Maghraby, C.H. Pentland, S. Iglauer, M.J. Blunt,A fast method to equilibrate carbon dioxide with brine at high pressure and elevated temperature including solubility measurements, The Journal of Supercritical Fluids, Volume 62,2012, Pages 55-59,ISSN 0896-8446, https://doi.org/10.1016/j.supflu.2011.11.002.

[107] N. Spycher, K. Pruess, CO2–H2O mixtures in the geological sequestration of CO2. II. Partitioning in Chloride brines at 12–100 ◦C and up to 600 bar, GeochimicaActa 69 (2005) 3309–3320.

[108] Duan, Z.H., Sun, R., 2003. An improved model calculating CO2 solubility in pure water and aqueous NaCl solutions from 273 to 533 K and from 0 to 2000 bar. Chemical Geology 193(3-4), 257-271. doi: 10.1016/S0009-2541(02)00263-2 Matter, J.M.&Kelemen, P. B. 2009. Permanent storage of carbon dioxide in geological reservoirs by mineral carbonation. Nature Geoscience, 2, 837–841.

[109] Takenouchi, S.,Kennedy, G.C., The solubility of carbon dioxide in NaCl solutions at high temperatures and pressures Am J Sci May 1, 1965 263:445-454; doi:10.2475/ajs.263.5.445

[110] Shock, E.L., Helgeson, H.C., 1988. Calculation of the thermodynamic and transport properties of aqueous species at high pressures and temperatures: correlation algorithms for ionic species and equation of state predictions to 5 kb and 1000 °C. Geochim. Cosmochim. Acta, 52, 2009–2036.

[111] Chou, L., Garrels R.M. et Wollast R. 1989. Comparative study of the kinetics and mechanics of dissolution of carbonate minerals, Chemical Geology, 1989, 78, p. 269-282.

[112] Busenberg, E., Plummer, L.N., 1986. A comparative study of the dissolution and crystal growth kinetics of calcite and aragonite. In: Mumptom, F.A.Ed.., Studies Diagenesis. U.S.G.S. Bull. 1578, pp. 139–168.

[113] Morse, J.W. and F.T. Mackenzie (1990) Geochemistry of Sedimentary Carbonates Volume 48. Elsevier science

[114] Langmuir, D., 1997. Aqueous Environmental Geochemistry. Prentice-Hall, Upper Saddle River, 600 pp.

[115] Folk, R. L., 1974, The natural history of crystalline calcium carbonate: effect of magnesium content and salinity: Jour. Sed. Petrology, v. 44, p. 40-53

[116] Moore, C.H. (2001) Carbonate Reservoirs, Porosity Evolution and Diagenesis in a Sequence Stratigraphic Framework. Vol. 55, Development in Sedimentology, Elsevier, Amsterdam, 444 p

[117] Lasaga, A. C. (1998). Kinetic theory in the earth sciences, Princeton University Press

[118] Shiraki, R., Rock, P.A., Casey, W.H., 2000. Dissolution kinetics of calcite in 0.1 M NaCl solution at room temperature: an atomic force microscopic (AFM) study. Aquatic Geochemistry 6, 87–108.

[119] Murphy, W.M., Oelkers, E.H., Lichtner, P.C., 1989. Surface reactions rate versus diffusion of aqueous species in the control of irreversible mineral hydrolysis in geochemical processes.Chem. Geol. 78, 357–380.

[120] Madé B. [1991] Modélisation thermodynamique et cinétique des réactions géochimiques dans les intéractions eau-roche. Thèse Université Strasbourg I, 323 pp

[121] Casey W. H. [1987] Heterogeneous kinetics and diffusion boundary layers: the example of reaction in a fracture. Journal of Geophysical Research 92 (B8), 8007-8013

[122] Morse J. W, Arvidson R.S and Lüttge A. Calcium Carbonate Formation and Dissolution. Chem. Rev. 2007, 107, 2, 342-381. doi.org/10.1021/cr050358j

[123] Pokrovsky, O.S., Golubev, S.V., Schott, J., Castillo, A., 2009. Calcite, dolomite and magnesite dissolution kinetics in aqueous solutions at acid to circumneutral pH, 25 to 150 °C and 1 to 55 atm pCO2: New constraints on CO2 sequestration in sedimentary basins. Chemical Geology 265, 20–32. https://doi.org/10.1016/j.chemgeo.2009.01.013

[124] Peng, C., Crawshaw, J.P., Maitland, G.C., Trusler, J.P.M., 2015. Kinetics of calcite dissolution in CO2-saturated water at temperatures between (323 and 373)K and pressures up to 13.8MPa. Chemical Geology 403, 74–85. https://doi.org/10.1016/j.chemgeo.2015.03.012

[125] Levenson, Y., Schiller, M., Kreisserman, Y., Emmanuel, S., 2015. Calcite dissolution rates in texturally diverse calcareous rocks. Geological Society, London, Special Publications 406, 81–94. https://doi.org/10.1144/SP406.14

[126] Lasaga, A.C., Lüttge, A., 2003. A model for crystal dissolution. European Journal of Mineralogy 15, 603–615. https://doi.org/10.1127/0935-1221/2003/0015-0603

[127] Bear, J. (1988). Dynamics of fluids in porous media. Courier Dover Publications, pp 764

[128] Hoefner, M.L., Fogler, H.S., 1988. Pore evolution and channel formation during flow and reaction in porous media. AIChE Journal 34, 45–54.

[129] Fredd, C.N., Fogler, H.S., 1999. Optimum conditions for wormhole formation in carbonate porous media: Influence of transport and reaction. Spe Journal 4, 196–205.hemical Modeling of Aqueous Systems II. American Chemical Society, Washington, DC, pp. 212–225.

[130] Daccord, G., Lenormand, R., Lietard, O., 1993. Chemical Dissolution of a Porous-Medium by a Reactive Fluid .1. Model for the Wormholing Phenomenon. Chem. Eng. Sci. 48, 169–178. https://doi.org/10.1016/0009-2509(93)80293-Y

[131] Fredd, C.N., Miller, M.J., 2000. Validation of carbonate matrix stimulation models, in: SPE International Symposium on Formation Damage Control. Society of Petroleum Engineers.

[132] Steefel, C.I., Lasaga, A.C., 1990. Evolution of Dissolution Patterns: Permeability Change Due to Coupled Flow and Reaction, in: Melchior, D.C., Bassett, R.L. (Eds.), C

[133] Steefel, C.I., Maher, K., 2009. Fluid-Rock Interaction: A Reactive Transport Approach. Reviews in Mineralogy and Geochemistry 70, 485–532. https://doi.org/10.2138/rmg.2009.70.11

[134] Fredd, C.N., Fogler, H.S., 1999. Optimum conditions for wormhole formation in carbonate porous media: Influence of transport and reaction. Spe Journal 4, 196–205.hemical Modeling of Aqueous Systems II. American Chemical Society, Washington, DC, pp. 212–225.

[135] Bazin, B., others, 2001. From matrix acidizing to acid fracturing: a laboratory evaluation of acid/rock interactions. SPE Production & Facilities 16, 22–29.

[136] Bekri, S., Thovert, J.F., Adler, P.M., 1995. Dissolution of porous media. Chemical Engineering Science 50, 2765–2791.

[137] Cohen, C.E., Ding, D., Quintard, M., Bazin, B., 2008. From pore scale to wellbore scale: Impact of geometry on wormhole growth in carbonate acidization. Chemical Engineering Science 63, 3088–3099. https://doi.org/10.1016/j.ces.2008.03.021

[138] Daccord, G., 1987. Chemical dissolution of a porous medium by a reactive fluid. Physical review letters 58, 479.

[139] Golfier, F., Zarcone, C., Bazin, B., Lenormand, R., Lasseux, D., & Quintard, M. (2002). On the ability of a Darcy-scale model to capture wormhole formation during the dissolution of a porous medium. Journal of fluid Mechanics, 457(213), C254.

[140] Menke, H.P., Andrew, M.G., Blunt, M.J., Bijeljic, B., 2016. Reservoir condition imaging of reactive transport in heterogeneous carbonates using fast synchrotron tomography — Effect of initial pore structure and flow conditions. Chemical Geology 428, 15–26. https://doi.org/10.1016/j.chemgeo.2016.02.030

[141] Tardy, P.M.J., Lecerf, B., Christanti, Y.: An experimentally validated wormhole model for self-diverting and conventional acids in carbonate rocks under radial flow conditions. In:European Formation Damage Conference. Society of PetroleumEngineers (2007)

[142] Algive, L., 2009. Évolution des propriétés pétrophysiques d'écoulement pendant une injection de CO2 et impact induit au niveau de l'injectivité (PhD Thesis). Institut National Polytechnique de Lorraine.

[143] Tartakovsky, A.M., Meakin, P., Scheibe, T.D., Eichler West, R.M., 2007. Simulations of reactive transport and precipitation with smoothed particle hydrodynamics. Journal of Computational Physics 222, 654–672. https://doi.org/10.1016/j.jcp.2006.08.013

[144] Buijse, M.A., 1997. Understanding wormholing mechanisms can improve acid treatments in carbonate formations, in: SPE European Formation Damage Conference. Society of Petroleum Engineers.

[146] Rojas,J.,Giot,D.,Le Nindre, Y.M.,Criaud,A., Fouillac,C., Brach,M. (1989) Caracterisation et modelisation du reservoir geothermique du Dogger, bassin Parisien, France. Technical Report CCE, EN 3G-0046-F(CD), BRGM R 30 IRG SGN 89(in french)

[147] Wendebourg, J., Lamiraux, C., 2002. Estimating the ultimate recoverable reserves of the Paris Basin, France. Oil & Gas Science and Technology 57, 621–629.

[148] Rigollet, C., Collin, P.-Y., Badinier, G. et Brosse, E., 2007. CO2 Geological storage in France (Dogger, Paris Basin) in depleted reservoirs and aquifers - Sedimentologists input. 11ème Congrès Français deSédimentologie, Caen, p. 261.

[149] Brosse, é., Badinier, G., Blanchard, F., Caspard, E., Collin, P.Y., Delmas, J., Dezayes, C., Dreux, R., Dufournet, A., Durst, P., Fillacier, S., Garcia, D., Grataloup, S., Hanot, F., Hasanov, V., Houel, P., Kervévan, C., Lansiart, M., Lescanne, M., Menjoz, A., Monnet, M., Mougin, P., Nedelec, B., Poutrel, A., Rachez, X., Renoux, P., Rigollet, C., Ruffier-Meray, V., Saysset, S., Thinon, I., Thoraval, A., Vidal-Gilbert, S., 2010. Selection and Characterization of Geological Sites able to Host a Pilot-Scale CO 2 Storage in the Paris Basin (GéoCarbone - PICOREF). Oil & Gas Science and Technology – Revue de l'Institut Français du Pétrole 65, 375–403. https://doi.org/10.2516/ogst/2009085

[150] Lopez, S., Hamm, V., Le Brun, M., Schaper, L., Boissier, F., Cotiche, C., Giuglaris, E., 2010. 40 years of Dogger aquifer management in Ile-de-France, Paris Basin, France. Geothermics, 39(4) :339–356. doi: 10.1016/j.geothermics.2010.09.005

[151] Delmas, J., Brosse, E., Houel, P. 2010. Petrophysical Properties of the Middle Jurassic Carbonates in the PICOREF Sector (South Champagne, Paris Basin, France). Oil Gas Sci. Technol. - Rev. IFP, 65(3) 405–434. doi : 10.2516/ogst/2010002

[152] Casteleyn, L., Robion, P., Collin, P.-Y., Menéndez, B., David, C., Desaubliaux, G., Fernandes, N., Dreux, R., Badiner, G., Brosse, E., Rigollet, C., 2010. Interrelations of the petrophysical, sedimentological and microstructural properties of the Oolithe Blanche Formation (Bathonian, saline aquifer of the Paris Basin). Sedimentary Geology 230, 123–138. https://doi.org/10.1016/j.sedgeo.2010.07.003

[153] Vincent, B., Fleury, M., Santerre, Y., Brigaud, B., 2011. NMR relaxation of neritic carbonates: An integrated petrophysical and petrographical approach. Journal of Applied Geophysics 74, 38–58. https://doi.org/10.1016/j.jappgeo.2011.03.002

[154] Kalo, K., Grgic, D., Auvray, C., Giraud, A., Drach, B., Sevostianov, I., 2017. Effective elastic moduli of a heterogeneous oolitic rock containing 3-D irregularly shaped pores. International Journal of Rock Mechanics and Mining Sciences 98, 20–32. https://doi.org/10.1016/j.ijrmms.2017.07.009

[155] Jobard E, Sterpenich J, Pironon J, Corvisier J, Jouanny M, Randi A (2013) Experimental simulation of the impact of a thermal gradient during geological sequestration of CO2: The COTAGES experiment. Inter J Greenhouse Gas Control 12:56–71, doi:10.1016/j.ijggc.2012.11.001

[156] Le Guen, Y., Renard, F., Hellmann, R., Brosse, E., Collombet, M., Tisserand, D., and Gratier, J.P., 2007. Enhanced deformation of limestone and sandstone in the presence of high Pco2 fluids. journal of geophysical research, vol. 112, B05421, doi:10.1029/2006JB004637

[157] Grgic, D., 2011. Influence of CO 2 on the long-term chemomechanical behavior of an oolitic limestone. Journal of Geophysical Research 116. doi:10.1029/2010JB008176

[158] Zinsmeister, L., Dautriat, J., Dimanov, A., Raphanel, J., Bornert, M., 2013. Mechanical evolution of an altered limestone using 2-D and 3-D digital image correlation (DIC), in: 47th US Rock Mechanics/geomechanics Symposium. American Rock Mechanics Association.

[159] Andrieu, S., Brigaud, B., Barbarand, J., Lasseur, E., Saucède, T., 2016. Disentangling the control of tectonics, eustasy, trophic conditions and climate on shallow-marine carbonate production during the Aalenian–Oxfordian interval: From the western France platform to the western Tethyan domain. Sedimentary Geology 345, 54–84. https://doi.org/10.1016/j.sedgeo.2016.09.005

[160] Burbaud-Vergneaud, M., 1987. Fracturation et interactions socle-couverture : le seuil du Poitou. Thèse. Université de Poitiers.

[161] Bourbiaux, B., J. P. Callot, B. Doligez, M. Fleury, F. Gaumet, M. Guiton, R. Lenormand, J. L. Mari, and H. Pourpak. 2007. Multi-Scale Characterization of an Heterogeneous Aquifer Through the Integration of Geological, Geophysical and Flow Data: A Case Study. Oil & Gas Science and Technology - Rev. IFP 63.

[162] Taylor, H.F.W. "Cement Chemistry", 2nd edn, Thomas Telford Publishing, London, 1997. 465 pp (ISBN:0-7277-2592-0)

[163] Legrand, C., Baron, J., Sauterey, R., 1982. Le béton hydraulique. Presses de l'Ecole National des Ponts et chaussées, Paris.

[164] Chanvillard., G. 1999. "Le matériau béton : Connaissances générales", Lyon, Editions Aléas.

[165] Wertz, F., Gherardi, F., Blanc, P., Bader, A.-G., Fabbri, A., 2013. Cement CO2-alteration propagation at the well–caprock–reservoir interface and influence of diffusion. International Journal of Greenhouse Gas Control 12, 9–17. doi:10.1016/j.ijggc.2012.10.019

[166] Parkhurst D.L., Appelo C.A.J. User guide to PHREEQC (Vesrion 2). A computer program for speciation, batc-reaction, on dimensional transport, and inverse geochemical calculations: U.S Geological Survey Water-Ressources Investigations Report 99-4259, 310p.

[167] Kervévan K., Lanini S., Audigane P. Etude comparative des algorithmes de couplage des codes chimie-transport utilisés au BRGM : premiers résultats à partir d'expérimentations numériques simples. BRGM/RP-54904-FR, 66 p., 11 Fig.

[168] Belgodere, C., Sterpenich, J., Pironon, J., Jobard, E., Randi, A., Birat, J.-P., 2013. CO2 Storage from Blast Furnace in the Triassic Sandstones of Lorraine, (Eastern Paris Basin, France): an experimental study. Energy Procedia 37, 5315–5322. https://doi.org/10.1016/j.egypro.2013.06.449

[169] Sterpenich, J., Jobard, E., El Hajj, H., Pironon, J., Randi, A., Caumon, M.-C., 2014. Experimental study of CO 2 injection in a simulated injection well: the MIRAGES experiment: Experimental study of CO 2 injection in a simulated injection well: the MIRAGES experiment. Greenhouse Gases: Science and Technology 4, 210–224. https://doi.org/10.1002/ghg.1389

[170] M.-H. Beddelem, F. Bugarel, L. HirsingerandM. Pujol,with the collaboration of G. Blount and K. O'Neil. (2015). Technical-economic feasibility and operational constraints of a geothermal loop including a CO2dissolution facility.BRGM/RP-65134-FR. 61p., 21illus.,0ann.

[171] Heat Transfer in Channel Flow. In: Heat Convection. 2006. Springer, Berlin, Heidelberg. https://doi-org.bases-doc.univ-lorraine.fr/10.1007/978-3-540-30694-8_6

[172] Gouze, P., Coudrain-Ribstein, A., 2000. Modeling permeability changes caused by hydrothermal circulation. Natural Resources Research 9, 157–166.

[173] Haffen, S., 2012. Caractéristiques géothermiques du réservoir gréseux du Buntsandstein d'Alsace. Université de Strasbourg.

[174] Sigismondi, M.E., Soldo, J.C., 2003. Curvature attributes and seismic interpretation: Case studies from Argentina basins. The Leading Edge 22, 1122–1126.

[175] Roberts, A., 2001. Curvature attributes and their application to 3 D interpreted horizons. First break 19, 85–100.

[176] Armstrong, R.T., Georgiadis, A., Ott, H., Klemin, D., Berg, S., 2014. Critical capillary number: Desaturation studied with fast X-ray computed microtomography: MICROTOMOGRAPHY IMAGED DESATURATION. Geophysical Research Letters 41, 55–60. https://doi.org/10.1002/2013GL058075

[177] Andrew, M., Menke, H., Blunt, M.J., Bijeljic, B., 2015. The Imaging of Dynamic Multiphase Fluid Flow Using Synchrotron-Based X-ray Microtomography at Reservoir Conditions. Transport in Porous Media 110, 1–24. https://doi.org/10.1007/s11242-015-0553-2

[178] Scanziani, A., Singh, K., Blunt, M.J., Guadagnini, A., 2017. Automatic method for estimation of in situ effective contact angle from X-ray micro tomography images of two-phase flow in porous media. Journal of Colloid and Interface Science 496, 51–59. https://doi.org/10.1016/j.jcis.2017.02.005

[179] Hege, H.-C., Seebass, M., Stalling, D., Zöckler, M., 1997. A generalized marching cubes algorithm based on non-binary classifications.

[180] Kohlmann, F.J. (2003). What is pH and how is it measured: atechnical handbook for industry.Hach Company. Available at: www.hach.com/quick.search-download.search.jsa?keywords=HANDBOOK

[181] Guo, H., Chen, Y., Hu, Q., Lu, W., Ou, W., Geng, L., 2014. Quantitative Raman spectroscopic investigation of geo-fluids high-pressure phase equilibria: Part I. Accurate calibration and determination of CO2 solubility in water from 273.15 to 573.15K and from 10 to 120MPa. Fluid Phase Equilibria 382, 70–79. doi:10.1016/j.fluid.2014.08.032

[182] Caumon, M.-C., Sterpenich, J., Randi, A., Pironon, J., 2016. Measuring mutual solubility in the H2O–CO2 system up to 200bar and 100°C by in situ Raman spectroscopy. International Journal of Greenhouse Gas Control 47, 63–70. doi:10.1016/j.ijggc.2016.01.034

[183] Deville de Periere, M., Durlet, C., Vennin, E., Lambert, L., Bourillot, R., Caline, B., Poli, E., 2011. Morphometry of micrite particles in cretaceous microporous limestones of the Middle East: Influence on reservoir properties. Marine and Petroleum Geology 28, 1727–1750. doi:10.1016/j.marpetgeo.2011.05.002

[184] André, L., Audigane, P., Azaroual, M., Menjoz, A., 2007. Numerical modeling of fluid–rock chemical interactions at the supercritical CO2–liquid interface during CO2 injection into a carbonate reservoir, the Dogger aquifer (Paris Basin, France). Energy Conversion and Management 48, 1782–1797. doi:10.1016/j.enconman.2007.01.006

[185] Fleury, M., Soualem, J., 2009. Quantitative analysis of diffusional pore coupling from T2-store-T2 NMR experiments. Journal of Colloid and Interface Science 336, 250–259. doi:10.1016/j.jcis.2009.03.051

[186] Noiriel, C., Renard, F., Doan, M.-L., Gratier, J.-P., 2010. Intense fracturing and fracture sealing induced by mineral growth in porous rocks. Chemical Geology 269, 197–209. doi:10.1016/j.chemgeo.2009.09.018

[187] Ochs, M., Mallants, D., Wang, L., 2016. Radionuclide and Metal Sorption on Cement and concrete, Topics in Safety, Risk, Reliability and Quality. Springer International Publishing, Cham.

[188] Berner, U.R., 1992. Evolution of pore water chemistry during degradation of cement in a radioactive waste repository environment. Waste management 12, 201–219.

[189] Andra., 2005. Référentiel de comportement des radionucléides et des toxiques chimiques d'un stockage dans le Callovo-Oxfordien jusqu'à l'homme, Site de Meuse/Haute-Marne, Tome 1/2: Chapitres 1 à 4, Dossier 2005 Argile.

[190] Carroll, S., Carey, J.W., Dzombak, D., Huerta, N.J., Li, L., Richard, T., Um, W., Walsh, S.D.C., Zhang, L., 2016. Review: Role of chemistry, mechanics, and transport on well integrity in CO2 storage environments. International Journal of Greenhouse Gas Control 49, 149–160. https://doi.org/10.1016/j.ijggc.2016.01.010

[191] Marty, N.C.M., Tournassat, C., Burnol, A., Giffaut, E., Gaucher, E.C., 2009. Influence of reaction kinetics and mesh refinement on the numerical modelling of concrete/clay interactions. Journal of Hydrology 364, 58–72. https://doi.org/10.1016/j.jhydrol.2008.10.013value of pH can combine the Ca+ ion sreleas from the cement to the carbonate in solution provided by the reactive solution.

[192] Duguid, A., Radonjic, M., Bruant, R., Mandecki, T., Scherer, G., Celia, M., 2004. The effect of CO2 sequestration on oil well cements, in: Greenhouse Gas Technologies Conference (GHGT–7).

[193] Brunet, J.-P.L., Li, L., Karpyn, Z.T., Kutchko, B.G., Strazisar, B., Bromhal, G., 2013. Dynamic Evolution of Cement Composition and Transport Properties under Conditions Relevant to Geological Carbon Sequestration. Energy & Fuels 27, 4208–4220. https://doi.org/10.1021/ef302023v

[194] Duguid, A., Scherer, G.W., 2010. Degradation of oilwell cement due to exposure to carbonated brine. International Journal of Greenhouse Gas Control 4, 546–560. https://doi.org/10.1016/j.ijggc.2009.11.001

[195] Randi, A., Sterpenich, J., Thiéry, D., Kervévan, C., Pironon, J., Morlot, C., 2017. Experimental and Numerical Simulation of the Injection of a CO 2 Saturated Solution in a Carbonate Reservoir: Application to the CO 2 -DISSOLVED Concept Combining CO 2 Geological Storage and Geothermal Heat Recovery. Energy Procedia 114, 2942–2956. https://doi.org/10.1016/j.egypro.2017.03.1423

[196] Jobard, E., Sterpenich, J., Pironon, J., Corvisier, J., Randi, A., 2018. Experimental Modelling of the Caprock/Cement Interface Behaviour under CO2 Storage Conditions: Effect of Water and Supercritical CO2 from a Cathodoluminescence Study. Geosciences 8, 185. https://doi.org/10.3390/geosciences8050185

[197] Andac, M.; Glasser, F.P. 1999. Long-term leaching mechanisms of Portland cement-stabilized municipal waste fly ash in carbonated water. Cem. Concr. Res., 29, 179–186. https://doi.org/10.1016/S0008-8846(98)00194-X

[198] Guichet X., Schott J., Oelkers E.H., Vincent B., Magnier C. and Brosse E., 2005, Reactive transport experiments and modelling of CO2 sequestration in deep aquifers, Geochim. and Cosmochim. Acta (Abstracts of the 15th Goldschmidt Conference, Moscow Idaho, USA), 69(N.10S):A 179;

[199] Menke, H.P., Bijeljic, B., Blunt, M.J., 2017. Dynamic reservoir-condition microtomography of reactive transport in complex carbonates: Effect of initial pore structure and initial brine pH. Geochimica et Cosmochimica Acta 204, 267–285. https://doi.org/10.1016/j.gca.2017.01.053

[200] Ortoleva, P., Merino, E., Moore, M., Chadam, J., 1987. Geochemical self-organization I; reaction-transport feedbacks and modeling approach. American Journal of Science December 1987, 287 (10) 979-1007; DOI: https://doi.org/10.2475/ajs.287.10.979

[201] Ortoleva, P., Chadam, J., Merino, E., Sen, A., 1987. Geochemical self-organization II; the reactive-infiltration instability. American Journal of Science December 1987, 287 (10) 1008-1040; DOI: https://doi.org/10.2475/ajs.287.10.1008

[202] Ellis, B., Peters, C., Fitts, J., Bromhal, G., McIntyre, D., Warzinski, R., Rosenbaum, E., 2011. Deterioration of a fractured carbonate caprock exposed to CO2-acidified brine flow. Greenhouse Gases: Science and Technology 1, 248–260.

[203] Smith, M.M., Hao, Y., Carroll, S.A., 2017. Development and calibration of a reactive transport model for carbonate reservoir porosity and permeability changes based on CO 2 core-flood experiments. International Journal of Greenhouse Gas Control 57, 73–88. https://doi.org/10.1016/j.ijggc.2016.12.004

[204] Noiriel, C., 2015. Resolving Time-dependent Evolution of Pore-Scale Structure, Permeability and Reactivity using X-ray Microtomography. Reviews in Mineralogy and Geochemistry 80, 247–285. https://doi.org/10.2138/rmg.2015.80.08

[205] Daccord, G., Touboul, E., Lenormand, R., 1989. Chemical dissolution of a porous medium: Limits of the fractal behaviour. Geoderma 44, 159–165

[206] Qiu, X., Aidagulov, G., Ghommem, M., Edelman, E., Brady, D., Abbad, M., 2018. Towards a better understanding of wormhole propagation in carbonate rocks: Linear vs. radial acid injection. Journal of Petroleum Science and Engineering 171, 570–583. https://doi.org/10.1016/j.petrol.2018.07.075

[207] Frick, T.P.: "Production and Stimulation Mechanisms of Horizontal Wells," Ph.D. thesis (1993), Mining University Leoben, Austria.

[208] Hung, K.M., Hill, A.D., Sepehrnoori, K., 1989. A mechanistic model of wormhole growth in carbonate matrix acidizing and acid fracturing. Journal of petroleum technology 41, 59–66.

[209] Magee, J., Buijse, M., and Pongratz, R., Method for Effective Fluid Diversion When Performing a Matrix Acid Stimulation in Carbonate Formations, Middle East Oil Show and Conference, Society of Petroleum Engineers, 1997.

[210] Cheng, H., D. Zhu, and A. D. Hill, 2016, The Effect of Evolved CO2 on Wormhole Propagation in Carbonate Acidizing: SPE Production & Operations, no. February, p. 24-26, doi:10.2118/178962-PA.

[211] Aidagulov, G., Gwaba, D., Kayumov, R. et al. 2019. Effects of Pre-Existing Fractures on Carbonate Matrix Stimulation Studied by Large-Scale Radial Acidizing Experiments. Paper presented at the SPE Middle East Oil and Gas Show and Conference, Manama, Bahrain, 18–21 March. SPE-195153-MS. https://doi.org/10.2118/195153-MS.

[212] Huang, T, D Zhu, and AD Hill. 1999. Prediction of wormhole population density in carbonate matrix acidizing." SPE European Formation Damage Conference. Society of Petroleum Engineers.

[213] Schechter, R.S., Gidley, J.L., 1969. The change in pore size distribution from surface reactions in porous media. AIChE Journal 15, 339–350.

[214] Detwiler, R.L., Glass, R.J., Bourcier, W.L., 2003. Experimental observations of fracture dissolution: The role of Péclet number on evolving aperture variability: FRACTURE DISSOLUTION. Geophysical Research Letters 30. doi:10.1029/2003GL017396

[215] Elkhoury, J.E., Ameli, P., Detwiler, R.L., 2013. Dissolution and deformation in fractured carbonates caused by flow of CO2-rich brine under reservoir conditions. International Journal of Greenhouse Gas Control 16, S203–S215. https://doi.org/10.1016/j.ijggc.2013.02.023

[216] Gdanski R. (1999) A fundamentally new model of acid wormholing in carbonates, in: Proceedings of the SPE European Formation Damage Conference, Society of Petroleum Engineers, The Hague, Netherlands, pp. 1–10.

[217] C.-E. Cohen, Modélisation et simulation de la stimulation acidedes puits carbonatés, Ph.D. thesis, Institut National Polytech-nique de Toulouse, 2007.

[218] Oltéan, C., Golfier, F., Buès, M.A., 2013. Numerical and experimental investigation of buoyancy-driven dissolution in vertical fracture: BUOYANCY-DRIVEN DISSOLUTION IN FRACTURE. Journal of Geophysical Research: Solid Earth 118, 2038–2048. https://doi.org/10.1002/jgrb.50188

[219] Dijk, P.E., Berkowitz, B., Yechieli, Y., 2002. Measurement and analysis of dissolution patterns in rock fractures: MEASUREMENT AND ANALYSIS OF DISSOLUTION IN ROCK FRACTURES. Water Resources Research 38, 5–1–5–12. https://doi.org/10.1029/2001WR000246

[220] Mainhagu, J., Golfier, F., Oltéan, C., Buès, M.A., 2012. Gravity-driven fingers in fractures: Experimental study and dispersion analysis by moment method for a point-source injection. Journal of Contaminant Hydrology 132, 12–27. https://doi.org/10.1016/j.jconhyd.2012.02.004

[221] Berkowitz, B., 2002. Characterizing flow and transport in fractured geological media: A review. Advances in Water Resources 25, 861–884. https://doi.org/10.1016/S0309-1708(02)00042-8

[222] Svec, R.K., Grigg, R.B., 2001. Physical effects of WAG fluids on carbonate core plugs, in: SPE Annual Technical Conference and Exhibition. Society of Petroleum Engineers.

[223] Le Guen, Y., 2006, Etude expérimentale du couplage chimie-mécanique lors de la percolation d'un fluide réactif dans des roches sous contrainte, dans le contexte de la séquestration géologique du CO2 : Ph.D thesis, Université Joseph Fourier, Grenoble, France.

[224] Noiriel, C., Gouze, P., Madé, B., 2013. 3D analysis of geometry and flow changes in a limestone fracture during dissolution. Journal of Hydrology 486, 211–223. https://doi.org/10.1016/j.jhydrol.2013.01.035

[225] Noiriel, C., Steefel, C.I., Yang, L., Ajo-Franklin, J., 2012. Upscaling calcium carbonate precipitation rates from pore to continuum scale. Chemical Geology 318-319, 60–74. https://doi.org/10.1016/j.chemgeo.2012.05.014

[226] Qajar, J., François, N., Arns, C., 2012. Micro-tomographic Characterization of dissolution-induced local porosity changes including fines migration in carbonate rock. SPE Journal 18, 545-562. Doi : 10.2118/153216-PA

[227] Fischer, C., Lüttge, A., 2017. Beyond the conventional understanding of water–rock reactivity. Earth Planet. Sci. Let., 457, 100–105, doi:10.1016/j.epsl.2016.10.019.

[228] Ellis, B.R., Fitts, J.P., Bromhal, G.S., McIntyre, D.L., Tappero, R., Peters, C.A., 2013. Dissolution-Driven Permeability Reduction of a Fractured Carbonate Caprock. Environmental Engineering Science 30, 187–193. https://doi.org/10.1089/ees.2012.0337

[229] Marcu, A., Alberola, E., Caneill,J.Y., Mazzoni, M., Schleicher, S., Vailles, C., Stoefs, W., Vangenechten, D., et Cecchettil. F. (2019). I4CE. State of the EU ETS Report. https://www.i4ce.org/wp-core/wp-content/uploads/2019/05/2019-State-of-the-EU-ETS-Report-1.pdf

[230] Thèse Hassiba Teghidet. Etude de la cristallisation contrôlée de la calcite par voie électrochimique. Effet des ions étrangers au système calcocarbonique sur la nucléation-croissance de la calcite.. Autre. Université Pierre et Marie Curie - Paris VI, 2012. Français. <tel-00788536>

[231] Cailleux P., Jacquin, C., Dragone, D., Girou, A., Roques, H., Humbert, L., Influence des ions étrangers et de la matière organique sur la cristallisation des carbonates de calcium. Rev. Inst. Fr. Pét., 34 1 (1979) 83-112. Published online: 2006-11-01. https://doi.org/10.2516/ogst:1979003

[232] Steefel ,C.I. and Van Cappellen, P., 1990. A new kinetic approach to modeling water-rock interaction: The role of nucleation, precursors, and Ostwald ripening. Geochim. Cosmochim. Acta54, 2657–2677.

[233] Nielsen, A.E., 1964. Kinetics of precipitation. Pergamon

[234] Mutaftschiev, B., 1993. Nucleation. In: Handbook on Crystal Growth. Hurle DTJ (ed) North–Holland, Amsterdam, p 187-248C

[235] Fleury, M., Pironon, J., Le Nindre, Y.M., Bildstein, O., Berne, P et al.. 2010. Evaluating sealingefficiency of caprocks for CO2 storage: an overview of the Geocarbone Integrity program and results.Oil & Gas Science and Technology - Revue d'IFP Energies nouvelles, Institut Français du Pétrole, 65 (3), pp.435-444. 0.2516/ogst/2010007.

[236] Garrels, Robert M., and Charles L. Christ. 1965. Solutions, minerals, and equilibria. New York: Harper & Row.

[237] Ottonello, G., 1997. Principles of Geochemistry. xii 894 pp. New York: Columbia University Press. ISBN 0 231 09984 3. Geological Magazine, 135(5), 723-732. doi:10.1017/S0016756898268981

[238] Kielland, J. 1937. Individual Activity Coefficients of Ions in AqueousSolutions.J. Res. Natl. Bur. Stand. 59, 1675−1678

LISTE DES FIGURES (LIST OF FIGURES)

Figure 1: Liste des installations de CSC à grande échelle en opération, en construction ou en phase de projet (Source : Global CCS Institut (2018). Global status of CCS 2018)._____ 37

Figure 2: Représentation schématique du concept CO2-DISSOLVED combinant le stockage du CO_2 sous forme dissoute et la récupération de chaleur géothermique via un système de doublet.. (http://co2-dissolved.brgm.fr/).(@BRGM)_____ 42

Figure 3: Petits à moyens émetteurs industriels de CO_2 (ca. 10-150 kt/yr) et sites géothermiques sur la carte géologique de la France simplifiée (Castillo et al., 2014 [28] ; (Points jaunes, données IREP 2011))._____43

Figure 4: Pi-CO2 : Prototype de technologie de captage du CO_2 par absorption avec un système de transfert de masse en cascade (adsorber) (@BRGM)._____ 44

Figure 5: Composition des oolithes marines récentes et plus anciennes [79].____ 51

Figure 6: Les différents types de pores._____ 53

Figure 7: Classification des familles de taille de pores dans la matrice rocheuse en fonction du diamètre d'entrée de pore [82]._____ 53

Figure 8: Classification des différents types de porosité d'une roche carbonatée selon Choquette et Pray [83]._____ 54

Figure 9: Observations MEB sur calcaire de Lavoux sain de la surface 1) d'un monocristal de calcite (sparite) et d'une calcite finement cristallisée (microsparite) et 2) d'un cortex micritique microcristallin._____ 56

Figure 10: Représentation schématique de l'hétérogénéité réactive du mécanisme de dissolution à la surface d'un cristal de calcite par la répartition des différents sites de dissolution préférentielle [94]._____ 57

Figure 11: Classification des roches carbonatées selon la texture de dépôt par Duhnam [96]._____ 59

Figure 12: Texture d'un calcaire cristallin ou dolomie cristalline._____ 59

Figure 13: a) Solubilité du CO_2 dans l'eau pure en fonction des paramètres pression et température [108] et b) pour différentes concentrations de NaCl en fonction de la pression [108 ; 109]._____ 61

Figure 14: Solubilité de la calcite magnésienne en fonction de la teneur en $MgCO_3$ dans la roche (Morse et Mackenzie., 1990) [113]: données pour la calcite, Mg-calcite et aragonite, Langmuir., 1997 [114] : données pour la calcite et l'aragonite)._____ 64

Figure 15 : Habitus des croissances des cristaux de calcite en fonction du ratio Mg/Ca en condition naturelle [115, 116]._____ 65

Figure 16 : Evolution des coefficients d'activité de Ca^{2+} et CO_3^{2-} calculés à l'aide de la loi de Debye-Hückel en fonction de la force ionique de la solution à 60°C._____ 66

Figure 17: Schéma représentant les cinq étapes élémentaires observées lors des processus de dissolution/précipitation d'un minéral à son interface avec la solution aqueuse. A droite du schéma, il est possible de visualiser l'évolution des concentrations au sein de la couche interfaciale lors du contrôle de la dissolution d'un solide (a) par le transport diffusif, (b) contrôle mixte, ou (c) par la réaction de surface (modifié d'après Madé 1991 [120])._____ 67

Figure 18: Vitesses de dissolution de la calcite en fonction de a) la P_{CO2} à différentes températures [123] et b) de l'inverse de la température pour différentes pression de CO_2 . ◆, P_{CO_2} = 6 MPa; ■, P_{CO_2} = 10 MPa et ▲, P_{CO_2} = 13.8 MPa [124]._____ 68

Figure 19: Comparaison des spectres représentant la distribution des vitesses de dissolution à la surface d'un monocristal et d'une micrite. Les images AFM correspondent aux états de surface propres à chaque échantillon [125]. b) Simulation de la formation d'un puits de dissolution sur le site d'un défaut de dislocation avec la génération d'ondes progressives de dissolution [126]._____ 69

Figure 20: Représentation schématique des différents mécanismes intervenant lors du transport hydraulique d'éléments conservatifs dans un milieu poreux saturé a) Mise en évidence de l'influence de la tortuosité et de la géométrie des pores sur le mécanisme de dispersion ; les images représentent l'accumulation de stacks acquis par tomographie aux rayons X sur les échantillons de calcaire (cette étude) b) Influence des phénomènes de friction sur le mécanisme de dispersion au sein d'un pore et c) mécanisme de diffusion._____ 72

Figure 21: Représentation schématique des différents régimes d'altération obtenus expérimentalement aux échelles microscopiques [130] et macroscopiques [131]._ 74

Figure 22: Représentation schématique des régimes de dissolution [140] (a) de type wormholing et (b) de type " channeling ". L'espace poreux est représenté en noir ; les points noirs correspondent à la porosité intra-granulaire ; la solution réactive est en bleu et la roche en blanc._____ 75

Figure 23: Diagramme de prédiction des transitions entre les différentes figures de dissolution en fonction des nombres adimensionnels *Pe-Da* [139]._____ 76

Figure 24: Geological SW-NE cross-section. Source BRGM, modified. http://sigespoc.brgm.fr/spip.php?article33_____ 82

Figure 25: Location of the major faults in the studied area on a simplified geological map of the Poitou-Charentes region. Source BRGM, modified. http://sigespoc.brgm.fr/spip.php?article33_____ 83

Figure 26: Main directions of the regional fractures [160]._____ 83

Figure 27: Dominant dip [160]._____ 83

Figure 28: Simplified model for the pre-dimensioning of the MIRAGES-2 experiment._____ 86

Figure 29: Evolution of the pH values of (a) the aqueous solution in the core sample and (b) the aqueous solution in the reactor with time depending on the injection flowrate._____ 88

Figure 30: Evolution of (a) the porosity of the core sample with time depending on the injection flowrate and (b) evolution of the saturation index for calcite in the reactor with time and for different injection flowrates._____ 89

Figure 31: Evolution of the pH values of (a) the aqueous solution in the core sample and (b) the aqueous solution in the reactor with time depending on the $P_{(CO_2)}$ of the injected solution._____ 89

Figure 32: Evolution of (a) the porosity of the core sample with time as a function of the $P_{(CO_2)}$ and (b) evolution of the saturation index for calcite in the reactor with time as a function of the $P_{(CO_2)}$ in the injected solution._____ 90

Figure 33: Evolution of the total $P_{(CO_2)}$ in (a) the core sample and (b) in the reactor with time depending on the $P_{(CO_2)}$ in the injected solution._____ 90

Figure 34: (a) View of the injection well scale-model. (b) Schematic view of the injection well of the MIRAGES-2 experiment. Dimensions are given in millimeters._92

Figure 35: (a) Typical injection well design [170] with the maximum provided angle (red circle) at the open hole depth. (b) Core sampling of the sample simulating the borehole angle on the field._____ 92

Figure 36: Global view of the MIRAGES-2 radial flowthrough test bench._____ 93

Figure 37: Schematics of the MIRAGES-2 MIRAGES-2 radial flowthrough test bench._____ 94

Figure 38: 5 liters mixing device plan (solubilization system)._____ 95

Figure 39: Double syringe pump (@Teledyne ISCO, model 500D)._____ 96

Figure 40: (a) Schematic drawing of the radial injection device MIRAGES-2 (b) Top view of the MIRAGES-2 lid (c) Front view of the various pressure measuring transducer and in-situ probe locations in the system._____ 97

Figure 41: Workflow on the rock analysis._____ 103

Figure 42: Data acquisition device of nitrogen permeability: 1) Hassler cell, 2) Confining system, 3) “head” system and 4) “foot” system._____ 104

Figure 43: Plan of a penetrometer used for the measurements of porosity by injection of mercury. The cannula is covered with a metallic film._____ 105

Figure 44: a) Curves obtained by injection of mercury on a 20 x 20 mm sample of Lavoux limestone used in this study ($\varnothing_{free}$ = free porosity, $\varnothing_{trapped}$ = trapped porosity). b) Histogram of distribution of entrance radii of pores for bulk porosity of limestone (1st injection of Hg porosity)._____ 106

Figure 45: Location of the 20 mm diameter X 20 mm height cylinders sampled for the post-experimental petrophysical analysis._____107

Figure 46: Model of preparation protocol of thin sections used in the study (example of the sample extracted from the blank experiment): (a) The core-plug is first split in two identical parts by following the diameter of the core, (b) Sugars are cut in specific areas of the core-plug (c) and sugar are finally polished at 30 µm before carbon covering._____ 107

Figure 47: (a) Schematic layout of X-Ray microtomograph. (b) Voxel size and 3-D voxel resolution depending of the sample size of this study (example of the 10 x 10 cm cylindrical sample)._____ 110

Figure 48: a) 2-D-slice of the reconstructed raw image encoded in 16-bit with the corresponding histogram of the grey level. It should be noticed that the circled part at the right end of the histogram corresponds to the stainless steel injection tube. b) 2-D Image filtered using an anisotropic diffusion filter with the corresponding filtered histogram of the grey level. The red line corresponds to the solid/void interface. This step made the artifacts related to the injection tube disappear. c) 2-D image of the delimitation of the porous network (in blue) within the segmented image (using the thresholding value). d) Projection of 3-D reconstruction in the XY plane using a generalized marching cubes algorithm._____ 112

Figure 49: Definition of curvature κ : the curvature at a considered point P on a curve is defined as the rate of change of an angle dω with respect to the arc length *dS*. The "ideal" tangent circle (which best fits the arc) is called the “osculating circle” and the curvature correspond to: $\kappa = \frac{d\omega}{dS} = \frac{2\pi}{\pi R} = \frac{1}{R}$. N are the vectors normal to the curve at each point P. The convergence (convexity), divergence (concavity) or parallelism (flatness) of nearby surface normal vectors allow to define the sign of the curvature which are respectively positive, negative or zero._____ 114

Figure 50: a) Reproduction in 3-dimensions of the tangential and normal radial plans at a P point of a curved surface, b) Curvature in three-dimensions ([174] modified): a 3-D surface is intercepted by an infinity of orthogonal plans with their associated curvature (κ_1 and κ_2 for example). For the definition of the key curvature indicator, only the minimum (κ_{min}) and maximum (κ_{max}) values of the curvature, which are called major curvatures, are used. c) Illustration of the local appearance of the surface according to the sign of the main curvatures (the colored part on the figure refers to a 3-D simulation of a dissolved volume observed in this study)._____ 115

Figure 51: Simplified diagram of the surface meshing algorithm by cell triangulation. [179]._____ 116

Figure 52: Image processing for surface curvature analysis workflow a) Typical 3-D reconstruction of a post-experimental dissolution arrays after tomographic image processing (threshold volume in voxel). (b) Reconstruction of the 3-D image (rock/void interface) by smoothing the surface in triangular coordinates. The colorations correspond to the different values of surface mean curvatures (c) Illustration of the curvature calculation at a given point. The black and withe arrows represents the

orthogonal eigenvectors of the surface curvature in the plane T tangential to the surface. The red arrow corresponds to the normal eigenvector. The module calculates the major normal surface curvatures of the curve located at the interception between the surface defined by a given number of neighboring triangles (numbers in red) and the radial plane. d) Mean curvature color map with considered extreme value. e) Inside view of the porosity network depicting the idea of convexity and concavity of curvatures. f) Evolution of the curvature of the rock-void interface for the selected interface. The black line corresponds to the distribution of the raw data surface curvature and the red line to the smoothing of these data (moving average) g) Mean curvature color map across the initial rock/void interface analyzed._____117

Figure 53: a) HP/HT in situ pH probe with its cable and 316SS tee allowing it implementation in the MIRAGES-2 test bench. b) Scheme of the probe with the different components (@Hendress and Hauser Conducta INC)._____119

Figure 54: Calibration curves of high pressure pH probes showing the electrode potential as a function of pH for two different calibration steps, before and after the end of the 21d injection experiment without salt (a) Output of the 5L mixing autoclave and (b) output of the MIRAGES-2 autoclave._____121

Figure 55: Description of Kaiser RXN1 Raman spectrometer (a). Implementation of the probe on the test bench (b): the probe is crimped to a 316 SS tee with ¼" connection, the laser is focused at the center of the tee where the solution flows continually._____ 122

Figure 56: Typical Raman spectra of dissolved CO_2 in pure water acquired with the in-situ Raman probes at 20°C/30bar._____ 123

Fig. 57: (a) Evolution of Raman spectra of dissolved CO_2 in water with time after CO_2 injection (T = 0 min). The peaks at 1276 cm^{-1} and at 1384 cm^{-1} correspond to the Fermi doublet characteristic of the dissolved CO_2 and the peak at 1640 cm^{-1} is the H_2O bending vibration band. The peak at 1555 cm^{-1} comes from atmospheric O_2 trapped in the probe. The spectra are offset for clarity. (b) Diagram representing the evolution of the ratio I_{CO2}/I_{H2O} and the corresponding solubility in mole/kg with time after CO_2 injection until equilibrium._____ 124

Figure 58: I_{CO2}/I_{H2O} peak intensity ratio as a function of CO_2 solubility ($mol.kg^{-1}_{water}$) calculated from the thermodynamic model of Duan and Sun (2003) [108] at 20°C. 125

Figure 59: Illustration of the Lavoux limestone texture: (a) microscopic observation on a fresh sample, (b) microscopic observation on thin section (polarized light). We can see the fabric of the rock with the ooids (Ool) and the syntaxial cementation (Synt-cem) around an echinoderm fragment (Eq) and also the oolitic fringe (ool-b). The dark areas correspond to the porosity, (c) SEM observation (in SE Secondary Electrons mode) of Lavoux limestone. Overview of the surface showing the ooid (oolite), syntaxial cement (synt-cem) and macropores (M-pore) (d) with micritic cortex and sparitic equant cement (Spar-equ-cem).(e) Syntaxial cement with dissolution pits (f) Focus on the micritic cortex and the microporosity (µ-por)._____ 131

Figure 60: Classification of micritic micro-textures from Deville de Periere et al., 2011 [183], mainly based on crystal morphology and type of inter-crystal contact.____ 132

Figure 61: CT scans of a sample of the Lavoux limestone (resolution 5 µm) with the rock fabric in grey and the porosity in black. (a) Sub-horizontal cross-section showing the arrangement. Of Oolites and cements. The nucleus of some oolites are partially dissolved. Some potential micro-fracture are also visible (double red arrows) (c) Focus on the oolites and sparitic cement: The CT-scan displays stylolitic contacts of ooids (red circles arrows) and some grains interpenetration due to a chemical compaction during burial (large red arrows)._____ 132

Figure 62: CT scans of a sample of the Lavoux limestone (resolution 5 µm) with the rock fabric in grey and the porosity in black. (a) Sub-vertical cross-section: the dark area in the ooids corresponds to a partial secondary dissolution of the intra-porosity and the large red arrows show some grains interpenetration due to a chemical compaction during burial._____ 133

Figure 63: Purcell test (Hg porosimetry) on the Lavoux limestone (first injection). Pore size distribution (porous spectrum) is for bulk porosity._____ 135

Figure 64: Evolution of temperature and CO_2 pressure in the mixing autoclave (5 Liters) for the 21d experiment without salt._____136

Figure 65: Evolution of pressures (confining and injection), temperatures (confining and injection), ΔP (between injection and confining) and injection flowrate in the MIRAGES-2 autoclave during the 21d experiment without salt._____137

Figure 66: pH measurements of the injected solution and of the solution at the outlet of the core-plug during the different experiments._____ 139

Figure 67: 21d experiment injection of CO_2 laden equilibrated solution without salt: Evolution of the pH values and total inorganic carbon concentrations at the inlet and outlet of the core-plug with time (in kg per kg of solution)._____ 140

Figure 68: 20d experiment injection of CO_2 laden equilibrated solution with salt: Evolution of the pH values and total inorganic carbon concentrations at the inlet and outlet of the core-plug with time._____141

Fig 69: Chemical analysis (ICP-AES) of the samples collected during the different experiments. The concentrations of (a) sulfates ions, (b) calcium, (c) magnesium, (d) strontium, (e) aluminum and (f) iron were measured at the outlet of the core-plug are plotted as a function of the duration of experiment. (Sal.sol corresponds to saline solution)._____ 142

Figure 70: Evolution of the Mg/Ca and Sr/Ca ratios as a function of time for the long-term experiment without (10d and 21d) and with (20d) salt in the reactive solution. The data are compared with the initial element ratio in the cement and the fresh rock. 143

Figure 71: View of the samples after experiment and after drying for 24h at room temperature. For the blank and 21d experiment without salt, focus are carried out in order to check the external surface state of the core-plug._____144

Figure 72: a) Cross section of the core-sample showing the different materials (rock, cement) for the blank, 2.5d and 20 d experiment without salt and 21d experiment with salt. The red dotted lines correspond to the area selected for microscopic observations of the cement/rock interface. b) Overview of the injection well of the core plug after experiments with the zone of appearance of the wormholes._____145

Figure 73: 3D display of dissolution patterns from X-ray tomography. (Side and top views). Experiments: blank, from 12h to 21d without salt and 20d with salt. The blue color corresponds to the void areas in the core with a resolution of 60 µm._____ 146

Figure 74: XZ side view (Square images surrounded by red dotted lines) and XY TOP View (Circular images surrounded by red dotted lines) projection of all wormholes by superimposition of CT-scans on a thickness defined on the XZ view (purples lines). a) 12h, b) 24h, c) 2.5d, d) 10d, e) 21d experiment without salt and f) 20d experiment with salt. The red dotted arrows located in the injection well highlight the axisymmetry of the wormholes' origin sites. The white dotted lines in b), c) and d) underline a drastic change of the initial direction of predominant wormholes. The presence of the nut corresponding to the fluid outlet gives information on the orientation of the core at the end of the experiment._____ 147

Figure 75: a) Detail of the thin section of the rock-cement interface with altered zone of the cement (with arrows) delimited by the red line. The red square corresponds to a focus on the transition between reacted (whitish and brown color) and unreacted cement (dark color) delimited by a red dotted line. b) SEM (BSE) picture showing the cement alteration divided in three zones for the 21d experiment without salt. c) Binarization of the SEM image (ImagJ software)._____148

Figure 76: 21d experiment with salt a) Detail of the thin section of the rock-cement interface with altered zone of the cement (with arrows) delimited by the red line. The red square corresponds to a focus on b) the transition between reacted (orange-brown color) and unreacted cement (dark color) delimited by a red dotted line. b) SEM (BSE) picture showing the cement alteration divided in 2 zones._____ 149

Figure 77: Evolution of the average pore size distribution with time from the sample drilled at different location in the post-experimental core-plug._____ 150

Figure 78: Figure 78: SEM images (in SE Secondary Electrons mode) of the surface state of fresh fractured rock of (a) the initial microstructure of the Lavoux limestone composed of oolitic grains, microporous micritic matrix, sparitic rhombohedral calcite (Spar-Eq-Cem) and syntaxial cement (Syn-Cem). SEM images of the wall of the well from (b) the blank (c) 2.5, (d) 21d experiment without salt and (e) 20d experiment with salt. Holes of dissolution appear in the micritic matrix (white arrows) for all experiments. This new intra-oolitic porosity is from 5 to 20 µm in diameter._____ 152

Figure 79: SEM images (in SE mode) of the micritic microtextures observed (a) in the natural limestone rock before experiment on the wall of the injection well (b) after 20d injection of unsaturated distillated water and (c) after 21d injection of aggressive CO_2-charged water and (d) salt. Red arrows correspond to the initial intra-oolitic microporosity and white arrows to an increase of this micoporosity._____ 153

Figure 80: SEM images (Secondary electrons) focusing the observation of fibrous crystal (white arrows) covering (a) the surface of the entry of a wormhole in the blank experiment with unsaturated distillated water and the internal walls of wormholes for experiment of (d) 2.5d and (c) 21d of injection of dissolved CO_2. (d) (BSE mode) Surface state of the wellbore after injection for the 20d experiment with salt.____ 154

Figure 81: SEM observation (BSE mode): 21d experiment without salt: (a) Aggregates of euhedral micro-calcite (µCal) crystals covering the surface of the oolith at the cement-rock interface. The dotted white square corresponds to aragonite needles (b) Clusters of smooth rhombohedral calcite growing on the wall of a secondary wormhole and (c) Aggregates of neo-formed polyhedral micro-calcite on the surface of ooliths located on the wall of secondary wormholes. 20d experiment with salt: (d) Clusters of smooth rhombohedral calcite growing on the wall of a secondary wormhole._____ 155

Figure 82: Schematic diagrams of the evolution of the pore water pH as a function of the number of water exchange cycles. It illustrates the different stages of cement degradation due to the infiltration of a calcite equilibrated water at 25°C and depicts the major solid phase controlling the fluid composition and the corresponding pore water pH. Ochs (2016) [186] modified from Berner (1992) [188] and Andra (2005) [189]._____ 159

Figure 83: Evolution of the total dissolved calcium weight for each experiment.__ 162

Figure 84: Quantitative schematic diagram representing the dissolution pattern depending on Péclet and Damköhler numbers [139]. The Red Cross corresponds to the theoretical estimated *Pe-Da** numbers values._____ 167

Figure 85: (a) 3D display from X-ray tomography analysis results of wormholes initiated from the surface of the well (10d injection experiment without salt). (b) Schematic view of the wormholes' formation on rock surface [277]. Huang et al 1999_____ 169

Figure 86: (a) Time dependent evolution of the well geometry. The large blue arrows indicate the fluid inlet within the injection well. The background photo illustrates the well shape of an initial sample. The different color dotted lines show the final geometry of the well for several time of acidic injection. (b) Example of Numerical buoyancy-dominated dissolution patterns obtained for *Pe-Da* numbers expected at the injection well after the core-plug breakthrough for intermediate to high value of the Richardson dimensionless number which reflects the significance of the buoyancy force. *g* is defined as the gravity vector ($L.T^{-2}$).[Oltéan]_____ 170

Figure 87: XY TOP view and XZ side view of projections of wormholes initiated at the bottom part of the well by superimposition of the CT-scan. The thickness of the projection for the XY Top views is defined on the XZ view (purples lines) for the short-term (a) 2.5d, and long-term experiments (b) without and c) with salt._____ 172

Figure 88: Extraction of a 3D model of an isolated wormhole after the analysis of the curvature distribution of its surface for (a) the blank experiment and (b) 21d experiment without salt. (c) Inside view of the isolated wormholes from the blank experiment

displaying the surface triangles used to determine the distribution of curvatures. The color of the triangle depends on the sign and the value of the calculated curvatures and from (d) 21 d experiment without salt. (e) Color map corresponding to the rate of concave (toward the interior of the wormhole) or convex (toward the rock matrix) curvatures. SEM observation (secondary electrons) of the walls of the dead wormholes for (f) the blank with a micritic cortex and syntaxial cement partially dissolved and for (g) 21d experiment without salt with a dissolved micritic cortex and a possible re-precipitated rhombohedral calcite._____ 173

Figure 89: 3D model of the analyzed wormholes for experiments without salt (a) 2.5d injection: in green the wormholes initiated at the top of the well and in light blue at the bottom of the well. b) 21d injection: in dark blue the wormholes initiated at the top of the well and in green and red at the bottom of the well._____ 174

Figure 90: Time dependent histogram of the total surface mean curvature of the walls for “dead wormhole” selected (a) at the upper part of the well and (b) at the bottom part of the well. (c) Comparison of the cumulative frequency of curvatures with strong concavity (Radius of curvature from 200 to 400 µm) for the wormholes generated from the upper part of the well according to the different experiments and (d) from the bottom part of the well._____ 175

Figure 91: a) SEM (BSE) picture showing the cement alteration divided in three zones and the unaltered cement for the 21d experiment without salt. Red crosses correspond to the analysis points. b) Evolution of **Mg** concentrations (black line) and **Mg/Ca** ratio (red line) along the cement. c) Evolution of **Ca** concentrations._____ 177

Figure 92: Evolution of Calcite and dolomite solubility with the **Mg** concertation in solution._____ 178

Figure 93: Location of the main risk events related to the CO2-DISSOLVED project_____ 214

LISTE DES TABLEAUX (LIST OF TABLES)

Tableau 1 : Paramètres de l'équation (19) décrivant la dépendance du taux de dissolution de la calcite à la P_{CO_2} (pour 4,8<pH<5,2)._____ 70

Table 2: Chemical composition (weight %) of the Portland class G anhydrous powder (ICP-OES analysis): Major components and trace elements._____ 84

Table 3: Mineralogical composition of the class G hydrated cement. [165]_____ 85

Table 4: Chemical composition (Weight %) of injection tube steel (316SS) (@Autoclave Maxitech)_____ 85

Table 5: Sum up of experiments. The angle of the core-drilling orientation in the limestone boulder is done with respect to the bedding._____ 102

Table 6: Acquisition parameters for X-ray tomography of the whole core-plug used in the different experiments and for the cylindrical sample used for the characterization of the rock. The radiographies numbers is the number of images acquired by the detector, it depends on the angular interval between two successive radiographies._____ 110

Table 7: Petro-physical properties (Total, free and trapped porosity, permeability k_v and k_h) of Lavoux limestone: initial cylindrical samples cored in the direction perpendicular and parallel to the horizontal sedimentary bedding._____134

Table 8: Chemical composition of the Lavoux limestone (ICP-ES)._____136

Table 9: Concentration of the total inorganic carbon in the injected and experimental solutions at different period of the "ageing" of the 21d injection experiment without salt. Distribution of carbonated species $CO_{2(aq)}$ and HCO_3^- in the experimental solution._____140

Table 10: Concentration of the total inorganic carbon in the injected and experimental solutions at different period of the "ageing" of the 21d injection experiment without salt. Distribution of carbonated species and in the experimental solution._____141

Table 11: pH at equilibrium with different mineral phases at 60°C. Calculation with PHREEQC and Themoddem database._____159

Table 12: Total Amount of dissolved calcite after each experiment._____ 162

Table 13: Parameters used for the dimensionless number calculations._____166

– APPENDIXES –

– ANNEXES –

APPENDIX A

Détails des calculs de l'évolution du coefficient d'activité des ions CO_3^{2-} et Ca^{2+} en fonction de la force ionique de la solution à 60°C

L'évolution des coefficients d'activité de Ca^{2+} et CO_3^{2-} calculés à l'aide de la loi de Debye-Hückel (Equation 33) en fonction de la force ionique de la solution à 60°C.

$$\log\gamma_i = \frac{-Az_i^2\sqrt{I}}{1+B\overset{o}{a}\sqrt{I}} \quad (32)$$

Avec *A* et *B* les paramètres de Debye-Hückel qui varient avec la température et la pression, z_i la charge de l'ion, $\overset{o}{a}$ le paramètre de taille de l'ion et I la force ionique de la solution.

La liste des valeurs des constantes utilisées dans la théorie de Debye-Hückel exprimée selon l'équation 33 en fonction de la température sont visibles tableau A.1 :

Temperature (°C)	*A*	*B*
0	0.4883	0.3241
5	0.4921	0.3249
10	0.496	0.3258
15	0.5	0.3262
20	0.5042	0.3273
25	0.5085	0.3281
30	0.513	0.329
35	0.5175	0.3297
40	0.5221	0.3305
45	0.5271	0.3314
50	0.5319	0.3321
55	0.5371	0.3329
60	0.5425	0.3338

Tableau A.1 : liste des valeurs des constantes A et B utilisées dans la théorie de Debye-Hückel (source Garells and Christ., [236])

Les paramètres de tailles en fonction des ions simples et complexes inorganiques en solution aqueuses sont données tableau A.2 [237]:

$\mathring{a}$	Ions simples et complexes inorganiques en solution aqueuse
2.5	Rb^+, Cs^+, NH_4^+, Tl^+, Ag^+
3	K^+, Cl^-, Br^-, I^-, CN^-, NO_2^-, NO_3^-
3.5	OH^-, F^-, NCS^-, NCO^-, HS^-, ClO_3^-, ClO_4^-, BrO_3^-, IO_4^-, MnO_4^-
4	Hg_2^{2+}, SO_4^{2-}, $S_2O_3^{2-}$, $S_2O_8^{2-}$, SeO_4^{2-}, CrO_4^{2-}, HPO_4^{2-}, $S_2O_6^{2-}$, PO_4^{3-}
	$Fe(CN)_6^{3-}$, $Cr(NH_3)_6^{3+}$, $Co(NH_3)_5^{3+}$, $Co(NH_3)_5H_2O^{3+}$
4-4.5	Na^+, $CdCl^+$, ClO_2^-, IO_3^-, HCO_3^-, $H_2PO_4^-$, HSO_3^-, $H_2AsO_4^-$, $Co(NH_3)_4(NO_2)_2^+$
4.5	Pb^{2+}, CO_3^{2-}, SO_3^{2-}, MoO_4^{2-}, $Co(NH_3)_5Cl^{2+}$, $Fe(CN)_5NO^{2-}$
5	Sr^{2+}, Ba^{2+}, Ra^{2+}, Cd^{2+}, Hg^{2+}, S^{2-}, $S_2O_4^{2-}$, WO_4^{2-}, $Fe(CN)_6^{4-}$
6	Li^+, Ca^{2+}, Cu^{2+}, Zn^{2+}, Sn^{2+}, Mn^{2+}, Fe^{2+}, Ni^{2+}, Co^{2+}, $Co(S_2O_3)(CN)_5^{4-}$
8	Mg^{2+}, Be^{2+}
9	H^+, Al^{3+}, Fe^{3+}, Cr^{3+}, Sc^{3+}, Y^{3+}, La^{3+}, Ce^{3+}, Pr^{3+}, Nd^{3+}, Sm^{3+}, In^{3+}, $Co(SO_3)_2(CN)_4^{5-}$
11	Th^{4+}, Zr^{4+}, Ce^{4+}, Sn^{4+}

Tableau A.2 : Paramètres de taille des ions simples et complexes inorganiques en solution aqueuses. (Ottonello., 1997 [237]; d'après Kielland., 1937 [238])

Les résultats obtenus sont visibles dans le tableau A.3 :

Force ionique (M)	γCa^{2+}	γCO_3^{2-}
0	1	1
4.00E-04	0.908388187	0.907540042
0.05	0.462233641	0.433284982
0.1	0.3800763	0.34258773
0.2	0.307659882	0.262725206
0.25	0.286998406	0.240088731
0.3	0.271146859	0.222805417

Tableau A.3 : Résultats des calculs de m'évolution des coefficients d'activité de Ca^{2+} et CO_3^{2-} calculés à l'aide de la loi de Debye-Hückel en fonction de la force ionique de la solution à 60°C.

APPENDIX B

Investigation of heat transfer in the injection tube of the core-plug between the reactive fluid and the confinement simulating the geological conditions. This modelling is based on a protocol defined in [171]

The flow regime has to be initially specified according to the dimensionless REYNOLDS number.

$$\mathrm{Re} = \frac{\rho \bar{v} D_h}{\mu} \quad (33)$$

Where ρ is the density of the fluid (kg.m^{-3}), $\bar{v}$ the mean velocity between the two concentric cylinders (m.s^{-1}), D_h the hydraulic diameter (m) and μ the dynamic viscosity (kg.m^{-1}.s^{-1}).

The values used in this calculation are as follow: ρ = 1,015 kg.m^{-3} (experimentally measured by the Coriolis flowmeter), $\bar{v}$ = 4.83 x 10^{-3} m.s^{-1}, and μ = 1.003 X 10^{-3} kg.m^{-1}.s^{-1} (the standard dynamic viscosity of water at 20°C)

The hydraulic diameter is equal to:

$$D_h = \frac{4S}{P_w} \quad (34)$$

Where S is the cross section of the flow stream (m²) and P_w the wetted perimeter by the flow stream (m) (Fig. B.1a). With S = 8.5 x 10^{-6} m²

The wetted perimeter P_w in two concentric tube is given by:

$$P_w = \Pi(D_e + D_1) \quad (35)$$

Where D_e is the internal diameter of the injection (m) and D_i the external diameter of the thermocouple pocket (Fig. B.1b). With D_e = 4.57 X 10^{-3} m and D_i = 3.175 X 10^{-3} m.

For the imposed flowrate of 150 g.h^{-1} corresponding to a fluid velocity in the injection tube equal to 4.83 x 10^{-3} m.s^{-1}, the calculated Re is equal to 6.83 corresponding to a unidirectional laminar flow.

For the modelling of the heat transfer in our experimental system, the model is based on 2 tubes arranged in a concentric way in respect to a flow axis on x (Fig. B.1b). The external tube is submitted to a uniform surface temperature T_{conf} of 60°C after 10 days of cure. The inlet temperature T_{inj} of the fluid is of 20°C. The mean temperature

variation is noted Tm (x) and the heat flow (in Joules) exchanged through the lateral wall area *dS* between the abscissa x and $x+dx$ noted dq_S.

Based on these initial assumptions of a uniform surface temperature of 60°C, a steady state during the fluid flow, that no energy is generated, that kinetic and potential energy are negligible and that no axial conduction occurs, the equation of conservation of energy applied to the element dq_S are written under the form of:

$$dq_s = mCpdT_m \quad (36)$$

Where m is the mass flowrate (kg.s^{-1}) equal to 4.17 · 10^{-5} kg.s^{-1} and Cp the specific heat in J.kg^{-1}.°C^{-1}. We approximate the specific heat capacity Cp by taking the value of pure water Cp = 4,180 J.kg^{-1}.°C^{-1} and dTm the difference in temperature before and after heat transfer between x and $x+dx$.

And the Newton law for surface flux:

$$dq_S = h(x)\left[T_{conf} - T_m(x)\right]Pdx \quad (37)$$

Where $h(x)$ is the average heat transfer coefficient (W.m^{-2}.°C^{-1}) between the fluid and the injection tube and P the thermal exchange perimeter of the internal tube diameter (m).

Equation (36) and (37) are combined:

$$\frac{dT_m}{T_{conf} - T_m(x)} = \frac{P}{mc_p}h(x)dx \quad (38)$$

Integrating from x = 0 ($dT_m = T_m(0) = T_{inj}$) to x ($T_m = T_m(x)$)

$$\ln\left[\frac{T_m(x) - T_{conf}}{T_{inj} - T_{conf}}\right] = -\frac{P}{mC_p}\int_0^x h(x)dx \quad (39)$$

It is then necessary to determine $h(x)$ by introducing $\overline{h}$:

$$\overline{h} = \frac{1}{x}\int_0^x h(x)dx \quad (40)$$

By replacing (40) in (39), the temperature field along the tube can be determined by the relation

$$T_m(x) = T_{conf} + \left(T_{inj} + T_{conf}\right)\exp\left[\frac{P\bar{h}}{mCp}x\right] \quad (41)$$

The evaluation of the average convection exchange coefficient $\bar{h}$ value is determined using the dimensionless number of Nusselt:

$$Nu = \frac{hD_e}{\lambda} \quad (42)$$

With D_e the heat exchange diameter (m), k (the thermal conductivity of the fluid ($W.m^{-1}.°C^{-1}$). For pure water at 20°C and 120 bar, λ = 0.607 $W.m^{-1}.°C^{-1}$. For laminar flow, we consider that $h = \bar{h}$.

In a regime of forced convection in laminar flow, the experimental correlations of Lévêque can be applied to determine the Nu values as a function of the distance of fluid progression in the tubing.

$$\xi = \frac{1}{\mathrm{Re.Pr}}\frac{x}{D_e} \quad (43)$$

Where Pr is the PRANDLT dimensionless number corresponding to the ratio between the diffusivity of the quantity of movement (kinematic viscosity) and that of heat (thermal diffusivity):

$$\mathrm{Pr} = \frac{\mu C_p}{\lambda} \quad (44)$$

These correlations are expressed:

$$Nu = 3.66 \text{ for } \xi \geq 0.05$$
$$Nu = 1.06\xi^{-0.4} \text{ for } \xi \leq 0.05$$

The evolution of the temperature is calculated with a 1 mm pitch over the 120 mm of the injection tube. The results tables can be consulted below. Figures B.1a displays the graph of the evolution of the temperature of the percolating reactive fluid along the tube down to the injection point.

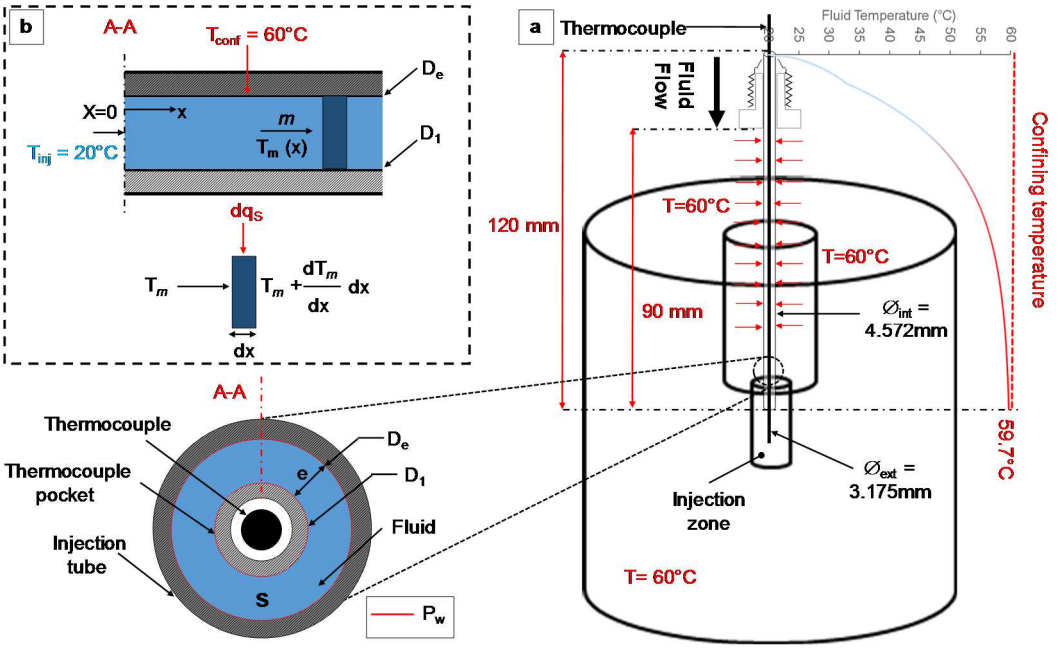

Figure B.1: (a) Schematic of the sample with the different elements and parameters considered for the calculation of the heat transfer between the fluid in the injection tube and the surrounding medium. The graph displays the temperature evolution of the fluid as it flows through the tube. The focus represents a horizontal cross section of the injection tube. (b) Model for the heat transfer investigation.

The calculations as well as the associated results tables are:

x(m)	ξ	Nu(ξ)	h(x)	T_{fluid} (x)
0.000	0.000	∞	∞	20.0
0.001	0.005	9.095	1208	23.8
0.002	0.009	6.893	916	25.6
0.003	0.014	5.861	779	27.0
0.004	0.019	5.224	694	28.2
0.005	0.023	4.778	635	29.2
0.006	0.028	4.442	590	30.1
0.007	0.032	4.176	555	31.0
0.008	0.037	3.959	526	31.7
0.009	0.042	3.777	502	32.4
0.010	0.046	3.621	481	33.1
0.011	0.051	3.660	486	34.3
0.012	0.056	3.660	486	35.3
0.013	0.060	3.660	486	36.2
0.014	0.065	3.660	486	37.2
0.015	0.070	3.660	486	38.1
0.016	0.074	3.660	486	38.9
0.017	0.079	3.660	486	39.8
0.018	0.083	3.660	486	40.6
0.019	0.088	3.660	486	41.3
0.020	0.093	3.660	486	42.1
0.021	0.097	3.660	486	42.8
0.022	0.102	3.660	486	43.4
0.023	0.107	3.660	486	44.1
0.024	0.111	3.660	486	44.7
0.025	0.116	3.660	486	45.3
0.026	0.121	3.660	486	45.9
0.027	0.125	3.660	486	46.4
0.028	0.130	3.660	486	47.0
0.029	0.134	3.660	486	47.5
0.030	0.139	3.660	486	48.0
0.031	0.144	3.660	486	48.5
0.032	0.148	3.660	486	48.9
0.033	0.153	3.660	486	49.3
0.034	0.158	3.660	486	49.8
0.035	0.162	3.660	486	50.2
0.036	0.167	3.660	486	50.6
0.037	0.172	3.660	486	50.9

x(m)	ξ	Nu(ξ)	h(x)	T_{fluid} (x)
0.038	0.176	3.660	486	51.3
0.039	0.181	3.660	486	51.6
0.040	0.185	3.660	486	52.0
0.041	0.190	3.660	486	52.3
0.042	0.195	3.660	486	52.6
0.043	0.199	3.660	486	52.9
0.044	0.204	3.660	486	53.1
0.045	0.209	3.660	486	53.4
0.046	0.213	3.660	486	53.7
0.047	0.218	3.660	486	53.9
0.048	0.223	3.660	486	54.2
0.049	0.227	3.660	486	54.4
0.050	0.232	3.660	486	54.6
0.051	0.237	3.660	486	54.8
0.052	0.241	3.660	486	55.0
0.053	0.246	3.660	486	55.2
0.054	0.250	3.660	486	55.4
0.055	0.255	3.660	486	55.6
0.056	0.260	3.660	486	55.8
0.057	0.264	3.660	486	55.9
0.058	0.269	3.660	486	56.1
0.059	0.274	3.660	486	56.2
0.060	0.278	3.660	486	56.4
0.061	0.283	3.660	486	56.5
0.062	0.288	3.660	486	56.7
0.063	0.292	3.660	486	56.8
0.064	0.297	3.660	486	56.9
0.065	0.301	3.660	486	57.0
0.066	0.306	3.660	486	57.2
0.067	0.311	3.660	486	57.3
0.068	0.315	3.660	486	57.4
0.069	0.320	3.660	486	57.5
0.070	0.325	3.660	486	57.6
0.071	0.329	3.660	486	57.7
0.072	0.334	3.660	486	57.8
0.073	0.339	3.660	486	57.9
0.074	0.343	3.660	486	57.9
0.075	0.348	3.660	486	58.0
0.076	0.352	3.660	486	58.1
0.077	0.357	3.660	486	58.2
0.078	0.362	3.660	486	58.2
0.079	0.366	3.660	486	58.3
0.080	0.371	3.660	486	58.4

x(m)	ξ	Nu(ξ)	h(x)	T_{fluid} (x)
0.081	0.376	3.660	486	58.4
0.082	0.380	3.660	486	58.5
0.083	0.385	3.660	486	58.6
0.084	0.390	3.660	486	58.6
0.085	0.394	3.660	486	58.7
0.086	0.399	3.660	486	58.7
0.087	0.403	3.660	486	58.8
0.088	0.408	3.660	486	58.8
0.089	0.413	3.660	486	58.9
0.090	0.417	3.660	486	58.9
0.091	0.422	3.660	486	59.0
0.092	0.427	3.660	486	59.0
0.093	0.431	3.660	486	59.0
0.094	0.436	3.660	486	59.1
0.095	0.441	3.660	486	59.1
0.096	0.445	3.660	486	59.1
0.097	0.450	3.660	486	59.2
0.098	0.454	3.660	486	59.2
0.099	0.459	3.660	486	59.2
0.100	0.464	3.660	486	59.3
0.101	0.468	3.660	486	59.3
0.102	0.473	3.660	486	59.3
0.103	0.478	3.660	486	59.4
0.104	0.482	3.660	486	59.4
0.105	0.487	3.660	486	59.4
0.106	0.492	3.660	486	59.4
0.107	0.496	3.660	486	59.5
0.108	0.501	3.660	486	59.5
0.109	0.505	3.660	486	59.5
0.110	0.510	3.660	486	59.5
0.111	0.515	3.660	486	59.5
0.112	0.519	3.660	486	59.6
0.113	0.524	3.660	486	59.6
0.114	0.529	3.660	486	59.6
0.115	0.533	3.660	486	59.6
0.116	0.538	3.660	486	59.6
0.117	0.543	3.660	486	59.6
0.118	0.547	3.660	486	59.6
0.119	0.552	3.660	486	59.7
0.120	0.556	3.660	486	59.7

APPENDIX C

Experimental procedure for the Raman calibration of dissolved CO_2 concentration measurements at 20°C:

Before experiments, a calibration is needed. This calibration of the Raman probe is carried out by measuring the area pic ratio of CO_2/H_2O (I_{CO_2}/I_{H_2O}) at 20°C (temperature of the solubilization experiment) for different pressures. The ratio is calculated and plotted as a function of dissolved CO_2 concentration. The solubility of CO_2 in water is calculated as a function of pressure and temperature using the thermodynamic model of Duan et al (2003) [108].
The concentration of dissolved CO_2 is also determined gravimetrically to confirm the calculated CO_2 solubility.

The procedure included the following steps:

- The 5 Liters mixing autoclave is filled with 4.5 Liters of fresh MilliQ water (18.2 MΩ.cm) and closed
- The temperature is set to 20°C thanks to a controlled heat transfer fluid (water).
- Once the temperature is reached, the pure water is pumped by the syringe pump through the tee where the Raman analysis is performed (constant flow rate 1 ml/min).
- A first series of Raman spectra is recorded to check the intensity of the Raman signal.
- Then the CO_2 is added at the wanted pressure. Raman spectra are acquired continuously using *iC* Raman software (Kaiser Optical Systems, Inc.). The number of Raman spectra acquired successively when equilibrium is reached varies between 4 and 149. For each spectrum, pressure/temperature data are recorded.
- Together with the Raman analyses, several samplings are done for gravimetric measurement of dissolved CO_2.

Once the correlation found between the peak intensity ratios I_{CO_2}/I_{H_2O} and the CO_2 dissolved in solution ($mol.kg^{-1}_w$), the amount of CO_2 dissolved in water before the injection in the core-plug is continually measured during our experiments. A sampling of the solution is done from time to time in order to check with the gravimetric method, if there is no drift of the Raman measurement during the 20 days of experiment.

Experimental procedure for the gravimetric method of total carbonate concentration measurement:

The equilibrated CO_2/water solution is sampled in order to measure the total carbonate concentration under specified pressure and temperature conditions. The results are compared with those calculated at the same temperature and pressure using the thermodynamic model of Duan and Sun (2003) [108]. This method is developed to experimentally validate the Raman calibration. The gravimetric method basically consists of precipitating all the carbonates as $BaCO_3$ after mixing with $BaCl_2$.

The procedure included the following steps:

- Preparation of a 0.5 M barium chloride ($BaCl_2$) solution,
- A 30 mL sampling cell, filled with 25 mL of the 0.5 M $BaCl_2$ solution is connected to the liquid sampling valve of the by-pass and filled with the solution. NaOH is added to the solution in order to have a basic solution with a pH of 12-13 and to favor the precipitation of $BaCO_3$.
- $BaCO_3$ precipitates inside the cell for about 1 to 2 days at room temperature until the CO_2 overpressure becomes negligible (all the initial carbonates are then precipitated).
- The solution is filtered to collect the $BaCO_3$,
- Filtered $BaCO_3$ is dried and weighted.

Validation of the method: In order to validate the protocol and check the accuracy of the gravimetric method, solutions containing well-known concentration of CO_3^{2-} have been prepared. Sodium carbonate (Na_2CO_3) is dissolved in fresh MilliQ water (18.2 MΩ.cm) at different concentrations (0.2 – 0.4 – 0.6 – 0.8 mole/kg). Barium Chloride ($BaCl_2$) solution is prepared with and without NaOH to check the pH influence on the reaction. The precipitated carbonates ($BaCO_3$) from the reaction is filtered and weighted. The measured concentration is finally compared to the initial quantity of carbonates in solution. The error on the balance measuring the weigh at the different step of the protocol is of $\pm$ 0.01g.

The flasks after reaction between $BaCl_2$ and Na_2CO_3 for different Na_2CO_3 concentrated solution are presented in figure C.1.

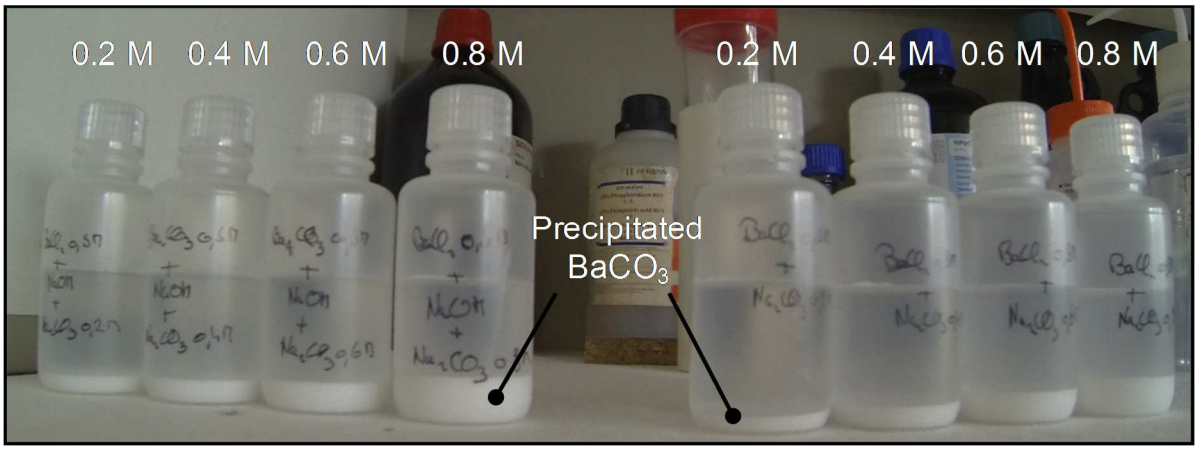

Figure C.1: Results of the validation test of the gravimetric method of total inorganic carbon concentration measurement: $BaCl_2$ reacts with Na_2CO_3 according to the reaction $Ba^{2+} + CO_3^{2-} = BaCO_3(solid)$. The flasks on the left side contain precipitated $BaCO_3$ in presence of NaOH (pH=12.5). The flasks on the right side contain precipitated $BaCO_3$ without NaOH (pH=4.3).

Table C.1 (with NaCl) and table C.2 (without NaCl) show the results of the validation test. Figures C.2 and C.3 represent the concentration of carbonate in solution measured thanks to the gravimetric method as a function of the concentration of carbonate initially present in the solution.

Initial carbonate molality in solution (mole.kg^{-1})	Carbonate molality *measured* by the gravimetric method (mole kg^{-1})	Error (%)
0.2	0.203	-1.58
0.2	0.198	0.95
0.35	0.348	0.66
0.4	0.399	0.37
0.4	0.398	0.53
0.45	0.448	0.44
0.6	0.597	0.52
0.6	0.596	0.67
0.8	0.797	0.35
0.8	0.793	0.85

Table C.1: Results of the validation test of the gravimetric method in presence of NaOH.

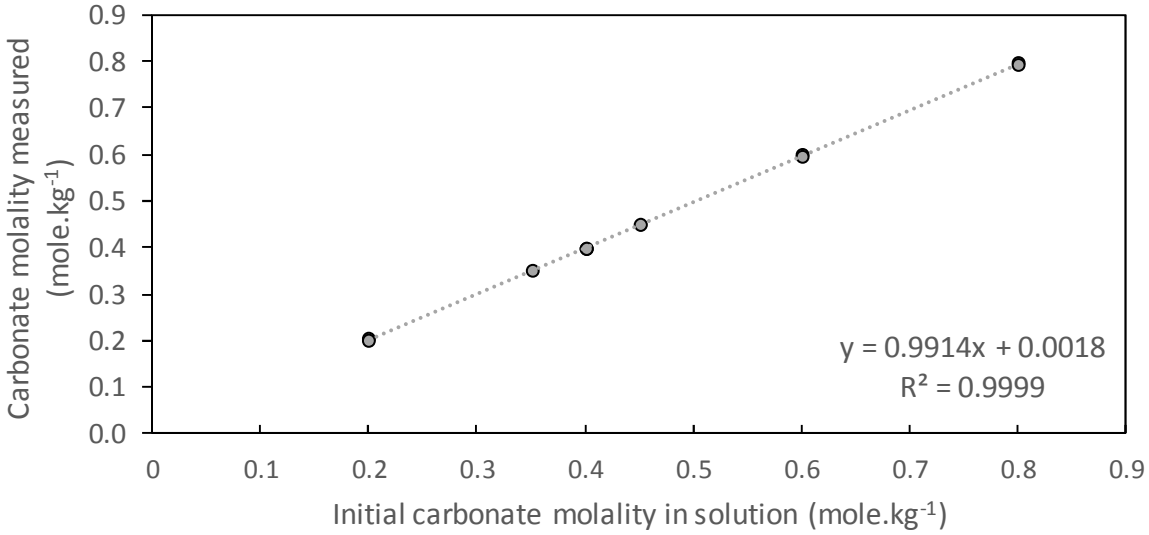

Figure C.2: Carbonate molality measured by the gravimetric method as a function of the initial carbonate molality in solution in presence of NaOH.

The results demonstrate the efficiency of the gravimetric method. The carbonate concentrations measured correspond to the expected values with accuracy close to 1%. The slops of the test curve are close to 1 with an adjusted R^2 equal to 0.9999. The results in presence of NaOH are slightly better than without NaOH. The use of barium chloride with sodium hydroxide has been chosen also in order to have faster kinetics of reaction.

Initial carbonate molality in solution (mole.kg^{-1})	Carbonate molality *measured* by the gravimetric method (mole kg^{-1})	Error (%)
0.2	0.2017	-0.83
0.4	0.4024	-0.59
0.6	0.6033	-0.55
0.8	0.8002	-0.02
0.2	0.1981	0.93
0.5	0.4956	0.88
0.8	0.7993	0.09
0.9	0.8996	0.04
0.95	0.9444	0.59
1	0.9953	0.47

Table C.2: Results of the validation test of the gravimetric method under basic conditions.

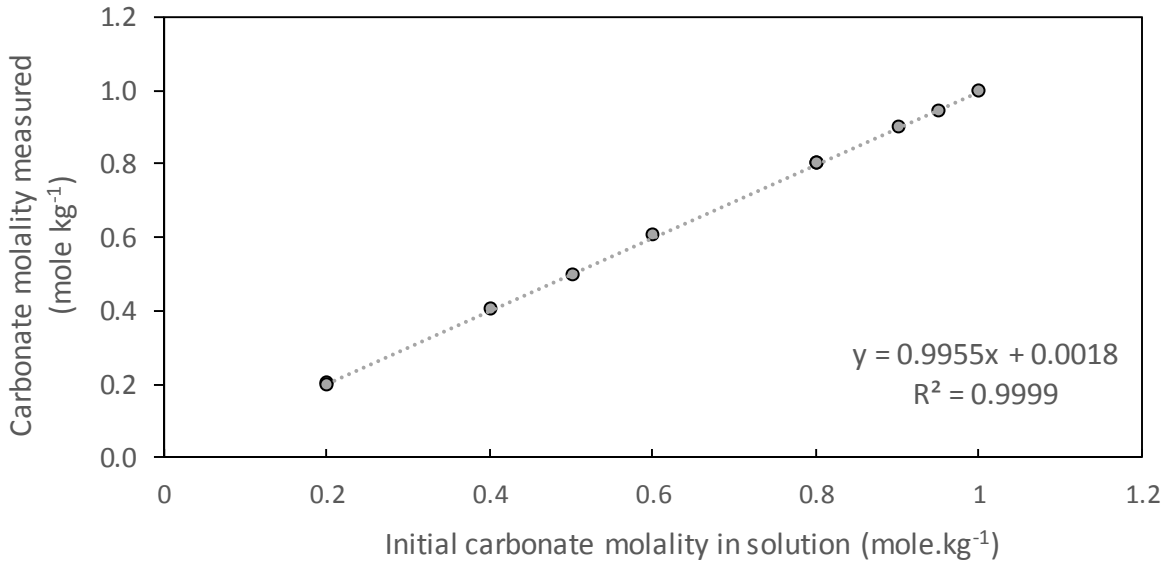

Figure C.3: Curve represented the results of the validation test of the gravimetric method under basic conditions.

Results of the Gravimetric method: Five pressure conditions (20 – 25 – 30 – 35 and 40 bar) in the CO_2–H_2O system are used at 20°C to impose different total carbonate concentrations. 17 experimental conditions are performed with 3 sampling for each conditions. The CO_2 solubility in water measured gravimetrically are compared with those calculated using the thermodynamic model of Duan and Sun., 2003 [108]. The results are summarized in Table C.3.

These results show that our experimental data are accurately reproduced by the Duan model with a difference from 1.5 to 8.5%.

Table C.3: Results of the study of the consistency between the solubility data of CO_2 in water from the model of Duan and the data measured with the gravimetric method in the pressure-temperature domain of the experiments. The values of CO_2 solubility measured by the gravimetric method are the mean of 3 measurements at a given pressure

Temp (°C)	P_{CO2} (bar)	CO_2 solubility (s_{CO2}) calculated (mole.kg$^{-1}_{water}$) (Duan)[a]	CO_2 solubility (s_{CO2}) mesured by the gravimetric method (mole.kg$^{-1}_{water}$)[b]	s_{CO2} calculated - s_{CO2} measured (mole.kg$^{-1}_{water}$)
20.46	30.13	0.932	0.920	0.012
20.34	29.66	0.915	0.894	0.021
20.40	19.74	0.657	0.667	-0.010
20.28	25.67	0.818	0.808	0.010
20.37	29.92	0.917	0.895	0.022
20.09	19.96	0.674	0.713	-0.039
20.33	30.69	0.919	0.944	-0.025
20.32	19.63	0.669	0.636	0.032
20.37	29.92	0.948	0.922	0.026
20.37	29.92	0.948	0.935	0.013
20.37	29.92	0.948	0.911	0.037
20.20	25.16	0.809	0.769	0.040
20.20	25.16	0.809	0.739	0.070
20.20	25.16	0.809	0.781	0.027
20.30	34.72	1.047	1.004	0.043
20.30	34.72	1.047	1.022	0.024
20.30	34.72	1.047	1.018	0.028

[a] Calculated after Duan and Sun (2003) [108].

[b] Gravimetric measurement ($BaCO_3$).

The differences from the experimental data and data obtained with the Duan model are represented in figure C.4. The standard deviation 2.05σ at 95% is determined from the 51 measurements performed. Most of the data remain mainly inferior to ± 2.05σ. This implies that the experimental data are in agreement with the model of Duan demonstrating the reliability between the experimental results and the thermodynamic model. In the P/T conditions of our experiments, the use of the theoretical model of Duan and Sun., 2003 to calibrate the Raman data is justified.

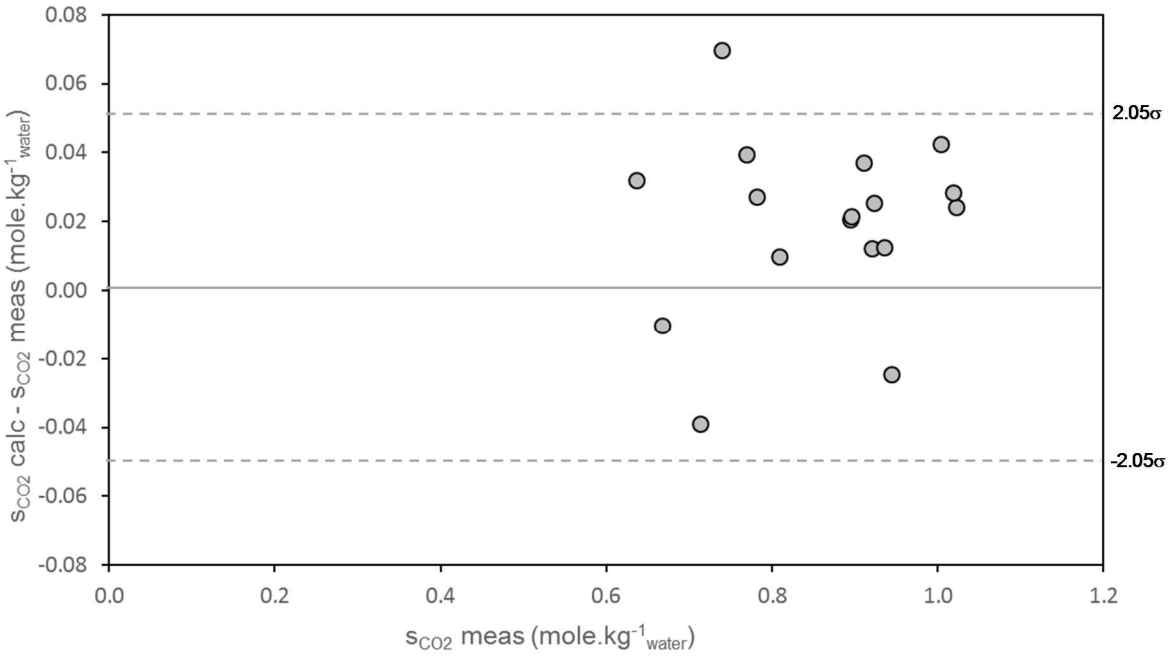

Figure C.4: Differences between the gravimetrically measured concentration of dissolved CO_2 and the dissolved CO_2 concentration calculated using the Duan and Sun (2003) model in the CO_2-H_20 system.

APPENDIX D

Results of the in situ Raman calibration of measurement of dissolved CO_2 at 20°C

Temp (°C)	P_{CO_2} (bar)	I_{CO_2}/I_{H_2O} [a]	number of measurment at equilibrium	Standard uncertainty σ	Relative standard uncertainty σ_r	CO_2 solubility (s_{CO2}) calculated (mole.kg$^{-1}_{wat}$) (Duan) [b]
20.4	24.93	3.443	10	0.031	0.009	0.797
20.57	24.41	3.360	14	0.040	0.011	0.780
20.42	40.31	4.840	19	0.061	0.014	1.149
20.22	19.71	2.841	125	0.031	0.003	0.657
20.37	39.38	4.823	55	0.078	0.010	1.132
20.8	38.55	4.934	4	0.030	0.015	1.104
20.13	40.47	5.184	18	0.079	0.019	1.160
20.2	31.1	3.762	36	0.093	0.015	0.955
20.2	36.2	4.576	45	0.083	0.013	1.070
20.46	30.13	3.784	11	0.036	0.011	0.932
20.34	29.66	3.709	84	0.069	0.008	0.915
20.40	19.74	2.566	139	0.017	0.001	0.657
20.28	25.67	3.362	149	0.039	0.003	0.818
20.37	29.92	3.732	16	0.037	0.009	0.917
20.09	19.96	3.125	18	0.023	0.005	0.674
20.33	30.69	4.119	10	0.066	0.007	0.919
20.32	19.63	2.766	37	0.025	0.004	0.669
20.37	29.92	3.732	16	0.037	0.009	0.948
20.37	29.92	3.732	16	0.037	0.009	0.948
20.37	29.92	3.732	16	0.037	0.009	0.948
20.20	25.16	3.481	50	0.027	0.004	0.809
20.20	25.16	3.481	50	0.027	0.004	0.809
20.20	25.16	3.481	50	0.027	0.004	0.809
20.30	34.72	4.318	11	0.041	0.004	1.047
20.30	34.72	4.318	11	0.041	0.004	1.047
20.30	34.72	4.318	11	0.041	0.004	1.047

[a] Ratio between integrated intensity of the Raman stretching bands ($\nu_1 + 2\nu_2$) of CO_2 and the OH vibration bending band at 1640 cm^{-1}.

[b] Calculated after Duan and Sun (2003) [108]

APPENDIX E

Recording of the Pressure, temperature and flowrates parameters evolution with time for all the experiments are presented figures E.1 to E.11.

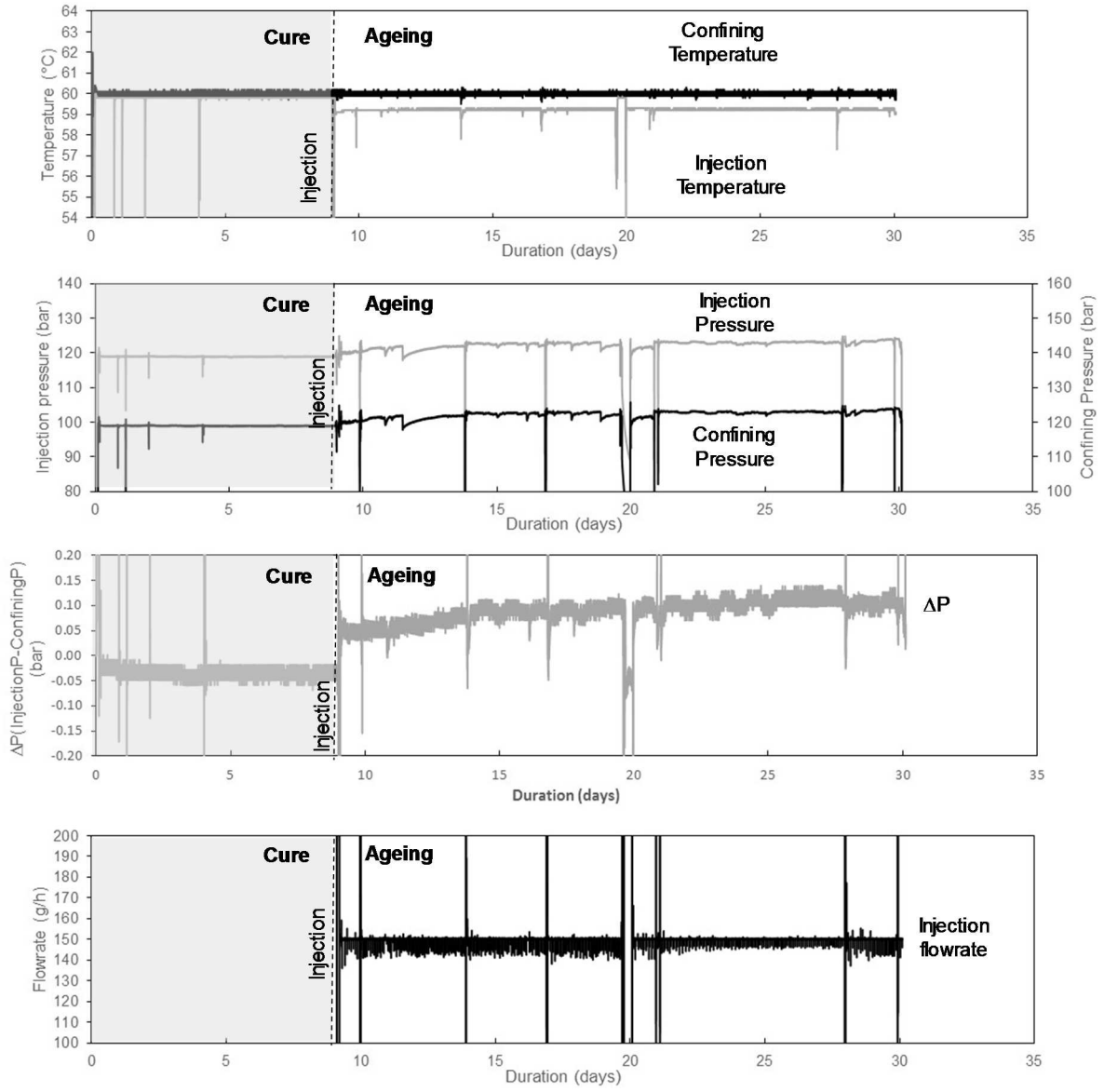

Figure E.1: Evolution of pressures (confining and injection), temperatures (confining and injection), ΔP (between injection and confining) and injection flowrate in the MIRAGES-2 autoclave during the blank experiment (pure water).

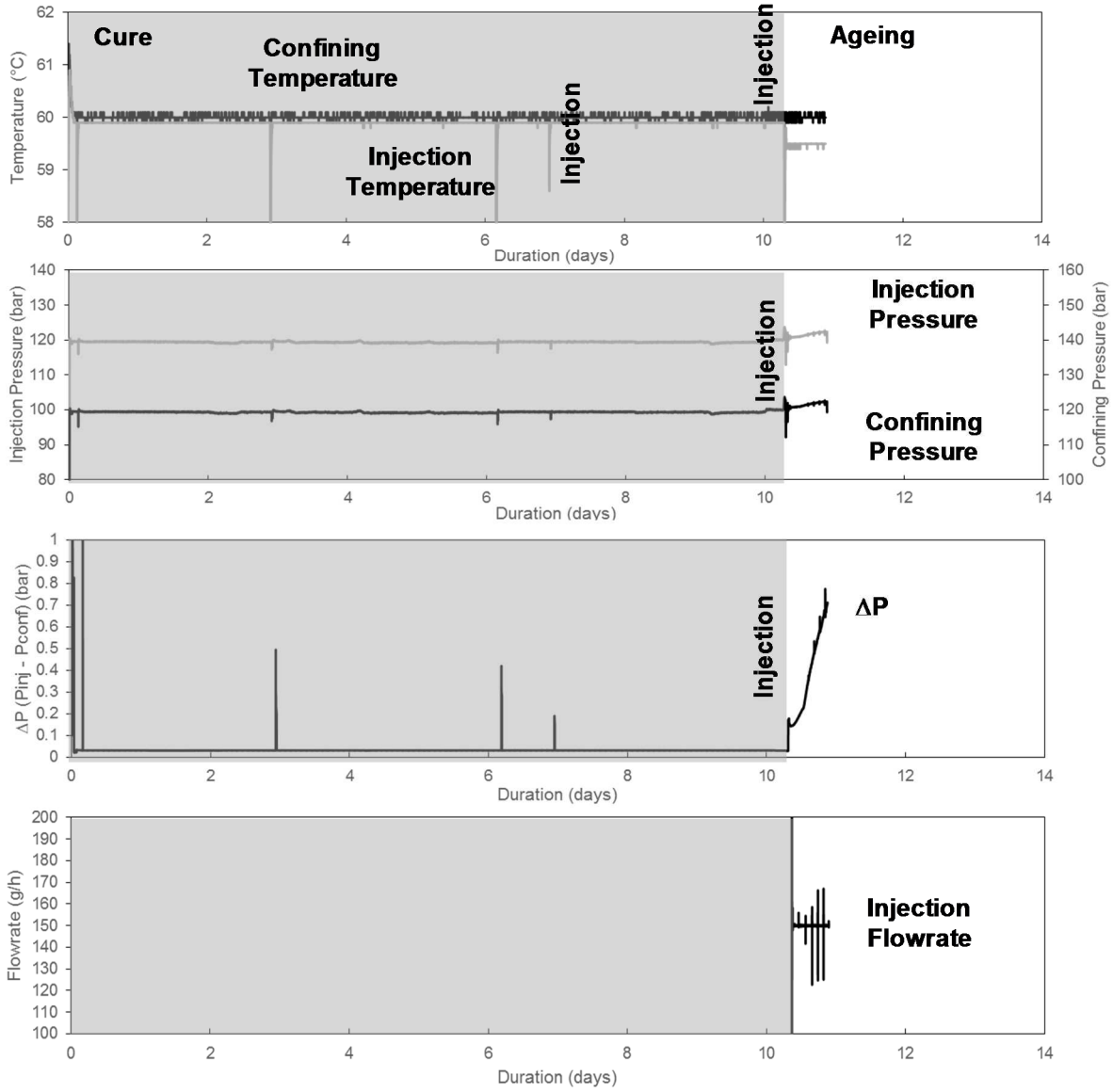

Figure E.2: Evolution of pressures (confining and injection), temperatures (confining and injection), ΔP (between injection and confining) and injection flowrate in the MIRAGES-2 autoclave during the 12h experiment without salt.

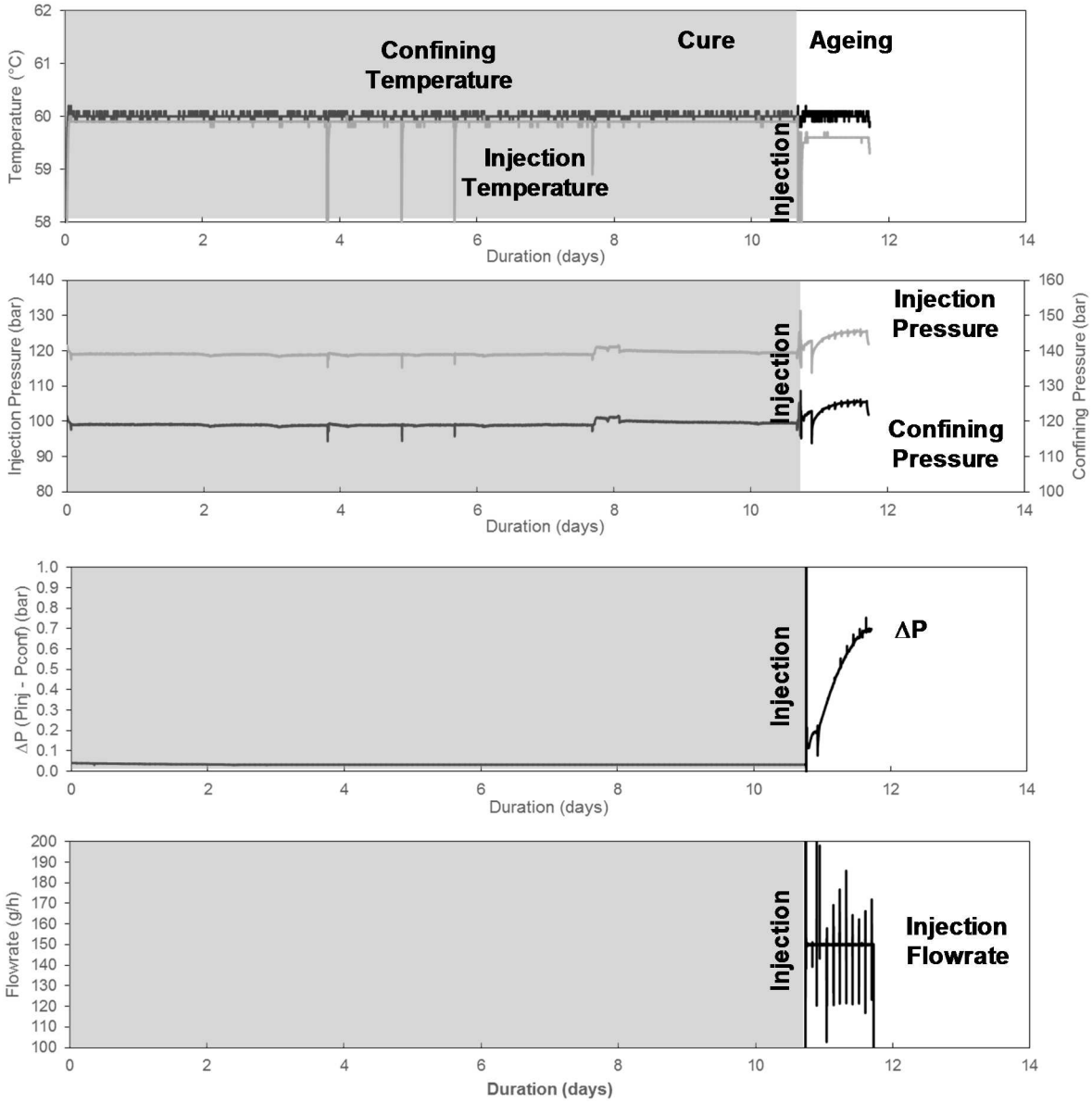

Figure E.3: Evolution of pressures (confining and injection), temperatures (confining and injection), ΔP (between injection and confining) and injection flowrate in the MIRAGES-2 autoclave during the 24h experiment without salt.

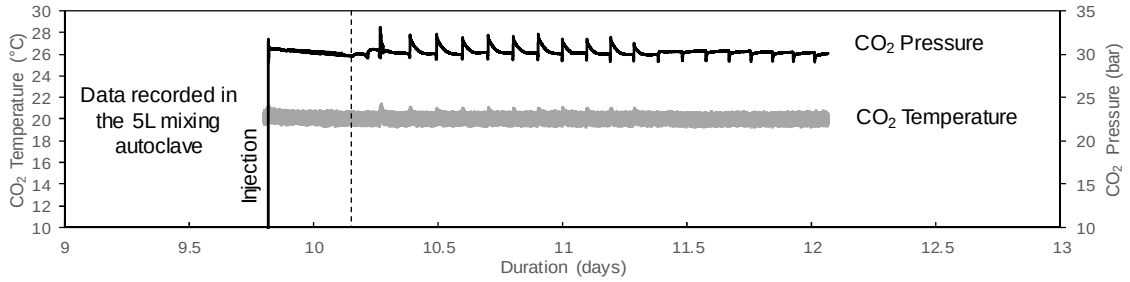

Figure E.4: Evolution of temperature and CO_2 pressure in the mixing autoclave (5 L) for the 2.5d experiment without salt.

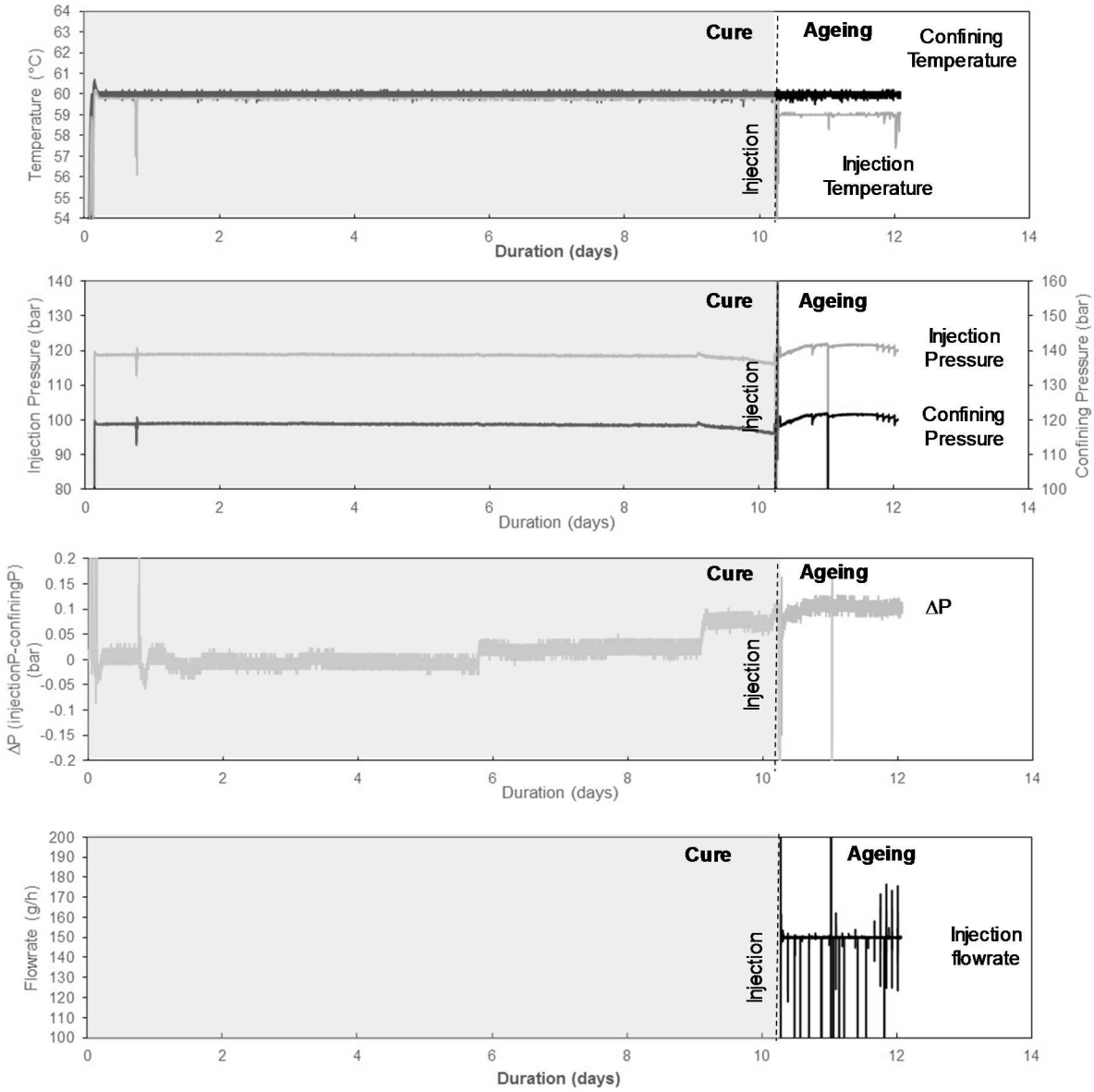

Figure E.5: Evolution of pressures (confining and injection), temperatures (confining and injection), ΔP (between injection and confining) and injection flowrate in the MIRAGES-2 autoclave during the 2.5d experiment without salt.

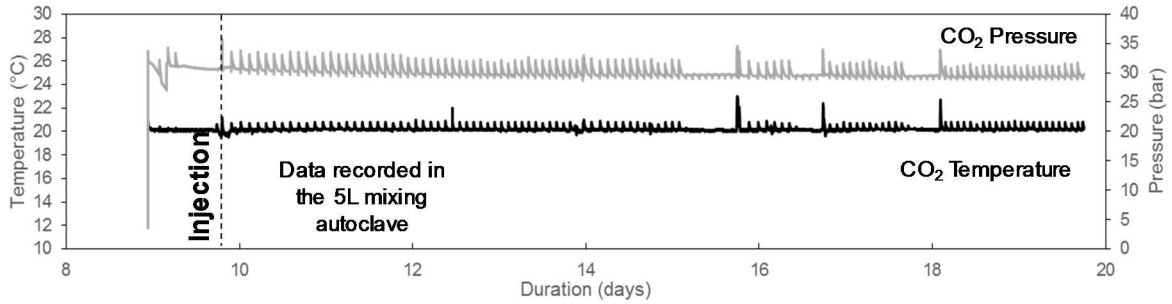

Figure E.6: Evolution of temperature and CO_2 pressure in the mixing autoclave (5 L) for the 10d experiment without salt.

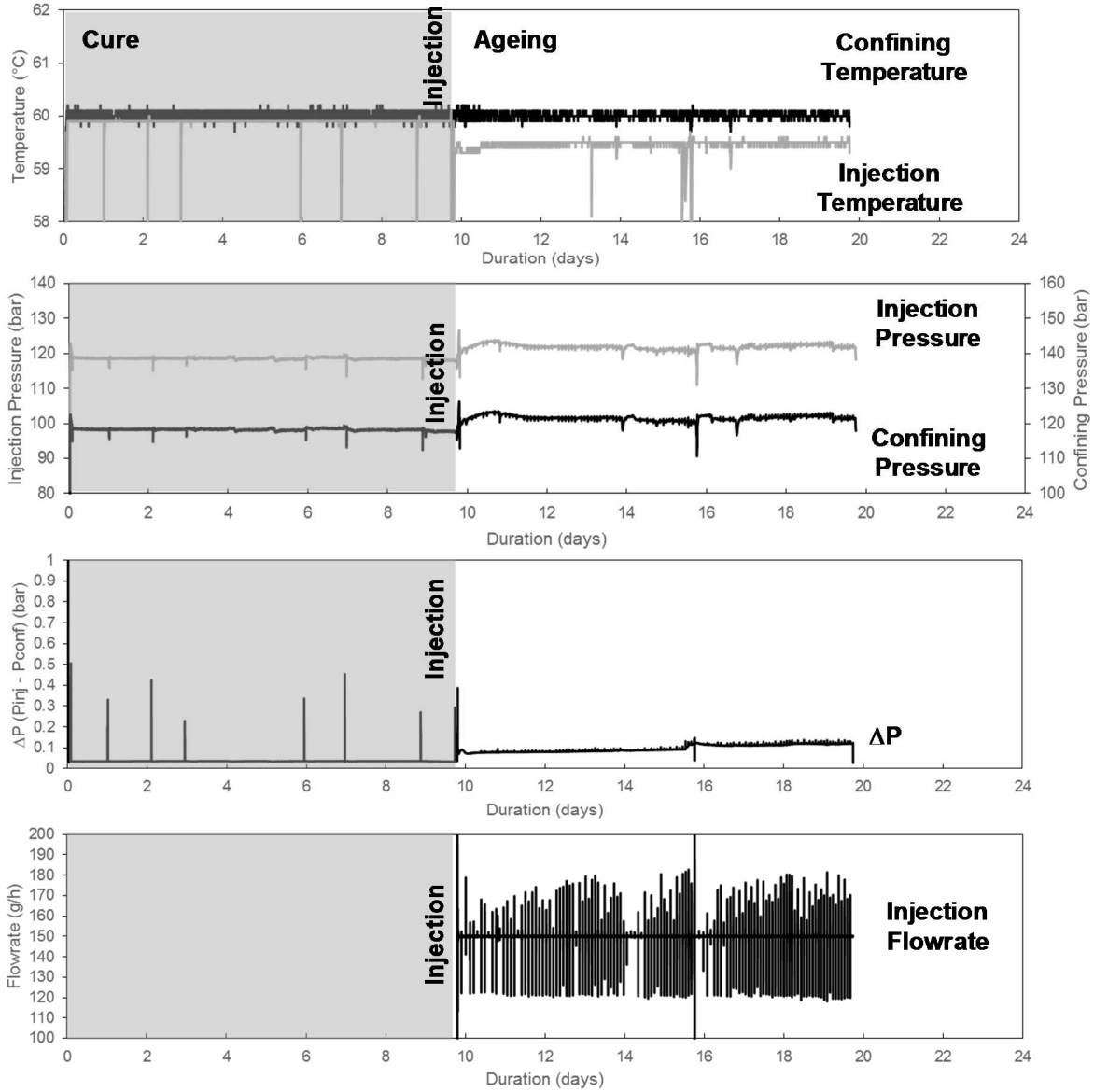

Figure E.7: Evolution of pressures (confining and injection), temperatures (confining and injection), ΔP (between injection and confining) and injection flowrate in the MIRAGES-2 autoclave during the 10d experiment without salt.

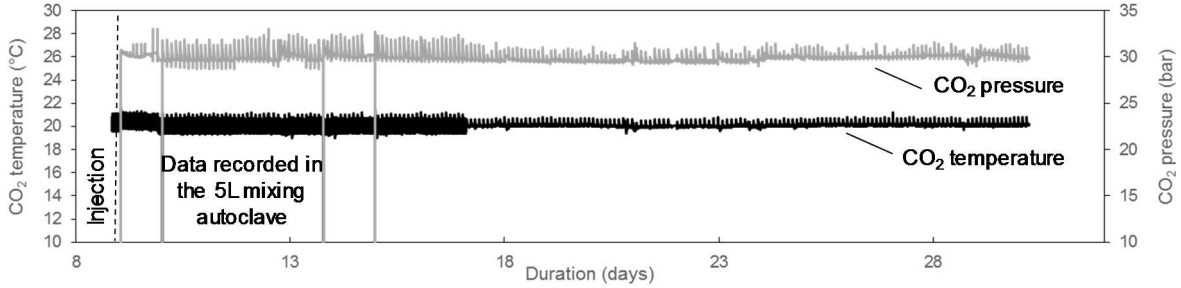

Figure E.8: Evolution of temperature and CO_2 pressure in the mixing autoclave (5 Liters) for the 21d experiment without salt.

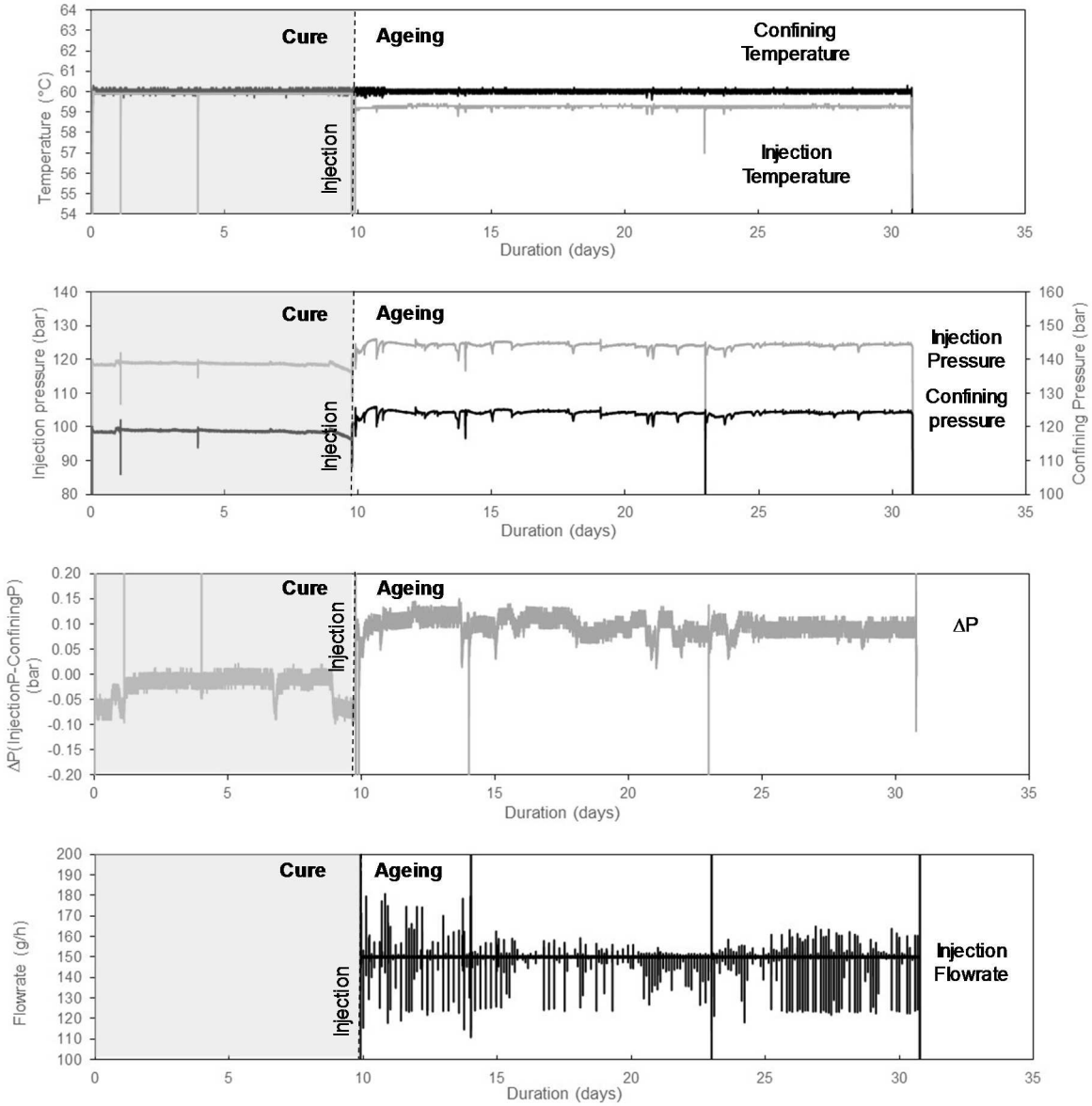

Figure E.9: Evolution of pressures (confining and injection), temperatures (confining and injection), ΔP (between injection and confining) and injection flowrate in the MIRAGES-2 autoclave during the 21d experiment without salt.

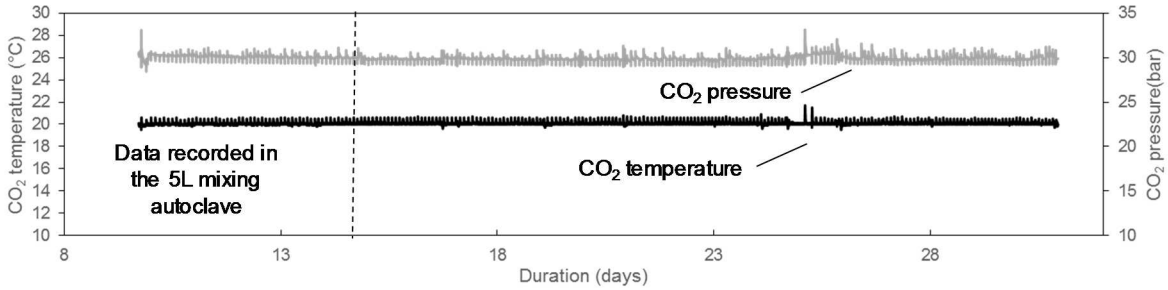

Figure E.10: Evolution of temperature and CO_2 pressure in the mixing autoclave (5 Liters) for the 20d experiment with salt.

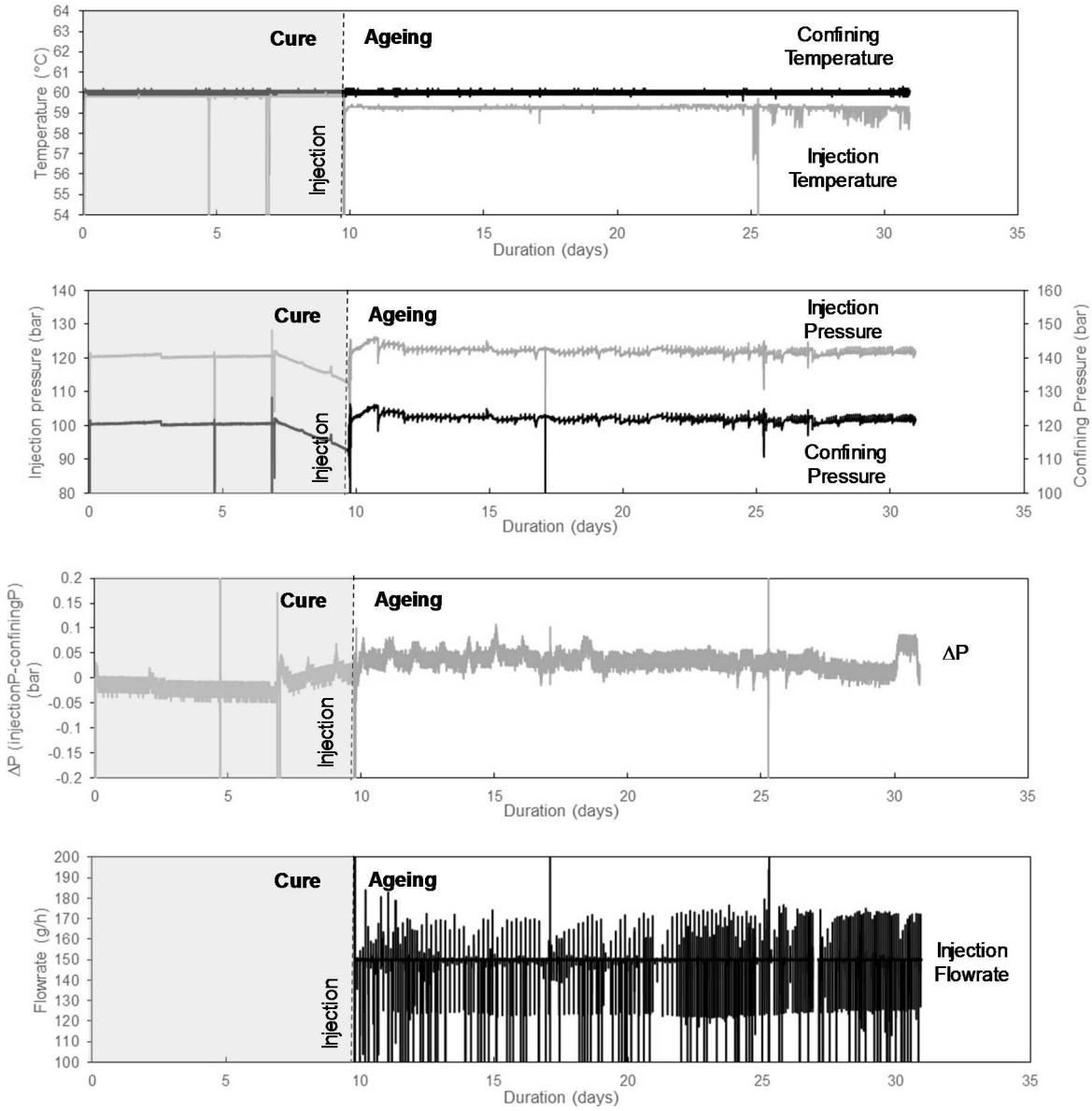

Figure E.11: Evolution of pressures (confining and injection), temperatures (confining and injection), ΔP (between injection and confining) and injection flowrate in the MIRAGES-2 autoclave during the 20d experiment with salt.

APPENDIX F

Experimental data recorded during the different experiments.

	Experiments	Exp #1 (21 days water injection)	Exp #2 (12hours water/CO_2 injection)	Exp #3 (24hours water/CO_2 injection)	Exp #4 (2.5 days water/CO_2 injection)
	Solutions	fresh MilliQ water	fresh MilliQ water + 15mg/kg_w $CaCO_3$	fresh MilliQ water + 15mg/kg_w $CaCO_3$	fresh MilliQ water + 15mg/kg_w $CaCO_3$
	Duration of the cure (days)	9.1	10.37	10.77	10.27
	Duration of the ageing	21 days	12H35min	23h50min	2.6 days
	Injected volume of solution (Liters)	71.18	2	3.49	10.322
CO_2 solubility data of the injected solution	Pressure of dissolution of CO_2 (bar)	atmospheric conditions	31.0 ± 0.3	30.1 ± 0.2	30.2 ± 0.2
	Temperature of dissolution (°C)	20 ± 1.5	20.0 ± 1.6	20.1 ± 1.5	20.2 ± 1.5
	Injection flowrate (g/h)	149.2 ± 0.01	151 ± 0.01	150 ± 0.01	149.9 ± 0.01
Pressure during the cure	Pressure of injection (bar)	118.9 ± 1.5	119.4 ± 1.5	119.2 ± 1.5	118.6 ± 1.5
	Pressure of confinement (bar)	118.9 ± 1.5	119.4 ± 1.5	119.2 ± 1.5	118.6 ± 1.5
Pressure during the ageing	Pressure of injection (bar)	121.8 ± 1.5	120.5 ± 1.5	123.8 ± 1.5	120.7 ± 1.5
	Pressure of confinement (bar)	121.7 ± 1.5	120.5 ± 1.5	123.8 ± 1.5	120.6 ± 1.5
Temperature during the cure	Temperature of injection (°C)	59.7 ± 1.5	59.9 ± 1.6	59.9 ± 1.5	59.8 ± 1.5
	Temperature of confinement (°C)	60 ± 1.5	60.0 ± 1.6	60.0 ± 1.5	59.9 ± 1.5
Temperature during the ageing	Temperature of injection (°C)	59.2 ± 1.5	59.5 ± 1.6	59.7 ± 1.5	58.9 ± 1.5
	Temperature of confinement (°C)	60 ± 1.5	60.0 ± 1.6	60 ± 1.5	60 ± 1.5

	Experiments	Exp #5 (10 days water/CO_2 injection/55°)	Exp #6 (21 days water/CO_2 injection)	Exp #7 (21 days NaCl/CO_2 injection)
	Solutions	fresh MilliQ water + 15mg/kg_w $CaCO_3$	fresh MilliQ water + 15mg/kg_w $CaCO_3$	fresh MilliQ water + 30mg /kg_w $CaCO_3$ + 15g/L NaCL
	Duration of the cure (days)	9.8	9.9	9.78
	Duration of the ageing	9.95 days	20.9 days	21.2 days
	Injected volume of solution (Liters)	35.15	73.7	74.32
CO_2 solubility data of the injected solution	Pressure of dissolution of CO_2 (bar)	30.0 ± 0.2	29.9 ± 0.2	30 ± 0.2
	Temperature of dissolution (°C)	20.2 ± 1.5	20.1 ± 1.5	20.1 ± 1.5
	Injection flowrate (g/h)	150 ± 0.01	150 ± 0.01	150 ± 0.01
Pressure during the cure	Pressure of injection (bar)	118.5 ± 1.5	118.7 ± 1.5	119.5 ± 1.5
	Pressure of confinement (bar)	118.5 ± 1.5	118.7 ± 1.5	119.5± 1.5
Pressure during the ageing	Pressure of injection (bar)	121.8 ± 1.5	122.2 ± 1.5	122.0 ± 1.5
	Pressure of confinement (bar)	121.5 ± 1.5	122.1 ± 1.5	121.9 ± 1.5
Temperature during the cure	Temperature of injection (°C)	59.9 ± 1.5	59.9± 1.5	59.8± 1.5
	Temperature of confinement (°C)	60.0 ± 1.5	60± 1.5	60± 1.5
Temperature during the ageing	Temperature of injection (°C)	59.5 ± 1.5	59.3± 1.5	59.3 ± 1.5
	Temperature of confinement (°C)	60.0 ± 1.5	60 ± 1.5	60 ± 1.5

APPENDIX G

Results of the evolution of the sulfate concentration in solution during all the experiments

	Exp #1 (Blank)	Exp#3 (24 hours)	Exp #4 (2.5 days)	Exp #5 (10 days)	Exp #6 (21days)	Exp #7 (21days) NaCl
Duration (days)	$[SO_4^{2-}]$ (mg/kg)		$[SO_4^{2-}]$ (mg/kg)		$[SO_4^{2-}]$ (mg/kg)	
0.00	0.00	0.00	0.00	0.00	0.00	0.00
2.00	12.31 ± 0.74					
3.81		13.3 ± 0.8				
4.02					13.49 ± 0.81	
4.70						6.84 ± 0.41
6.85						6.42 ± 0.38
6.97				3.8 ± 0.23		
8.78					12.50 ± 0.75	
9.01	11.3 ± 0.68					
9.74				3.6 ± 0.21		
9.75						
10.26			12.69 ± 0.76			
10.67		14 ± 0.84				
10.93						0.00
11.69		0.16 ± 0.02				
11.85						0.00
12.02				0.00		
12.08			0.19 ± 0.02			
12.83						0.00
13.76						
13.88				0.00		0.00
15.00					0.00	
16.13				0.00		
16.81	0.12 ± 0.02					
18.69				0.00		
19.05						0.00
19.73				0.00		
20.84					0.29 ± 0.01	
20.91						0.00
21.01	0.07 ± 0.02					
23.70					0.00	
24.09						0.00
25.92						0.00
27.81					0.00	
27.88	0.14 ± 0.02					
30.07						0.00
30.11	0.28 ± 0.02					
30.74					0.00	
30.95						0.00

APPENDIX H

Chemical composition of the outlet solution of the core-plug (cations in mg/kg of solution) as a function of time for the experiment without salt.

	Duration (days)	Ca (mg/L)	Mg (mg/L)	Sr (mg/L)	Si (mg/L)	Al (mg/L)	Fe (mg/L)	K (mg/L)	Mn (mg/L)	Na (mg/L)	Ti (mg/L)
BLANK (Exp #1)	2.00	**1.8 ± 0.09**	**< 5 ppb**		*2.62 ± 0.131*		**< 5 ppb**	*32.7 ± 1.635*	*< 5 ppb*	*6.16 ± 0.308*	
	9.01	**0.84 ± 0.042**	**< 5 ppb**		*2.42 ± 0.121*		**< 5 ppb**	*38.2 ± 1.91*	*< 5 ppb*	*6.94 ± 0.347*	
	16.81	**7.76 ± 0.39**	**< 5 ppb**		*0.251 ± 0.012*		**< 5 ppb**	*1.35 ± 0.067*	*< 5 ppb*	*0.687 ± 0.034*	
	21.01	**8.01 ± 0.4**	**< 5 ppb**		*0.227 ± 0.011*		**< 5 ppb**	*0.685 ± 0.034*	*< 5 ppb*	*0.778 ± 0.039*	
	27.88	**8.1 ± 0.4**	**< 5 ppb**		*0.236 ± 0.012*		**< 5 ppb**	*0.726 ± 0.036*	*< 5 ppb*	*0.73 ± 0.036*	
	30.11	**7.84 ± 0.39**	**< 5 ppb**		*0.2 ± 0.01*		**< 5 ppb**	*0.622 ± 0.031*	*< 5 ppb*	*0.857 ± 0.043*	
Exp#3 (24hours)	0.00	**4.25 ± 0.21**	**< 5 ppb**	**0.011 ± 0.001**	*0.08 ± 0.004*	**0.04 ± 0.003**	**0.106 ± 0.005**	*< 5 ppb*	*< 5 ppb*	*< 5 ppb*	*0.05 ± 0.002*
	3.81	**1.65 ± 0.08**	**0.22 ± 0.01**	**0.039 ± 0.002**	*0.09 ± 0.005*	**0.2 ± 0.01**	**0.027 ± 0.001**	*42.56 ± 2.13*	*< 5 ppb*	*11.18 ± 0.56*	*0.01 ± 0.001*
	10.67	**1.86 ± 0.09**	**0.11 ± 0.006**	**0.107 ± 0.005**	*0.1 ± 0.005*	**0.32 ± 0.02**	**0.017 ± 0.001**	*43.4 ± 2.17*	*< 5 ppb*	*11.49 ± 0.57*	*< 5 ppb*
	11.69	**216.88 ± 10.84**	**3.6 ± 0.23**	**1.01 ± 0.05**	*0.09 ± 0.005*	**0.065 ± 0.003**	**0.039 ± 0.002**	*8.41 ± 0.42*	*0.042 ± 0.002*	*2.64 ± 0.13*	*< 5 ppb*
Exp #4 (2days)	< 5 ppb	**5.34 ± 0.27**	**< 5 ppb**	**< 5 ppb**	*< 5 ppb*	**< 5 ppb**	**< 5 ppb**	*0.115 ± 0.01*	*< 5 ppb*	*0.162 ± 0.008*	*< 5 ppb*
	10.26	**1.74 ± 0.09**	**< 5 ppb**	**< 5 ppb**	*1.292 ± 0.065*	**0.103 ± 0.005**	**< 5 ppb**	*32.724 ± 1.636*	*< 5 ppb*	*11.867 ± 0.593*	*< 5 ppb*
	12.08	**127.7 ± 6.39**	**1.451 ± 0.07**	**0.174 ± 0.009**	*0.926 ± 0.046*	**< 5 ppb**	**< 5 ppb**	*1.393 ± 0.07*	*< 5 ppb*	*0.652 ± 0.033*	*< 5 ppb*
Exp#5 (10 days)	0.00	**4.25 ± 0.21**	**< 5 ppb**	**0.011 ± 0.001**	*0.085 ± 0.004*	**0.042 ± 0.002**	**0.106 ± 0.005**	*< 5 ppb*	*< 5 ppb*	*< 5 ppb*	*0.05 ± 0.002*
	6.97	**2.52 ± 0.13**	**0.08 ± 0.004**	**0.106 ± 0.005**	*0.109 ± 0.005*	**0.17 ± 0.009**	**0.08 ± 0.004**	*33.41 ± 1.67*	*< 5 ppb*	*4.48 ± 0.24*	*0.05 ± 0.002*
	9.74	**1.98 ± 0.1**	**0.06 ± 0.003**	**0.15 ± 0.008**	*0.075 ± 0.004*	**0.21 ± 0.01**	**0.009 ± 0**	*33.89 ± 1.69*	*< 5 ppb*	*5.32 ± 0.27*	*0.01 ± 0.001*
	12.02	**212.03 ± 10.60**	**3.23 ± 0.16**	**0.59 ± 0.03**	*0.094 ± 0.005*	**0.06 ± 0.003**	**0.08 ± 0.004**	*1.86 ± 0.09*	*0.048 ± 0.002*	*0.42 ± 0.02*	*< 5 ppb*
	13.88	**207.17 ± 10.36**	**2.83 ± 0.14**	**0.49 ± 0.02**	*0.05 ± 0.003*	**0.07 ± 0.003**	**0.09 ± 0.004**	*1.405 ± 0.07*	*0.047 ± 0.002*	*0.26 ± 0.01*	*< 5 ppb*
	16.13	**198.83 ± 9.94**	**2.59 ± 0.13**	**0.44 ± 0.02**	*0.08 ± 0.004*	**0.07 ± 0.003**	**0.05 ± 0.002**	*1.35 ± 0.07*	*0.049 ± 0.002*	*0.26 ± 0.01*	*< 5 ppb*
	18.09	**196.40 ± 9.82**	**2.43 ± 0.12**	**0.41 ± 0.02**	*0.08 ± 0.004*	**0.075 ± 0.004**	**0.07 ± 0.004**	*1.323 ± 0.06*	*0.048 ± 0.002*	*0.22 ± 0.01*	*< 5 ppb*
	19.73	**192.17 ± 9.61**	**2.38 ± 0.12**	**0.39 ± 0.02**	*0.08 ± 0.004*	**0.075 ± 0.004**	**0.08 ± 0.004**	*1.22 ± 0.06*	*0.047 ± 0.002*	*0.20 ± 0.01*	*< 5 ppb*
Exp #6 (21 days)	0.00	**5.34 ± 0.7**	**0.00**	**0.00**	*0.00*	**0.00**	**0.00**	*0.12 ± 0.01*	*0.00*	*0.16 ± 0.01*	*0.00*
	4.02	**2.072 ± 0.1**	**0.00**	**0.00**	*1.14 ± 0.06*	**0.12 ± 0.01**	**0.00**	*26.78 ± 1.33*	*0.00*	*9.34 ± 0.467*	*0.00*
	8.78	**1.38 ± 0.07**	**0.00**	**0.031 ± 0.005**	*1.25 ± 0.06*	**0.21 ± 0.01**	**0.00**	*29.50 ± 1.47*	*0.00*	*10.88 ± 0.54*	*0.00*
	9.94	**126.6± 6.33**	**1.54 ± 0.08**	**0.175 ± 0.005**	*1.14 ± 0.06*	**0.20 ± 0.01**	**0.00**	*28.35 ± 1.42*	*0.00*	*10.23 ± 0.51*	*0.00*
	15.00	**125.7 ± 6.29**	**1.44 ± 0.07**	**0.17 ± 0.009**	*0.89 ± 0.04*	**0.00**	**0.00**	*0.40 ± 0.02*	*0.00*	*0.40 ± 0.02*	*0.00*
	20.84	**120.7 ± 6.04**	**1.22 ± 0.06**	**0.12 ± 0.006**	*0.718 ± 0.04*	**0.00**	**0.01 ± 0.0 5**	*0.39 ± 0.02*	*0.00*	*0.37 ± 0.02*	*0.00*
	23.70	**117.2 ± 5.86**	**1.15 ± 0.06**	**0.106 ± 0.005**	*0.67 ± 0.03*	**0.00**	**0.00**	*0.31 ± 0.02*	*0.00*	*0.34 ± 0.02*	*0.00*
	27.81	**117.6 ± 5.88**	**1.14 ± 0.06**	**0.103 ± 0.005**	*0.66 ± 0.03*	**0.00**	**0.051 ± 0.005**	*0.37 ± 0.02*	*0.00*	*0.34 ± 0.02*	*0.00*
	30.74	**114.8 ± 5.74**	**1.11 ± 0.06**	**0.098 ± 0.005**	*0.65 ± 0.03*	**0.00**	**0.083 ± 0.005**	*0.36 ± 0.02*	*0.00*	*0.34 ± 0.02*	*0.00*

APPENDIX I

Chemical composition of the outlet solution of the core-plug (cations in mg/kg of solution) as a function of time for the experiment with saline solution (15g.L^{-1} of NaCl)

	Duration (days)	Ca (mg/L)	Mg (mg/L)	Sr (mg/L)	*Si (mg/L)*	Al (mg/L)	Fe (mg/L)	*K (mg/L)*	*Mn (mg/L)*	*Ti (mg/L)*
Exp #7 (20 days with salted solution)	0.00	**10.2 ± 0.5**	**0.01 ± 0.005**	**0**	*1.1 ± 0.05*	**0.02 ± 0.005**	**0**	*0.32 ± 0.02*	*0*	*0*
	4.70	**5.1 ± 0.3**	**0.20 ± 0.01**	**0.06 ± 0.005**	*1.57 ± 0.07*	**0.25 ± 0.01**	**0.02 ± 0.005**	*54.56 ± 2.72*	*0*	*0*
	6.85	**4.2 ± 0.2**	**0.1 ± 0.005**	**0.08 ± 0.005**	*1.72 ± 0.08*	**0.31 ± 0.01**	**0.01 ± 0.005**	*52.2 ± 2.6*	*0*	*0*
	9.75	**3.8± 0.2**	**0.06 ± 0.005**	**0.11 ± 0.006**	*1.87 ± 0.09*	**0.34 ± 0.02**	**0.01 ± 0.005**	*55.22 ± 2.76*	*0*	*0*
	10.93	**635.9 ± 31.8**	**4.94 ± 0.25**	**0.34 ± 0.02**	*1.58 ± 0.08*	**0.02 ± 0.005**	**0.22 ± 0.01**	*8 ± 0.4*	*0.054 ± 0.005*	*0*
	11.85	**632.8 ± 31.6**	**4.08 ± 0.20**	**0.28 ± 0.01**	*1.21 ± 0.06*	**0.02 ± 0.005**	**0.11 ± 0.005**	*2.27 ± 0.1*	*0.05 ± 0.005*	*0*
	12.83	**615.2 ± 30.8**	**3.59 ± 0.18**	**0.24 ± 0.01**	*1.12 ± 0.06*	**0.02 ± 0.005**	**0.1 ± 0.005**	*1.12 ± 0.06*	*0.047 ± 0.005*	*0*
	13.76	**596.3 ± 29.8**	**3.31 ± 0.16**	**0.22 ± 0.01**	*1.14 ± 0.06*	**0.02 ± 0.005**	**0.1 ± 0.005**	*0.93 ± 0.05*	*0.046 ± 0.005*	*0*
	16.73	**577.4 ± 28.9**	**3.00 ± 0.15**	**0.19 ± 0.01**	*1.4 ± 0.07*	**0.03 ± 0.005**	**0.1 ± 0.005**	*1.35 ± 0.07*	*0.046 ± 0.005*	*0*
	19.05	**535.3 ± 26.8**	**2.69 ± 0.13**	**0.18 ± 0.01**	*1.59 ± 0.08*	**0.03 ± 0.005**	**0.16 ± 0.007**	*0.64 ± 0.03*	*0.046 ± 0.005*	*0*
	20.91	**517.8 ± 25.9**	**2.58 ± 0.13**	**0.17 ± 0.01**	*1.64 ± 0.08*	**0.03 ± 0.005**	**0.16 ± 0.008**	*0.56 ± 0.03*	*0.045 ± 0.005*	*0*
	24.09	**516.1 ± 25.8**	**2.52 ± 0.12**	**0.16 ± 0.01**	*1.72 ± 0.09*	**0.03 ± 0.005**	**0.18 ± 0.008**	*0.53 ± 0.03*	*0.045 ± 0.005*	*0*
	25.92	**531.0 ± 26.6**	**2.57 ± 0.13**	**0.16 ± 0.01**	*1.86 ± 0.09*	**0.03 ± 0.006**	**0.18 ± 0.009**	*0.66 ± 0.03*	*0.045 ± 0.005*	*0*
	30.07	**514.4 ± 25.7**	**2.47 ± 0.12**	**0.15 ± 0.01**	*1.64 ± 0.08*	**0.03 ± 0.007**	**0.22 ± 0.01**	*0.5 ± 0.02*	*0.046 ± 0.005*	*0*
	30.95	**491.1 ± 24.6**	**2.33 ± 0.12**	**0.15 ± 0.01**	*1.63 ± 0.08*	**0.04 ± 0.005**	**0.19 ± 0.01**	*0.80 ± 0.04*	*0.044 ± 0.005*	*0*

APPENDIX J

An open access article was published in the peer-rewied journal Energy Procedia: 13th International Conference on Greenhouse Gas Control Technologies, GHGT-13, 14-18 November 2016, Lausanne, Switzerland

Edited by Tim Dixon, Lyesse Laloui, Sian Twinning

Volume 114,

Pages 1-7666 (July 2017)

Experimental and numerical simulation of the injection of a CO_2 saturated solution in a carbonate reservoir: application to the CO_2-DISSOLVED concept combining CO_2 geological storage and geothermal heat recovery

A. Randi[1], J. Sterpenich[1], D. Thiéry[2], C. Kervévan[2], J. Pironon[1]

[1]Université de Lorraine, CNRS, CREGU, GeoRessources laboratory, BP 70239, 54506 Vandœuvre-lès-Nancy, France

[2]BRGM, 3 av. Claude-Guillemin, BP 36009, 45060 Orléans Cedex 2, France

Available online at www.sciencedirect.com

ScienceDirect

Energy Procedia 114 (2017) 2942 – 2956

Energy Procedia

www.elsevier.com/locate/procedia

13th International Conference on Greenhouse Gas Control Technologies, GHGT-13, 14-18 November 2016, Lausanne, Switzerland

Experimental and numerical simulation of the injection of a CO2 saturated solution in a carbonate reservoir: application to the CO2-DISSOLVED concept combining CO2 geological storage and geothermal heat recovery

A. Randi[1]*, J. Sterpenich[1], D. Thiéry[2], C. Kervévan[2], J. Pironon[1], C. Morlot[1]

[1]*Université de Lorraine, CNRS, CREGU, GeoRessources laboratory, BP 70239, 54506 Vandœuvre-lès-Nancy, France*
[2]*BRGM, 3 av. Claude-Guillemin, BP 36009, 45060 Orléans Cedex 2, France*

Abstract

The CO2-DISSOLVED project explores the technical and economic feasibility of a promising concept combining CO_2 storage and geothermal heat extraction. The CO_2 released by low CO_2 emitters is dissolved in the extracted brine via a doublet heat exchanger system. To study the effect to CO_2-rich and thus acidic solution in the geothermal doublet, three reactive flow-through experiments mimicking the injection of a CO_2 rich solution were performed. The chemical interactions in the near-injection well area between the reservoir rock, the cement phases and the acidic CO_2-rich solution was investigated under geothermal reservoir conditions. The main results are i) the formation of a highly permeable network due to specific dissolution pattern called wormholes, and ii) the preservation of mechanical cohesion the cement/rock interface despite the cement carbonation. The experimental results are compared with those obtained by chemical-transport modelling with the coupled PHREEQC-MARTHE codes

Peer-review under reponsability of the organizating comitte of GHGT-13

Keywords: geological storage; geothermal energy; dissolved CO2; limestone; class G Portland cement; wormhole, numerical simulation

* Corresponding author. Tel.: +33 3-83-68-47-07; fax: +33 3-83-68-47-01.
E-mail address: aurelien.randi@univ-lorraine.fr

Peer-review under responsibility of the organizing committee of GHGT-13.
doi: 10.1016/j.egypro.2017.03.1423

1. Introduction

To tackle the issue of climate change, a lot of Carbon Capture and Storage (CCS) projects [1] have been launched to develop strategies and technologies that safely and permanently store carbon dioxide (CO_2). CCS involves a combination of technologies to capture CO_2 from large emission sources like fossil fuel plants and industrial facilities, transport it to a suitable location and bury it into deep geological formation. These projects generally plan for the injection of CO_2 under supercritical state, thus maximizing the stored quantities that can reach several millions of tons per year. Novel CCS concepts emerge and consist in injecting dissolved CO_2 in brine instead of supercritical phase. This option offers substantial benefits in terms of lower brine displacement risks, lower CO_2 escape risks, lower to none pressure buildup in the storage aquifer, and the potential for more rapid mineralization. Thereon, the synergy between geothermal heat recovery and CCS appears as a promising alternative as it offers a way to offset some of the cost of storage [2]. The CO2-DISSOLVED concept [3-4] combines the injection of dissolved CO_2 close to an emitting source and the recovery of the geothermal heat from the extracted brine. The proposed project opens new potential opportunities for local storage solutions dedicated to low emitters (< 150 000 t/years) and constitutes an interesting way of valorizing the brine reinjection, demonstrating that an actual synergy between CO_2 storage and geothermal activities may exist. This approach relies on the geothermal doublet technology (commonly used in the Paris Basin, France), where the warm water is extracted at the production well and the cooled brine re-injected in the same aquifer via a second well (injection well).

The acidification of the brine caused by the presence of dissolved CO_2 involves complex phenomena in the near wellbore region that should be accounted for the design and the sizing of the whole system. Indeed, the injection of CO_2-rich acidified water has an effect on the chemical reactivity of fluid and solid phases resulting in dissolution and potentially, carbonate precipitation [5,6,7,8,9,10]. The CO_2-saturated brine-limestone reactions provokes changes in petrophysical properties of the host formation which are characterized by an increase of porosity and permeability [6,11,12,13,14] especially at the immediate vicinity of the injection well. The long term behavior of the reservoir will be modified in term of injectivity, storage efficiency and integrity. Similarly, acidified water will be much more aggressive for the well casing than standard cold brine in classical geothermal doublets. It could also induced mechanisms of chemical alteration of well cement weakening the mechanical cohesion between the different interfaces (cement-rock and cement-steel tube). Well integrity can be thus compromised because of the potential development of leaks [15,16,17,18].

A good understanding of the mechanical impact near the injection well induced by the injection of CO_2 acidified solution is essential for producing reliable model for risk assessment. Specific work, focusing on the near-injection well area and relying on both new experimental and modeling approaches are carried out in the framework of the CO2-DISSOLVED project. The so-called MIRAGES2 (acronym, in French, for “Radial Model for Greenhouse Gas Injection”) experimental device is designed by the GeoRessources laboratory for injection of a CO_2-rich aqueous solution in an injection well at the centimeter scale under realistic storage conditions (60°C – 120 bar) [19]. Three flow-through reactive experiments were performed on cylindrical samples composed of Lavoux limestone, a class G Portland cement and a well casing made of stainless steel in order to quantify the effect of CO_2-enriched solution on reservoir and well properties. The main transformations of the materials (cement, steel and limestone) were investigated in terms of mineral dissolutions, precipitations, and petrophysical properties. The ongoing monitoring of injection and confining pressures and temperatures as well as the flowrate of the injected solution and the pH of the solution outside of the core plug were implemented. The evolution of the porous network in samples was also investigated after each experiment using 3D X-Ray micro-tomography. The evolution of the cement phase, its carbonation, and the different interfaces were analyzed using the Scanning Electron Microscopy (SEM). The Raman spectroscopy enabled the determination of the nature of the calcite polymorphs precipitated in the cement phase during experiments.

Simultaneously of the experiments, geochemical modelling were performed using the coupled MARTHE-PHREEQC codes [20,21]. The data gathered during experiments were compared with results from numerical reaction-transport codes used to predict the behavior of the geothermal doublet with time. This study combining experimentation and modelling carrying out at the laboratory scale is very important in understanding and predicting the rock behavior at the reservoir scale.

2. Experimental methodology

2.1. Sample description

The Lavoux limestone is a Dogger (Mid-Jurassic) oolitic limestone from the Oolithe Blanche Formation of the Paris Basin. Due to its high storage capacity, the deep formation of the Dogger of the Paris Basin was identified as a relevant target for supercritical CO_2 storage [24,25] and has been used for hydro-geological and geothermal purposes for 40 years. This study was carried out on plugs sampled on quarry in Chauvigny in the Southwest of the Paris basin. From a structural point of view, the Lavoux limestone is a packstone to grainstone mainly composed of oolites, peloids, and bioclasts linked by a $CaCO_3$ cement (Fig. 1). The oolitic carbonate contains a micritic matrix. Locally, the cement is made up by large size syntaxial sparites (100 – 200µm) and moderate size rhomboedral calcites (10 – 50 µm, Fig. 1c). Petrophysical analyses are performed with focus on porosity and permeability parameters. The total bulk connected porosity is 25.38%. The porosity is mainly composed of pores of 0.03 to 1.46 µm corresponding to the inter-oolites pores. Two other families of pores of about 3 µm and 200 µm correspond to the inter-oolitic porosity (or macroporosity). The permeability of the rock is of 1.1 x 10^{-13} m^2 (88.2 mD). From a chemical viewpoint, the Lavoux limestone is composed of 98% of calcium carbonate (calcite and low magnesium calcite). This sample was selected as being representative of a potential good candidate area for a future implementation of the CO2-DISSOLVED concept.

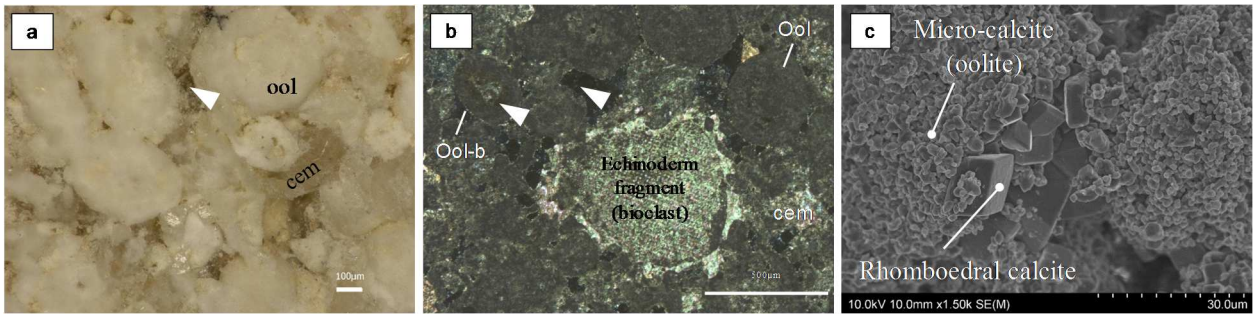

Fig. 1: Illustration of the oolitic facies: Microscopic view of the rock surface (a). Cathodoluminescence image of thin section of the limestone with the oolites (ool), the syntaxial cementation (cem) in polarized-analyzed light, the oolitic belt (ool-b) and the porosity (arrow). (b). SEM image (Secondary Electrons) of LAVOUX limestone showing micritic crystals and cement.

Concerning the well material, the cement is a class G Portland cement commonly used for deep well applications. After hydration the cement is mainly composed by portlandite ($Ca(OH)_2$), calcium silica hydrate (CSH), non-hydrated bi/tri calcic silicate (C2S and C3S) and other minor phases containing aluminium and sulfates (ettringite) and iron. The steel used in our experiment is an austenitic stainless steel 316 (EN standard steel name X5CrNiMo17-12-2).

The core assemblage used to reproduce a scaled-down injection well (Fig. 2) is described in Randi et al. [19]. It is made of the steel tube that is fixed to the core plug with the class G Portland cement.

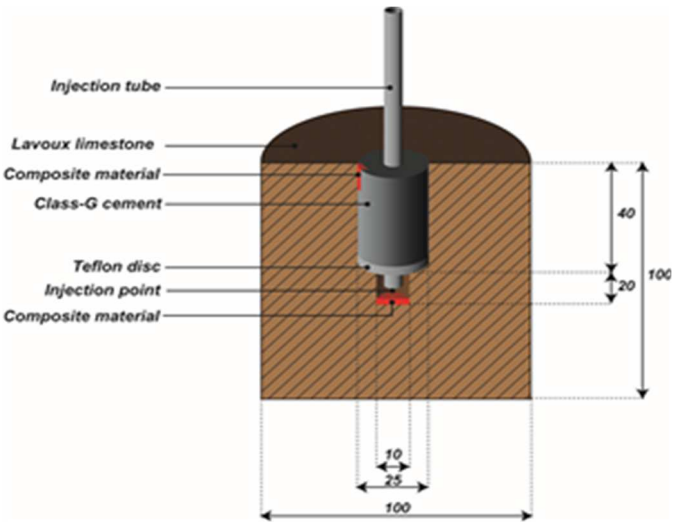

Fig. 2: Schematic view of the injection well of the MIRAGES-2 experiment. Dimensions are given in millimeters.

2.2. Experimental conditions

The so-called MIRAGES2 experimental device is extensively described in Randi and al. [19]. It allows to perform continuous and constant injections of CO_2 dissolved in aqueous solution (pure water or brine) under pressures and temperatures representative of CO_2 storage conditions in the Dogger formations of the Paris basin at 1500 m depth. The core plug samples of limestones are loaded into a 2 Liters "injection autoclave". The injection of the CO_2-enriched fluid is performed at constant flow rate using a double syringe pump coupled to a liquid mass Coriolis flow meter. A mixing autoclave located upstream of the continuous flowrate injection system provides a controlled mixture of dissolved CO_2 in solution. During the experiments, regular measurements of the pH are carried out with in situ probes at the inlet and the outlet of the samples. The experimental procedure consists in two steps: i) a cure period during which the sample is subjected to reservoir conditions in a close system. This period lasts approximately 10 days and allows the hydration of the cement phase under the reservoir conditions. ii) a 21 days injection period in which the fluid is injected radially in the injection zone of the rock sample (Fig. 2).

A set of 3 experiments forcing the cores samples to different regimes of injections of specific fluids are performed at 60°C and 120 bar total pressure with a constant rate of $150 g.h^{-1}$. The first experiment is carried out with pure water in equilibrium with atmospheric CO_2 corresponding to the blank experiment (exp #1). The second one is a short-term experiment with the injection of a CO_2-rich solution (exp #2), and the third one is a long-term experiment, also with the injection of a CO_2-rich solution (exp #3). $CaCO_3$ is added to pure water in order to limit the dissolution of the core-plug during the cure period. Finally, the CO_2 concentration in the injected solution is always kept below the limit of solubility of CO_2 in the solution in the experimental conditions. This step keeps the injected phase monophasic and prevent from any CO_2 bubbling in the "injection autoclave". The conditions of performed experiments are summarized in Table 1.

Table 1. Overview of experimental conditions

Experimental conditions	Exp #1: 21 days water	Exp #2 : 2.5 days CO_2/water	Exp #3 : 21 days CO_2/water
Chemistry of the injected solution	pure water	equilibrated water (15mg.kg^{-1} $CaCO_3$)	equilibrated water (15mg/kg^{-1} $CaCO_3$)
CO_2 concentration in the injected solution (P/T)	equilibrated with atmosphere	0.93 mol.kg^{-1} (30 bar / 20°C)	0.93 mol.kg^{-1} (30 bar / 20°C)
Time of cure	9.1 days	10.5 days	9.9 days
Time of injection	21.0 days	2.5 days	20.9 days

2.3. X-ray tomography

The X-ray computed microtomography (CT) is a non-destructive technique used to explore the architecture of a solid sample with a resolution of tens of microns for our samples. This technic produces a 3D-imagery of the internal structure of the sample measuring the X-ray attenuation of the material. In this study, the whole core-plugs with 100×100 mm dimensions are analyzed before and after injection. The several different parameters of acquisition are defined depending on the sample (Table 2). These configurations allow the acquisition of images with a final resolution between 59 and 105 µm.voxel^{-1}. The 3D reconstruction of the sample is performed using the Datos-Rec software. The CT images are interpreted in terms of porous (voids) and solid phases by segmentation thanks to the Interactive thresholding module on the AVISO© software.

The data acquisition are performed at the GeoRessources laboratory using a Nanotom Phoenix (GE).

Table 2: Acquisition parameters for X-ray tomography of the whole core-plug for the different experiments. The resolution (µm.voxel^{-1}) depends on the span length between the X-Ray source and the sample; the radiography number is the number of images acquired by the detector, it depends on the angular interval between two successive radiographies.

EXPERIMENTS	Resolution (µm/voxel)	Angular interval (°)	radiographies number	Exposure time (ms)	X-ray tube of nanofocus tension (kV)	Beam intensity (µA)
Exp #1	100	0.24	1500	1250	110	100
Exp #2	105	0.35	1020	1250	110	50
Exp #3	59.57	0.24	1500	1000	145	300

3. Modelling approach

The experiments of dissolution of a calcite core have been modelled with the MARTHE-PHREEQC numerical code [20]. This code results from the coupling of the MARTHE code [21, http://marthe.brgm.fr/] for flow and transport in porous media, and PHREEQC modules for geochemistry [22, 23].

In the first modelling, as a simplifying assumption, the cement has been assumed to be impermeable and non-reactive. In the second modelling, the reactions with the Portland cement have been considered. Both simulations have been performed with a radial grid, supposing a radial symmetry around the well. This makes it possible to greatly reduce the number of cells and hence the calculations time, which is quite long, as it will be shown.

3.1. Geometry of the core and the chamber

The modelled chamber (injection autoclave) is a cylinder of radius 6.25 cm and 16.25 cm height (volume 1.99 liter). The modelled sample is a cylinder of radius 5.0 cm and 10.0 cm height (volume 0.78 liter). The radial irregular grid comprises 35 rows of 19 columns (665 cells). The rows represent circular slices in the vertical direction, and the columns represent the widths in the radial distance. The vertical slice thickness ranges from 0.25 cm to 1.25 cm, and the radial width from 0.25 cm to 0.50 cm. The model grid is displayed in fig.3.

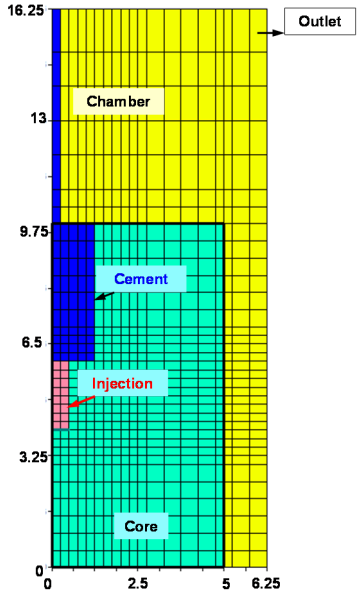

Fig. 3. Modelling radial grid. (Dimensions are in cm). The horizontal axis is the radial distance.

3.2. Flow and transport parameters

The hydraulic parameters are:

- Calcite sample: porosity 10 %, hydraulic conductivity 1 mD
- Cement: porosity 28 %, hydraulic conductivity nearly 0 (10^{-20} mD)
- Injection and external chamber: porosity 100 %, hydraulic conductivity = 50 mD

The flow is injected at a rate of 9.375 cm^3/hour in each of the 16 cells representing the injection chamber (total flow is 150 cm^3/hour). The outlet is set in the upper right corner with a prescribed arbitrary hydraulic head of 20 cm (0.2 bar). The hydro-dispersive parameters are: molecular dispersion = 10^{-9} m^2/s, dispersivity = 1 cm

4. Results

4.1. Evolution of the limestone reservoir

The in situ measurements of pH during experiments (Fig. 4) indicate an increase during the cure period up to values between 9.2 and 10 depending on the experiments. The ettringite and the portlandite of the cement phase act as a buffer and control the pH of the solution.

For the blank experiment (exp #1), a slight decrease of the pH occurs during the 8 first days of the injection in the core-plug of pure water at equilibrium with the atmospheric CO_2 with a value dropped from 9.8 to 9.4. The pH then remains relatively constant until the end of the experiment. For experiments with dissolved CO_2 (exp#2 and #3), as soon as the CO_2-rich acidified solutions with a pH value of 3.6 is injected, the pH at the outlet of the core-plug dropped to 6 during the first 30 minutes of injection due the formation and dissociation of the carbonic acid. Then a sill lasting 1 or 2 days is followed by a new acidification with values reaching 5.4. This phenomenon demonstrates a competition between the carbonates and the cement phases to control the pH.

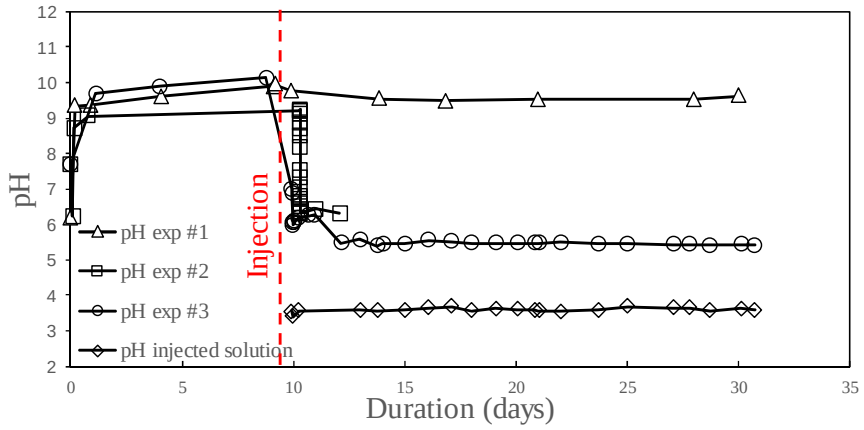

Fig. 4: pH measurements of the injected solution and of the solution at the outlet of the core-plug during the different experiments. The pH of the injected CO_2-rich solution is given for comparison.

The observations of the core-plug removed from the autoclave after experiment with pure water does not reveal visible changes neither apparent trace of dissolution on the outer part of the sample (Fig. 5a). Experiments #2 and #3 with CO_2-rich solutions lead to the formation of millimetric to centimetric holes visible on the wall of the core plug. These holes appear after only 2.5 days of injection (Fig. 5b) and increase in diameter when the alteration time increases (Fig. 5c).

The CT analysis shows the development of a radial porous network induced by the injection of the different fluids (Fig 5). Despite the alkaline environment, a dissolution pattern resulting on the injection of pure water is observed and corresponds to a ramified and complex wormhole structure mainly at the bottom of the injection point (Fig 5a bottom part). These wormholes can be defined as dominant with branches formation. No modification of the well geometry is noticed at the injection point. After 2.5 days of injection of aggressive fluid (exp #2), significant dominant wormhole structure is also observed at the bottom of the injection point. However, in this case, a main wormhole forms from the upper part of the well to the outer part of the core-plug. Secondary channels branching from the predominant channel of dissolution are also visible (Fig. 5b bottom part). The appearance of this large diameter wormhole after 2.5 days of injection demonstrates that the injection of the acidic solution leads to a rapid and directional dissolution of the carbonate minerals. However, after this experiment, the geometry of the well has not changed near the injection point. The continuous renewal of the acidic fluid during 21 days (exp #3) increases significantly the diameter of the main wormhole at the upper part of the well (from 9.8 mm after 2.5 days to 13.3 mm after 21 days, on average). Radial channel branching is also present at the bottom of the well with a radial extent length similar to exp #2. This largest wormhole carries the majority of the injected fluid, resulting in a constant and rapid increase of its diameter at the expense of the shorter wormhole [26] located at the bottom of the well that seems to stop growing and eventually to close up. After 21 days of injection, the well with initial cylindrical shape becomes conical.

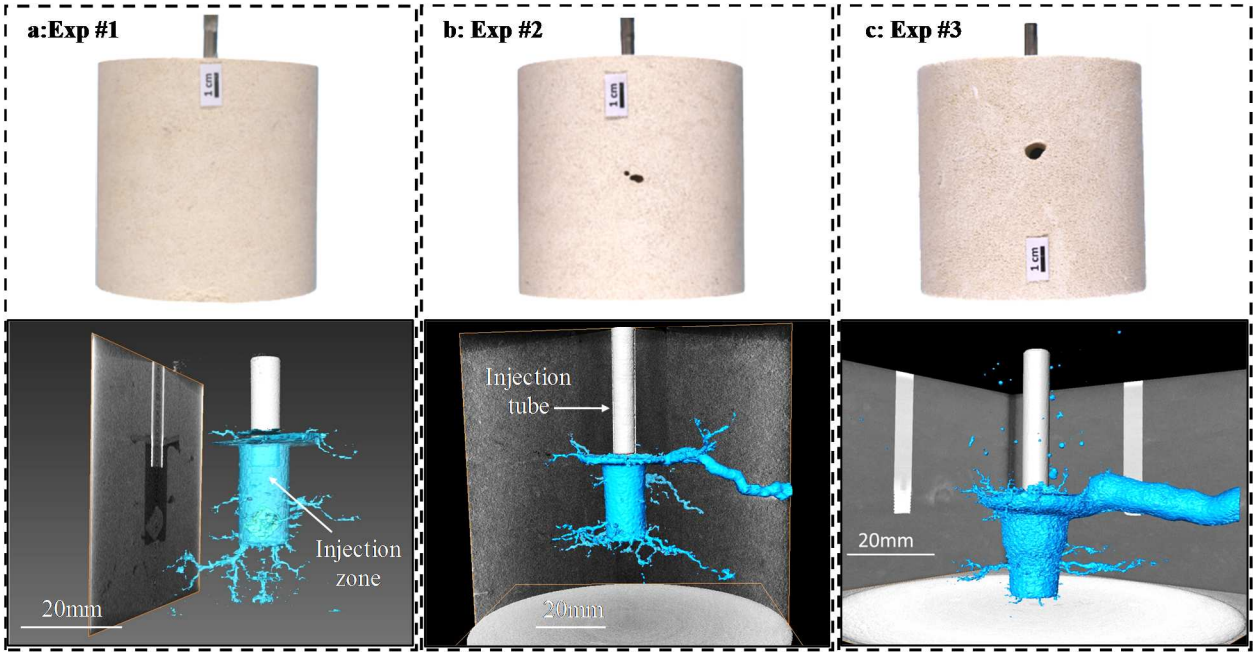

Fig. 5: View of the samples after experiment and after drying for 24h at room temperature (upper part) and comparison of dissolution patterns (3D models) based on results of X-ray computed tomography (CT) (bottom part) for (a) pure water in equilibrium with atmospheric CO_2 (exp #1), (b) short-term experiment with CO_2-rich solution (exp #2) and (c) long-term experiment with CO_2-rich solution (exp #3).

4.2. Results of the cement/rock interface evolution.

Observation of the cement/rock interface is realized from polished cross sections of the core-plugs. Experiments exp #1 (Fig. 6) and exp #3 (Fig. 7) with the same duration of alteration are compared. The detail observation of the interfaces reveals a good mechanical cohesion and the absence of fractures or cracks between the cement and the limestone for both experiments. Nevertheless, a reactive zone parallel to the interface develops from the interface into the cement zone. The optical images of the thin sections (Fig.6b and 7b) highlight this zone (red line).

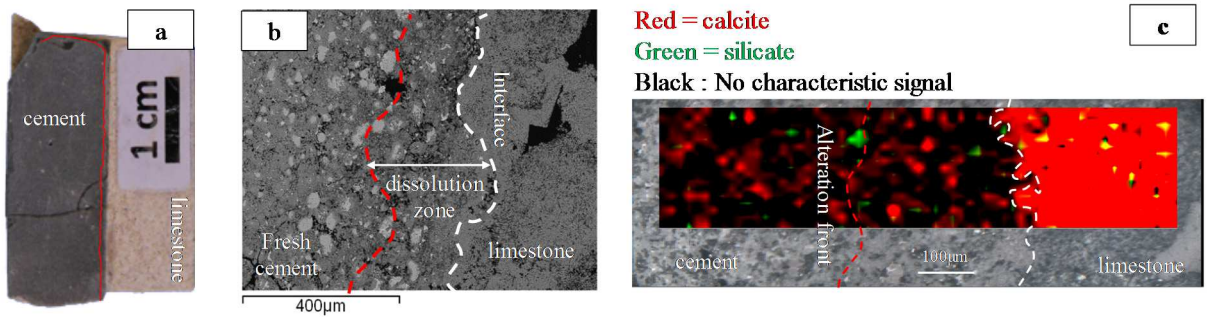

Fig. 6: Experiment exp #1 (pure water): a) Sampling at the rock/cement interface, b) SEM (BSE) picture showing the cement alteration and the cement/limestone interface and c) Raman mapping at the rock/cement interface shows a limited calcite precipitation in the cement phase.

In the blank experiment (exp #1), the thickness of the alteration zone is about 450 µm corresponding to an averaged alteration speed of $0.88 \mu m.h^{-1}$. The SEM observations reveal an increase of the porosity of the cement matrix at the cement/limestone interface (dissolution zone, Fig. 6b). This is due to the leaching of the calcium bearing phase (C2S, C3S and CSH) of the cement by the injected solution. The Raman mapping shows also a limited carbonation of the cement phases (red dots in the cement).

In the case of the injection of the acidic solution (exp 2 and #3), the thickness of the alteration front is around 457 µm after 2.5 days of injection and 1,518 µm after 21 days corresponding to an average speed of alteration of 7.61 and 3.03 $\mu m.h^{-1}$ respectively. The reaction zone can be subdivided in 3 zones corresponding to different chemical processes (Fig. 7). A first zone (Z1), with a higher porosity, where the CSH matrix is dissolved, can be identified. The Raman mapping shows the presence of the C2S and C3S silicate phases (green dots in the cement). In the two other zones (Z2 and Z3), the SEM observation (Fig. 7b) reveals a dense CSH matrix with a precipitation intimately related to the matrix. Raman analysis indicates that this secondary precipitation corresponds to aragonite (Fig. 7c). In Z2 and Z3, the C2S and C3S are replaced by an amorphous silica phase. The area close to the interface with the rock (Z3) appears more porous than the intermediate zone (Z2).

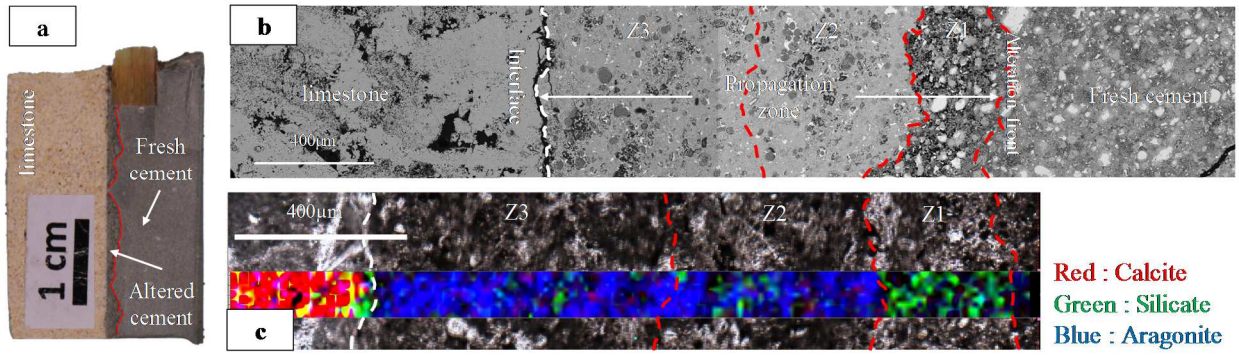

Fig. 7: Experiment #3 (CO_2-rich solution): a) Sampling at the rock/cement interface with an altered zone of the cement delimited by the red line, b) SEM (BSE) picture showing the cement alteration divided in three zones and c) Raman mapping at the rock/cement interface showing a strong carbonation of the cement with aragonite precipitation.

5. Discussion

5.1. Dissolution of the limestone reservoir

The thermodynamics instability triggered by the massive injection of dissolved CO_2 into a carbonated reservoirs induces a dissolution front at the vicinity of the injection well. The acidic solution in contact with the rock formation reacts with the porous matrix and leads to the increase of the local permeability and thus of the mass transfer resulting in an increasing of porosity. Conversely, precipitation phenomenon can be observed due to an enrichment in cations, especially Ca^{2+}, induced by carbonate dissolution and a local oversaturation of the solution with respect to carbonates. The prominence of the processes depends on reactive transport mechanisms, i.e. on the coupling between dissolution/precipitation and diffusion/advection. An anisotropic evolution of the system was highlighted during experimental studies and was dependent on different factors as the intrinsic characteristics of the rock (nature, permeability, heterogeneity, reactivity,…), the process parameters (injection flowrate, CO_2 concentration,…) and thermodynamics conditions (Pressure, Temperature). Percolation experiments of a CO_2-enriched fluid through a core-flood carbonated rock sample have been performed in geological reservoirs conditions closed to our experiments by different authors [6,8,9,10]. These results underline the diversity of the dissolution patterns as a function of the operating conditions influencing the mass transfer in the geological environment. A high flowrate generally stimulates the growth of a very localized dissolution with the appearance of highly conductive channels, referred as wormholes. The distribution and the geometry of these channels are controlled by the heterogeneity of the pore structure. The wormhole leads to a preferential flow path at the expense of the porous matrix [10]. It is important to remark that acidic solution penetrates predominantly within local domains of pre-existing fractures [27,28] and vuggy carbonates [29]. Moreover, depending on the P_{CO2} in the system, uniform dissolution can also be observed [6] far from the injection point. The determination of the dissolution pattern and the impact on the petrophysical properties of the host reservoir remains complex mainly because of the competition of the acidic effect (decrease of the pH) induced by the injection of a CO_2-rich solution and the transport phenomena which can lead to local oversaturation. Dimensionless numbers (the Péclet-Damköhler numbers) characteristic of the reactive transport problem can help to characterize the dissolution regimes. The Péclet number Pe represents the significance of the advective rate on the diffusion rate and is defined as:

$$Pe = \frac{\upsilon \times l}{D}$$

where l (cm) is the representative pore lenght and could be taken as the square root of the permeability, D is a coefficient of effective molecular diffusion ($cm^{-2}.s^{-1}$), and υ is the interstitial velocity ($cm.s^{-1}$) defined here as the Darcy velocity ν ($cm.s^{-1}$) divided by the porosity ϕ.

The Damköhler number represents the ratio of the dissolution to the advective rates and is defined as:

$$Da = \frac{k \times l}{\upsilon}$$

where, k is a reaction rate (s^{-1}). The k constant is calculated multiplying the mineral dissolution rate R ($mol.cm^{-2}.s^{-1}$) by the specific surface area S_{spec} of the calcium carbonate ($cm^2.mole^{-1}$). According to our experimental conditions, the calculated Péclet number ranges from 0.0152 to 0.1 with a diffusion coefficient for Ca^{2+} ranging from 7.5 x 10^{-6} $cm^2.s^{-1}$ [6] to 2 x 10^{-5} $cm^2.s^{-1}$ [8]. For the determination of the Damköhler number, the kinetic constant is determined using the empirical law of Pokrovsky et al [30], $k=10^{-7.51}$ $mol.cm^{-2}.s^{-1}$ and a specific surface area from 10^6 to 1.5 × 10^6 $cm^2.mole^{-1}$ [31]. The calculated values range from Da = 0.033 to 0.05.

According to the Péclet/Damköhler diagram obtained from Golfier et al [32] in a system close to our experiments (Fig.8), the results tend to indicate that a dominant wormhole dissolution and potentially conical wormhole pattern could be initiated at small scale near the injection point. Initiation of compact or uniform dissolution pattern seems less probable because the transport mechanism is strongly dominated by advection rather than diffusion.

The development of the shape of the wormholes is mainly subjected to a dominant advection effect at the early stage of the injection. Once the big wormhole crosses the core plug radius, the diffusive effect tends to erode its walls inducing an increase of the channel diameter and the modification of the shape of the well in a conical aspect.

It is important to underline that prominent anisotropy of the multilevel dissolution pathways are observed, while the injection process is basically isotropic from the bottom hole. Different assumptions can explain this anisotropic patterns. The first assumption is the presence of an initial anisotropy of the porous network. This phenomenon could be also induced by the mechanical consequences of the sample preparation procedure or could be due to the regional stress field linked to the geological history of the Lavoux formation. Another explanation could be the geometry of the experimental test bench constraining a preferential pathway for the fluid circulation. Anyway, the injection of aggressive fluids induces a dominant dissolution regime that will be responsible for the modification of the porosity and permeability of the rock at a large scale.

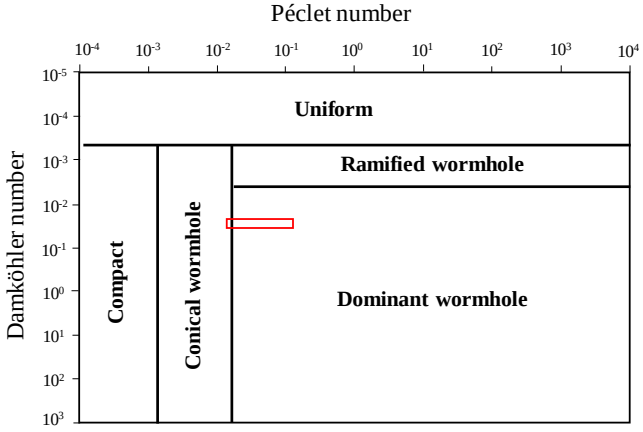

Fig. 8: Diagram representing the dissolution regime and pattern depending on Péclet and Damköhler numbers in a system close to our experiment. [29] The red box corresponds to the dissolution pattern expected in our experimental conditions.

5.2. Evolution of the cement/limestone interface

The injection of the fluids, pure or CO_2-rich water, in the rock during 21 days doesn't alter the mechanical cohesion between the cement and the limestone. However, a reactive zone parallel to the interface appears in the cement phase. During the week of cure, the cement phase is hydrated under geological conditions of pressure and temperature and imposes, together with the limestone, an alkaline environment to the system with initial pH around 10. The injection of water, more or less acidic as a function of the experiment, induces chemical reactions with calcium silicate phases of the Portland cement. The reactivity leads to the dissolution of portlandite and a part of the CSH phases, the leaching of C2S and C3S and the precipitation of carbonates in the cement matrix. All these chemical reactions imply petrographic changes mainly in the cement phase close to the interface with the limestone. Porous zones are the result of dissolution processes and are adjacent to carbonates zones, where aragonite precipitate, clogging the porosity between the CSH.

SEM microscopic observations and Raman mapping highlight three different alteration zones (Z1, Z2 and Z3) widely described in the literature and corresponding to the different processes described above. The portlandite (CH) of the cement matrix is dissolved by the CO_2-enriched solution and is responsible for calcium release in solution. Another calcium contribution comes from the dissolution of CSH and the leaching of C2S and C3S leading to the development of the zone Z1. The diffusion of the calcium coupled to the diffusion of the carbonate ions induces the precipitation of secondary carbonates, mainly aragonite, responsible for the low permeability and carbonated zones Z2 and Z3. The zone Z3 located at the rock/limestone interface undergoes, in a second step, the action of the renewed acidic solution and thus the partial dissolution of the secondary carbonates. This secondary dissolution implies a localized increase of the porosity by comparison with zone Z2.

Despite the chemical reactivity of the Portland cement used in the experiment, the interface between cement and limestone keeps a good mechanical cohesion. The carbonation processes don't seem to damage the physic-chemical properties of the cement, with a possible profitable effect linked to the decrease of the porosity of the carbonated zones. Moreover, it has been shown that the mean rate of cement alteration decreases with the duration of the experiment, likely because the carbonated zone plays the role of a diffusion barrier. However, the zone Z3 has to be carefully studied since a secondary dissolution is observed, which could lead to a possible opening of the interface. This zone could be a weakness of the injection well.

5.3. Chemical-Transport modelling

The modelling will explore thee aspects to compare to experimental results. This is the general dissolution of the limestone reservoir, the wormholing phenomenon and the influence of the Portland cement.

5.3.1. Results from the flow modelling

The computed hydraulic pressure difference between inflow and outflow is 5.2 bar.

The residence time in cells in the radial direction from the center of the injection chamber depends on velocity and also on the cell size. This residence time is 7.8 seconds in the cell at 0.5 cm from the injection, 11 seconds in the cell at 0.75 cm and 28 seconds in the cell at 2 cm. The total residence time in the sample in the radial direction is 1050 seconds.

5.3.2. Reactive transport modelling with kinetic: limestone only

For this simulation MARTHE-PHREEQC has been used, with parallel computation of the chemical reactions. In the simulation it has been assumed, for simplification purpose, that there is no coupling between the progressive mineral dissolution and the variation of flow due to the modification of porosity and of permeability.

The chemical database which has been used is "Phreeqc Thermoddem" (release 1.10, 12/11/2014) developed at BRGM (French Geological Survey).

The initial solution in the sample has a temperature of 60°C, a pH of 8.23, and a CO_2(g) saturation of -3.45. The injected acidified solution contains 0.93 mol of CO_2 per kg_w at a temperature of 60°C, resulting in a pH of 3.165.

In order to get accurate results it is very important to use an adequate calculation time step. A first guess is on the order of the residence time in the cells, which corresponds to a Courant number equal to unity. It has been seen that this residence time ranges from 8 seconds, near the injection chamber to 30 seconds 2 cm away. The adequacy of the time step has been verified by decreasing it until results do not vary significantly. It has been found that a value of 2.4 seconds gives accurate results. The total simulation period being 20 days, this corresponds to 0.72 million calculation time steps which is considerable. With a 9 processors 2015 workstation the duration of the calculation is 27 hours, (82 % of it for the geochemistry calculations).

The calculation shows that after 10 days the calcite is dissolved in a radius of about 2.0 cm, i.e. 1.5 cm from the injection chamber (Fig. 9) which is coherent with the observations. The profile is relatively sharp, however attenuation is observed due to dispersion and dissolution kinetics.

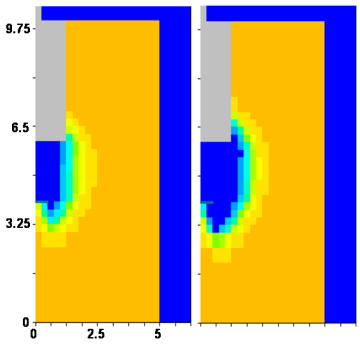

Fig. 9. Calcite concentration in the sample calculated after 5 days (left) and 10 days (right).
Dark blue = Fully dissolved, Orange color = No dissolution.

5.3.3. Modelling with channeling effects

In order to address the channeling effect due to heterogeneity which has been observed in the laboratory experiments, a simulation has been performed with a radial zone with a higher permeability. The higher permeability induced a higher velocity (and a higher dispersion) which pushed away more rapidly the water enriched in Ca ions resulting from the calcite dissolution. In this zone the dissolution is then faster.

For this modelling, in order to simulate a fracture or a fissured zone, the hydraulic conductivity has been increased in a radial slice of vertical thickness of 2.5 mm intercepting the injection chamber. In this slice the hydraulic conductivity was increased by a factor of 100.

Fig 10 shows calcite concentration after 2 days, 5 days, 10 days and 15 days. It appears that the dissolution is fast. After 10 days, the calcite has already been totally dissolved into the circular “fracture”. The dissolution near the injection chamber is decreased, obviously because it is concerned by less flow.

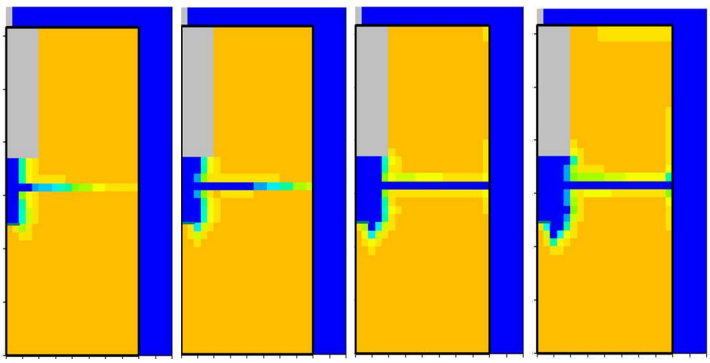

Fig. 10: Modelling of the channeling effect: calcite concentration in the sample after 2 days, 5 days, 10 days and 15 days.
Dark blue = Fully dissolved, Orange colore= No dissolution.

5.3.4. Reactive transport taking into account the cement

For this simulation, the cement is taken into account assuming a 100% Portlandite composition. The calculated pH of the initial equilibrated solution in the portlandite is 11.37. In order to speed up the calculations, the dissolution kinetic of the minerals has been neglected which is acceptable as it has been verified in preliminary simulations.

The portlandite dissolution calculated after 10 days and 20 days is displayed in Fig. 11. The calcite concentration calculated in the sample with reaction with the cement is quite similar to the simulation results considering only calcite. However it appears that, as was expected, there is calcite precipitation near the border of the zone where portlandite was present.

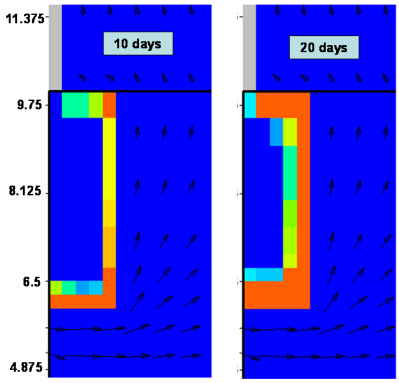

Fig. 11. Portlandite dissolution in the sample calculated after 10 days (left) and 20 days (right).
Dark blue = No dissolution, Red = Fully dissolved (21.96 mol/L of sample).

6. Conclusion and perspective

The MIRAGES2 experiment is designed to perform the injection of CO_2-rich solutions under the geological conditions of a combined "geothermal heat recovery/CO_2 sequestration" site. This 1/20th scale model of an injection is used to perform experiments under realistic conditions of injection and gives important information on i) the evolution of the reservoir, in terms of petro-physical properties, ii) the reactivity of the well materials, Portland cement and steel, submitted to an aggressive fluid, and iii) the evolution of the cement/rock interface which could be a source of leakage in case of weakness. The experiments performed at 60°C and 120 bar, with CO_2 aqueous concentration up to 0.93 mol.kg$_w^{-1}$, have shown that i) the main dissolution process in the limestone reservoir is wormholing, ii) the carbonation of the Portland cement does not seem to damage the physico-chemical properties of the cement, iii) despite a strong dissolution of the reservoir, the cement/rock interface remains cohesive all along the duration of the experiments. However, the interface between rock and cement has to be studied on longer periods since secondary dissolution of carbonated cement can occur at this interface implying a possible weakness.

The MIRAGES2 laboratory experiments have been modelled with the MARTHE-PHREEQC code [21] from BRGM. The numerical simulations reproduce reasonably well the experimental observations. This validates the use of the MARTHE-PHREEQC code for this experiment modelling to contribute in the prediction of the long term effects of the injection of a CO_2-rich aqueous solution in a limestone aquifer.

Acknowledgements

This study was financially supported by the French National Research Agency (ANR CO2-DISSOLVED-12-SEED-0009).

References

[1] D'Aprile A. Advances and slowdowns in Carbon Capture and Storage technology development. ICCG Reflection No. 48, May 2016
[2] Basava-Reddi L. IEAGHG, "Geothermal Energy and CO2 Storage", 2010/TR3, August, 2010
[3] Kervévan C, Bugarel F, Galiègue X, Le Gallo Y, May F, O'Neil K, Sterpenich J. -CO2-DISSOLVED- A Novel Approach to Combining CCS and Geothermal Heat Recovery. Ed In: EAGE, Sustainable Earth Sciences, Technologies for Sustainable Use of the Deep Sub-surface, Pau, France,.30 Sept.- 4 Oct. 2013.

[4] Kervévan C, Beddelem M. H, and O'Neil K. -CO 2-DISSOLVED- A novel concept coupling geological storage of dissolved CO2 and geothermal heat recovery. Part 1: Assessment of the integration of an innovative low-cost, water-based CO2 capture technology. Energy Procedia 63; 2014. p. 4508–4518.
[5] Fredd CN, Fogler HS. Influence of transport and reaction on wormhole formation in porous media. AIChE J. 44 (9); 1998. p. 1933–1949.
[6] Luquot L, Gouze P. Experimental determination of porosity and permeability changes induced by injection of CO2 into carbonate rocks. Chem Geol 265; 2009. p. 148–59.
[7] Noiriel C, Luquot L, Madé B, Raimbault L, Gouze Ph, Van der Lee J. Changes in reactive surface area during limestone dissolution: an experimental and modelling study. Chem. Geol. 265 (1–2); 2009. p. 160–170.
[8] Smith MM, Sholokhova Y, Hao Y, Carroll SA. CO2-induced dissolution of low permeability carbonates. Part I: Characterization and experiments. Advances in Water Resources 62, Part C; 2013. p 370–387.
[9] Gharbi O, Bijeljic B, Boek E, Blunt MJ. Changes in pore structure and connectivity induced by CO2 injection in carbonates: a combined pore-scale approach. Energy Procedia 37; 2013. p. 5367–5378
[10] Ott H and Oedai S. Wormhole formation and compact dissolution in single- and two-phase CO2-brine injections. Geophys. Res. Lett., 42; 2015.p. 2270–2276.
[11] Rosenbauer RJ, Koksalan T, Palandri JL. Experimental investigation of CO2–brine–rock interactions at elevated temperature and pressure: Implications for CO2 sequestration in deep-saline aquifers. Fuel Processing Technology 86; 2005. p. 1581–1597.
[12] Noiriel C, Bernard D, Gouze Ph., Thibaut X. Hydraulic properties and microgeometry evolution in the course of limestone dissolution by CO2-enriched water. Oil Gas Sci. Technol. 60 (1); 2005. p. 177–192.
[13] Le Guen Y, Renard F, Hellmann R, Brosse E, Collombet M, Tisserand D, Gratier J-P. Enhanced deformation of limestone and sandstone in the presence of high Pco2 fluids. Journal of geophysical research 112; 2007. 21pp.
[14] Grgic D. Influence of CO2 on the long-term chemomechanical behavior of an oolitic limestone. Journal of geophysical research 116; 2011. 22 pp.
[15] Kutchko BG, Strazisar BR, Lowry GV, Thaulow N. Degradation of Well Cement by CO2 under Geologic Sequestration Conditions. Environ. Sci. Technol. 41; 2007. p. 4787–4792.
[16] Carey JW, Svec R, Grigg Reid, Zhang Jinsuo, Crow W. Experimental investigation of wellbore integrity and CO2-brine flow along the casing-cement microannulus. International Journal of Greenhouse Gas Control 4; 2009. p. 272–282.
[17] Carey JW. Geochemistry of Wellbore Integrity in CO2 Sequestration: Portland Cement-Steel-Brine-CO2 Interactions. Mineralogy and Geochemistry 77; 2013. p. 505–539.
[18] Carroll S, Carey JW, Dzombak D, Huerta N, Li L, Richard T, Um W, Walsh S, Zhang L. Review: Role of chemistry, mechanics, and transport on well integrity in CO2 storage environments. International Journal of Greenhouse Gas Control 49; 2016. p. 149–160.
[19] Randi A, Sterpenich J, Morlot C, Pironon J, Kervévan C, Beddelem MH, Fléhoc C. CO2-DISSOLVED: a Novel Concept Coupling Geological Storage of Dissolved CO2 and Geothermal Heat Recovery - Part 3: Design of the MIRAGES-2 Experimental Device Dedicated to the Study of the Geochemical Water-Rock Interactions Triggered by CO2 Laden Brine Injection. Energy Procedia 63; 2014. p. 4536–4547.
[20] Thiéry, D. – Modélisation 3D du Transport Réactif avec le code de calcul MARTHE v7.5 couplé aux modules géochimiques de PHREEQC. Rapport BRGM/RP-65010-FR ; 2015. 164 p., 88 fig.
[21] Thiéry, D. – Code de calcul MARTHE - Modélisation 3D des écoulements dans les hydrosystèmes - Notice d'utilisation de la version 7.5. Rapport BRGM/RP-64554-FR; 2015. 306 p., 150 fig.
[22] Parkhurst, D.L. and Appelo C.A.J. - Description of Input and Examples for PHREEQC Version 3 - A Computer Program for Speciation, Batch-Reaction, One-Dimensional Transport, and Inverse Geochemical Calculations. U.S. Department of the Interior, U.S. Geological Survey Techniques and Methods 6–A43; 2013.
[23] Parkhurst D.L. and Wissmeier L. - PhreeqcRM: A reaction module for transport simulators based on the geochemical model PHREEQC. Advances in Water Resources 83; 2015. p 176 189.
[24] Vidal-Gilbert S, Nauroy J-F, Brosse E. 3D geomechanical modelling for CO2 geologic storage in the Dogger carbonates of the Paris Basin. International Journal of Greenhouse Gas Control (3); 2009. p. 288–-299.
[25] Brosse E, Badinier G, Blanchard F, Caspard E, Collin PY, Delmas J, Dezayes C, Dreux R, Dufournet A, Durst P, Fillacier S, Garcia D, Grataloup S, Hanot F, Hasanov V, Houel P, Kervévan C, Lansiart M, Lescanne M, Menjoz A, Monnet M, Mougin P, Nedelec B, Poutrel A, Rachez X, Renoux P, Rigollet C, Ruffier-Meray V, Saysset S, Thinon I, Thoraval A, Vidal-Gilbert S. 2010. Selection and Characterization of Geological Sites able to Host a Pilot-Scale CO2 Storage in the Paris Basin (GéoCarbone-PICOREF). Oil & Gas Science and Technology – Rev. IFP, Vol. 65, No. 3; 2010. p. 375–403.
[26] Hoefner M.L, Fogler HS. Pore evolution and channel formation during flow and reaction in porous media. AIChE J. 34 (1); 1988. p. 45–54.
[27] Detwiler RL, Glass RJ, Bourcier WL. Experimental observations of fracture dissolution: The role of Péclet number on evolving aperture variability. Geophysical Research Letters vol 30 n°12 1648; 2003. p. 50-1–50-4.
[28] ElkhouryJE, Ameli P, Detwiler RL. Dissolution and deformation in fractured carbonates caused by flow of CO2-rich brine under reservoir conditions. International Journal of Greenhouse Gas Control 16S; 2013. p. S203–S215.
[29] Izgec O, Zhu D, Hill AD. Numerical and experimental investigation of acid wormholing during acidization of vuggy carbonate rocks. Journal of Petroleum Science and Engineering 74; 2010.p 51–66.
[30] Pokrovsky OS, Golubev SV, Schott J, Castillo A. Calcite, dolomite and magnesite dissolution kinetics in aqueous solutions at acid to circumneutral pH, 25 to 150 °C and 1 to 55 atm pCO2: New constraints on CO2 sequestration in sedimentary basins. Chemical Geology 265; 2009. p 20–32.
[31] Holford ICR and Mattingly GEG. Surface areas of calcium carbonate in soils. Geoderma 13; 1975. p 247--255
[32] Golfier F, Zracone C, Bazin B, Lenormand R, Lasseux D, Quintard M. On the ability of a Dracy scale model to capture wormhole formation during dissolution of a porous medium. J. Fluid Mech. 457; 2002. p 213–254.

RESUME

Les travaux réalisés s'inscrivent dans le cadre de l'étude de faisabilité d'un concept hybride couplant l'exploitation d'énergie géothermique et le stockage géologique de CO_2 sous forme dissoute. Ils visent à i) quantifier et simuler l'impact hydrodynamique et géochimique de l'injection dans une roche carbonatée de la solution enrichie en CO_2 et ii) déterminer le comportement des matériaux constituant le puits d'injection (ciment, casing acier) afin de s'assurer de la sécurisation de l'injection.

Le développement d'un dispositif expérimental innovant appelé MIRAGES-2 a permis de reproduire à l'échelle du laboratoire l'injection "radiale" d'une solution saturée en CO_2 dans un puits miniature scellé dans un échantillon de roche dans les conditions de pression et de température attendues dans le réservoir géothermique. Ce banc est composé d'un dispositif amont de solubilisation du CO_2 dans l'eau de formation et d'un dispositif aval simulant l'injection dans le modèle réduit de puits. En plus des contrôles éprouvés de la pression et de la température, des outils originaux (sonde Raman HP/HT, sonde pH HP/HT, débitmètre) permettant l'acquisition *in situ* de données physico-chimiques au cours des expériences (concentrations des différentes espèces en solution, pH, débit) ont été intégrés et validés. Enfin, une méthode de traitement d'images acquises sur les échantillons post-expérimentaux par la technique de micro-tomographie aux rayons X a permis une reconstruction 3D de l'architecture du réseau poreux mesoscopiques. Ce protocole expérimental a alors permis le suivi de l'évolution physico-chimique :

- des différentes interfaces ciment/acier, ciment/réservoir,
- de la région proche-puits du réservoir,
- du fluide injecté.

Une série de 7 expériences a été réalisée afin d'étudier les effets des durées d'injection (12h, 24h, 2.5j, 10j, 21j), de la salinité de la solution injectée et de l'orientation du puits d'injection par rapport à la stratification de la roche.

Les expériences ont permis de montrer le développement et la propagation, à partir du point d'injection, d'une dissolution non-uniforme de la roche carbonatée sous forme de chemins préférentiels appelés « wormholes » et dont la densité tend à décroître globalement après le perçage de la carotte. Malgré la prédominance de ce phénomène localisé, une évolution des caractéristiques pétrophysiques de la roche dans des régions éloignées des wormholes a été observée. Suite au renouvèlement continu de la solution acidifiée, une dissolution uniforme en partie haute de puits a été mise en évidence. L'analyse de la rugosité de surface des wormholes couplée à des observations microscopiques a montré la présence de précipitations de calcite qui conduisent à la fermeture de wormholes secondaires.

L’étude du vieillissement du ciment au contact de la solution réactive montre qu’il est à l’origine de déséquilibres chimiques localisés. Les valeurs de concentration en magnésium, inhibiteur de la précipitation de la calcite et principalement liées à l’altération du ciment gouvernent les états locaux de saturation de la solution interstitielle vis-à-vis de la calcite. Elles seraient donc à l’origine des précipitations observées dans un milieu pourtant principalement sous-saturé vis-à-vis de la calcite.

Les expériences ont également démontré le rôle important de la salinité de la solution injectée qui permet de dissoudre jusqu’à cinq fois plus la roche encaissante qu’une solution d’eau douce.

Enfin, une étude structurale multi-échelle a été menée et a établi la relation étroite entre la distribution des défauts structuraux générés par la tectonique régionale et l’orientation des réseaux de dissolution observés dans nos expériences. Ces résultats affinent l’analyse et l’évaluation des impacts et des risques environnementaux dans le contexte du projet étudié. Ils permettent de définir le rôle des discontinuités présentes dans la roche et leur contrôle sur les chemins de dissolution à l’échelle du réservoir.

Mots-clefs : modélisation expérimentale, stockage de CO_2, région proche puits, aquifère salin, CO_2 dissous, interface ciment-roche, MIRAGES-2, géothermie, micro-tomographie à rayons-X

ABSTRACT

This work was conducted in the framework of the technical assessment of a novel Carbon Capture and Storage (CCS) concept integrating aqueous dissolution of CO_2 and injection via a geothermal doublet. This study focuses on i) the quantification and modelling of the hydrodynamic and geochemical impact induced by the injection of a CO_2-laden solution in a reservoir rock and ii) the evaluation of long term integrity of the well materials (cement, steel casing) in order to ensure a safe injection protocol.

A dedicated experimental device named MIRAGES.2 was developed to mimic, at the lab scale, the continuous radial injection of a CO_2-enriched solution under realistic conditions of a geological reservoir. The miniature well consists in a steel tube that is cemented to the core plug with a class G Portland cement. The test bench is divided in two parts: the first one is devoted to the CO_2-solution mixing process, and the second one enables to perform the injection of the solution in the core-plug. In addition, the implementation of original in situ measurement techniques (in-situ HP/HT Raman and pH probes, flowmeter) was carried out in order to ensure optimal acquisition of physical and chemical data (pressure, temperature, pH, concentrations of different species in solution...) during the experiments. A method of image processing acquired on post-experimental samples by X-ray micro-tomography has been developed. This technique revealed the 3D architecture of the mesoscopic porous network. This experimental protocol revealed the physicochemical evolution of:

- the different interfaces between cement and steel, and between cement and reservoir,
- the near-well region of the reservoir,
- The injected fluid.

A set of 7 experiments was performed. The injection duration (12 h, 24 h, 2.5 d, 10 d and 21 d), the fluid salinity and the core drilling inclination with respect to the bedding were investigated.

The experiments demonstrate the non-uniform propagation of the acidic solution from the injection point in the form of preferential pathways called « wormholes ». Once a single wormhole breaks through the core-plug, all the other competing wormholes stop growing and their density tend to decrease as the solution is injected. Despite a predominant localized phenomenon, changes in petrophysical properties of the rock in regions far from the wormholes was observed. Following the continuous renewal of the acidic solution, a uniform dissolution in the upper part of the injection well was also highlighted. Roughness surface measurements coupled with microscopic observations have revealed the presence of calcite precipitation which induces the clogging of secondary wormholes.

Cement ageing in contact with the reactive solution induces localized chemical imbalances. Changes in magnesium concentration, inhibitor of calcite precipitation, released during cement alteration, govern the local calcite saturation states of the interstitial solution. These phenomena could explain the observed precipitation in a medium mainly undersaturated with respect to the calcite.

The experiments also demonstrated the important role of the salinity of the injected solution, which dissolves up to five times more host rock than a freshwater solution.

Finally, a multi-scale structural study was carried out and established the close relationship between the distribution of structural defects generated by regional tectonics and the orientation of the dissolution networks observed in our experiments. These results refine the analysis and assessment of environmental impacts and risks in the context of the CO_2 injection in a geothermal doublet. They demonstrate the discontinuities present in the rock control the dissolution paths at the reservoir scale.

Key-words: experimental modeling, CO2 storage, near well region, saline aquifer, dissolved CO_2, rock-cement interface, MIRAGES-2, geothermal energy, X-ray micro-tomography